Exploring excimeric interactions in mono- and dinuclear cyclometallated platinum(II) complexes for deep-red/near-infrared emission

REBECCA JANE SALTHOUSE

Exploring excimeric interactions in mono- and dinuclear cyclometallated platinum(II) complexes for deep-red/near-infrared emission

Rebecca Salthouse

A thesis submitted for the degree of Doctor of Philosophy

Department of Chemistry

September 2022

Abstract

The work described in this thesis is concerned with the development of new molecular materials that emit deep-red or near-infrared (NIR) light upon excitation. Molecules that emit efficiently in these regions of the electromagnetic spectrum are important in a variety of security, technological, and biological applications. The focus is on platinum-containing molecules, the key role of the metal being to enhance spin-orbit coupling and thus facilitate the formally forbidden emission from triplet states that is necessary to produce efficient devices. A range of platinum(II) complexes with cyclometallating ligands have been synthesised and their photophysical properties studied. The luminescence both from isolated molecules and from species comprised of two or more molecules has been evaluated, with the aim of establishing reliable strategies for tuning the emission further into the NIR.

Chapter 2 describes complexes featuring symmetric, tridentate N^C^N-coordinating ligands and one monodentate ligand, X. Organic light-emitting diodes (OLEDs) fabricated using some of these complexes as the emissive layer display NIR electroluminescence through the formation of aggregates. The identity of X is found to influence the aggregation: the change from X = Cl to I is accompanied by a 4-fold increase in the external quantum efficiency (EQE) of the device, whilst X = SCN red-shifts the emission to λ_{EL}^{max} = 940 nm, apparently the longest-wavelength emission reported to date for a device employing a non-porphyrinic platinum(II) complex.

The work of Chapter 3 introduces related complexes featuring asymmetrically-substituted N^C^N ligands: it establishes that the wavelength of the unimolecular emission tends to follow that of the corresponding parent symmetric complex of lowest excited-state energy. Complexes of ligands that incorporate 3-substituted isoquinoline are found to have a particularly high propensity to excimer formation, whilst 4-trifluoromethylpyridine ligands lead to a red shift in the emission, both unimolecular and excimer/aggregate.

Chapters 4 and 5 focus on the strategy of covalently linking two complexes through a rigid xanthene scaffold, with a view to facilitating their face-to-face interaction. Complexes with tridentate and bidentate ligands are discussed in the two chapters, respectively. They mostly display broad, long-wavelength emission at all concentrations in solution, likely arising from intramolecular excimers, with impressive quantum yields ranging from 0.11 to 0.61. The interactions are further favoured using a second xanthene to generate “molecular squares” which display purely excimeric emission.

Finally, in Chapter 5, a series of novel dinuclear platinum compounds is presented that feature bidentate N^C-coordinating ligands. The emission wavelengths are influenced both by structural modifications of the N^C moiety and by intramolecular excimeric interactions, the most red-shifted of which has λ_{PL}^{max} of 777 nm.

Declaration

The research described herein was undertaken at the Department of Chemistry at Durham University between October 2018 and December 2021. All of the work is my own, except where specifically stated otherwise. No part of it has previously been submitted for a degree at this or any other university.

Statement of copyright

Acknowledgements

I have had the best experience over the last few years doing my PhD, despite the Covid-19 pandemic. This would not have been possible without the funding bodies that have supported me during my studies; thank you to the EPSRC and Durham University. The biggest thank you must go to my supervisor Professor Gareth Williams for his invaluable experience and support, and for giving me the opportunity the undertake this project. I am especially thankful for his understanding through some tough personal circumstances. I could not have completed this project without you!

I am extremely grateful to have been a part of the JAGW lab, where no day felt like a workday as we had so much fun together. In particular, thank you to Chris, Yana and Amit for sharing most of my PhD journey with me and being my best friends. Chris has been with me since the beginning of my PhD, my fumehood neighbour, and the first person I taught in the group. It paid off because now he teaches me many things so thank you for being so intelligent. Thanks for putting up with my attempts at a Northern Irish accent (and rrr) and TMI. (P.S sorry for the hexane grease situation, you were right.) I miss annoying Amit and vice versa, though I am sure this will continue, and you will always be my BFI. Thank you for all your synthesis wisdom and your friendship. Yana, I always enjoyed our drives home together and sticking up for each other against the boys. Thanks for also being my conference roommate, we have to be friends for life now (not temporary besties), you know too much! I hope we can all always be friends and I will always be your Mother Becky.

I would also like to thank David and Mel for being the first ones to show me the ropes in the lab. Without my incredible MChem experience I may not have decided to undertake this PhD. A big thank you also to Piotr Pander in the Physics Department for all his hard work making the OLED devices, even sometimes with only a few mg of compound! Thank you to everyone in the department including all the service staff for their amazing work, particularly Dmitry Yufit for solving all the crystal structures, and Juan Aguilar for collecting the NMR spectra of my extremely insoluble complexes. Thanks also to all the friendly faces around the department, Gary at solvents, Annette at stores, Clare, and particularly Ivan at tea-time. Thanks also to my postdoc supervisor Professor Martin Bryce.

Thanks, and love, to all my friends in Durham, past and present, not least Jamie, Yazmin, Aisha, Jaime, Exe, Brad, Rayan, and Zoe (particularly for listening to my chemistry rants as a non-chemist flatmate), and to CG104+. Thanks also to all my ‘home’ friends for not understanding anything I do but supporting me anyway.

Finally, I would like to thank my family for all the love and support (financially and emotionally). Mum, Dad and Dan, you’re the best, I’m so lucky to have you. Thank you so much for everything you do for me. Grandad, I hope you would be proud.

Ah sí, y gracias a mi novio Rigo por todo. Te amo mucho.

Abbreviations

acac	Acetylacetone
ASAP	Atmospheric solids analysis probe
B_2pin_2	Bis(pinacolato)diboron
bpy	2,2'-Bipyridine
bzim	Benzimidazole
bzox	Benzoxazole
bzoxb	Bis(benzoxazolyl)benzene
bzth	Benzothiazole
COD	1,5-Cyclo-octadiene
COSY	Correlation spectroscopy
Cp	Cyclopentadiene
CT	Charge transfer
DCM	Dichloromethane
DFT	Density functional theory
DME	Dimethyoxyethane
DMF	Dimethylformamide
dpm	Dipivaloylmethane
dppf	1,1'-Bis(diphenylphosphino)ferrocene
dpybH	1,3-Di(2-pyridyl)benzene
EDG	Electron-donating group
EL	Electroluminescence
EML	Emissive layer
E^{ox}	Oxidation potential
EQE	External quantum efficiency
EWG	Electron-withdrawing group
FPT	Freeze-pump-thaw
HAT-CN	1,4,5,8,9,11- Hexaazatriphenylenehexacarbonitrile
HMBC	Heteronuclear multiple-bond correlation spectroscopy

HOMO	Highest occupied molecular orbital
HRMS	High resolution mass spectrometry
HSQC	Heteronuclear single-quantum correlation spectroscopy
IC	Internal conversion
ILCT	Intra-ligand charge transfer
ISC	Intersystem crossing
ITO	Indium tin oxide
k_{nr}	Non-radiative rate constant
k_{obs}	Observed rate constant
k_r	Radiative rate constant
k_{SQ}	Self-quenching rate constant
LC	Ligand centred
LCD	Liquid crystal display
LMCT	Ligand-to-metal charge-transfer
LUMO	Lowest unoccupied molecular orbital
MC	Metal centred
MLCT	Metal-to-ligand charge-transfer
MMLCT	Metal-metal to ligand charge-transfer
MO	Molecular orbital
NIR	Near-infrared
NMR	Nuclear magnetic resonance
NOESY	Nuclear overhauser effect spectroscopy
OLED	Organic light emitting diode
PES	Potential energy surface
phbpy	6-Phenyl-2,2'-bipyridine
PL	Photoluminescence
PLQY	Photoluminescence quantum yield
PO-T2T	2,4,6-Tris[3-(diphenylphosphinyl)phenyl]-1,3,5-triazine
ppy	Phenylpyridine

PtOEP	Platinum(II) octaethylporphyrin
PVK	Poly(*N*-vinylcarbazole)
RT	Room temperature
S_0	Singlet ground state
sh	Shoulder
S_n	n^{th} singlet excited state
SOC	Spin orbit coupling
TCSPC	Time-correlated single photon counting
TD-DFT	Time-dependent density functional theory
thpy	2-(2-thienyl)pyridine
TLC	Thin layer chromatography
T_n	n^{th} triplet excited state
TSBPA	4,4'-(Diphenylsilanediyl)bis(N,N-diphenylaniline)
TTA	Triplet-triplet annihilation
WOLED	White organic light emitting diode
λ_{abs}	Absorption wavelength
λ_{EL}	Electroluminescence wavelength
λ_{em}	Emission wavelength
λ_{max}	Wavelength maximum
τ_0	Lifetime at infinite dilution
τ_{aer}	Lifetime in air-equilibrated solution
τ_{deg}	Lifetime in degassed solution
Φ	Quantum yield

Table of contents

Chapter 1

1. Introduction

Square-planar platinum(II) complexes containing N^C^N-coordinating ligands, generally based on 1,3-di(2-pyridyl)benzene (dpybH), are often brightly luminescent, emitting from triplet states with high efficiency. They have attracted growing attention over the past two decades due to their high phosphorescence quantum yields and their ability to display interfacial interactions. Such face-to-face interactions lead to excimer or aggregate emission that is almost unique to d^8 square-planar complexes over other luminescent metal complexes such as those of pseudo-octahedral iridium(III).[1] Efficient spin orbit coupling (SOC) of heavy metals such as platinum facilitates fast intersystem crossing (ISC) to the triplet excited state and subsequent relaxation of the spin selection rule; hence $T_1 \rightarrow S_0$ phosphorescence is promoted in these complexes leading to high phosphorescence quantum yields under ambient conditions and relatively short triplet lifetimes (τ) of a few μs.[2]

Potential applications of these luminescent transition metal complexes are numerous; they include dopants in organic light emitting devices (OLEDs)[3–6], chemosensors[7–10], photocatalysts[11,12], and as time-resolved bioimaging agents.[13–16] An attractive property of cyclometallated complexes is the ability to tune the excited state energy[4,17,18], and hence emission colour, through the introduction of electron-donating and/or -withdrawing substituents in aryl or heterocyclic rings. This strategy is being exploited in the preparation of white OLEDs (WOLEDs)[19–21] for the next generation of solid-state lighting, and near-infrared (NIR) OLEDs,[22–25] which are currently highly desired for a range of new technologies in medicine[16,26–29], communications[30] and security.[31–33]

This thesis presents the design, synthesis and photophysical properties of a range of Pt(II) complexes featuring bi- and tridentate ligands with an aim of achieving emission in the NIR region of the electromagnetic spectrum. This chapter offers a general introduction to some of the key principles and archetypal complexes in the field. Each of the subsequent chapters that describe the results of experimental work will begin with a focused review of the literature that is most relevant to the research presented in that chapter.

1.1 Luminescence

The term photoluminescence (PL) refers to the emission of light that occurs after excitation of an atom or molecule following absorption of electromagnetic radiation in the UV, visible, or NIR regions. Photoluminescence can be broadly divided into two categories: fluorescence and phosphorescence. Fluorescence is the emission of light from an excited state of the same spin multiplicity as the ground state, usually singlet. ISC to a triplet excited state may occur after excitation to a singlet excited state, or there may be some direct excitation to the triplet manifold, albeit with low probability. Either way, the resulting relaxation of the molecule from a triplet state through a radiative transition is known as phosphorescence (**Figure 1.1**).

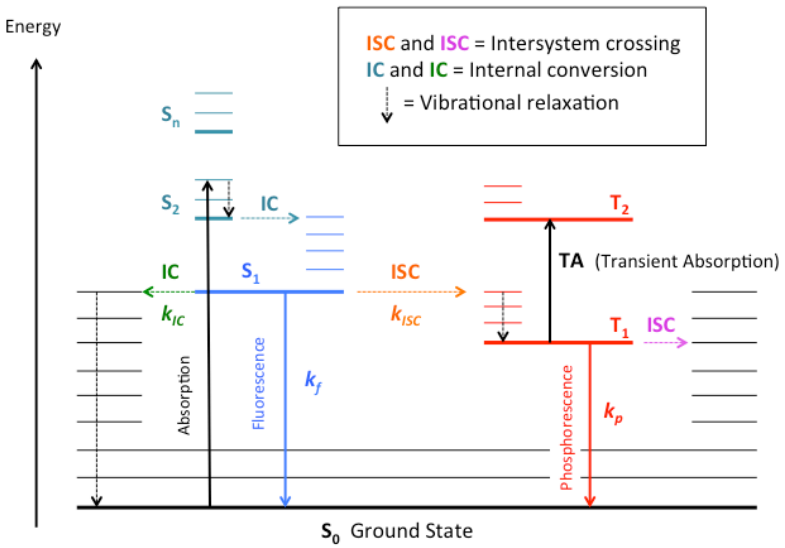

Figure 1.1: *A generalised Jablonski diagram illustrating possible electronic transitions.*

Phosphorescence is formally a spin-forbidden process; the rate of phosphorescence is slower than fluorescence. Heavy metals, such as Pt, with high SOC constants, can relax the spin-selection rule and thus promote phosphorescence. Both fluorescence and phosphorescence occur at a longer wavelength than the excitation wavelength due to vibrational relaxation prior to emission, known as the Stokes shift. Non-radiative decay pathways may compete with the radiative processes such as through intramolecular energy transfer into vibrations and subsequent dissipation of energy to the surroundings. The luminescence efficiency is measured by the quantum yield, Φ_{lum}, which is defined as the ratio of emitted photons to photons absorbed. Assuming that the excited state is formed with unit efficiency, Φ_{lum} can be expressed in terms of the relative rate constants for radiative (k_r) and non-radiative (k_{nr}) decay (**Equation 1.1**).

$$\Phi_{\mathrm{lum}} = \frac{k_{\mathrm{r}}}{k_{\mathrm{r}} + k_{\mathrm{nr}}} \tag{1.1}$$

In organometallic compounds, the emissive state, which is usually the lowest energy excited state following Kasha's rule, can generally be described as one of four types of state depending on the character of the molecular orbitals involved in the transition (**Figure 1.2**): metal centred (MC) d-d state, metal-to-ligand charge transfer

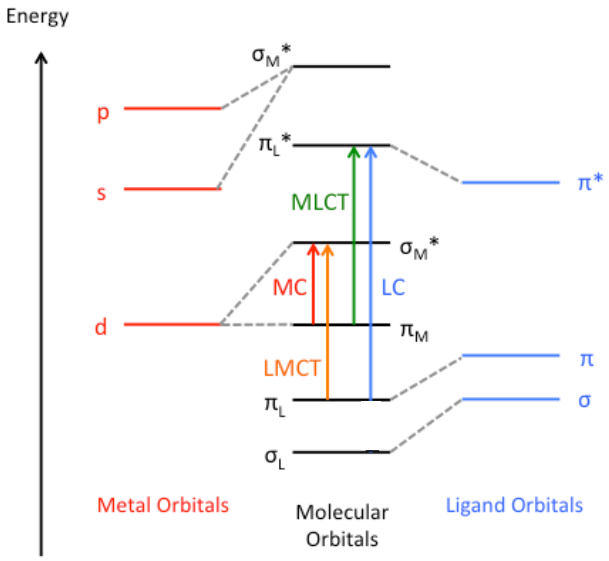

Figure 1.2: *Simplified molecular orbital (MO) diagram for a generic transition metal complex showing the various excited states and transitions possible.*

(MLCT), ligand-to-metal charge transfer (LMCT) and ligand-centred π-π* (LC).[16] Such assignments are, however, an over simplification, particularly in cyclometallated complexes which feature a high degree of covalency. Orbitals can possess significant contributions from both the metal and the ligand, giving rise to transitions of mixed character; the emissive state of many Pt(II) complexes is of mixed MLCT and LC character.

To achieve efficient luminescence from Pt(II) complexes, the emissive state should lie low enough in energy relative to the non-emissive MC state so that the non-radiative decay pathway is not thermally accessible.[34] Low-lying MC d-d states are typically strongly distorted compared to the ground state, as their formation involves population of strongly antibonding e_g orbitals[1], for example the unoccupied $d_{x^2-y^2}$ orbital in d^8 Pt(II) complexes.[35] Utilising ligands with low-lying excited states, for example porphyrins, lowers the energy of the emissive state relative to the non-emissive MC state and hence leads to efficient luminescence.[35] Suppression of k_{nr} is also key to achieving efficient luminescence. Excited-state distortion is detrimental to emission as it provides a means of efficient non-radiative decay; the overlap of the vibrational wavefunctions of excited and ground electronic states is favoured by a large displacement of potential energy surfaces (**Figure 1.3**).[31] Therefore, designing complexes with rigid structures can help minimise k_{nr}.

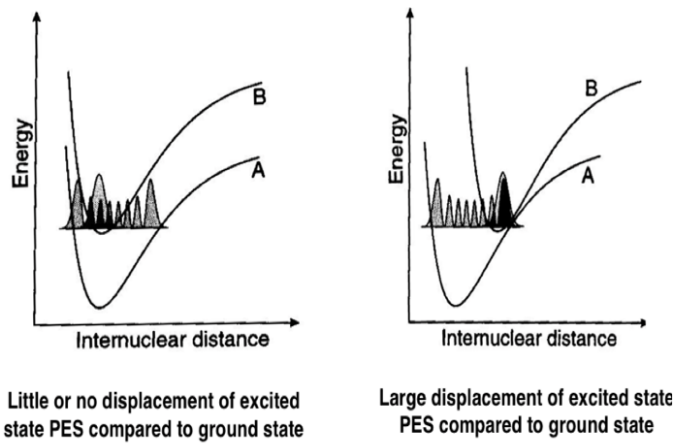

Figure 1.3: *Effect of excited-state distortion on non-radiative decay; a more distorted excited state leads to faster non-radiative decay.*

1.2 Cyclometallation

Another approach to achieve efficient luminescence and reduce non-radiative decay is to introduce strong field cyclometallating ligands to raise the energy of the MC state.[35–37] Cyclometallated complexes contain metal-carbon bonds and are often particularly stable with respect to metal-ion dissociation.[31] These complexes are formally organometallic compounds; however, they possess the character of coordination complexes. The synergistic combination of a strongly σ-donating metalated aryl ring and π-accepting heterocyclic rings helps minimise non-radiative decay processes by raising the energy of the d-d state, diminishing its deactivating effect and providing stability to such a complex (**Figure 1.4**).[36] The favourable formation of 5-membered chelating rings adds to the stability of these complexes through the chelate effect.

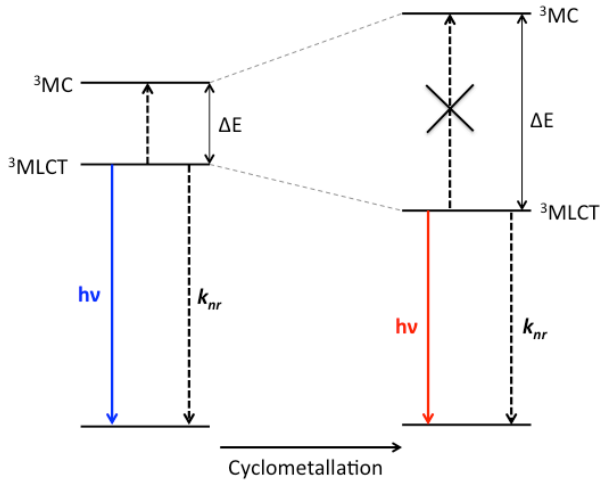

Figure 1.4: *Illustration of the influence of cyclometallation on the energies of MLCT and MC states (adapted from ref. 1).*

In order to generate efficient triplet emission with a high radiative rate constant, the excited state of the emitting complex should normally have significant MLCT character.[31] Metal character is necessary for efficient SOC, partly in order to promote ISC, but particularly to allow the formally forbidden triplet-to-singlet emission to occur. Complexes incorporating cyclometallating ligands typically provide more participation from the metal, hence more efficient SOC and larger k_r values.

Introducing conjugated ligands with π-accepting pyridyls in conjunction with oxidisable metals also serves to lower the energy of MLCT states.[1]

Cyclometallation thus often leads to emission at longer wavelengths, compared to analogous non-cyclometallated complexes, as the emissive MLCT state is lower in energy. The fact that cyclometallated complexes often have higher quantum yields, due to the inhibition of non-radiative decay as the energy gap to the non-emissive MC state increases, contradicts what is expected on the basis of the "energy-gap law" where quantum yields and lifetimes tend to decrease as the emission energy decreases due to more efficient non-radiative decay over smaller energy gaps.[38] However, this usually only applies for blue- and green-emitting complexes. For those that emit at long wavelengths (e.g. in the orange and red region) the gap to the MC state is usually sufficiently large that it is insignificant as a non-radiative pathway.

1.3 Pt(II) complexes featuring tridentate N^C^N ligands

Prior to a study by Williams *et al.* in 2003, there were relatively few examples of charge-neutral phosphorescent Pt(II) complexes possessing tridentate ligands.[36] The most widely studied complexes incorporated N^N^C-coordinating 6-phenyl-2,2'-bipyridine (phbpy)[39–41] (**2**) and the only reported N^C^N complex was Pt(dpyb)Cl (**1**), where dpyb is 1,3-di(2-pyridyl)benzene, in 1999 from a synthetic viewpoint only (**Figure 1.5**).[42] Since then, a plethora of N^C^N-coordinating Pt(II) complexes have been studied and recognised for their excellent photophysical properties and scope to tune emission colour through simple structural modifications of each constituent moiety of the tridentate ligand.[19]

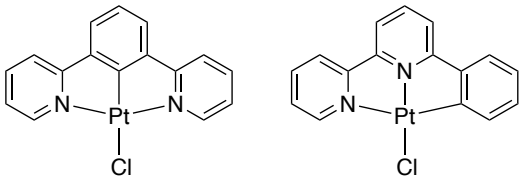

1 Pt(dpyb)Cl **2** Pt(phbpy)Cl

Figure 1.5: *Pt(II) complexes with tridentate ligands featuring N^C^N (left) and N^N^C (right) coordination.*

Rausch et al.[43] probed the excited states of Pt(dpyb)Cl and bidentate analogues through high-resolution optical spectroscopy at cryogenic temperatures and concluded that the key difference between **3** and **4** (**Figure 1.6**) was a smaller geometry change between the singlet ground state, S_0, and triplet excited state, T_1, owing to the higher rigidity of the complex with the tridentate ligand; Pt(N^C^N) complexes show greater luminescence efficiencies as a result. Furthermore, Pt(N^C^N) systems may offer higher emission colour purity than their related Pt(N^C) compounds, a desirable quality for OLED applications, as shown for **3** which is a purer blue emitter compared to the bidentate analogue. The high rigidity ensures that emission is concentrated in the (0,0) band, with a lower contribution of the green-to-yellow low-energy (0,1), (0,2), and (0,3) vibrational bands.[44]

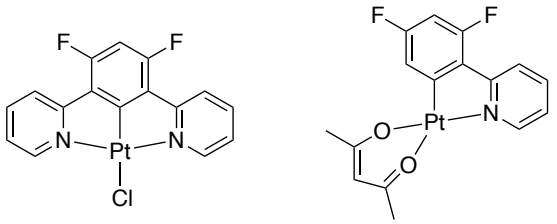

3 Pt(F_2dpyb)Cl **4** Pt(F_2ppy)(acac)

Figure 1.6: *Blue-emitting complexes featuring closely related tridentate and bidentate cyclometallating ligands. Complex **3** displays higher colour purity than **4**, as the emission is largely concentrated in the (0,0) band.*

The position of the cyclometallating phenyl ring in isomers of tridentate ligands can also lead to significant differences in their properties. Comparing N^N^C-coordinated Pt(phbpy)Cl to N^C^N-coordinated Pt(dpyb)Cl (**Figure 1.5**), it is found that the Pt–C bond in the latter is considerably shorter, leading to a stronger ligand field.[1] This serves to raise the energy of the d-d excited state even further in the N^C^N-coordinated Pt(dpyb)Cl, effectively cutting off the pathway of non-radiative deactivation.[36] Consequently, the properties of N^C^N-coordinated complexes are usually significantly superior, e.g. Φ = 0.60 and 0.03 for Pt(dpyb)Cl and Pt(phbpy)Cl respectively in deoxygenated CH_2Cl_2 at RT. Note that emission data throughout this thesis is reported in deoxygenated solution as O_2 is an efficient quencher of phosphorescence due to its triplet electronic ground state.

A theoretical analysis based on density functional theory (DFT)/time-dependent DFT (TD-DFT) highlighted that the ligand-field strength is not the only contributing factor in determining the emissive properties of Pt(II) complexes.[45] An analogous C^N^C complex Pt(C^N^C)(CNPh) (where C^N^C = 2,6-diphenylpyridyl^{2-}) was studied alongside Pt(dpby)Cl and Pt(phbpy)Cl, a fair comparison despite the different co-ligand as the excited state is usually largely localised on the C^N^C unit for Pt(C^N^C) complexes.[46] Their findings showed that despite the stronger ligand-field imposed by the two cyclometallated rings of the C^N^C unit of Pt(C^N^C)(CNPh), the complex is non-emissive. By considering both the SOC and the electronic structures of the above complexes at their respective optimised singlet ground (S_0) and first triplet (T^1_{opt}) excited states, Tong and Che were able to rationalise the experimental findings that Pt(dpyb)Cl is a stronger emitter whilst Pt(phbpy)Cl is only weakly emissive in dichloromethane (DCM) solution at room temperature and Pt(C^N^C)(CNPh) is non-emissive; the N^N^C- and C^N^C-coordinated complexes displayed Jahn-Teller and pseudo-Jahn-Teller effects for the S_0 to T^1_{opt} transition, leading to large excited-state structural distortions and hence faster non-radiative decay. Furthermore, a strong ligand field may increase the dd splitting so much so that the SOC effect is small and k_r is low.[45]

1.4 Synthesis of N^C^N-coordinating proligands based on dipyridylbenzene

The first examples of N^C^N-coordinated complexes were those of ruthenium(II) and osmium(II) developed by Sauvage and Collin in the 1990s.[1] Their approach to synthesising dpybH involved the reaction of 1,3-dicyanobenzene with potentially explosive acetylene gas under 10 atm pressure at 130°C, catalysed by Co(Cp)(COD), where Cp is cyclopentadiene and COD is 1,5-cyclo-octadiene.[47] Although the reaction proceeded in a high yield of 90%, a milder way of synthesising dpybH, which also allows for the incorporation of substituents in the pyridyl rings, is by palladium-catalysed cross-coupling reactions to form the required interannular C-C bonds.

Aryl halides or triflates undergo cross-coupling with "metalloaryl" substrates (Ar−E) such as aryl-boronic acids or esters (E' = $-B(OR)_2$, Suzuki)[48], aryl-stannanes (E = $-SnR_3$, Stille)[49] or aryl-zinc reagents (E = −ZnCl, Negishi)[50] to form aryl-aryl bonds. There are two different approaches that can be adopted to make dpybH and derivatives in this way, according to whether the "E" functionality is in the aryl or heterocyclic unit (**Scheme 1.1**).[1]

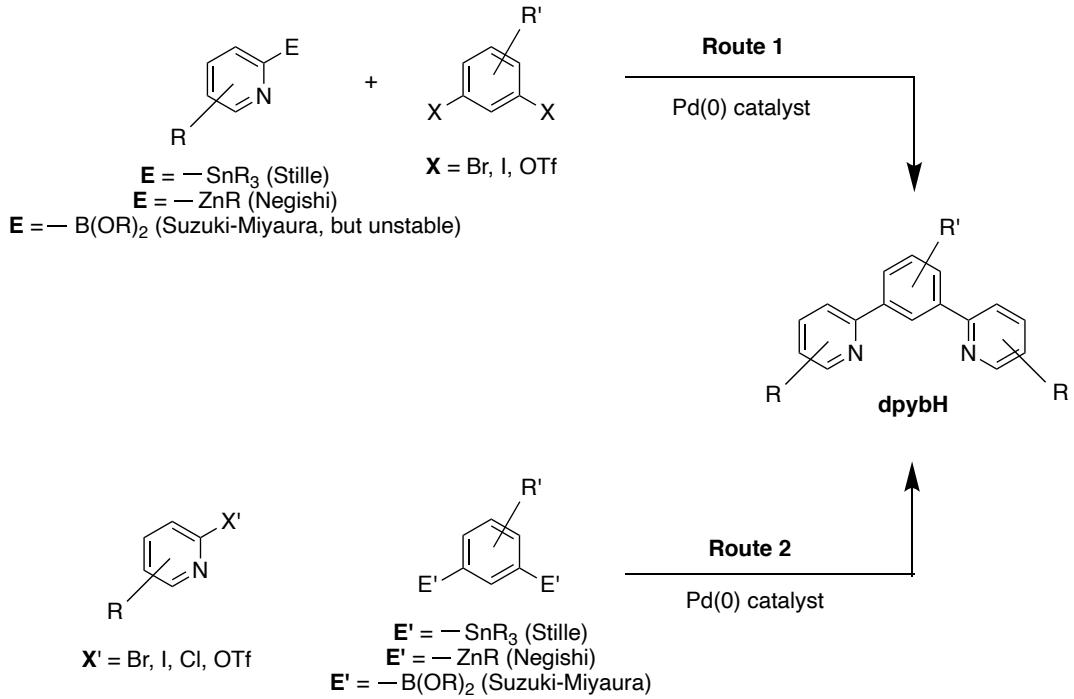

Scheme 1.1: *Generic cross-coupling reactions for the synthesis of dpybH. Route 1: 1,3-dihalogenated cores cross-coupled with a 2-pyridyl substrate with "E" functionality. Route 2: cross-coupling in the "reverse sense".*[1]

Low-cost catalysts such as $Pd(PPh_3)_4$ or $Pd(PPh_3)_2Cl_2$ can be used for these cross-coupling reactions. Suzuki cross-coupling is generally favoured over the use of stannanes due to the benign nature of the borate side-products compared to toxic organotin reagents.[1] However, unprotected pyridyl-2-boronic acids are unstable, and so if Suzuki couplings are to be used, they must be carried out using Route 2. A number of dpybH derivatives have been prepared by Williams' group and others over the last decade using sequential Suzuki and Stille chemistry to incorporate functional groups into the central aryl ring by using substituted precursors or by functional group conversion after coupling.[51,52]

The neopentylglycolate, or pinacolato esters, of 1,3-di(2-pyridyl)benzene-5-boronic acid (dpyb-B) are useful intermediates in the divergent synthesis of dpybH ligands that are functionalised with aryl groups at the 5-position of the central ring[53]. They can be easily synthesised from the corresponding halogenated compound *via* a Miyaura reaction.[48,53] This provides a potentially more versatile strategy for synthesis making use of Route 2 (**Scheme 1.2**).[52] This route has previously been utilised to prepare new complexes incorporating electron rich substituents on the central phenyl ring such as amines, phenols, oxacrown and azacrown ethers.[52]

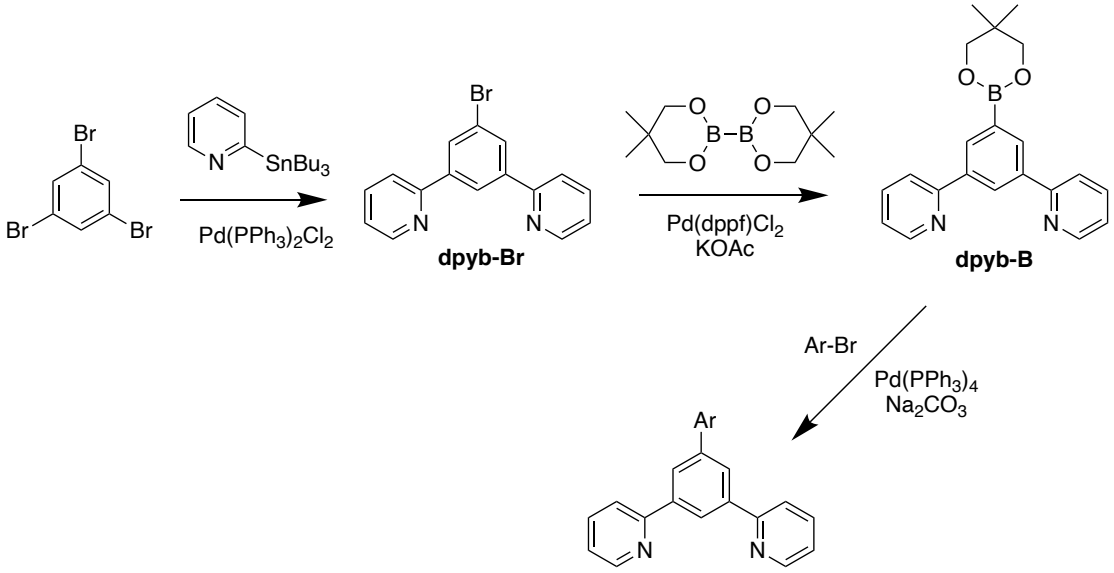

Scheme 1.2: *Synthesis of 5-substituted dpyb derivatives via dpyb-B.*[52]

1.5 Electrochemical and photophysical properties

1.5.1 Electronic spectroscopy

Pt(dpyb)Cl and derivatives have been studied in great detail. The parent complex Pt(dpyb)Cl is intensely luminescent in dilute solution: λ_{max} = 498 nm, Φ = 0.60 and τ = 7.2 μs in deoxygenated DCM.[1] The emission spectrum of Pt(dpyb)Cl is highly structured (**Figure 1.7**) with a very small Stokes shift between the highest energy emission band and the weak but distinct $S_0 \rightarrow T_1$ absorption band, implying a predominant $^3\pi$-π^* assignment for the emissive state with very little excited state distortion relative to the ground state geometry.[1] However, DFT studies demonstrate

significant d-π* (or MLCT) contribution, which accounts for the high triplet radiative rate constants through efficient SOC.[43]

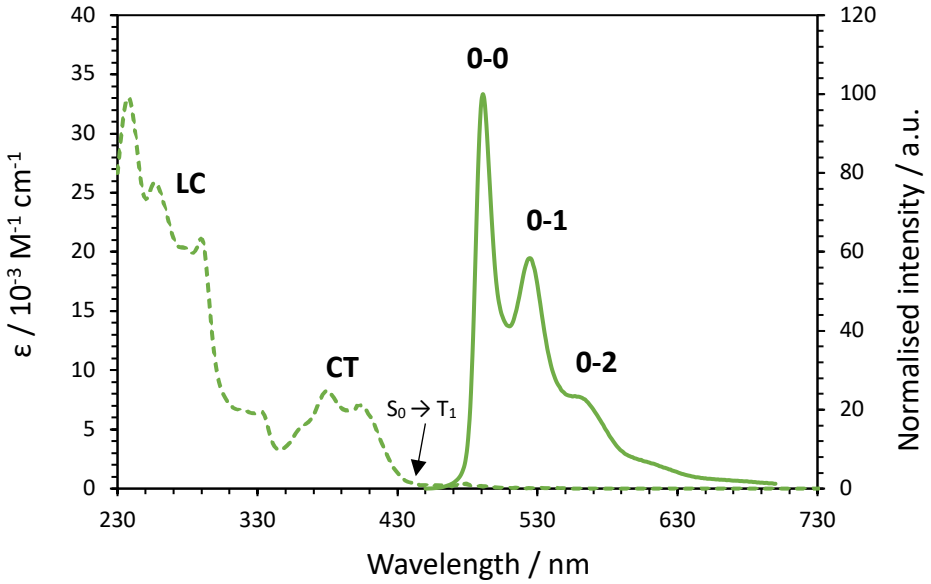

Figure 1.7: *Absorption (dashed line) and emission spectrum (solid line) of Pt(dpyb)Cl in degassed DCM solution (c = 10^{-5} M) highlighting the characteristic LC absorption bands below 300 nm, and CT bands likely involving the metal between 330 and 430 nm. The emission spectrum is highly structured due owing to the rigidity of the complex.*

For Pt(dpyb)Cl and similar complexes, the vibrational component of highest intensity in the $T_1 \rightarrow S_0$ emission is the 0-0 band owing to the rigidity of the complexes. According to the Franck-Condon principle, electronic transitions occur most favourably when the nuclear structure of the initial and final states are most similar.[54] The nuclear displacement between the ground and excited state therefore determines the shape of the emission spectrum.[55] In the case where excited state displacement is small, as for these complexes (**Figure 1.8a**), the 0-0 vibrational transition is the most probable and a highly structured emission profile is observed. On the other hand, when the displacement in the excited state is large (**Figure 1.8c**), the overlap of the ground state level with the v=0 excited state level is much smaller, and the maximum intensity will be observed for higher vibrational levels.

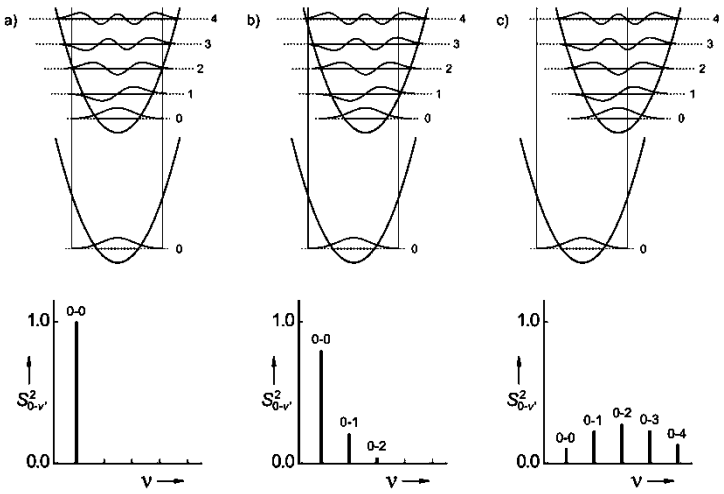

Figure 1.8: *Illustration of the quantum mechanical model for Franck-Condon overlap with increasing excited state distortion from a-c (ref. 55).*

1.5.2 Electrochemistry

Oxidation and reduction potentials, determined by cyclic voltammetry, can be beneficial in interpreting excited state energies of Pt(dpyb)Cl derivatives,[31] as some correlation may be observed between the emission energy and oxidation peak potentials.[56] The oxidation potential provides an indication of the energy of the highest occupied molecular orbital (HOMO), as an electron is removed from this MO, whilst the reduction potential reflects the energy of the lowest unoccupied molecular orbital (LUMO), where an electron is gained.[31,51] Thus, they may determine the MLCT energy. Cocchi *et al*. synthesised a number of Pt(dpyb)Cl derivatives with varying substituents at the 4-position of the central phenyl ring (C_1 = cyclometallated carbon).[57] They observed that the reduction potentials were similar for all complexes, suggesting that the LUMO is located primarily on the metal-coordinated pyridyl rings (**Figure 1.9**), as this part of the complex was unchanged between each

derivative. The oxidation potentials (E^{ox}) revealed more variation; introduction of an electron-donating methyl group decreased E^{ox} as the HOMO is destabilised, leading to easier oxidation and also an observed red shift in emission as the HOMO-LUMO gap decreases. Adding an electron-withdrawing substituent had the opposite effect, implying that the HOMO is localised on the metal-phenyl fragment.

Conversely, a study by Wang *et al.* found that addition of an electron-withdrawing fluorine group in the 4-position led to an increase in oxidation potential as expected, but also a significant decrease in reduction potential.[56] Their use of a different solvent system may be the reason for this, or it may simply highlight that the link between electrochemical and optical data must be approached with caution, as the excited state molecule is a different chemical species from the ground-state molecule.[31] The contrasting inductive withdrawal of F and resonance donation may also play a role. Moreover, the position of the substituent as well as its nature is important; substituents influence the HOMO and LUMO energies, and hence the oxidation and reduction potentials to different extents according to the position. TD-DFT is often used in conjunction with electrochemistry to confirm the location of the frontier molecular orbitals.[4,31]

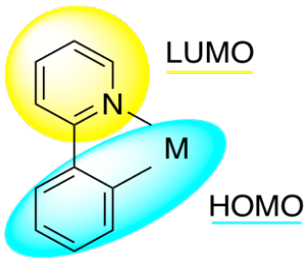

Figure 1.9: *The location of the HOMO and LUMO for cyclometallated Pt(II) complexes.*

1.5.3 Colour tuning

Based on the location of the frontier orbitals in Pt(N^C^N)Cl complexes, a red-shift of the PL can be achieved by introducing electron-donating substituents into the cyclometallated aryl ring to raise the energy of the HOMO, and/or electron-withdrawing substituents into the heterocycle to lower the LUMO energy.[31] Consequently, the HOMO-LUMO gap will decrease, and the emission will be lower in energy. A blue shift can be achieved by applying the reverse principle (**Figure 1.10**)[31]. The focus of the work described in this thesis is on shifting the emission to the NIR.

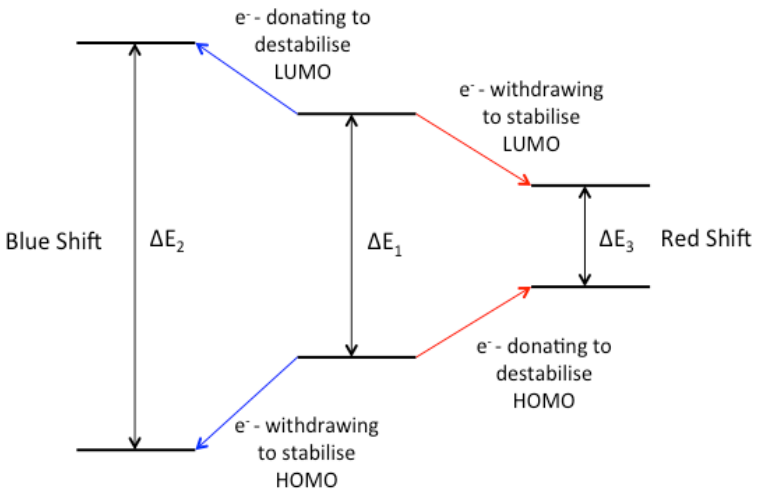

Figure 1.10: *The effect of electron-withdrawing and electron-donating groups on the frontier orbital energies of Pt(N^C^N)Cl complexes, hence the energy gap and emission colour; $\Delta E_2 > \Delta E_1 > \Delta E_3$.*

Incorporation of increasingly electron-rich substituents into the 4-position of the central aryl ring of Pt(dpyb)Cl leads to a rise in the HOMO energy without significantly affecting the LUMO, hence a red shift in the emission (**Figure 1.11**),[51] which can be rationalised by contribution of this position to the frontier orbitals from DFT calculations.[31] The emission can be shifted further to the red by stabilising the LUMO through introduction of electron-withdrawing substituents in the pyridyl rings as demonstrated in a later study.

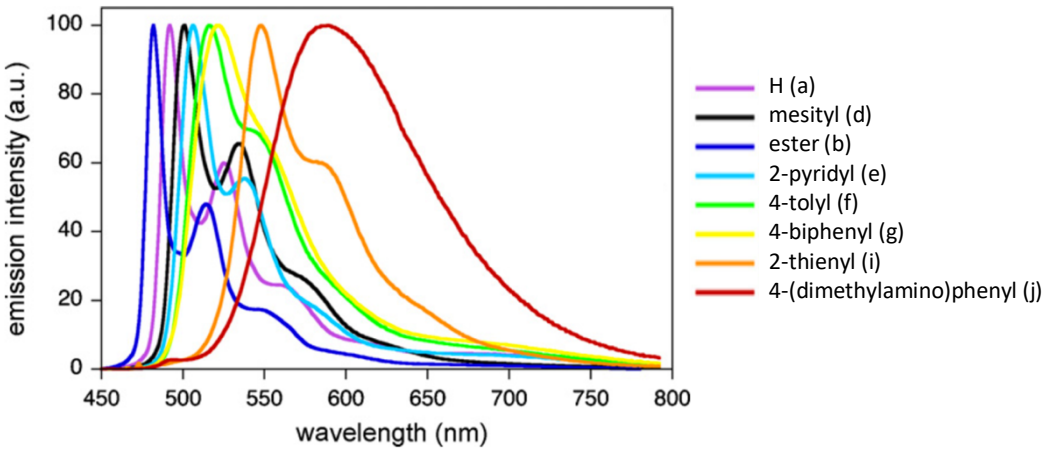

Figure 1.11: *Emission spectra for Pt(N^C^N) complexes can be tuned from Pt(dpyb)Cl (purple line) by addition of electron-donating or electron–withdrawing substituents at the 4-position of the aryl ring. Spectra are recorded in DCM at 298 K with λ_{ex} = 400 nm and normalised to the peak maximum (figure taken from ref 51).*

A strong electron-donating 4-(dimethylamino)phenyl substituent in the 4-position of the aryl ring (complex j in **Figure 1.11**) led to a particularly facile oxidation, and also to a switch in nature of the lowest energy emissive state from $^3\pi$-π^* to primarily intra-ligand charge transfer (ILCT), hence to a broader, structureless and red-shifted emission spectrum.[57] This highlights the potential of the N^C^N family of complexes to switch between different highly luminescent excited states with distinct properties through simple structural modification.[52]

A red (bathochromic) shift can also be achieved by increasing the conjugation in a molecule, which also lowers the HOMO-LUMO gap. This idea can be exploited to achieve red or NIR-emitting complexes by incorporating ligands with increasingly extended conjugation[56], for example Pt(II) porphyrins[58] and complexes containing ligands based on isoquinoline in place of pyridine as presented in this report.

The two possible isomers containing 1- and 3-substituted isoquinoline ligands are shown in **Figure 1.12**. The emission spectrum of complex **5** features two maxima of similar intensity λ = 595 and 642 nm) whereas that of complex **6** (λ = 559 nm for monomer emission) is dominated by an excimeric broad band at 668 nm unless in

very dilute solution; complex **6** has a high propensity to excimer formation (see Section 1.6).[56,59]

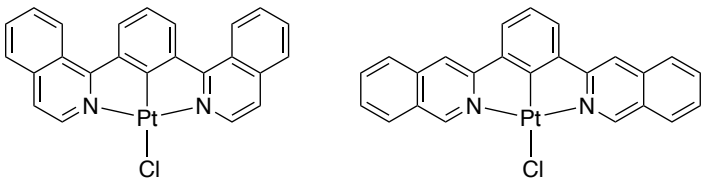

5 **6**

Figure 1.12: *Pt(N^C^N)Cl complexes based on 1- and 3-isoquinoline (**5** and **6** respectively) that show red-shifted emission compared to Pt(dpyb)Cl due to the extended conjugation.*

Changing the pyridine rings for electron-deficient pyrimidine moieties could also be a successful strategy for colour tuning the emission (**Figure 1.13**), as the presence of the extra nitrogen atom in the ring should effectively lower the energy of the LUMO and hence lead to a red shift in emission, as seen for complex **8** compared to the corresponding pyridine complex (λ_{max} = 560 and 547 nm respectively).[56,60] Having said that, a slight blue shift in the emission is actually observed for complex **7** compared to Pt(dpyb)Cl (λ_{max} = 484 and 490 nm respectively),[56,60] suggesting that the pyrimidine rings may also serve to stabilise the HOMO somewhat, as well as the LUMO.

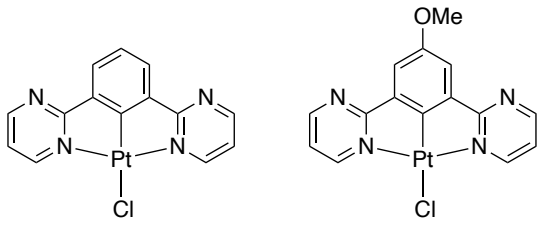

7 **8**

Figure 1.13: *Structure of pyrimidine containing complexes.*

1.6 Excimers and aggregates

Pt(II) complexes have the potential to undergo face-to-face Pt···Pt and π–π stacking interactions along the z-axis due to their planar geometry, leading to the formation of aggregates or excimers (excited dimers). The distinction between the two is made on the basis of whether the bimolecular species pre-exists in the ground state

(aggregate) or only forms after excitation of one of the constituent molecules and thus exists only in the excited state (excimer). Excimers form due to the existence of a shallow minimum in the potential energy surface (PES) for the combination of M* (excited state molecule) and M (ground state molecule) and do not exist in the ground state as the PES is repulsive (**Figure 1.14**).[1] Excimer formation is a dynamic process, requiring some motion of the molecules relative to one another.

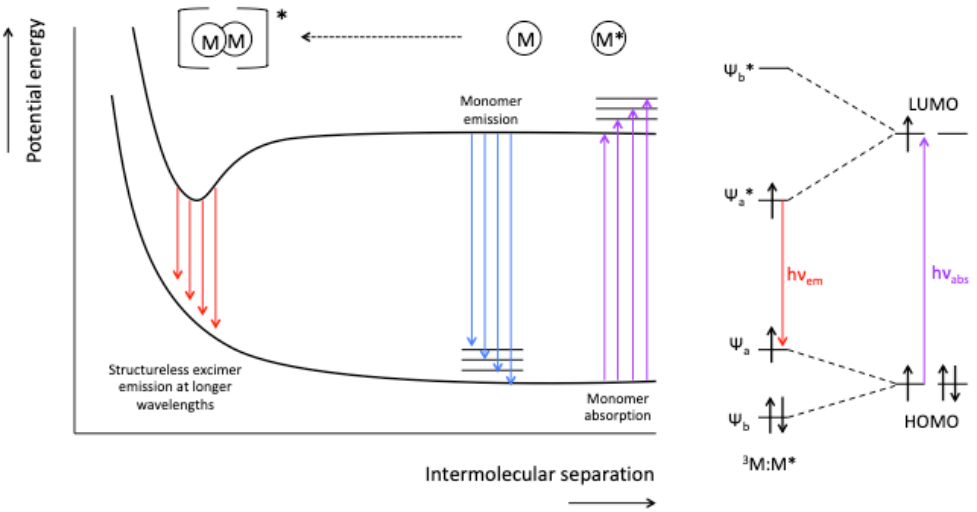

Figure 1.14: *Schematic potential energy diagram for excimer emission. M/M* denotes a molecule in the ground/excited state.*

The formation of excimers or aggregates is often undesirable as they may cause self-quenching of emission at high-concentrations, through triplet-triplet annihilation (TTA). However, Pt(dpyb)Cl derivatives efficiently form excimers at elevated concentrations that are themselves intensely emissive with quantum yields of excimer luminescence that can be as high as 0.35, as well as having short lifetimes, and so they can be intentionally exploited for OLED applications.[1,51,61] The term excimer strictly applies to excited dimers formed in solution; however, emission observed in films of such complexes clearly emanates from a similar species.[57]

Conventionally for excimer formation, one of the dimer components is in its excited state and the other in the ground state with a filled valence shell of electrons. The mechanism of excimer formation and phosphorescence can be described by

Equation 1.2, where v_{ex} is the excitation frequency, $v_{excimer}$ is the frequency of excimer emission and M_1 and M_2 denotes two separate molecules in the ground state.[62]

$$h\nu_{ex} + M_1 \rightarrow {}^1M_1^* \rightarrow {}^3M_1^* \quad (1.2)$$
$$^3M_1^* + M_2 \rightarrow {}^3|M_1M_2\rangle^* \rightarrow h\nu_{excimer} + M_1 + M_2$$

Upon excitation of one molecule, its HOMO and LUMO, now both singly occupied, interact with the HOMO and LUMO of a neighbouring molecule in the ground state, which induces splitting of the energy levels and therefore stabilisation (usually through these Pt d_z^2-d_z^2 interactions) which subsequently drives excimer formation (**Figure 1.14**).[63] The resulting species have lower energy excited states than the isolated molecules or monomers, leading to the characteristic structureless red-shifted emission.[64]

1.6.1 Factors affecting excimer emission energy

Excimers have been known for a long time and many molecules have been investigated and discussed in the literature for their excimer-forming properties, particularly those of aromatic molecules such as pyrene in the 1960s.[65,66] Emission of monomeric molecules can be controlled in a reasonably predictable manner through appropriate substitution of the ligand, as highlighted in Section 1.5.3.[22] On the other hand, factors governing excimer energy have been studied to a lesser extent and are therefore less clear-cut; excimer emission energy is influenced by steric as well as electronic factors. The wavelength of excimer emission is similar for most Pt(dpyb)Cl derivatives with various substituents at the 4-aryl position, with λ_{max} centred around 700 nm.[1] Nonetheless, scope for tuning the excimer emission is emerging.[67,68]

The introduction of electron-donating groups into the pyridyl rings of Pt(dpyb)Cl tends to blue-shift the excimer emission, as for the monomer.[69] Rossi *et al.* also presented the opposite, in that addition of an electron-withdrawing $–CF_3$ group onto the pyridyl ring led to stabilisation of the excimer manifest through a significant red shift of its emission. The position of the substituent also plays a crucial role, with the

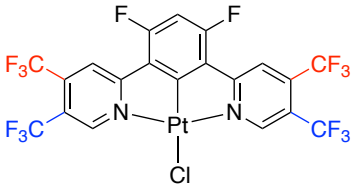

Figure 1.15: *Complexes synthesised by Rossi et al. with -CF_3 substitution at the 4- (red) or 5-position (blue) on the pyridyl rings.*

complex substituted at the pyridyl 4-position showing a greater red shift than the 5-position (**Figure 1.15**). This can potentially be explained by the relative contributions of those positions to the frontier orbitals: the 4-position of the pyridyl rings is a node for the HOMO, whereas the 5-position contributes to the HOMO as well as the LUMO, thus stabilising both and diminishing the energy gap difference.[22]

In addition to substituent effects, the relative proportion of excimer and monomer species in the excited state is strongly dependent on sample concentration and particularly the polarity of the solvent.[70] Kalinowski *et al.* highlighted the influence of solvent polarity on the ability of two derivatives of Pt(dpyb)Cl to form bi-molecular species. The negative solvatochromism they observed (a blue shift with increasing solvent polarity) upon the initial addition of H_2O to a solution of the Pt(dpyb)Cl-type complex in MeCN is consistent with an excimeric excited state of lower polarity than the ground state. They also observed the appearance of an even lower energy band at high concentration of H_2O that had a different excitation spectrum and was hence assigned to an excited ground state dimer. They concluded that a strongly polar solvent facilitates the formation of ground-state dimers or aggregates whilst excimers occur mostly in non-polar or weakly polar solvents.[70]

A recent study by Cho *et al.* aimed to elucidate interactions between the frontier molecular orbitals that are crucial for efficient excimer formation.[63] Planar Pt(II) complexes are ideal model compounds for this study as the HOMO and LUMO moieties are often clearly separated. They found that adding bulky $–SiPh_3$ substituents on either the pyridine (LUMO) or phenyl (HOMO) component of phenylpyridine would hinder certain interactions and force a specific orientation of the molecules (**Figure 1.16**). For **9**, only a HOMO-HOMO interaction could occur and interestingly no excimer emission was observed for this complex.

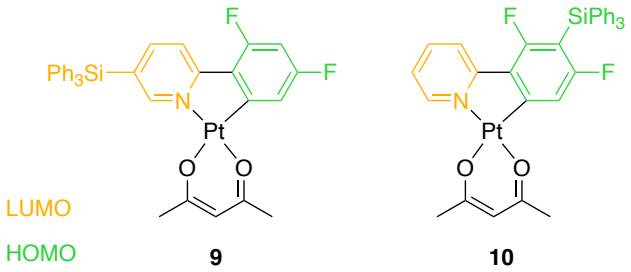

Figure 1.16: *Complexes synthesised by Cho et al. The position of the bulky -$SiPh_3$ substituent on either the LUMO (**9**) or the HOMO (**10**) affects the ability of the complex to form excimers.*

Conversely, with **10** a LUMO-LUMO interaction is possible and excimer emission was seen for this complex, suggesting that such an interaction is a crucial precondition for excimer formation. The switch in emission properties between **9** and **10** was also accompanied by a significant reduction in the quantum yield, which was almost unity for **9** but 0.28 for **10**; excimer emission is often linked to low quantum yields in accordance with the energy-gap law. Despite this, excimer emission has been exploited as a tool to design promising NIR-emitting materials.[23,33]

1.6.2 Achieving NIR emission

The shift to the NIR region of the electromagnetic spectrum is intrinsically challenging.[71] Luminescence quantum yields tend to decrease with decreasing excited state energy, reflecting the tendency for non-radiative decay processes to increase rapidly through energy transfer into vibrations,[72] controlled by the Franck-Condon overlap between the vibrational wavefunctions of the excited and ground states. Furthermore, the coefficient of spontaneous emission varies with ν^3 (where ν is the frequency of light emitted) such that k_r declines for longer wavelength emission.[31] The energy-gap law is always anticipated to be a major determinant in the efficiency of NIR emitters.[73] Consequently, to achieve NIR emitters with a high photoluminescence quantum yield (PLQY), it is necessary to suppress non-radiative decay as much as possible.

Despite the challenges associated with achieving NIR emission, the highest PLQY of a thin film Pt(II) complex to date reaches an impressive 81% with λ_{max} = 740 nm, due to exciton-like emission along the molecular aggregate and the d_z^2 orbital, which

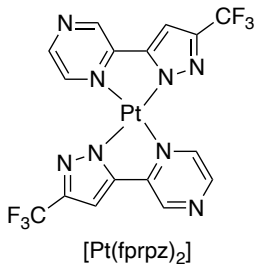

Figure 1.17: *Structure of NIR-emitter reported by Chi et al. possessing a very high EQE.*

greatly suppresses exciton-optical phonon coupling.[74] OLEDs were also fabricated with this 2-pyrazinyl pyrazolate Pt(II) complex [Pt(fprpz)$_2$] (**Figure 1.17**); an external quantum efficiency (EQE) of 24% was achieved for an OLED device that was increased to 55% upon optimisation of the device architecture.

It is clear that the factors governing the efficiency of NIR emission are complicated and must be better understood in order to design efficient NIR-emitting materials. According to Fermi's golden rule (**Equation 1.3**), reducing the strength of the vibronic couplings, represented by the reorganisation energy term (C = coupling constant, ω_M = frequency of the normal vibrations of maximum frequency, λ_M = collective reorganisation energy of the maximum frequency modes and ΔE = the energy gap between the two electronic states), will result in a slower non-radiative transition rate. Qualitative factors such as the molecular rigidity and delocalisation length of the extended π-conjugation system are generally used to implicate the strength of vibronic couplings; therefore, a further quantitative understanding is needed.

$$W = \frac{C^2\sqrt{2\pi}}{\hbar\sqrt{\hbar\omega_M \Delta E}} \exp\left(-\frac{\lambda_M}{\hbar\omega_M}\right) \exp\left\{-\frac{\Delta E}{\hbar\omega_M}\left[\log\left(\frac{\Delta E}{\lambda_M} - 1\right)\right]\right\} \quad (1.3)$$

In a study in 2019, Chen *et al.* applied DFT to a series of high-efficiency square-planar Pt(II) complexes in both the monomeric and dimeric forms in order to investigate vibronic coupling effects.[73] They revealed that the magnitude of the internal reorganisation energy (λ_{in}), defined as the extent of vibronic coupling between two electronic states, can be significantly reduced for the dimers compared to monomers through the formation of MMLCT excimeric states on the lowest triplet excited-state potential energy surface (**Figure 1.18**). They also used the transition density between

the excited and ground state as a tool to rationalise the relative magnitudes of the reorganisation energies and ligand substituent effects.

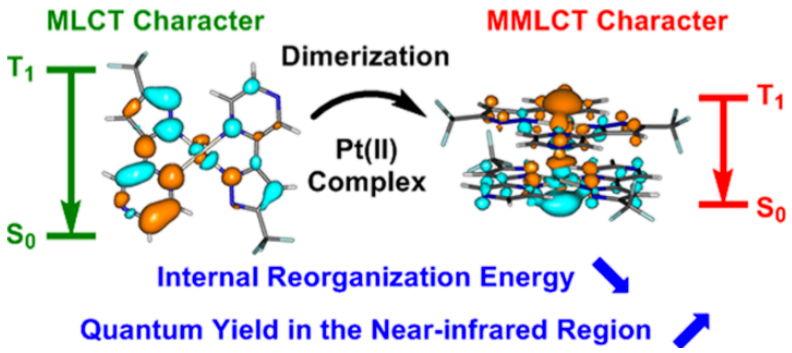

Figure 1.18: *Schematic representation of the transition densities of a monomeric (left) and dimeric/excimer (right) Pt(II) complex, highlighting the red shift and reduction in internal reorganisation energy following excimer formation.*[73]

The group extended their theory to 45 Pt(II) complexes in the literature and demonstrated a strong correlation between the experimental PLQY and the calculated λ_{in}; reduction of internal reorganisation energy should be considered a critical factor for improving the performance of NIR emitters. Their study offered valuable insights and suggests that transition density can be used as a tool for theoretical guidance to help identify all possible suitable ligand positions for substitutions with minimal impacts on λ_{in}, potentially pointing to novel design principles for improved NIR emitters by controlling vibronic couplings through metallophilic interactions in molecular aggregates.[73]

1.7 Applications

1.7.1 OLEDs

Organic light emitting diodes (OLEDs) are increasingly competing with other display technologies such as liquid crystal displays (LCDs) as they can provide thinner, more flexible and brighter displays, as well as being self-emitting, eliminating the need for a backlighting source.[75] An OLED has a similar structure to a conventional LED but

instead of using layered n- and p-type semiconductors, organic molecules are used to transport electrons and holes (**Figure 1.19**).

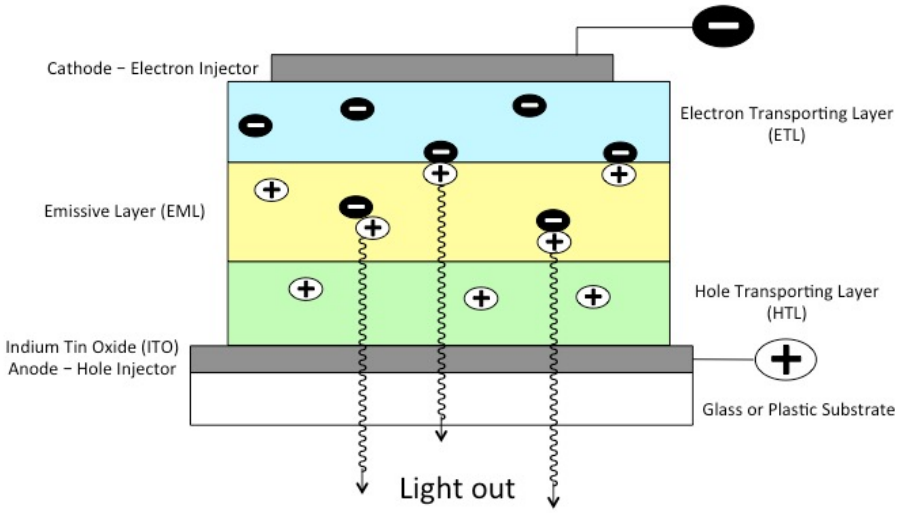

Figure 1.19: *Basic OLED device structure; a voltage is applied across the anode and cathode.*

When a hole recombines with an electron to produce an exciton, energy is released in the form of light (**Figure 1.20**) from the singlet excited state due to the spin selection rule.[31] However, spin statistics based on relative degeneracies (**Scheme 1.3**) imply a 3:1 ratio in favour of the non-emissive triplet state being formed upon charge recombination. In order to improve device efficiency, complexes of heavy metals are employed as "triplet harvesting agents" to exploit the high SOC constants and theoretically achieve 100% electron-to-photon conversion by promoting emission from the triplet states. Platinum(II) complexes of the type reported in the preceding sections have attracted a great deal of attention in the literature as phosphorescent dopants in the emissive layer of OLEDs due to their high phosphorescence quantum yields, very high electroluminescence (EL) efficiencies, and scope for tuning the emission colour.[57]

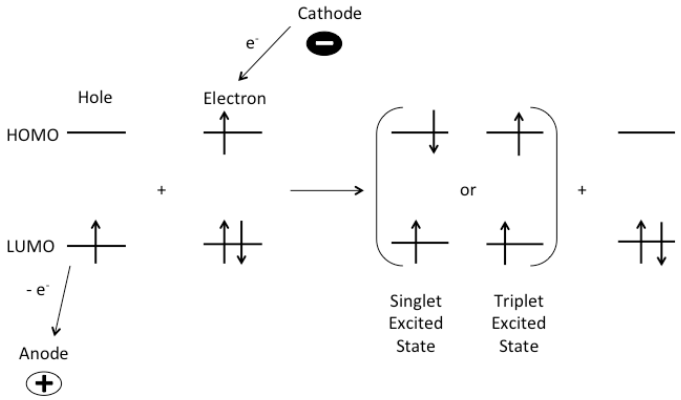

Figure 1.20: *Illustrative energy level diagram for the charge recombination process in an OLED.*

$$|\uparrow\uparrow\rangle \;,\; |\downarrow\downarrow\rangle \;,\; \frac{1}{\sqrt{2}}\left(|\uparrow\downarrow\rangle + |\downarrow\uparrow\rangle\right)$$

$$\frac{1}{\sqrt{2}}\left(|\uparrow\downarrow\rangle - |\downarrow\uparrow\rangle\right)$$

Scheme 1.3: *Triplet and singlet states resulting from charge recombination. Top: 3 symmetric triplet states. Bottom: 1 antisymmetric singlet state.*

Devices fabricated with Pt(dpyb)Cl derivatives as the emissive layer (EML) at low wt % doping concentration tend to show EL that closely resembles that of the PL in dilute solution. This allows the emission colour tuning methods of Section 1.5.3 to be applied to OLED applications.[57] The relatively short lifetimes of these complexes is also an attractive property as it helps to suppress the decrease in EL efficiency, or "roll-off", with increasing voltage, which results from the effects of induced exciton quenching, TTA and charge-carrier-exciton interactions on long lived excited states.[57]

1.7.2 White OLEDs

Excimer emission from Pt(dpyb)Cl-based complexes can be exploited in the preparation of white OLEDs (WOLEDs) for lighting applications by combining monomer and excimer emission to achieve white light from a single dopant.[1,76,77] This simplified structure is advantageous over common WOLEDs that combine red, green and blue emitters to realise white light, as charge recombination is easier to control

and problems of colour quality changing over time, stemming from different degradation rates of multiple dopants, will be eradicated.[35] "Short-circuiting" is also often seen for systems that rely on a combination of emitters mixed in a single layer, to the lowest energy (red) emitter.[76] The undesirable use of higher concentrations of green and blue emitters is required to compensate for that.

1.7.3 NIR OLEDs

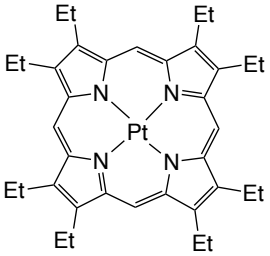

Figure 1.21: *Structure of PtOEP.*

Platinum(II) octaethylporphyrin (PtOEP, **Figure 1.21**) was the first reported complex tested successfully as an OLED emissive layer dopant that demonstrated high EL efficiency (Φ = 0.5 and τ = 91 μs in both solution and a polystyrene film at room temperature).[78] The highly conjugated nature of porphyrin ligands leads to deep red emission, λ_{max} = 650 nm, making Pt(II) porphyrins a competitor for use as dopants in NIR OLEDs.[79–83] Emission energies can be further shifted to the NIR, albeit with a decrease in the solution PLQY, by extending the π-conjugation of the porphyrin macrocycle.[62,84] However, the relatively long radiative lifetimes lead to a decrease in EL efficiency, especially at high currents and high doping concentrations, due to TTA of the excited state (**Equation 1.4**).[31,70] Complexes based on Pt(dpyb)Cl, as well as others containing cyclometallating ligands, are superior for NIR OLED applications due to the improved k_r and shorter lifetimes from the enhanced SOC influence of the metal as a result of cyclometallation.[33,85] Excimer emission can also be exploited in the fabrication of NIR OLEDs; neat films of the luminescent material as the emissive layer can yield exclusively excimeric emission, at longer wavelengths than the corresponding monomer.[31]

$$4\ (^3M^* + {}^3M^*) \rightarrow {}^1M^* + 3\ {}^3M^* + 4\ M \qquad (1.4)$$

A potential exciting application of NIR OLEDs is for integrated silicon-OLED displays and touch sensor panels, allowing for in-screen fingerprint detection that is not currently available in the technology market.[86] Moreover, the NIR emission range

(700-1000 nm) coincides with the semitransparency window of biological tissue, enabling NIR OLEDs to be employed in a variety of biomedical and bio-sensing applications.[33]

1.8 Concluding remarks and project aims

The overall aim of the work in this thesis is to design and synthesise luminescent platinum complexes that exhibit red-shifted emission, with a goal to achieve emission that is more squarely in the NIR region of the spectrum without any "contamination" from visible light. Pt(N^C^N)Cl complexes featuring isoquinoline/quinoline rings may offer a route to this goal, due to extended conjugation and ease of excimer formation. Asymmetric Pt(N^C^N)Cl complexes, featuring two different or differently substituted heterocycles, will also be studied, as this is an area that has not been explored in the literature and may provide some insight into factors governing excimer emission energy; the ability to tune excimer emission energy is highly desirable towards the goal of NIR emission. An alternative approach that will be explored is to try to force excimer emission by introducing a rigid scaffold, such as xanthene, to covalently lock two Pt(II) complexes in a geometry that favours interfacial interactions.

Chapter 2

2. Pt(II) complexes featuring symmetric tridentate N^C^N-coordinating ligands

2.1 Introduction

As described in Section 1.3, Pt(II) complexes incorporating N^C^N-coordinating ligands have attracted interest, particularly as potential triplet-harvesting phosphors for OLED applications.[3–6] Pt(N^C^N) complexes usually show higher luminescence efficiencies than analogous (N^N^C) and (C^N^C) structures, along with scope to tune the colour of the emission through simple modifications of the N^C^N ligand. DFT studies have shown that the LUMO is based primarily on the pyridine rings and the HOMO on the central phenyl ring and the platinum moiety, as referenced in Section 1.5.3.[31] Colour tuning of these complexes can thus be achieved by adding electron-donating (EDG) or electron-withdrawing (EWG) substituents to either the pyridine ring or central phenyl ring. The 4-position of the pyridine ring has been found to be the ideal position for substitution as it contributes greatly to the LUMO but not to the HOMO so the overall change in the energy gap will be greater leading to a larger shift in λ_{max}.[87] Rossi *et al.* showed that substitution at this position also had a greater effect on the emission energy of the excimer.[22]

Moreover, the ancillary monodentate ligand offers additional scope to tune the excited-state properties. For example, replacement of the chloride ligand of the parent complex with an electron-rich thiolate leads to a significant red shift in the emission, from the characteristic, highly phosphorescent structured bands of Pt(N^C^N)Cl in the green region, to a broad, structureless emission band in the red

region (**Figure 2.1**).[15] Such thiolate complexes can be formed readily upon treatment of the Pt(N^C^N)Cl complex with the corresponding potassium thiolate KSR in solution at room temperature. The red shift in emission can be explained by the change in nature of the lowest-energy singlet and triplet excited states, to ones assigned to charge transfer from the thiolate, mixed with some metal character, to the N^C^N ligand. Although the resulting quantum yields for these thiolate complexes are lower than those of the chloro parents, the values of up to 0.16 are unusually high for Pt(II) complexes that emit at such low energy. One possible drawback is that the complexes have low stability in solution, due to the lability of the Pt–S bond, although they are reported to be stable indefinitely in the solid state.

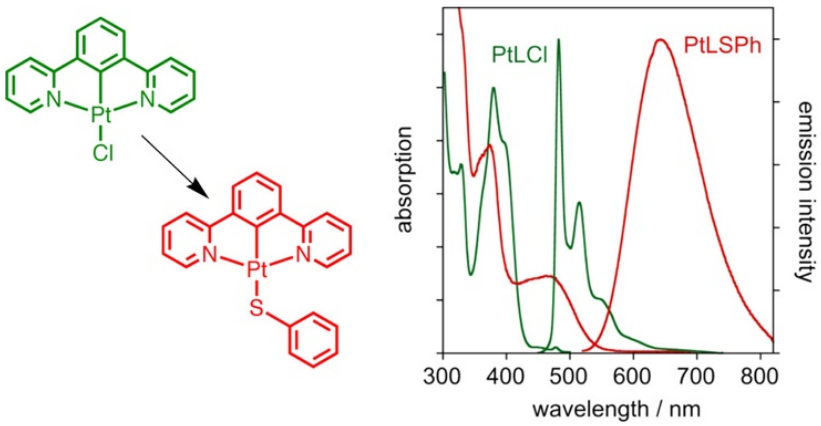

Figure 2.1: *Replacement of chloro with a thiolate ancillary ligand leads to broad, red-shifted emission in solution. Figure taken from reference 15.*

The replacement of the chloro ligand by -NCS in one Pt(N^C^N) complex (**Figure 2.2**) was found to significantly red shift the emission in the solid state, despite having little effect on the emission in solution.[23] Crystal structure determination reveals that the molecules pack in a head-to-head arrangement with short Pt···Pt interactions for X = NCS, leading to a low-energy aggregate excited state of MMLCT character, in which the HOMO is raised in energy. This effect was exploited to fabricate OLEDs that emit squarely in the NIR region (855 nm). The NCS co-ligand was deduced by IR spectroscopy to be N-bound, as observed by X-ray crystallography. A tentative conclusion from that work was that the change from Cl to an NCS co-ligand appears to favour metal-metal interactions and thus brings MMLCT states into play.

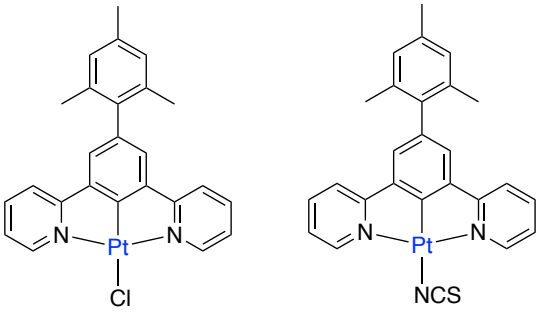

Pt-Cl **Pt-NCS**

Figure 2.2: *Structure of X = -Cl and X = -NCS complexes incorporated into OLEDs.*

The luminescence properties, along with the ability to tune the colour of emission through simple structural modifications of the N^C^N tridentate ligand and ancillary ligand, inspired the choice of Pt(N^C^N) complexes as a focal point in the research described in this thesis.

2.2 Aims and objectives

With the overarching aim of this work to red shift the emission more fully into the deep red and/or near-infrared (NIR) region of the electromagnetic spectrum, target complexes are proposed with EWGs, such as trifluoromethyl (-CF_3), added to the pyridine ring to stabilise the LUMO, lowering its energy and consequently decreasing the HOMO-LUMO gap and therefore emission energy. EDGs, such as *tert*-butyl, can also be added to the central phenyl ring to raise the energy of the HOMO, whilst improving solubility. The approach applied in designing the target molecules is shown in **Figure 2.3**.

Complexes with methyl groups at the 2- and 4-positions of the central ring, i.e. *meta* to the metal, have also been targeted, as DFT studies have shown that these positions contribute greatly to the HOMO energy but lie on a node in the LUMO; adding electron-donating groups to these positions should destabilise the HOMO without affecting the LUMO and hence lead to a red shift in the emission. An alternative approach applied to red shift the emission is to extend the conjugation by replacing the pyridine rings with quinoline/isoquinolines. A series of substituted Pt(II)

complexes bearing isoquinoline rings were synthesised and their photophysical properties investigated. The influence of the ancillary ligand on luminescence was also investigated by replacing the chloro group with -NCS and -I.

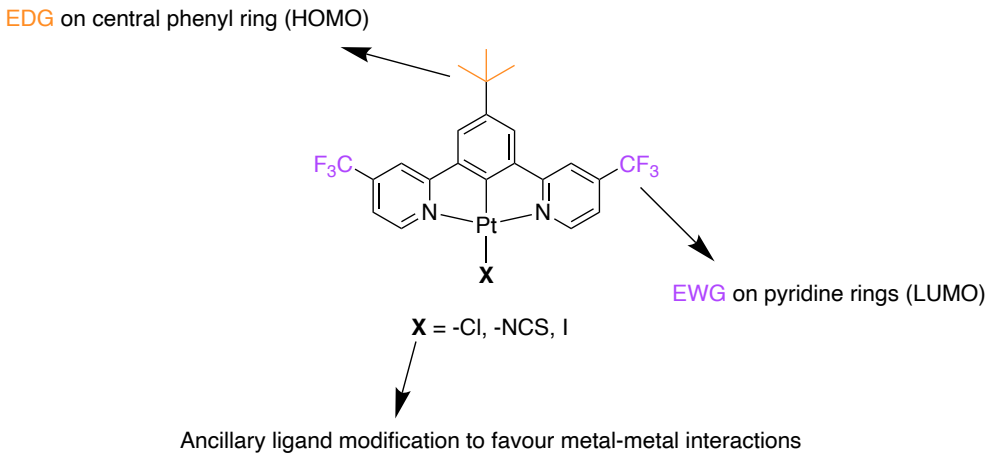

Figure 2.3: *The design strategy for symmetric Pt(II) complexes to achieve NIR emission through structural modification.*

2.3 Results and Discussion

2.3.1 Synthesis

Ligand synthesis

All proligands discussed in this chapter, HL^{1-11}, were synthesised by multi-step Suzuki-Miyaura and/or Stille cross-coupling reactions.[48,49] Bispinacolatoborate esters created by the Miyaura reaction proved invaluable in this work. The synthesis of HL^{1-2} was achieved first by borylation of 1,3-dibromo-5-*tert*-butylbenzene with bispinacolatodiboron (B_2pin_2) to give **P1**, followed by a Suzuki cross-coupling to introduce the CF_3-substituted pyridine (HL^1) or pyrimidine ring (HL^2) (**Scheme 2.1**).

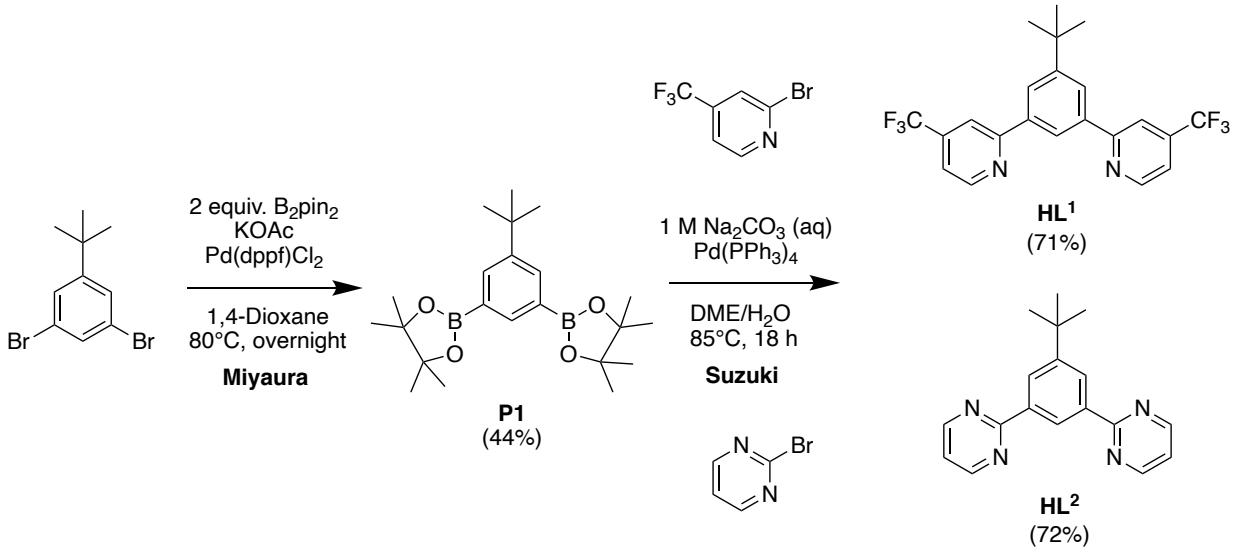

Scheme 2.1: *Synthesis of ligands HL[1] and HL[2] through the precursor 1,3-dibromo-5-t-butylbenzene (**P1**).*

HL[3-5] were synthesised in a similar manner from a one-step Suzuki cross-coupling reaction of the commercially available 1,3-phenylenediboronic acid with the corresponding chloro- or bromo-substituted quinoline or isoquinoline (**Scheme 2.2**) followed by purification by column chromatography to give the pure proligands in good yields. The higher yield of HL[4] may reflect the higher reactivity of bromo-isoquinoline compared to the other isoquinoline/quinoline starting materials that feature a chloro leaving group. HL[3-5] and their Pt complexes are known compounds[56]

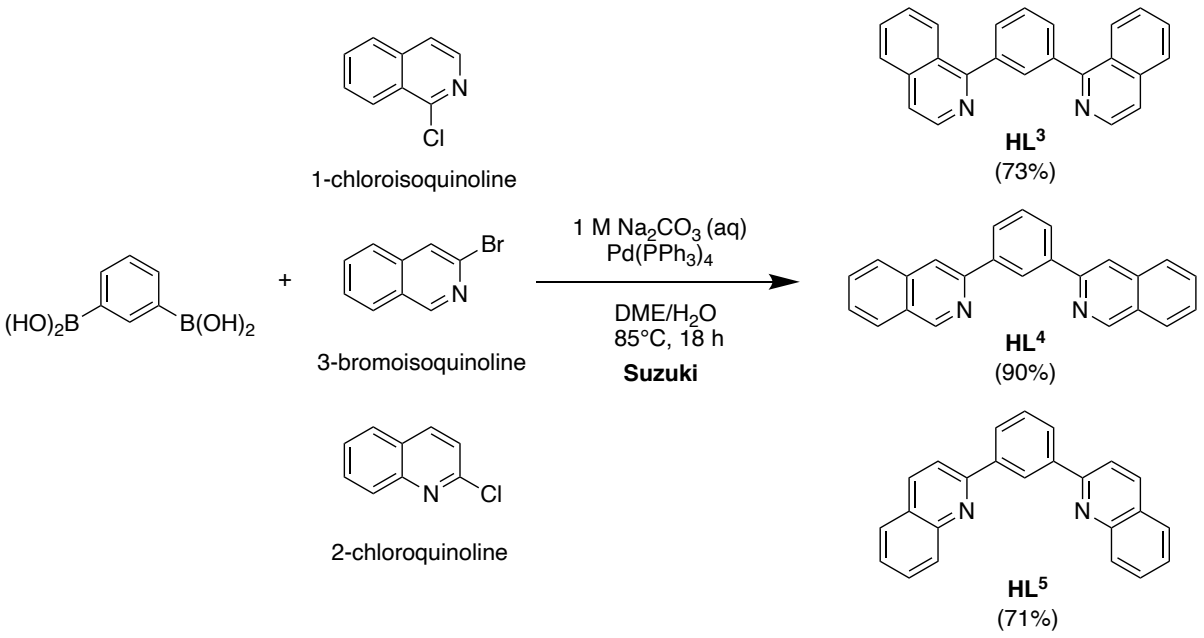

Scheme 2.2: *Synthesis of HL[3-5].*

that have been synthesised here to study the corresponding complexes in detail and to use them as models against which the new complexes can be compared.

HL[4] and derivatives were initially made from the precursor 3-isoquinolyl triflate. This compound was prepared in three steps as shown in **Scheme 2.3**. The amide **I1**, formed by reaction of benzylamine with ethyl diethoxyacetate,[88] was treated with concentrated sulphuric acid to form isoquinolin-3-ol,[89] which was converted to the triflate upon reaction with triflic anhydride.[90] During the course of this project, 3-bromoisoquinoline became available commercially at an acceptable price, and was used henceforth instead of synthesising the triflate.

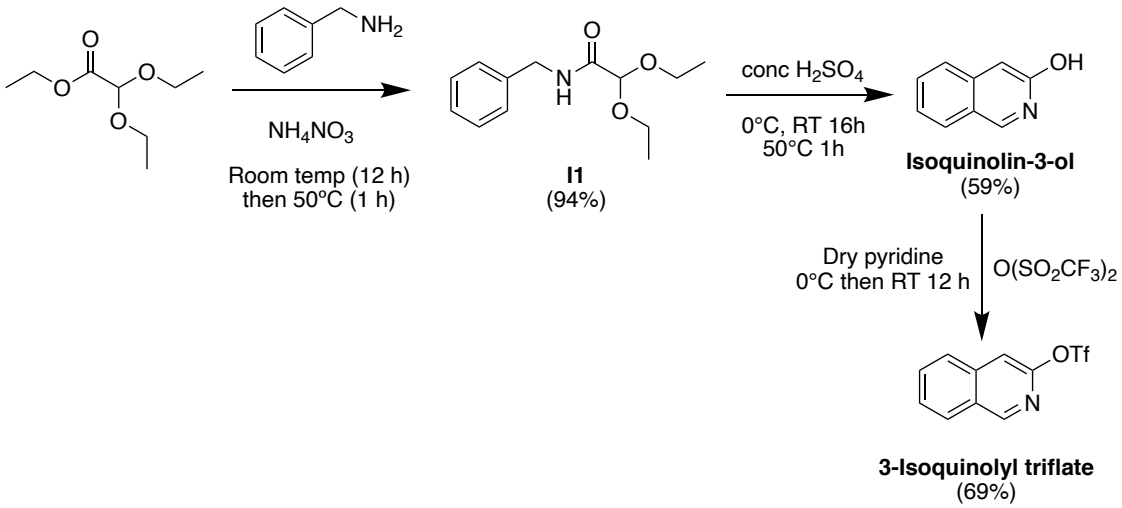

Scheme 2.3: *Synthesis of 3-isoquinolyl triflate through the intermediates **I1** and isoquinolin-3-ol.*

HL[6-11] were synthesised in a similar manner to HL[3-5]. They differ in that they have substituents in the central phenyl ring, either methyl groups in the 2- and 4-positions, or *t*-butyl in the 5-position. The requisite precursor in the former case, **P2**, was prepared as shown in **Scheme 2.4**, while **P1** was used for the *t*-butyl systems. A summary of the reagents, products and yields of the final Suzuki cross-coupling step is shown in **Table 2.1**.

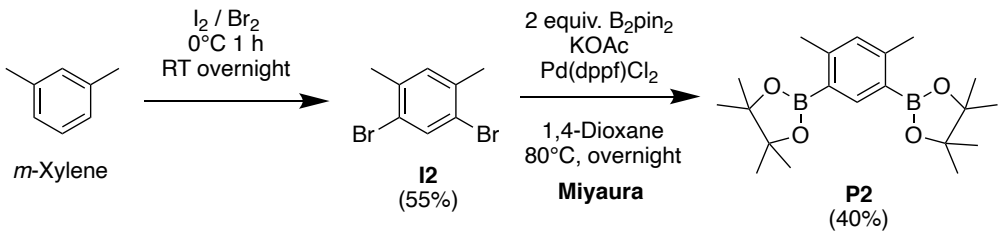

Scheme 2.4: *Bromination of meta-xylene and synthesis of the boronate ester precursor **P2**.*

***Table 2.1**: Synthesis of HL[6-11] by Suzuki cross-coupling reaction; 1 M Na_2CO_3, $Pd(PPh_3)_4$, DME/H_2O, 85 ℃, 18 h.*

Starting material	Precursor	Product	Yield
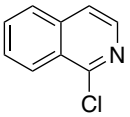	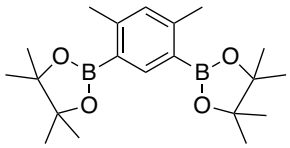 **P2**	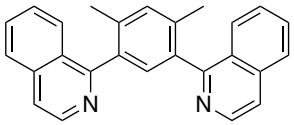 **HL[6]**	66%
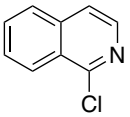	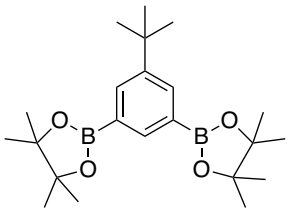 **P1**	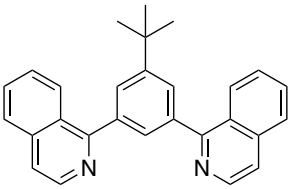 **HL[7]**	70%
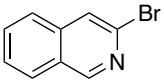	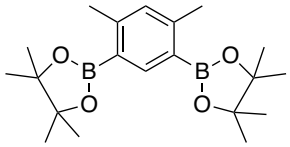 **P2**	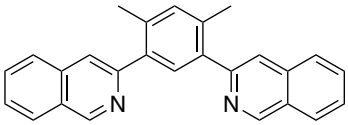 **HL[8]**	64%
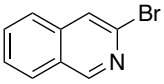	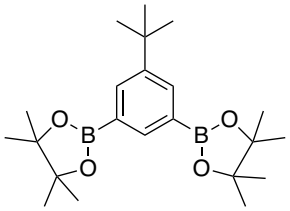 **P1**	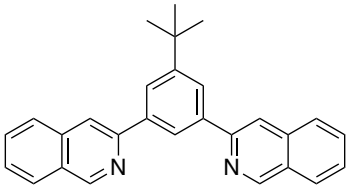 **HL[9]**	64%
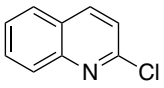	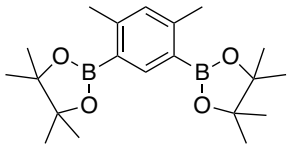 **P2**	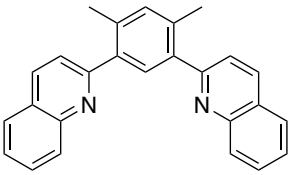 **HL[10]**	60%
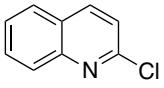	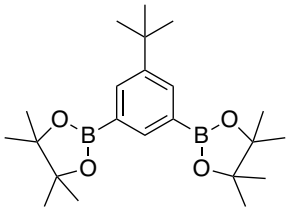 **P1**	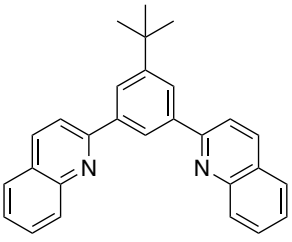 **HL[11]**	16%

Complexation

The preparation of the N^C^N-coordinated Pt(II) complexes of the form PtL^nCl was carried out by reacting the corresponding proligand HL^n with potassium tetrachloroplatinate(II) in acetic acid at reflux for 60 h under an atmosphere of nitrogen (**Scheme 2.5**). The complexes precipitated as brightly coloured solids, ranging from green-yellow to red, and were washed with water, methanol and diethyl ether before extraction into DCM to give the desired products in yields ranging from 27 to 87% (**Figure 2.4**). Note the change in atom labelling upon complexation: the cyclometallated carbon becomes C1.

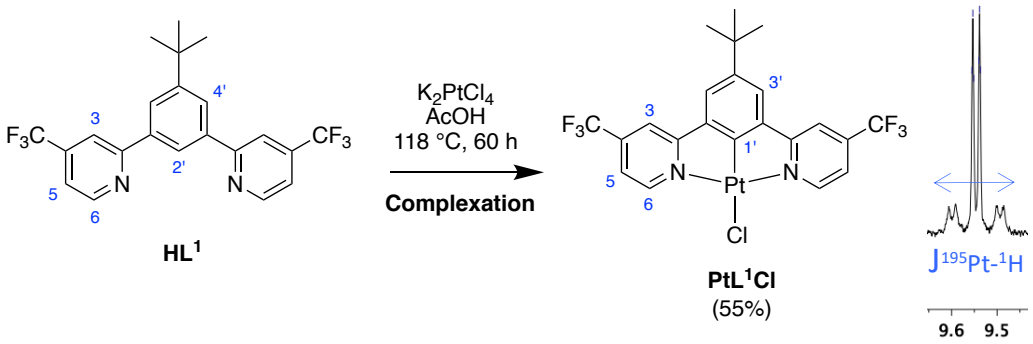

Scheme 2.5: *Complexation of HL^1 and a section of the ^1H NMR spectrum of PtL^1Cl in $CDCl_3$ highlighting the coupling of H^6 to ^{195}Pt, the spin-$^1/_2$ isotope of Pt that constitutes 34% of naturally occurring Pt ($J\ ^{195}Pt\text{-}^1H$ = 44 Hz measured using a 400 MHz spectrometer).*

Analytically pure samples of $PtL^{10}Cl$ and $PtL^{11}Cl$ could not be achieved, despite evidence of their presence in the mass spectra, which showed molecular ion peaks. The ^1H spectra showed persistent additional peaks. It is notable that the corresponding unsubstituted complex featuring 2-substituted quinolines has particularly low solubility.

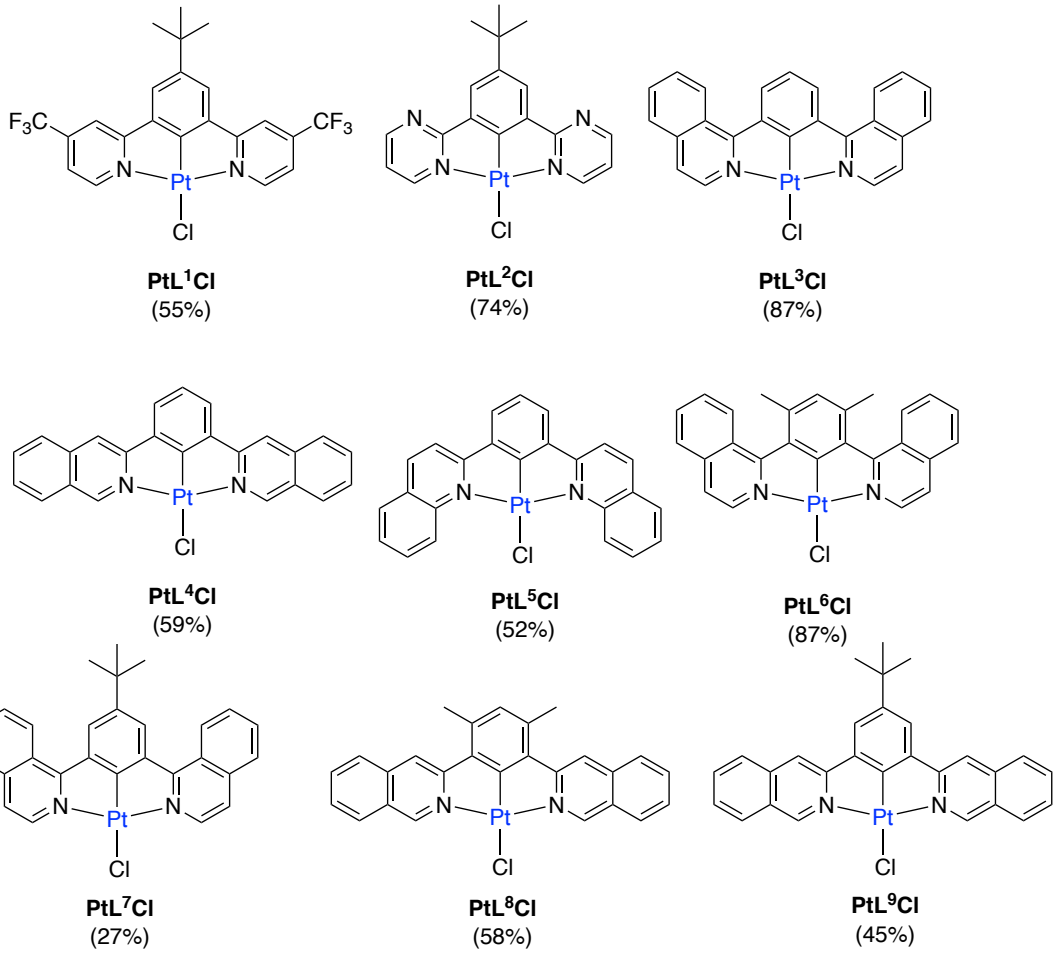

Figure 2.4: *Pt(N^C^N)Cl complexes prepared and discussed in this chapter, and their yields.*

As a representative example, **Figure 2.5** draws comparisons between the ^{1}H NMR spectrum of the ligand HL^{6} and its corresponding complex PtL^{6}Cl. Aside from the obvious loss of the H$^{6'}$ resonance, the main difference between the spectra is the noticeable shift of the H^{3} peak of the isoquinoline ring to higher frequency upon complexation (δ = 8.58 and 9.31 ppm for the ligand and complex respectively). The signal for the proton directly opposite the cyclometallated carbon (H$^{4'}$ in the complex and H$^{3'}$ in the ligand) also moves to a lower chemical shift. This effect has been reported for related complexes and is due to increased shielding within the central phenyl ring, brought about by the increase in electron density that accompanies cyclometallation.[51] Coupling with ^{195}Pt in the form of "satellites" can often be observed for these types of complexes. However, ^{195}Pt-^{1}H couplings become poorly resolved at high fields, owing to chemical shift anisotropy,[91] as can be seen upon

comparing the H^3 satellites in **Figure 2.5** recorded at 700 MHz, with those of H^6 in **Scheme 2.5** at 400 MHz.

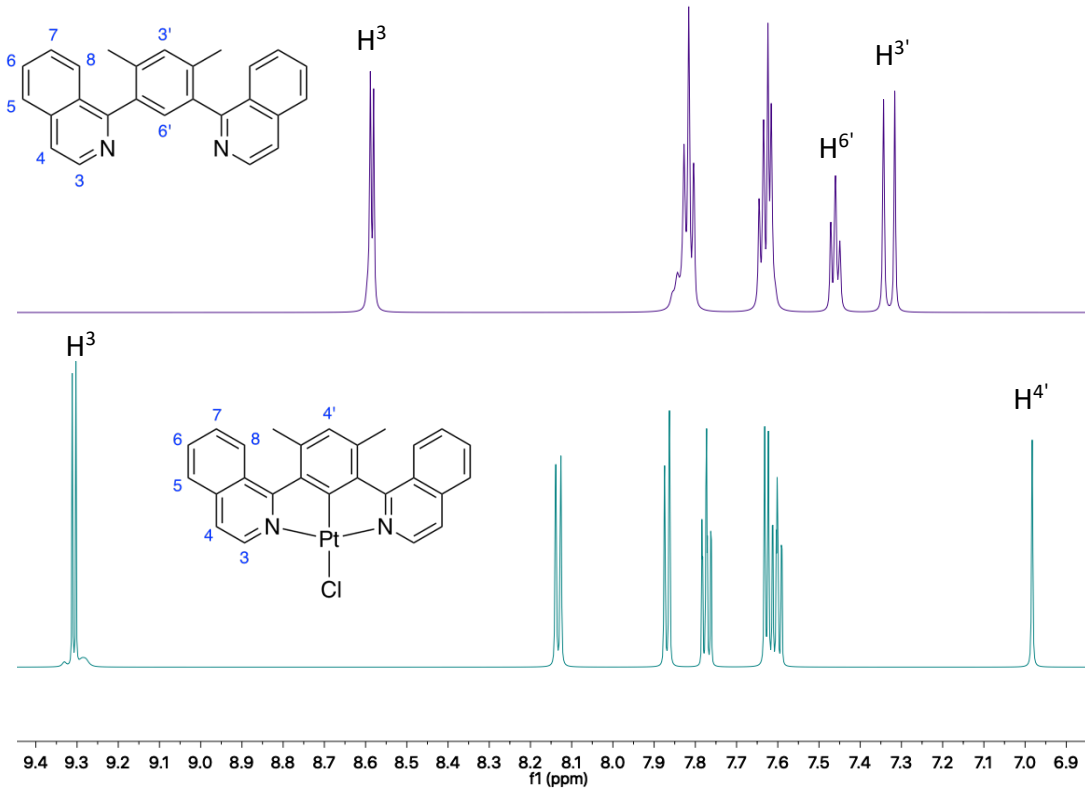

Figure 2.5: *^{1}H NMR spectrum of H^6 (top) and PtL^6Cl (bottom) in $CDCl_3$ at 700 MHz.*

2.3.2 Molecular and crystal structures in the solid state

Crystals of a number of complexes were obtained during this work, suitable for analysis by X-ray diffraction. The structures obtained in this way were solved by Dr Dmitry Yufit. Tabulated crystal and unit cell data in each case are provided in the Appendix.

Yellow crystals of PtL^1Cl suitable for X-ray diffraction were obtained by slow evaporation of the solvent from a solution in chloroform. The molecular structure (**Figure 2.6** left) is as expected, with an almost planar geometry of the constituent aromatic rings around the Pt(II) centre. The crystal packing (**Figure 2.6** right) reveals a slightly off-centre head-to-tail arrangement of the complexes with overlap between the pyridine ring of one complex and the phenyl ring of its neighbour. The

intermolecular distance is 3.638(18) Å suggesting a weak π–π stacking interaction. The shortest Pt···Pt distance is 5.7896(5) Å, longer than the sum of the van der Waals' radius (3.50 Å), implying no metallophilic interactions in this polymorph.

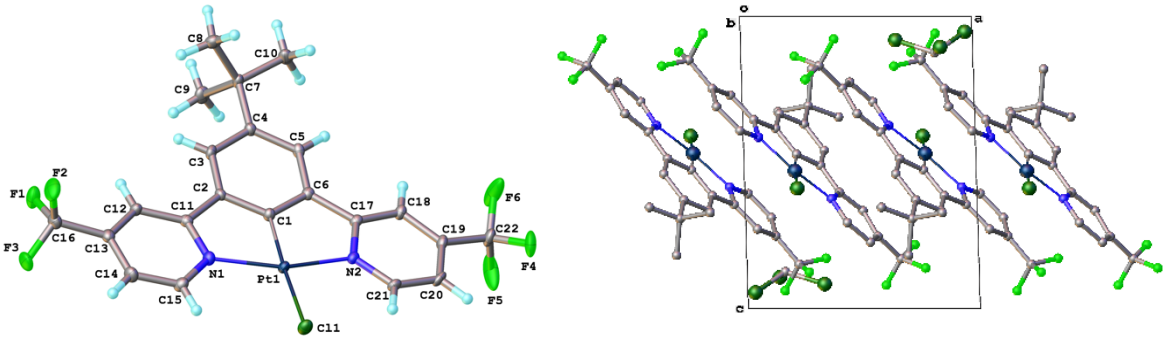

Figure 2.6: *Molecular and crystal structure (polymorph 1) of PtL[1]Cl showing head-to-tail packing and a $CHCl_3$ molecule in the unit cell (T = 120.0 K). The crystals were yellow in colour.*

A second, pseudo-polymorph red crystal (a MeOH solvate) was obtained by slow evaporation from DCM/MeOH. The methanol solvated crystal structure contains two identical complexes with one of the CF_3-groups disordered in each and packs in a twisted head-to-head arrangement with close Pt···Pt contacts of 3.2137(3) Å (**Figure 2.7**). Interestingly, it was noted that PtL[1]Cl formed either a yellow or red solid upon evaporation; fast evaporation from DCM led to the former, whereas slow evaporation gave the red solid. Such observation might suggest that the red form is

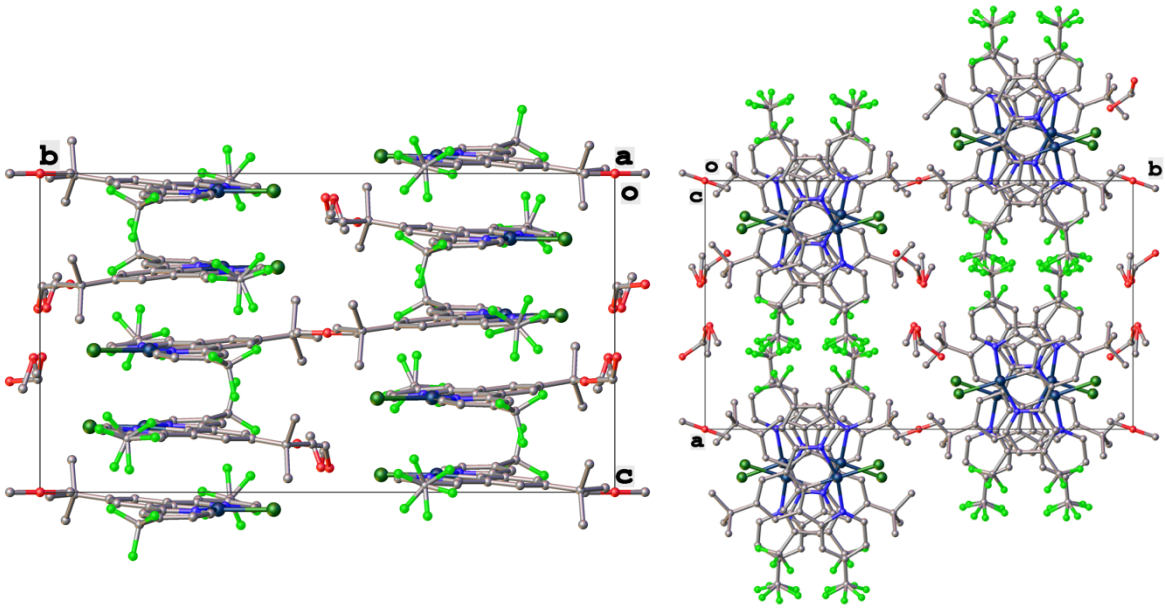

Figure 2.7*: Crystal structure (polymorph 2) of PtL[1]Cl showing head-to-head packing and close Pt···Pt contacts. The crystals were red in colour.*

thermodynamically favoured (perhaps owing to the stabilising face-to-face interactions) but there is a kinetic preference for the formation of the yellow form.

This highlights how different arrangements of the molecules may have very similar energies and effects favouring one over another may be subtle. Such observations has been noted in the literature,[92] in particular a study in 2020 by Lien *et al.* showed powders of a Pt(N^C^N) complex with a bulky pentiptycene co-ligand could be obtained that show pure monomer (green) or pure excimer (red) emission depending on the rate of precipitation from solutions.[93] We tentatively link the packing arrangement of PtL^1Cl (MeOH solvate) to the presence of excimer formation in the solid state (see Section 2.3.5).

PtL^2Cl (crystals grown by Dr Amit Sil by evaporation from a DCM/MeOH solution of the complex) packs in a head-to-tail arrangement with a shortest Pt···Pt distance of 4.393(1) Å, indicating no metallophilic interactions (**Figure 2.8**) due to the slightly offset arrangement of neighbouring molecules relative to one another. The interplanar distance of 3.40(1) Å, does however, suggest intermolecular interactions are present. PtL^3Cl also packs in a head-to-tail arrangement with no significant Pt···Pt

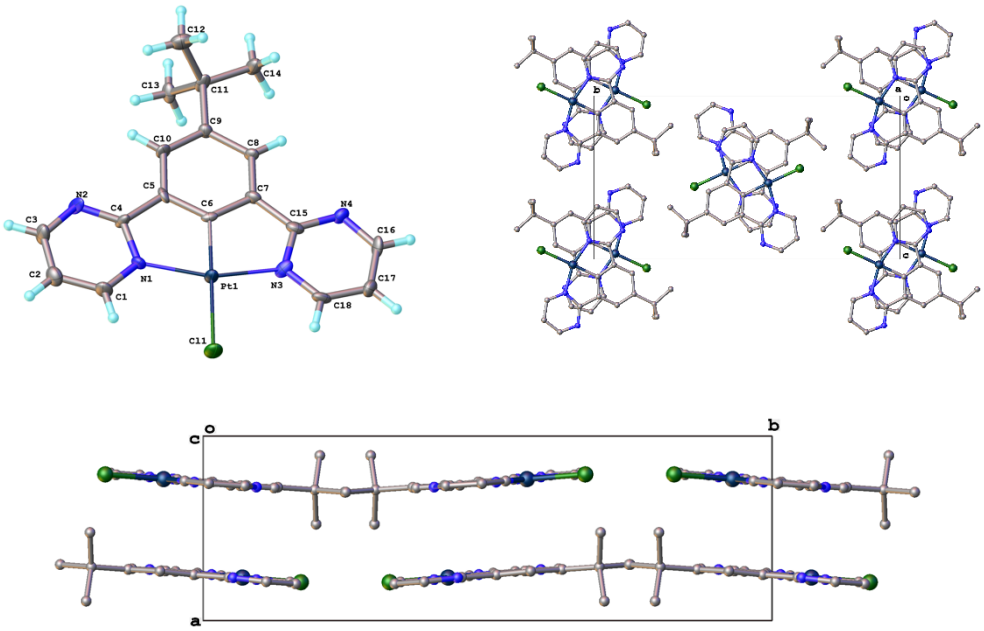

Figure 2.8: *Molecular structure and crystal packing of PtL^2Cl.*

interactions (shortest Pt···Pt distance = 5.1914(7) Å, **Figure 2.9**), though again with an interplanar distance of 3.582(3) Å suggesting the molecules are sufficiently close for some weak π–π interactions to be implicated.

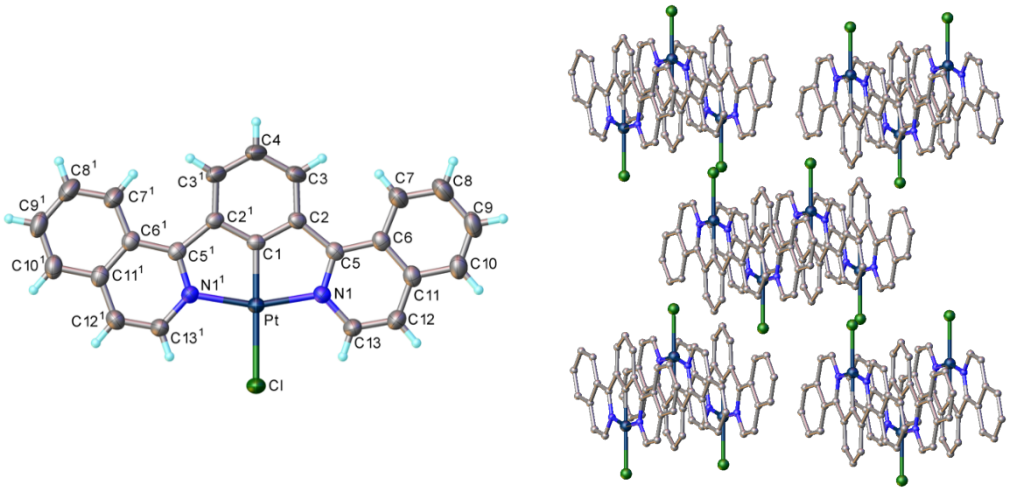

Figure 2.9: *Molecular structure and crystal packing of PtL[3]Cl.*

PtL[6]Cl packs in an off-centre head-to-tail fashion and is noticeably non-planar (**Figure 2.10**). The calculated bond angle between the plane of the phenyl ring and each isoquinoline ring is 29.52(5)° for one ring and 31.44(8)° for the other, with twists in the same direction. The twisting is evidently a result of steric clash between the methyl groups and H[8] of the isoquinoline rings. No metallophilic interactions are present in this structure (**Table 2.2**).

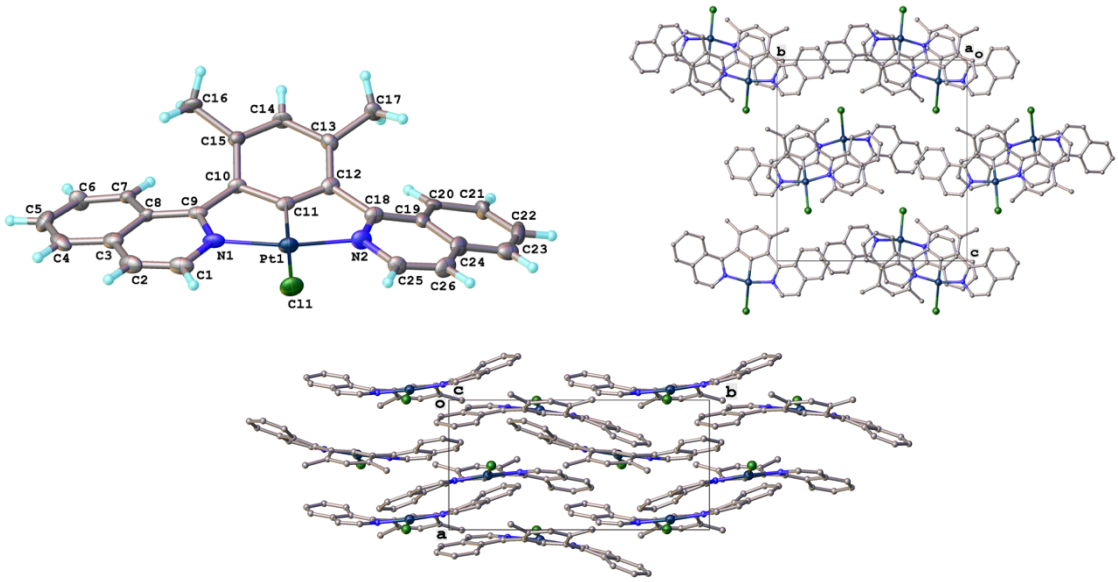

Figure 2.10: *Molecular structure and crystal packing of PtL[6]Cl highlighting the non-planarity.*

PtL^7Cl (**Figure 2.11**) and PtL^8Cl (**Figure 2.12**) pack in a head-to-tail arrangement. The latter is a methanol solvate, the crystal having been obtained from a solution in MeOH/DCM. The packing of PtL^7Cl is off-centre, with only slightly twisted isoquinoline rings relative to the phenyl ring (bond angles between the plane of each isoquinoline ring and phenyl ring of 17.98(9)° and 14.33(8)°) compared to PtL^6Cl. A summary of the Pt···Pt and interplanar distances, along with the packing arrangement (i.e. head-to-head or head-to-tail) is shown in **Table 2.2**.

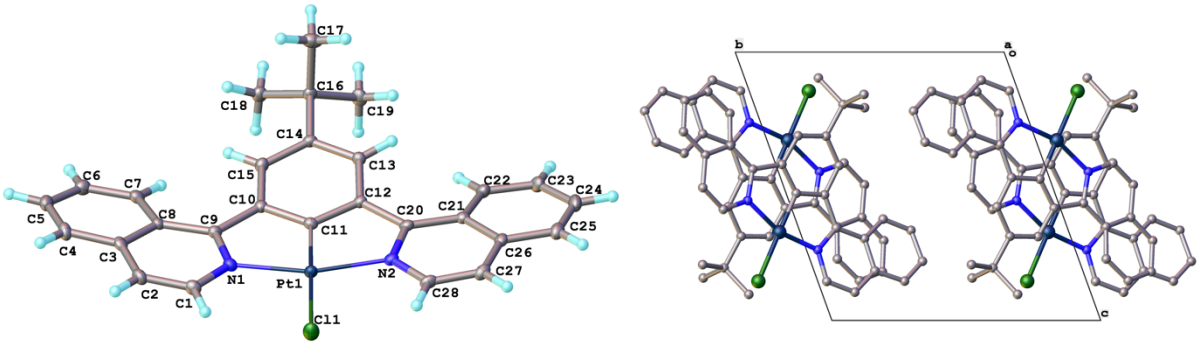

Figure 2.11: *Molecular structure and crystal packing of PtL^7Cl.*

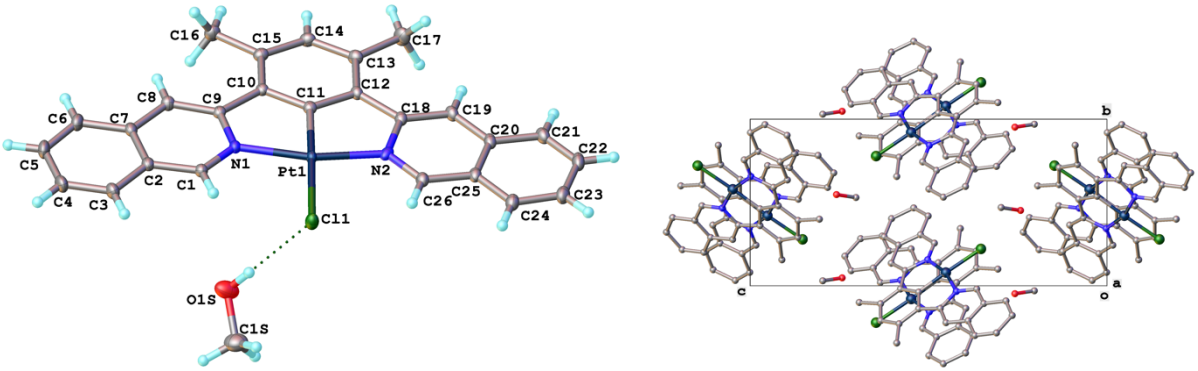

Figure 2.12: *Molecular structure and crystal packing of PtL^8Cl.*

Table 2.2: *A summary of intermolecular distances and packing arrangements in the crystal structures presented.*

Complex	Pt···Pt distance / Å	Interplanar distance / Å	Packing arrangement
PtL^1Cl ($CHCl_3$)	5.7896(5)	3.638(18)	Head-to-tail
PtL^1Cl (MeOH)	3.2137(3)	3.759(3)	Head-to-head
PtL^2Cl	4.3927(11)	3.399(12)	Head-to-tail
PtL^3Cl	5.1914(7)	3.582(3)	Head-to-tail
PtL^6Cl	6.0509(9)	3.833(8)	Head-to-tail
PtL^7Cl	5.222(15)	3.170(3)	Head-to-tail
PtL^8Cl	6.2543(5)	3.8463(16)	Head-to-tail

2.3.3 Chloride metathesis

The parent chloro complex, PtL^nCl, was readily converted into the iodo and thiocyanate derivatives in two steps (**Scheme 2.6**). Initial treatment with silver trifluoromethanesulfonate in acetone at room temperature led to the removal of the Cl ligand, which precipitated as AgCl and was separated by centrifugation. Acetone presumably enters the coordination sphere as a weakly bound, easily displaced ligand. The addition of KI or KNCS to the solution led to a precipitate of the desired complex with the new ancillary ligand. The products were purified by washing and recrystallisation.

The identities of the products were confirmed by ^1H NMR spectroscopy as a noticeable difference in the chemical shift of the H^6 proton adjacent to the metal (numbered H^3 in PtL^3NCS and PtL^7NCS) can be seen upon changing the ancillary ligand (shown in **Figure 2.13** for PtL^1X as a representative example). Compared to the parent chloro complex, PtL^1Cl, this signal is shifted to lower frequency in the SCN derivative and to higher frequency in the iodo derivative.

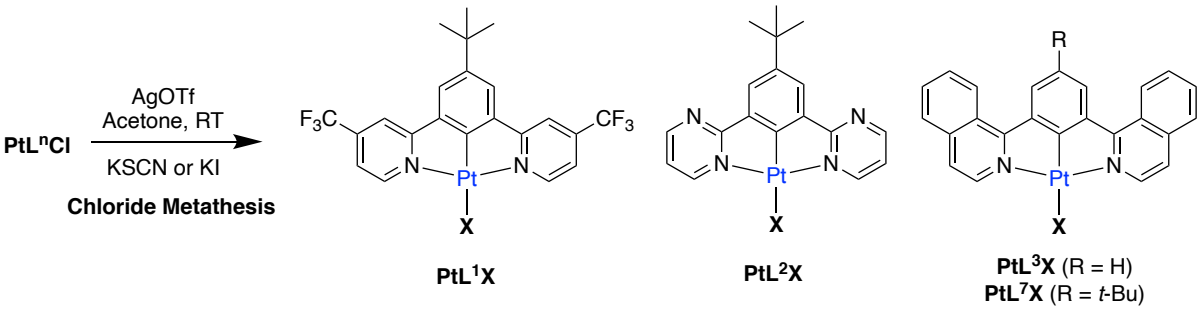

PtL^{1}X **PtL^{2}X** **PtL^{3}X** (R = H) **PtL^{7}X** (R = *t*-Bu)

	X = I	**X** = NCS
PtL^{1}X	60%	64%
PtL^{2}X	27%	42%
PtL^{3}X	-*	95%
PtL^{7}X	58%*	39%*

Scheme 2.6: *Synthesis of PtL$^{1-3}$X where X = I or SCN/NCS with yields. *PtL^{7}I and PtL^{7}NCS were synthesised by James Smith, Durham University MChem project student, under my supervision. The synthesis of PtL^{3}I yielded no isolable material likely due to insolubility of the product.*

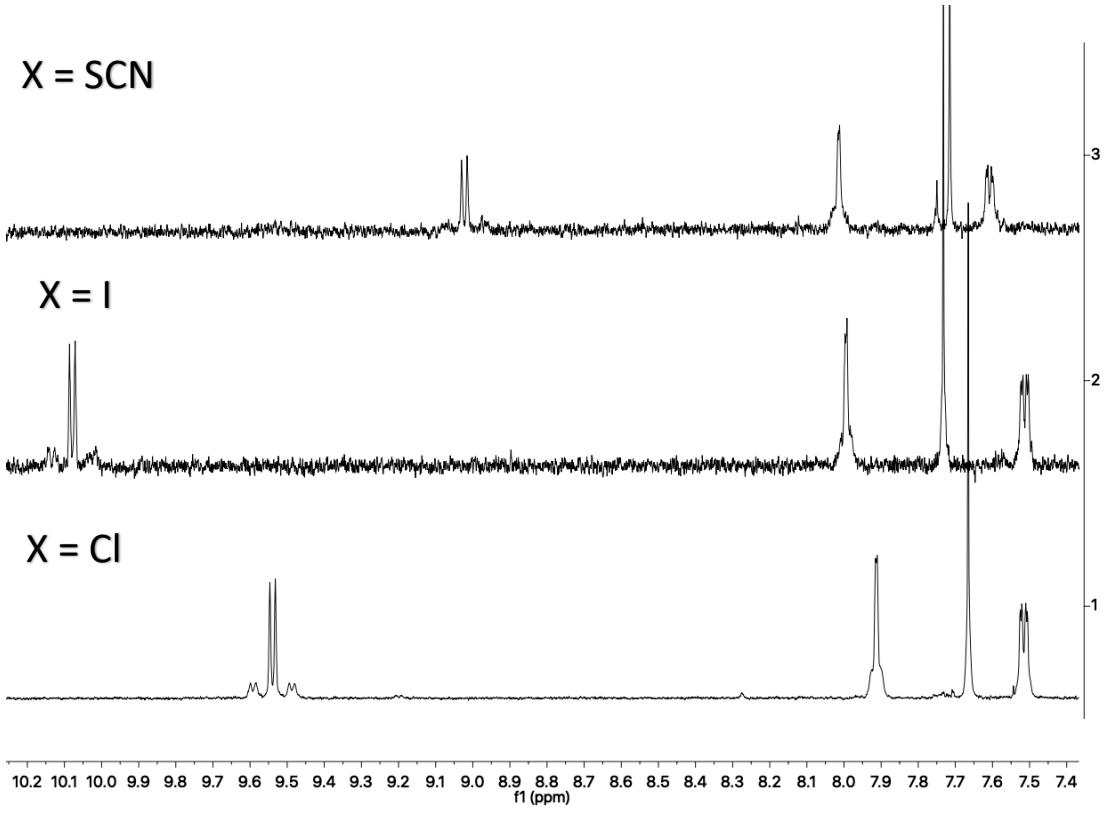

Figure 2.13: *NMR spectra of PtL^{1}Cl (1, bottom), PtL^{1}I (2, middle) and PtL^{1}SCN (3, top) in CD_2Cl_2 at 400 MHz highlighting the noticeable difference in the chemical shift of the H^6 proton.*

Note the different labelling of the thiocyanate ligand as either SCN or NCS; SCN is used to indicate S-bound and NCS indicates N-bound. Both binding modes have been observed in this research. The binding mode will be discussed in the following sections.

Crystals of PtL^2I suitable for x-ray diffraction were obtained by slow evaporation from DMF. The crystal structure of PtL^2I shows packing in a head-to-tail arrangement with no significant metal-metal interactions (**Figure 2.14**). The closest Pt···Pt distance is 5.0619(5) Å, though the interplanar distance is 3.4634(8)° indicative of weak π–π stacking interactions.

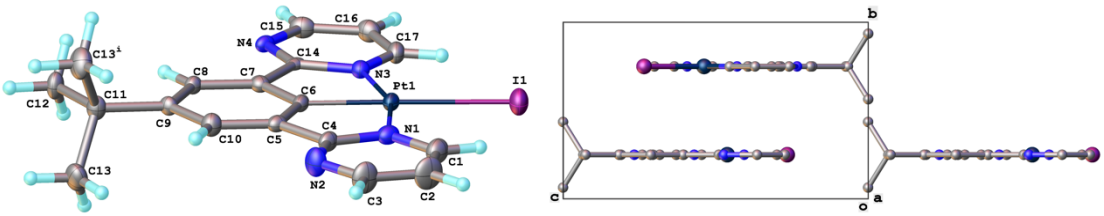

Figure 2.14: *Molecular structure and crystal packing of PtL^2I.*

Crystals of PtL^1SCN suitable for X-ray diffraction were grown by slow evaporation from $CDCl_3$ in an NMR tube and the structure showed a mixed Cl/SCN disorder, apparently due to degradation of the complex in chloroform (**Figure 2.15**). For all subsequent SCN/I complexes, the NMR spectrum was recorded in CD_2Cl_2 to avoid this issue. The molecule packs in a head-to-tail arrangement, though the packing may be influenced by the presence of the chloro impurity so no valid conclusion can be drawn about Pt···Pt interactions from this crystal structure (the shortest Pt···Pt distance here being 5.360(9) Å). As we have shown for PtL^1Cl, subtle changes in solvent for crystal growth can influence the packing and thus Pt···Pt/interplanar distances. Despite the disorder in the structure, it does reveal how the ancillary ligand is bound, namely through the sulphur atom (i.e. thiocyanate not isothiocyanate). This contrasts with the previous literature report of a

Pt(N^C^N)(NCS) complex that showed the monodentate ligand to be N-bound (refer back to **Figure 2.2**).[23]

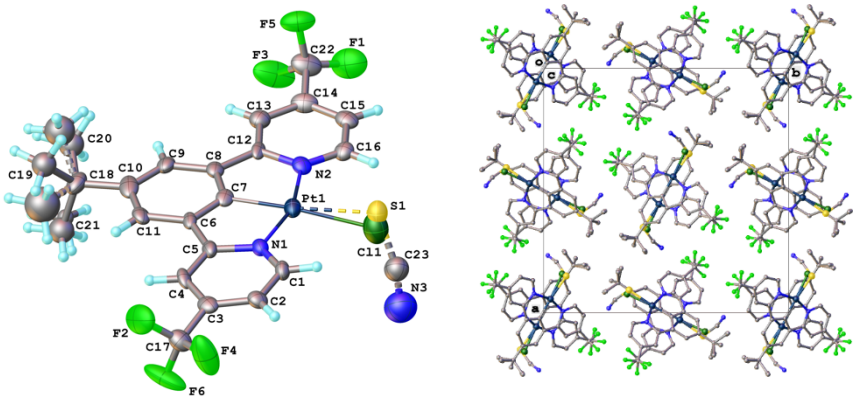

Figure 2.15: *Molecular structure and crystal packing of PtL[1]SCN showing a disordered structure with PtL[1]Cl and linkage to Pt via S.*

The crystal structure of PtL[3]NCS indicates that the ancillary thiocyanate ligand is N-bound and packs in a head-to-head arrangement with a Pt···Pt distance of 3.1594(4) Å indicative of metallophilic interactions (**Figure 2.16**). The corresponding parent PtL[3]Cl complex was arranged in a head-to-tail manner with no significant Pt···Pt interactions (**Figure 2.9**). The binding mode of the ancillary thiocyanate ligand likely depends on the nature of the N^C^N-coordinating ligand of the Pt complex. Reports have shown that the ligand can isomerise with changes in temperature and solvent[94–

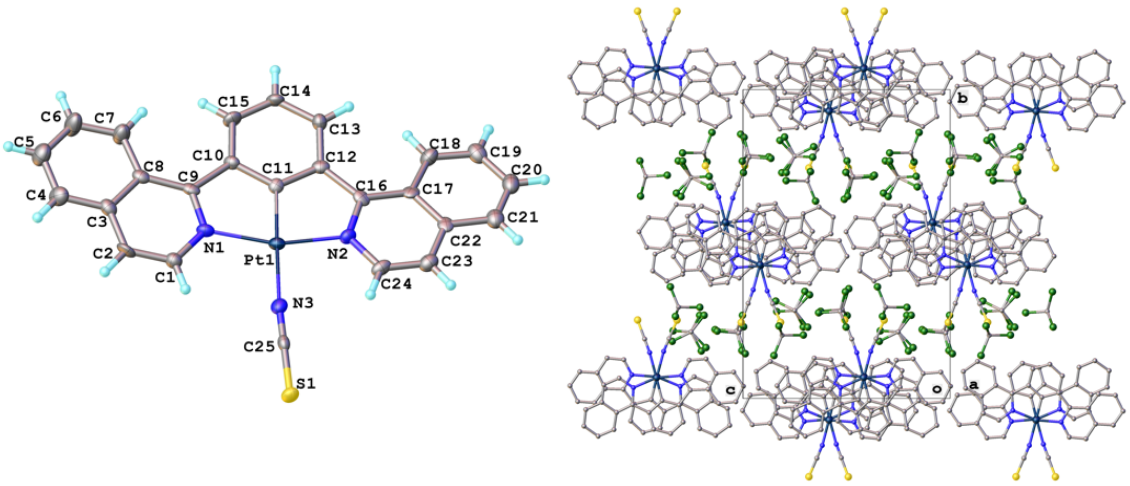

Figure 2.16: *Molecular structure and crystal packing of PtL[3]NCS shows the N-bound ancillary ligand and metallophilic interactions.*

[97]; the binding mode of the thiocyanate ancillary ligand may thus not be determinable solely by a crystal structure that is not necessarily representative of the bulk.

Infrared (IR) spectra were recorded of powders of each thiocyanate complex; the NCS/SCN stretching frequencies are given in **Table 2.3**. Interestingly, PtL^2NCS showed two bands at 2108 cm^{-1} and 2082 cm^{-1}. It was noted that this complex formed either a burgundy red or dark green powder depending upon the rate of solvent evaporation, in a similar manner to PtL^1Cl as discussed in Section 2.3.2. This is likely evidence that the thiocyanate ligand is isomerising in solution. As we know from the crystal structure that PtL^1SCN is S bound, the lowest energy stretching frequency of 2082 cm^{-1} for PtL^2NCS can be tentatively assigned to the S bound isomer, and the higher energy band at 2108 cm^{-1} the N bound complex. PtL^7NCS showed only one band at 2108 cm^{-1} suggesting the complex exists as only the N bound isomer. Only a small amount of pure PtL^3NCS was isolated, insufficient for IR analysis; the crystal structure revealed the ligand to be N bound.

Table 2.3: *IR stretching frequencies of the thiocyanate complexes.*

Complex	$\nu_{SCN/NCS}$ / cm^{-1}
PtL^1SCN	2074
PtL^2NCS	2108 and 2082
PtL^7NCS	2108

$^{15}N/^{195}Pt$ NMR may be a useful tool to further probe the binding mode of the thiocyanate ligand and could be used to monitor the reaction to see if one isomer is thermodynamically favoured and the other kinetically.

2.3.4 Solution-state photophysics

Photophysical data for complexes $PtL^{1\text{-}9}Cl$ can be found in **Table 2.4**. The absorption spectra of complexes $PtL^{1\text{-}9}Cl$ were measured in DCM at RT (**Figure 2.17**). The Beer-Lambert law, $A\,(\lambda) = \varepsilon\,(\lambda)\,cl$, is obeyed for all, at least for concentrations up to 10^{-4} M. Intense high-energy bands occur at $\lambda < 300$ nm ($\varepsilon > 20{,}000$ mol^{-1} dm^3 cm^{-1}) assigned to LC $\pi\rightarrow\pi^*$ transitions, whilst the somewhat weaker lower-energy bands are characteristic of CT.[52] They are observed due to transitions involving the metal or induced within the ligand as a result of cyclometallation, consistent with an increase in electron density on the metal.

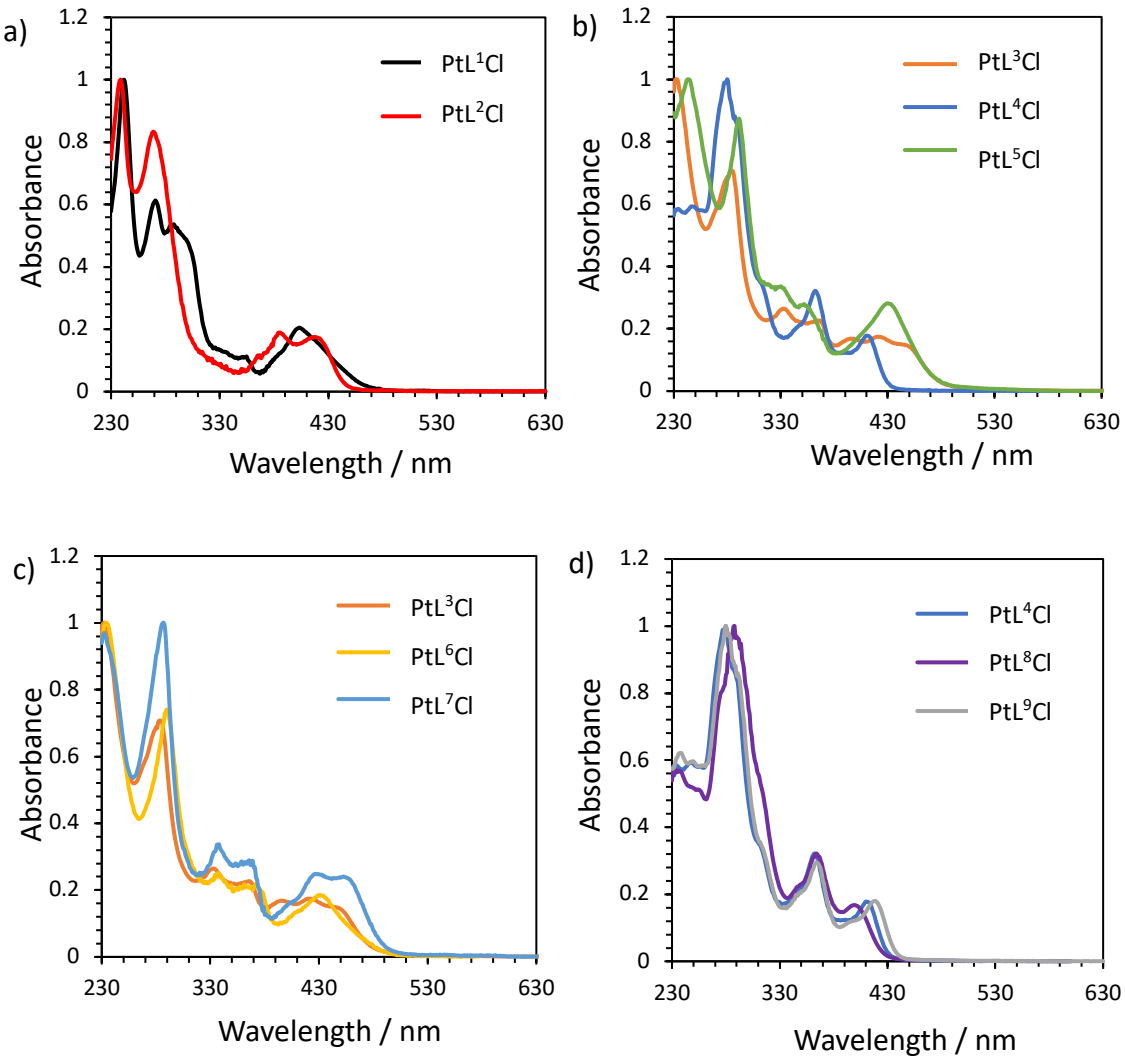

***Figure 2.17**: Absorption spectra of $PtL^{1\text{-}9}Cl$ in DCM at 295 K, normalised to λ_{max}.*

Figure 2.17 (a) shows the absorption spectra of complexes PtL^1Cl and PtL^2Cl; the former has a CT band peaking at 405 nm whilst the latter shows two peaks in this region at 387 and 420 nm. The energies of these CT bands are comparable to that of the parent Pt(dpyb)Cl which peaks at 402 nm (**Table 2.4**). **Figure 2.17** (b) compares the absorption spectra of the parent complexes bearing different isoquinoline/quinoline rings. The lower energy CT band is significantly red-shifted by approx. 40 nm for PtL^3Cl (1-isoquinoline) and PtL^5Cl (quinoline) compared to PtL^4Cl (3-isoquinoline).

Figure 2.17 (c) compares the absorption spectra of the 1-substituted isoquinoline complexes; the tail of the lowest energy absorption band is slightly red-shifted for PtL^7Cl, perhaps due to the slightly electron-donating *t*-butyl substituent on the central phenyl ring. **Figure 2.17** (d) shows the absorption spectra of the 3-substituted isoquinoline complexes. The spectral profile is similar for each complex in the series, with the lowest energy absorption band slightly red shifting in the order PtL^8Cl < PtL^4Cl < PtL^9Cl, with the parent sitting in the middle. The fact that the band is slightly blue-shifted for PtL^8Cl suggests that the methyl groups on the 2- and 4-positions of the central phenyl ring also affect the LUMO energy (to a greater extent) as well as the HOMO. PtL^9Cl is red-shifted as expected with the *t*-butyl substituent on the central phenyl ring.

Emission spectra were recorded in degassed DCM solution at RT (**Figure 2.18**). All complexes are brightly luminescent with most displaying structured spectra in dilute solution, attributed to unimolecular emission (i.e. isolated molecules as opposed to dimers or excimers). The excitation wavelength for each complex was chosen based on the tail of the lowest-energy absorption band. Experimental details are outlined in Section 7.1. The reported PLQY in all cases is determined from the emission spectrum in dilute deoxygenated DCM solution at a concentration of ~ 10^{-6} M.

The monomer emission for PtL^2Cl is blue-shifted compared to PtL^1Cl (**Figure 2.18a**), suggesting the 4-substituted CF_3-pyridine has a greater stabilising effect on the LUMO energy than the pyrimidine rings. The emission of both complexes is red-

shifted compared to Pt(dpyb)Cl. The emission spectra of complexes $PtL^{3-5}Cl$ containing isoquinoline/quinoline rings are shown in (b). The λ_{max} of monomer emission follows the order $PtL^4Cl < PtL^5Cl < PtL^3Cl$ with the most red-shifted emission seen for PtL^3Cl, the complex of 1-isoquinoline. This trend follows the trend in absorption spectra, except the tail of the lowest energy absorption band is almost identical for PtL^5Cl and PtL^3Cl. The spectral profile of PtL^4Cl potentially suggests that the complex is not as rigid, with the (0,2) or (0,3) transition now the most intense.

Table 2.4: *Photophysical parameters for $PtL^{1-9}Cl$ in deoxygenated (aerated in parentheses) DCM solution at 298 K, with references if quoted from the literature.*[i]

Complex	λ_{abs} / nm [a] (ε / M^{-1} cm^{-1})	λ_{em} / nm [b] (monomer)	λ_{em} / nm [c] (excimer)	Φ_{lum} [d] [aer]	τ / ns [e] [aer]	τ_0 / μs [f]	k_r / 10^3 s^{-1} [g]	$\sum k_{nr}$ / 10^3 s^{-1} [h]	k_{SQ} / 10^9 M^{-1} s^{-1} [i]	$k_Q(O_2)$ / 10^8 M^{-1} s^{-1} [j]
PtL^1Cl	244 (36200), 272 (23000), 290 (19800), 305 (16700), 358 (3460), 382sh (4250), 405 (7630)	533, 570	750	0.91 [0.11]	6500 [790]	6.5	140	10	1.0	5.0
PtL^2Cl	240 (26100), 270 (22100), 362sh (2550), 387 (4830), 420 (4480)	500, 531, 584sh	701	0.60 [0.04]	7400 [400]	7.9	81	54	1.5	10.6
PtL^3Cl	285 (41200), 333 (12700), 363 (11500), 397 (7800), 423 (11500), 446 (9800)	597, 637, 684sh	801	0.13	4300 [3600]	3.1	30	200	2.0	0.2
PtL^4Cl	276 (71400), 285sh (60400), 315sh (27500), 360 (22900), 408 (12600)	515, 556, 602	669	0.28	30000 [680]	35	5 (ref[56])	20 (ref[56])	2.0	6.6
PtL^5Cl	245 (36500), 292 (33000), 333 (11800), 355 (9570), 430 (10800)	577sh, 607	-	0.43 [0.07]	5700 [820]	6.4	76	100	3.4	4.7

[i] a) λ_{abs} values with corresponding molar extinction coefficients; b) λ_{max} value for unimolecular emission bands; c) λ_{max} value for the excimer band; d) Luminescence quantum yield in dilute deoxygenated solution, measured using $[Ru(bpy)_3]Cl_2$ (aq) as the standard (Φ_{PL} = 0.04).[161] Self-quenching is negligible under these dilute conditions, such that the Φ_{lum} values refer specifically to the unimolecular photoluminescence. The associated error is approx. ± 20%; e) Lifetime of the most dilute solution used to measure Φ_{lum} in both degassed and aerated solution. The associated error is approx. ± 15% or better; f) Lifetime at infinite dilution, estimated by extrapolation of a plot of $1/\tau$ versus concentration, c, to c = 0; g and h) Estimates of k_r and k_{nr} assuming that the emitting state is formed with unit efficiency such that $k_r = \Phi/t$ and $k_{nr} = (1 - \Phi)/\tau$; i) Self-quenching rate constant estimated from the gradient of the plot of $1/\tau$ versus concentration; j) Oxygen-quenching rate constant estimated from the lifetimes in degassed and aerated solution using $1/\tau_{aer} = k_r + k_{nr} + k_Q[O_2]$ where $[O_2]$ is the concentration of O_2 in DCM at a pressure of 1 atm air at RT (2.2 mmol dm^{-3}). These parameters will be used throughout this thesis, defined as stated here.

Complex	λ_{abs} / nm [a] (ε / M^{-1} cm^{-1})	λ_{em} / nm [b] (monomer)	λ_{em} / nm [c] (excimer)	Φ_{lum} [d] [aer]	τ / ns [e] [aer]	τ_0 / μs [f]	k_r / 10^3 s^{-1} [g]	$\sum k_{nr}$ / 10^3 s^{-1} [h]	k_{SQ} / 10^9 M^{-1} s^{-1} [i]	$k_Q(O_2)$ / 10^8 M^{-1} s^{-1} [j]
PtL^{6}Cl	240 (35300), 291 (32100), 340 (9910), 368 (8950), 380 (7340), 430 (14200)	625, 660	-	0.11 [0.02]	2900 [480]	2.9	37	300	0.15	8.0
PtL^{7}Cl	289 (31300), 340 (14100), 370 (12200), 402 (6940), 433 (10400), 455 (10200)	603, 652	710	0.16 [0.02]	3500 [490]	3.6	46	240	1.6	7.9
PtL^{8}Cl	286 (62300), 360 (19600), 395 (10800)	517, 552, 608	680	0.23	23000	41	4	14	3.0	-
PtL^{9}Cl	281 (10900), 345sh (14800), 365 (24400), 399sh (9220), 420 (13900)	524, 566, 615, 672sh	687	0.51 [0.01]	58000 [550]	65	9	8	1.4	8.2
Pt(dpyb)Cl (ref[36])	332 (6510), 380 (8690), 401 (7010), 454 (270), 485 (240)	491, 524, 562	700	0.60 [0.04]	7200 [500]	7.2	83	55	5.3	-

The value of k_r is significantly lower for PtL^4Cl than for PtL^3Cl with values of 5×10^3 s^{-1} and 40×10^3 s^{-1} respectively, though counterintuitively PtL^4Cl has a higher PLQY than PtL^3Cl with values of 0.28 and 0.09 respectively. The difference in the emission spectra of PtL^3Cl and PtL^4Cl, rationalised by considering the frontier orbitals from DFT calculations, was discussed by Louise Parkes in her PhD thesis.[59] In PtL^3Cl the LUMO is evenly distributed over the entire tridentate ligand with a 96% contribution and only 4% localisation on Pt. Conversely, the density of the LUMO of PtL^4Cl is concentrated on the outer isoquinolyl rings with virtually no localisation on the central phenyl ring.[59] This ensures a very distinct separation of the HOMO and LUMO for PtL^4Cl, which might explain the low k_r value; the radiative rate constant is dependent upon the overlap integral of the HOMO-LUMO. The higher PLQY for PtL^4Cl compared to PtL^3Cl can be explained by the increased metal contribution to the HOMO for PtL^4Cl (57% compared to 48% for PtL^3Cl), which leads to higher SOC.

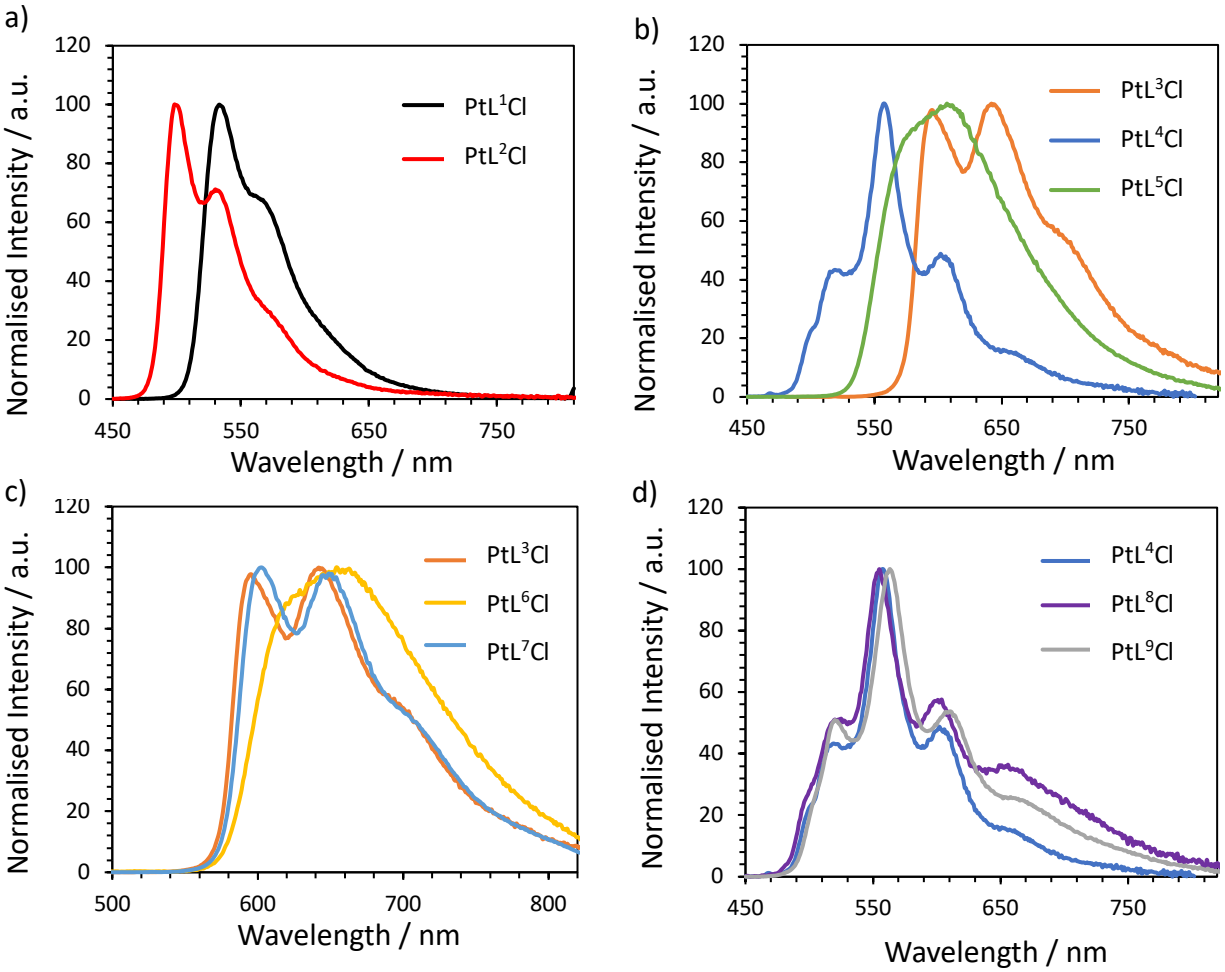

Figure 2.18: *Emission spectra of $PtL^{1-9}Cl$ in dilute (10^{-5} M) degassed DCM solution highlighting monomeric emission.*

The emission spectra of complexes substituted with 1-isoquinoline are shown in **Figure 2.18** (c). The spectral profile and wavelength of emission for *t*-butyl substituted PtL^7Cl is almost identical to that of the parent PtL^3Cl whereas PtL^6Cl exhibits red-shifted and less structured emission, more comparable to that of PtL^5Cl. The crystal structure of PtL^6Cl was noticeably non-planar (**Figure 2.10**), which could be the reason for this difference in the emission profile as the LUMO will presumably no longer be delocalised over the entire ligand.

Finally, **Figure 2.18** (d) shows the emission spectra of complexes substituted with 3-isoquinoline rings. The emission is almost identical for each complex, with the (0,0) component no longer being the most intense band. Along with their parent, PtL^4Cl, PtL^8Cl and PtL^9Cl also have relatively low k_r values (4×10^3 s^{-1} and 3×10^3 s^{-1} respectively) when compared to all other Pt(N^C^N)Cl complexes presented, for reasons discussed above for 3-substituted isoquinoline complexes. Moreover, the complexes show unusually long lifetimes in the range of 23 – 58 µs. An additional, broad, low-energy band between 650 and 750 nm can be seen even in dilute solution, attributed to the formation of excimers. This effect was studied further by recording the emission spectra of each complex in solutions of increasing concentration.

All complexes show concentration-dependent figures for Φ and τ due to self-quenching and a lower QY of any resulting excimer, with a much higher emissive lifetime observed in dilute solution. The emission lifetime of the monomer at infinite dilution, τ_0, and the apparent rate-constant of self-quenching, k_{SQ}, were determined (**Equation 2.1**) from the linear Stern-Volmer variation of the observed emission decay rate constant, k_{obs}, as a function of the concentration of the complex, [Pt]. A high value of k_{SQ} indicates very efficient excimer formation. All values obtained are typical for a diffusion-controlled process, as is excimer formation (**Table 2.4**).[98]

$$k_{\mathrm{obs}} = {}^{1}/_{\tau_0} + k_{\mathrm{SQ}}[\mathrm{Pt}] \qquad (2.1)$$

PtL^1Cl shows the formation of a low energy broad emission band at 750 nm at elevated concentration, attributed to excimer formation (**Figure 2.19**). This excimer

band is red shifted by 50 nm compared to that of Pt(dpyb)Cl, suggesting that the CF_3-substituted pyridine and *t*-butyl substituent on the phenyl ring stabilise the excimer as well as the monomer.

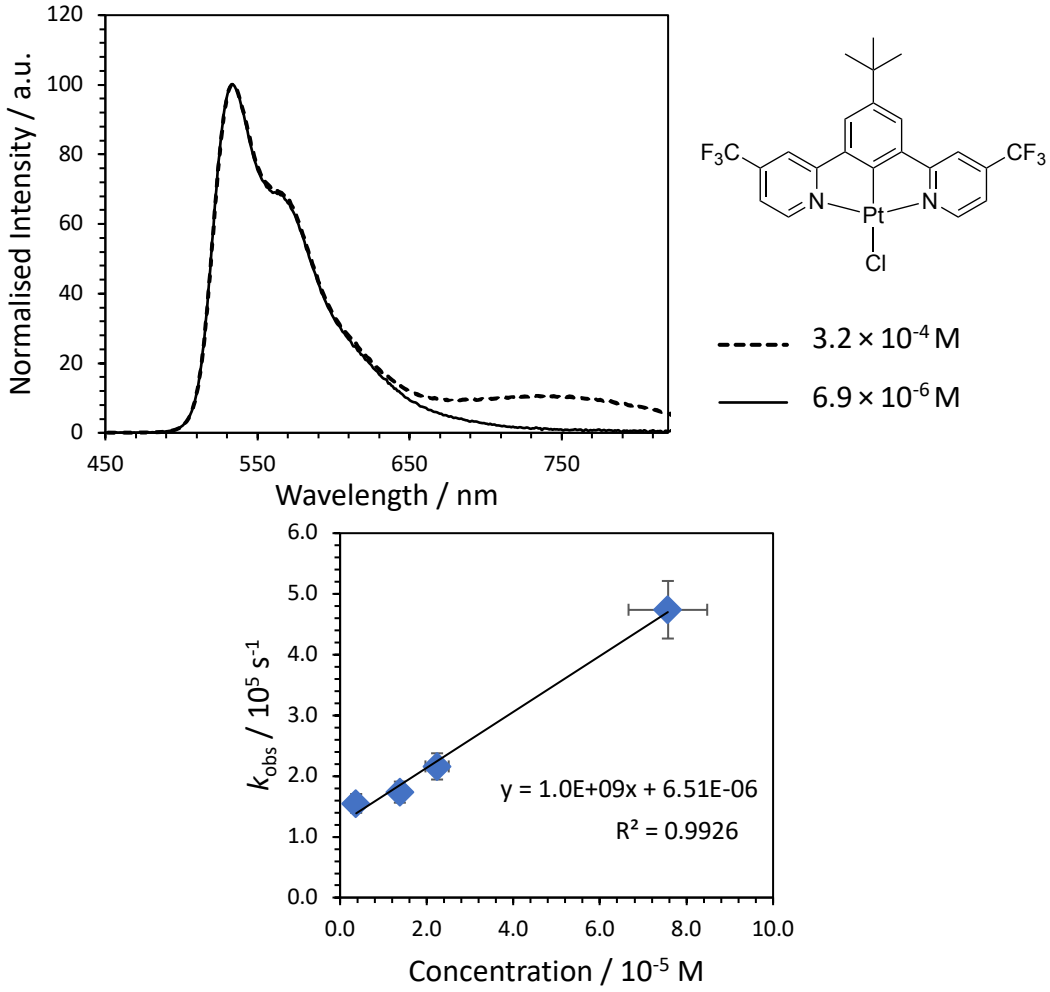

Figure 2.19: *Emission spectra of PtL^1Cl at 6.9 × 10⁻⁶ M (solid line) and 3.2 × 10⁻⁴ M (dashed line) in degassed DCM solution at RT (top) and the corresponding Stern-Volmer plot (bottom) at these and two other intervening concentrations. Errors are discussed in Section 7.1.*

The emission spectra of PtL^2Cl in dilute and concentrated degassed DCM solution are shown in **Figure 2.20**. The ratio of the excimer to monomer band is larger for PtL^2Cl compared to PtL^1Cl, despite the concentration of the saturated solution of the former being lower. The value of k_{SQ} for PtL^2Cl is also double that of PtL^1Cl (10.6×10^8 M^{-1} s^{-1} and 5.0×10^8 M^{-1} s^{-1} respectively). This suggests that the pyrimidine rings increase the propensity to excimer formation with respect to CF_3-substituted pyridine. The energy of the excimer is lower for PtL^2Cl than for PtL^1Cl, with a λ_{max} of 701 nm, the

same as the parent Pt(dpyb)Cl. Thus it appears that pyrimidine rings red shift the monomer emission but seem to have little effect on excimer emission. The PLQY for PtL^2Cl is also identical to Pt(dpyb)Cl (0.60) whereas the PLQY of PtL^1Cl is significantly higher at 0.91, reflecting the simultaneous enhancement of k_r and reduction of k_{nr} (**Table 2.4**).

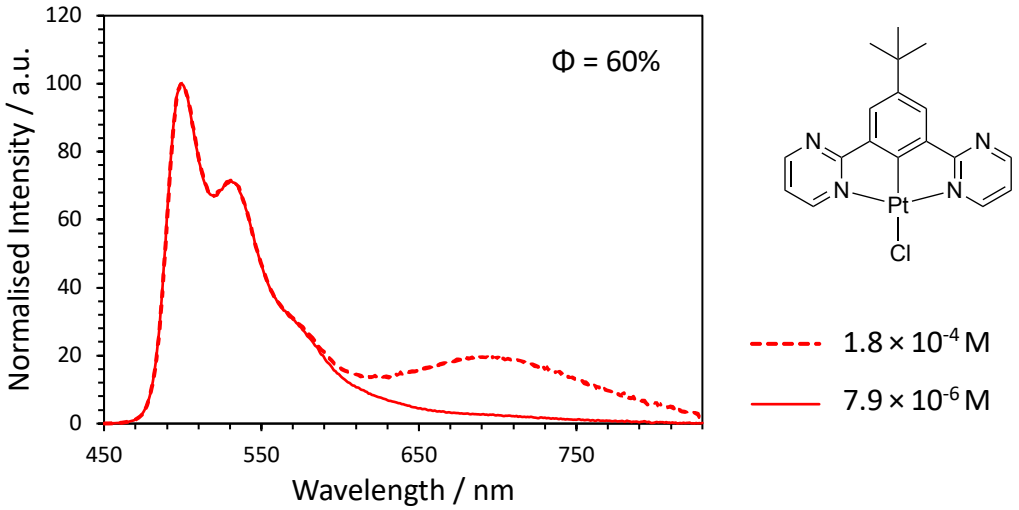

Figure 2.20: *Emission spectra of PtL^2Cl at 7.9×10^{-6} M (solid line) and 1.8×10^{-4} M (dashed line) in degassed DCM solution at RT.*

Complexes of 1-isoquinoline (PtL^3Cl, PtL^6Cl and PtL^7Cl) were overall less prone to excimer formation. Excimer emission was seen for PtL^3Cl only in concentrated solution (3×10^{-4} M), peaking in the NIR region of the spectrum around 800 nm. **Figure 2.21** depicts the emission spectra of PtL^3Cl in dilute and concentrated degassed DCM solution at RT. The excimer emission is difficult to separate from the (0,4) unimolecular emission peak as they overlap. PtL^6Cl, substituted with methyl groups at the 2- and 4-positions of the central phenyl ring, showed no evidence of excimer formation over the concentration range investigated (up to 5×10^{-4} M). This is possibly due to the non-planarity of the complex affecting its ability to pack, as highlighted in the crystal structure (**Figure 2.10**). This is also reflected in the low value of k_{SQ} at 0.15×10^9 M^{-1} s^{-1} compared to 2.0×10^9 M^{-1} s^{-1} for the parent PtL^3Cl and 1.6×10^9 M^{-1} s^{-1} for PtL^7Cl (substituted with *t*-butyl).

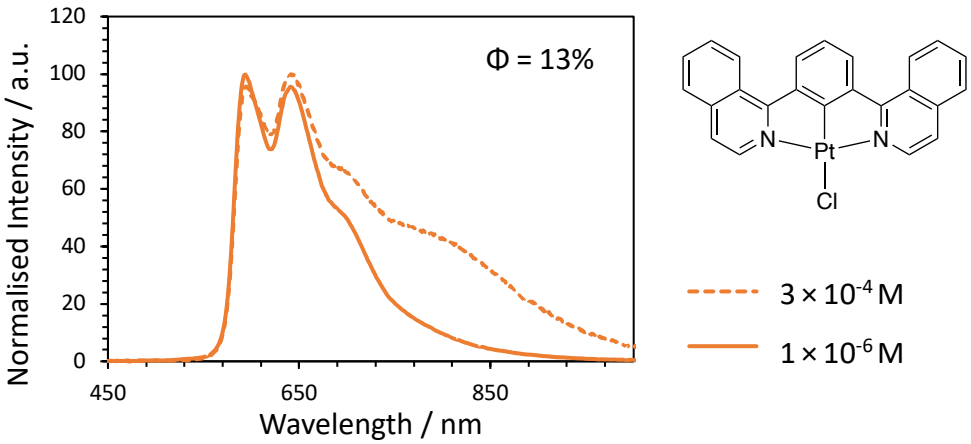

Figure 2.21: *Emission spectra of PtL[3]Cl at 1 × 10[-6] M (solid line) and 3 × 10[-4] M (dashed line) in degassed DCM solution. Measurements run by Dr Piotr Pander using a CCD detector that offers sensitivity further into the NIR.*

PtL[7]Cl displayed excimer emission centred around 800 nm (**Figure 2.22**). Complexes of 1-isoquinoline exhibit the most red shifted excimer emission spectra, following the trend for the monomer emission. PtL[5]Cl, featuring quinoline rings, showed no sign of excimer formation over the concentration range investigated (limited to 1×10^{-4} M due to solubility).

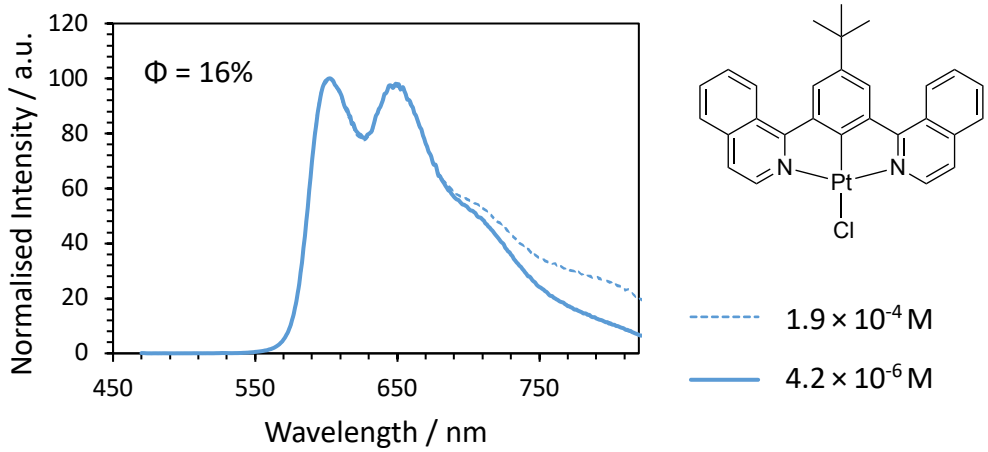

Figure 2.22: *Emission spectra of PtL[7]Cl at 4.2 × 10[-6] M (solid line) and 1.9 × 10[-4] M (dashed line) in degassed DCM solution at RT.*

Complexes of 3-isoquinoline (PtL[4]Cl, PtL[8]Cl and PtL[9]Cl) all exhibit concentration-dependent emission with the appearance of a broad structureless red-shifted band, assigned to excimer formation, at elevated concentrations (**Figure 2.23** and **Figure**

2.24). These complexes with 3-substituted isoquinoline rings in particular show a high propensity to excimer formation, reflected in the relative intensity of the excimer band which greatly surpasses the monomer intensity at high concentrations of solution. The wavelength of excimer emission is red shifted for the substituted complexes compared to the parent PtL^4Cl (λ_{max} = 669 nm); it is also slightly different for each substituted complex in the series (680 and 687 nm for PtL^8Cl and PtL^9Cl respectively) despite the monomer emission being almost identical. This suggests that the various substituents on the central phenyl ring are altering the intermolecular interactions and hence the excimer emission energy.

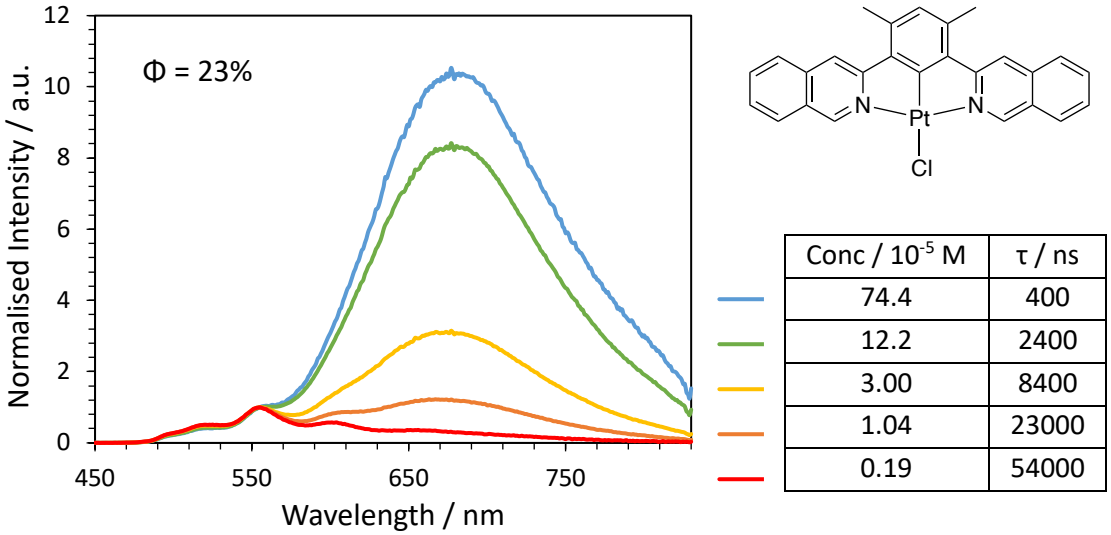

Conc / 10^{-5} M	τ / ns
74.4	400
12.2	2400
3.00	8400
1.04	23000
0.19	54000

Figure 2.23: *Concentration-dependent emission of PtL^8Cl in degassed DCM solution at RT, normalised to 555 nm.*

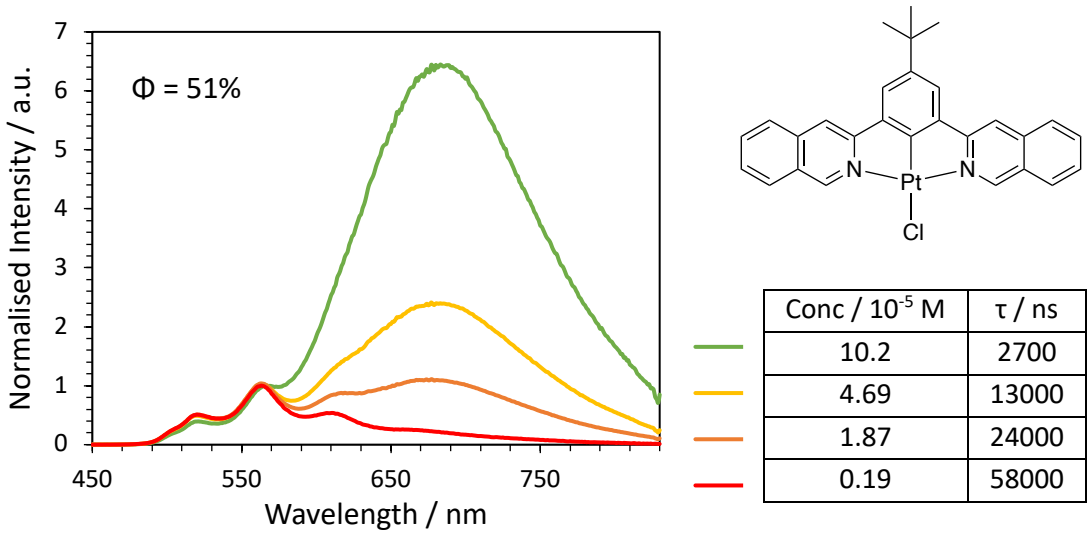

Conc / 10^{-5} M	τ / ns
10.2	2700
4.69	13000
1.87	24000
0.19	58000

Figure 2.24: *Concentration-dependent emission of PtL^9Cl in degassed DCM solution at RT, normalised to 567 nm.*

Time-correlated single photon counting (TCSPC) measurements can be used to support the assignment of the long wavelength bands to the presence of excimers and not aggregates. Temporal evolution of the low energy emission of all complexes displaying this feature (shown in **Figure 2.25** for PtL^9Cl as a representative example) is compared to the monomeric emission, with the latter appearing to reach its peak instantaneously, within the timescale of the initial data collection. On the other hand, the emission at 680 nm for PtL^9Cl takes time to reach its maximum, clearly showing a rise-time of several hundred nanoseconds. This indicates that the long wavelength emission, or at least some of it, is due to a species that takes time to form, i.e. an excimer that relies on diffusion of an excited state molecule to find and interact with a ground state molecule. If the emission was due to a pre-existing aggregate, one would expect the emission to appear instantaneously. Once formed, the excimer appears to decay with the same kinetics as the monomer.

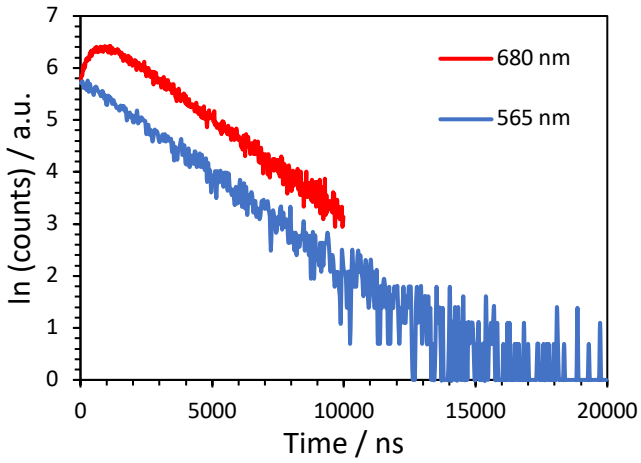

Figure 2.25: *TCSPC measurements for PtL^9Cl probing the monomer at 565 nm (blue) and excimer at 680 nm (red).*

Additional studies on the excimer formation mechanism and kinetics of complexes $PtL^{1\text{-}3}Cl$ were carried out by Dr Piotr Pander (Durham University Physics Department). Detailed information can be read in the paper arising from this work.[99]

PtL^nX Complexes where X = I or NCS

The absorption and photoluminescence emission spectra of PtL^1X (where X = Cl, SCN or I) in dilute solutions are shown in **Figure 2.26**. It is apparent that the ancillary ligand

has little effect on unimolecular emission as all complexes display similar luminescence in solution. Nevertheless, there are some differences. PtL^1I displays slightly red-shifted photoluminescence compared to X = SCN, and a small red shift of the lowest energy absorption band. The most remarkable results to note are the high PLQY values obtained upon substitution of the ancillary ligand, which are close to unity for PtL^1SCN and PtL^1I (**Table 2.5**) due to the low non-radiative decay values (0 and 10×10^3 s^{-1} respectively).

Weak, broad, long-wavelength emission can be seen for each complex in solution upon increasing the concentration (**Figure 2.27**), indicative of excimer formation. It appears that the energy of the excimer emission in solution is slightly red shifted in the order PtL^1SCN < PtL^1Cl < PtL^1I, though the excimer emission for PtL^1I is so weak that this complex was not probed further.

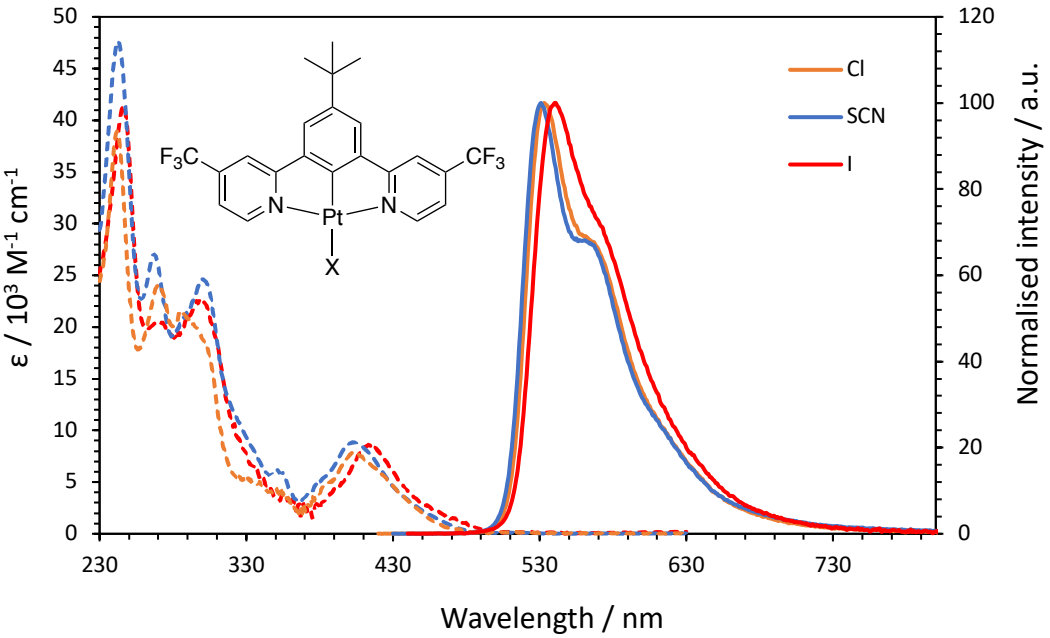

Figure 2.26: *Comparison of absorption (dashed line) and photoluminescence (solid line) spectra in degassed DCM solution of complexes PtL^1X where X = Cl (orange), SCN (blue) or I (red).*

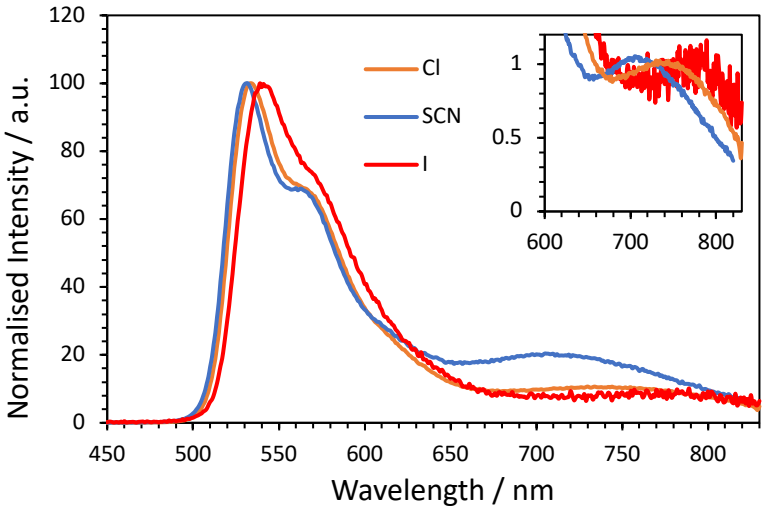

Figure 2.27: *Emission spectra of complexes PtL[1]X where X = Cl, SCN and I, in concentrated degassed DCM solution at RT (3 x 10[4], 3 x 10[-4] and 5 x 10[-4] M respectively) showing weak excimer emission (normalised to excimer inset).*

The absorption and photoluminescence emission spectra of PtL[2]X (where X = Cl, NCS or I) in dilute solutions are shown in **Figure 2.28**. Like the analogous PtL[1]X series, there is no significant difference in the absorption or emission spectra upon changing the ancillary ligand. The PLQYs increase upon going from X = Cl to NCS and then to I, with values of 0.49, 0.67 and 0.86 respectively. These values are a little lower than the PtL[1]X series.

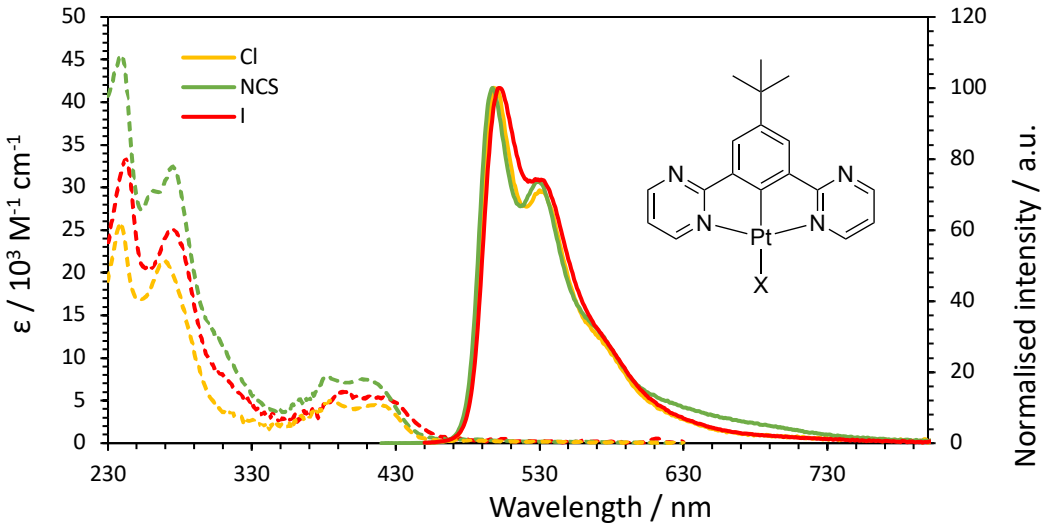

Figure 2.28: *Comparison of absorption (dashed line) and photoluminescence (solid line) spectra in degassed DCM solution of complexes PtL[2]X where X = Cl (yellow), NCS (green) or I (red).*

Each complex in the series shows an additional lower energy excimer band at high concentration (**Figure 2.29**). The emission band is similar in both intensity and wavelength for PtL^2Cl and PtL^2I, but blue-shifted for PtL^2NCS by approx. 50 nm. PtL^2NCS also has the highest propensity to excimer formation as the self-quenching constant is the largest (**Table 2.5**). Concentration-dependent emission of this complex is shown in **Figure 2.30**.

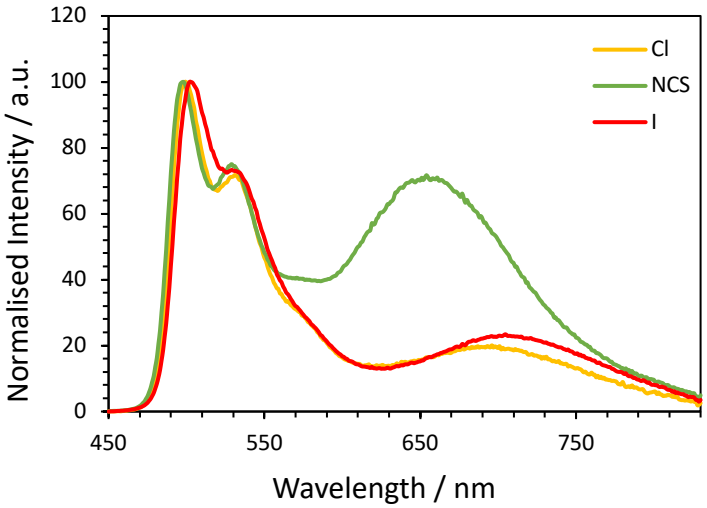

Figure 2.29: *Emission spectra of complexes PtL^2X where X = Cl, NCS and I, in concentrated degassed DCM solution at RT (all at 2 x 10^4 M) showing excimer emission.*

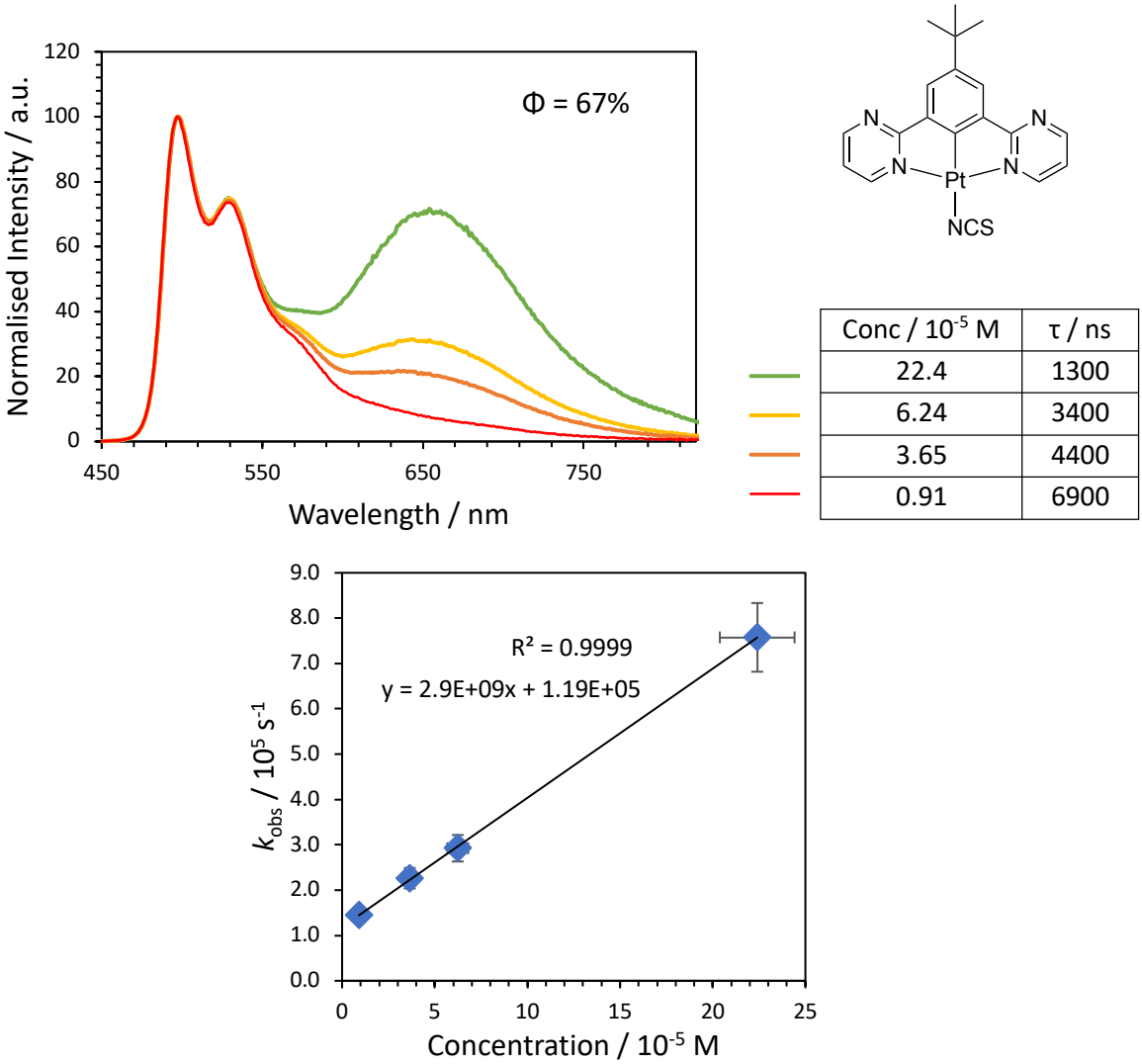

Figure 2.30: *Concentration-dependent emission spectra of PtL²NCS in degassed DCM solution, with lifetimes of the monomer emission band. Bottom: corresponding Stern-Volmer plot. See Section 7.1 for a discussion of the errors.*

Table 2.5: *Summary of spectroscopic properties of PtL^nX, where X = Cl, SCN/NCS or I, in degassed (aerated in parentheses) DCM solution at 298 K.*

Complex	λ_{abs} / nm (ε / M^{-1} cm^{-1})	λ_{em} / nm (monomer)	λ_{em} / nm (excimer)	Φ_{lum} [aer]	τ / ns [aer]	τ_0 / μs	k_r / 10^3 s^{-1}	$\sum k_{nr}$ / 10^3 s^{-1}	k_{SQ} / 10^9 M^{-1} s^{-1}	$k_Q(O_2)$ / 10^8 M^{-1} s^{-1}
PtL^1Cl	244 (36200), 272 (23000), 290 (19800), 305 (16700), 358 (3460), 382sh (4250), 405 (7630)	533, 570	750	0.91 [0.11]	6500 [790]	6.5	140	10	1.0	5.0
PtL^1SCN	245 (45800), 269 (26100), 305 (23000), 356 (5400), 405 (8700)	531, 567	744	1.0 [0.19]	6900 [880]	7.3	190	0	1.4	4.5
PtL^1I	248 (38800), 274 (19700), 304 (20800), 360 (3520), 415 (8300)	541, 573	-	0.92 [0.11]	5700 [650]	6.1	160	10	2.0	6.2
PtL^2Cl	240 (26100), 270 (22100), 362sh (2550), 387 (4830), 420 (4480)	500, 531, 584sh	701	0.60 [0.04]	7400 [410]	7.9	81	54	1.5	10.6
PtL^2NCS	266 (35500), 279 (29000), 359 (4120), 388 (7400), 400 (7180), 417 (7080)	497	657	0.67 [0.05]	6900 [450]	8.4	100	50	2.9	9.4
PtL^2I	244 (32300), 279 (23100), 400 (4980), 420 (5010)	502	710	0.86 [0.05]	6200 [340]	6.6	140	20	2.4	12.6
PtL^3NCS	237 (9550), 282 (8390), 342 (3560), 368sh (2690), 405sh (1970), 420 (2490), 443sh (1960)	590, 641, 699sh	760	0.16 [0.02]	3900 [510]	3.9	40	220	0.24	7.7
PtL^7NCS	285 (16630), 344 (6660), 369 (4890), 403 (2940), 430 (3750), 446sh (3160)	602, 649, 707sh	770	0.21 [0.01]	3900 [470]	4.0	50	200	0.5	8.6
PtL^7I	282 (36600), 344 (15400), 368sh (10700), 410sh (6480), 435 (9960), 450 (9460)	606, 649, 704sh	780	0.16 [0.02]	3500 [470]	3.4	50	240	2.5	8.3

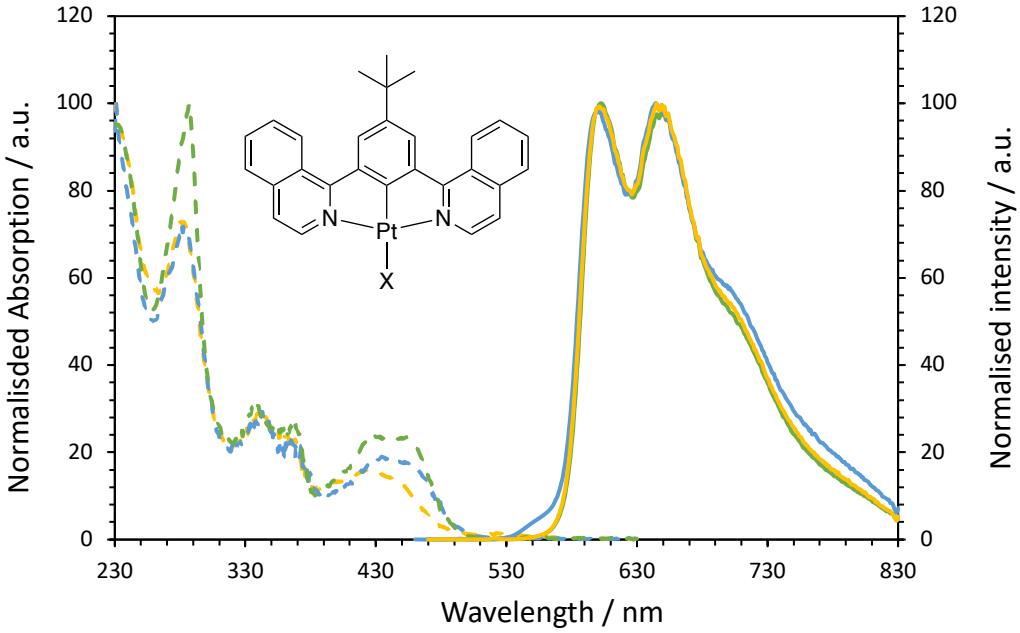

Figure 2.31: *Comparison of absorption (dashed line) and photoluminescence (solid line) spectra in degassed DCM solution of complexes PtL^{7}X where X = Cl (green), NCS (blue) or I (yellow).*

The absorption and photoluminescence spectra of PtL^{7}X (where X = Cl, NCS or I) are shown in **Figure 2.31**. This series of complexes follows the same pattern as PtL^{1}X and PtL^{2}X: the photoluminescence in solution is almost identical, and the excimer emission is more prominent for PtL^{7}NCS, albeit still weak in intensity (**Figure 2.32**). This excimer band may also be blue shifted for PtL^{7}NCS, though that is hard to distinguish as it overlaps with the (0,4) transition peak.

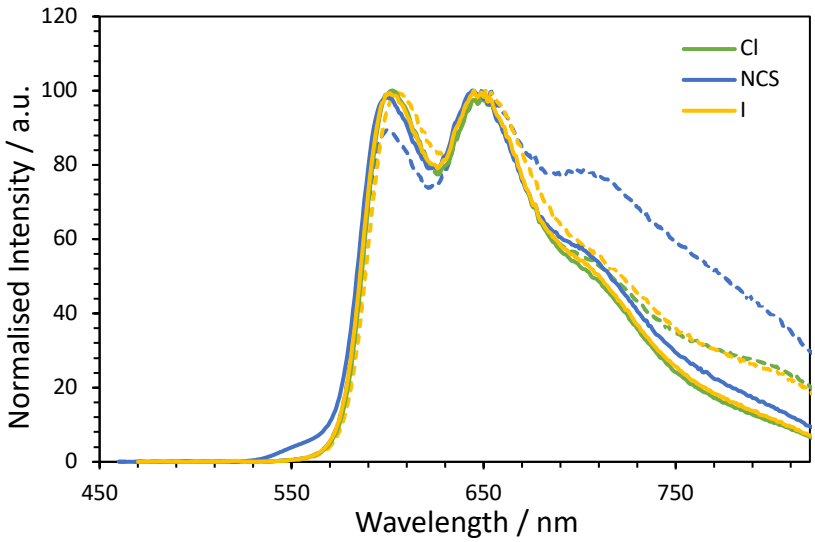

Figure 2.32: *Emission spectra of PtL^{7}X (where X = Cl, NCS or I) in dilute (solid line) and concentrated (dashed line) degassed DCM solution, highlighting weak excimer formation in the latter.*

The absorption and photoluminescence spectra of PtL^3X (where X = Cl and NCS) at low and high concentrations in degassed DCM solution are shown in **Figure 2.33**. Once again, the unimolecular emission is unchanged upon substitution of the ancillary ligand, though the excimeric emission observed at high concentration appears to be blue shifted for PtL^3NCS compared to the parent PtL^3Cl. Moreover, PtL^3NCS has an interestingly low self-quenching constant, an order of magnitude less than the parent PtL^3Cl, with values of 0.2×10^9 M^{-1} s^{-1} and 2.0×10^9 M^{-1} s^{-1} respectively (**Table 2.5**), despite both complexes forming excimers (albeit weakly) in solution.

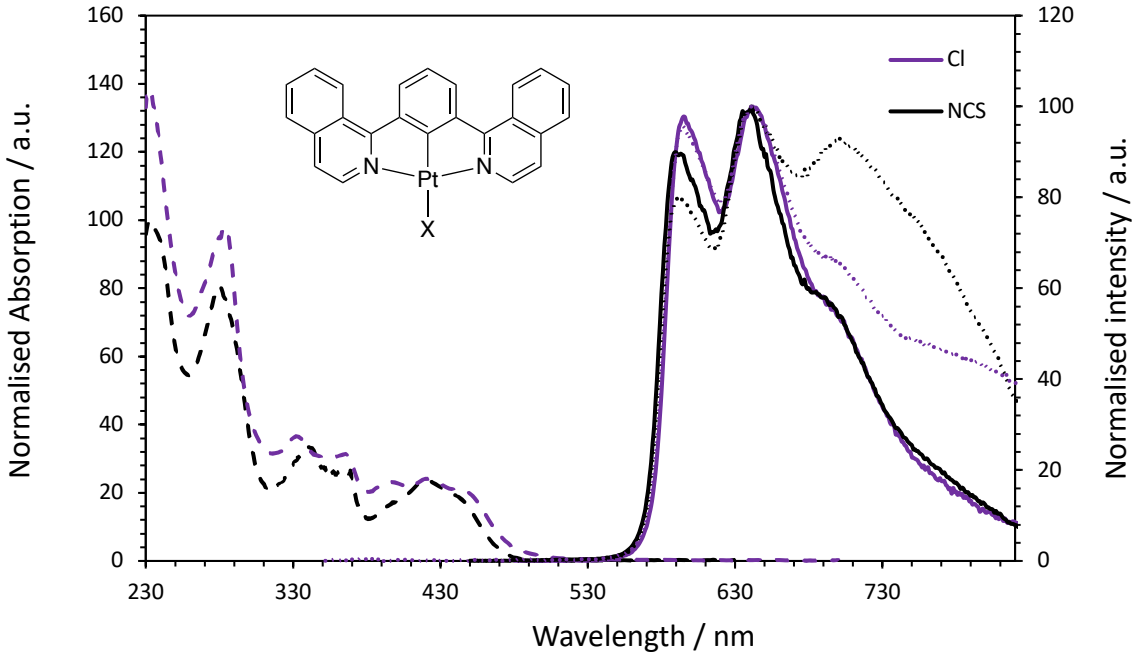

Figure 2.33: *Absorption (dashed line) and photoluminescence spectra of PtL^3X (where X = Cl and NCS) at low (solid line) and high concentration (dotted line) of degassed DCM solution at RT.*

The ancillary ligand is clearly playing a role in the intermolecular interactions and thus excimer emission in solution: lower energy excimers are observed for X = -I and higher energy for X = -NCS/SCN. Nevertheless, the differences in the emission spectra of these complexes in solution are minor. Solid-state photoluminescence and electroluminescence tells another story, as postulated,[23] and will be discussed in the following section for PtL^1X and PtL^2X (where X = Cl, NCS/SCN and I).

2.3.5 Solid-state photophysics and OLED devices

PtL^nCl

Thin-film emission and OLED studies on a number of the complexes discussed in this chapter were carried out by Dr Piotr Pander (Department of Physics, Durham University). Poly(*N*-vinylcarbazole) (PVK) was chosen as the polymer host to study emission in the solid state, due to its chemical similarity to hosts used in OLEDs. Firstly, PtL^nCl complexes will be discussed before moving onto PtL^nX, where X = SCN/NCS or I. The PL spectra of complexes $PtL^{1\text{-}3}Cl$ in solution-processed film are shown in **Figure 2.34**. The spectrum of PtL^3Cl in film resembles that in dilute solution, irrespective of the loading wt %. There is almost no evidence of a long wavelength excimer/aggregate band in film, despite the complex showing NIR excimer emission in concentrated solution (**Figure 2.21**). This complex was ruled out for use in NIR-OLEDs.

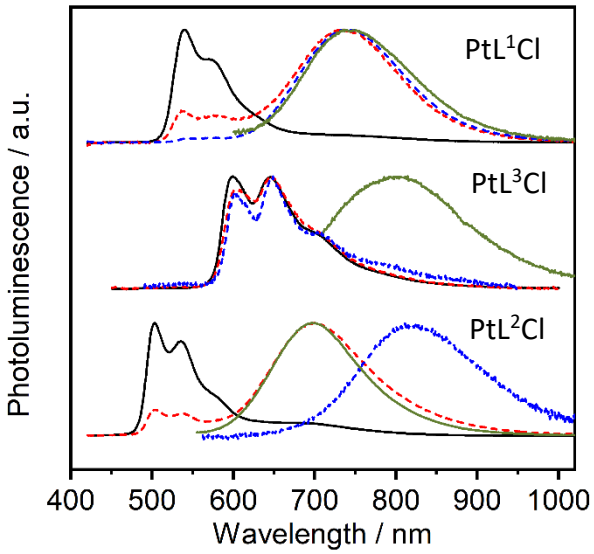

Figure 2.34: *PL spectra of complexes $PtL^{1\text{-}3}Cl$ in solution-processed film: 5% load in PVK (black continuous line); 20% load in PVK (red dashed line); pristine film prepared from solution (blue dashed line). The PL spectra in solution of the excimer emission deconvoluted from that of the monomer (green continuous line) are displayed for comparison).*

In contrast, PtL^1Cl and PtL^2Cl show a large increase in the long-wavelength band (λ_{max} approx. 740 and 700 nm respectively) at 20 % concentration in PVK films, relative to the structured shorter-wavelength emission that dominates at 5% loading (**Figure 2.34**). This long wavelength band resembles that of the excimer emission in DCM

solution, implying a similar, bimolecular nature to the excited state responsible in film.

In neat films, the behaviour changes. For PtL^2Cl there is a large red shift of 120 nm of the long wavelength band relative to that at 20% in PVK (λ_{max} = 820 nm in neat film compared to 701 nm in 20 % PVK film). The occurrence of such a profound red shift with increasing concentration in the film is highly suggestive of the formation of new emissive species in neat film, comprising of more than two molecules, *i.e.* trimers, tetramers, *etc.*, that are not present in significant amounts at lower loadings. DFT studies of the excimers of these complexes, in both a *syn* and *anti* geometry, were carried out by Dr Piotr Pander (**Figure 2.35**).[99] The model suggests that the molecules adopt an *anti* geometry in the excimer as this geometry is an excellent match to the experimental excimer energy in solution. The model was extended to trimers and tetramers and showed that the T_1 geometry, considered as the emissive state in these systems, of the trimer and tetramer of PtL^2Cl matched with the experimental PL in film. This conclusion is in line with another recent study on Pt(II) NIR OLED emitters reported by Chi *et al.* that form aggregates comprising of more than two

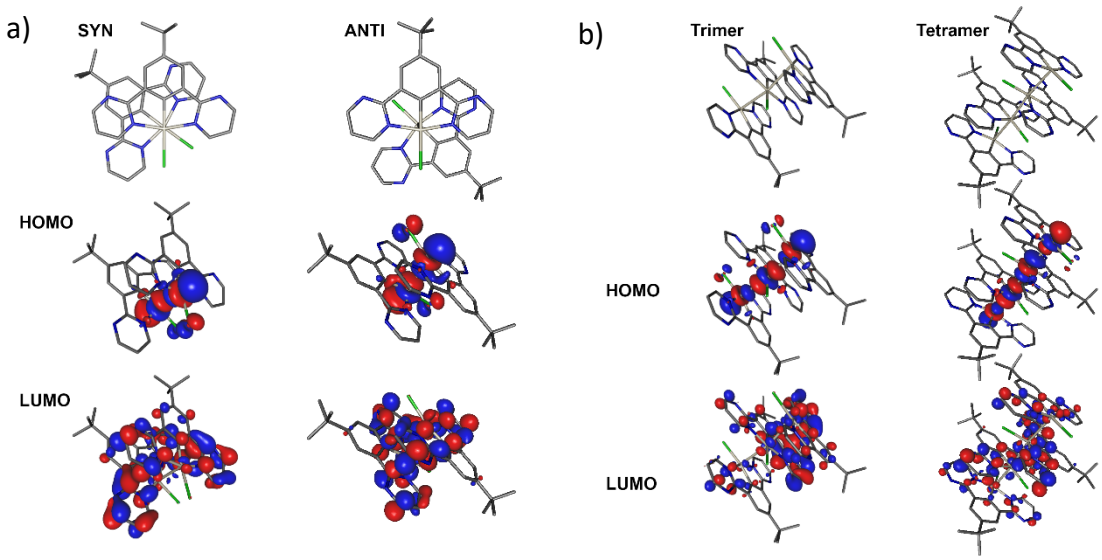

Figure 2.35: *Structural geometry and frontier molecular orbital contour plots for a) the excimer of PtL^1Cl and PtL^2Cl, and b) anti-trimer and anti-tetramer of PtL^2Cl at T_1 geometry.The energy-minimised T_1 geometry of the excimer, trimer and tetramer was evaluated using BP86/def2-SVP with subsequent single-point energy calculation using B3LYP/def2-SVP/CPCM(CH_2Cl_2).*

molecules to generate long-wavelength PL and EL in the NIR region of the spectrum.[100]

In solution, excimers can be recognised by their distinctive kinetic behaviour (*i.e.,* biexponential decay and rise time)[101,102] as shown in **Figure 2.25**, but in solid film, the mono- and bimolecular excited states behave as if they were not forming an equilibrium and decay independently of each other. Due to the limited mobility of molecules in the solid state, short intermolecular distances are required in the ground state in order to generate excimer-like species emitting at long wavelengths, giving a similar picture to aggregation. This is highlighted in the appearance of an additional absorption band in film that is not present in solution, assigned to the Pt···Pt MMLCT transition of ground state dimers or aggregates (**Figure 2.36**).

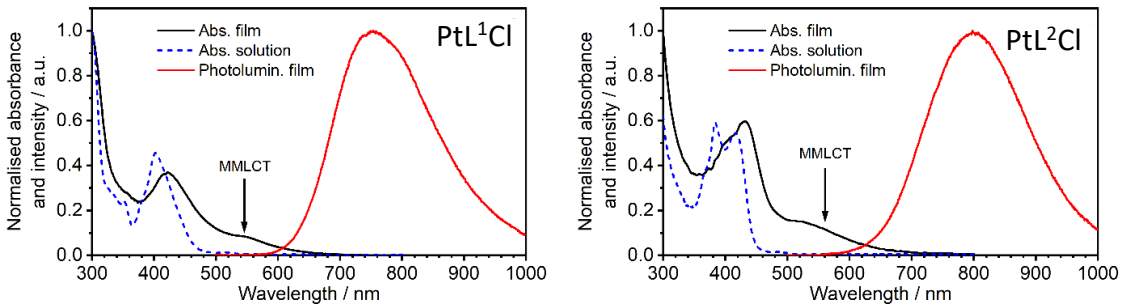

Figure 2.36: *Absorption (black solid line) and PL spectra of complexes PtL¹Cl and PtL²Cl in vacuum-deposited films. The absorption of the complexes in solution is included for comparison (blue dashed line) to highlight the appearance of an MMLCT band in film.*

Figure 2.36 depicts the absorption and PL spectra of complexes PtL¹Cl and PtL²Cl in vacuum-deposited films. The slightly blue-shifted λ_{max} of PtL²Cl compared to the solution-processed film likely reflects subtly different proportions of trimers and tetramers in the films formed by the two methods. There is a notable overlap between the absorption and PL in the 600-650 nm region, which may seem inconsistent with a triplet emitter. To investigate this, emission spectra were recorded over a range of excitation wavelengths (**Figure 2.37**). For $\lambda_{ex} < 500$ nm, the PL spectra are identical, consistent with direct excitation of individual Pt(II) units within the oligomer (aggregate). However, longer wavelength excitation leads to a progressive red shift of the emission spectrum, indicating that lower energy emissive

excited states are associated with those species displaying longer-wavelength absorption bands, i.e. trimers and tetramers. This supports the idea that different sizes of aggregates are present in the film.

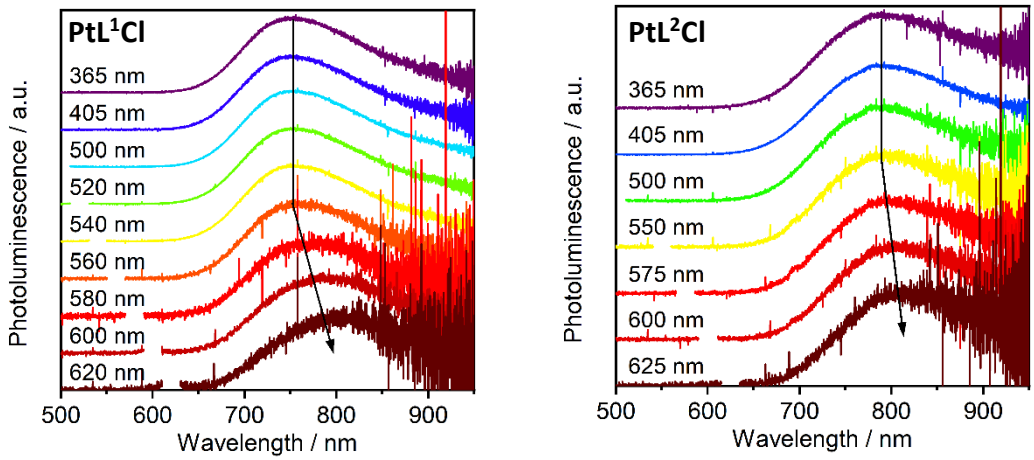

Figure 2.37: *PL spectra of PtL¹Cl and PtL²Cl in vacuum-deposited films at various excitation wavelengths (given on the graphs).*

Complexes PtL¹Cl and PtL²Cl were chosen for study in NIR OLEDs due to their long wavelength emission in neat films. The OLED device architecture used consists of the EML sandwiched between layers of hole-blocking 2,4,6-tris[3-(diphenylphosphinyl)-phenyl]-1,3,5-triazine (PO-T2T) and electron-blocking 4,4'-(diphenylsilanediyl)-bis(N,N-diphenylaniline) (TSBPA) (structures of which can be seen in **Figure 2.38**). These materials have HOMO and LUMO energies close to the respective energy levels

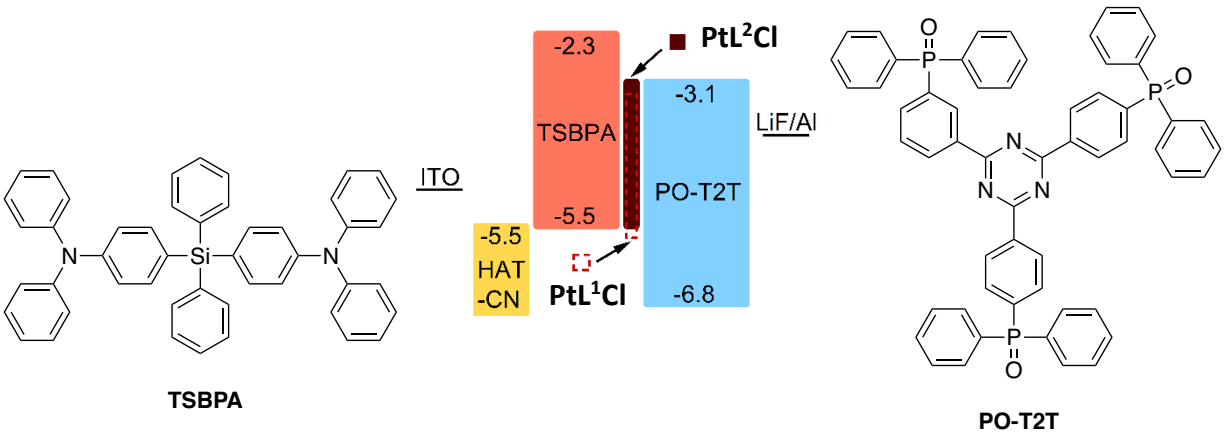

Figure 2.38: *Structure of Devices 1-6 where the EML is indicated either as a filled brown rectangle (PtL²Cl) or dashed red rectangle (PtL¹Cl). The width of rectangles roughly represents the relative thickness of each layer. Structures of electron-blocking TSBPA and hole-blocking PO-T2T materials are also shown.*

of the emitters (**Figure 2.38**). The device structure was ITO | HAT-CN (10 nm) | TSBPA (35 nm) | **PtL^{1}Cl** or **PtL^{2}Cl** (*x* nm) | PO-T2T (50 nm) | LiF (0.8 nm) | Al (100 nm). The material HAT-CN (1,4,5,8,9,11-hexaazatriphenylenehexacarbonitrile) is the hole injection layer, while the thin layer of LiF facilitates electron injection. The EL characteristics of the OLED devices are presented in **Table 2.6**.

Table 2.6: *Characteristics of OLED devices fabricated with PtL^{1}Cl and PtL^{2}Cl as emitters.*

Device	Complex	Φ_{PL} [a]	*EML thickness x*, nm [b]	λ_{EL}, nm [c]	% λ > 700 nm [d]	EQE_{max}, % [e]	Max. radiosity, mW cm^{-2}
Dev 1	PtL^{1}Cl	0.02 ± 0.01	1	541, 734	67	0.9 ± 0.1	1.54
Dev 2			2	765	89	0.8 ± 0.1	1.04
Dev 3			10	790	97	0.9 ± 0.1	1.19
Dev 4	PtL^{2}Cl	0.03 ± 0.01	1	819	96	1.1 ± 0.1	1.33
Dev 5			2	817	95	1.2 ± 0.1	1.46
Dev 6			10	820	97	1.2 ± 0.1	1.31

a) *PLQY of the emissive layer in nitrogen; b) Emissive layer (EML) thickness; c) EL maxima; d) % of spectral power at wavelengths above 700 n; e) device maximum external quantum efficiency.*

The EML thickness typically used in NIR OLEDs involving neat films of platinum(II) complexes is typically ~20–40 nm or more.[70,74,100,103–106] Devices featuring three different thicknesses of EML (10, 2 and 1 nm) were studied (**Figure 2.39**). For both PtL^{1}Cl and PtL^{2}Cl as emitters, the resulting EL characteristics of the 10 and 2 nm OLEDs are very similar, with the same efficiency and almost identical spectra. Even Device 4 with a 1 nm EML of PtL^{2}Cl demonstrates similar characteristics to Devices 5 and 6 with 2 and 10 nm EMLs respectively. This suggests that the minimum practical EML thickness can be as low as 1-2 nm in this case, allowing a reduction of the consumption of the precious metal complexes by over 90%, without compromising on the efficiency and EL spectrum. A notable result is the EQE of devices using PtL^{2}Cl as the EML which reaches 1.2 ± 0.1 % at λ_{EL} = 817 nm with a maximum radiosity of 1.46 mW cm^{-2} (Device 5, **Figure 2.39 c** and **d**). We note also that Devices 5 and 6 demonstrate negligible roll-off, with the EQE only dropping marginally to 0.90 % at

~100 mA cm^{-2}. We demonstrate efficient NIR OLEDs can be fabricated using very thin layers of the emissive Pt complexes.

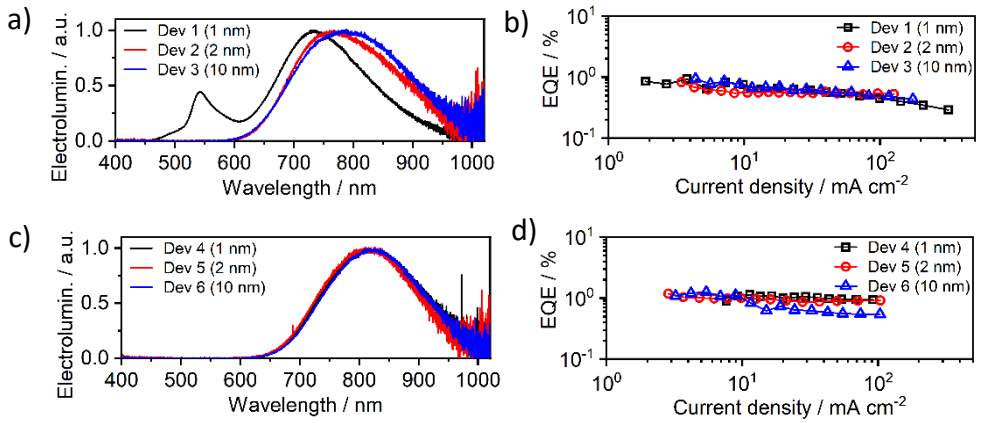

***Figure 2.39**: Electroluminescence spectra of Devices 1-3 containing PtL^{1}Cl as EML (a) and of Devices 4-6 containing PtL^{2}Cl as EML (c), along with the corresponding EQE of the devices as a function of current density (b and d for PtL^{1}Cl and PtL^{2}Cl respectively).*

PtL^{1}Cl demonstrates significant changes in the EL spectra upon changing the EML thickness (**Figure 2.39a**); a blue shift is observed upon decreasing the EML thickness, with values of λ_{EL} = 780, 765 and 734 nm for Devices 3, 2 and 1 respectively (10, 2 and 1 nm EML thicknesses). This can be rationalised as follows. Given the molecular dimensions of the studied Pt complexes of around 1 × 1 × 0.4 nm, it can be expected that mono- or bimolecular coverage should be the dominating mode in a 1–2 nm thick film, unless aggregation offers sufficient energetic advantage. With the thinning of the EML, it becomes less likely that the vacuum-deposited films of PtL^{1}Cl will contain aggregates larger than dimers; one would expect a smaller proportion of the higher aggregates in a 2 nm EML compared to one of 10 nm, a prediction that is consistent with the blue shift of the EL λ_{max} in Device 2 compared to Device 3 (**Table 2.6**).

Moreover, an additional band appears at λ_{EL} = 541 nm for Device 1 which does not match the unimolecular PL band observed in PVK films or in solution. However, we still conclude that this band is indeed due to unimolecular emission of PtL^{1}Cl, with the difference between solution/PVK film and OLED possibly being related to the way the complex packs and interacts with mCP in a blend and at the TSBPA/PO-T2T

interfaces in a vacuum-deposited film (the shoulder at ~500 nm in the electroluminescence spectrum of Device 1 is consistent with the known EL of the TSBPA:PO-T2T exciplex[107]). In Device 1, the average layer thickness is so small that probably only bi- and monomolecular excited states can be formed. In areas between molecules of PtL^1Cl in the film, direct contact between TSBPA and PO-T2T layers may become possible, leading to a small contribution of the aforementioned exciplex to the EL spectrum. On the other hand, complex PtL^2Cl shows such a strong propensity to aggregation that preferential formation of aggregates probably occurs at *any* [average] layer thickness, leading to the EL spectrum being invariant with EML thickness.

PtL^nX where X = SCN/NCS or I

Photoluminescence and absorption spectra of complexes PtL^1X and PtL^2X (where X = SCN/NCS or I) in neat film are shown in **Figure 2.40**. For each complex, the absorption band in film around 400-450 nm matches that recorded in solution and so is attributed to the absorption of individual molecules. An additional low energy band appears in the absorption spectra of the films, forming a weak shoulder at around 500-600 nm for the iodo-substituted complexes but an intense band for the thiocyanate complexes, where it spans from 500 to 700-800 nm forming a clear maximum at 629 nm and 552 nm (for PtL^1SCN and PtL^2NCS respectively). This band is attributed to MMLCT, supported by computational studies.

All four complexes display NIR emission in neat films with the onset PL and absorption spectra showing a perfect match. The occurrence of the additional MMLCT absorption bands indicates that the long wavelength PL originates from excited states of aggregates formed in the film. The film emission of complexes PtL^1I and PtL^2I resembles that of the respective excimers in solution, with λ_{PL} = 740 nm and 733 nm respectively. The longest wavelength luminescence is observed for complexes PtL^1SCN and PtL^2NCS featuring the SCN ancillary ligand with values of λ_{PL} = 950 nm and 872 nm respectively.

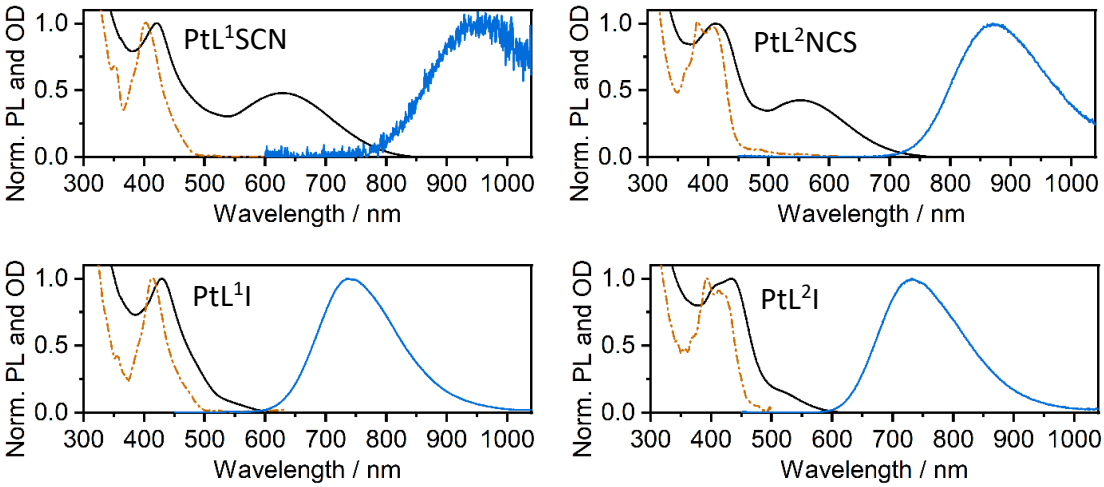

Figure 2.40: *Photoluminescence (blue continuous line) and absorption (black continuous line) spectra of complexes PtL^1X and PtL^2X (where X = SCN/NCS or I) in thermally evaporated neat films, with corresponding absorption spectra in dilute DCM solution (red dashed and dotted line) for comparison.*

Similar behaviour is observed for these complexes as seen for PtL^1Cl and PtL^2Cl in the preceding section; the PL spectrum is red-shifted when a longer excitation wavelength is used, with the exception of PtL^1I, implying aggregates with more molecules involved in the interaction are present in the neat films, *i.e.* trimers and tetramers.

Theoretical calculations, carried out by Dr Piotr Pander, helped provide additional insight into the binding mode of the thiocyanate ancillary ligand. The previously established correlation between the calculated excimer/dimer energy and experimental emission maximum or onset calibrated for DCM solution was used to validate the calculations he performed. The triplet excited-state properties were simulated for systems composed of 2, 3, 4 and 5 molecules (only 2 and 3 molecules for PtL^1I and PtL^2I) with a face-to-face orientation. We observe that the predicted excimer energy (for the *anti* configuration, using the established methodology described above for PtL^1Cl and PtL^2Cl) is close to the experimental value for the iodo derivatives (**Figure 2.41**). The excimer energy for the thiocyanate complexes generally depends on the binding mode of the ancillary ligand: the -NCS mode yielded a higher energy excited state, thus a more blue shifted PL than -SCN.

The difference in the calculated T_1 energy between PtL^{1}SCN and PtL^{1}NCS exceeds 0.4 eV and while the former demonstrates a perfect agreement with the excimer PL spectrum (both λ_{max} and λ_{onset}), the latter does not match the experiment at all (**Figure 2.41**). This result strongly suggests that the binding of the ancillary ligand to the metal centre in this complex occurs through the sulphur atom, rather than nitrogen, which is in line with the crystal structure presented in **Figure 2.15**. The theoretical energy of the isomeric PtL^{2}SCN and PtL^{2}NCS excimers is much more similar than for PtL^{1}SCN/PtL^{1}NCS with only ~0.1 eV energy difference between them. Here, the -NCS isomer appears to be a better fit, suggesting that this binding mode should be dominating for PtL^{2}NCS.

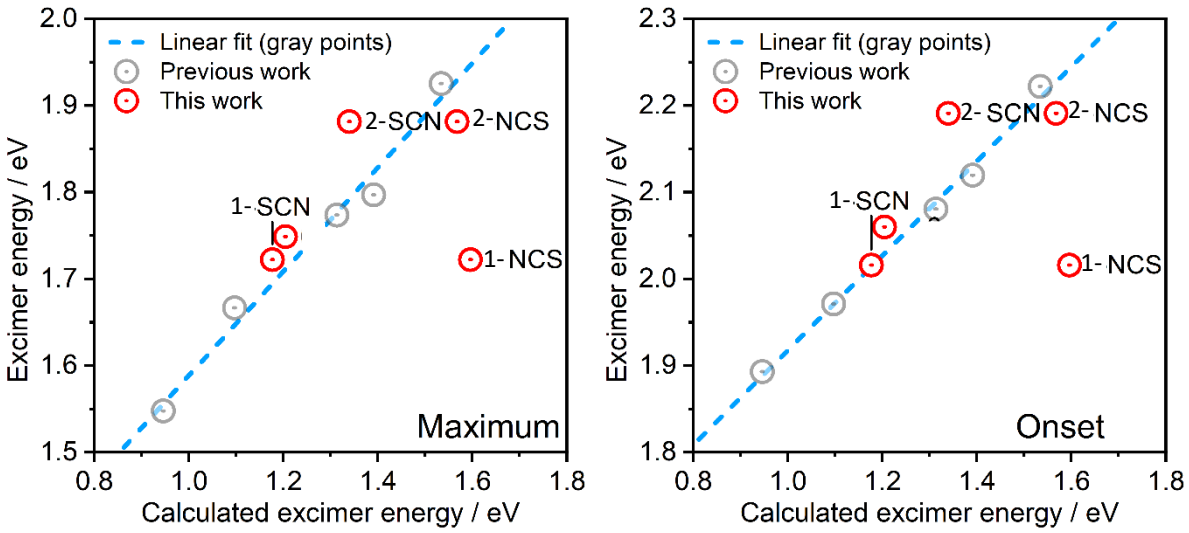

Figure 2.41: *Correlation between the computed excimer energy and the experimental λ_{max} values (left) or emission onsets (right) obtained from the PL spectra in DCM solution. The grey points represent previous calculations for PtL^{1}Cl and PtL^{2}Cl discussed above using the same methodology. Calculations performed by collaborator Dr Piotr Pander (Department of Physics, Durham University).*

OLEDs were fabricated (by Dr Piotr Pander) with PtL^{1}X and PtL^{2}X (where X = SCN/NCS or I) as the EML and the results shown in **Figure 2.42** and **Table 2.7**. The device architecture was produced in the same way as for PtL^{1}Cl and PtL^{2}Cl discussed in the preceding section with EML thicknesses of 1, 2 and 10 nm. Amongst the results, two points stand out as the most impressive. Firstly, the EQE for PtL^{1}I is drastically improved compared to the parent PtL^{1}Cl (from 0.8 to 3%), despite showing similar λ_{EL}. This can possibly be attributed to the beneficial role of the heavier halogen atom

in reducing molecular vibrations in aggregates and contributing to slowing down non-radiative decay. Secondly, the EL for PtL^1SCN is significantly red-shifted compared to PtL^1Cl, peaking at 942-945 nm in Devices 1-3 (compared to 765 nm for the latter) with an EQE ≈ 0.3-0.4 %.

Table 2.7: *Characteristics of OLED devices fabricated with PtL^1SCN, PtL^1I, PtL^2NCS and PtL^2I as emitters.*

Device	Complex	Φ_{PL}	x, nm	λ_{el}, nm	% λ > 700 nm	EQE_{max}, %	Max. radiosity, mW cm^{-2}
Dev 1	**PtL^1SCN**	~0.01*	1	945	> 99	0.4	0.91
Dev 2			2	944	100	0.3	0.78
Dev 3			10	942	100	0.3	0.94
Dev 4	**PtL^1I**	0.09 ± 0.02	1	558, 736	78	4.1	4.49
Dev 5			2	736	80	2.5	3.38
Dev 6			10	742	84	2.3	3.78
Dev 7	**PtL^2NCS**	0.02 ± 0.02	1	842	98	1.1	2.88
Dev 8			2	857	99	1.1	3.04
Dev 9			10	868	100	0.7	2.54
Dev 10	**PtL^2I**	0.12 ± 0.03	1	512, 541, 726	74	4.7	5.09
Dev 11			2	734	79	4.2	5.92
Dev 12			10	735	80	4.6	6.34

* The accuracy of the Φ_{PL} value is low in this instance due to the low intensity and long wavelength of the luminescence.

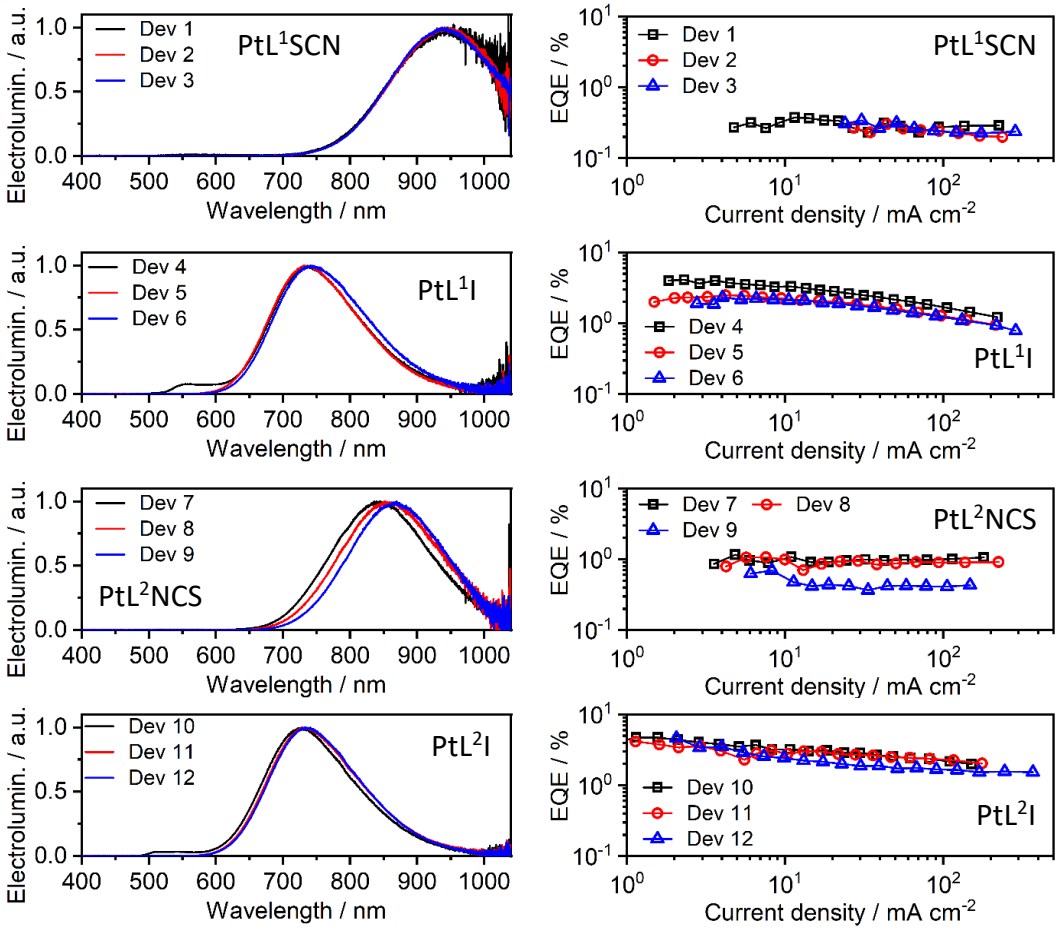

Figure 2.42: *Electroluminescence spectra of Devices 1-12 and corresponding EQE as a function of current density.*

We believe that PtL¹SCN shows the longest wavelength electroluminescence reported for a platinum(II) complex aggregate; the EQE and λ_{EL} of reported NIR OLEDs in the literature are compared to the values for our devices in **Figure 2.43**, with references and device information in **Table 2.8**. Note that the emitter with λ_{el} = 1005 nm is a platinum porphyrin. Such long wavelength luminescence of PtL¹SCN is likely owed to a combination of factors promoting the low triplet energy of the excited state aggregate, in particular the -SCN binding mode of the ancillary ligand.

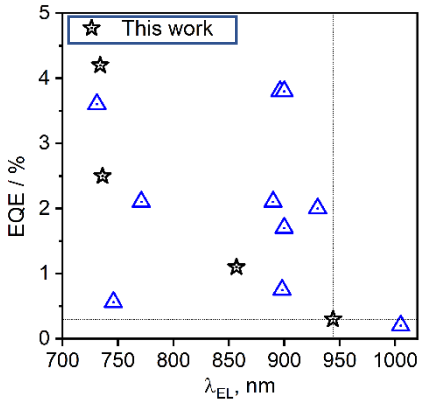

Figure 2.43: *EQE and EL spectra maxima of sample NIR OLEDs using Pt(II) complexes as emitters (blue triangles) compared to devices presented in this work (black stars).*

Table 2.8: *Compilation of reported NIR OLED efficiency (λ_{el} ≈ 700-1000 nm) of Pt(II) complexes.*

Emitter type	OLED fabrication method	λ_{el} / nm	EQE / %	Reference
Mono-Pt(II)	Thermal evaporation	896	3.8	[108]
Mono-Pt(II)	Solution-processed	771	2.1	[84]
Mono-Pt(II)	Thermal evaporation	773	8.0	[84]
Mono-Pt(II)	Solution-processed	898	0.75	[84]
Mono-Pt(II)	Thermal evaporation	900	3.8	[84]
Mono-Pt(II)	Solution-processed	1005	0.2	[84]
Di-Pt(II)	Solution-processed	731	3.6	[109]
Di-Pt(II)	Solution-processed	746	0.56	[110]
Excimer/aggregate	Thermal evaporation	724	16.7	[105]
Excimer/aggregate	Thermal evaporation	740	24	[111]
Excimer/aggregate	Thermal evaporation	900	1.7	[100]
Excimer/aggregate	Thermal evaporation	890	2.1	[100]
Excimer/aggregate	Thermal evaporation	930	2.0	[100]
Excimer/aggregate	Solution-processed	692	6.3	[112]
Excimer/aggregate	Solution-processed	700	8.1	[112]
Excimer/aggregate	Solution-processed	704	8.9	[112]
Excimer/aggregate	Solution-processed	716	5.1	[113]

2.4 Chapter 2 summary

The synthesis of nine Pt(II) complexes (seven of which are new materials) of the type Pt(N^C^N)Cl is reported with yields varying from 27 to 87%. The symmetric N^C^N-coordinating ligand in each case features electron-deficient substituted pyridine rings, pyrimidine or quinoline/isoquinoline (LUMO), as well as slightly electron-donating alkyl groups on the central phenyl ring (HOMO), in order to red shift the emission. Reported crystal structures reveal mainly head-to-tail packing with no significant Pt···Pt interactions (4.4 – 6.3 Å), though with interplanar distances small enough to expect π–π interactions (3.2 – 3.8 Å). A MeOH solvate of PtL^1Cl differs in that it shows a head-to-head packing arrangement in the crystal with close Pt···Pt contacts of 3.2137(3) Å. This suggests that Pt···Pt interactions cannot be ruled out for all complexes if isolated under conditions that favour them (e.g. solvent, temperature, rate of evaporation).

Solution-state photophysical studies were carried out on all complexes, with PLQYs ranging from 0.11 to 0.91%, with the lowest values obtained for the most red emitting complexes featuring 1-isoquinoline rings (namely PtL^3Cl, PtL^6Cl and PtL^7Cl). Unimolecular or monomeric emission was observed in dilute degassed DCM solution for all complexes, with values of λ_{max} ranging from 500 – 625 nm. Unimolecular emission was red-shifted in the order PtL^2Cl (pyrimidine) < PtL^1Cl (4-trifluoromethyl pyridine) < PtL^4Cl (3-isoquinoline) < PtL^3Cl (1-isoquinoline), considering only 'parent' complexes. All complexes showed red shifted emission with respect to Pt(dpyb)Cl.

Most complexes exhibited the presence of a broad, long-wavelength band at elevated concentration, assigned to the formation of excimers, as reported for the parent Pt(dypb)Cl. Complexes featuring 3-isoquinoline rings (namely PtL^4Cl, PtL^8Cl and PtL^9Cl) showed the highest propensity to excimer formation, with the emission in saturated solution originating almost solely from the excimer species. Excimer emission was red-shifted in the order PtL^4Cl (3-isoquinoline) < PtL^8Cl (3-isoquinoline) < PtL^9Cl (3-isoquinoline) < PtL^2Cl (pyrimidine) < PtL^7Cl (1-isoquinoline) < PtL^1Cl (4-

trifluoromethyl pyridine) < PtL^3Cl (1-isoquinoline), which roughly follows the trend of monomeric emission, with the exception of the 3-isoquinoline substituted complexes which show the most blue-shifted excimer emission.

Chloride metathesis was carried out on PtL^1Cl, PtL^2Cl, PtL^3Cl and PtL^7Cl to replace the chloro ancillary ligand with iodo or thiocyanate. Yields of 27 to 95% were achieved. Crystal structures revealed different binding modes for the thiocyanate co-ligand dependent upon the nature of the N^C^N ligand. PtL^1SCN was bound through the S atom, not N as previously reported in the literature for another similar complex (**Figure 2.2**).[23] The binding mode was confirmed by theoretical calculations (by Dr Piotr Pander) to compare the calculated and experimental excimer energy of the complexes with -NCS or -SCN binding modes. Similar energies were seen for both binding modes for PtL^2NCS. IR spectra suggest that both binding modes could be present in the solid state depending upon how the powder was obtained (i.e. solvent, and rate of solvent evaporation).

Solution-state photophysical analysis for the PtL^nX complexes (where X = I or SCN/NCS) revealed no significant change upon substitution of the ancillary ligand. The solution-state excimer was slightly higher in energy for X = SCN/NCS and lower in energy for X = I in each case. However, in moving to the solid-state, the excimer/aggregate emission significantly red shifted for complexes with X = SCN/NCS, especially for the S bound PtL^1SCN up to λ_{max} = 940 nm. NIR OLEDs were fabricated by Dr Piotr Pander (Department of Physics, Durham University) with PtL^1X (X = Cl, I and SCN) and PtL^2X (X = Cl, I and NCS) as the emissive layers, with thicknesses of 1, 2 and 10 nm. Similar characteristics were achieved for devices with 2 and 10 nm emissive layers. This is beneficial as a thinner layer can be used, minimising the use of the precious heavy metal complexes. The most remarkable results to observe were the increased EQE for PtL^1I compared to PtL^1Cl (3 and 0.8% respectively), as well as the red-shifted EL for PtL^1SCN peaking around 940 nm with the onset after 700 nm, deep into the NIR region, albeit with an EQE of 0.3%. The extreme red shifts were attributed to the presence of aggregates featuring more than two Pt units. We believe PtL^1SCN to be the lowest energy emitter of its kind (excluding Pt porphyrins).

Chapter 3

3. Pt(II) complexes featuring asymmetrically substituted tridentate N^C^N-coordinating ligands

3.1 Introduction

There are few reported examples of Pt(N^C^N) complexes in which the two heterocycles are different from one another, or that feature differently substituted pyridines.[114–117] It is of interest to study a range of such complexes to explore whether the presence of different heterocycles affects intermolecular interactions and excimer formation. One study by Develay *et al.* in 2008 found that the replacement of one of the pyridyl rings in Pt(dpyb)Cl by an electron rich pyrazole destabilised the excimer without affecting the monomer (**Figure 3.1**).[114]

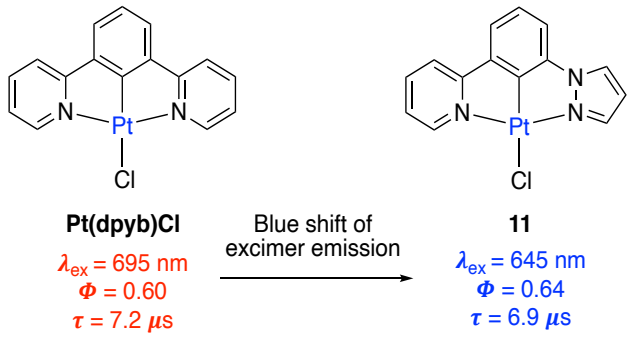

Figure 3.1: *Asymmetric pyridyl-pyrazolyl complex **11** shows blue-shifted excimer emission but similar monomer emission compared to Pt(dpyb)Cl. The data are in degassed CH_2Cl_2 solution.*

This asymmetric complex shows characteristics of both the bis-pyrazole and bis-pyridyl complexes. The monomer emission of **11** is similar to that of Pt(dpyb)Cl, which can be rationalised by DFT studies. The LUMO for complex **11** is asymmetrically

distributed, localised solely on the lower energy pyridyl ring with effectively no contribution from the pyrazole (**Figure 3.2**). Moreover, the presence of the pyrazole only exerts an influence on the emission properties at higher concentrations, namely the rate of self-quenching is reduced by almost an order of magnitude and the excimer emission is dramatically blue shifted by 50 nm (**Figure 3.1**). Another complex was studied whereby a slightly electron-donating methyl group was added to the 4-position of the central phenyl ring, with two pyrazole rings completing the N^C^N ligand. This was enough to disrupt intermolecular interactions; no excimer emission was observed for this complex.[114] This result contrasts with the previously observed insensitivity of the excimer emission energy in Pt(dpyb)Cl systems to substituents.[1] It is clear that more research into the factors governing excimer emission is needed.

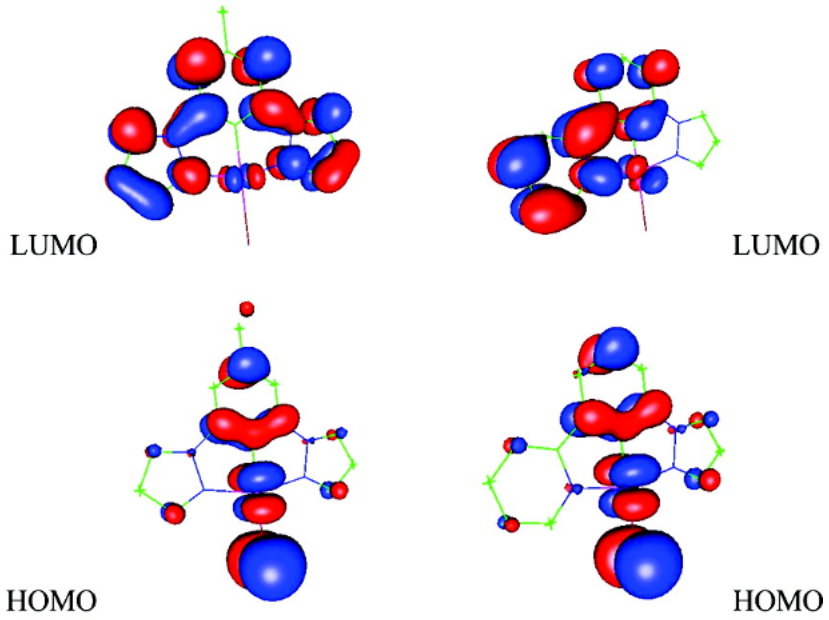

Figure 3.2: *Frontier orbital plots of complex **11** (right) and the corresponding di-pyrazole complex (left); the LUMO is asymmetrically distributed for the former, featuring the pyridine but not the pyrazole ring. Figure taken from reference 114.*

Another example of an asymmetric Pt(N^C^N) complex incorporates one benzoxazole (bzox) and one benzthiazole (bzth) ring, complex **12** (**Figure 3.3**).[115] This complex is compared with the corresponding symmetric complex Pt(bzoxb)Cl, where bzoxb is bis(benzoxazolyl)benzene. The bzth unit of complex **12** induces a red shift in the emission maximum of 13 nm when compared to Pt(bzoxb)Cl due to the presence of the less electronegative sulphur atom compared to oxygen; the HOMO-

LUMO gap is decreased as the LUMO energy is lowered whilst the HOMO level remains unchanged. The introduction of the CF_3 group into the *para* position of the benzene ring in complex **13** did not alter the emission energy as this group lowered the energy of both the HOMO and the LUMO. The presence of the benzimidazole (bzim) substituent in **14** likewise did not significantly affect the emission spectrum. All three complexes display similar emission profiles with well-resolved vibronic structured bands, as the lowest-energy emissive state involves the bzth moiety in each case (shown in red). As for complex **11**, TD-DFT studies confirmed an asymmetry in the LUMOs of the asymmetric complexes, which were mainly located on the bzth ring due to its better conjugation, hence a smaller HOMO-LUMO gap.[115] The report made no mention of whether excimer emission was observed at elevated concentrations.

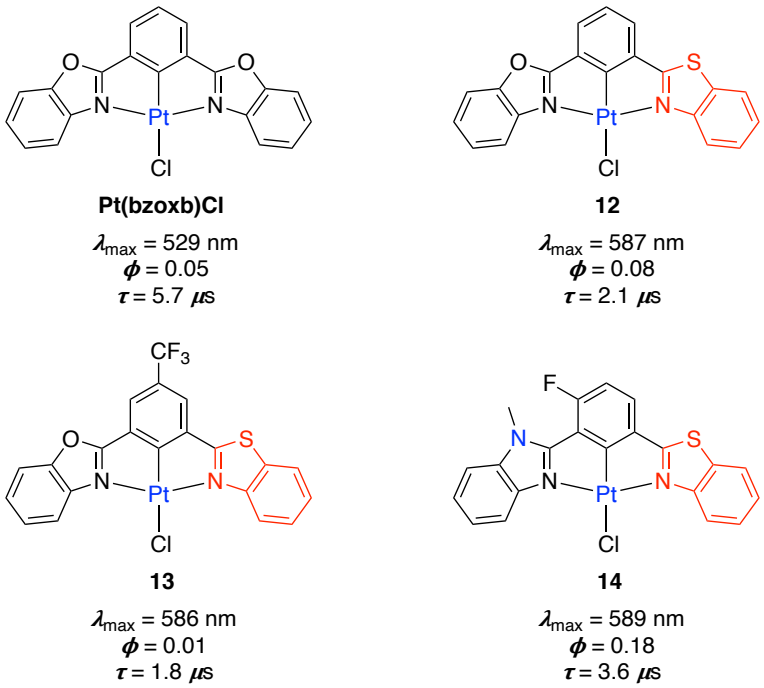

Figure 3.3: *Asymmetric complexes presented by Dang et al. based on the ligand bis(benzoxazolyl)benzene (bzoxb) and their emission data in degassed CH_2Cl_2 solution at 298 K.*

The most recently reported asymmetric N^C^N-Pt(II) complex incorporates a 1,2,3-triazole chelate (**16** in **Figure 3.4**) utilising Click chemistry for the synthesis of the proligand.[116] It bears both a pyridine and a 1,2,3-triazole ring, which is known to raise the energy of the π^* orbitals, and displays intense green emission with a slightly

higher PLQY than that of the reference symmetric complex **15** containing two pyridine rings. The absorption spectrum of complex **16** combines features of both **15** and the bis-triazole complex **17**, with electronic transitions involving the π^* orbitals of both the pyridine ring and the 1,2,3-triazole. Conversely, the emission spectrum of **16** is identical to that of **15**, suggesting that the LUMO is localised on the lower energy pyridine ring as seen for pyrazole-containing complex **11**; DFT confirms this hypothesis. No excimer emission was seen for **16,** due to the deliberate addition of the bulky mesityl group preventing intermolecular interactions, perhaps also the reason for the higher observed PLQY.

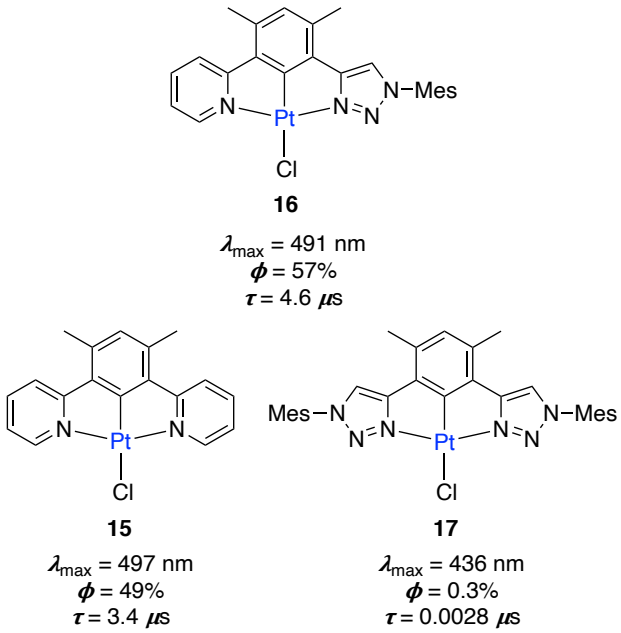

Figure 3.4: *An asymmetric 1,2,3-triazole complex **16** and the corresponding reference symmetric complexes **15** and **17**.*

Asymmetric complexes seem to possess emission characteristics similar to the corresponding parent symmetric complex that features the lowest energy heterocycles, at least for monomeric emission, due to localisation of the LUMO on the heterocycle with the lower energy π^* orbitals. Despite this, it is clear that research to date has not adequately probed the effect of the identity of the second ring on excimer formation and emission. The synthesis and detailed study of a wider range of asymmetric complexes could be the key to ascertain a better understanding

of excimeric interactions and factors affecting the emission energy. This constitutes the primary objective of the work described in this chapter.

3.2 Aims and objectives

Target complexes have been designed featuring differently substituted pyridines, isoquinoline, and pyrimidine rings, all of which will have different LUMO energies, with the aim of achieving a better understanding of the factors governing excimeric interactions and therefore emission energy. A selection of target complexes showing the types of groups employed in this work is shown in **Figure 3.5**. Complexes were proposed featuring a "donor-acceptor" type design with an EDG group on one pyridine ring and an EWG on the other in order to modify the intermolecular interactions and rationalise the effect, if any, on the energy of the excimer (top left complex in **Figure 3.5**).

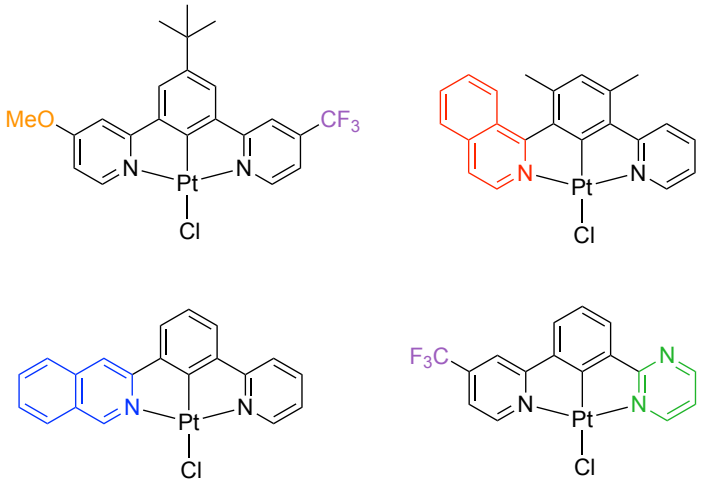

Figure 3.5: *A selection of target asymmetric Pt(II) complexes.*

The series of asymmetric Pt(II) complexes presented here were designed in the hope of tackling both objectives of probing intermolecular excimeric interactions whilst tuning the bimolecular emission further to the deep-red/NIR region by incorporating electron-deficient heterocycles into the molecular design as in Chapter 2.

3.3 Results and Discussion

3.3.1 Synthesis

Ligand synthesis

All of the asymmetric proligands and their complexes presented here are novel compounds. The synthesis of the proligands was achieved by multi-step Suzuki-Miyaura and/or Stille cross-coupling reactions. Inherently, the synthesis of asymmetric ligands requires multiple steps to achieve (if not employing a 'one-pot' method and relying on isolating the desired asymmetric target molecule), involving stoichiometric incorporation of one pyridine unit and subsequent Miyaura borylation before a second Suzuki cross-coupling step. A key precursor in the synthesis of asymmetric N^C^N ligands, where one heterocycle is pyridine, is 2-(3-bromophenyl)pyridine (**P3**). Two routes to this compound were explored: Stille and Suzuki cross-couplings (**Scheme 3.1**). The Suzuki reaction, utilising 3-bromophenylboronic acid, was preferable due to the higher yields, shorter reaction time (< 24 h compared to 48 h), and benign nature of the borate compounds compared to the toxic organotin reagents required for Stille reactions. There was no evidence of self-coupling of the 3-bromophenylboronic acid in the Suzuki reaction as the bromopyridine is more reactive than the bromobenzene.

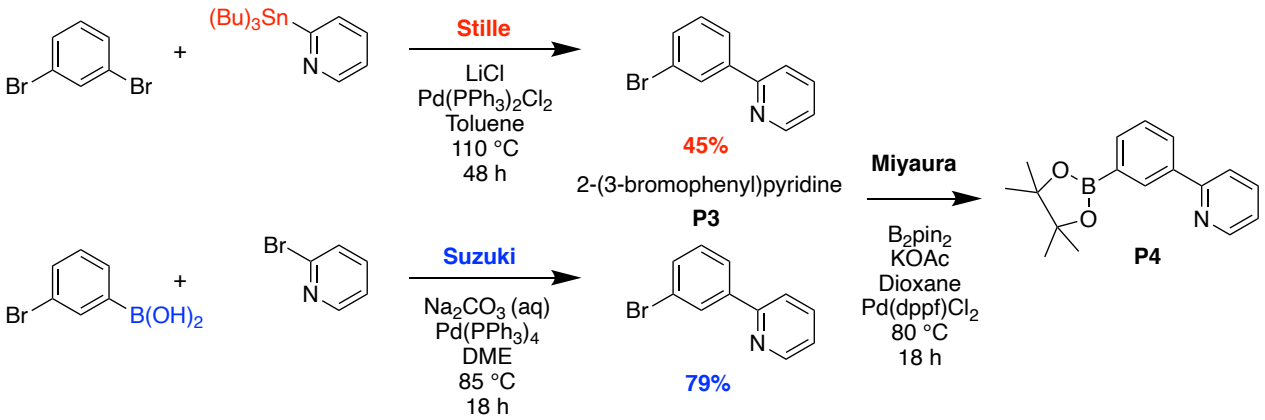

Scheme 3.1: *Alternative synthetic routes to the asymmetric ligand precursor 2-(3-bromophenyl)pyridine* ***P3****, and hence* ***P4****.*

Borylation of **P3** with B_2Pin_2 yielded the boronate ester **P4** that could be reacted in a further Suzuki cross-coupling to achieve a range of proligands. Difficulties arose when purifying **P4** by column chromatography, perhaps due to the presence of the nitrogen lone pair on the pyridyl ring which could interact with the boronate ester. There was no evidence of the product after elution with a hexane/DCM gradient, typically used for other boronate ester products, so the column was flushed with methanol to disrupt any possible interactions between B_2Pin_2 or silica and the desired product. The product co-eluted with impurities at 25% methanol. In subsequent preparations, therefore, most similar boronate ester products were used in the next steps in their crude form without chromatographic purification, albeit giving relatively low yields of final target asymmetric proligands.

Proligands were targeted by systematically varying the heterocycle on each unit of the N^C^N ligands. The synthesis of asymmetric proligands bearing isoquinoline rings, HL^{12-15}, is shown in **Scheme 3.2**. Ligands substituted with methyl groups at the 2- and 4-positions of the central phenyl ring were accessed through the precursor **P5**, synthesised by a Stille cross-coupling reaction from **I2**, chosen as only one step was required instead of a Miyaura and subsequent Suzuki cross-coupling.

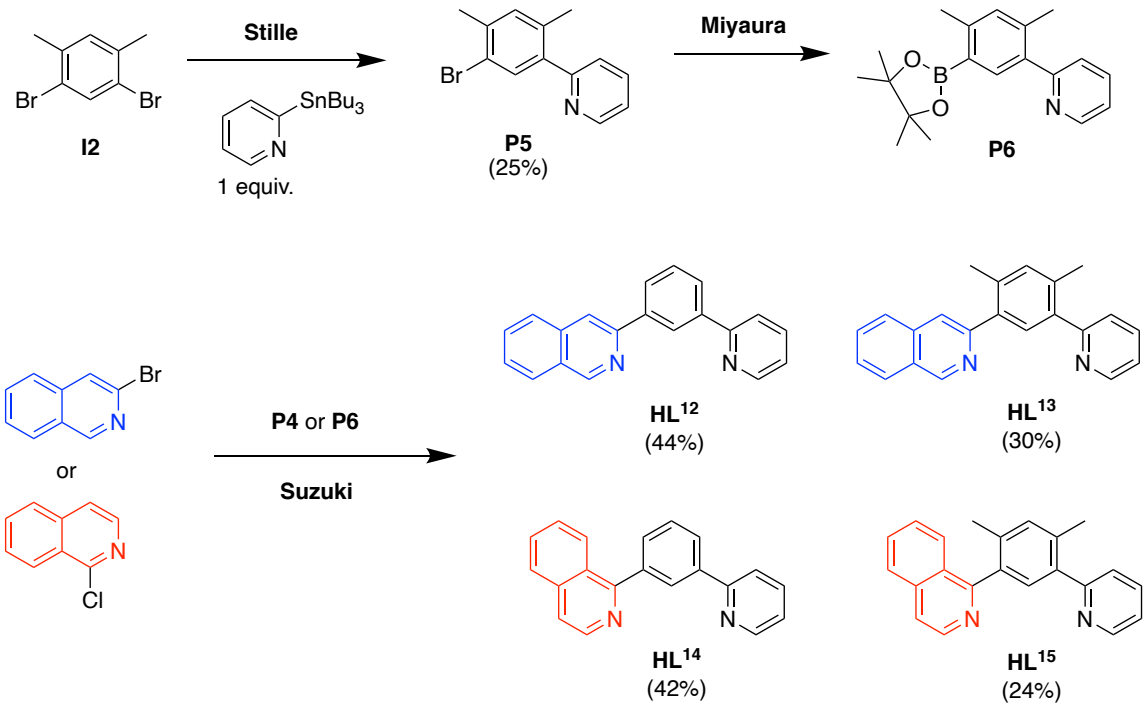

Scheme 3.2: *Synthetic route to HL^{12-15} with yields.*

Further proligands in the 1-isoquinoline series were targeted. To synthesise proligands with two different heterocycles, where neither is unsubstituted pyridine, there are two possible routes depending on which group is added first. Route 1, adding the CF_3-substituted pyridine first, *via* the precursor **P7**, resulted in a very low yield of the final Suzuki step for HL[16]. This proligand was better prepared in relatively high yield *via* the opposite Route 2 in which the 1-isoquinoline group is first added followed by the CF_3-pyridine (**Scheme 3.3**). HL[17] was prepared similarly by Route 2 for the same reason (**Scheme 3.4**).

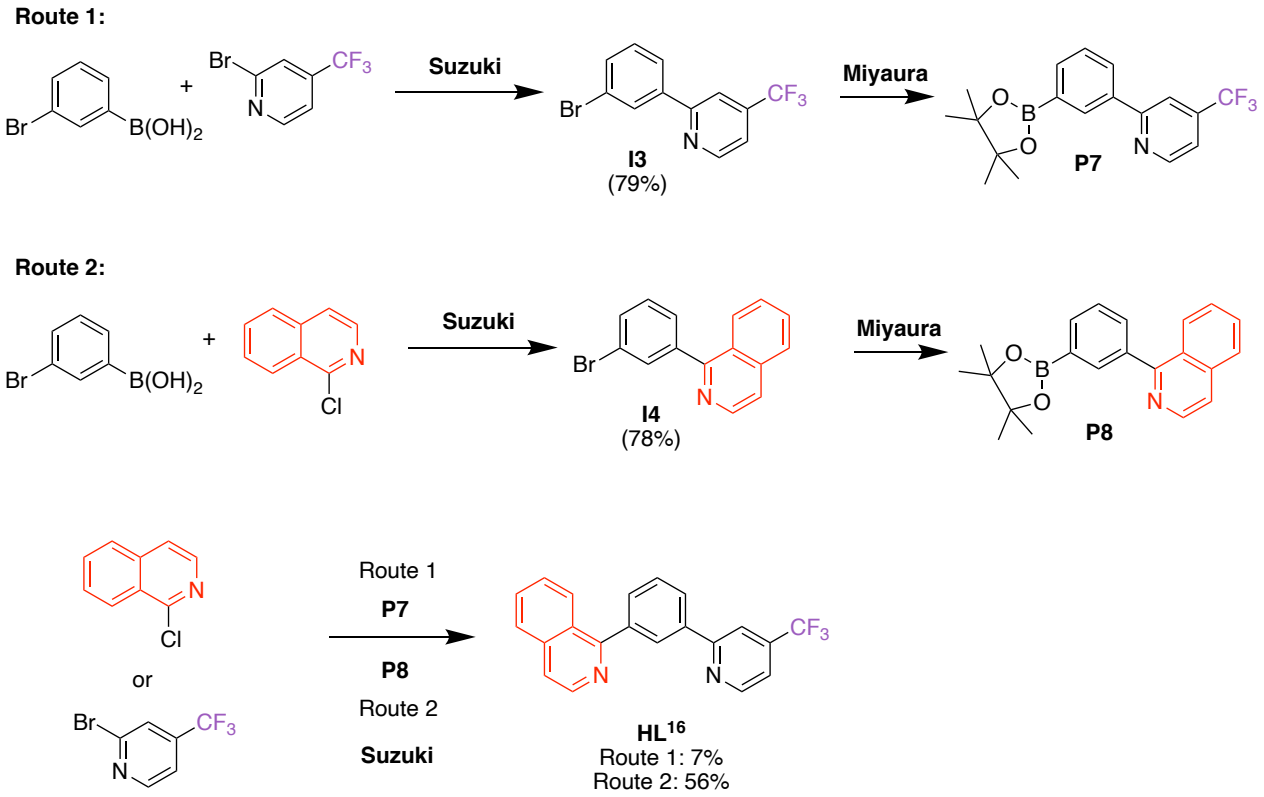

Scheme 3.3: *Different routes to HL[16].*

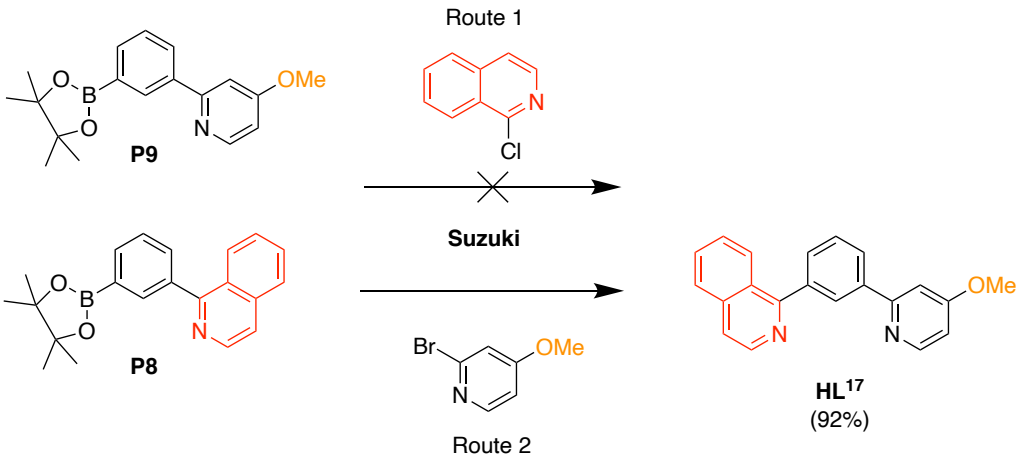

Scheme 3.4: *Synthesis of HL[17].*

A series of asymmetric proligands featuring the electron-deficient pyrimidine were synthesised according to **Scheme 3.5**. HL[18] and HL[19] were synthesised from the precursors **P4** and **P6**, which were also used for other syntheses. The synthesis of HL[20] and HL[21], where neither heterocycle is unsubstituted pyridine, required the synthesis of the pyrimidine-based precursor **P10**.

A target molecule HL[22] was proposed with an electron-donating -OMe group on one pyridyl ring and an electron-withdrawing –CF_3 group on the other to analyse whether "donor-acceptor" interactions between the differently substituted pyridine rings in adjacent complexes would facilitate excimer formation. The synthesis of this proligand would require either **P7** or **P9** as a precursor, both of which proved problematic in subsequent reactions (**Scheme 3.3** and **Scheme 3.4**). The chosen synthetic route involved the incorporation of the CF_3-containing pyridyl ring first; HL[22] was synthesised in 8% yield (**Scheme 3.6**). The corresponding ligands with just one substituted pyridine featuring either OMe or CF_3 were also synthesised as models for comparison of photophysical properties of the resulting complexes.

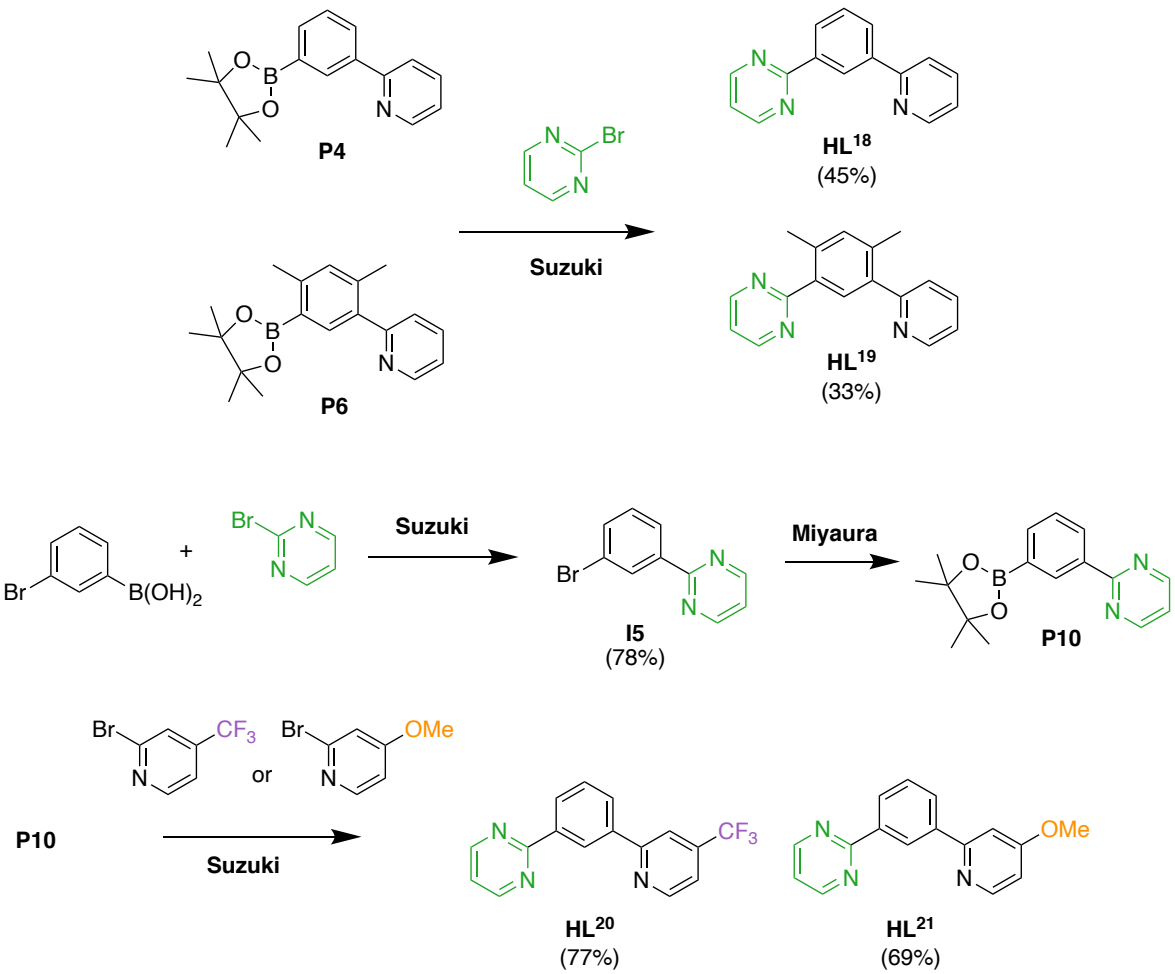

Scheme 3.5: *Synthesis of HL[18-21].*

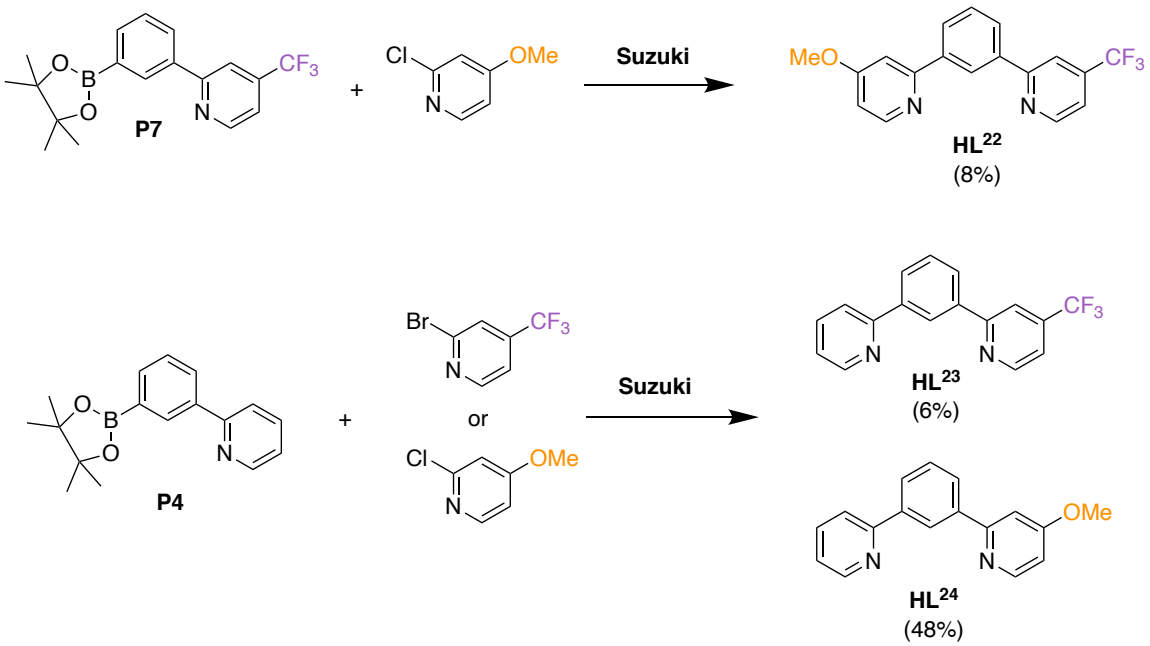

Scheme 3.6: *Synthesis of the "donor-acceptor" proligand HL[22] and respective mono-substituted proligands HL[23-24].*

To increase the solubility of the final target complex, a derivative of HL[22] was prepared that incorporates an additional *t*-butyl functionality on the central phenyl ring, HL[25] (**Scheme 3.7**). It was also of interest to see what effect, if any, the steric bulk of the *t*-butyl group would have on the intermolecular interactions. The synthesis of HL[25] required an additional step, relying on the statistical addition of one Bpin unit to give the mono-borylated intermediate **I6**, which was then reacted in its crude form.

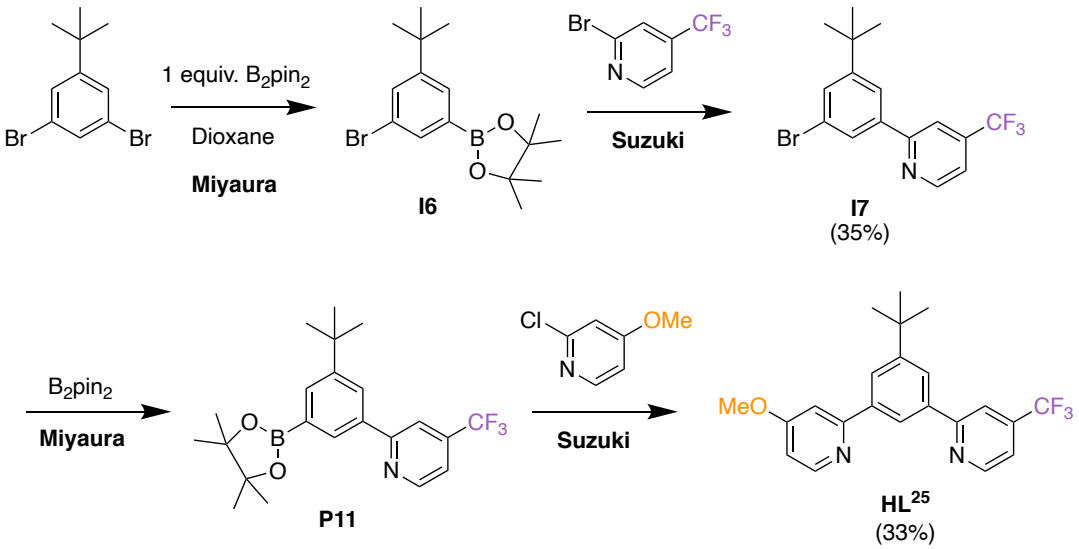

Scheme 3.7: *Synthesis of HL[25].*

Another novel "donor-acceptor" proligand functionalised with methyl groups at the 2- and 4-positions of the central phenyl ring was also targeted (**Scheme 3.8**). However, the yield of HL[26] was low (12 mg, 9%) giving insufficient material for complexation. This reaction could be repeated on a larger scale in future work to obtain PtL[26]Cl for comparison of photophysical properties.

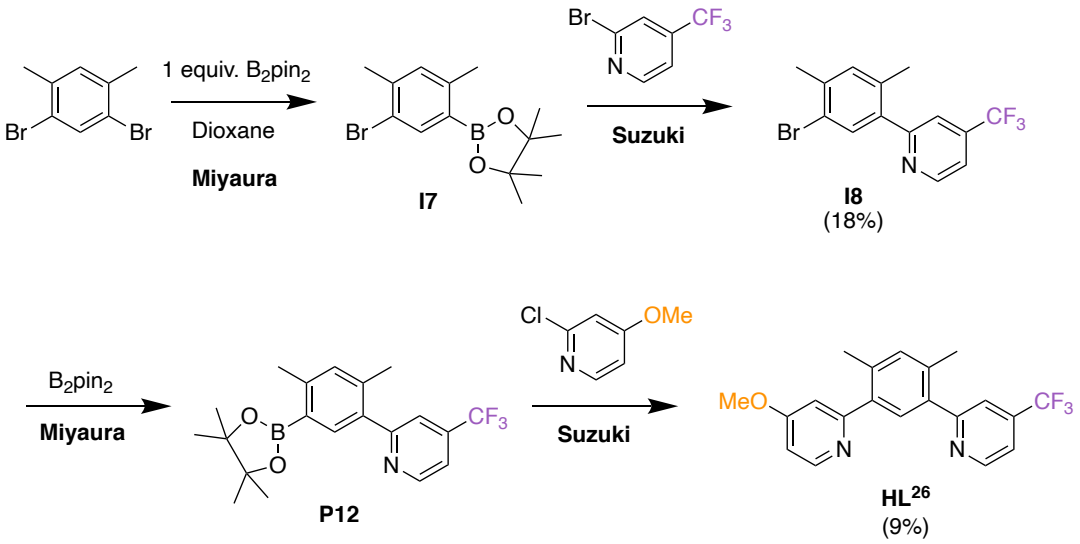

Scheme 3.8: *Synthesis of HL[26].*

Further asymmetric ligands were designed incorporating various polyazaheterocycles: pyrazine (HL[27]), quinazoline (HL[28]) and quinoxaline (HL[29]). These benzannulated quinazoline and quinoxaline rings were incorporated into the ligand design in an attempt to further red shift the emission of the respective complex due to the extended conjugation. The synthetic route to each proligand is reported in **Scheme 3.9**. Quinazoline-containing HL[28] could not be isolated, despite there being evidence of the molecular ion peak in the mass spectrum and an additional spot appearing on the TLC plate. Similar problems were observed by Chris

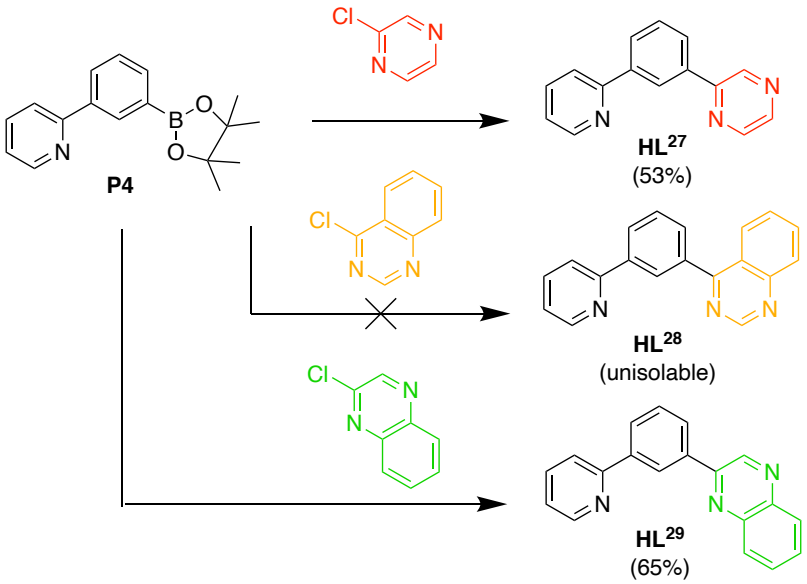

Scheme 3.9: *Synthesis of asymmetric ligands containing polyazaheterocycles was carried out by a Suzuki cross-coupling reaction (Na_2CO_3 (aq), DME, $Pd(PPh_3)_4$, 18 h, 85 °C).*

Hogg (another JAGW group member) when attempting to synthesise the symmetric N^C^N ligand containing two quinazoline rings.

Interestingly, a side product of a reaction targeting a potential bis-coordinating ligand yielded **P13**, which was reacted with phenylboronic acid to achieve the asymmetric proligand HL^{30} (**Scheme 3.10**). The addition of the extra phenyl group to the pyrazine ring allowed the synthesis of the complex $PtL^{30}Cl$ with no problems and is the only pyrazine-containing N^C^N-coordinated Pt(II) complex known to date, to the best of our knowledge.

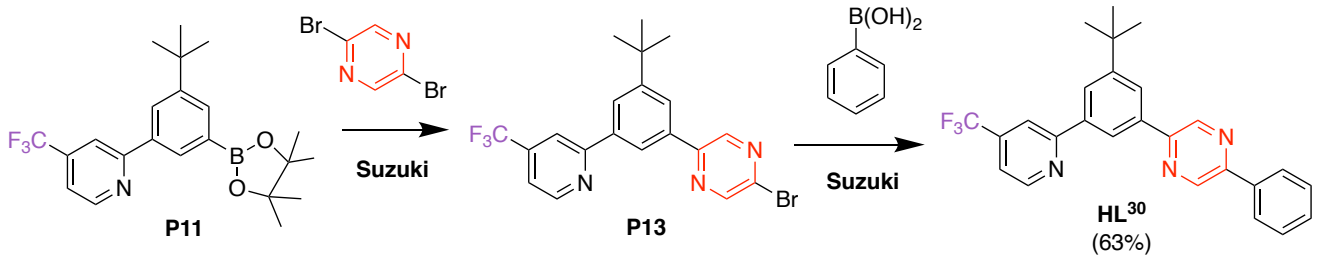

Scheme 3.10: *Synthesis of pyrazine-containing proligand HL^{30}.*

Complexation

Complexation to achieve asymmetric N^C^N-coordinated Pt(II) complexes of the form PtL^nCl was carried out in the same way as outlined in Chapter 2 for the symmetric complexes, by reacting the relevant proligand HL^n with K_2PtCl_4 in acetic acid at reflux for 60 h under an atmosphere of nitrogen. The complexes precipitated as bright solids that were washed with water, methanol and diethyl ether before extraction into DCM, from which the final products were obtained in yields ranging from 34 to 85% (**Figure 3.6**). Neither of the complexation reactions for proligands HL^{27} and HL^{29} featuring polyazaheterocycles resulted in products, only insoluble material. The only platinum(II) complexes of pyrazine-containing ligands reported to date feature bidentate ligands as opposed to tridentate.[118,119] $PtL^{30}Cl$ is a novel pyrazine-containing N^C^N-coordinating Pt(II) complex.

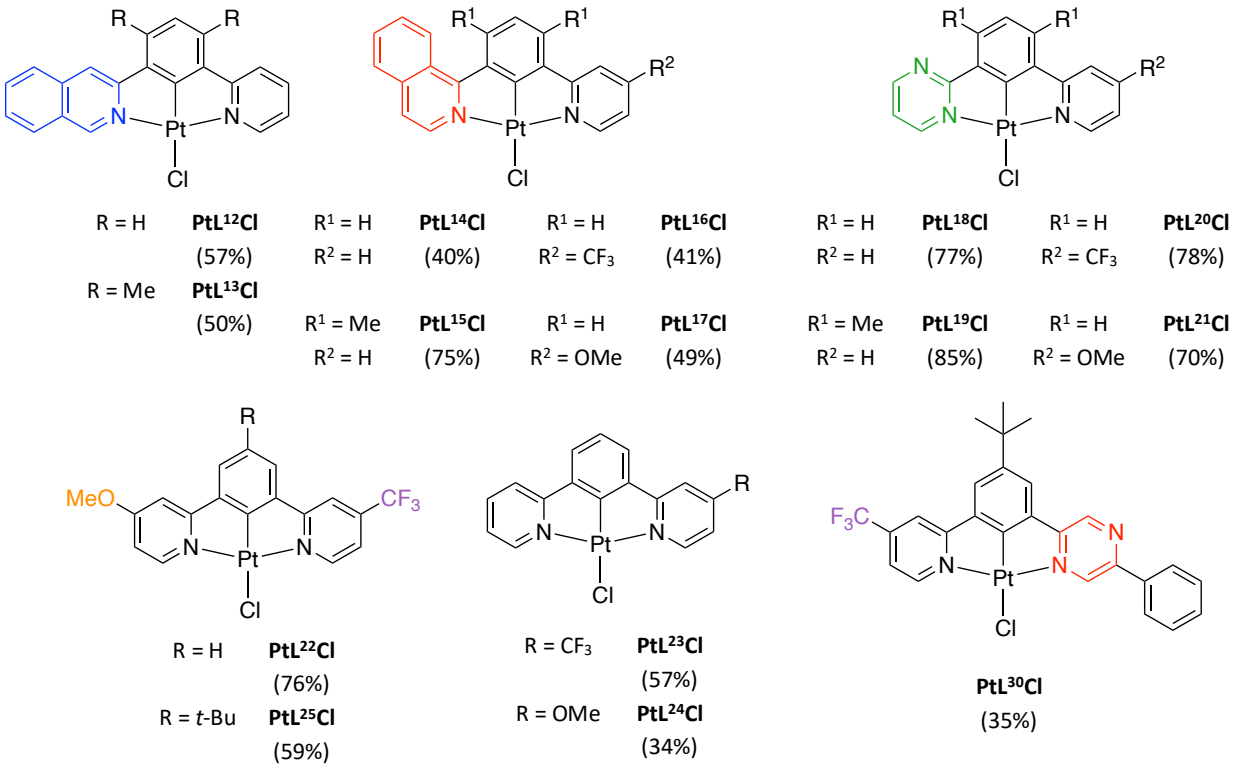

Figure 3.6: *Structures and yields of all the complexes prepared that feature asymmetric N^C^N-coordinating ligands.*

Crystals of $PtL^{12}Cl$ suitable for X-ray diffraction were grown by slow evaporation in DCM/MeOH. The molecules pack in a head-to-tail arrangement with overlap between the pyridine ring of one complex and isoquinoline ring of an adjacent complex. They are arranged in pairs, in almost perpendicular layers (**Figure 3.7**). There are no metallophilic interactions, the shortest Pt···Pt distance being 5.3724(7) Å, which is much longer than the sum of the van der Waals' radii for two Pt atoms (3.50 Å). The closest intermolecular distance was measured at 3.494(2) Å.

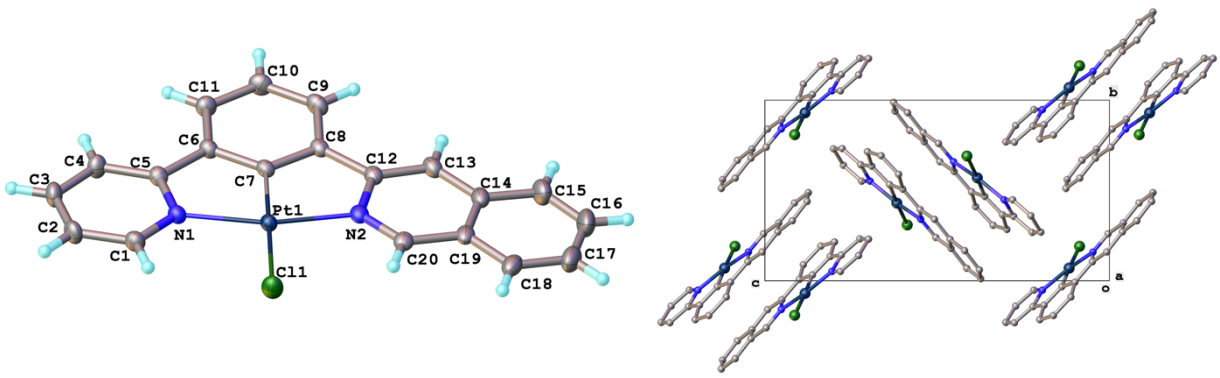

Figure 3.7: *Molecular structure and packing of $PtL^{12}Cl$ in the crystal at T = 120 K.*

Crystals of $PtL^{14}Cl$ were grown by slow evaporation of the complex from DCM/MeOH and analysed by X-ray diffraction. Its structure is shown in **Figure 3.8**, highlighting the head-to-tail packing arrangement, forming layers arranged in a zig-zag pattern. There are no metallophilic interactions with the closest Pt···Pt distance measuring 5.5064(8) Å, though the closest intermolecular distance is 3.361(5) Å indicative of π–π stacking. There is also a MeOH molecule in the unit cell which may affect the intermolecular interactions of the complex.

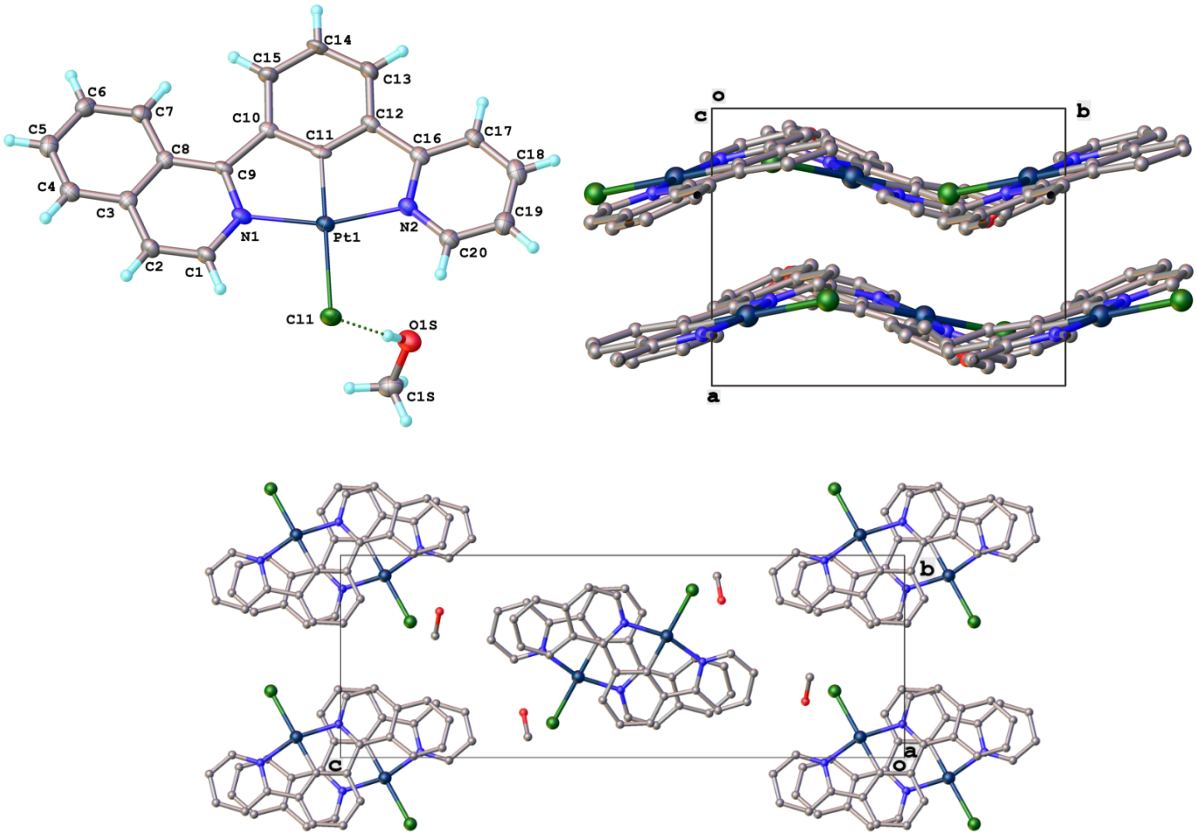

***Figure 3.8**: Molecular and crystal structure of $PtL^{14}Cl$ at T = 120 K highlighting a head-to-tail packing arrangement and formation of zig-zag type layers.*

Crystals of $PtL^{18}Cl$ were obtained by slow evaporation from DCM/MeOH and the molecular structure and crystal packing are shown in **Figure 3.9**. This complex crystallises in a non-centrosymmetrical space group as a racemic twin, with disordered pyridine and pyrimidine rings and antiparallel stacks of the complex along the a-axis. The shortest Pt···Pt distance is 5.1151(8) Å and the intermolecular distance is 3.352(15) Å, implying that no metallophilic interactions are present and only weak π–π stacking interactions.

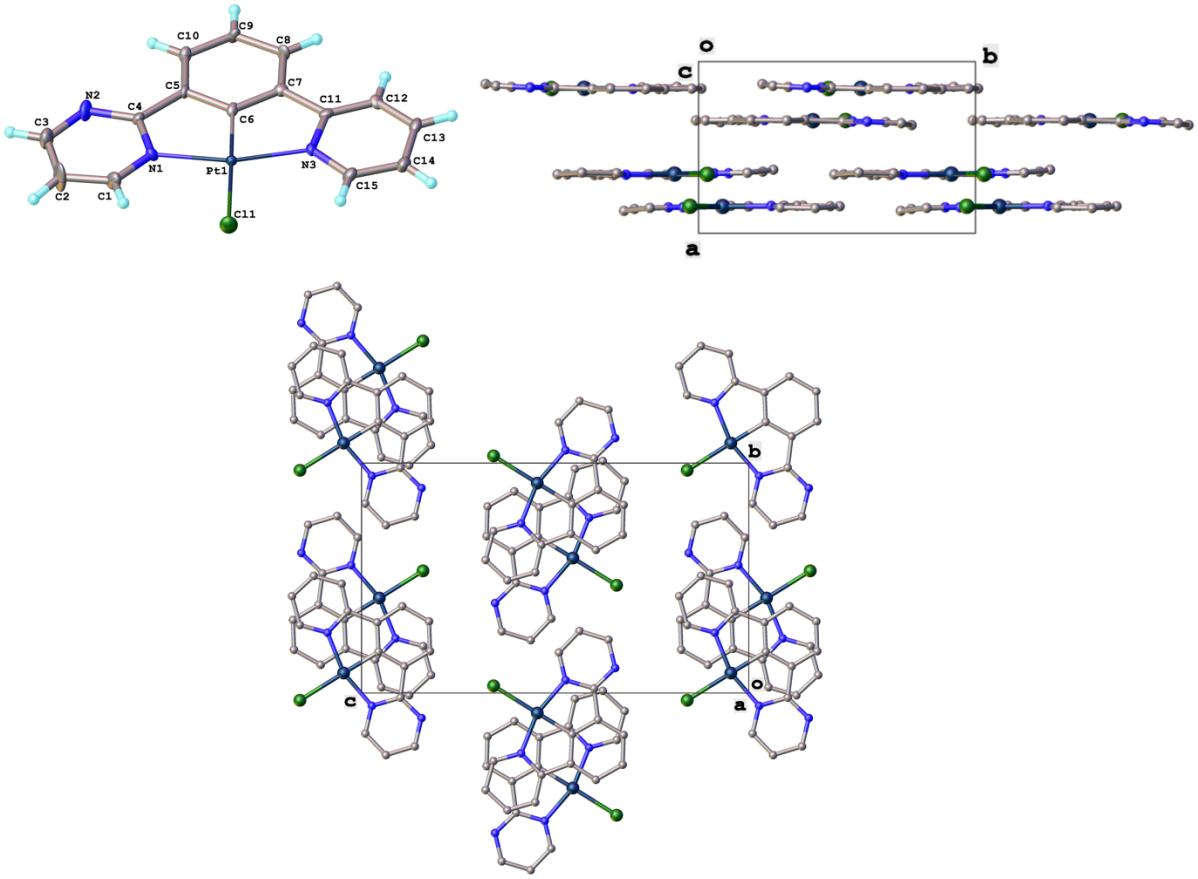

Figure 3.9: *Molecular structure and crystal packing of PtL[18]Cl at T = 120 K.*

A crystal of PtL[19]Cl was obtained by slow evaporation from $CDCl_3$ and the crystal structure determined (**Figure 3.10**). This polymorph of the complex crystallises in the monoclinic $P2_1/c$ space group. The independent part of the unit cell contains three virtually identical complexes and two chloroform molecules and in one of the complexes, pyridine and pyrimidine cycles are disordered. Adjacent complexes are stacked in pairs in a head-to-head configuration, with head-to-tail interactions between the pairs. The shortest Pt···Pt distance is 3.293(2) Å between the pair of complexes stacked in a head-to-head arrangement, indicative of Pt···Pt interactions, compared to 5.4387(6) Å for the complexes that interact in a head-to-tail manner. Presumably such interactions are promoted by the pyrimidine rings as no such interactions have been reported for Pt(dpyb)Cl or its derivatives. The shortest interplanar distances for the head-to-head pairs and head-to-tail pairs are 3.443(4) Å and 3.531(4) Å respectively, implying that any π–π stacking interactions do not

depend on the packing arrangement (i.e. head-to-head or head-to-tail) and hence the Pt···Pt distance.

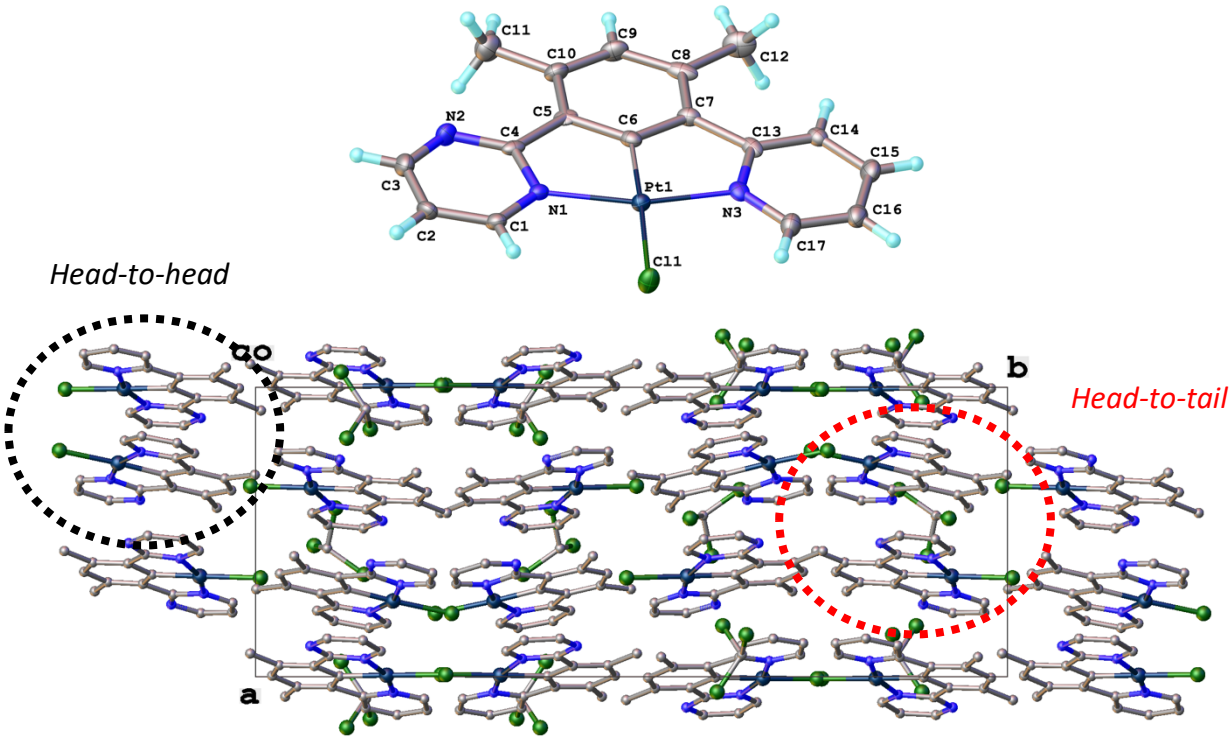

Figure 3.10: *Molecular structure and crystal packing of PtL[19]Cl highlighting the combination of head-to-tail (red) and head-to-head (black) packing.*

Crystals of PtL[20]Cl were grown by Dr Amit Sil by slow diffusion of MeOH into a DCM solution of the complex. Its structure reveals a slightly off-centre head-to-tail packing arrangement between adjacent molecules in the unit cell (**Figure 3.11**), allowing a shorter Pt···Pt distance than seen for other complexes that pack in a head-to-tail manner of 4.3465(4) Å. The interplanar distance of 3.4160(18) Å, measured between a pyridine unit of one complex and a pyrimidine unit of an adjacent complex, is indicative of weak π–π stacking interactions.

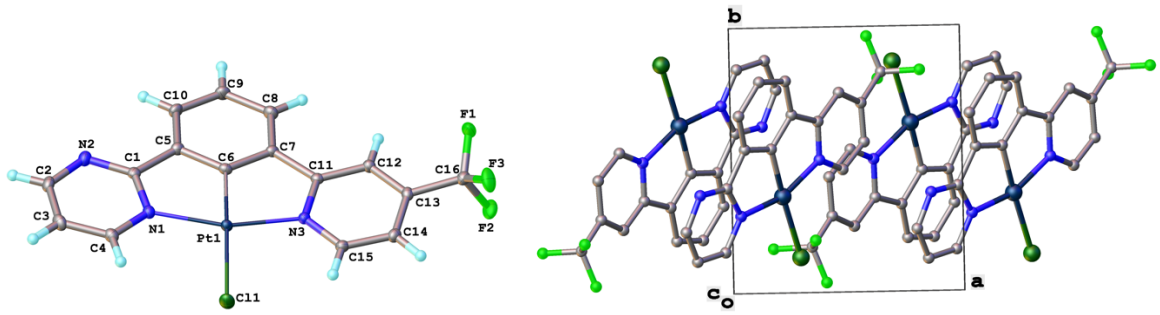

Figure 3.11: *Molecular structure and crystal packing of PtL[20]Cl at T = 120 K.*

The crystal structure of PtL[22]Cl is depicted in **Figure 3.12**. The complex crystallises in the triclinic P-1 space group and the crystal was obtained by slow evaporation from $CDCl_3$. The crystal packing reveals a slightly off-centre head-to-tail arrangement with overlap between the CF_3-substituted pyridine of one complex and the OMe-substituted pyridine of an adjacent molecule in an ordered manner, with an intermolecular distance of 4.3647(16) Å, too large to show any interactions. However, the shortest interplanar distance is 3.7559(18) Å, measured between the pyridine ring of one complex and the phenyl ring of another, indicative of weak π-π stacking interactions. The shortest Pt···Pt distance is 5.1394(5) Å indicating that no metallophilic interactions are present in this polymorph.

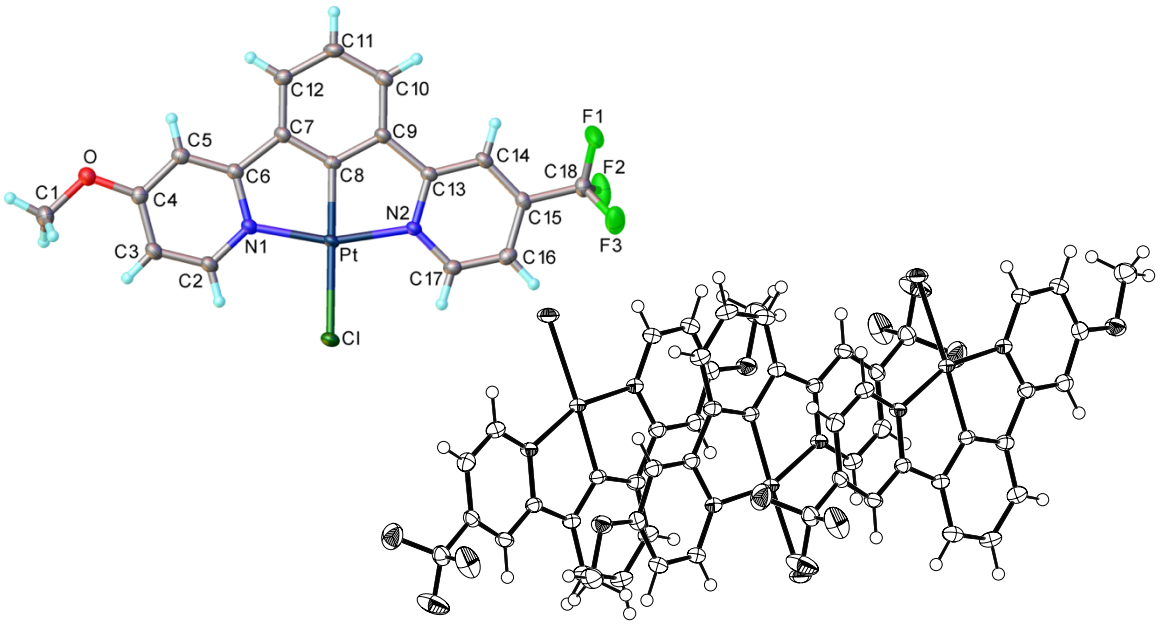

Figure 3.12: *Molecular structure and crystal packing of PtL[22]Cl.*

Crystals of $PtL^{23}Cl$ were grown from a DCM solution of the complex by adding MeOH and slowly evaporating the solution. The crystal structure is shown in **Figure 3.13**, highlighting a zig-zag type pattern involving the interaction of multiple complexes forming an interdigitated structure. No metallophilic interactions are present with a Pt···Pt distance of 5.2323(6) Å, but weak π–π interactions are likely as the shortest interplanar distance is 3.389(4) Å.

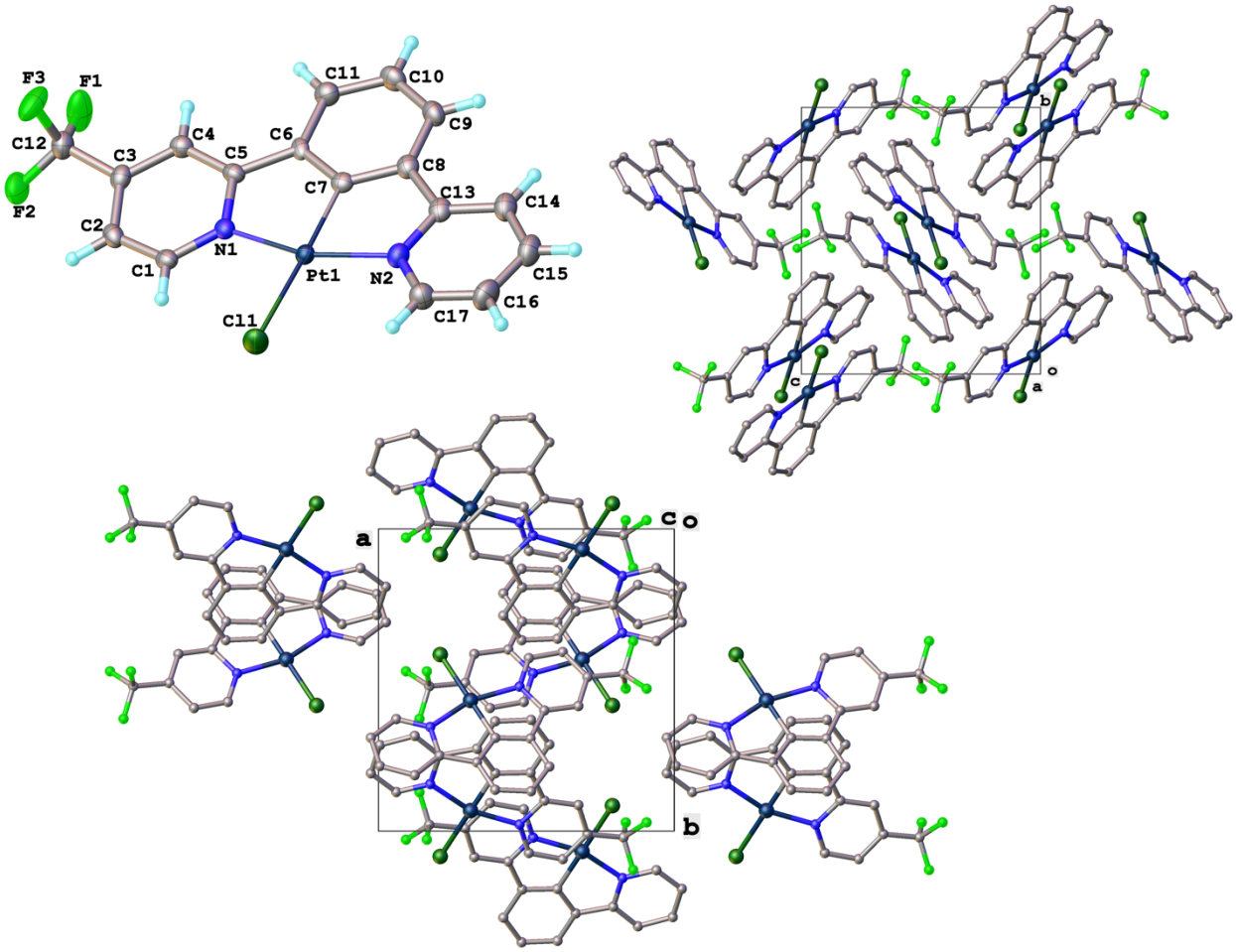

Figure 3.13: *Molecular structure and crystal packing of $PtL^{23}Cl$.*

The crystal structure of $PtL^{25}Cl$ is shown in **Figure 3.14**, obtained from crystals that were grown by slow evaporation from a DCM solution of the complex. The molecules pack in an off-centre, head-to-tail arrangement with barely any overlap between adjacent complexes in each layer suggesting that no intermolecular interactions are present, possibly due to the bulky substituents on the N^C^N ligand. The intermolecular distance is 4.1472(13) Å. Due to the off-centre arrangement, these

interactions are between two pyridine rings substituted with OMe groups, as opposed to PtL^{22}Cl (with no *t*-butyl group) where the CF_3-pyridine interacted with the OMe-pyridine of the adjacent molecule.

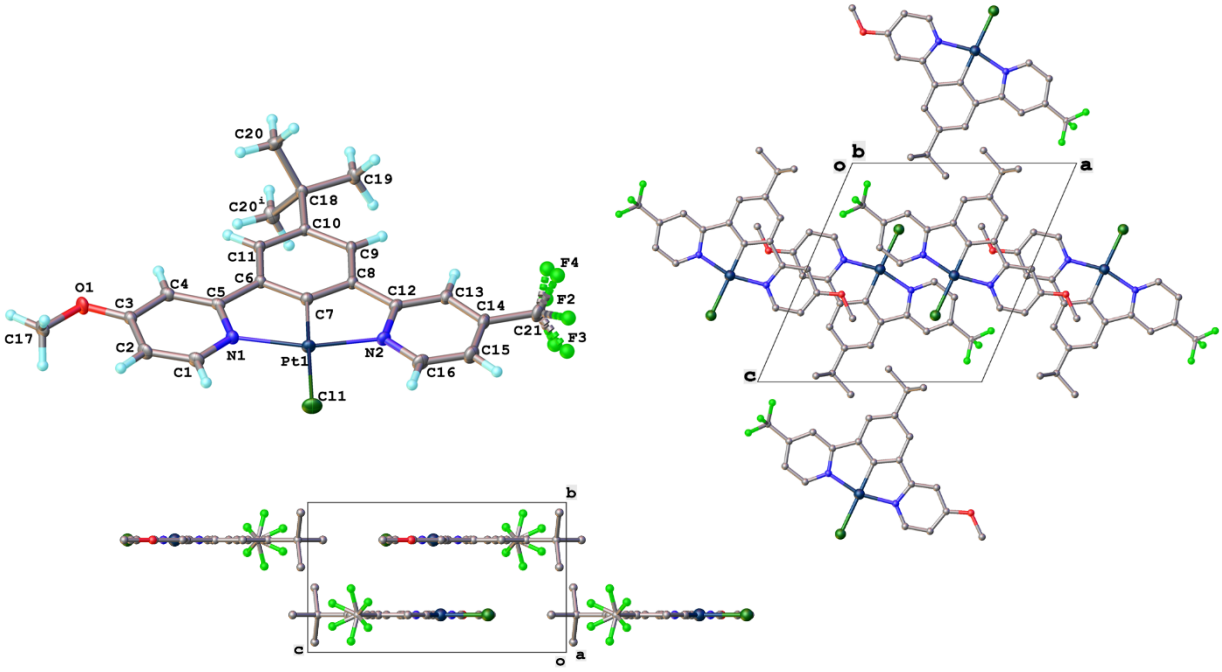

Figure 3.14: *Molecular structure and crystal packing of PtL^{25}Cl.*

Crystals of PtL^{30}Cl suitable for X-ray diffraction were obtained by slow diffusion of MeOH into a DCM solution of the complex. The crystal structure contains two independent molecules with a slightly different orientation of substituents and a DCM molecule in the unit cell (**Figure 3.15**). Crystal packing reveals an off-centre, head-to-tail packing arrangement with a Pt···Pt distance of 4.7067(9) Å. The molecules arrange themselves in columnar stacks with an intermolecular distance of 3.317(7) Å implying weak π–π stacking interactions.

In general, most complexes in this asymmetric series display head-to-tail interactions in the crystal structure, with no metallophilic interactions present. A summary of all the interactions and distances is shown in **Table 3.1**. Only PtL^{19}Cl packs in a head-to-head arrangement with short Pt···Pt contacts, but this crystal structure contains a mix of molecules packing in both a head-to-head arrangement and a head-to-tail arrangement.

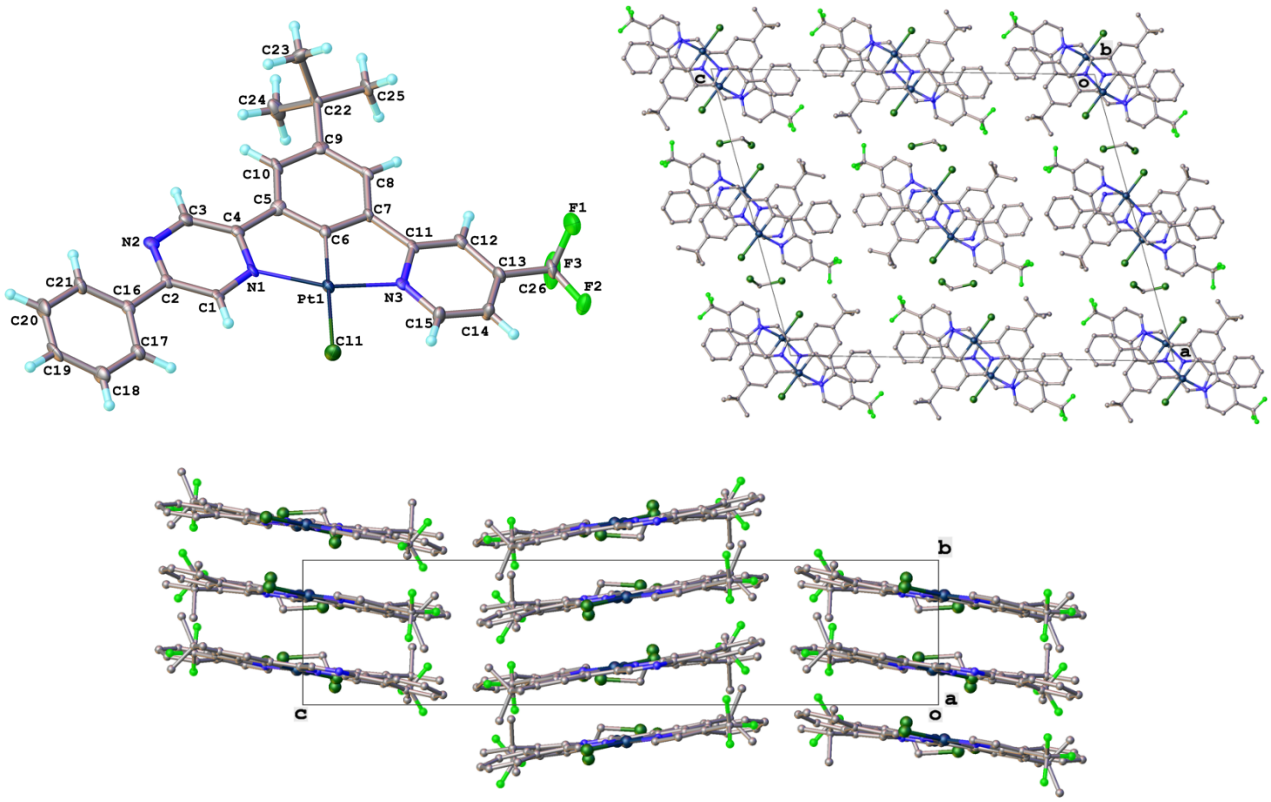

Figure 3.15: *Molecular structure and crystal packing of PtL^{30}Cl.*

Table 3.1: *A summary of intermolecular distances and packing arrangements in the crystal structures presented.*

Complex	Pt···Pt distance / Å	Interplanar distance / Å	Packing arrangement
PtL^{12}Cl	5.3724(7)	3.494(2)	Head-to-tail
PtL^{14}Cl	5.5064(8)	3.361(5)	Head-to-tail
PtL^{18}Cl	5.1151(8)	3.352(15)	Head-to-tail
PtL^{19}Cl	3.293(2) 5.4387(6)	3.443(4) 3.531(4)	Head-to-head Head-to-tail
PtL^{20}Cl	4.3465(4)	3.4160(18)	Head-to-tail
PtL^{22}Cl	5.1394(5)	3.7559(18)	Head-to-tail
PtL^{23}Cl	5.2323(6)	3.389(4)	Head-to-tail
PtL^{25}Cl	6.8899(3)	4.1472(13)	Head-to-tail
PtL^{30}Cl	4.7067(9)	3.317(7)	Head-to-tail

3.3.2 Photophysical properties

$PtL^{12\text{-}17}Cl$: Featuring 1- or 3-isoquinoline

A summary of the photophysical data of $PtL^{12\text{-}17}Cl$, the asymmetric complexes incorporating 1- or 3-isoquinoline, is given in **Table 3.2**. Absorption spectra of these complexes in DCM at 298 K are similar to those of the symmetric complexes of Chapter 2 (**Figure 3.16**). They display intense high-energy bands at $\lambda < 300$ nm, assigned to LC $\pi \rightarrow \pi^*$ transitions, and somewhat weaker bands at lower energy typical of CT transitions. The spectra resemble those of the parent symmetric complex bearing the substituted heterocycle of lowest energy, in this case the isoquinoline unit.

Figure 3.16a compares the absorption spectra of the two complexes bearing 3-substituted isoquinoline rings, namely $PtL^{12}Cl$ and $PtL^{13}Cl$. The vibrational structure appears rather better resolved in $PtL^{12}Cl$. **Figure 3.16b** depicts the absorption spectra of the four complexes featuring 1-substituted isoquinoline, $PtL^{14\text{-}17}Cl$. The absorption spectral profile is almost identical for all except $PtL^{16}Cl$, which shows only one band with a shoulder in the lower energy part of the spectrum, as opposed to the rest which show two distinct bands in this region. The most striking difference between the spectra of the 3- and 1-substituted isoquinoline complexes is that the lowest

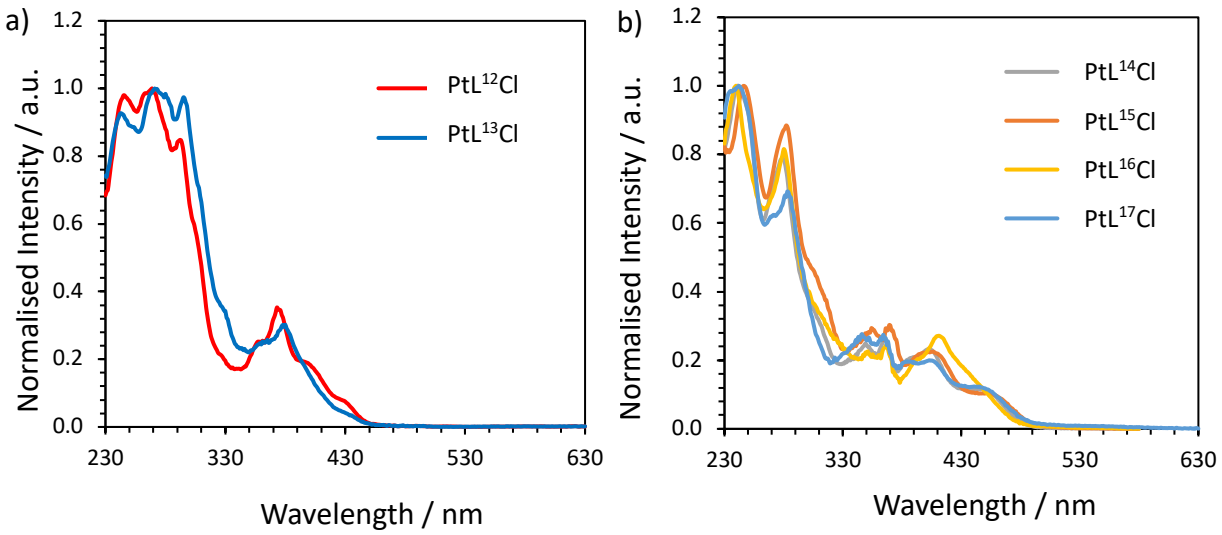

Figure 3.16: *Absorption spectra of complexes substituted with a) 3-isoquinoline and b) 1-isoquinoline in dilute DCM solution at 298 K.*

energy bands of the latter extend to significantly longer wavelengths up to about 490 nm (cf. 450 nm for the former).

The emission spectra for $PtL^{12}Cl$ and $PtL^{13}Cl$ in dilute and concentrated DCM solution are shown in **Figure 3.17**. The broad, structureless, long-wavelength excimer emission band is observed even in the most dilute solution, highlighting the propensity of these types of complexes functionalised with 3-isoquinoline to form excimers. The structured unimolecular emission between approx. 500 and 600 nm is a similar spectral profile for both complexes, differing only in the relative intensities of each peak. This shape of the monomer emission does not match Pt(dpyb)Cl where each peak can be assigned to the (0,0), (0,1) vibrational components and so forth, suggesting a contribution from both the 3-isoquinoline and pyridine unit to the vibrational modes and hence emission.

Both compounds form excimers at elevated concentration (**Figure 3.17**). The excimer emission energy maximum is blue-shifted by 34 nm for $PtL^{13}Cl$ (λ_{max} = 687 nm and 721 nm for $PtL^{12}Cl$ and $PtL^{13}Cl$ respectively), functionalised with methyl groups at the 2- and 4-positions of the central phenyl ring. This result is opposite to what was

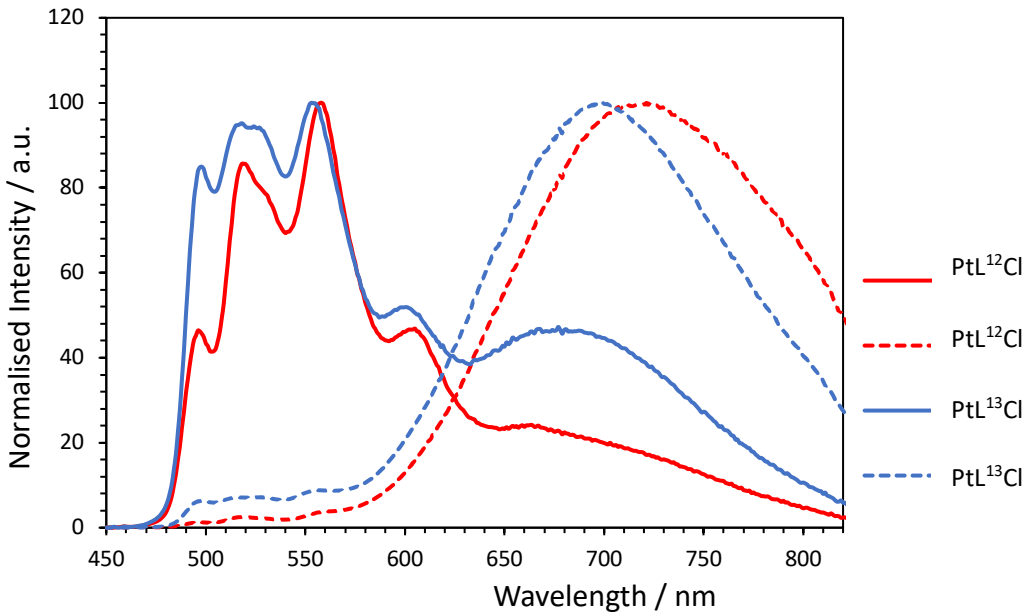

Figure 3.17: *Normalised emission spectra for $PtL^{12}Cl$ and $PtL^{13}Cl$ in dilute (1.6×10^{-6} M and 4.9×10^{-6} M) and concentrated degassed DCM solutions (1.8×10^{-3} M and 3.6×10^{-4} M) at 298 K for $PtL^{12}Cl$ and $PtL^{13}Cl$ respectively.*

predicted by the colour tuning principles for monomer emission, where addition of electron-donating methyl groups to the central phenyl ring should in principle increase the energy of the HOMO and lead to a red shift in the emission. Adding groups to this position may affect the ability of the complexes to interact and therefore shift the excimer to higher energy.

The excitation spectrum registered at 675 nm is identical to that registered at 520 nm, supporting the assignment of the broad, low-energy band that increases with concentration as being excimeric in nature. Both spectra match closely with the absorption spectrum (**Figure 3.18**). Compounds incorporating 3-isoquinoline (PtL^4Cl, PtL^8Cl and PtL^9Cl presented in Chapter 2) show unusually long lifetimes, particularly for compounds that form excimers with high efficiency, and these asymmetric derivatives, $PtL^{12}Cl$ and $PtL^{13}Cl$, are no exception (**Table 3.2**).

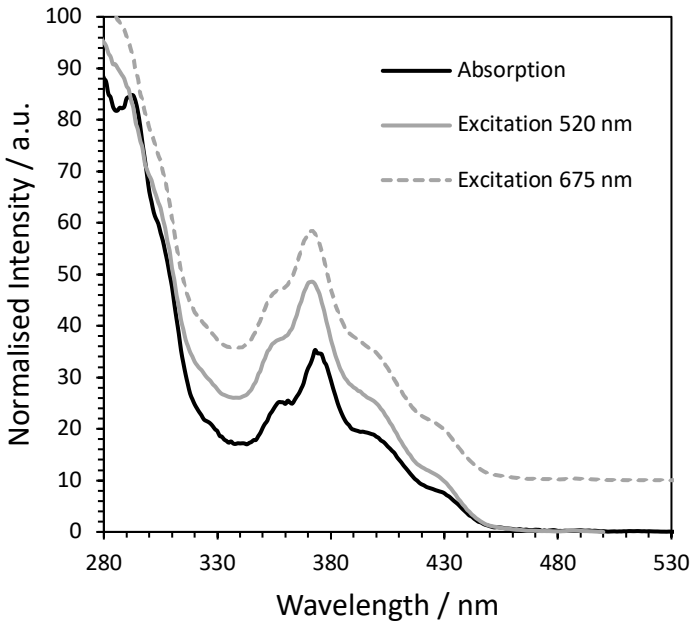

Figure 3.18: *Absorption and excitation spectrum at λ_{em} = 520 nm and 675 nm (offset by 10 nm) of $PtL^{12}Cl$ in dilute degassed DCM solution(1.6×10^{-6} M).*

Table 3.2: *Summary of photophysical properties of asymmetric complexes incorporating 1- or 3-substituted isoquinoline units ($PtL^{12\text{-}13}Cl$ and $PtL^{14\text{-}17}Cl$ respectively) in deoxygenated (aerated in parentheses) DCM solution at 298 K.*

Complex	λ_{abs} / nm (ε / M^{-1} cm^{-1})	λ_{em} / nm (monomer)	λ_{em} / nm (excimer)	Φ_{lum} [aer]	τ / ns [aer]	τ_0 / μs	k_r / 10^3 s^{-1}	$\sum k_{nr}$ / 10^3 s^{-1}	k_{SQ} / 10^9 M^{-1} s^{-1}	$k_Q(O_2)$ / 10^8 M^{-1} s^{-1}
$PtL^{12}Cl$	250 (36600), 272 (37400), 295 (30800), 360 (9450), 375 (13200), 405 (6180), 430 (2690)	500, 522, 533, 561, 610	721	0.62 [0.03]	49000 [870]	36	13	8	3.3	5.2
$PtL^{13}Cl$	245 (38500), 273 (41600), 286 (38900), 298 (38800), 330 (14200), 366 (11000), 381 (13000), 425 (2100)	500, 520, 530, 557, 605	687	0.55 [0.01]	25000 [510]	32	22	18	3.7	8.7
$PtL^{14}Cl$	245 (36400), 281 (28800), 351 (8870), 366 (9680), 390 (7810), 405 (8650), 450 (4360)	600, 646, 698	-	0.11 [0.02]	3500 [580]	3.5	32	260	0.5	6.6
$PtL^{15}Cl$	249 (39000), 284 (34600), 356 (11300), 371 (11700), 405 (4850), 445 (4070)	623sh, 661	-	0.05 [0.01]	2700 [470]	2.7	20	350	0.05	8.0
$PtL^{16}Cl$	240 (36400), 281 (31900), 353 (7870), 368 (8460), 393 (7570), 410 (10500)	599, 646, 700	770	0.09 [0.01]	3400 [470]	3.5	26	270	0.7	8.4
$PtL^{17}Cl$	246 (44800), 273sh (28600), 286 (31100), 349 (11900), 367 (11300), 392 (8230), 410 (8110) 445 (5290)	597, 643, 698	-	0.13 [0.02]	3200 [520]	3.2	40	280	0.6	7.4

The variation of the emission spectrum of PtL[12]Cl over a range of concentrations is shown in **Figure 3.19**. The broad longer wavelength excimer band dominates the spectrum in concentrated solution, with almost no contribution from the unimolecular emission, once again highlighting the propensity of these complexes featuring 3-substituted isoquinoline to form excimers.

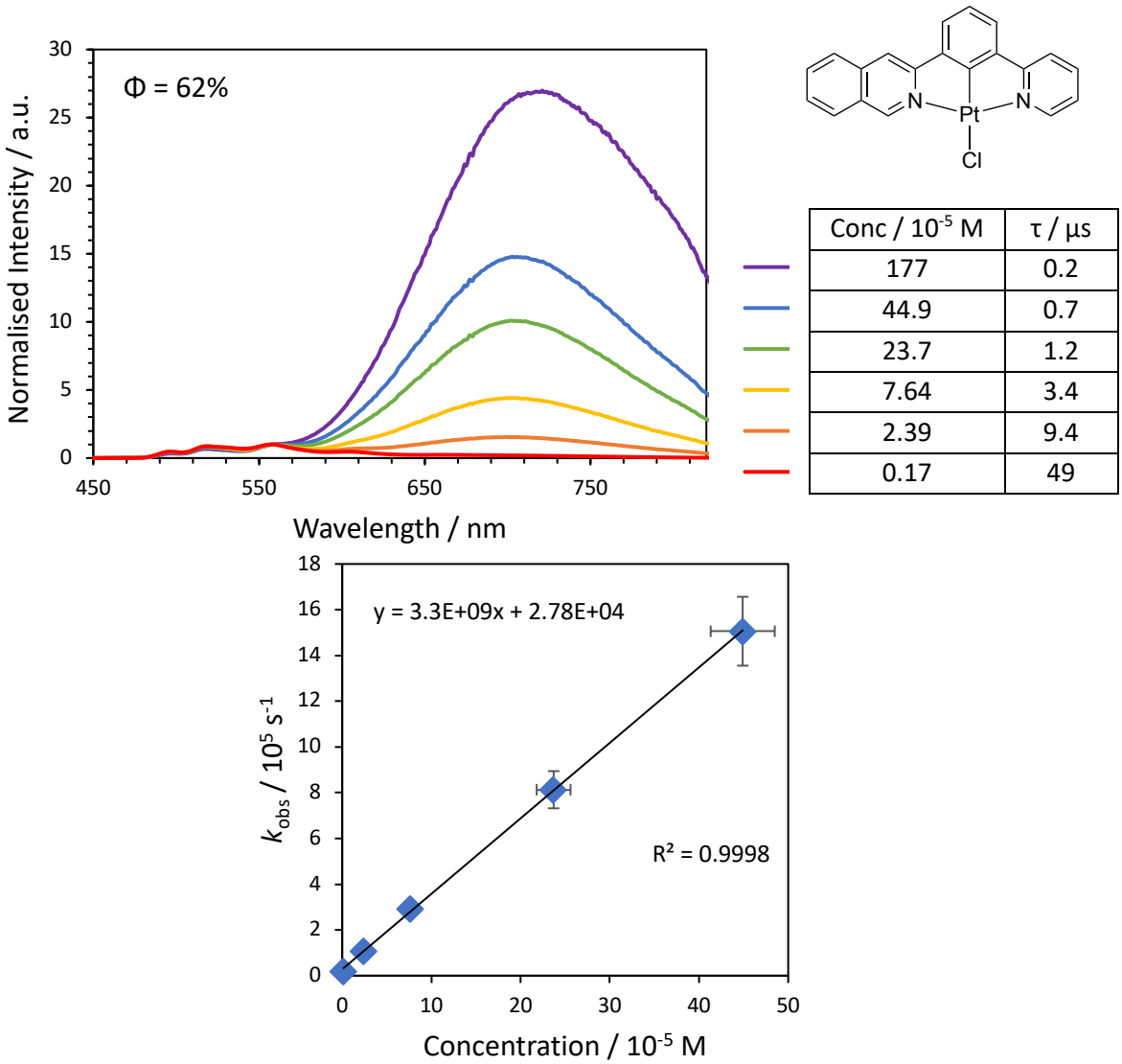

Conc / 10^{-5} M	τ / µs
177	0.2
44.9	0.7
23.7	1.2
7.64	3.4
2.39	9.4
0.17	49

Figure 3.19: *Concentration-dependent emission of PtL[12]Cl in degassed DCM solution at 298 K with the corresponding Stern-Volmer plot (bottom). Errors are discussed in Section 7.1.*

Figure 3.20 shows the concentration-dependent emission of PtL[13]Cl in degassed DCM solution. Again, the emission spectrum is dominated by the broad longer wavelength excimeric emission unless in dilute solution. The high propensity of these complexes featuring 3-substituted isoquinoline to form excimers is reflected in the relatively high self-quenching

constants, with values of 3.3×10^9 M^{-1} s^{-1} and 3.7×10^9 M^{-1} s^{-1} for $PtL^{12}Cl$ and $PtL^{13}Cl$ respectively (**Table 3.2**). The assignment of the lower energy band to excimer formation is supported by the excitation spectrum, which matches the absorption spectrum (**Figure 3.21**). The lifetimes reported in **Figure 3.19** and **Figure 3.20** are measured for the monomer emission; lifetimes recorded of the long wavelength excimeric band in each case were identical (within error). This is highlighted in the TCSPC decays, where a rise time can be seen for the excimeric emission in each case, but once it reaches the maximum, the species decays with the same lifetime as the monomer (**Figure 3.22**).

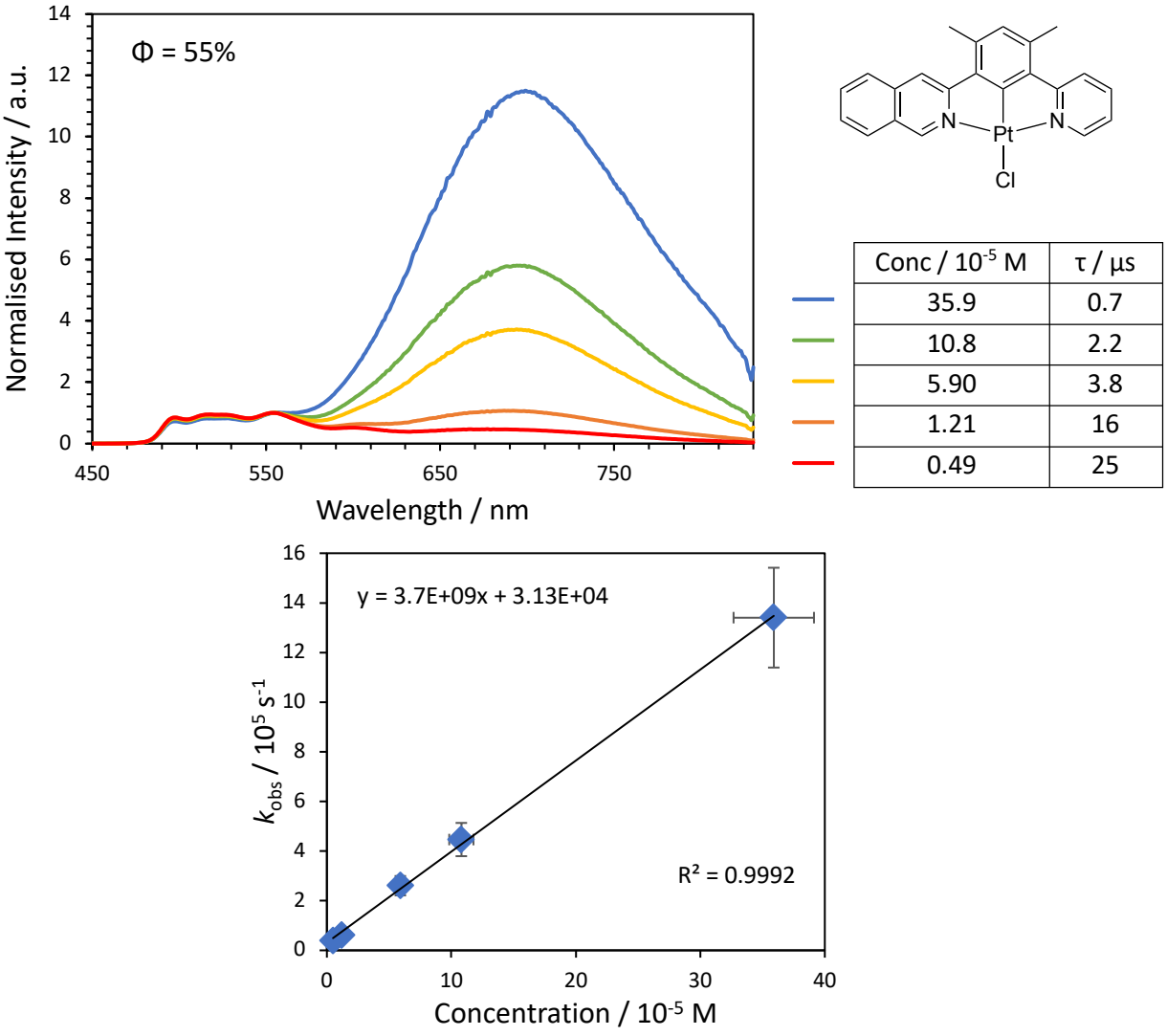

Figure 3.20: *Concentration-dependent emission of $PtL^{13}Cl$ in degassed DCM solution at 298 K, with the corresponding Stern-Volmer plot (bottom). Errors are discussed in Section 7.1.*

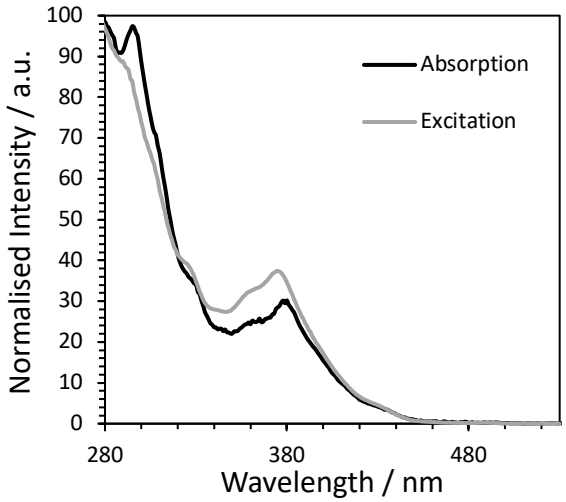

***Figure 3.21**: Absorption and excitation (λ_{em} = 555 nm) spectra of PtL^{13}Cl.*

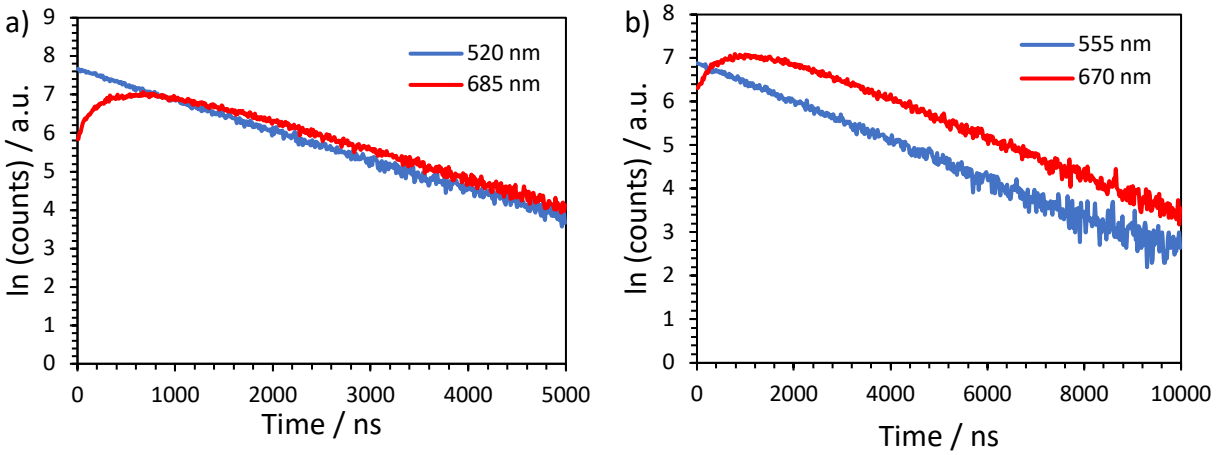

***Figure 3.22:** TCSPC decays of a) PtL^{12}Cl at λ_{em} = 520 nm (monomer) and 685 nm (excimer), and b) PtL^{13}Cl at λ_{em} = 555 nm (monomer) and 670 nm (excimer). All measurements are in degassed DCM solution at 298 K (3 × 10^{-4} M and 10^{-4} M for PtL^{12}Cl and PtL^{13}Cl respectively.*

Figure 3.23 compares the RT emission spectra of complexes incorporating 1-substituted isoquinoline in dilute degassed DCM solution. The spectra of all the complexes are identical, with the exception of PtL^{15}Cl. This is indicative of an excited state that has a contribution only from the isoquinoline ring as this is the common motif in all the complexes in this series. PtL^{15}Cl displays an emission shape identical to that of its parent symmetric complex PtL^{6}Cl, (**Figure 2.18c**), which interestingly resembles the emission of complexes featuring quinoline not 1-substituted isoquinoline. The spectrum is not vibronically resolved like the other complexes in the series. This may reflect a greater degree of distortion in the excited state

associated with repulsion between the isoquinoline H^8 and the central methyl group *ortho* to the pyridine—isoquinoline bond.

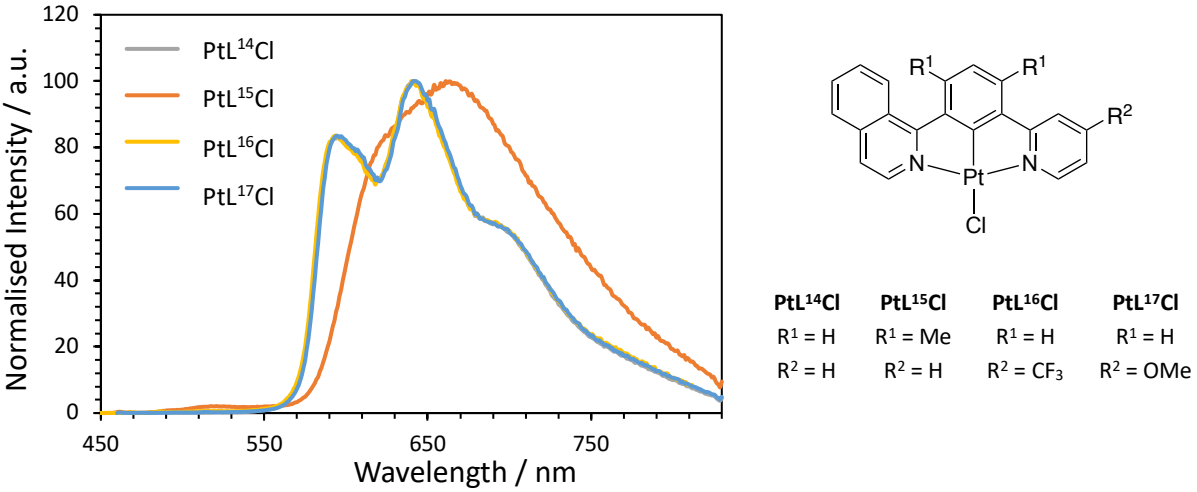

Figure 3.23: *Emission spectra of $PtL^{14-17}Cl$ in dilute (~ 10^{-6} M) degassed DCM solution at 298 K.*

$PtL^{16}Cl$ is the only complex in this series to exhibit significant excimer formation at elevated concentration, highlighted by the appearance of the broad longer wavelength band at around 770 nm (**Figure 3.24**). There is potentially some evidence of excimer formation for $PtL^{14}Cl$ in the most concentrated solution (4×10^{-4} M). All other complexes in the series show solution-state emission spectra that are

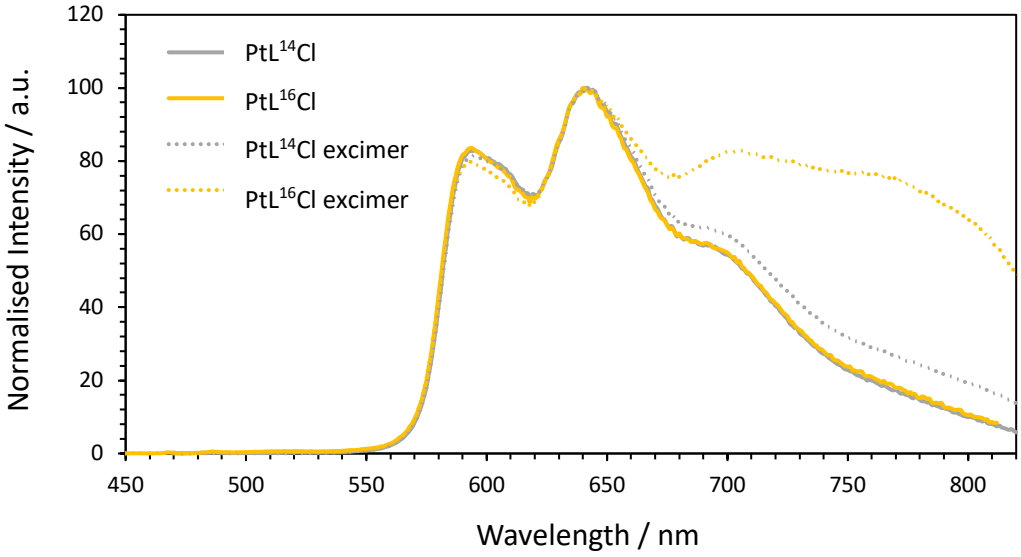

Figure 3.24: *Emission spectra of $PtL^{14}Cl$ and $PtL^{16}Cl$ in dilute (1.5×10^{-5} M and 7.7×10^{-6} M) and concentrated (4.0×10^{-4} M and 3.0×10^{-4} M) degassed DCM solution at 298 K, highlighting excimer formation, stronger for the latter.*

independent of concentration over the range investigated (up to 3×10^{-4} M). The k_{SQ} value for $PtL^{14}Cl$ is higher at 0.5×10^9 M^{-1} s^{-1}, along with excimer-forming $PtL^{16}Cl$ at 0.7×10^9 M^{-1} s^{-1} compared to 0.05×10^9 M^{-1} $s^{-1}$for $PtL^{15}Cl$ which shows no evidence of excimer formation in solution. The CF_3-substituted pyridine may promote intermolecular interactions for $PtL^{16}Cl$.

$PtL^{18\text{-}21}Cl$: Featuring pyrimidine

Absorption spectra of complexes $PtL^{18\text{-}21}Cl$ that feature pyrimidine are shown in **Figure 3.25**. All spectra are similar to one another, with the most noticeable difference being the additional band between 310 and 350 nm for $PtL^{19}Cl$. The tail of the lower energy CT absorption band is also red shifted slightly for $PtL^{20}Cl$.

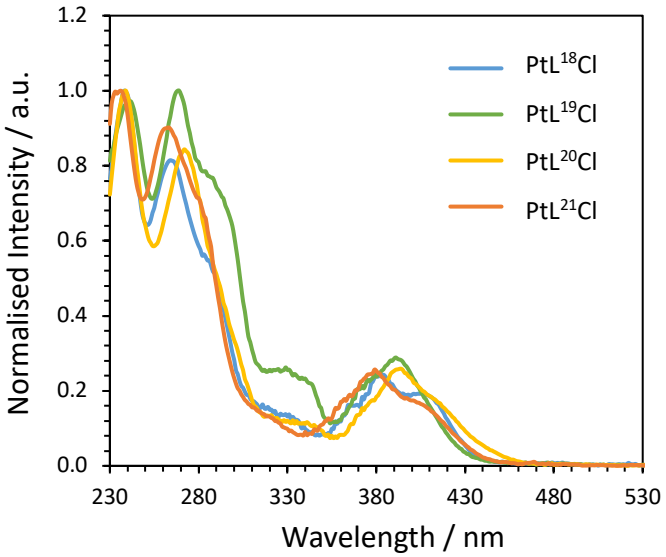

Figure 3.25: *Absorption spectra of $PtL^{18\text{-}21}Cl$ featuring pyrimidine, in dilute DCM solution at 298 K.*

The emission spectra for these complexes, $PtL^{18\text{-}21}Cl$, in dilute solution are shown in **Figure 3.26a**. The monomer emission for each complex is almost identical, differing only in the ratio of each peak and a slight shift in λ_{max}, suggesting that the emission profile is dictated by the pyrimidine ring. $PtL^{20}Cl$ displays a significantly red-shifted monomer emission due to the presence of the lower energy CF_3-substituted pyridine ring, which matches with the absorption spectrum showing a longer tail to the CT band.

Despite the monomer emission showing negligible change upon change of substituents, the excimer emission is more greatly affected, as observed upon increasing the concentration. **Figure 3.26b** depicts the excimer emission of each complex, normalised to the maximum of the monomer emission. The excimer emission red shifts in the order $PtL^{21}Cl < PtL^{18}Cl < PtL^{19}Cl < PtL^{20}Cl$.

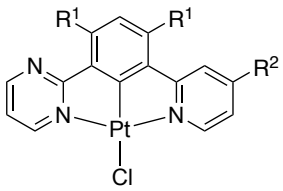

$PtL^{18}Cl$	$PtL^{19}Cl$	$PtL^{20}Cl$	$PtL^{21}Cl$
R^1 = H	R^1 = Me	R^1 = H	R^1 = H
R^2 = H	R^2 = H	R^2 = CF_3	R^2 = OMe

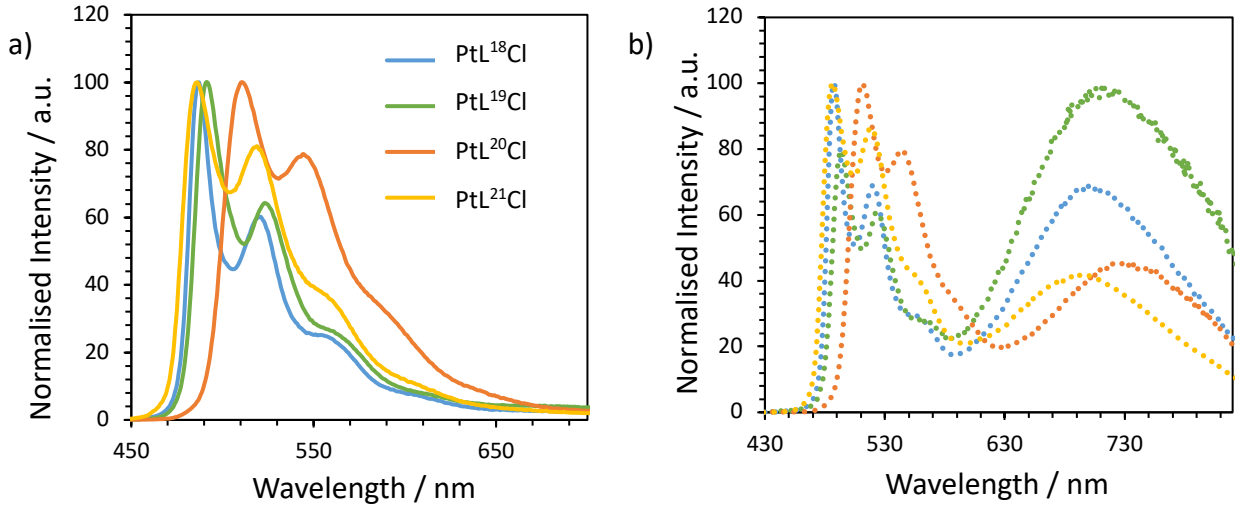

Figure 3.26: *Emission spectra of complexes featuring pyrimidine, $PtL^{18\text{-}21}Cl$, in a) dilute solution showing monomer emission, and b) saturated solution showing excimer emission. All measured in degassed DCM solution at 298 K.*

The concentration of the saturated solutions in **Figure 3.26b** are 8.3×10^{-4} M, 1.4×10^{-3} M, 8.0×10^{-4} M and 6.1×10^{-4} M, in numerical order for $PtL^{18\text{-}21}Cl$, which reflect the relative solubilities of the complexes in DCM solution. The intensity of excimer emission can therefore only be compared for $PtL^{18}Cl$ and $PtL^{20}Cl$ as these were measured at roughly the same concentration. The presence of the CF_3-substituted pyridine decreases the intensity of excimer emission, at the same time as red shifting the emission. From the study of this series, it is suggested that adding an EDG such

as OMe to the 4-position of the pyridine ring blue shifts the excimer, whereas adding an EWG to the same position red shifts the excimer, as previously reported for 4-substituted CF_3-pyridine.[21,87]

Each complex has a relatively high quantum yield, ranging from 0.57 to 0.64 (**Table 3.3**). The self-quenching constants are also relatively high (ranging from 3.4×10^{-9} M^{-1} s^{-1} to 4.7×10^{-9} M^{-1} s^{-1}), reflecting the formation of excimers for all complexes in this series.

Table 3.3: *Summary of photophysical properties of asymmetric complexes substituted with pyrimidine ($PtL^{18\text{-}21}Cl$) in deoxygenated (aerated in parentheses) DCM solution at 298 K.*

Complex	λ_{abs} / nm (ε / M^{-1} cm^{-1})	λ_{em} / nm (monomer)	λ_{em} / nm (excimer)	Φ_{lum} [aer]	τ / ns [aer]	τ_0 / μs	k_r / 10^3 s^{-1}	$\sum k_{nr}$ / 10^3 s^{-1}	k_{SQ} / 10^9 M^{-1} s^{-1}	$k_Q(O_2)$ / 10^8 M^{-1} s^{-1}
$PtL^{18}Cl$	240 (31200), 268 (25100), 290 (15900), 335 (3850), 365 (4720), 384 (7720), 405 (6080)	488, 523, 563, 610sh	700	0.59 [0.06]	5300 [480]	7.5	111	78	4.7	8.7
$PtL^{19}Cl$	244 (33800), 270 (35800), 290 (26600), 331 (9040), 345 (7000), 377 (7970), 390 (9890)	493, 528, 568	716	0.59 [0.04]	5600 [320]	6.8	105	74	4.5	13.3
$PtL^{20}Cl$	240 (35700), 274 (29800), 329 (4540), 348 (3690), 373sh (5550), 395 (9250), 416sh (5890)	514, 548, 595 sh	730	0.64 [0.12]	5000 [890]	5.6	128	73	3.4	4.2
$PtL^{21}Cl$	239 (34300), 265 (31400), 283 (23900), 325 (4360), 382 (8600), 400 (6090)	488, 522, 560	698	0.57 [0.05]	4500 [400]	5.3	127	97	4.0	10.5

PtL$^{22\text{-}25}$Cl: 'Donor-acceptor' and related complexes

The absorption spectra for complexes featuring an EDG (OMe-substituted pyridine) and/or an EWG (CF_3-substituted pyridine) are shown in **Figure 3.27a**. The spectra are almost identical for all complexes except PtL^{24}Cl. The tail of the lower energy CT absorption band of this complex is blue-shifted, or it could be explained in the opposite way in that the tail of the CT band for all the other complexes seems to have a shoulder that absorbs out to lower enegry. This is suggesting that the CF_3-substituted pyridine is the moiety responsible for the CT bands for all complexes, as PtL^{24}Cl is the only complex without this substituent.

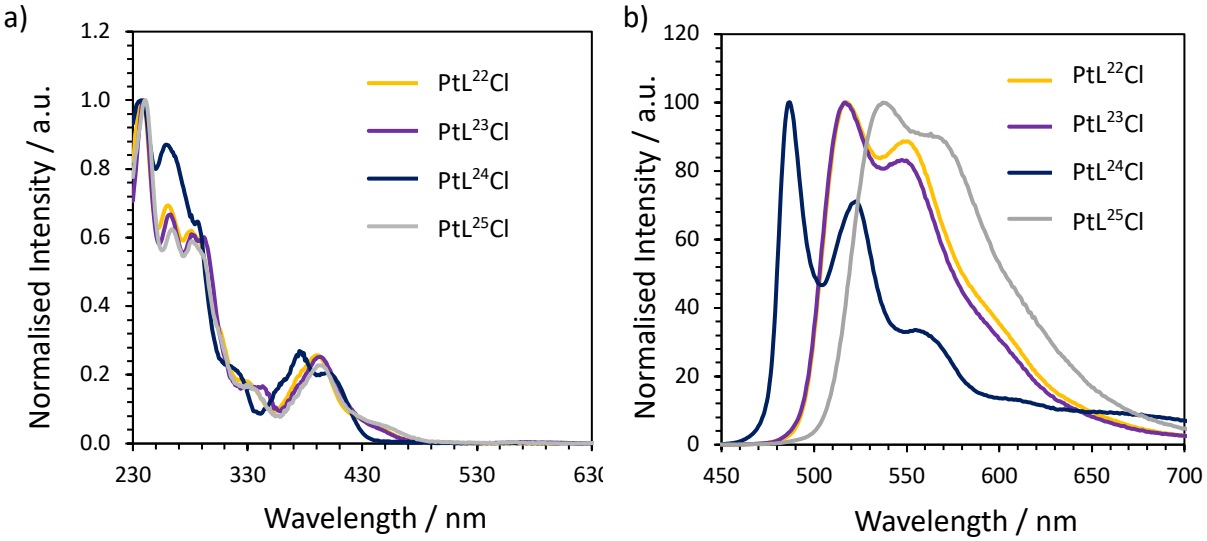

***Figure 3.27**: a) Absorption spectra of PtL$^{22\text{-}25}$Cl featuring 'donor-acceptor' type ligands and their corresponding parent complexes, in dilute DCM solution at 298 K; b) Monomeric emission of PtL$^{22\text{-}25}$Cl in dilute degassed DCM solution at 298 K.*

The monomeric emission spectra for these complexes are shown in **Figure 3.27b** and a summary of all the photophysical parameters can be found in **Table 3.4**. The emission profile of PtL^{22}Cl is almost identical to that of PtL^{23}Cl, implying that the LUMO is solely based on the CF_3-substituted pyridine. The monomer emission of PtL^{24}Cl is significantly blue-shifted in comparison, likely due to the EDG raising the energy of the LUMO. Addition of an electron-donating *t*-butyl group at the 4-position of the central phenyl ring to give PtL^{25}Cl red-shifts the monomer emission maximum by 17 nm whilst also increasing the quantum yield from 0.57 (for PtL^{22}Cl) to 0.77.

The excimeric emission spectra of PtL$^{22\text{-}25}$Cl are shown in **Figure 3.28**, normalised to λ_{max}. Interestingly, in addition to having identical unimolecular emission, PtL^{22}Cl and PtL^{23}Cl exhibit identical excimeric emission, peaking at 745 nm. Incorporation of the OMe-substituted pyridine to create the "donor-acceptor" type design (PtL^{23}Cl) has no effect on the emission, which must only be influenced by the lower energy CF_3-substituted pyridine which is present in both PtL^{22}Cl and PtL^{23}Cl. The excimer emission λ_{max} of PtL^{24}Cl is significantly blue shifted to 672 nm in comparison to the rest of the complexes in the series. Its excimer emission is also blue shifted by 30 nm in relation to Pt(dpyb)Cl (λ_{max} = 700 nm), suggesting that the OMe-substituted pyridine is responsible for the blue-shifted excimer.

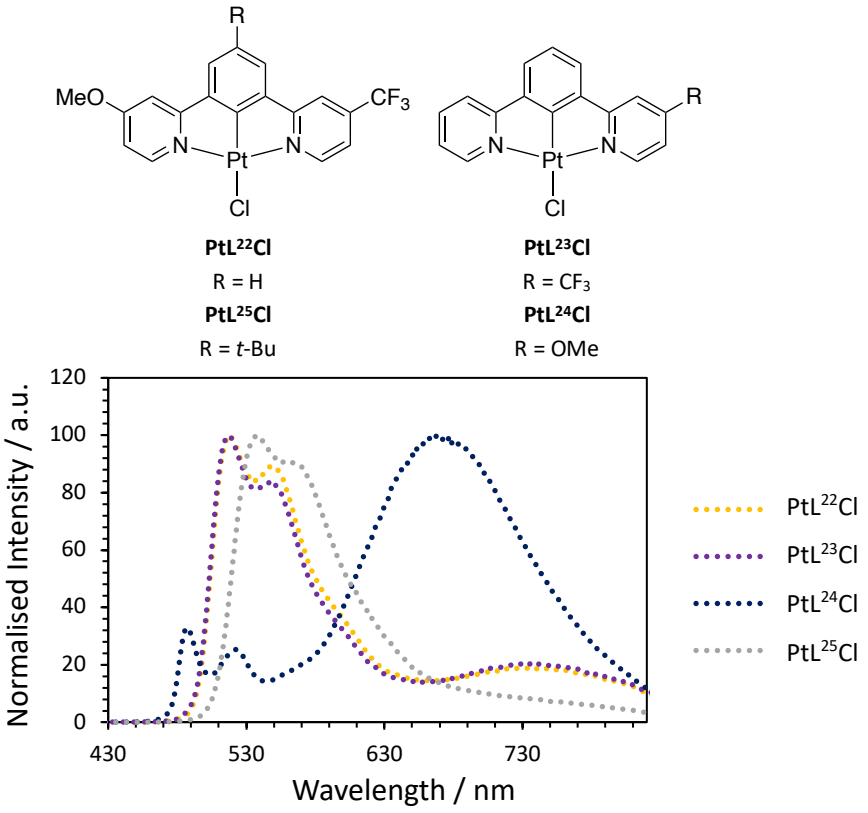

Figure 3.28: *Excimer emission of PtL$^{22\text{-}25}$Cl in saturated DCM solution (~ 10^{-4} M).*

PtL^{24}Cl also appears to have a higher propensity to excimer formation, as the excimer emission intensity surpasses that of the monomer in saturated solution (6.9×10^{-4} M), and this is reflected in the larger k_{SQ} value (**Table 3.4**). Incorporation of a *t*-butyl group to the central phenyl ring (PtL^{25}Cl) seems to decrease the propensity to form excimers, possibly due to the extra steric hindrance and inability to form close intermolecular interactions. This could explain the observed increase in PLQY compared to PtL^{22}Cl (with no *t*-butyl group).

Table 3.4: *Photophysical properties of asymmetric complexes featuring OMe-substituted pyridine and/or CF_3-substituted pyridine ($PtL^{22\text{-}25}Cl$) in degassed (aerated in parentheses) DCM solution at 298 K.*

Complex	λ_{abs} / nm (ε / M^{-1} cm^{-1})	λ_{em} / nm (monomer)	λ_{em} / nm (excimer)	Φ_{lum} [aer]	τ / ns [aer]	τ_0 / μs	k_r / 10^3 s^{-1}	$\sum k_{nr}$ / 10^3 s^{-1}	k_{SQ} / 10^9 M^{-1} s^{-1}	$k_Q(O_2)$ / 10^8 M^{-1} s^{-1}
$PtL^{22}Cl$	240 (35800), 263 (24800), 287 (21500), 337 (5600), 391 (9280), 430 (2450)	522, 555, 600sh	745	0.57 [0.09]	3900 [620]	5.4	147	112	3.4	6.1
$PtL^{23}Cl$	240 (31900), 265 (21200), 286 (19600), 296 (18100), 345 (5420), 395 (7980), 440sh (1560)	520, 555, 600sh	745	0.67 [0.10]	4800 [680]	6.1	140	69	3.7	5.7
$PtL^{24}Cl$	242 (32400), 266 (28800), 290 (20000), 320 (7680), 360 (6340), 379 (9060), 400 (7300)	488, 525, 562, 615sh	672	0.66 [0.05]	5100 [410]	5.3	129	67	4.7	10.1
$PtL^{25}Cl$	243 (55300), 267 (25900), 292 (23700), 336 (6820), 395 (9810), 448 (2230)	539, 572	-	0.77 [0.08]	6400 [610]	7.0	121	36	1.6	6.7

PtL^{30}Cl: Featuring pyrazine

Finally, the photophysical properties of the pyrazine containing complex PtL^{30}Cl were studied (**Table 3.6**). Its absorption spectrum is shown in **Figure 3.29** where two strong, lower energy CT bands are observed. The tail of the CT band is red shifted for PtL^{30}Cl compared to that of PtL^{1}Cl, the symmetric CF_3-pyridine-based complex. As predicted, the monomer emission λ_{max} is also significantly red shifted by 50 nm for PtL^{30}Cl in comparison to PtL^{1}Cl (**Figure 3.30**). It is difficult to compare the excimer emission in solution as it is not prominent in the most concentrated solution of either complex.

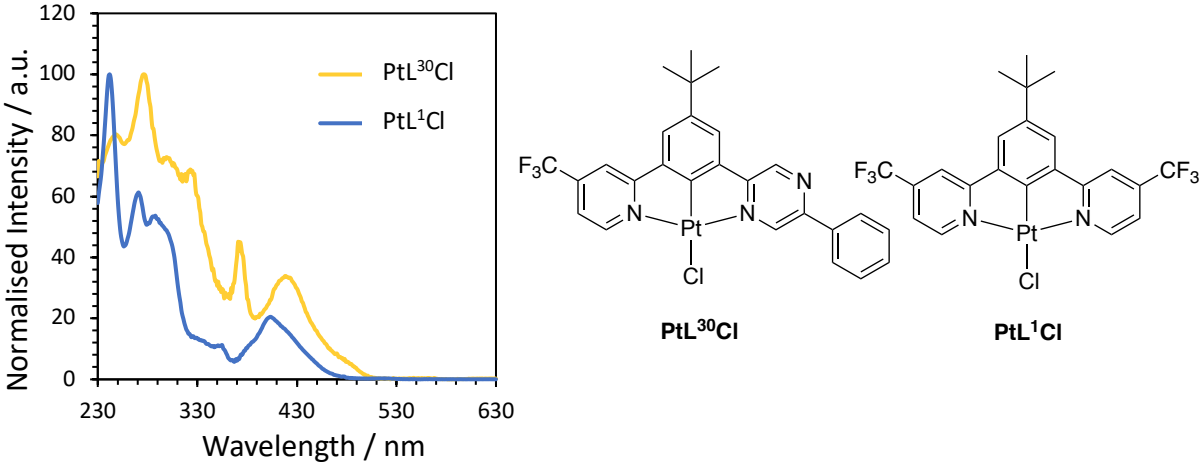

Figure 3.29: *Absorption spectra of PtL^{30}Cl and PtL^{1}Cl for comparison in DCM solution (10^{-5} M) at 298 K.*

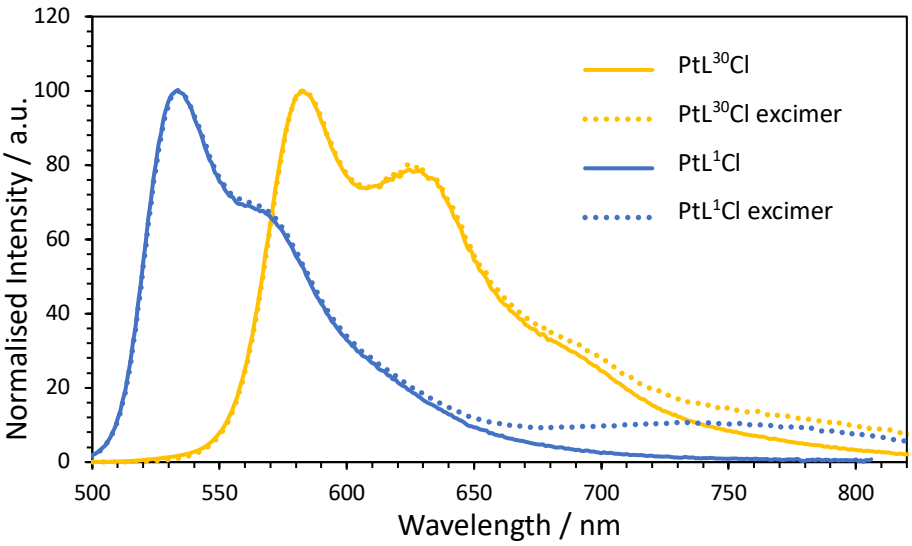

Figure 3.30: *Monomer and excimer emission of PtL^{30}Cl compared with PtL^{1}Cl in dilute (~ 10^{-6} M) and concentrated (~ 10^{-4} M) DCM solution.*

Comparison of all complexes

As a final comparison of effects of substituents on emission energy, **Figure 3.31** shows the monomer emission of complexes bearing one unsubstituted pyridine. The emission spectra for $PtL^{18}Cl$ and $PtL^{24}Cl$ are almost identical, suggesting for pyrimidine and OMe-substituted pyridine, the emission is dominated purely by the unsubstituted pyridine unit in the complex. This is expected for the electron-donating OMe group, but pyrimidine is an electron-deficient heterocycle so it would be expected to decrease the energy of the LUMO,[120] if the LUMO resides here. Substituting the pyridine with an electron-withdrawing CF_3 group red shifts the monomer emission, seen here for $PtL^{23}Cl$. Additionally, increasing the conjugation by swapping the pyridine ring for an isoquinoline red shifts the emission as seen for $PtL^{12}Cl$ and $PtL^{14}Cl$, with the latter being the most red-shifted amongst the 1-isoquinoline complexes.

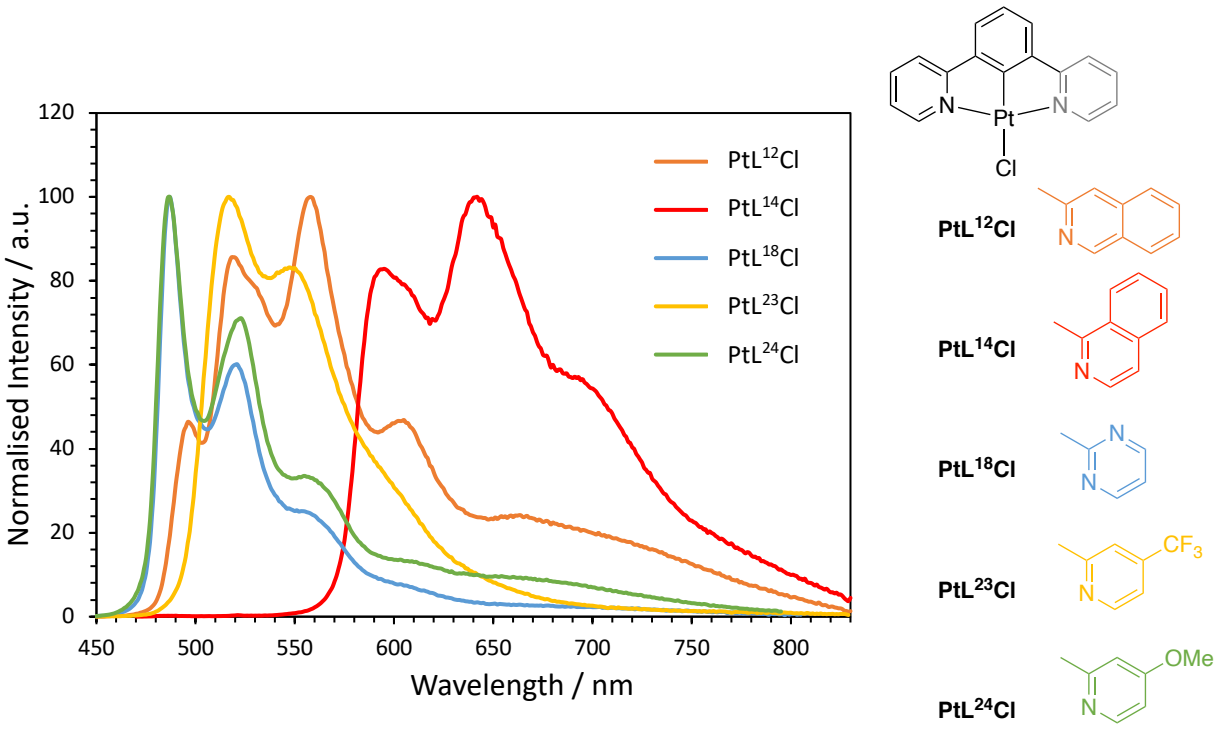

Figure 3.31: *Photoluminescence emission spectra of complexes bearing one unsubstituted pyridine ring in dilute (~ 10^{-6} M) degassed DCM solution.*

Figure 3.32 compares the emission spectrum of each complex in concentrated DCM solution, normalised to λ_{max}. All complexes show the appearance of a broad unstructured band at lower energy assigned to excimer formation, with the

exception of $PtL^{14}Cl$. The excimer emission shifts to lower energy in the order $PtL^{24}Cl$ < $PtL^{18}Cl$ < $PtL^{12}Cl$ < $PtL^{23}Cl$. This supports our argument that EDGs on the pyridine ring can blue shift the excimer, whilst EWGs red shift the excimer emission. Pyrimidine comes somewhere in between, with the conjugated 3-isoquinoline also leading to slightly red-shifted excimer emission in comparison to Pt(dpyb)Cl whilst increasing the propensity to form excimers. These results form a strategy for tuning excimer emission energy to achieve red/NIR emission.

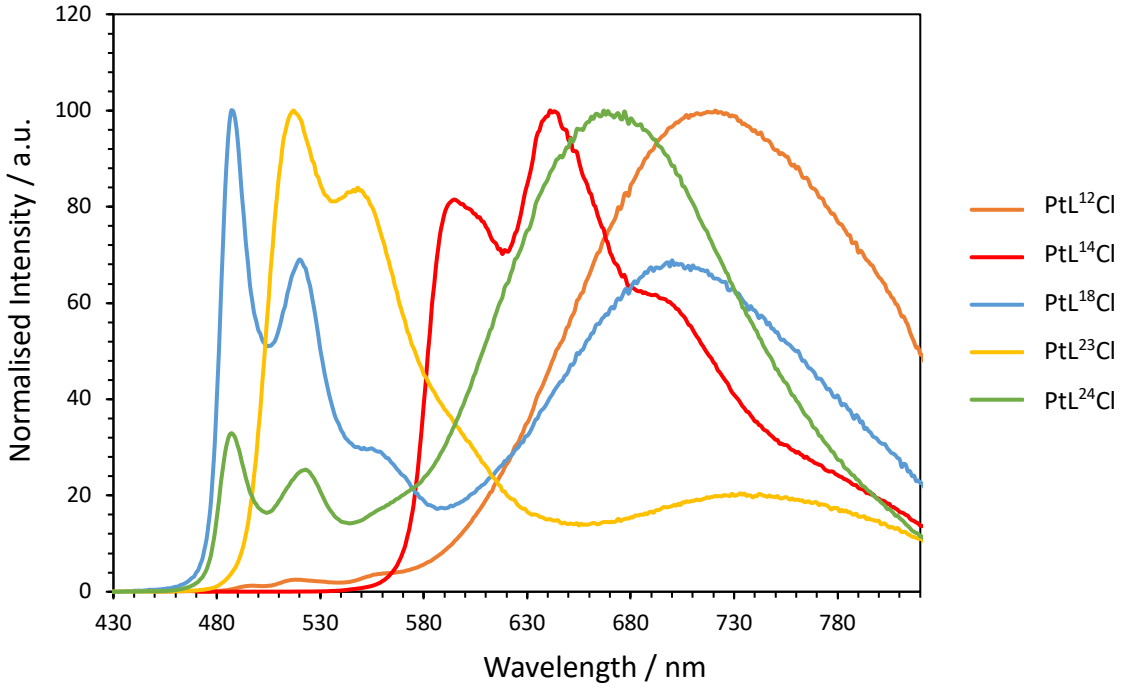

Figure 3.32: *Photoluminescence emission spectra of complexes bearing one unsubstituted pyridine ring in concentrated (~ 10^{-4} M) degassed DCM solution a 298 K showing excimer formation. Spectra are normalised to λ_{max}, which is the excimer emission for $PtL^{12}Cl$ and $PtL^{24}Cl$.*

3.3.3 Chloride Metathesis

Metathesis of the chloro ligands of $PtL^{16}Cl$ and $PtL^{19}Cl$ by SCN was attempted. $PtL^{16}Cl$ was selected as it is the only complex in the 1-isoquinoline series that showed excimer emission in solution, and because 4-substituted CF_3-pyridine had been shown to red shift the excimer emission. Exchanging -Cl for -SCN was anticipated to further promote intermolecular interactions and red shift the emission in the solid state. $PtL^{19}Cl$ was also chosen as this complex has the highest propensity for excimer

formation in the pyrimidine series and is relatively soluble. Chloride metathesis was carried out as in Section 2.3.1 to give the complexes shown in **Figure 3.33**.

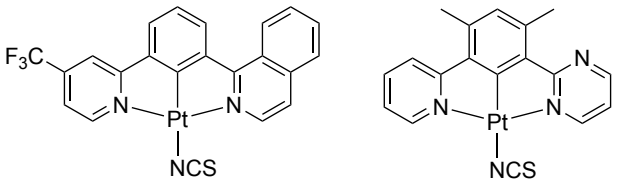

PtL[16]NCS (32%) **PtL[19]NCS** (19%)

Figure 3.33: *Structure of NCS-substituted asymmetric complexes.*

IR spectra were recorded for powders of each thiocyanate complex; the NCS/SCN stretching frequencies are given in **Table 3.5**. Comparing the data to those for symmetric complexes with X = SCN/NCS presented in Chapter 2, it is likely that both complexes are N-bound. The only S-bound complex, PtL[1]SCN, had a much lower stretching frequency of 2074 cm^{-1}.

Table 3.5: *IR stretching frequencies of the thiocyanate complexes.*

Complex	$\nu_{\underline{SCN}/\underline{NCS}}$ / cm^{-1}
PtL[16]NCS	2088
PtL[19]NCS	2097

The absorption spectra for PtL[16]NCS and PtL[16]Cl are shown in **Figure 3.34a**. The spectra do not significantly change upon variation of the ancillary ligand, apart from an additional band at approx. 320 nm for PtL[16]NCS. The emission spectra for both complexes are also identical in dilute DCM solution (**Figure 3.34b**). Both complexes show evidence of excimer formation at elevated concentration, more intense for PtL[16]Cl. The excimer energy may be blue shifted for PtL[16]NCS as seen for other thiocyanate complexes in Chapter 2, and hence is less visible as it overlaps more with the (0,4) transition. For a complete analysis of properties, solid-state emission must be studied.

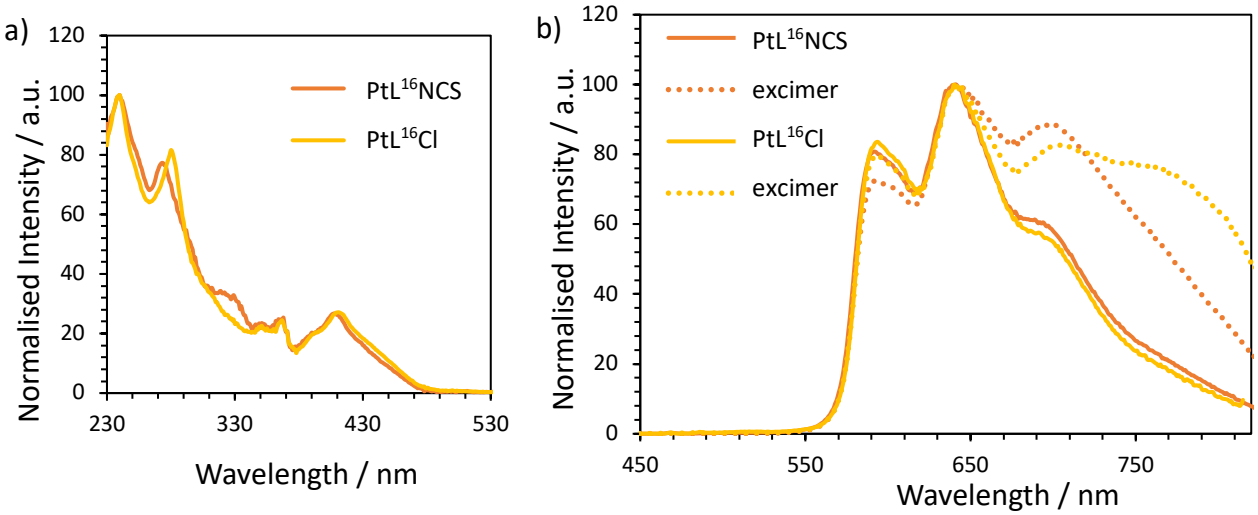

Figure 3.34: *a) Absorption spectra and b) photoluminescence spectra of PtL[16]SCN compared to the parent PtL[16]Cl in degassed DCM solution (solid line ~ 10^{-6} M, dashed line ~ 10^{-4} M).*

Figure 3.35 depicts the absorption and photoluminescence spectra of PtL[19]NCS and PtL[19]Cl in DCM solution. Again, both complexes exhibit almost identical absorption spectra and monomer emission. However, the excimer emission for PtL[19]NCS is significantly blue shifted by almost 50 nm compared to the chloro parent. These results verify those seen for the symmetric thiocyanate complexes presented in Chapter 2. Thin film emission should be carried out in future work. The photophysical

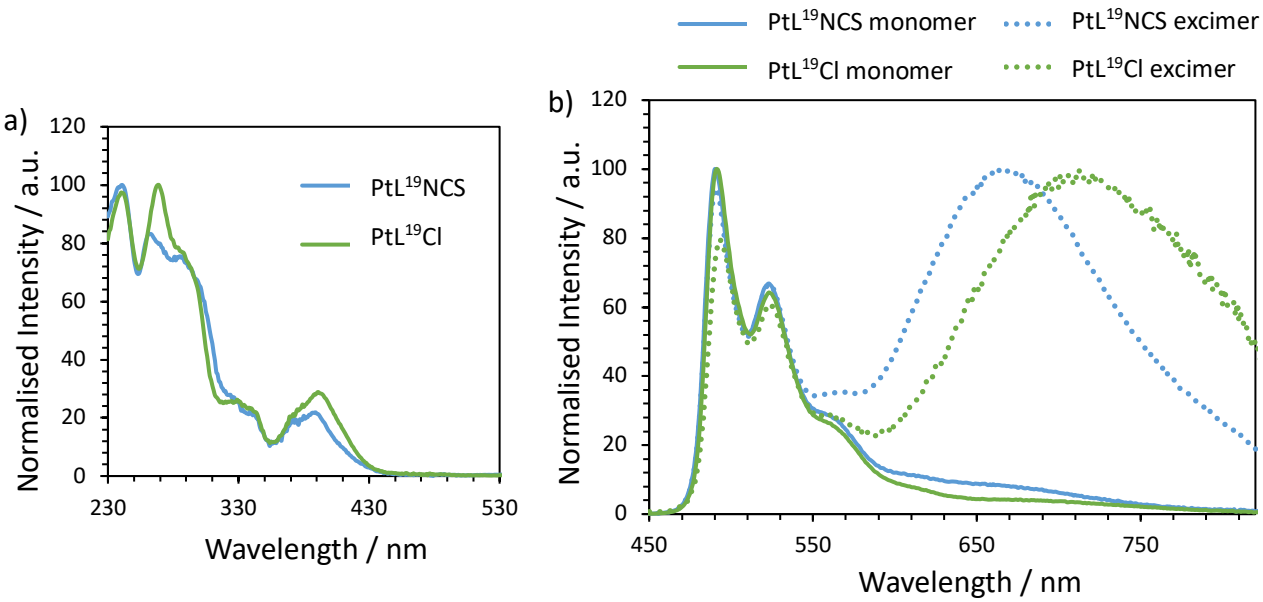

Figure 3.35: *a) Absorption spectra and b) photoluminescence spectra of PtL[19]SCN and PtL[19]Cl in degassed DCM solution (solid line ~ 10^{-6} M, dashed line ~ 10^{-4} M).*

parameters for these complexes are reported in **Table 3.6**. Exchanging the chloro ancillary ligand for -NCS results in an increased PLQY of the complex, reflected in the larger k_r and smaller k_{nr} values.

Table 3.6: *Photophysical parameters for $PtL^{30}Cl$, $PtL^{16}SCN$ and $PtL^{19}SCN$ in degassed (aerated in parentheses) DCM solution at 298 K. $PtL^{16}Cl$ and $PtL^{19}Cl$ data are repeated for ease of comparison.*

Complex	λ_{abs} / nm (ε / M^{-1} cm^{-1})	λ_{em} / nm (monomer)	λ_{em} / nm (excimer)	Φ_{lum} [aer]	τ / ns [aer]	τ_0 / μs	k_r / 10^3 s^{-1}	$\sum k_{nr}$ / 10^3 s^{-1}	k_{sQ} / 10^9 M^{-1} s^{-1}	$k_Q(O_2)$ / 10^8 M^{-1} s^{-1}
$PtL^{30}Cl$	256 (6440), 279 (8010), 308 (5690), 328 (5270), 376 (3210), 420 (2700)	582, 632	688	0.47 [0.04]	7900 [730]	8.6	59	67	0.38	5.7
$PtL^{16}NCS$	241 (48500), 274 (38500), 323 (16500), 355 (11200), 367 (11900), 394sh (9900), 410 (12800)	596, 641, 694	761	0.12 [0.02]	3500 [590]	3.6	35	249	1.3	6.4
$PtL^{19}NCS$	242 (8450), 265 (7020), 289 (6630), 327 (2320), 343sh (1740), 376sh (1610), 390 (1880)	490, 524, 561	669	0.81 [0.04]	6200 [420]	5.2	132	31	0.8	10.1
$PtL^{16}Cl$	240 (36400), 281 (31900), 353 (7870), 368 (8460), 393 (7570), 410 (10500)	599, 646, 700	770	0.09 [0.01]	3400 [470]	3.5	26	270	0.7	8.4
$PtL^{19}Cl$	244 (33800), 270 (35800), 290 (26600), 331 (9040), 345 (7000), 377 (7980), 390 (9890)	493, 528, 568	716	0.59 [0.04]	5600 [320]	6.8	105	74	4.5	13.3

3.4 Chapter 3 Summary

A range of novel N^C^N-Pt(II) complexes with asymmetrically substituted ligands have been synthesised and their photophysical properties studied. Complexes were synthesised in yields of 34 – 85%, with the lowest yields observed for complexes featuring the electron-rich OMe-substituted pyridine. Crystal structures revealed mainly head-to-tail packing arrangements with no significant metallophilic interactions, only weak π–π stacking. The crystal structure of $PtL^{19}Cl$ revealed a mixture of both head-to-head and head-to-tail interactions, with the former leading to close Pt···Pt contacts of 3.293(2) Å.

The unimolecular emission for each complex tends to follow the emission profile of the parent symmetric complex of lowest energy. For complexes featuring 3-substituted isoquinoline, the excited state appears to be mixed as there are more vibronic peaks likely originating from both the 3-isoquinoline and pyridine.

Most complexes studied form excimers in concentrated DCM solution. Complexes featuring 3-substituted isoquinoline in particular have a high propensity to excimer formation. Systematically varying the heterocycle in these asymmetric complexes has allowed investigation into the subsequent excimer energies and substituent effects. An electron-withdrawing CF_3 group at the 4-position of the pyridine ring leads to a red shift in the excimer energy, whilst an electron-donating OMe group at the same position blue shifts the excimer. Pyrimidine lies somewhere in between the two, whilst 3-substituted isoquinoline slightly red shifts the excimer, likely due to increased conjugation. Complexes featuring 1-substituted isoquinoline are less prone to excimer formation, but, when they do form, the excimer λ_{max} is significantly red shifted (λ_{max} = 770 nm for $PtL^{16}Cl$ compared to 700 nm for Pt(dpyb)Cl).

Exchanging the chloro monodentate ligand for thiocyanate to give $PtL^{16}NCS$ and $PtL^{19}NCS$ led to a blue shift in the excimer emission, as seen for symmetric

thiocyanate complexes in Chapter 2. These complexes were also accompanied by an increase in the monomer PLQY reflected in the increased values of k_r and lower k_{nr} values. Overall, the synthesis and study of these complexes has revealed strategies to tune the excimer emission energy.

Chapter 4

4. Dinuclear Pt(II) complexes featuring tridentate ligands

4.1 Introduction

The incorporation of a second metal ion to generate dinuclear complexes can be a route towards efficient red or NIR emitters that display unusually high triplet radiative decay rates, and therefore high PLQYs.[121–124] A second Pt(II) ion in an appropriate geometry within a complex can promote interfacial interactions whilst potentially increasing the SOC. Alternatively, additional metals such as Ir(III) can be incorporated to generate multinuclear mixed-metal species that allow additional control over excited state properties of important phosphorescent materials.

4.1.1 Mixed-metal Ir(III)/Pt(II) complexes

Despite quantum yields for pseudo-octahedral Ir(III) complexes generally being higher than those of Pt(II) complexes, achieving red emission from Ir(III) complexes proves difficult due to non-radiative decay. Previous strategies to red-shift the emission include increasing the conjugation within the ligand, or replacing the cyclometallating phenyl ring by a more electron rich unit, such as a thienyl ring.[125,126] Incorporating Pt(II) into an Ir(III) complex can be an effective strategy to shift the emission further to the red without compromising the high PLQYs.[121,127]

Given the importance of *fac*-Ir(ppy)$_3$ (**18**), the brightest Ir(III) green emitter to date, a tetranuclear complex **19** in which a *fac*-tris-cyclometallated Ir(III) centre is rigidly connected to three cyclometallated Pt(II) centres (**Figure 4.1**), was reported which absorbs strongly up to 600 nm and emits red light with unusually high efficiency due to its high k_r.[122] The target complex was synthesised in two steps, the first being incorporation of the iridium centre. The resulting complex was then reacted with K_2PtCl_4 (>3 equiv.) to give the target compound **19**.[122]

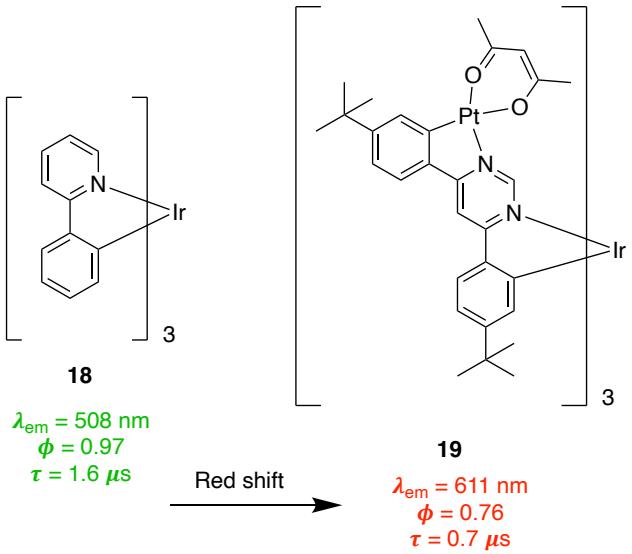

Figure 4.1: *Structures of the bright green emitter fac-Ir(ppy)$_3$ (**18**) and a mixed-metal complex containing an Ir(III) and three Pt(II) centres (**19**); the additional metal centres lead to a red-shift of the emission whilst a high PLQY is retained.*

The lifetime of complex **19** is unusually short at 720 ns, but the PLQY remains high; the complex must have a substantially enhanced radiative decay rate, as opposed to detrimental non-radiative decay. In fact, k_r for complex **19** is estimated as 1.1×10^6 s^{-1}, double that of complex **18**. This may be attributed to the effect of enhanced SOC associated with the presence of additional metal centres. The spin-allowed absorption bands are also enhanced. Moreover, an increase in the rigidity may be another factor contributing to the high PLQY, which helps to minimise excited state distortion and hence reduce competitive non-radiative decay. This high rigidity also leads to a narrow spectral profile, which is an important prerequisite for colour purity in display screen applications.

Complex **20** is a similarly bright red emitter incorporating the same 4,6-diphenylpyrimidine ligand as a rigid bridging unit between the two metal centres (**Figure 4.2**).[127] The complex is highly soluble, has a high PLQY of 85% and a short lifetime of 640 ns in degassed toluene. It was shown that the high efficiency of the $T_1 \rightarrow S_0$ transition probably originates from a strong SOC of the T_1 state with a manifold of excited singlet states, contributing to the record-breaking zero-field splitting of the T_1 state of 240 cm^{-1}. These examples help highlight that multinuclear mixed-metal complexes of Ir(III) and Pt(II) can be useful in the development of more efficient red and NIR emitters.[31,122,123]

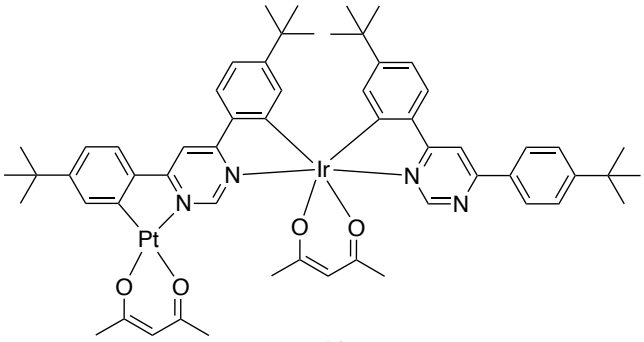

20

λ_{em} = 615 nm
ϕ_{PL} = 0.85
τ = 640 ns
Degassed toluene

Figure 4.2: *Structure of the bright red-emitting complex* ***20****.*

4.1.2 Rigidly linked Pt(II) complexes

Following the fact that excimer formation leads to red-shifted emission as seen for mononuclear complexes in the previous chapters, the linking together of two Pt(II) complexes in such a way that forces interfacial interactions can generate red-emitting complexes due to the formation of *intra*molecular as opposed to *inter*molecular excimers. The formation of intramolecular excimers or aggregates can involve Pt···Pt interactions and/or π-π interactions between conjugated ligands. The stabilisation arising from face-to-face interactions is attributed, in part, to the σ overlap of orthogonal molecular orbitals, $5d_z^2$ and $6p_z$, of adjacent metal centres (**Figure 4.3**).[63] In the case of dinuclear complexes without any aromatic ligands that

introduce low-energy π∗ orbitals, the MO diagram of **Figure 4.3a** is largely sufficient for an appreciation of the photophysical properties.

The presence of aromatic ligands, relevant to all complexes in this work, introduces additional π and π∗ orbitals into the MO description **Figure 4.3b**. The HOMO-LUMO gap is clearly reduced for the Pt_2 dimeric species compared to isolated molecules, leading to a red shift in the absorption and emission of aggregates relative to the isolated molecules.[123] The low-energy absorption that is introduced in this way is typically described as a metal-metal-to-ligand charge transfer transition (MMLCT or dσ∗–π∗), though π-π∗ transitions may equally well account for such effects, according to the relative energies of the MOs.

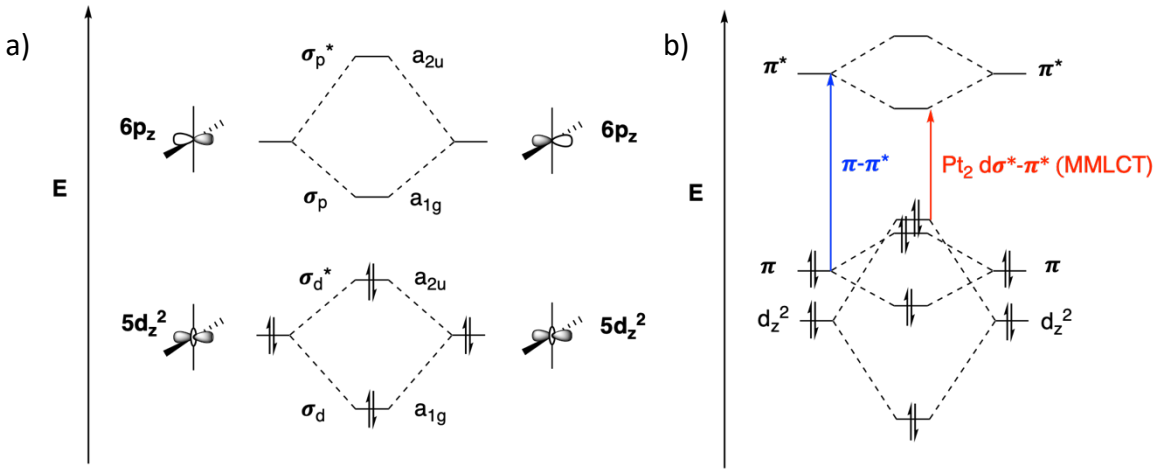

Figure 4.3: *Schematic MO diagram for interfacial interactions between square planar Pt(II) units; a) overlap of vacant $6p_z$ orbitals stabilises the $5d_z^2$ MO's through configuration interaction, decreasing the total energy; b) introducing aromatic ligands leads to additional π and π* orbitals and an MMLCT absorption band. Note that the relative energies are dependent on the specific complex.*

One potential model compound for locking Pt(N^C^N) units in the correct geometry to achieve such interactions used in this work is a 4,5-disubstituted xanthene.[128] The nature of the xanthene scaffold lends itself to two potential classes of complex, depending upon where the connection exists between the scaffold and the Pt(II) complex. We will use the term Class I to indicate the case where each complex is linked to the bridge *via* the central phenyl ring of the cyclometallating ligand[129] and

Class II where the chloride is replaced with an acetylide co-ligand to form a bridge to the xanthene scaffold (**Figure 4.4**).[130]

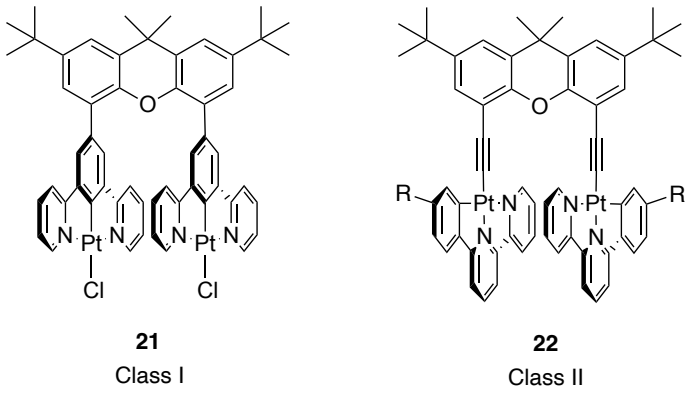

Figure 4.4: *Left: Class I xanthene complex linked by the central phenyl ring of the dpyb ligand. Right: Class II xanthene complex with an acetylide linkage to the Pt(N^N^C) complex.*

Class I complex **21**, in the work by Develay *et al.*, was found to display an intense broad unstructured emission band at λ_{max} = 690 nm (Φ_{lum} = 0.20 and τ = 1.7 μs in deoxygenated DCM) which is independent of concentration, over the range investigated.[129] The band closely resembles that of Pt(dpyb)Cl at elevated concentrations due to the diffusion-controlled formation of intermolecular excimers, though in the case of **21** there is no sign of any accompanied monomer emission; complex **21** rapidly forms intramolecular "excimers" at a rate that excludes any significant monomer emission. The absence of a detectable grow-in of emission on the nanosecond timescale following pulsed laser diode excitation implies that excimer formation is extremely rapid, as the two Pt(N^C^N) units are already held in close proximity. The absence of an additional low-energy band in the absorption/excitation spectrum, and the observation of exclusively monomer-like emission at 77 K, suggest that there are no significant interfacial ground-state interactions in **21**, supporting the excimeric assignment over the alternative explanation of a ground state interaction between the two units.[129]

Cárdenas *et al.* tethered two Pt(N^N^C) by a non-conjugated 4,5-diethynylxanthene derivative also holding them in a geometry that may facilitate interfacial interactions (**Figure 4.4**).[130] This Class II dinuclear complex **22** exhibits emission that is

substantially red-shifted to the NIR region of the spectrum (λ_{max} = 815 nm, Φ_{lum} = 0.26 and τ = 26 ns in de-aerated DCM) compared to the respective mono-substituted complex on the xanthene scaffold. This could be due to the formation of an MMLCT state involving the interaction of the two Pt(II) units. The lowest-energy absorption band of **22** is slightly enhanced to longer wavelength, indicative of a degree of interaction between the two Pt(N^N^C) moieties in the ground state. The emission of the mononuclear analogue of **22** (i.e. with the xanthene scaffold and only one Pt unit) is also red-shifted compared to the related N^N^C complex with a simple phenylacetylide co-ligand, namely Pt(phbpy)(C≡C-P), and non-radiative decay is surprisingly increased by an order of magnitude; the xanthene unit clearly influences the emission in some way and does not just act as an insulating scaffold. It is clear that this xanthene scaffold is a versatile platform for the design of red-emitting dinuclear Pt(II) complexes.

Employing various rigid backbones with different central ring sizes, as in xanthene, can be a tool to modulate the separation and angle, and thus the extent of interaction, between the Pt units in such complexes. A series of dinuclear Pt(II) aromatic Schiff base (salphen) complexes tethered in a co-facial manner by a rigid linker, either xanthene (**24**), dibenzofuran (**25**), or biphenylene (**26**), were reported by Chan *et al.* (**Scheme 4.1**).[131] Treatment of the respective bisboronic acids with 2 equivalents of "Pt-salphen" (**23**) in the presence of $Pd(PPh_3)_4$ and K_2CO_3 in degassed DMF solution afforded the desired dinuclear complexes **24**-**26** as dark red solids. Crystal structures of **24** and **26** revealed intra- and intermolecular π-stacking interactions as well as contrasting *syn* (**24**) and *anti* (**26**) configurations of the $(Pt\text{-salphen})_2$ moiety.

All of these salphen complexes are luminescent in solution, displaying structureless red emission centred between 630 and 640 nm in DCM at room temperature from a mixed-MLCT excited state. The red-shifted emission and lower QYs of **24** and **26** relative to **25** are attributed to enhanced intramolecular π-stacking interactions, as it is clear that the dibenzofuran linker in **25** holds the Pt-salphen units further apart. The group also investigated the selective responses of the complexes to metal ions,

in particular Pb^{2+}, highlighting another potential application of these types of complexes as phosphorescent molecular hosts and assemblies. A plausible binding mechanism is proposed based on occupation of the O(salphen)-binding cavity, which induces perturbation of intramolecular π–π interactions of the $(Pt\text{-salphen})_2$ unit, hence leading to a longer lifetime and blue shifted emission band in the presence of Pb^{2+}.

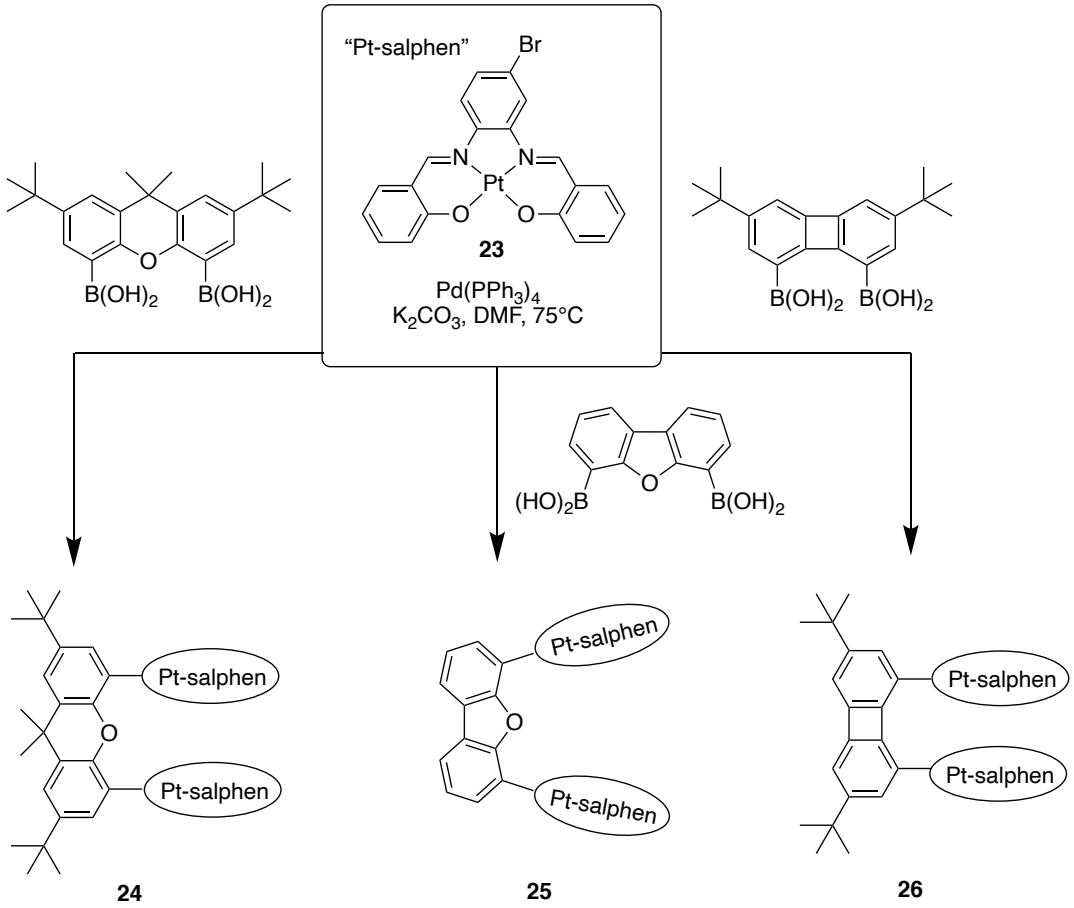

Scheme 4.1: *Structure of dinuclear "Pt-salphen" complexes with various rigid linkers: xanthene (**24**), dibenzofuran (**25**) and biphenylene (**26**).*

4.1.3 Flexibly linked Pt(II) complexes

Instead of a rigid scaffold such as xanthene that locks two adjacent Pt(II) complexes in a position that enables interfacial interactions, a flexible linker can be employed so that formation of intramolecular excimers is possible but not forced. Guerchais *et al.* achieved this by utilising a polyether bridge to connect two Pt(N^C^N) units *via*

the central phenyl ring of the tridentate dpyb ligand or as a phenylacetylide co-ligand (**Figure 4.5**).[132]

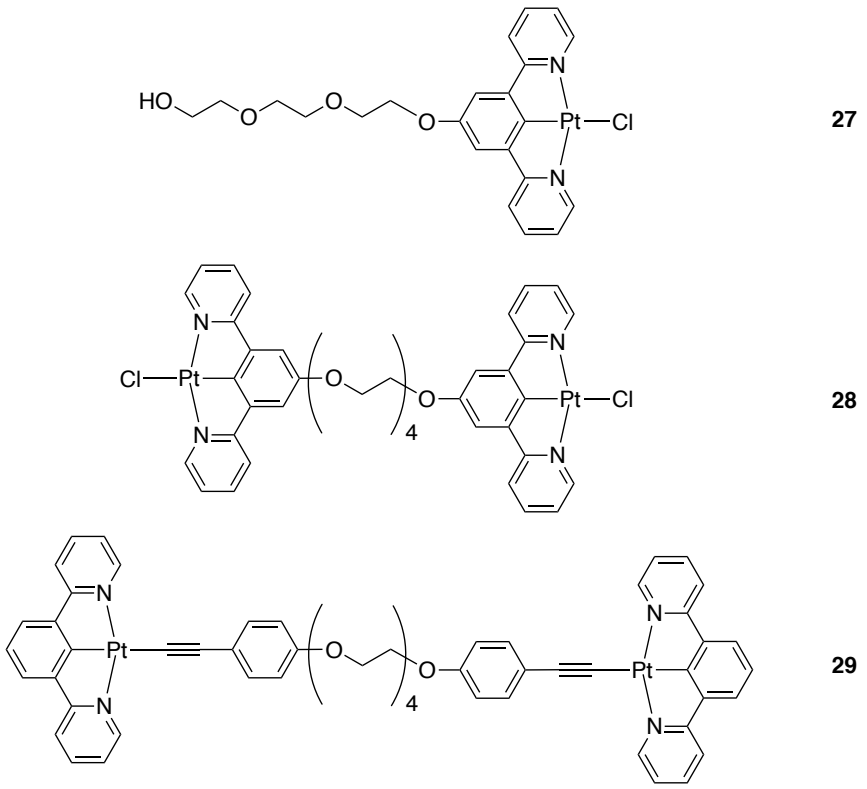

Figure 4.5: *Flexibly linked Pt(N^C^N) complexes joined by a polyether chain through either the dpyb ligand (**28**) or a phenylacetylide co-ligand (**29**) with the mononuclear complex (**27**) for reference.*[132]

There are three possible conformations of complexes **28** and **29**: an extended form that should display similar characteristics to complex **27** but with the added benefits of an additional metal centre (such as a potential increase in the PLQY), intramolecular face-to-face conformation and intermolecular head-to-tail association, an interaction that is impossible intramolecularly due to the length of the polyether chain (**Figure 4.6**).

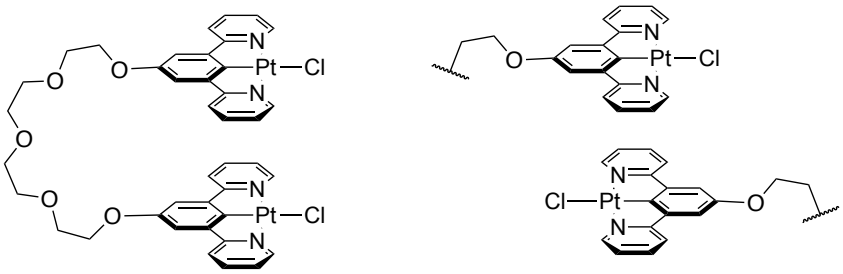

Figure 4.6: *Possible conformations of complexes **28** and **29** (displayed for complex **28**) showing intramolecular head-to-head interactions or intermolecular head-to-tail.*[132]

The emission spectra of complexes **27**-**29** are shown in **Figure 4.7**. The electron-donating alkoxy group linker is detrimental to excimer formation for **27**; the complex emits in the green-yellow region of the spectrum with the first band peaking at 547 nm (Φ_{lum} = 0.24 and τ = 11 µs in deoxygenated DCM). Environmental factors (temperature, solvent polarity and cation binding) affected the ability of **28** to adopt an intramolecular face-to-face conformation. In DCM solution (10^{-5} M), very broad band emission is observed featuring several peaks, which likely arises from the sum of two electronic transitions: monomer-like emission at 547 nm and a red-shifted intramolecular band at 670 nm assigned to excimer emission as it is present even at low concentration (10^{-5} M).

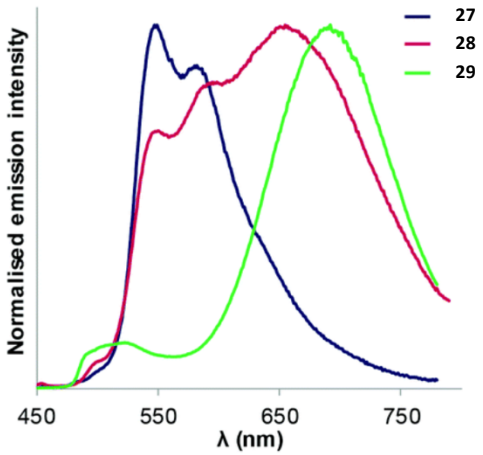

Figure 4.7*: Emission spectra of complexes **27**-**29** at 10^{-5} M in DCM.*[132]

For complex **29** at the same concentration, excimeric emission dominates. The low-energy emission band of **28** becomes more intense as the concentration increases whereas the absorption and excitation spectra do not change; the red-shifted band is likely to arise from Pt···Pt and π-π interactions that are strengthened in the face-to-face form when one of the two complexes is in its excited state (i.e. excimer not aggregate emission).[132] The ability to control excimer formation by flexibly linking complexes together in this way could enable the design of red/NIR-emitting complexes.

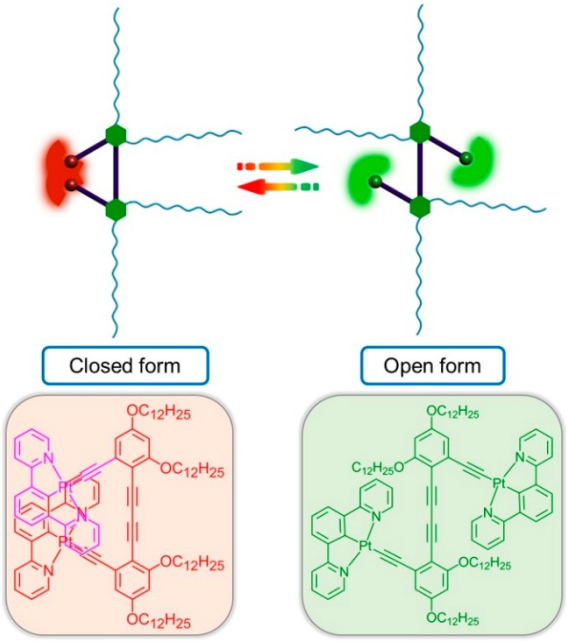

Figure 4.8: *Schematic representation of the rotary motion of the molecular hinge presented by Yam et al. (Figure reproduced from reference 133).*

Yam *et al.* reported a flexibly-linked dinuclear complex with a molecular hinge structure showing phosphorescence behaviour changes, using square-planar cyclometallated Pt(II) complexes and rigid aromatic alkynyl groups as the building blocks to construct the wings/flaps and axis respectively (**Figure 4.8**).[133] The molecular hinge wings can be opened or closed by rotary motion about the central rigid butadiynyl linker powered by solvent and temperature changes; DCM favours the closed form whereas nonpolar solvents such as hexane favour the open form. These changes can be conveniently monitored by their emission spectra as the closed hinge-like structure exhibits intramolecular π-π interactions leading to deep-red emission with a shift to green emission similar to that of the mononuclear counterparts when present in the open form.

Dinuclear pincer-type cyclometallated N^N^C-Pd(II) complexes with a similar but shorter foldable diarylacetylide linker were also reported in 2019.[134] These Pd(II)

complexes are highly phosphorescent in the red region (λ_{max} = 653 nm) in deoxygenated DCM solution with emission quantum yields of up to 48%, assigned to MMLCT emissive states. These high luminescence efficiencies are unusual for Pd(II) complexes due to the significantly lower ligand-field splitting of the Pd(II) ion, when compared to that of Pt(II) 5d-orbitals, leading to effective nonradiative decay through excited-state structural distortion by population of an antibonding orbital. These dinuclear complexes displayed emission spectra in DCM solution identical to those in the solid-state at 77 K, from which it was inferred that the emission originates from the folded conformation with short intramolecular Pd···Pd contact (**Figure 4.9**). Free rotation about the three ethylene moieties allows this favourable geometry for the two cyclometallated Pd(II) units interacting with each other through π-π stacking and Pd···Pd interactions.

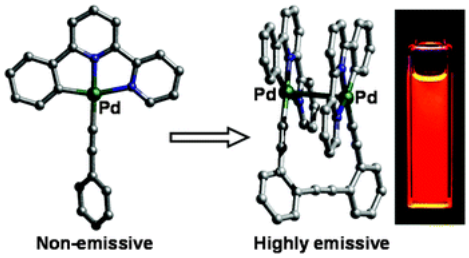

Figure 4.9: *Dinuclear pincer-type cyclometallated Pd(II) complexes displaying red emission. Figure taken from reference 134.*

4.2 Aims and objectives

Various complexes featuring two N^C^N-Pt(II) units linked onto a 4,5-disubstituted xanthene scaffold will be synthesised and their photophysical properties explored. The aim is to synthesise more of complex **21** (named $L^{31}(PtCl)_2$ in this work) in order to study the origin of the emission in more detail, and to design and synthesise further examples of Class I and Class II sandwich compounds in a bid to optimise NIR emission and elucidate the mechanism of emission, e.g. whether the excimer emission originates from inter- or intramolecular interactions, or a combination of

the two (**Figure 4.10**). Colour tuning strategies used in Chapters 2 and 3 will be employed, utilising 4-trifluoromethylpyridine and pyrimidine in place of pyridine in the dpyb unit of the xanthene-linked ligand. Additionally, Class I compounds allow additional synthetic flexibility through metathesis of the monodentate chloride co-ligand, e.g. by SCN^- or I^-. This strategy will be employed to investigate the effect on intramolecular interactions and hopefully red shift the emission further.

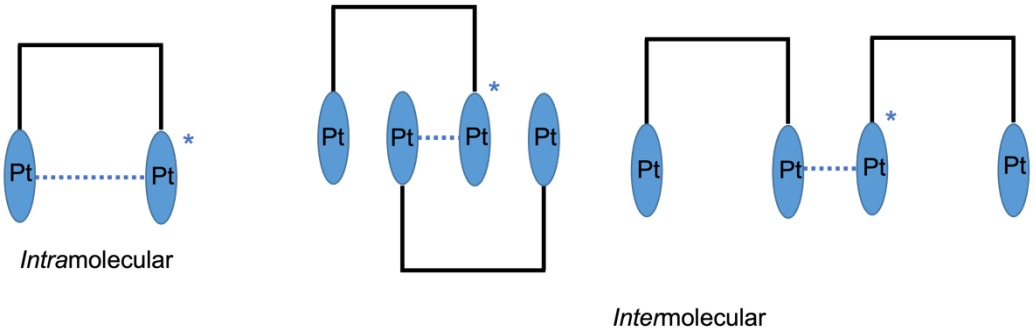

Figure 4.10: *Possible intra- and intermolecular interactions in Class I/II sandwich compounds.*

Other linkers have also been explored, varying the intramolecular distance between Pt units, to explore *inter*- as well as *intra*molecular excimers. For example, a linker that leads to longer intramolecular Pt···Pt distances should disfavour intramolecular interactions, allowing the study of intermolecular interactions. Flexibly linked dinuclear Pt(II) complexes were targeted, with linkers inspired by the publications outlined above, with the aim to achieve deep-red/NIR emission through intramolecular interactions. Diphenylacetylene has been utilised as a linker connected to the N^C^N-coordinating ligand through the central phenyl ring, in a manner similar to the rigidly linked Class I sandwich compounds. Rotation about the acetylene group should allow for intramolecular interactions (**Figure 4.11**). "Class II" versions have also been investigated using the diarylacetylide linker as reported but replacing the Pd with Pt, and the N^N^C ligand for N^C^N, to hopefully improve luminescence efficiency.

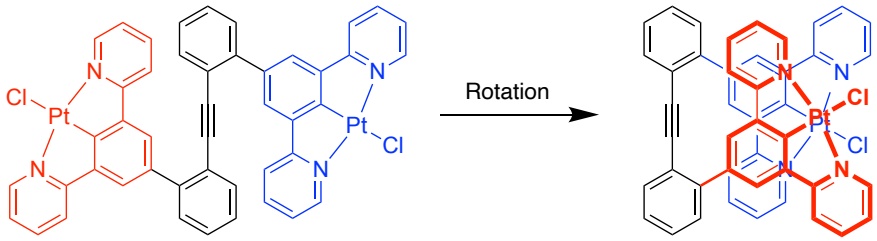

Figure 4.11: *Flexibly linked dinuclear target complex.*

4.3 Results and discussion

4.3.1 Class I sandwich compounds

4.3.1.1 Synthesis

The first step towards the synthesis of the parent Class I sandwich compound involves a Stille cross-coupling reaction between 1,3,5-tribromobenzene and 2-(tri-*n*-butylstannyl)pyridine (**Scheme 4.2**). This reaction proceeded in low yield (23%) as it is possible for the reaction to occur at the third bromine, or to occur at only one site, giving a mixture of products. The mass spectrum also showed a strong signal for dpybH, as competitive dehalogenation can occur. A Miyaura borylation reaction is required for the intermediate dpyb-Bpin, which was then reacted with the commercially available 4,5-dibromo-2,7-di-*tert*-butyl-9,9-dimethylxanthene ("xanthene-Br_2") in a Suzuki coupling to give the proligand H_2L[31] in relatively good yield (40%). It is worth noting that the synthesis reported by Develay *et al.* proceeded *via* the boronic acid $–B(OH)_2$ group[129] whereas here it has been shown that Bpin is sufficient for the subsequent Suzuki reaction.

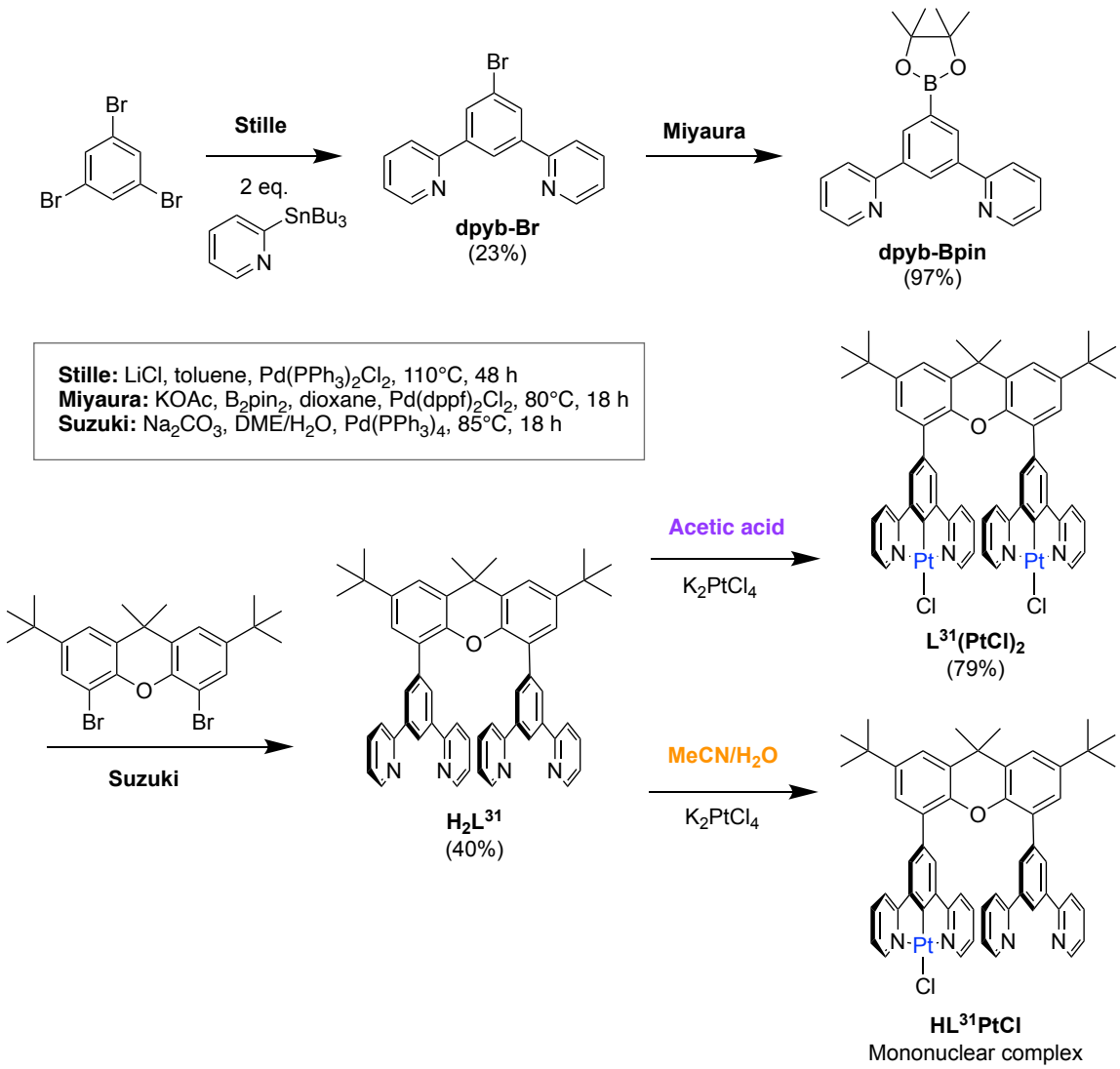

Scheme 4.2: *Synthesis of the parent Class I dinuclear sandwich complex $L^{31}(PtCl)_2$ and the mononuclear analogue.*

Complexation of H_2L^{31} with K_2PtCl_4 in acetic acid for 60 h led to the desired dinuclear complex $L^{31}(PtCl)_2$ in high yield (79%).[135] In the publication by Develay *et al.*, the reaction was conducted in $MeCN/H_2O$ and introduction of the second platinum centre required 11 days to go to completion.[129] The reaction was repeated here in $MeCN/H_2O$ over 72 h to yield a mixture of the mono- and dinuclear species, comprising of mainly the mononuclear complex. This could offer a possible route to hetero-dinuclear complexes through the introduction of a second transition metal centre.[130]

For all other sandwich compounds in the series, the synthetic route first involved stoichiometric borylation of 1,3,5-tribromobenzene (**Scheme 4.3**) to access substituted N^C^N boronates with CF_3-substituted pyridine, pyrimidine or 1-isoquinoline. The ditopic ligands were then prepared by a Suzuki reaction of the substituted dpyb-Bpin with xanthene-Br_2 which proceeded in high yields in two cases (**Scheme 4.4**).

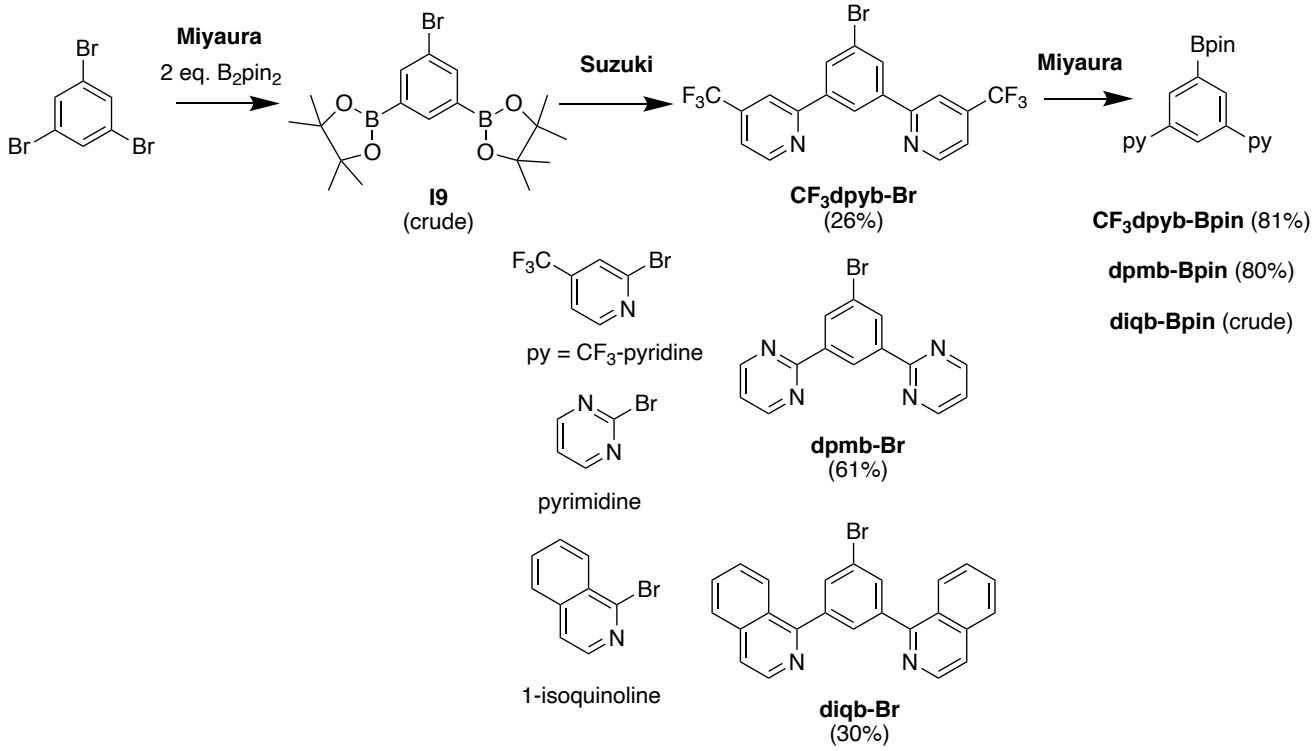

Scheme 4.3: *Synthesis of substituted N^C^N boronates.*

Note that for the analogue with 1-isoquinoline, the only product obtained was HL[34] containing just one N^C^N unit, most likely due to steric hindrance between the isoquinoline rings (**Scheme 4.4**). The same results were achieved in every repeat reaction and even after leaving the Suzuki step for a few days instead of the usual 18 h. The corresponding complex, obtained by reaction with K_2PtCl_4 in acetic acid (**Scheme 4.5**), is nevertheless a good mononuclear reference compound in order to study the effect of the xanthene scaffold on the emission of such complexes.

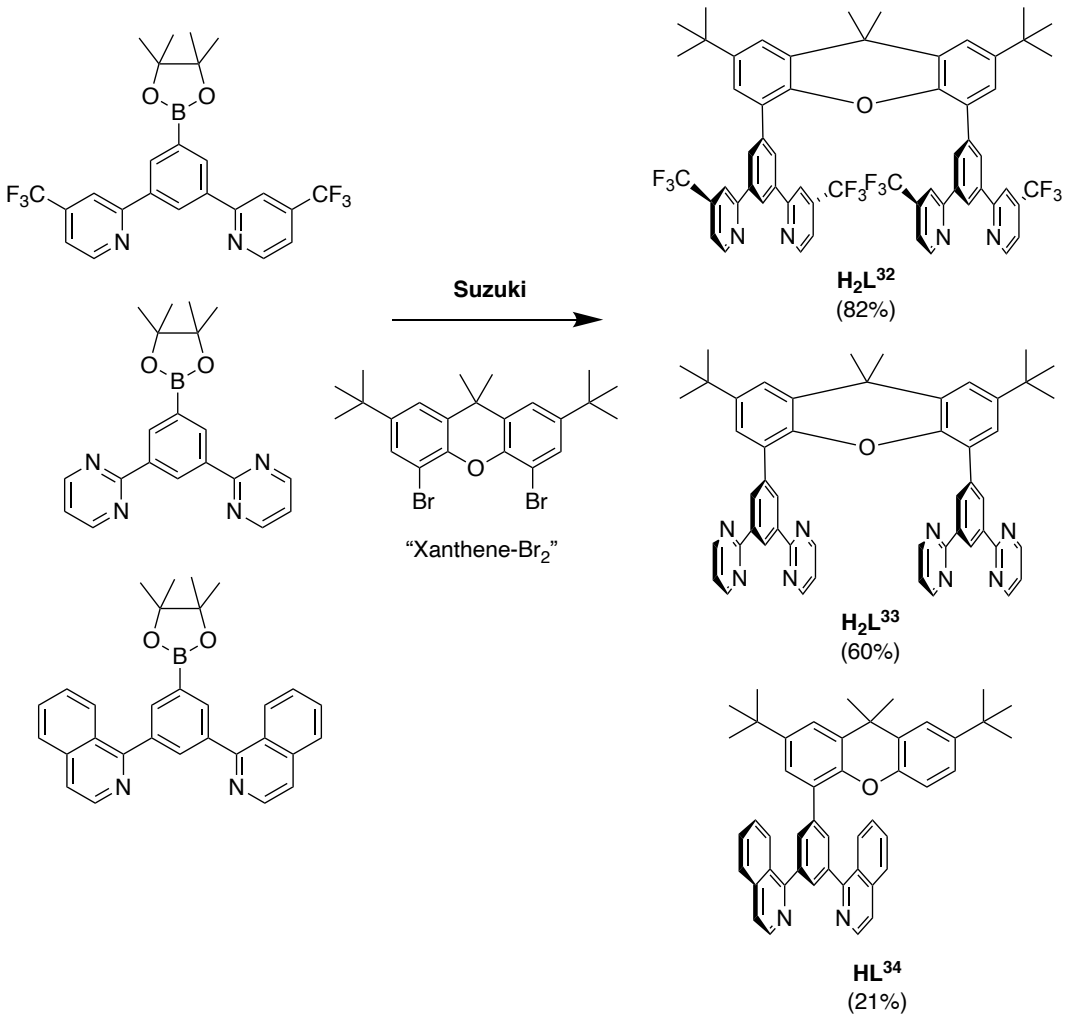

Scheme 4.4: *Synthesis of the Class I proligands.*

Complexation to form the dinuclear sandwich compounds was difficult to achieve, particularly to separate the dinuclear products from the mononuclear analogue, which was always present. The best method of complexation was found to be refluxing the ligand with an excess of K_2PtCl_4 (5 equivalents) in acetic acid for one week to drive the equilibrium towards the dinuclear product. Ratios of mono- to dinuclear product are shown in **Scheme 4.6** when the reaction was conducted for 60 h and for 1 week; the mononuclear derivative was always the major product. Reactions were tested in the microwave to attempt to reduce reaction times, but additional peaks were seen in the ^{1}H NMR spectrum suggesting decomposition, and the main product was still the mononuclear derivative. Purification required numerous steps involving a silica column (DCM/MeOH) and recrystallisations from DCM/hexane. The mono- and dinuclear derivatives were isolated for each complex

in the series (**Scheme 4.6**). All complexes are new compounds except $L^{32}(PtCl)_2$ which was synthesised by Melissa Walden.[135]

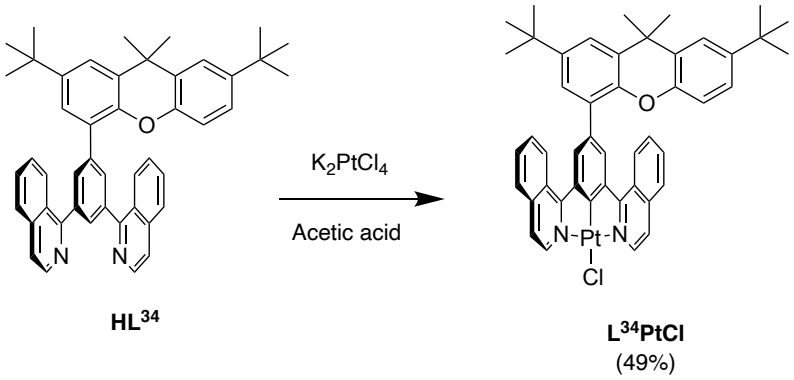

Scheme 4.5: *Synthesis of $L^{34}PtCl$ a mononuclear Class I compound.*

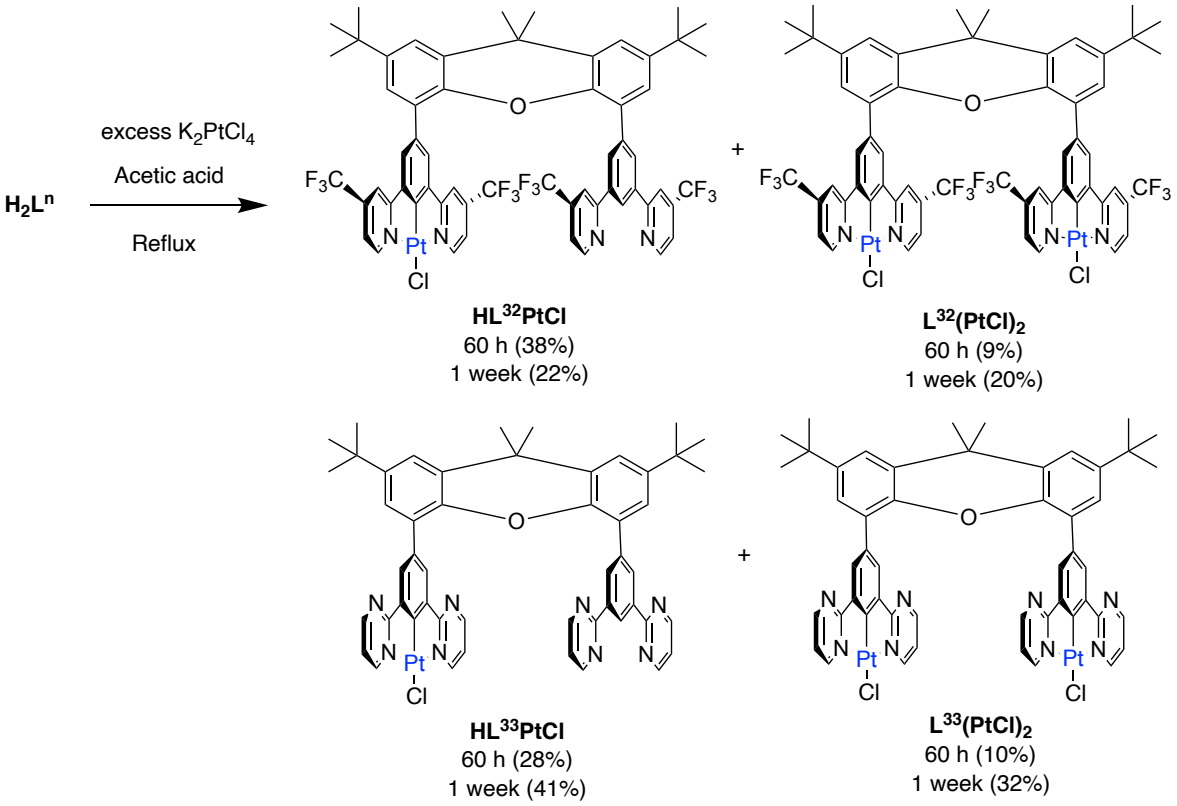

Scheme 4.6: *Synthesis of mono- and dinuclear Class I sandwich compounds, with reaction times and related yields of each derivative.*

4.3.1.2 Crystal structure determination

Small, weakly diffracting crystals of $L^{31}(PtCl)_2$ were obtained by slow evaporation from a solution of the complex in DCM/MeOH. The complex crystallises as a methanol mono-solvate belonging to the monoclinic $P2_1/c$ space group (**Figure 4.12**). The crystal structure reveals an intramolecular Pt···Pt distance of 4.7037(11) Å, larger than the sum of the van der Waals' radii of two Pt ions suggesting no intramolecular metallophilic interactions exist in the ground state. However, an interplanar distance of 3.572(8) Å was measured, implying there are π–π stacking interactions. The Pt(N^C^N) units are twisted relative to the xanthene at a torsion angle of 44.0°. Intermolecularly, the complex packs in a head-to-tail manner.

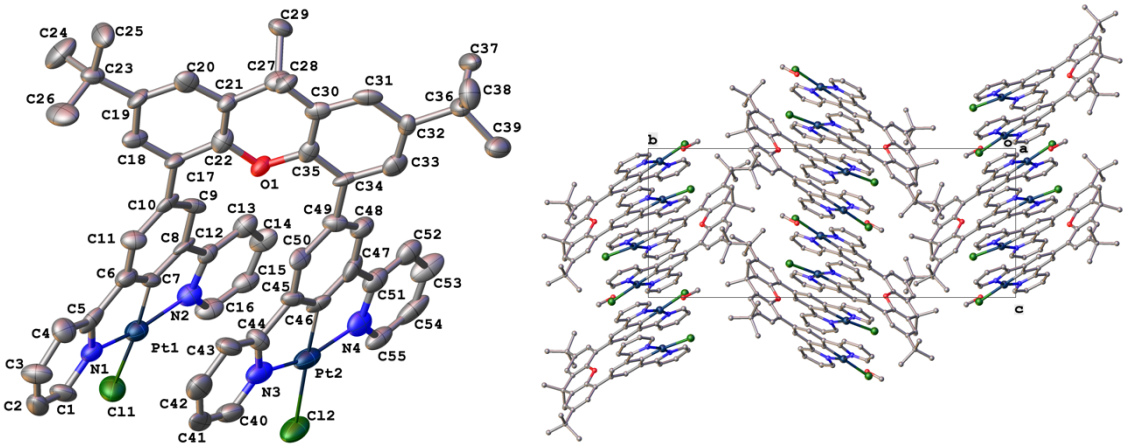

Figure 4.12: *Molecular and crystal structure of $L^{31}(PtCl)_2$ highlighting the packing.*

4.3.1.3 Chloride metathesis

The ancillary chloro ligands in $L^{32}(PtCl)_2$ and $L^{33}(PtCl)_2$ were replaced by thiocyanate or iodo by reacting the dinuclear chloro complexes with AgOTf in acetone. The AgCl precipitate was removed by centrifugation and then KSCN or KI added and stirred for 2 h. The resulting solid was washed with EtOH and Et_2O before extraction of the product into DCM to give the derivatives shown in **Figure 4.13** in excellent yields. $L^{33}(PtI)_2$ was not synthesised in this work due to time constraints but this could be made in future work to complete the series. $L^{33}(PtNCS)_2$ is also significantly less soluble than the chloro parent complex so unsuitable for OLED preparation.

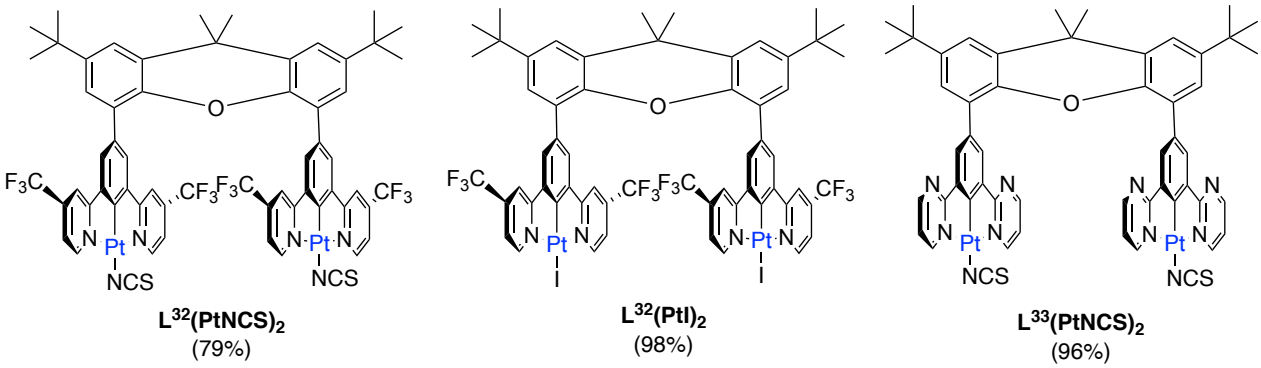

Figure 4.13: *Structure of the NCS/I derivatives.*

Binding mode of the NCS/SCN co-ligand

Crystals of $L^{32}(PtNCS)_2$ suitable for X-ray diffraction were grown by slow evaporation from DMF. The crystal structure reveals intrinsic disorder and a mixture of binding modes intramolecularly: one Pt is bound -SCN and the other -NCS (**Figure 4.14**). The Pt(N^C^N) units twist relative to the xanthene, at an angle of 53.3°, in a fashion that allows intramolecular metallophilic interactions with a Pt···Pt distance of 3.2531(37) Å. There are also *inter*molecular interactions with an intermolecular interplanar distance measured at 3.445(15) Å, highlighting the propensity of this compound to Pt···Pt and π-π interactions. Although the crystal structure is not necessarily

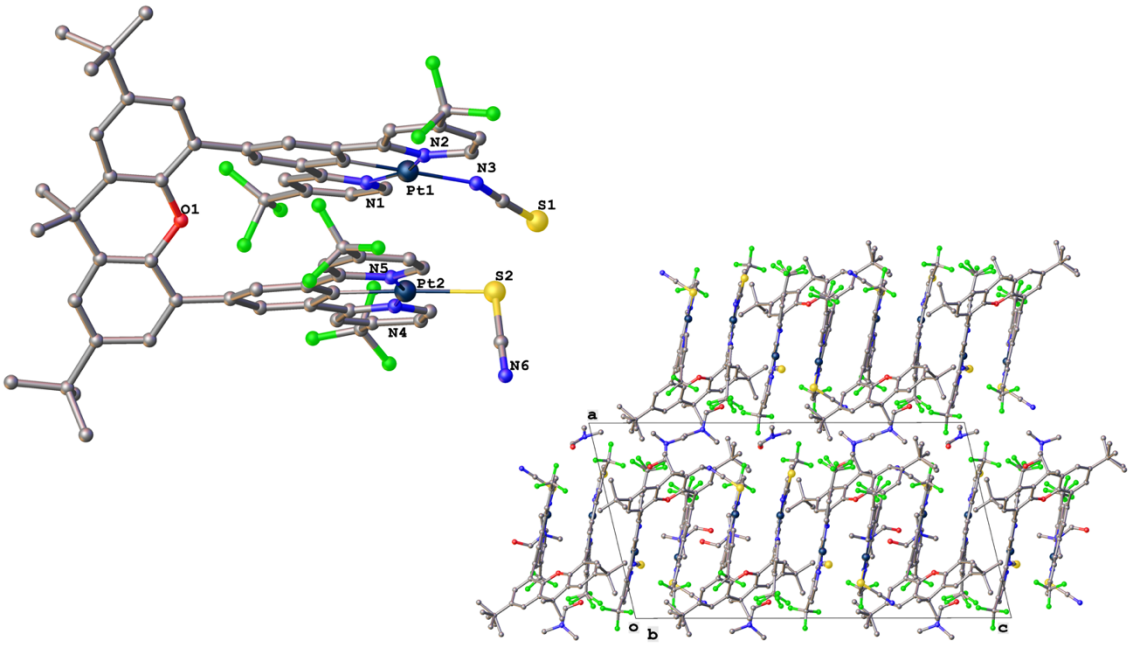

Figure 4.14: *Molecular structure and crystal packing of $L^{32}(PtSCN)_2$ revealing mixed SCN/NCS coordination.*

representative of the bulk, it seems that either there is no clear preference in the binding mode of the NCS ligand, or more likely that there exists some complementary in having both isomers within the same compound. The NMR spectrum suggests there is only one co-ligand environment (**Figure 4.15**), or that the ligand protons are magnetically equivalent regardless of the binding mode, though there is an additional small peak just next to the main H^6 peak.

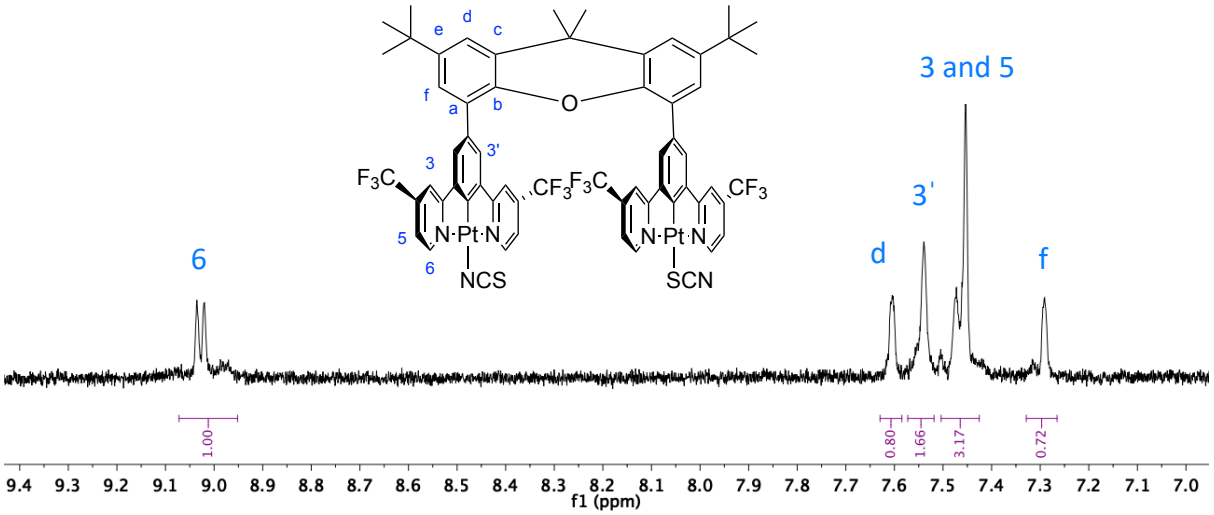

Figure 4.15: *^{1}H NMR spectrum of $L^{32}(PtNCS)_2$ in CD_2Cl_2 at 600 MHz.*

The IR spectrum reveals a short broad peak split at 2080 cm^{-1} with a FWHM of 60-70 cm^{-1}, more indicative of -NCS binding based on literature reports of Pt(NCS) complexes[95,136] (**Figure 4.16**), although no data is reported for similar complexes with N^C^N-coordinating ligands. The IR spectra were recorded for two different batches of reaction, both of which were carried out under identical conditions. The ratios of peaks change between batches, as well as a slight shift in the thiocyanate/isothiocyanate peak. The spectra of the complexes were recorded in their solid form. Further studies could be carried out with a reference compound such as salicylic acid for comparison as a potentially quantitative tool to confirm the ratio of complexes with SCN or NCS binding modes.[95] There is also potential for the complexes to isomerise in solution, with literature data of a square planar Pt[dmbp$(SCN)_2$] complex (where dmbp = 4,4'-dimethylbipyridine) suggesting the -SCN bound complex is the kinetic product whilst the -NCS bound is the

thermodynamically most favourable.[97] A catalogue of compounds of this type and more studies are needed to draw valid conclusions.

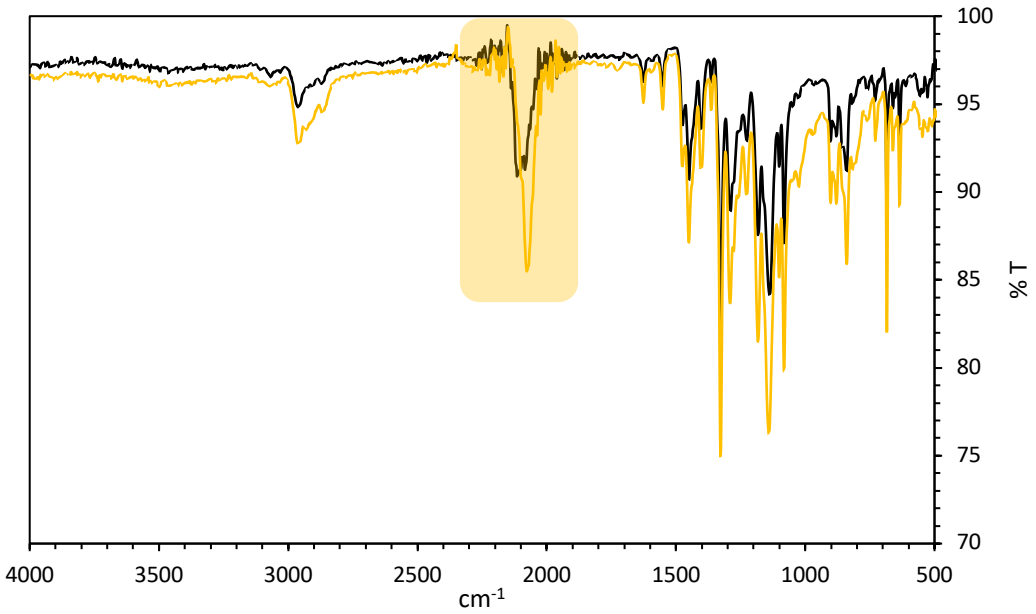

Figure 4.16: *IR spectrum of two batches of $L^{32}(PtNCS)_2$ highlighting the isothiocyanate/thiocyanate stretch.*

4.3.1.4 Photophysical properties

Absorption

A summary of all spectroscopic data for Class I compounds is displayed in **Table 4.1**. The absorption spectra of the dinuclear Class I compounds are shown in **Figure 4.17a**. All the compounds display similar absorption profiles to one another, with the tail of the absorption band being slightly red shifted in the order $L^{31}(PtCl)_2$ < $L^{33}(PtCl)_2$ < $L^{32}(PtCl)_2$. Bands in the higher energy region are attributed to LC transitions associated with the xanthene moiety, and lower energy bands between 350 and 450 nm are due to charge-transfer transitions likely involving the metal.

The absorption spectra of the mononuclear analogues (**Figure 4.17b**) are almost identical to their dinuclear counterparts. No conclusion can be drawn about $HL^{34}PtCl$ as no corresponding dinuclear complex could be synthesised. The absorption spectrum of this compound is significantly red-shifted compared to the parent

dinuclear complex $L^{31}(PtCl)_2$ by approx. 20 nm due to the presence of the conjugated isoquinoline rings in the N^C^N-coordinating ligand.

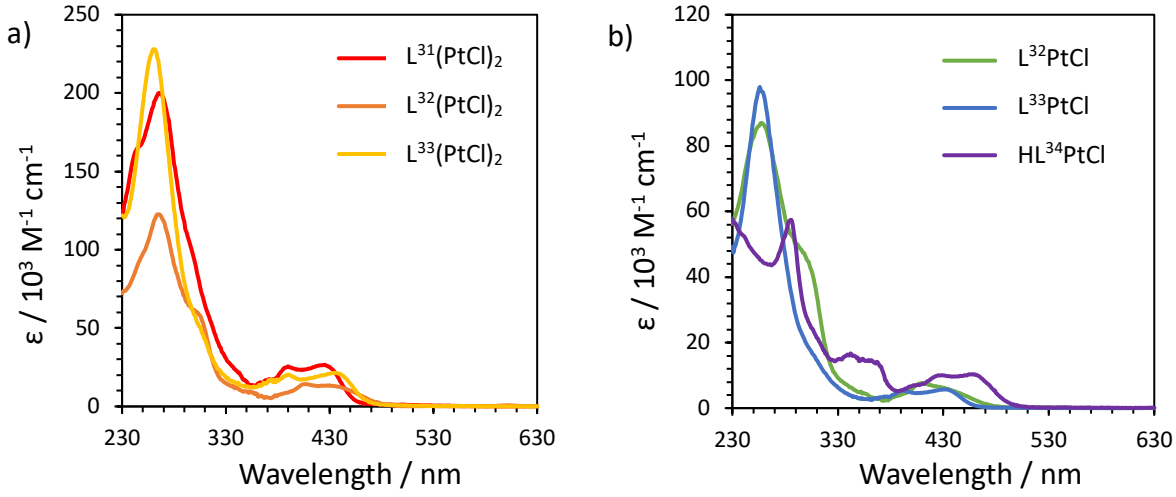

Figure 4.17: *Absorption spectra of a) dinuclear Class I complexes of the type $L^n(PtCl)_2$ and b) mononuclear Class I complexes $HL^{34}PtCl$, $L^{32}PtCl$ and $L^{33}PtCl$ all in dilute DCM solution.*

Figure 4.18 compares the absorption spectra for the mononuclear and dinuclear derivatives of each compound, highlighting their similarity, although the dinuclear derivatives have larger extinction coefficients due to the presence of the extra metal centre. This implies that the absorbing moiety is the same for both the mono- and dinuclear complexes, suggesting that only one metal is participating in the CT transition (i.e. the transition can be assigned to MLCT).

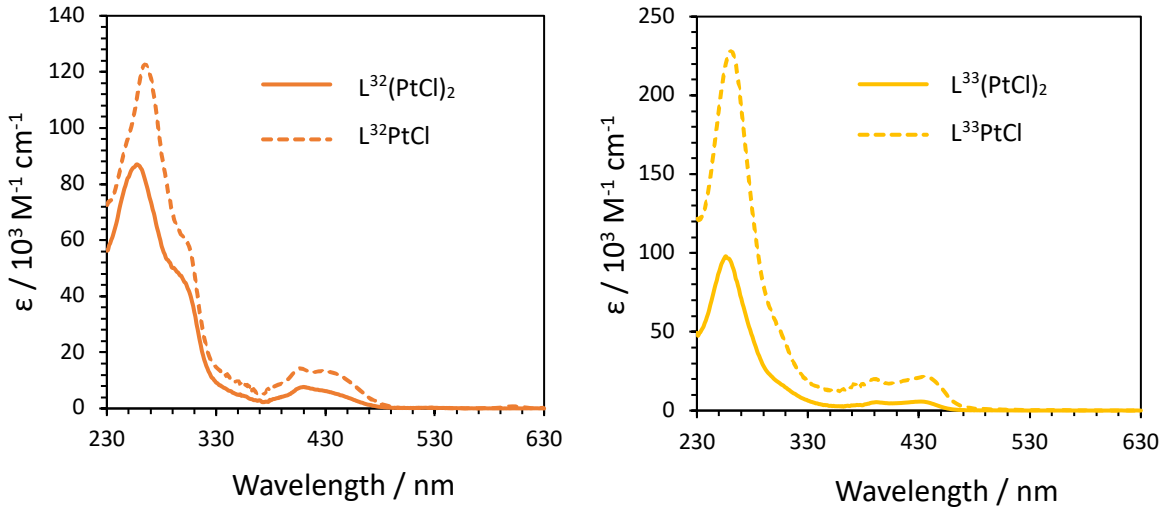

Figure 4.18: *Comparison of the absorption spectra of Class I mononuclear and dinuclear derivatives in dilute DCM solution.*

Emission

The emission of the parent complex, named $L^{31}(PtCl)_2$ in this work, has already been reported[129,135] but is included here for ease of comparison as the data were collected again in this project. As shown in **Figure 4.19**, the emission is almost exclusively excimer-like even in dilute solution (10^{-6} M) with a λ_{max} of 690 nm, hence the literature assignment to intramolecular excimer formation owing to the face-to-face conformation of the two Pt centres. The excimer emission is blue shifted by 10 nm compared to Pt(dpyb)Cl highlighting that the xanthene is not simply acting as an insulating scaffold, or that the intramolecular distance between Pt(N^C^N) units is different for $L^{31}(PtCl)_2$ compared to the intermolecular distance for Pt(dpyb)Cl.

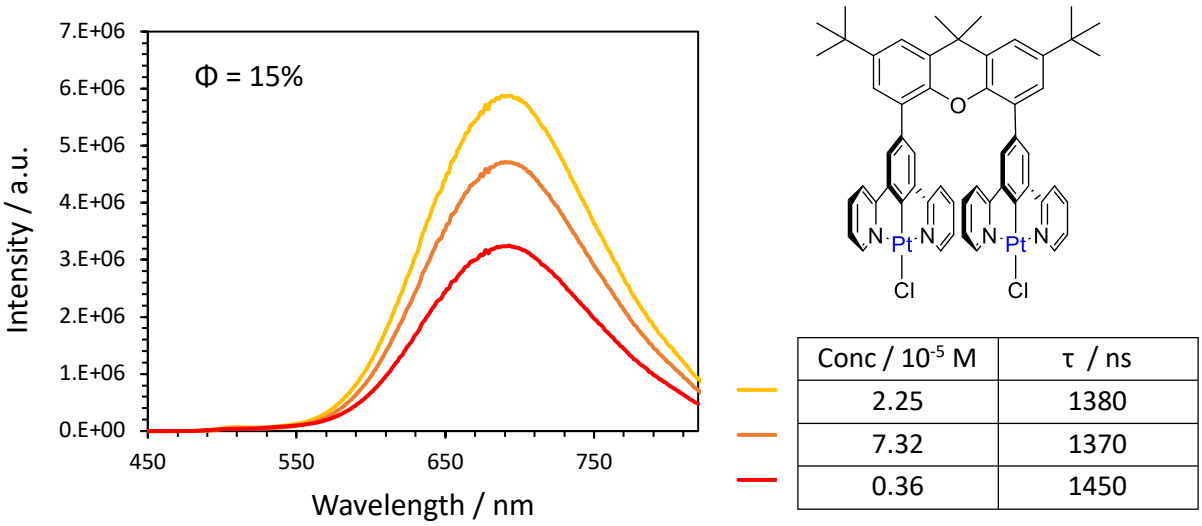

Conc / 10^{-5} M	τ / ns
2.25	1380
7.32	1370
0.36	1450

Figure 4.19: *Emission spectra and lifetimes of $L^{31}(PtCl)_2$ at various concentrations in degassed DCM solution.*

In contrast, complex $L^{32}(PtCl)_2$ functionalised with CF_3 groups at the 4-position of the pyridyl rings exhibits contributions from both a monomer- and excimer-like species to the emission at all concentrations over the range investigated (**Figure 4.20**) suggesting that both inter- and intramolecular interactions may lead to excimer formation. These interactions could be hindered by the presence of the CF_3 groups. The broad structureless excimer emission peaks in the NIR region at around 760 nm are red-shifted by a significant 70 nm compared to the parent complex. The emission is accompanied by a relatively high PLQY of 0.12 for the complex in degassed DCM solution. The peaks at 550 and 760 nm, for the monomer and excimer respectively,

possess different lifetimes suggesting that the two species are not in equilibrium. The lifetime measured at λ_{em} = 750 nm is 450 ns for each solution, and the lifetime measured at 545 nm is given in the table in **Figure 4.20**. The significantly shorter lifetime for the emission at 750 nm, as well as the absence of an observable rise time in the TCSPC decay, suggests the rate of excimer formation is not controlled by the diffusion of molecules and is therefore likely to be intramolecular in origin.

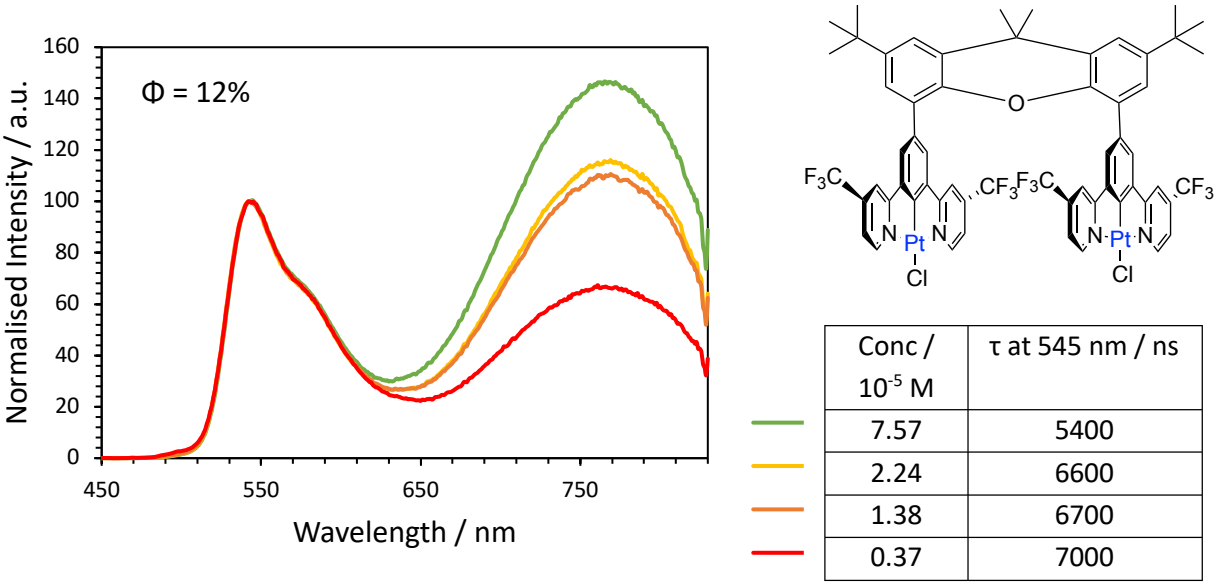

Conc / 10^{-5} M	τ at 545 nm / ns
7.57	5400
2.24	6600
1.38	6700
0.37	7000

Figure 4.20: *Emission spectra of $L^{32}(PtCl)_2$ in degassed DCM solution at various concentrations, normalised at 545 nm.*

To further investigate the mechanism of emission, the mononuclear analogue $HL^{32}PtCl$ was studied. The emission spectrum of $HL^{32}PtCl$ is dominated by monomer, with no excimer contribution even in saturated DCM solution. As seen in **Figure 4.21a**, the monomer emission matches perfectly with the monomer contribution for the dinuclear derivative. This, along with the absorption spectra matching for both $HL^{32}PtCl$ and $L^{32}(PtCl)_2$, indicates that the emissive species for the dinuclear derivative must be attributed to an excimer, i.e. a species that does not exist in the ground state, or the absorption spectrum would be noticeably different. This helps to confirm the excimer must be intramolecular in nature, or at least require two Pt centres within the same molecule to form the excimeric interaction. This is because the mononuclear derivative shows no sign of excimer formation even though, in

principle, an intermolecular excimer could exist with two mononuclear compounds if they slot together in a way similar to that depicted in **Figure 4.10**.

On the other hand, a Stern-Volmer plot (**Figure 4.21b**) for $L^{32}(PtCl)_2$ shows a linear correlation between the change in decay rates and concentration, implying some contribution to excimer formation from intermolecular interactions. This is corroborated by the values of k_{SQ} being much lower for $HL^{32}PtCl$ than for $L^{32}(PtCl)_2$, 0.1 × 10^9 and 0.6 × 10^9 M^{-1} s^{-1} respectively (**Table 4.1**), implying more efficient intermolecular interactions for the latter.

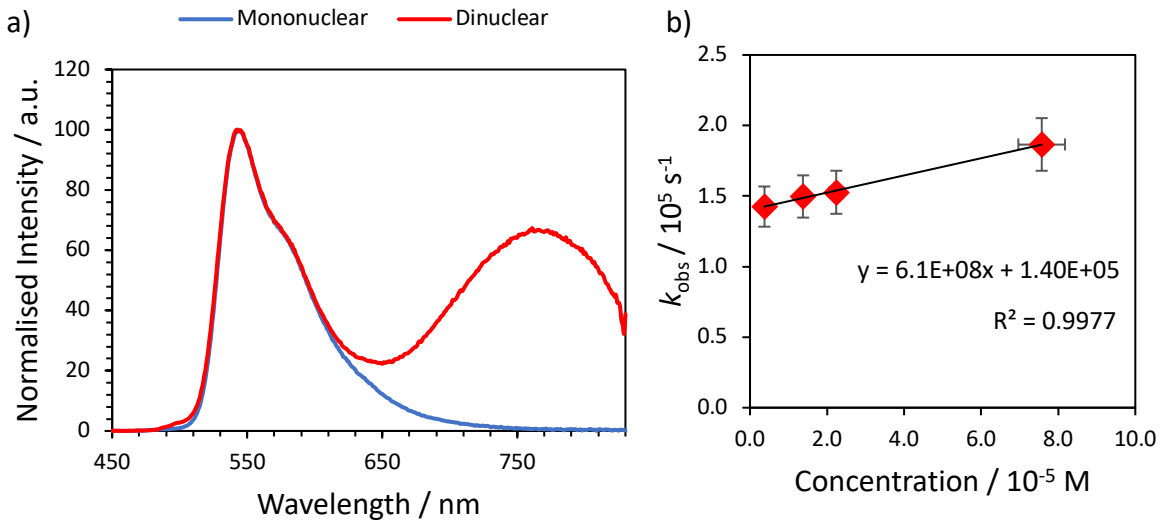

Figure 4.21: *a) Comparison of the emission of mononuclear complex $L^{32}PtCl$ and dinuclear analogue $L^{32}(PtCl)_2$ in dilute degassed DCM solution and b) Stern-Volmer plot for $L^{32}(PtCl)_2$. Errors are discussed in Section 7.1.*

Finally, the pyrimidine derivatives $L^{33}(PtCl)_2$ and $HL^{33}PtCl$ were investigated. Like the parent complex $L^{31}(PtCl)_2$, $L^{33}(PtCl)_2$ displays purely excimeric emission over the concentration range investigated (**Figure 4.22**) with a slightly red shifted λ_{max} of 700 nm owing to the electron deficient pyrimidine rings and a slightly enhanced QY of 0.16. The excimer-dominated emission demonstrates that the complex could be incorporated into an OLED at a low doping concentration to still achieve the same deep-red/NIR emission. The absorption spectrum is in good agreement with the excitation spectrum recorded at 690 nm (**Figure 4.23**) once again implying that the 'excimer' originates from intramolecular interactions. This is backed up by the

relatively short lifetime of ~700 ns at 700 nm, irrespective of concentration (**Figure 4.22**).

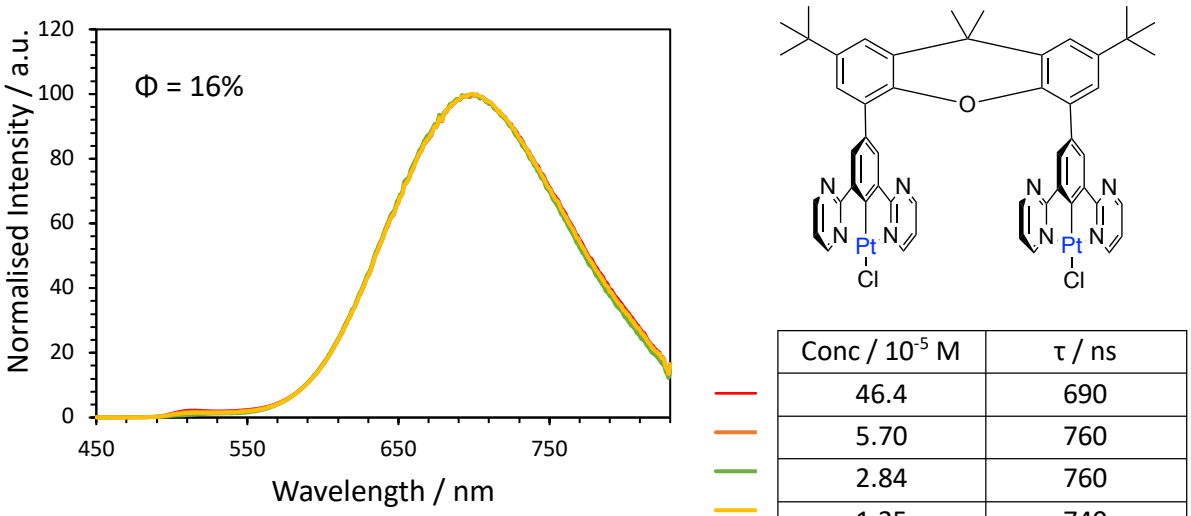

Conc / 10^{-5} M	τ / ns
46.4	690
5.70	760
2.84	760
1.25	740

Figure 4.22: *Emission of $L^{33}(PtCl)_2$ in degassed DCM solution at various concentrations.*

In comparison, and in agreement with the CF_3-substituted derivatives, the mononuclear analogue $HL^{33}PtCl$ displays mainly monomeric emission at all concentrations (**Figure 4.24**) with some slight evidence of excimer emission in the most concentrated solution (2.00×10^{-4} M). This suggests that intermolecular interactions are more prominent for this complex, or that the excimer involves π-stacking interactions between a Pt(N^C^N) and a N^C^N unit within the same

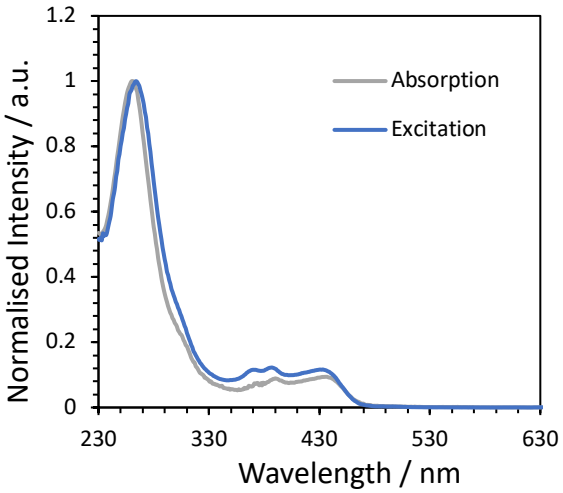

Figure 4.23: *Comparison of the absorption and excitation spectrum of $L^{33}(PtCl)_2$ in DCM solution (3×10^{-5} M).*

molecule. The self-quenching constant, k_{SQ}, for the dinuclear analogue is not significantly greater than the mononuclear, 0.32×10^9 M^{-1} s^{-1} compared to 0.24×10^9 M^{-1} s^{-1}, suggesting that intermolecular excimer formation is indeed possible with the mononuclear derivative also.

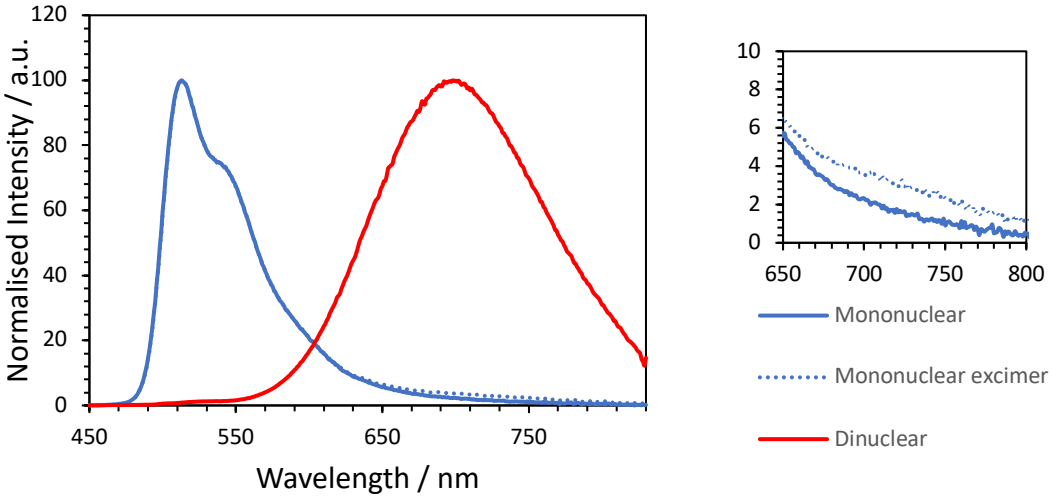

Figure 4.24: *Emission spectra for the mononuclear $HL^{33}PtCl$ at 1.4×10^{-5} M (solid blue line) and 2.0×10^{-4} M (dotted blue line) showing some slight excimer formation (inset: zoomed in), with comparison to the dinuclear analogue $L^{33}(PtCl)_2$ at low concentration, all in degassed DCM at RT.*

The low temperature emission spectra of each complex was recorded in EPA (ether, isopentane and ethanol in a ratio of 2:2:1 /v) at 77 K (**Figure 4.25**). Purely structured monomer-like emission is seen for $L^{31}(PtCl)_2$, as reported by Develay *et al.*, and also $L^{32}(PtCl)_2$. It was postulated that purely monomeric emission is seen at 77 K due to a lack of thermal activation needed to form the excimeric state, even if the interaction is intramolecular in nature, to allow movement of the Pt(N^C^N)Cl units relative to one another. Remarkably, $L^{33}(PtCl)_2$ displays some broad excimer-like emission even at such low temperatures in very dilute EPA glass, suggesting that the Pt(N^C^N)Cl units are already in a favourable orientation in the ground state and at low temperatures for the excimers to readily form. This supports the observation that some excimer formation was seen even for the mononuclear derivative $HL^{33}PtCl$.

However, the excimer emission is blue-shifted at 77 K from 700 nm to 660 nm, possibly due to a less stable excited state at low temperature.

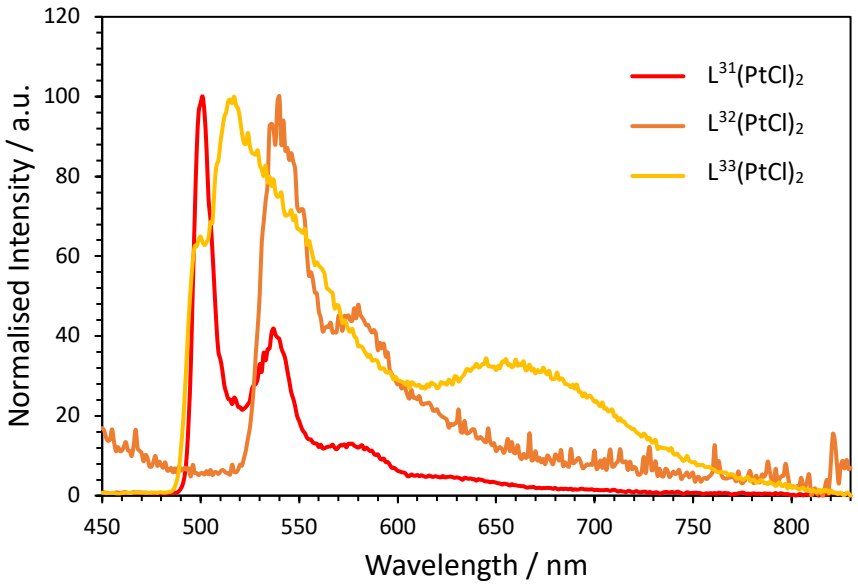

Figure 4.25: *77 K emission spectra of $L^n(PtCl)_2$ in EPA glass.*

Figure 4.26 highlights the comparison between the mono- and dinuclear derivatives of each compound in the series. The trend in excimeric emission follows the trend in absorption for the dinuclear derivatives; the emission is red shifted in the order $L^{31}(PtCl)_2 < L^{33}(PtCl)_2 < L^{32}(PtCl)_2$. The trend in monomer emission also follows the trend in the absorption for the mononuclear derivatives; the emission is red shifted in the order $HL^{33}PtCl < HL^{32}PtCl < L^{34}PtCl$.

The presence of isoquinoline rings in place of pyridine significantly red shifts the monomer, the (0,0) component peaking at 600 nm compared to 515 nm for the bluest emitting $L^{33}(PtCl)_2$, but no excimer emission is observed. To significantly red shift the excimer, incorporating pyridine rings functionalised with CF_3 groups at the 4-position is a good strategy, although this dinuclear complex $L^{32}(PtCl)_2$ displayed monomer emission in combination with the NIR excimer. Pyrimidine rings can also be incorporated to slightly red shift the excimer.

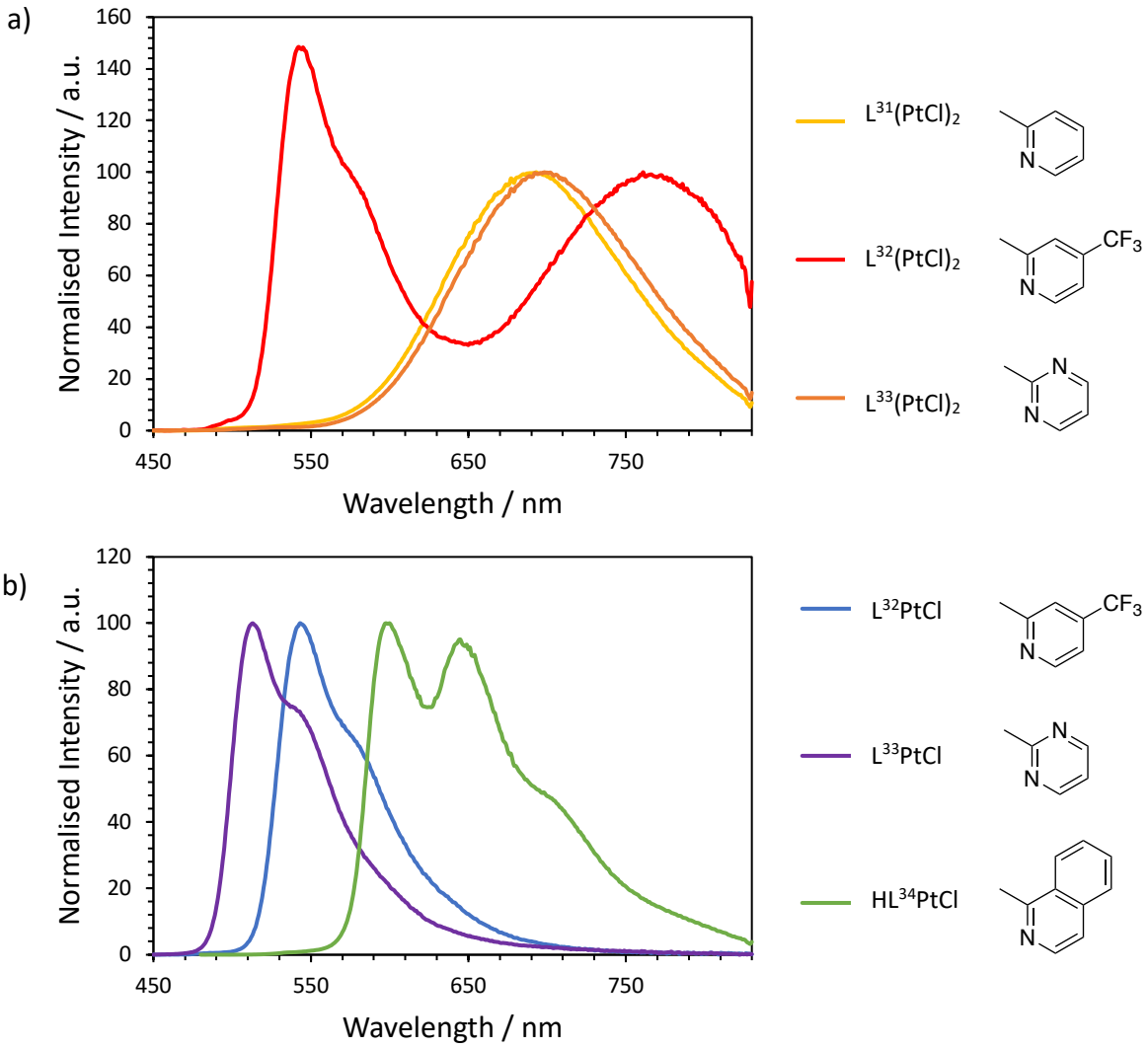

Figure 4.26: *Emission spectra in degassed dilute DCM solution at RT of a) dinuclear Class I sandwich complexes of the form $L^n(PtCl)_2$ and b) mononuclear complexes HL^nPtCl (with the exception of $L^{34}PtCl$ featuring only one N^C^N unit).*

Chloride metathesis

To try to shift the excimer emission further towards the NIR and investigate in more depth the mechanism of excimer formation, particularly for the CF_3-substituted dinuclear complex, the ancillary Cl ligand was replaced with NCS and I to give $L^{32}(PtNCS)_2$ and $L^{32}(PtI)_2$. The pyrimidine derivative $L^{33}(PtNCS)_2$ was also synthesised and studied, though the solubility is particularly poor so only one concentration of a DCM solution of the complex could be prepared.

The absorption spectra of complexes $L^{32}(PtNCS)_2$ and $L^{32}(PtI)_2$ are shown in **Figure 4.27**. The long wavelength CT absorption band is almost identical for both $L^{32}(PtNCS)_2$ and $L^{32}(PtI)_2$ implying that the transition is unaffected by the ancillary ligand.

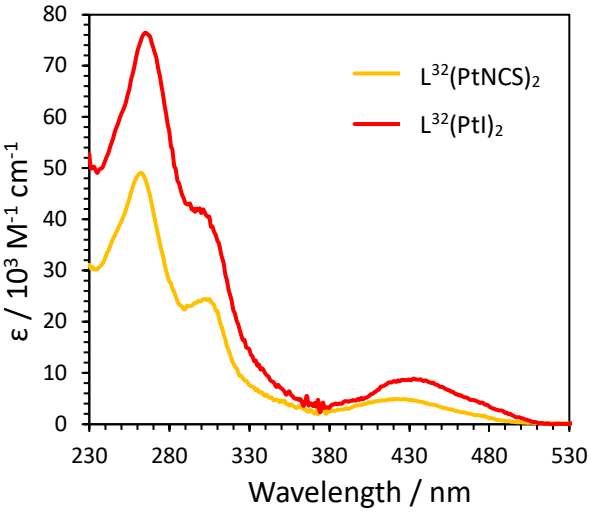

Figure 4.27: *Absorption spectra of complexes $L^{32}(PtNCS)_2$ and $L^{32}(PtI)_2$ in dilute DCM solution.*

Interestingly, changing the ancillary ligand from X = -Cl to X = -NCS resulted in a shift from almost equal contribution of monomer and excimer emission in the former, to purely excimeric emission at all concentrations investigated (6×10^{-6} to 8×10^{-5} M) for $L^{32}(PtNCS)_2$ (**Figure 4.28**), suggesting that -NCS promotes excimeric interactions. The excimer in solution is blue-shifted by a substantial 55 nm for $L^{32}(PtNCS)_2$ compared to $L^{32}(PtCl)_2$, following the trends seen for mononuclear NCS-substituted complexes in Chapters 2 and 3. It would be interesting to study this complex in the solid state to see if excimeric or aggregate emission can be generated emitting even further into the NIR.

On the contrary, replacing the ancillary ligand with -I leads to almost entirely monomeric emission, again with no change in concentration over the range investigated (from 4×10^{-6} to 5×10^{-5} M) (**Figure 4.28**). The PLQY of the iodo complex is also significantly reduced to 1% compared to 93% for $L^{32}(PtNCS)_2$ despite red-shifted emission usually being accompanied by lower quantum yields due to the energy gap law. The self-quenching constant is also much higher for $L^{32}(PtI)_2$, 9.8 ×

10^9 M^{-1} s^{-1} compared to 1.8×10^9 M^{-1} s^{-1} for the thiocyanate derivative, even though the emission of $L^{32}(PtI)_2$ is monomer dominated.

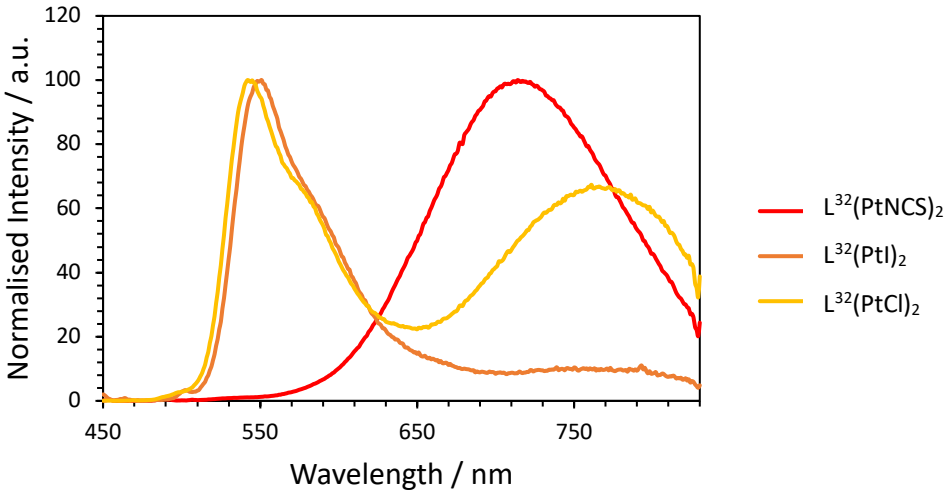

Figure 4.28: *Emission spectra of complexes $L^{32}(PtX)_2$ in dilute degassed DCM solution (4×10^{-6} M) highlighting the dependence of the excimer: monomer ratio on the ancillary ligand.*

The photophysical properties of $L^{33}(PtNCS)_2$ were studied only at one concentration as this complex is highly insoluble. The emission spectrum in degassed DCM solution shows mainly a broad red band at 680 nm with a small monomer-like band at 511 nm (**Figure 4.29**). The excitation spectra recorded at λ_{em} = 515 and 660 nm are comparable suggesting that the emissive species contributing to the long wavelength emission is arising from an excimer. **Figure 4.30** shows that the species emitting at 515 nm and 660 nm have different lifetimes, the lifetime of the excimer being much shorter. The excimer emission band is blue-shifted by approx. 20 nm for $L^{33}(PtNCS)_2$ compared to $L^{33}(PtCl)_2$, in line with the trend observed for all other thiocyanate complexes. Despite the challenges posed by the low solubility of some of these sandwich complexes, they are still valuable for proof-of-concept studies and investigating further the mechanism of excimer emission.

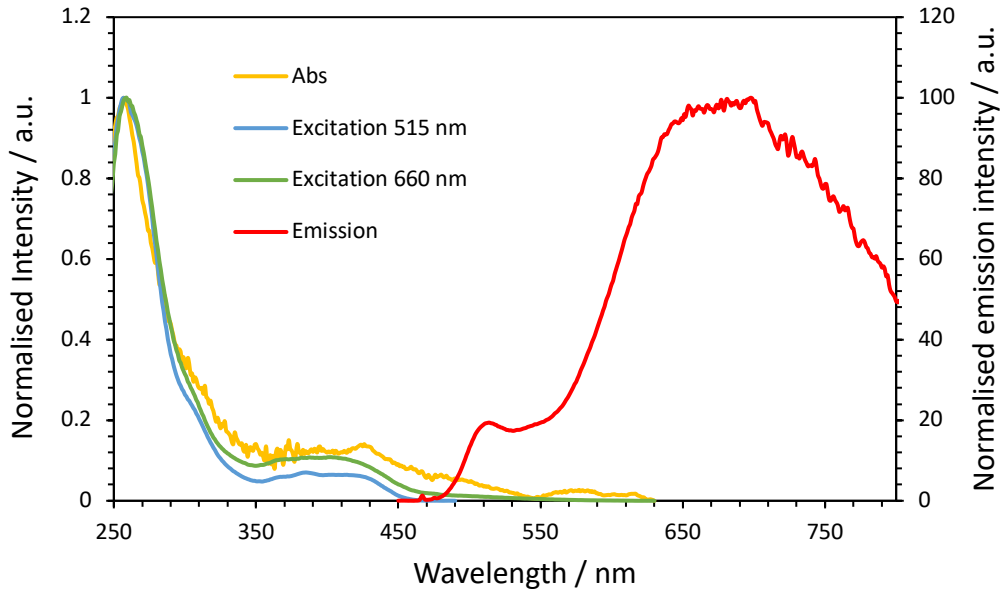

Figure 4.29: *Absorption spectrum, excitation spectra at 515 and 660 nm, and emission spectrum of $L^{33}(PtNCS)_2$ in degassed dilute DCM solution.*

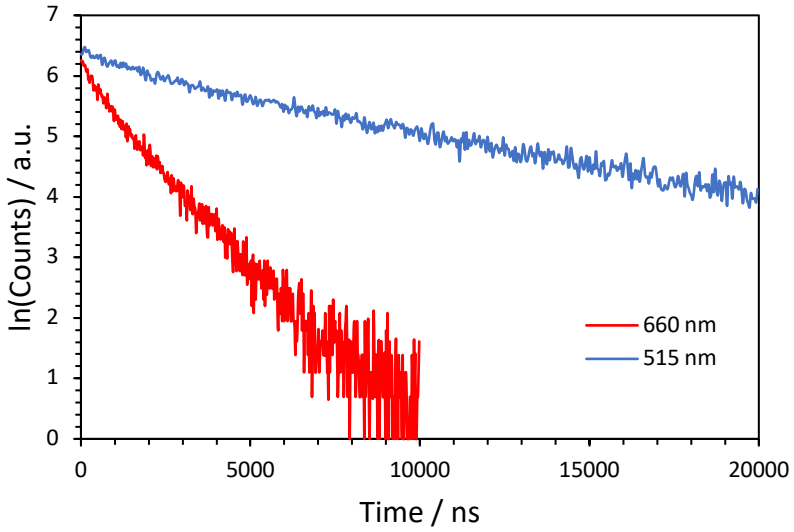

Figure 4.30: *TCSPC measurements for $L^{33}(PtNCS)_2$ at 515 nm (blue) and 660 nm (red) highlighting the different decay lifetimes for each emission band.*

Table 4.1: *A summary of the photophysical properties of Class I mono- and dinuclear sandwich complexes in degassed (aerated in parentheses) DCM solution at 298 K.*

Complex	λ_{abs} / nm (ε / M^{-1} cm^{-1})	λ_{em} / nm (monomer)	λ_{em} / nm (excimer)	Φ_{lum} [aer]	τ / ns [aer]	τ_0 / μs	k_r / 10^3 s^{-1}	$\sum k_{nr}$ / 10^3 s^{-1}	k_{SQ} / 10^9 M^{-1} s^{-1}	$k_Q(O_2)$ / 10^8 M^{-1} s^{-1}
$L^{31}(PtCl)_2$	246 (64900), 272 (76500), 371 (6590), 391 (9950), 425 (10400)	-	693	0.15 [0.02]	1500 [230]	1.5	103	587	1.9	17
$L^{32}(PtCl)_2$	270 (111000), 304 (56700), 357 (10300), 380 (8690), 412 (13700), 425 (13000)	542, 582	766	0.12 [0.05]	7000 450 [1200]	7.1	17	1.26	0.61	3.3
$L^{33}(PtCl)_2$	264 (22000), 374sh (1630), 390 (1900), 435 (2130)	-	698	0.16 [0.06]	760 [300]	0.8	209	1110	0.32	8.6
$L^{34}PtCl$	287 (58300), 345 (16500), 366 (14700), 406 (6960), 430 (9870), 460 (10100)	603, 650, 705	-	0.19 [0.03]	4100 [560]	4.1	47	197	0.8	7.0
$HL^{32}PtCl$	261 (79900), 298 (45200), 396 (4970), 413 (7360), 430 (6120)	543, 582	-	0.22 [0.04]	7100 [1300]	7.2	31	110	0.1	2.9
$HL^{33}PtCl$	259 (97600), 377sh (3840), 393 (5400), 430 (5670), 435 (5580)	513, 545	-	0.61 [0.05]	7900 [510]	8.1	77	50	0.24	8.3
$L^{32}(PtNCS)_2$	266 (40000), 310 (19600), 360 (3840), 425 (4650)	-	714	0.11 [0.06]	1200 [530]	1.2	93	740	1.60	4.7
$L^{32}(PtI)_2$	269 (80500), 308 (39000), 393 (5820), 435 (8390)	551, 584	-	0.01 [0]	6900 [1200]	9.8	1	144	9.76	3.2
$L^{33}(PtNCS)_2$	259, 427, 494	511	680	0.32 [0.04]	1500 [370]	-	219	456	-	9.4

4.3.2 Class II sandwich compounds

4.3.2.1 Synthesis

The synthesis of Class II sandwich compounds first requires the synthesis of the mononuclear complex before the chloride co-ligand is replaced with an acetylide linker, which forms a bridge to the xanthene scaffold. The precursor 2,7-di-*t*-butyl-4,5-diethynyl-9,9-dimethylxanthene (**H_2L^{35}**) can be accessed following the reported procedure[130] by reacting xanthene-Br_2 first with *n*BuLi and I_2 to give the iodo-substituted intermediate **I10**. A Sonagashira coupling followed by base deprotection gave H_2L^{35} in good yield (**Scheme 4.7**).

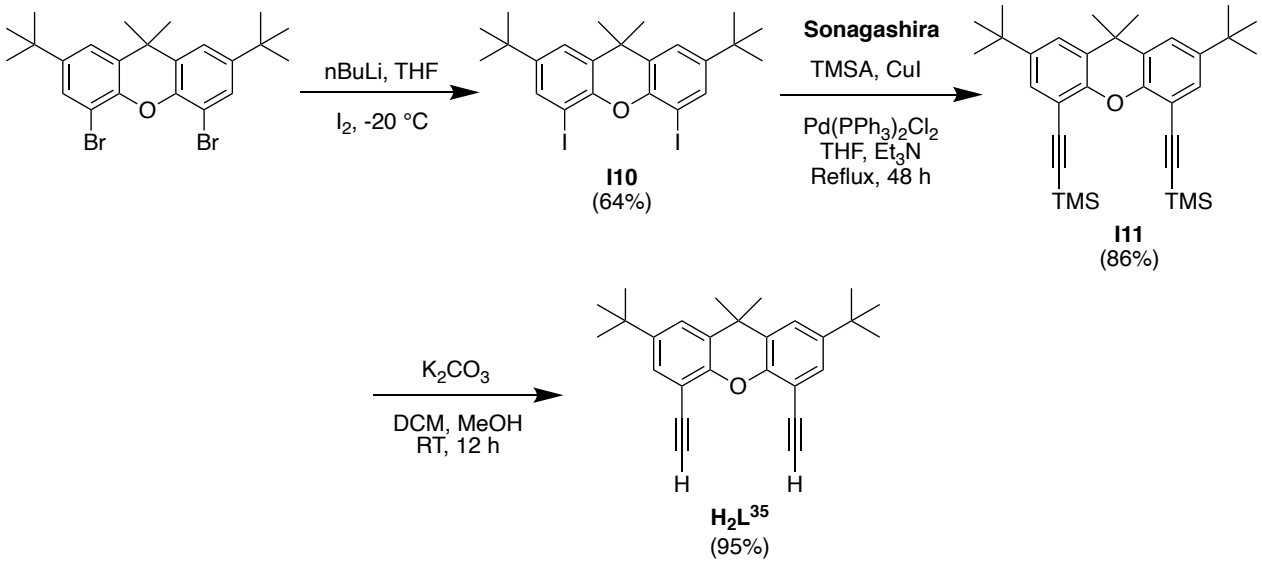

Scheme 4.7: *Synthesis of the xanthene-acetylene ligand precursor H_2L^{35}.*

The Class II complex $(L^3Pt)_2L^{35}$ was synthesised by reacting H_2L^{35} with PtL^3Cl in the presence of NaOMe as a base to deprotonate the acetylene (**Scheme 4.8**). Only a small amount of pure complex was obtained after several recrystallisations, with not enough for a full characterisation. The complex was found to transform back to the chloro mononuclear complex in $CDCl_3$ solution, perhaps due to the presence of trace HCl in the solvent.

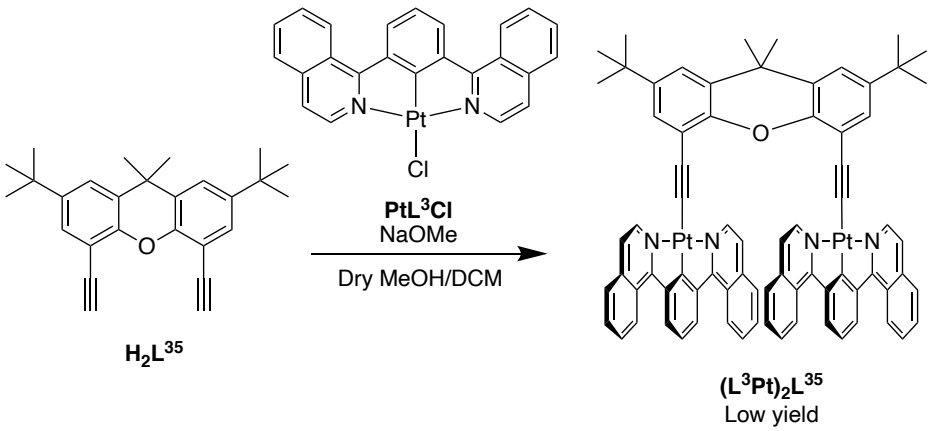

Scheme 4.8: *Synthesis of the Class II compound $(L^3Pt)_2L^{35}$ proceeded in low yield.*

The reaction was attempted with PtL^4Cl where the isoquinoline is linked to the phenyl ring by the 3-position (**Scheme 4.9**). This reaction resulted in an insoluble green/yellow solid that could not be characterised, and no trace of the desired product was observed in the mass spectrum. This might be due to steric hindrance of the isoquinoline rings preventing the chloride metathesis reaction.

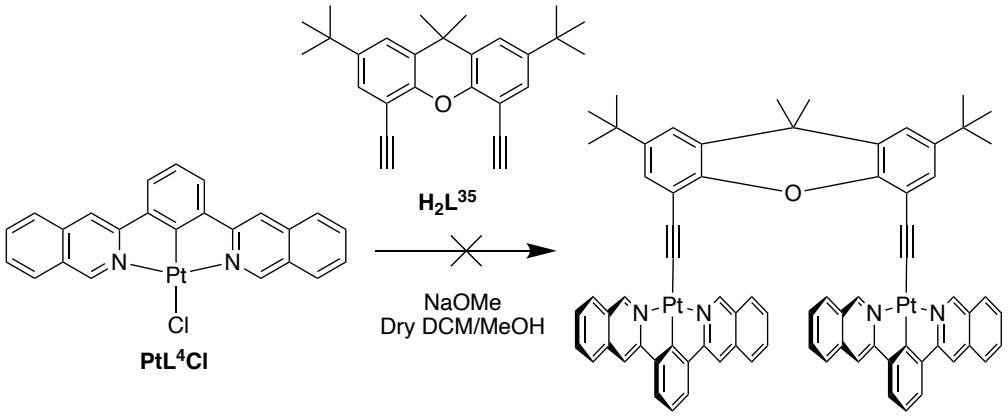

Scheme 4.9: *Reaction of PtL^4Cl to make the Class II complex was unsuccessful.*

Class II compounds were not studied in great detail in this work due to the difficulty with purification and problems with decomposition associated with the more labile acetylene linker. However, in order to improve the stability of Class II compounds, a molecular design based on a combination of Class I and Class II units was proposed and will be discussed in Section 4.3.3.

4.3.2.2 Photophysical properties

Solution-state photophysical analysis of $(L^3Pt)_2L^{35}$ (synthesised by Dr Melissa Walden) and PtL^3Cl (synthesised by me) was carried out by Dr Piotr Pander (Durham University, Department of Physics) and results shown in **Table 4.2**. The monomer emission is identical for both complexes peaking just before 600 nm. Whilst the monometallic complex PtL^3Cl only shows sign of some excimer emission in concentrated solution (3×10^{-4} M), the Class II bimetallic complex $(L^3Pt)_2L^{35}$ displays excimer emission of a similar intensity in dilute solution (3×10^{-6} M) highlighting the greater propensity for these interactions. Purely monomeric type emission can be seen for $(L^3Pt)_2L^{35}$ in very dilute solution (**Figure 4.31a**), in contrast to the Class I compounds above where excimeric emission can be seen even in very dilute solution. The excimer emission has λ_{max} around 800 nm for both complexes, greatly red-shifted in comparison to the excimer emission of Pt(dpyb)Cl (690 nm). $(L^3Pt)_2L^{35}$ has a solution QY of 9%, lower than other Class II compounds synthesised by Dr Melissa Walden (QYs ranging between 20 and 30%)[135] due to the extended conjugation of the isoquinoline unit, but significantly greater than the literature reported N^N^C

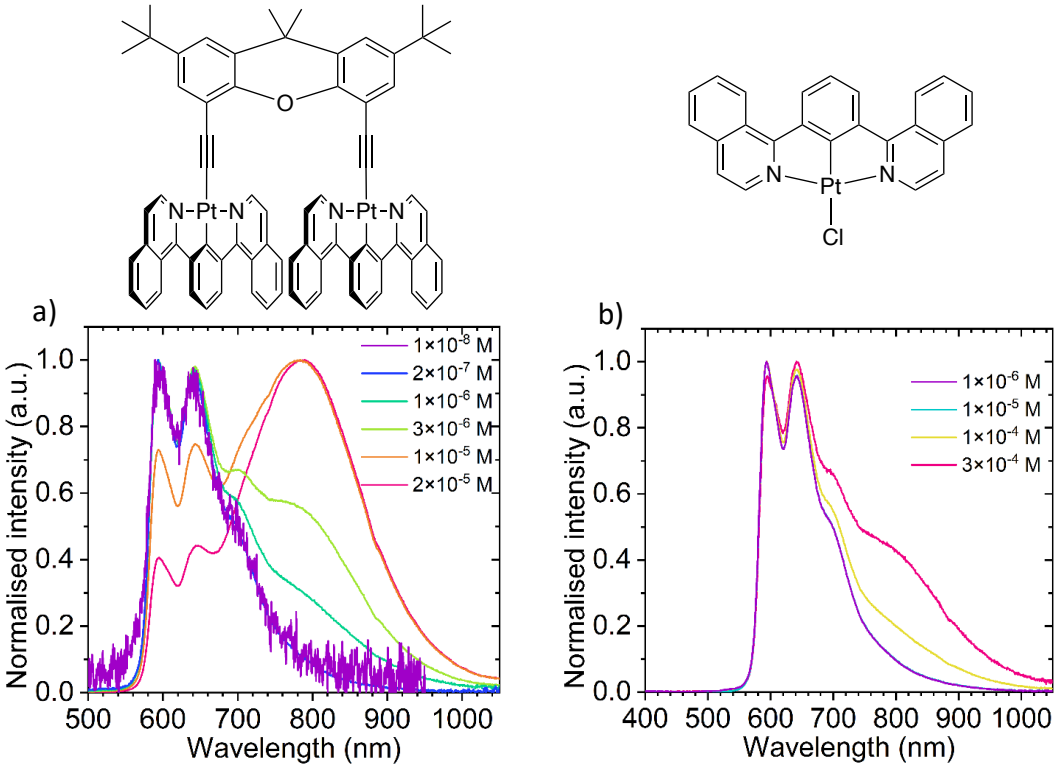

Figure 4.31: *Emission spectra at various concentrations in degassed DCM solution of a) $(L^3Pt)_2L^{35}$ and b) PtL^3Cl.*

compound **22** (QY = 0.0026% for λ_{max} = 817 nm).[130] This directly demonstrates the superior luminescence efficiency that can be achieved by the N^C^N arrangement of the cyclometallating ligand compared to N^N^C (see Section 1.3).

The emission spectra of $(L^3Pt)_2L^{35}$ collected at various concentrations show that the ratio between emission intensities of the monomer and excimer-type emissions changes with concentration. This observation clearly indicates that excimer formation is not supported by pure intramolecular interactions; if this was the case, the emission intensity ratio would be independent of concentration.

The absorption spectrum of $(L^3Pt)_2L^{35}$ obtained over a range of concentrations (**Figure 4.32a**) shows virtually no change between 1×10^{-6} and 2×10^{-5} M, which could indicate that no ground-state interactions are present. However, the excitation spectrum is a more sensitive tool to analyse changes in the ground state of photoluminescent systems, especially at low concentrations. The measurements were performed at a concentration of 3×10^{-6} M in order to ensure sufficient contribution of excimer-type emission, as well as to obtain sufficient signal-to-noise ratio. Probing the excitation spectrum at 800 nm and 600 nm to investigate the broad excimer-like emission and monomeric emission respectively, reveals different

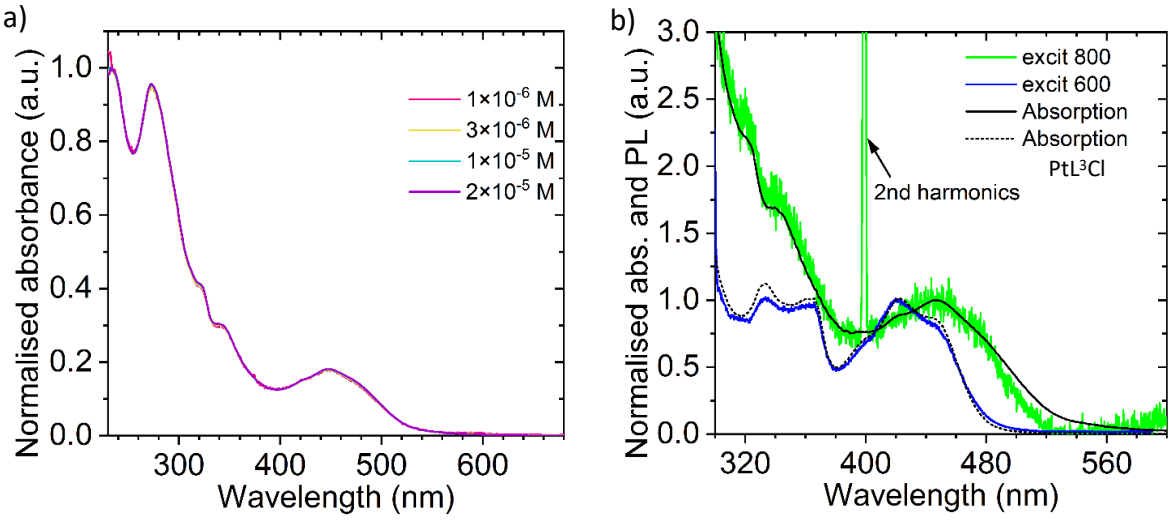

Figure 4.32: *a) Absorption spectra of $(L^3Pt)_2L^{35}$ at various concentrations, and b) excitation spectra of $(L^3Pt)_2L^{35}$ at 600 and 800 nm compared with its absorption spectrum (black solid line) and the absorption spectrum of the monometallic derivative PtL^3Cl (black dashed line).*

spectra for each, with the spectrum at 800 nm appearing red-shifted compared to that at 600 nm (**Figure 4.32b**). This shows that both emissions originate from different species and indicates the occurrence of ground-state interactions (dimer formation) as being responsible for the excimer-type emission.

Moreover, the excitation spectrum at 600 nm resembles the absorption spectrum of the respective monometallic analogue PtL^3Cl (**Figure 4.32b**). This observation indicates that each Pt(N^C^N) unit of the dinuclear complex behaves fundamentally like an individual, monometallic unit, or, that the complex is decomposing in solution to the mononuclear complex PtL^3Cl. The excitation spectrum of the dimer emission shows the best resemblance to the complex's absorption spectrum, showing that dimeric species are predominant in solution at concentrations above 1×10^{-6} M, where absorption spectra can be recorded with confidence.

4.3.3 Interlocked sandwich compounds

4.3.3.1 Synthesis

Interlocked sandwich compounds are defined here as having both a bond from a xanthene ring to the central phenyl ring of two N^C^N-coordinating Pt(II) units, as in Class I compounds, and additional bonds to another xanthene unit *via* acetylene co-ligands, as in Class II compounds. Their synthesis first requires the synthesis of the Class I complex which is then reacted with H_2L^{35} in the presence of NaOMe to form the square-like interlocked dinuclear complex. The parent complex was targeted first by reacting $L^{31}(PtCl)_2$ with H_2L^{35}. The resulting bright yellow solid was purified by washing with water, methanol and diethyl ether before extraction into DCM to give the product $L^{31}Pt_2L^{35}$ (**Scheme 4.10**).

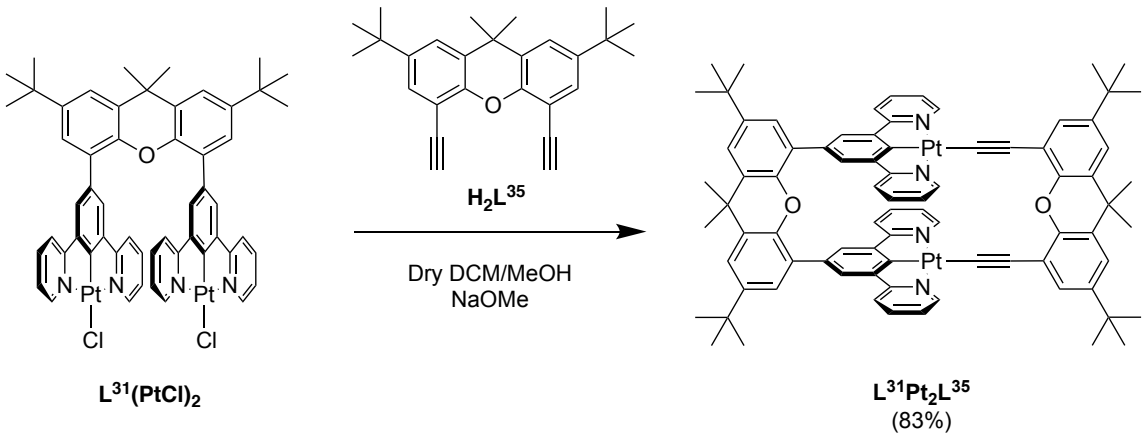

Scheme 4.10: *Synthesis of $L^{31}Pt_2L^{35}$ combining Class I and Class II sandwich compounds.*

The reaction was repeated with $L^{32}(PtCl)_2$ and $L^{33}(PtCl)_2$ to give $L^{31}Pt_2L^{35}$ and $L^{31}Pt_2L^{35}$ respectively (**Figure 4.33**). These derivatives required a column on silica with DCM/MeOH as the eluent to purify in order to separate the target complex from unreacted $L^n(PtCl)_2$. These complexes are significantly more soluble in DCM than their Class I analogues.

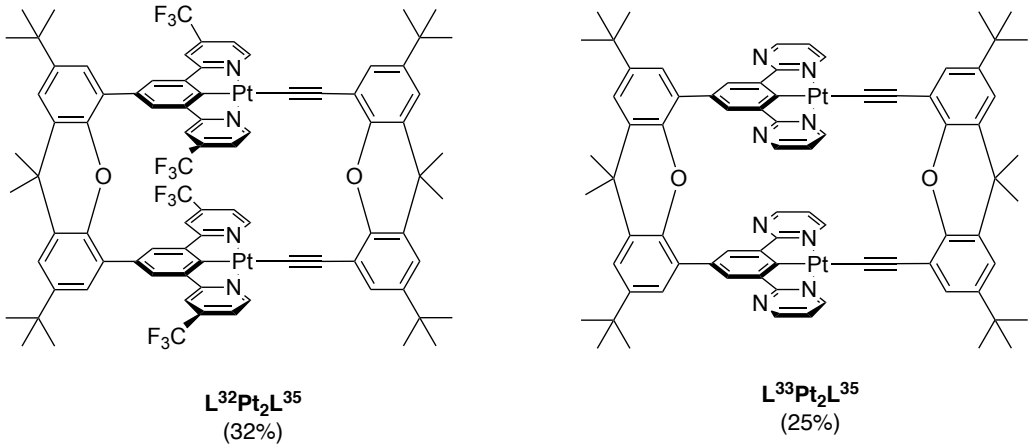

Figure 4.33: *Structure of interlocked sandwich complexes combining essences of both Class I and Class II compounds.*

4.3.3.2 Crystal structure determination

Crystals of $L^{31}Pt_2L^{35}$ suitable for X-ray diffraction were grown by slow evaporation of a solution of the complex in chloroform. The crystal structure is highly disordered but offers proof of connectivity (**Figure 4.34**). Numerous crystals were grown from different solvents and each one had the same disorder suggesting it is an intrinsic property of the way the molecule crystallises.

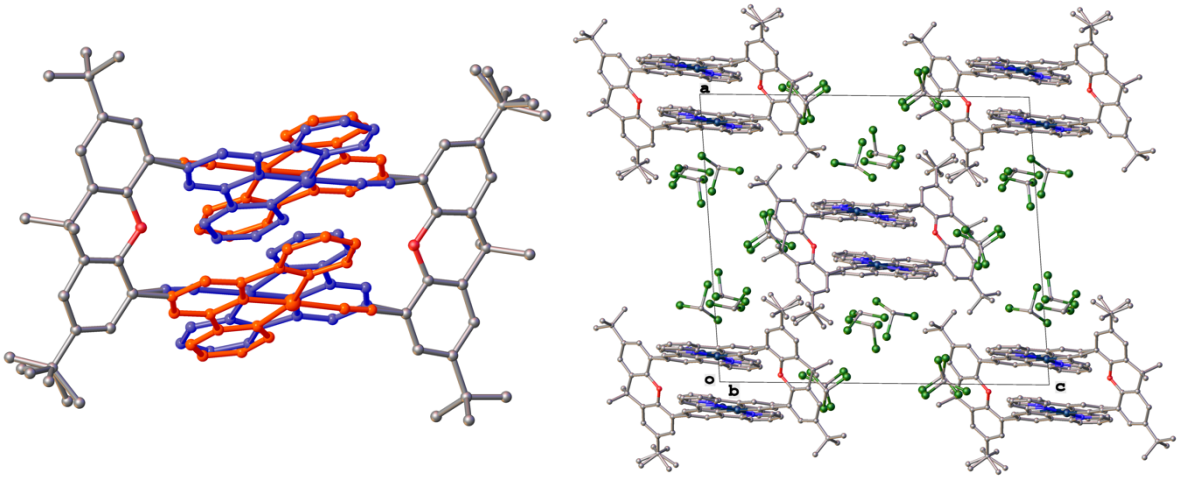

Figure 4.34: *Molecular structure and crystal packing of $L^{31}Pt_2L^{35}$ highlighting the disorder in the crystal.*

The Pt···Pt intramolecular distance is 4.2661(12) Å, shorter than that for the corresponding dinuclear Class I compound $L^{31}(PtCl)_2$ (4.7037(11) Å) but still larger than the sum of the van der Waals' radius for two Pt ions. The shortest interplanar distance, however, is measured as 3.387(7) Å implying intramolecular π-π stacking interactions are present. The Pt(N^C^N) units are twisted relative to the xanthene scaffold at an angle of 48.9° for one N^C^N unit and 59.1° for the other. No intermolecular interactions are present in the crystal structure between Pt(N^C^N) units, either Pt···Pt or π-π interactions.

The crystal structure of $L^{33}Pt_2L^{35}$ (**Figure 4.35**) also reveals similar disorder within the crystal. The crystal packing reveals a Pt···Pt distance of 4.3832(3) Å but an interplanar distance of 3.4129(2) Å measured between the Pt of one unit and a pyrimidine ring of another within the same molecule. The Pt(N^C^N) units are once again twisted

relative to the xanthene plane, at 48.0° for one unit and 45.0° for the other. There are no intermolecular interactions present between Pt(N^C^N) units but it is not impossible to imagine that the molecules could slot together and interact in an intermolecular fashion.

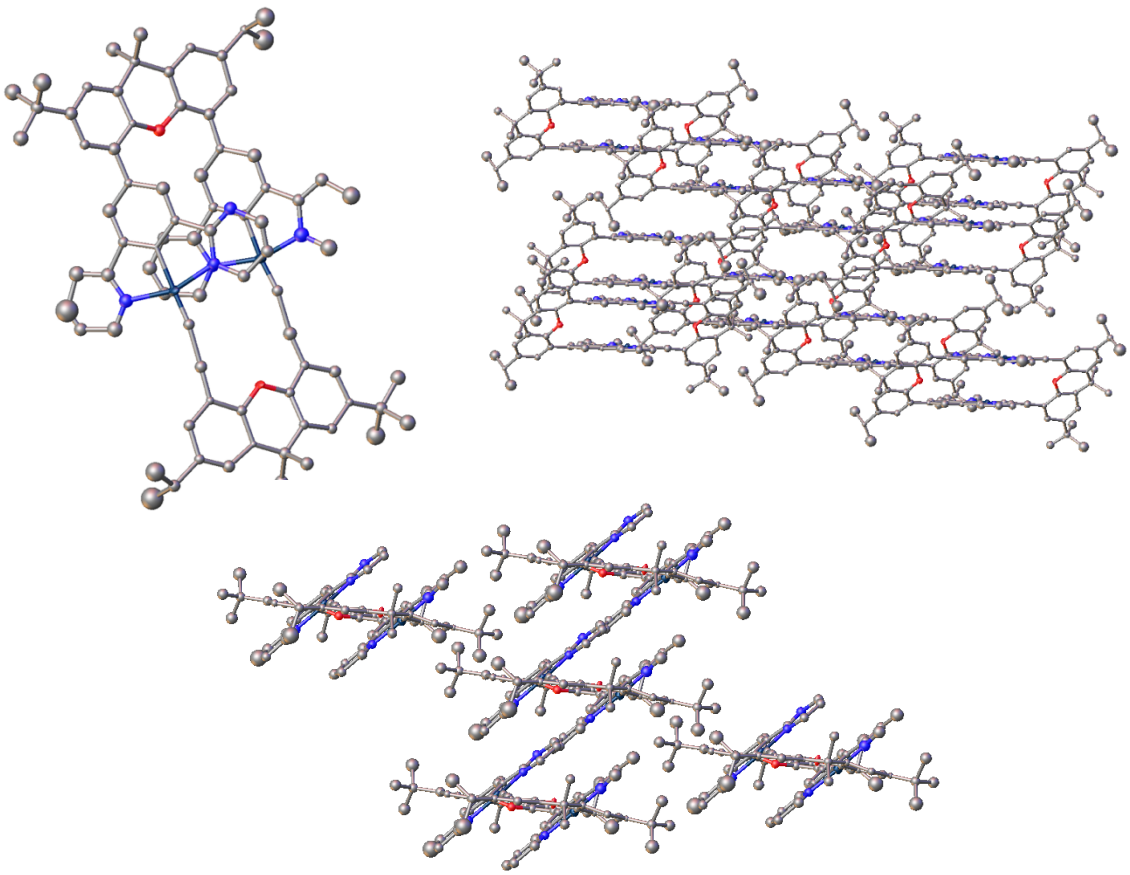

Figure 4.35: *Molecular and crystal structure of $L^{33}Pt_2L^3$, the second packing diagram highlighting the 45° twist of the Pt(N^C^N) units relative to the xanthene scaffold.*

4.3.3.3 Photophysical properties

Absorption

The absorption spectra of these interlocked complexes are shown in **Figure 4.36**. The tail of the lowest energy absorption band is red-shifted in the order $L^{31}Pt_2L^{35}$ < $L^{33}Pt_2L^{35}$ < $L^{32}Pt_2L^{35}$, following the same order as seen for the Class I derivatives. The extinction coefficients for the lowest energy absorbing complex $L^{32}Pt_2L^{35}$ are much lower than the other analogues in this series.

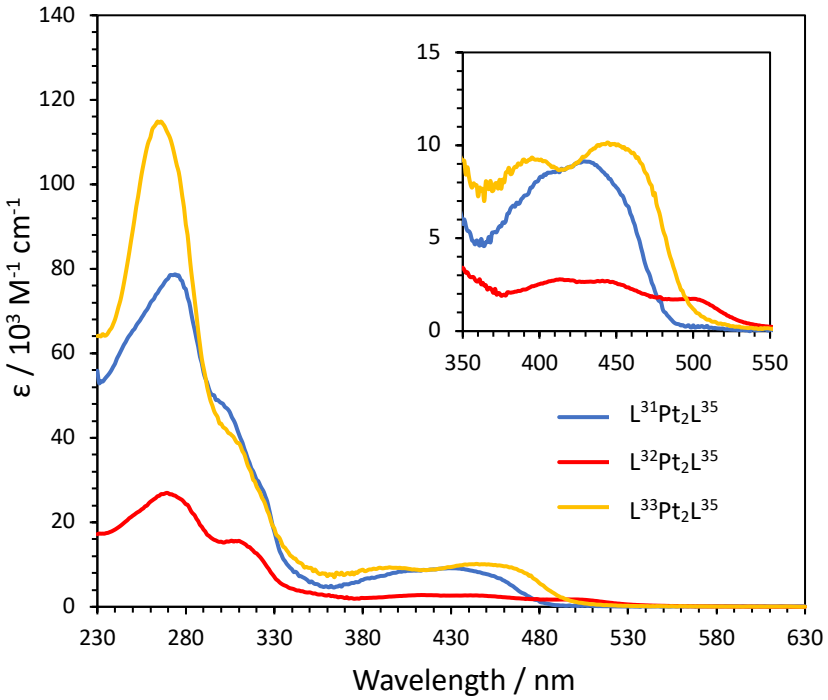

Figure 4.36: *Absorption spectra for $L^nPt_2L^{35}$ in DCM solution. Inset: zoomed in on the long wavelength region of the spectrum.*

When comparing the absorption of these interlocked $L^nPt_2L^{35}$ complexes to the analogous Class I compounds, the interlocked complexes exhibit red shifted absorption spectra as well as lower extinction coefficients for each band (**Figure 4.37**). $L^{31}Pt_2L^{35}$ has additional LC bands between 230 and 330 nm compared to $L^{31}(PtCl)_2$ (**Figure 4.37a**) probably owing to the additional xanthene ring. The same can be seen for $L^{32}Pt_2L^{35}$ which has an additional stronger peak at 315 nm compared to $L^{32}(PtCl)_2$ (**Figure 4.37b**) and for $L^{33}Pt_2L^{35}$ also showing an additional LC peak at 312 nm (**Figure 4.37c**).

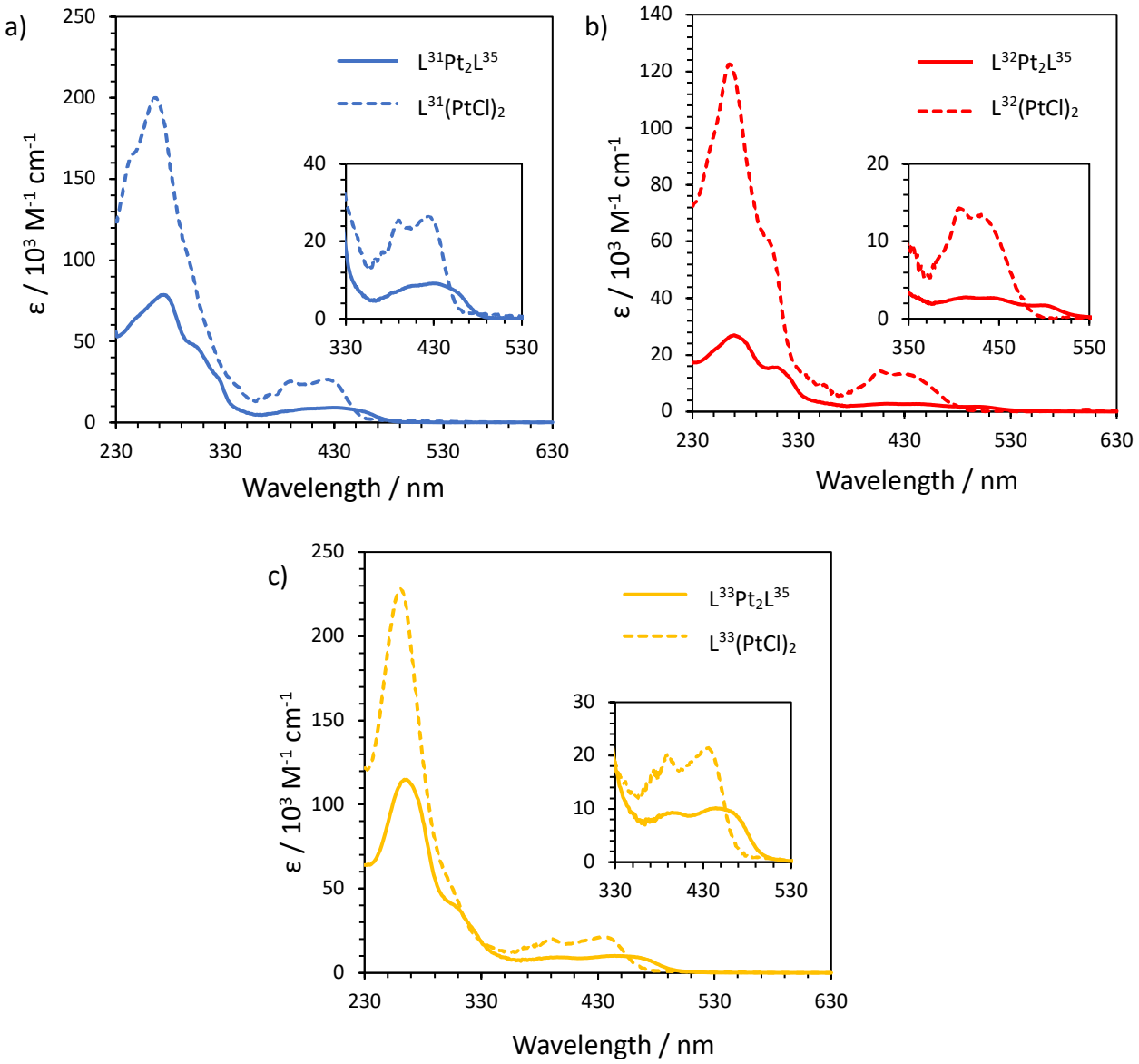

Figure 4.37: *Comparison of absorption spectra between $L^nPt_2L^{35}$ and the Class I derivatives $L^n(PtCl)_2$ in dilute DCM solution.*

Emission

All complexes are brightly luminescent in degassed DCM solution. The spectra are dominated by broad long-wavelength excimeric emission even in dilute solution, red-shifted in the order $L^{31}Pt_2L^{35}$ < $L^{33}Pt_2L^{35}$ < $L^{32}Pt_2L^{35}$ (**Figure 4.38**), in accordance with the absorption spectra.

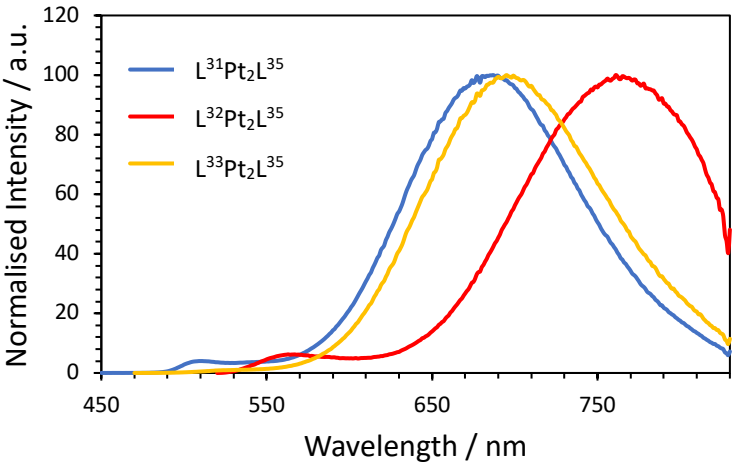

Figure 4.38: *Emission spectra of interlocked complexes $L^nPt_2L^{35}$ in DCM solution at 1 × 10^{-5} M.*

The emission of the series parent complex $L^{31}Pt_2L^{35}$ in degassed DCM solution recorded at various concentrations is shown in **Figure 4.39**. The complex exhibits purely excimer-like broad emission peaking at 690 nm at all concentrations investigated, with a very small monomer-like peak at 508 nm. The table in **Figure 4.39** shows that the lifetime does not change with concentration suggesting that this excimer is purely intramolecular in nature. This is supported by the lack of rise-time in the decay of the emission. Moreover, the absorption spectrum matches the excitation spectrum recorded at 680 nm implying that aggregation is unlikely, or that

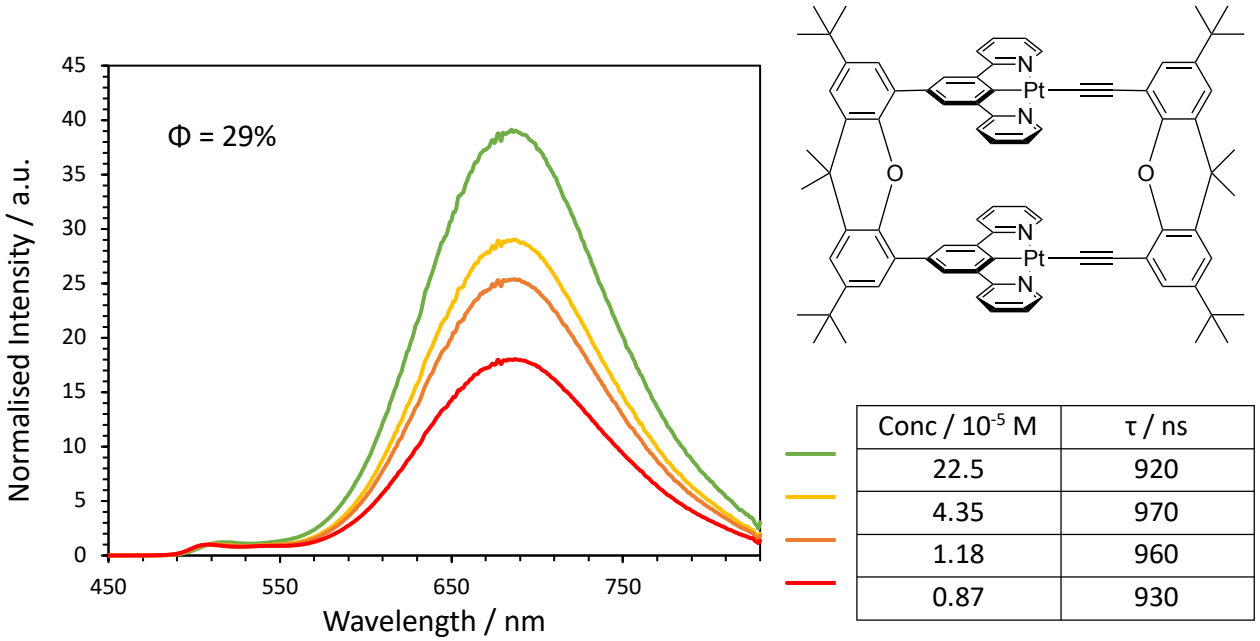

Conc / 10^{-5} M	τ / ns
22.5	920
4.35	970
1.18	960
0.87	930

Figure 4.39: *Emission spectra of $L^{31}Pt_2L^{35}$ in degassed DCM solution over a range of concentrations, normalised to 508 nm.*

these dimers are already present and predominant in the ground state for the measured concentrations (**Figure 4.40**).

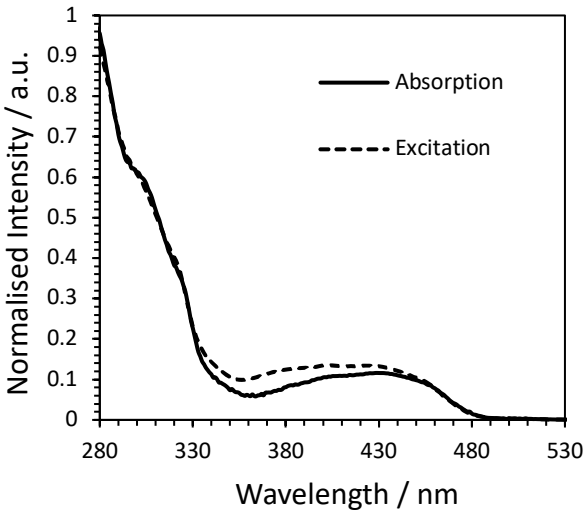

Figure 4.40: *Comparison of the excitation spectrum (at 680 nm) with the absorption spectrum for $L^{31}Pt_2L^{35}$ in DCM solution at 9×10^{-6} M.*

The emission profile of $L^{31}Pt_2L^{35}$ is almost identical to that of the Class I derivative $L^{31}(PtCl)_2$ (**Figure 4.41**). Interestingly, the quantum yield is enhanced for $L^{31}Pt_2L^{35}$ at 29%, almost double that of $L^{31}(PtCl)_2$ at 15% (**Table 4.2**).

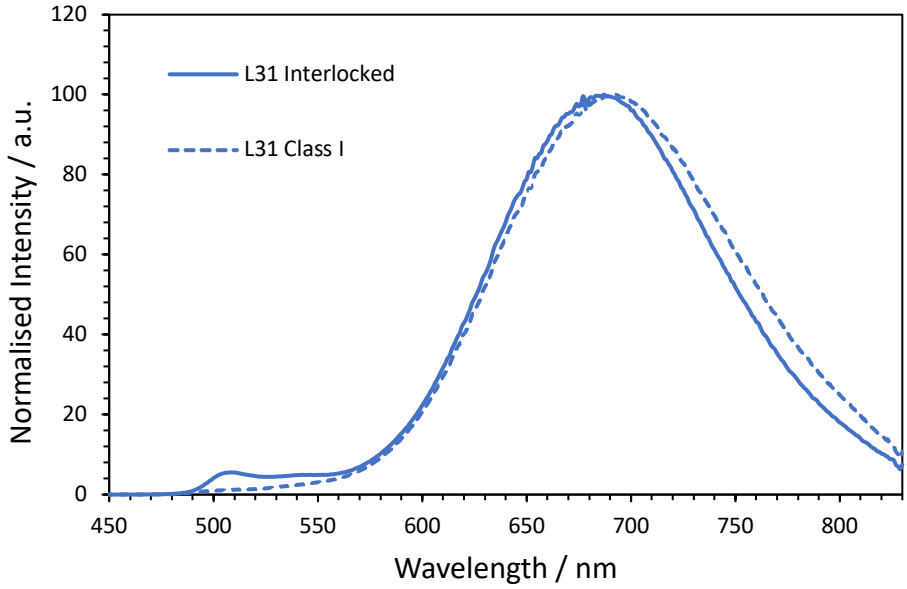

Figure 4.41: *Comparison of the emission spectra of $L^{31}Pt_2L^{35}$ and $L^{31}(PtCl)_2$ in dilute degassed DCM solution 5×10^{-6} M.*

The appearance of the complex $L^{31}Pt_2L^{35}$ as a bright yellow solid that glows brightly yellow green under long wave UV light prompted investigation into solid-state emission. Emission of the complex in polystyrene films at various doping concentrations (0.10%, 1%, 10% and 100%) was carried out by Dr Piotr Pander (Department of Physics, Durham University) and the results shown in **Figure 4.42**. At anything but high doping levels, the PL is dominated by monomer emission peaking at 530 nm; neat film is necessary to achieve excimer-dominated emission, with the broad long-wavelength band only appearing slightly at 10%. This is perhaps due to the Pt(N^C^N) units of the complex still requiring some motion relative to one another in order to achieve the favourable geometry for excimeric emission, which is not available in the solid-state.

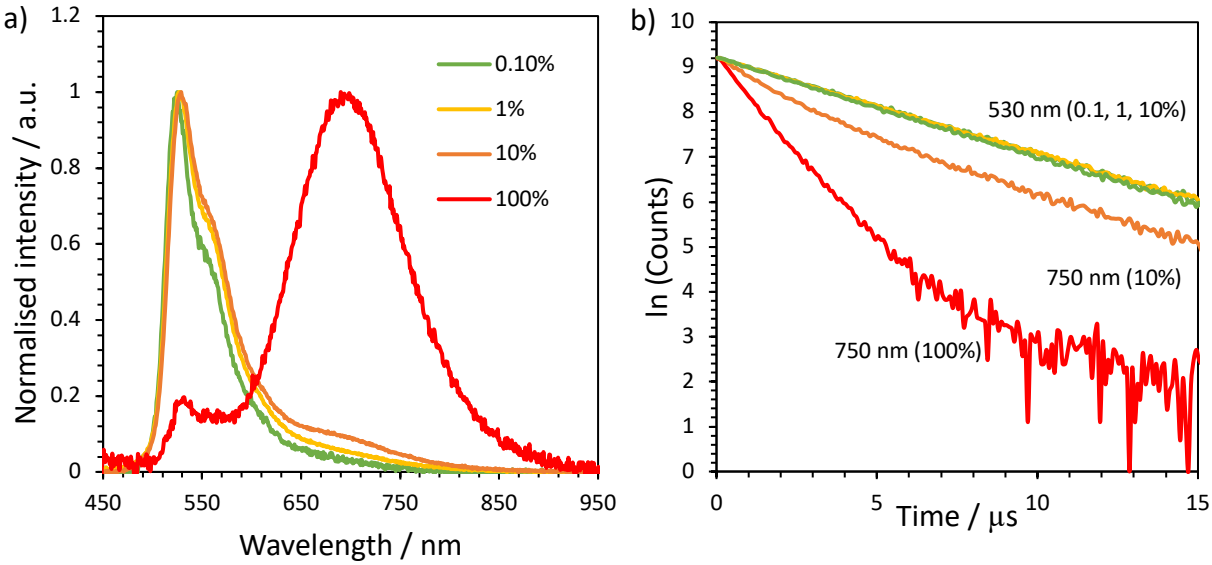

Figure 4.42: *a) Solid state emission of $L^{31}Pt_2L^{35}$ in polystyrene at various doping concentrations, and b) corresponding TCSPC decay of the emission.*

The concentration-dependent formation of the broad low energy band is likely to arise from aggregation, seen more often in the solid-state, and does not reflect the solution-state behaviour. The TCSPC decay of the emission at 750 nm (**Figure 4.42b**) highlights the two species emitting at 530 and 750 nm decay with different lifetimes (**Table 4.2**), suggesting they are not in equilibrium; this supports the assignment of the solid-state emission to aggregation.[99]

The solution-state emission spectrum of $L^{32}Pt_2L^{35}$ is dominated by the broad excimer band peaking at 765 nm (**Figure 4.43**). Incorporating this extra xanthene unit L^{35} has increased the propensity of this CF_3-substituted complex to form excimeric interactions, as the Class I derivative $L^{32}(PtCl)_2$ displayed almost equal contribution of the monomer and excimer species to the emission across all concentrations investigated (**Figure 4.44**). The additional xanthene unit most likely holds the two Pt(N^C^N) units in a favourable orientation to allow the formation of intramolecular excimers, whilst disfavouring intermolecular interactions due to steric hindrance. Even if intermolecular interactions are possible, they will always be outcompeted by intramolecular interactions.

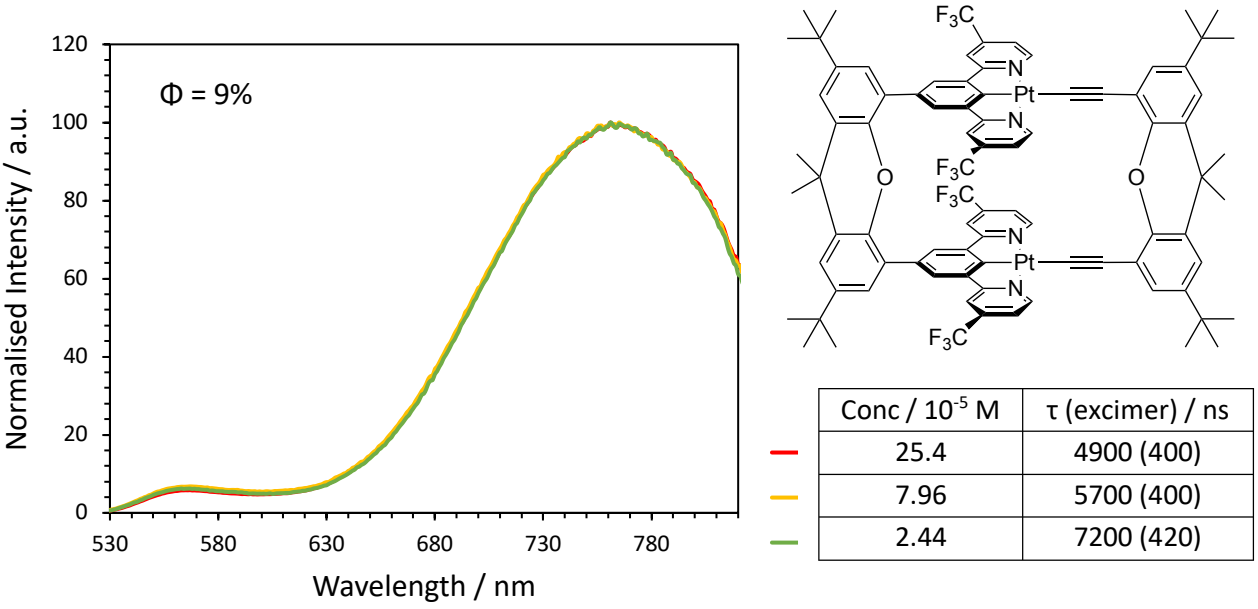

Conc / 10^{-5} M	τ (excimer) / ns
25.4	4900 (400)
7.96	5700 (400)
2.44	7200 (420)

Figure 4.43: *Emission spectra of $L^{32}Pt_2L^{35}$ in degassed DCM solution over a range of concentrations, and lifetimes measured at 565 nm (monomer) and 745 nm (excimer).*

The excimeric band is similar for both $L^{32}Pt_2L^{35}$ and $L^{32}(PtCl)_2$. The absorption spectrum of $L^{32}Pt_2L^{35}$ matches the excitation spectrum recorded at 745 nm confirming the assignment of this emissive species to an excimer (**Figure 4.45**). The excitation spectrum recorded at 545 nm is different, with just some peaks overlapping, implying that the two emitting species are not the same. The 'intramolecular excimer' is acting like an aggregate as the Pt(N^C^N) units are already held in close proximity in the ground state. Moreover, the excimer-like band

is not subject to self-quenching as there is no correlation between the concentration and the lifetime probed at 745 nm, once again implying the excimer is intramolecular in nature.

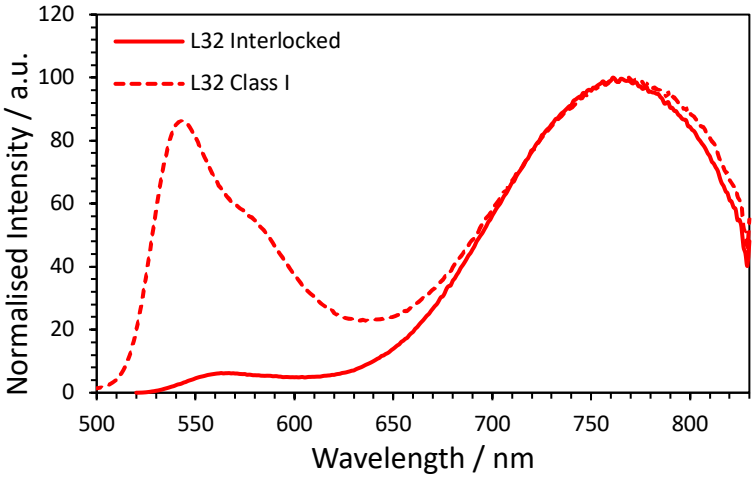

Figure 4.44: *Comparison of the emission spectra of the interlocked complex $L^{32}Pt_2L^{35}$ and the Class I derivative $L^{32}(PtCl)_2$ in DCM solution at 2×10^{-5} M.*

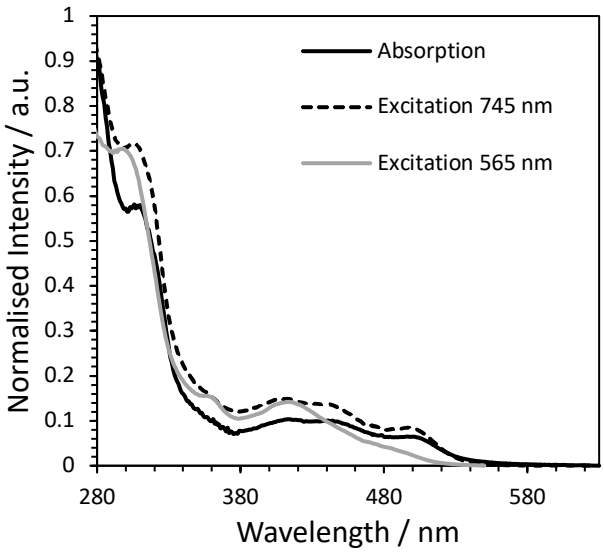

Figure 4.45: *Absorption spectrum and excitation spectra of $L^{32}Pt_2L^{35}$ at 565 and 745 nm to probe the monomer and excimer respectively, in DCM solution (2.4×10^{-5} M).*

The small band at λ_{em} = 565 nm does have a lifetime that varies with concentration indicating some degree of self-quenching; is this monomer band due to a trace amount of monomolecular complex present that would be subject to self-quenching, or do we always see some monomer contribution to the emission from the dinuclear

complexes, despite this species having a longer lifetime? The evidence presented suggests the latter though more experiments into the excited-state properties would be beneficial. This conclusion is also supported by the fact that the position of the monomer-like peak for $L^{32}Pt_2L^{35}$ does not match that of $L^{32}(PtCl)_2$, with the former being more red-shifted (**Figure 4.44**).

The emission spectra of $L^{33}Pt_2L^{35}$ in DCM at various concentrations are shown in **Figure 4.46**. This complex displays solely broad long-wavelength excimeric emission at all concentrations investigated, even in very dilute solution. The λ_{max} is 697 nm, slightly red-shifted compared to the parent $L^{31}Pt_2L^{35}$, but with a lower quantum yield (0.17 compared to 0.29). The lifetime of the excimeric band at 697 nm does not depend on concentration, implying that the emitting species is intramolecular in nature, as seen for the other complexes in this series. The assignment to an intramolecular excimer is supported by the excitation spectrum recorded at 680 nm which matches the absorption spectrum (**Figure 4.47**).

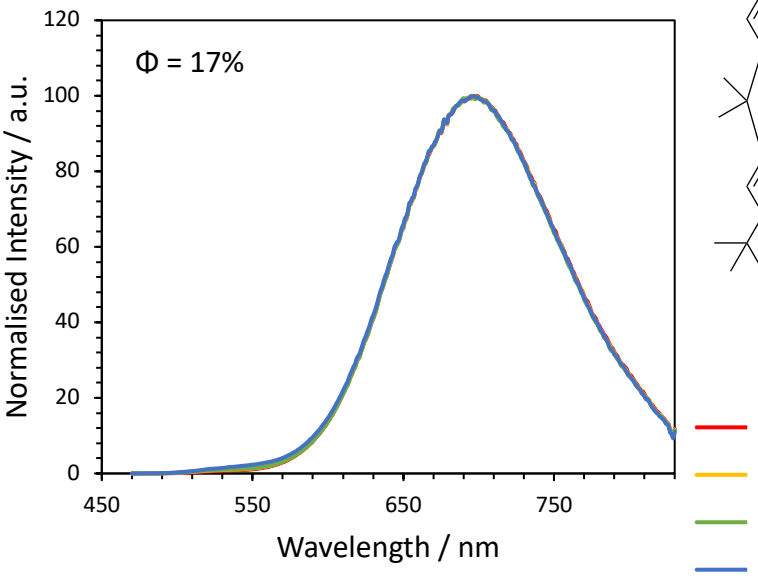

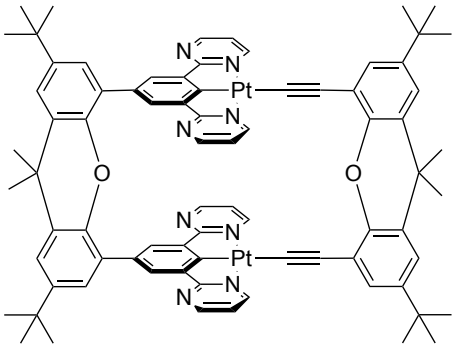

Conc / 10^{-5} M	τ at 680 nm / ns
22	730
4.7	720
1.2	680
6.4	720

Figure 4.46: *Emission spectra of $L^{33}Pt_2L^{35}$ in degassed DCM solution at various concentrations, normalised to λ_{max}.*

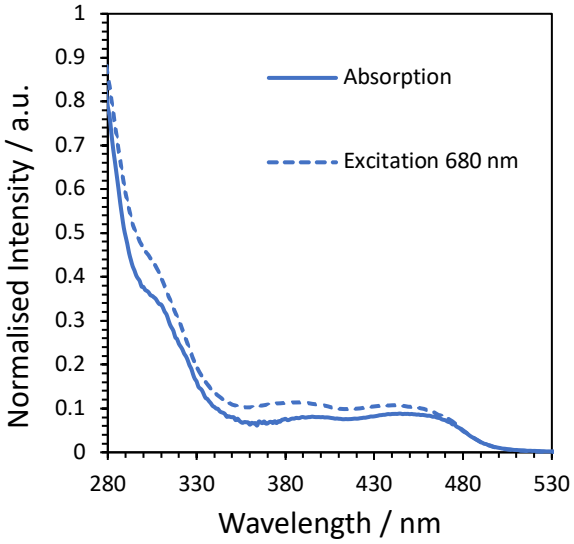

Figure 4.47: *Comparison of the absorption and excitation spectra of $L^{33}Pt_2L^{35}$ in DCM solution at 298 K.*

Finally, the emission spectrum of the interlocked $L^{33}Pt_2L^{35}$ matches that of its Class I analogue $L^{33}(PtCl)_2$ (**Figure 4.48**). As the crystal structures of these interlocked molecules revealed no preference for intermolecular interactions, it is likely that both the interlocked molecules and the Class I derivatives exhibit intramolecular excimers as the emitting species.

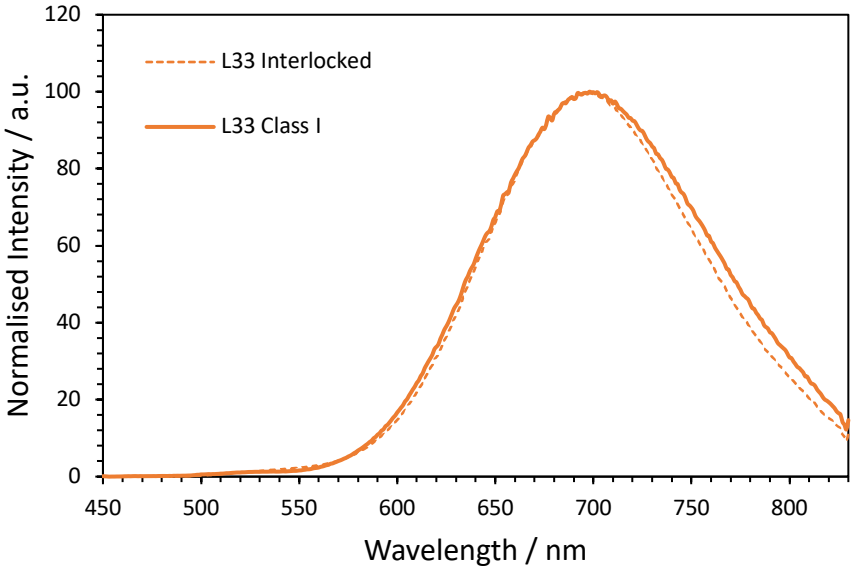

Figure 4.48: *Comparison of the emission spectra of $L^{33}Pt_2L^{35}$ and the Class I derivative $L^{33}(PtCl)_2$ in DCM solution at 3×10^{-5} M.*

The low temperature emission of this series of interlocked compounds follows the same trend seen for the Class I derivatives; $L^{31}Pt_2L^{35}$ and $L^{32}Pt_2L^{35}$ display purely structured monomeric emission whereas $L^{33}Pt_2L^{35}$ also displays some broad excimer-like emission peaking at 665 nm (**Figure 4.49**). The excimer emission of $L^{33}Pt_2L^{35}$ at 77 K is blue shifted by approx. 30 nm relative to the emission at 298 K. The observation of structured monomer emission at low temperature supports the argument that some motion is still required to form an excimer, even if it is intramolecular in nature.

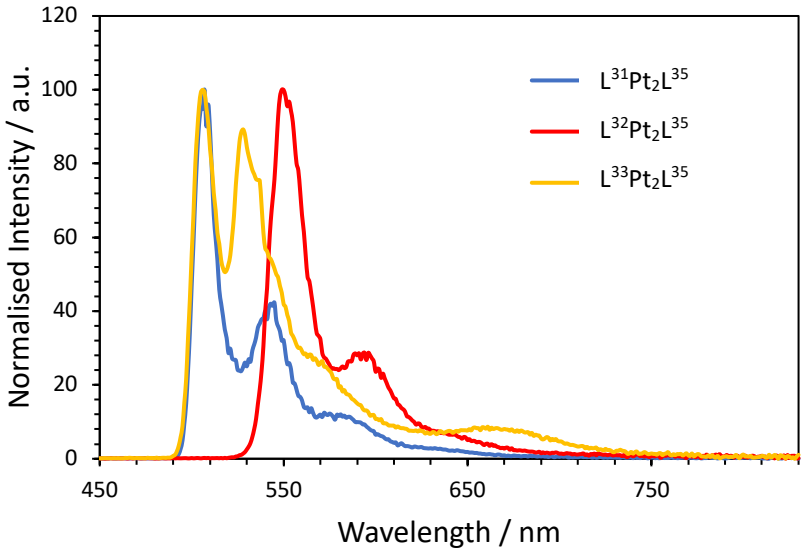

Figure 4.49: *77 K emission spectra of $L^nPt_2L^{35}$ in EPA glass.*

Table 4.2: *A summary of the photophysical parameters for the interlocked complexes $L^nPt_2L^{35}$ in dilute degassed (aerated in parentheses) DCM solution at 298 K.*

Complex	λ_{abs} / nm (ε / M^{-1} cm^{-1})	λ_{em} / nm (monomer)	λ_{em} / nm (excimer)	Φ_{lum} [aer]	τ / ns [aer]	τ_0 / μs	k_r / 10^5 s^{-1}	$\sum k_{nr}$ / 10^5 s^{-1}	k_{SQ} / 10^9 M^{-1} s^{-1}	$k_Q(O_2)$ / 10^8 M^{-1} s^{-1}
$L^{31}Pt_2L^{35}$	275 (78400), 306 (44300), 327 (23500), 405 (8540), 430 (9020)	511, 542	690	0.29 [0.06]	931 [192]	-	3.1	7.7	-	18.8
$L^{32}Pt_2L^{35}$	275 (27700), 313 (15900), 419 (2770), 451 (2590), 500 (1740)	566	761	0.09 [0.05]	422 [273]	7.0 (monomer band)	2.0	21.7	0.25	5.9
$L^{33}Pt_2L^{35}$	275 (78400), 315 (25500), 327 (23500), 397 (9250), 450 (9970)	-	697	0.17 [0.07]	722 [395]	-	2.3	11.5	-	12.3

4.3.4 Alternative Linkers

This section will focus on initial work carried out into alternative linkers to xanthene for dinuclear complexes to study inter- and/or intramolecular interactions and achieve red-shifted excimeric emission. The work is divided into two parts: complexes bearing a longer rigid linker similar to that of xanthene that will hold the Pt(N^C^N) units further apart in order to investigate intermolecular interactions in these complexes; and a flexible linker based on diphenylacetylene, forming 'foldamers'.

4.3.4.1 Long-distance linker

Synthesis

These compounds were synthesised in collaboration with Dr Amit Sil (Postdoctoral Researcher in the group). Inspiration was taken from examples of self-assembling molecules using **I13** as a scaffold.[137–139] Synthesis of the linker (**Scheme 4.11**) was carried out following reported literature procedures.[138]

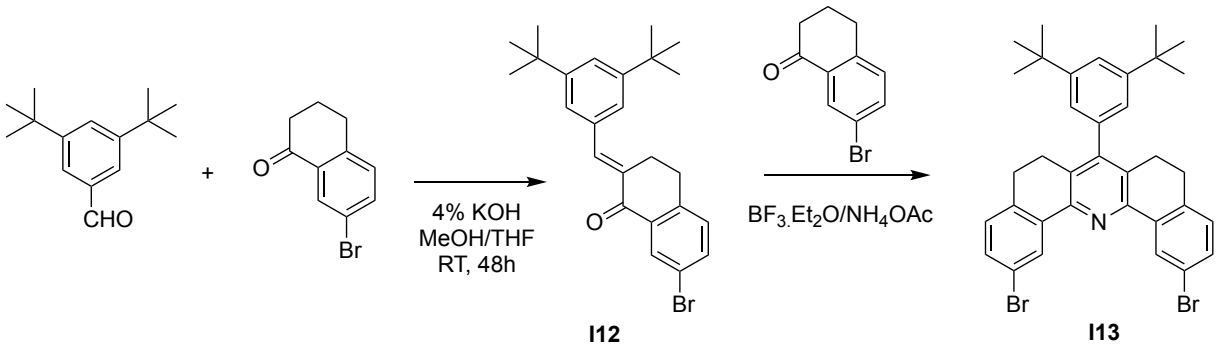

Scheme 4.11: *Synthesis of the long-distance linker I13.*

The proligands were then obtained by a Suzuki coupling between **I13** and the corresponding N^C^N-boronate ester (**Scheme 4.12**), the synthesis of which has been previously described and used for Class I sandwich compounds. Complexation was carried out by reacting the proligand with K_2PtCl_4 in acetic acid for approx. 1 week. Purification by column chromatography on silica in DCM/MeOH yielded the pure complexes shown in **Figure 4.50**. Complexation of H_2L[37] was not successful and

a mixture of products was isolated after the column. With more time this complex could potentially be isolated, however this was not possible within the time constraints of the project.

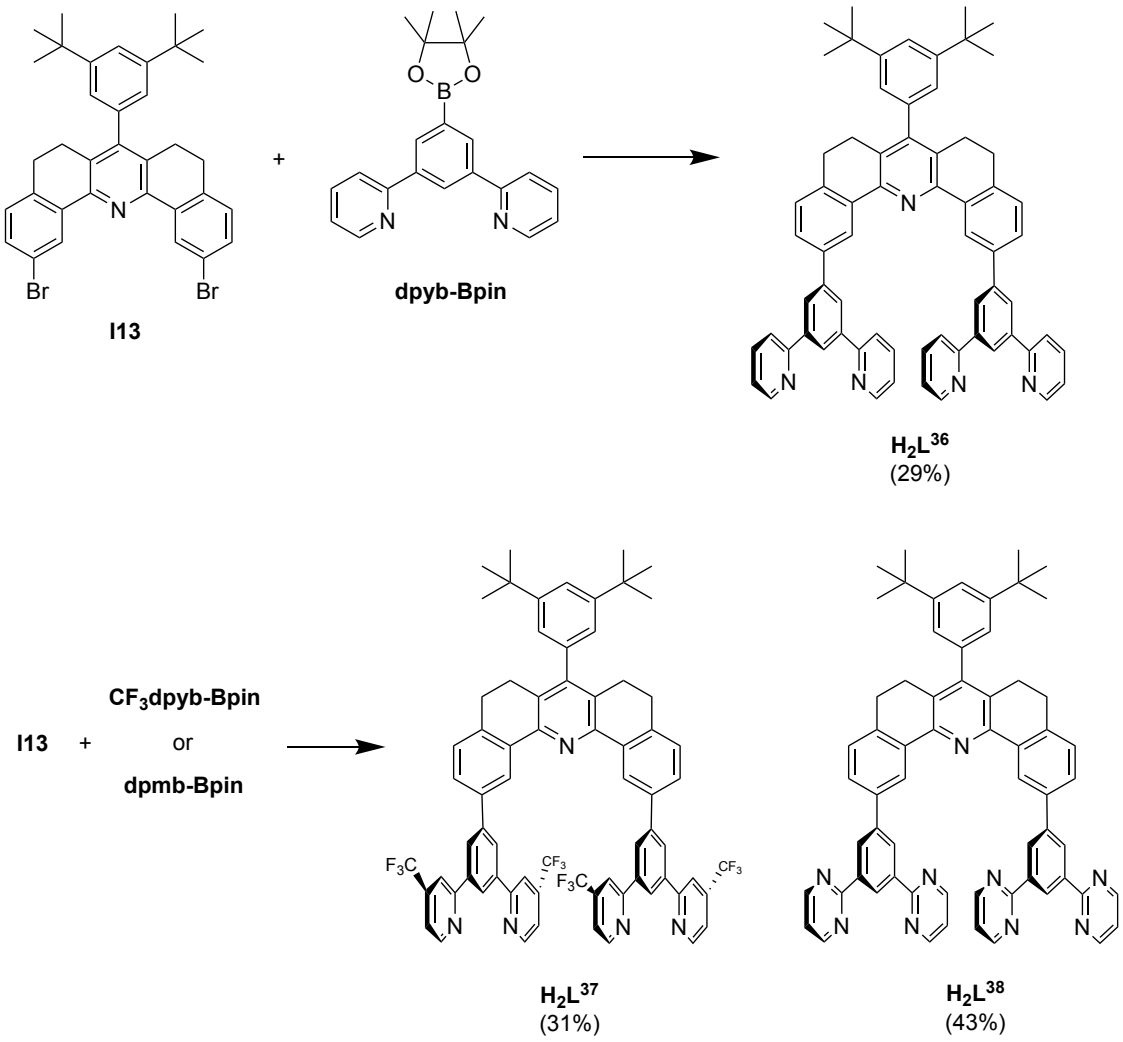

Scheme 4.12: *Synthesis of the proligands H_2L^{36-38}.*

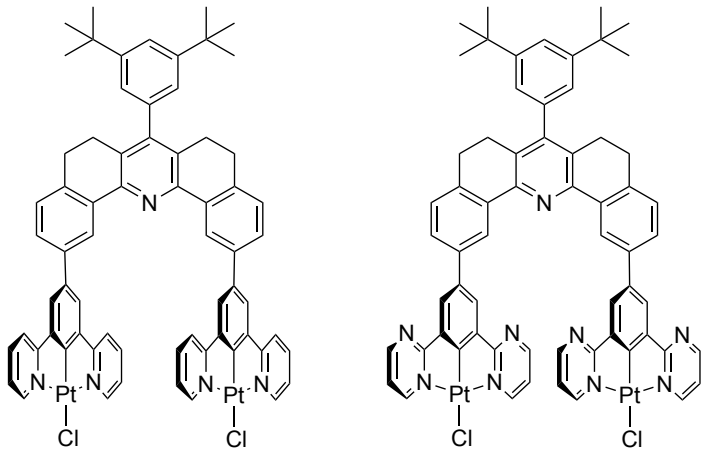

Figure 4.50: *Structures of complexes $L^n(PtCl)_2$ employing the long-distance linker.*

Crystal structure determination

Crystals of the linker ligand precursor **I11** suitable for X-ray diffraction were grown by slow evaporation from DMF. The molecular structure (**Figure 4.51**) reveals a distance of 7.3006(4) Å between the bromine atoms, which will be roughly the distance between Pt(N^C^N) units in the corresponding complexes. This linker was chosen as it should hold the Pt(N^C^N) units approx. 7 Å apart, twice the sum of the Van der Waals' radii of Pt, supporting the hypothesis that these complexes might form an interlocked zip-like structure (**Figure 4.52**). This will enable the study of intermolecular interactions in such complexes.

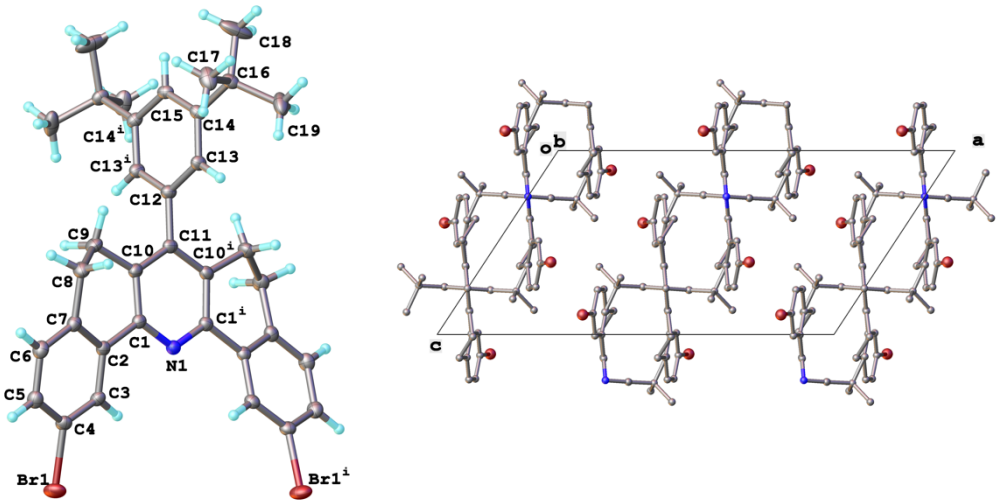

Figure 4.51: *Molecular and crystal structure of the long-distance linker precursor I11.*

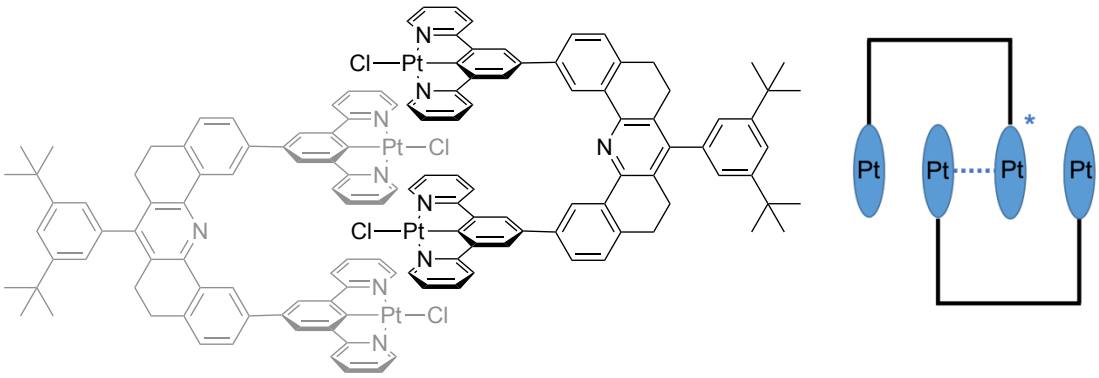

***Figure 4.52**: Proposed zip-like interactions that could occur in these linked Pt complexes.*

Photophysical properties

A summary of all photophysical properties can be found in **Table 4.3**. The absorption spectra of both complexes are similar, with the longest wavelength CT band being slightly red shifted for $L^{38}(PtCl)_2$ (**Figure 4.53**). This trend is emulated in the emission spectra in dilute DCM solution, where the monomeric emission is slightly red-shifted for $L^{38}(PtCl)_2$, as well as being less structured.

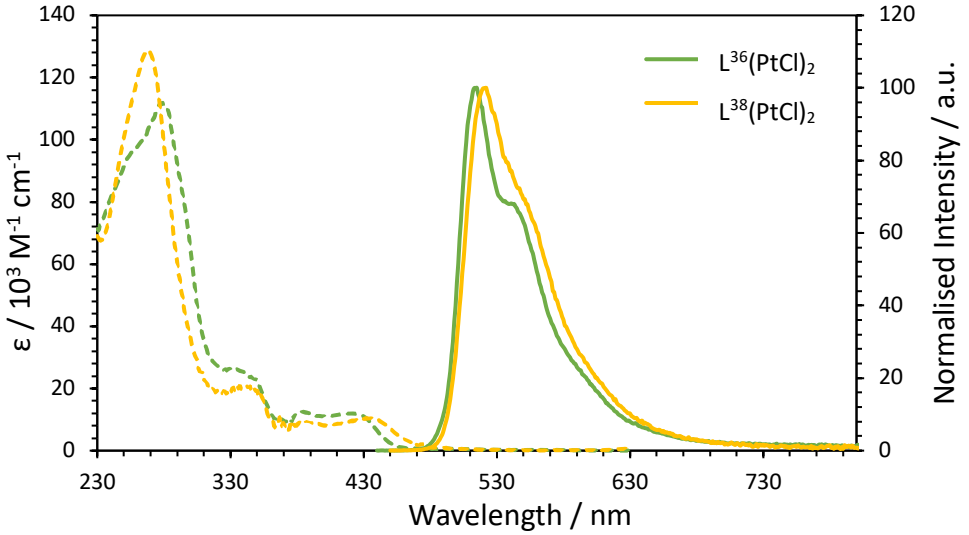

***Figure 4.53**: Absorption and emission spectra of $L^{36}(PtCl)_2$ and $L^{38}(PtCl)_2$ in dilute degassed DCM solution (5×10^{-6} M and 3×10^{-6} M respectively).*

Studying the emission of $L^{36}(PtCl)_2$ at elevated concentration reveals the appearance of a broad structureless red-shifted excimer band at 740 nm (**Figure 4.54**). The concentration dependence of this band, shown in the Stern-Volmer plot (**Figure**

4.55a), leads to an assignment of this emission to the presence of intermolecular excimers, as opposed to *intra*. Aggregation is also a viable explanation; there is potentially an additional long-wavelength absorption band observed for the most concentrated solution which would confirm aggregation (**Figure 4.55b**). Note the highest concentration studied was 8×10^{-5} M due to limited solubility of the complex.

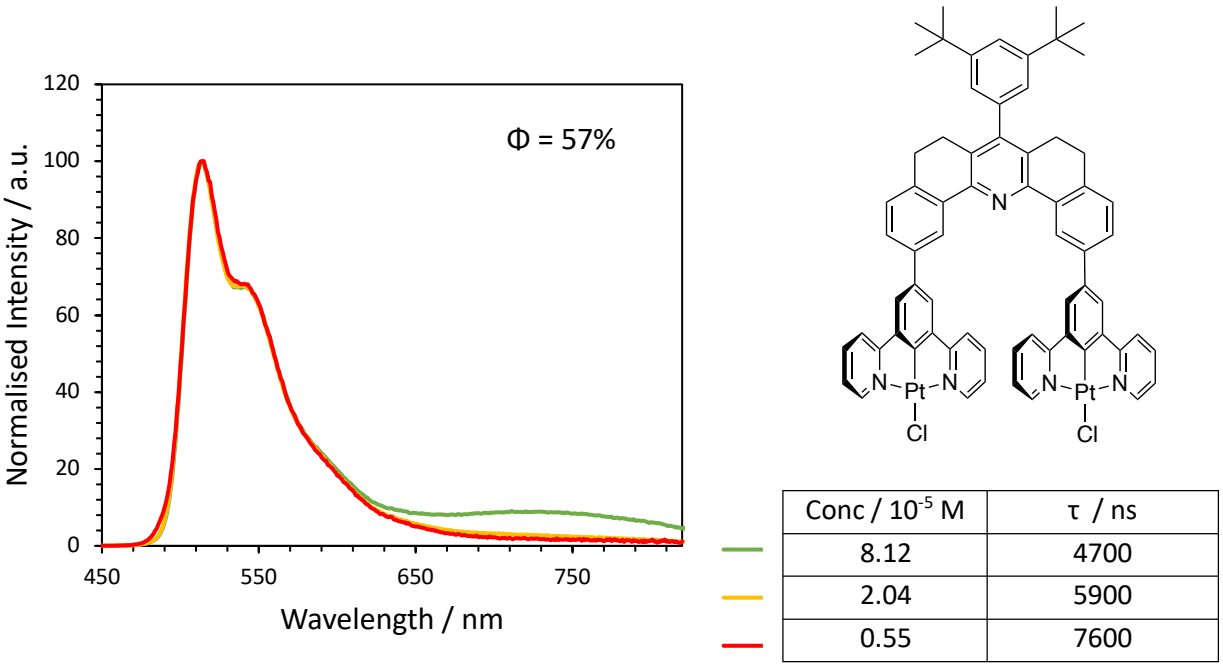

Conc / 10^{-5} M	τ / ns
8.12	4700
2.04	5900
0.55	7600

***Figure 4.54**: Concentration-dependent emission of $L^{36}(PtCl)_2$.*

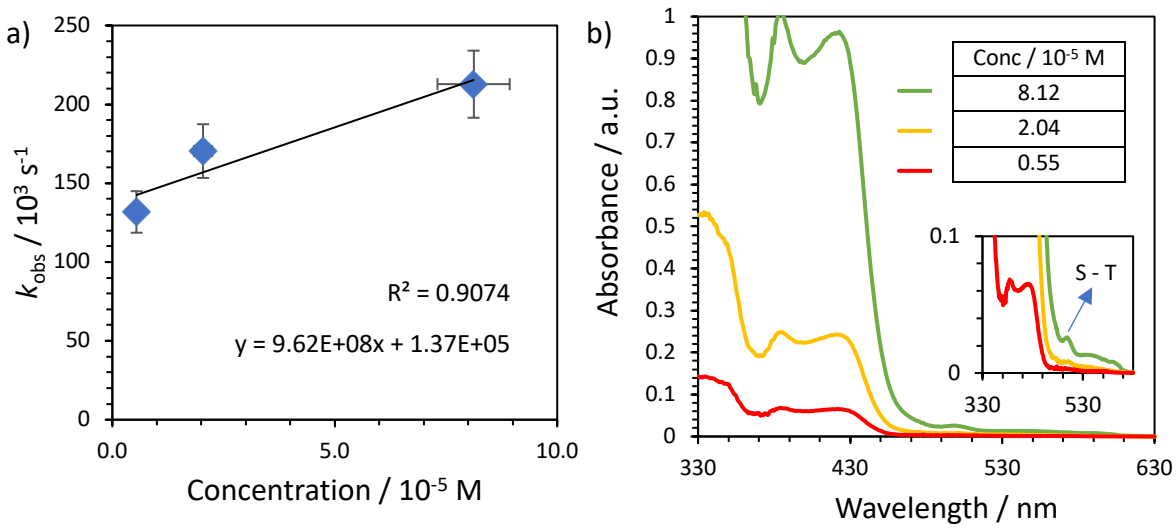

***Figure 4.55:** a) Stern-Volmer plot for $L^{36}(PtCl)_2$. Errors are discussed in Section 7.1; b) absorption spectra at various concentrations showing adherence to the Beer-Lambert Law, but with an additional low energy band appearing for the most concentrated solution (inset).*

The concentration-dependent emission of $L^{38}(PtCl)_2$ is shown in **Figure 4.56**. Excimer emission also appears for this complex at elevated concentrations, at a longer wavelength than the parent peaking at approx. 770 nm. This is surprising as the pyrimidine derivative of the Class I sandwich complexes, $L^{33}(PtCl)_2$, did not have a significantly red-shifted excimer when compared to the pyridine parent, $L^{31}(PtCl)_2$. This pyrimidine derivative $L^{38}(PtCl)_2$ also has a higher PLQY than the parent, at 0.77 compared to 0.57. Once again, due to the concentration dependence, this broad long-wavelength emission is attributed to either intermolecular excimers or aggregates (**Figure 4.57**). Inspection of the absorption spectra at various concentrations reveals the appearance of an additional long-wavelength band around 530 nm, suggesting this complex is indeed aggregating, and the additional band is likely MMLCT.

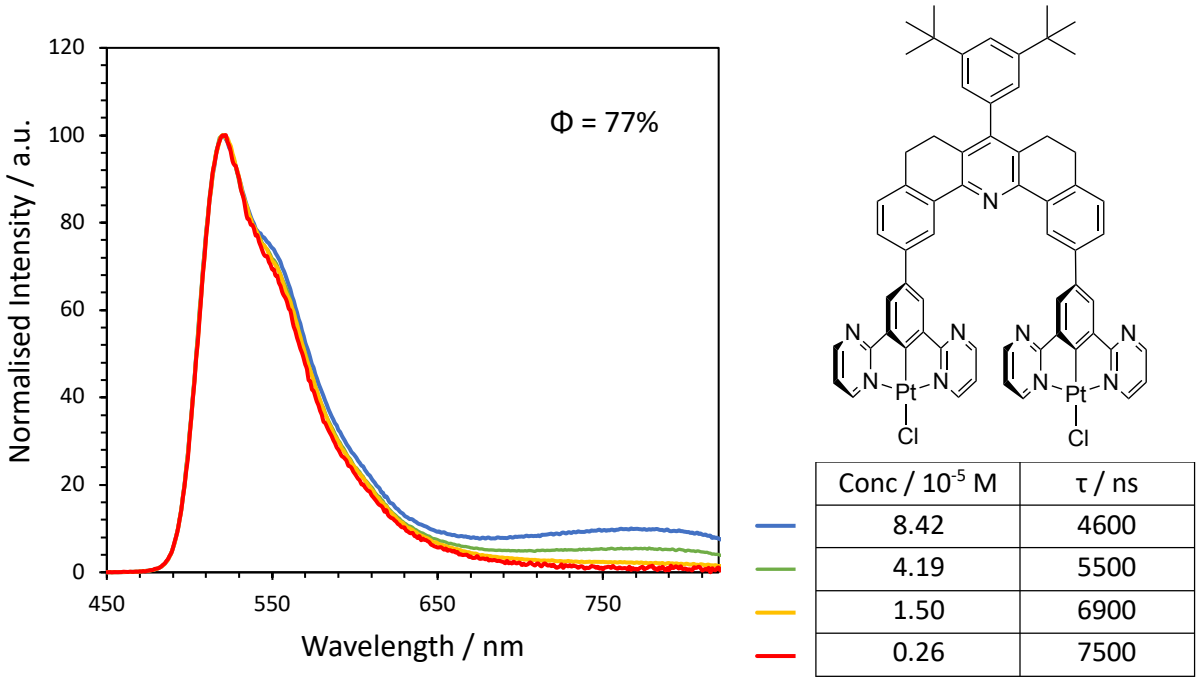

Conc / 10^{-5} M	τ / ns
8.42	4600
4.19	5500
1.50	6900
0.26	7500

Figure 4.56: *Concentration dependent emission of $L^{38}(PtCl)_2$ in degassed DCM solution at RT.*

These are only initial studies with just two complexes synthesised in the series, but we can already understand a lot from the collected data. The fact that the excimer band for each complex employing this 'long-distance' linker is significantly red-shifted compared to Pt(dpyb)Cl (50 nm for $L^{36}(PtCl)_2$ and 80 nm for $L^{38}(PtCl)_2$) supports the idea that a zip-like structure is being formed involving more Pt(N^C^N)

units in the interaction (i.e. not just dimers). This would explain the aggregation behaviour and the appearance of the MMLCT band. Mechanochromic properties have also been observed for $L^{38}(PtCl)_2$, which changes colour in the solid-state from dark green to orange when scraped with a spatula, and subsequently emits red light under long-wavelength UV light. This is evidence that suggests different types of interactions are present, though more work needs to be done in this area, especially looking at emission in the solid state.

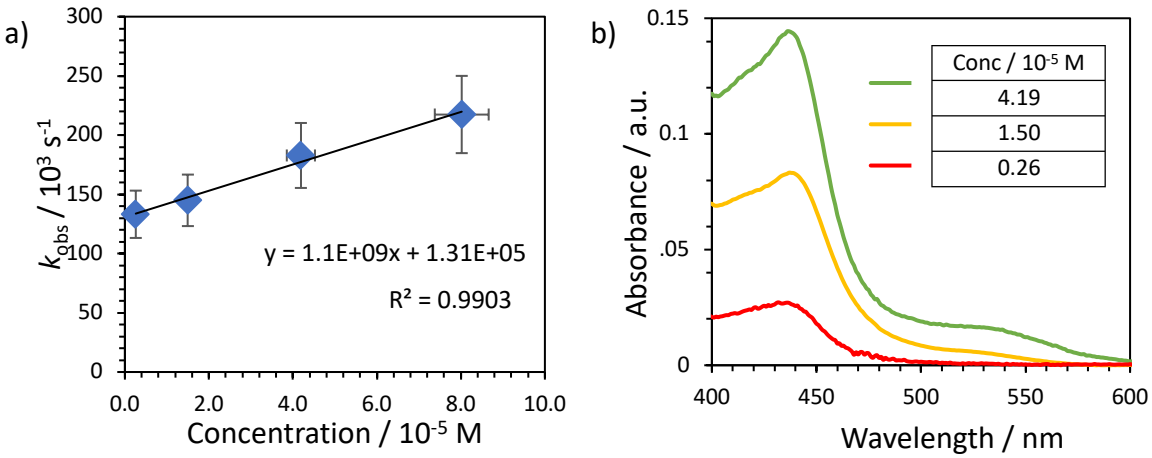

Figure 4.57: *a) Stern-Volmer plot for $L^{38}(PtCl)_2$. Errors are discussed in Section 7.1.; b) absorption spectra at various concentrations showing the appearance of an additional low energy band between 500 and 530 nm upon increasing the concentration.*

The low temperature emission spectra for $L^{36}(PtCl)_2$ and $L^{38}(PtCl)_2$ are shown in **Figure 4.58**. The bands are more vibronically resolved at 77 K as expected and show purely monomeric emission.

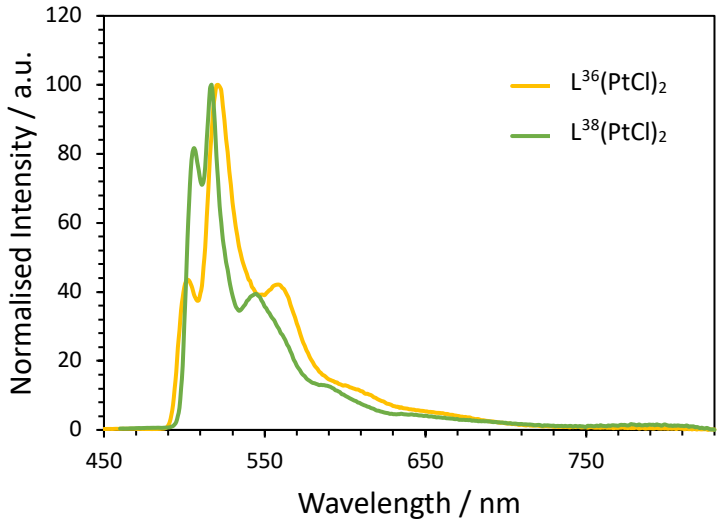

Figure 4.58: *77 K emission of $L^n(PtCl)_2$ in EPA glass.*

4.3.4.2 Foldamers

This section focuses on the synthesis and photophysical properties of 'foldamer' complexes, consisting of two Pt(N^C^N) units held together by a flexible diphenylacetylene linker that could enable intramolecular interfacial interactions between the Pt(N^C^N) units by rotation about the linker. An analogy can be drawn between the so-called 'foldamer' complexes presented here and the sandwich complexes presented earlier in the chapter, in the sense that two different class of complexes can be envisaged. Class I complexes here are where the N^C^N-coordinating ligand is linked to the diphenylacetylene flexible linker *via* the central phenyl ring of the N^C^N unit, and Class II is when the chloride in a Pt(N^C^N)Cl complex is replaced by an acetylene linker which forms a bridge to the diphenylacetylene flexible scaffold. In contrast to the sandwich complexes, this linker should allow flexibility so *intra*molecular interactions are possible but not forced.

Synthesis

The synthesis of the 'Class I' proligand H_2L^{39} was achieved by reacting dpyb-Bpin with I14 (synthesised by Dr Amit Sil following reported synthetic procedures[134,140]) using Suzuki cross-coupling conditions (**Scheme 4.13**). Complexation was carried out in degassed acetic acid with K_2PtCl_4 at reflux. A mixture of mono- and bis-substituted products were formed and separated by column chromatography on silica (DCM:

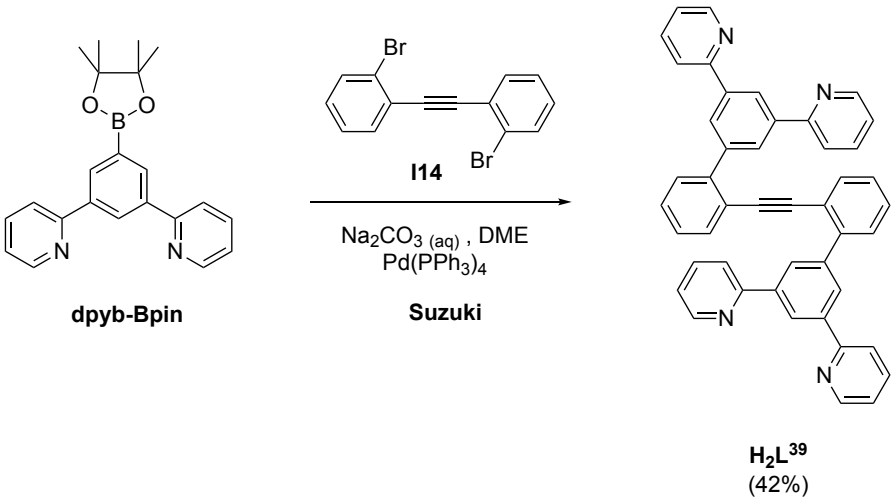

Scheme 4.13: *Synthesis of H_2L^{39}.*

MeOH), followed by recrystallisation of the desired dinuclear fraction to give $L^{39}(PtCl)_2$ (**Scheme 4.14**).

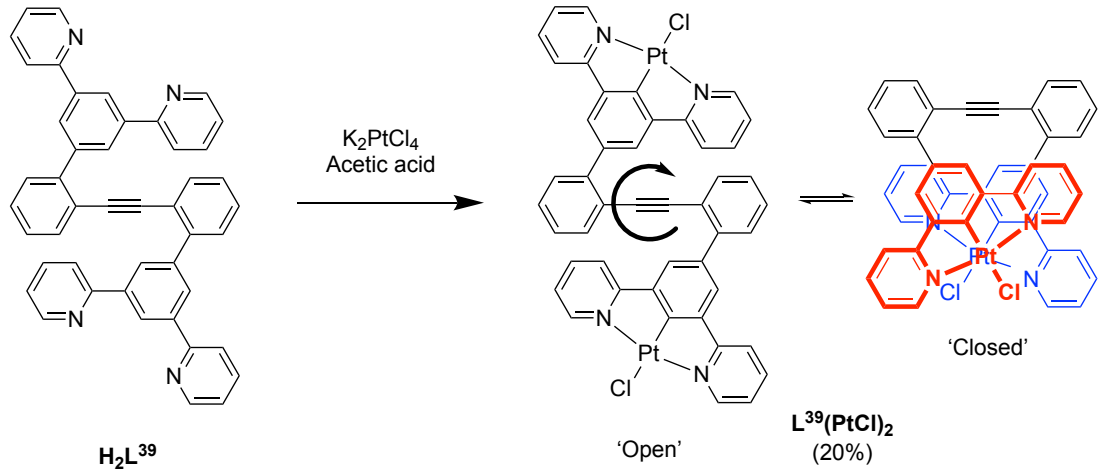

Scheme 4.14: *Synthesis of the Class I foldamer complex $L^{39}(PtCl)_2$ showing a schematic representation of the possible 'open' and 'closed' conformations of the complex interconverted by rotation about the diphenylacetylene linker. Pt(N^C^N) interactions could be anticipated in the 'closed' form.*

The Class II complex $L^{40}Pt_2L^1$ was synthesised by Dr Amit Sil following reported procedures[134,140] (**Scheme 4.15**). I purified the complex using a silica column with DCM as the eluent, and various recrystallisations, and collected the photophysical data.

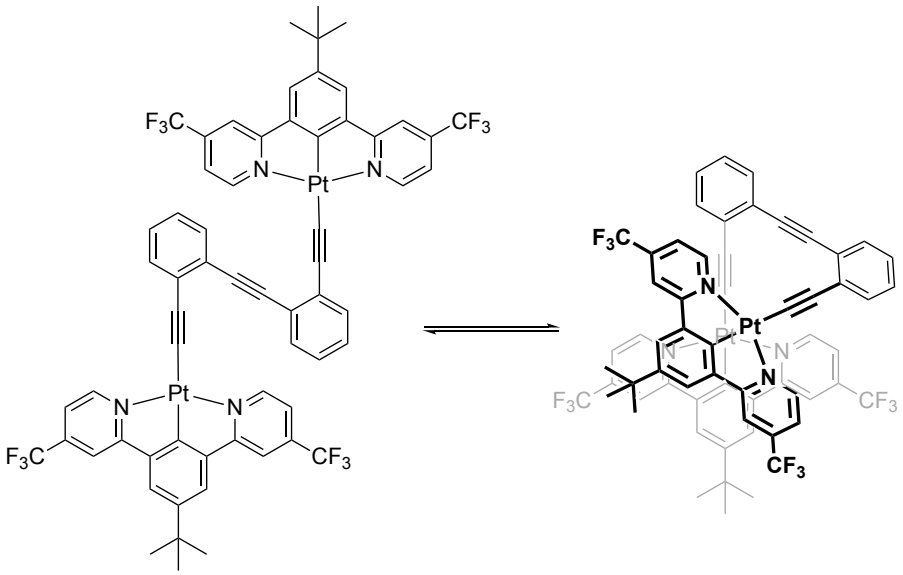

Scheme 4.15: *Possible 'open' and 'closed' conformations of $L^{40}Pt_2L^1$.*

Photophysical properties

The absorption spectrum of $L^{39}(PtCl)_2$ is presented in **Figure 4.59**, featuring only one main LC band at 280 nm and a CT band at 415 nm. The emission spectrum in degassed dilute DCM solution is dominated by broad structureless deep-red/NIR emission peaking at 679 nm. This emission is tentatively assigned to the presence of the 'closed' conformation of the complex in DCM solution, the relatively polar solvent likely enabling intramolecular interactions as seen for the molecular hinge complexes reported by Yam *et al.*[141] There is also a hint of some monomer-like species emitting below 500 nm, which has been present for all dinuclear complexes presented in this chapter that show primarily excimeric emission even in dilute solution. This was also seen for the flexibly linked complexes reported by Garoni *et al.* where even for complex **29** (**Figure 4.5**), for which the emission is dominated by the broad excimeric band, there is still a small contribution from monomeric emission.[132]

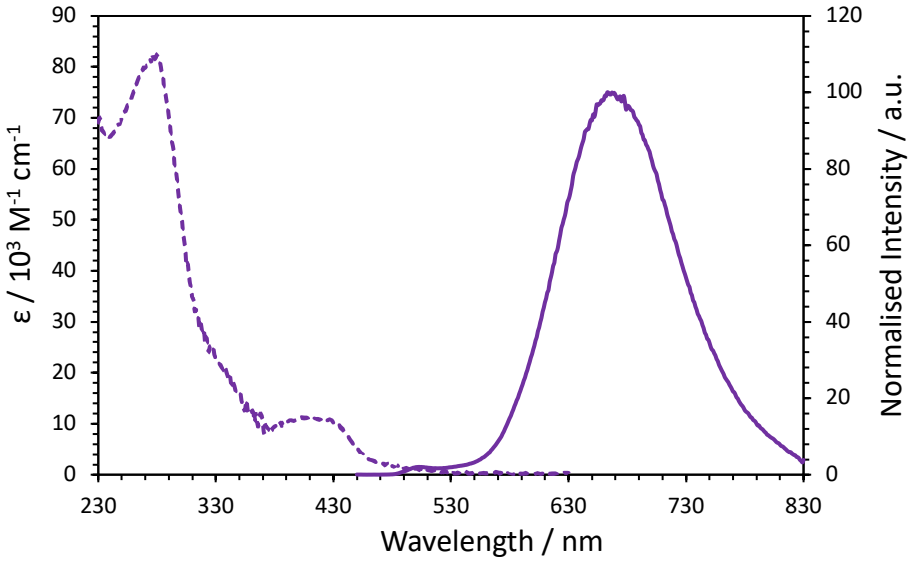

Figure 4.59: *Absorption and emission spectra of $L^{39}(PtCl)_2$ in degassed DCM solution (concentration = 2.25×10^{-6} M).*

The emission of this complex does not change with concentration (**Figure 4.60**), supporting the assignment to an intramolecular excimer due to the complex adopting the closed conformation. Inspection of the absorption spectra at increasing concentrations does not reveal the appearance of an additional band (except for the direct singlet to triplet absorption becoming more apparent) suggesting that no

aggregates are present. Moreover, the absorption spectrum matches the excitation spectrum of the long wavelength band (**Figure 4.61a**); this supports the assignment to an intramolecular excimer, or that the dimeric species is already predominant in solution at concentrations above 1 × 10^{-6} M, where absorption spectra can be recorded with confidence. There is, however, a Stern-Volmer correlation of the lifetime implying some concentration quenching (**Figure 4.61b**) with a self-quenching rate constant of 0.24 × 10^{9} M^{-1} s^{-1}.

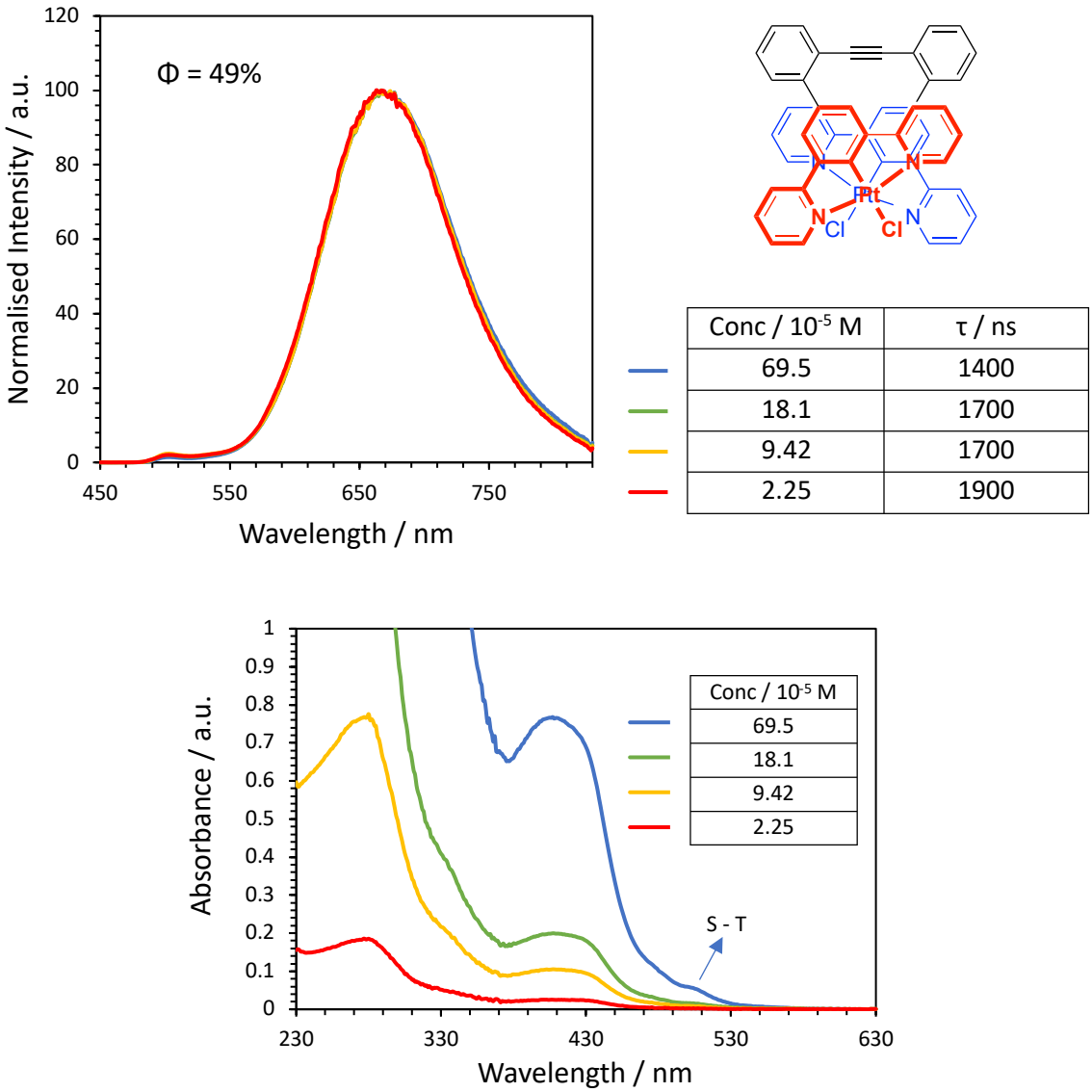

Figure 4.60: *Absorption and emission spectra of $L^{39}(PtCl)_2$ at various concentrations in degassed DCM solution.*

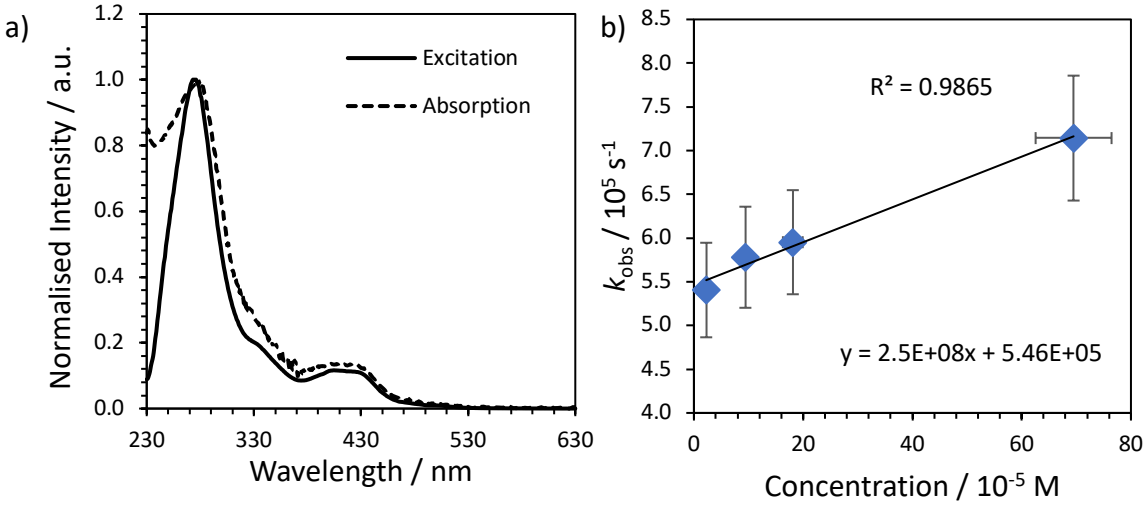

Figure 4.61: *a) Comparison of the absorption and excitation spectra (at 660 nm) of $L^{39}(PtCl)_2$ in DCM solution (2.25×10^{-5} M); b) Stern-Volmer plot for $L^{39}(PtCl)_2$. Errors are discussed in Section 7.1.*

Emission of $L^{39}(PtCl)_2$ at 77 K in EPA glass reveals some structured monomer bands between 450 and 550 nm, but a main contribution from a broad long-wavelength band (**Figure 4.62**). The presence of this band at 77 K could suggest aggregation is present, although for this complex, an 'intramolecular excimer' would indeed behave as an aggregate if the complex is already present in the closed form in the ground state. This suggests the preferential geometry of this complex is to form intramolecular interactions between the Pt(N^C^N) units and exist in the closed form.

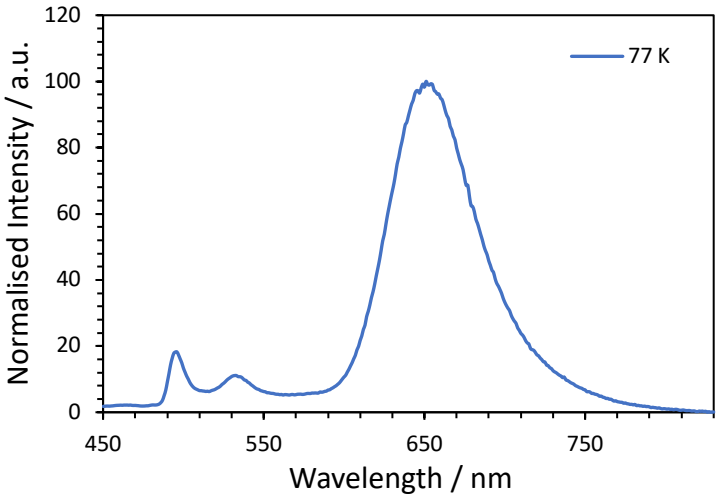

Figure 4.62: *Emission spectrum of $L^{39}(PtCl)_2$ at 77 K in EPA glass.*

The absorption and emission spectra of the Class II foldamer complex $L^{40}Pt_2L^1$ in dilute degassed DCM solution are shown in **Figure 4.63**. Comparing the absorption spectrum of $L^{40}Pt_2L^1$ with the Class I foldamer $L^{39}(PtCl)_2$ reveals absorption that spans further into the long wavelength region of the spectrum for the former. The extinction coefficients are also larger for $L^{40}Pt_2L^1$ indicating a larger oscillator strength for the $S_0 \rightarrow S_1$ transition compared to $L^{39}(PtCl)_2$.

The emission of $L^{40}Pt_2L^1$ has contributions from both a broad, long-wavelength, excimer-like band and from a more structured monomer-like band, assigned to an impurity of the monomolecular complex PtL^1Cl; the excitation spectrum at 535 nm perfectly matches the excitation spectrum of PtL^1Cl (**Figure 4.64**). This compound was found to degrade over time in solution. The impurity must only be small as the absorption spectrum of $L^{40}Pt_2L^1$ matches the excitation spectrum of the complex measured at 750 nm, although the monomolecular complex is so bright that it shows up intensely in the emission spectrum. For the purpose of this discussion, we will only consider the longer wavelength peak.

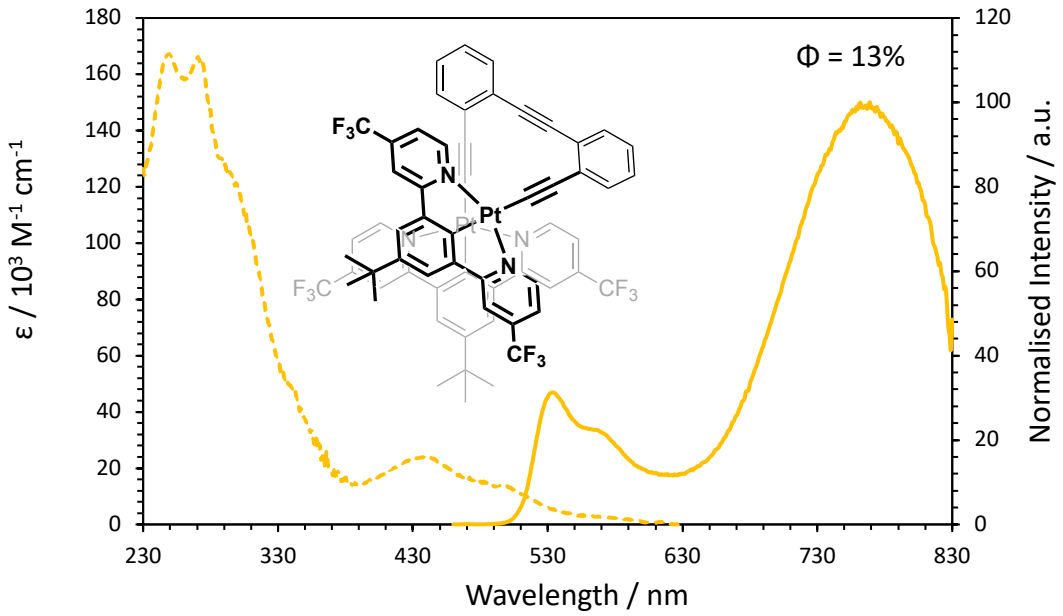

***Figure 4.63**: Absorption and emission spectrum of the Class II foldamer complex $L^{40}Pt_2L^1$ in degassed DCM solution (concentration = 1.34 × 10^{-6} M)*

Peaking at 766 nm, the excimeric emission for this complex is significantly red-shifted compared to the reported Pd(N^N^C) complexes using this diphenylacetylene scaffold, for which the lowest energy emission obtained in DCM was λ_{max} = 653 nm.[134] This highlights the effects of both changing the position of the cyclometallating ring and using Pt in place of Pd, which can reduce the HOMO-LUMO gap and lead to red-shifted emission. The electron-withdrawing trifluoromethyl-substituted pyridine rings are also likely playing a role in red shifting the excimer, as seen for mononuclear complexes in Chapter 2 and 3. However, the quantum yield of $L^{40}Pt_2L^1$ is reduced compared to $L^{39}(PtCl)_2$ (0.49 compared to 0.13), and others reported by Lin *et al.*, probably owing to the lower energy of the emission for the former. There exists an overlap between the absorption and emission spectrum of $L^{40}Pt_2L^1$ (**Figure 4.63**); the impurity emission peak at 510 nm overlaps with the MMLCT absorption, likely arising from 'aggregating' units (those existing in the closed form in the ground state). This suggests some re-absorption of the high energy emission will occur. The measured PLQY is an over-estimate of the true value for $L^{40}Pt_2L^1$ due to the PtL^1Cl impurity.

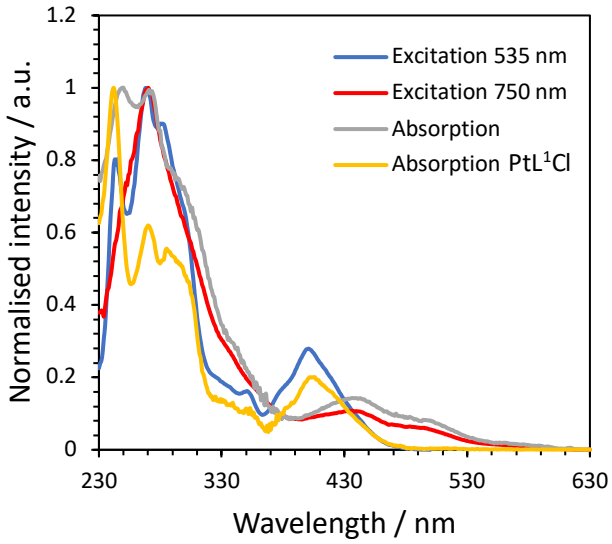

Figure 4.64: *Comparison of the absorption spectrum of $L^{40}Pt_2L^1$ with the absorption of monomolecular complex PtL^1Cl, and the excitation spectra for $L^{40}Pt_2L^1$ measured at 535 and 750 nm to probe the monomer- and excimer-like emission respectively.*

The emission spectrum of $L^{40}Pt_2L^1$ does not change with concentration, as expected for a complex that forms intramolecular excimers. The lifetime of the excimeric band

also does not change with concentration within error (τ = 700 ns). $L^{40}Pt_2L^1$ obeys the Beer-Lambert law, with no additional peaks appearing in the absorption spectrum over the concentration range investigated (**Figure 4.65**). This confirms the assignment to an 'intramolecular excimer' that behaves as an aggregate at all concentrations, as the complex is already present in the 'closed' conformation in the ground state.

This work proves the superiority of the Class I versions of dinuclear complexes for this diphenylacetylene linker with respect to complex stability, despite the red-shifted emission achieved for the Class II complex. The acetylene-linker has proven unstable as a co-ligand for this particular complex and may limit the potential applications of these complexes. No report was made towards the stability of the dinuclear Pd complexes reported with the diphenylacetylene linker,[134] perhaps due to the N^N^C linkage as opposed to N^C^N; the strong ligand field of the cyclometallating C can destabilise a strong σ-donating acetylide linker in the para position for N^C^N-linked complexes. Having said that, the acetylide linked 'molecular hinge' reported by Ai *et al.* with Pt(N^C^N) units (**Figure 4.8**) showed no signs of decomposition from what they reported suggesting stable complexes of this type are possible, albeit with syntheses requiring challenging purification steps.

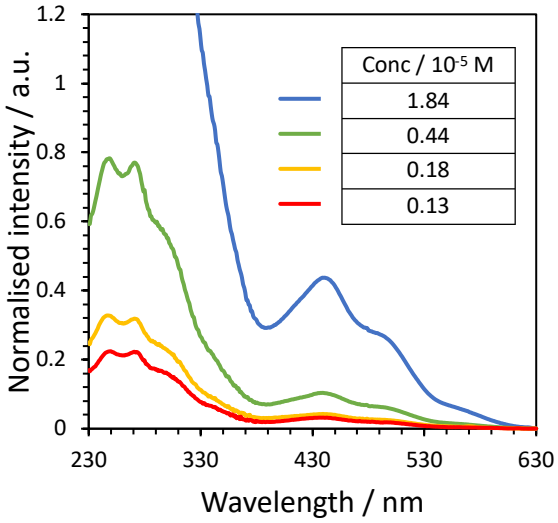

Figure 4.65: *a) Concentration dependent absorption of $L^{40}Pt_2L^1$ in DCM solution; b) Stern-Volmer plot for $L^{40}Pt_2L^1$, for lifetimes observed at 750 nm to probe the excimer.*

Table 4.3: *A summary of the photophysical parameters for complexes employing the long-distance linker, $L^{36}(PtCl)_2$ and $L^{38}(PtCl)_2$, and the foldamer complexes, $L^{39}(PtCl)_2$ and $L^{40}Pt_2L^1$, in dilute degassed (aerated in parentheses) DCM solution at 298 K.*

Complex	λ_{abs} / nm (ε / M^{-1} cm^{-1})	λ_{em} / nm (monomer)	λ_{em} / nm (excimer)	Φ_{lum} [aer]	τ / ns *excimer [aer]	τ_0 / μs	k_r / 10^3 s^{-1}	$\sum k_{nr}$ / 10^3 s^{-1}	k_{SQ} / 10^9 M^{-1} s^{-1}	$k_Q(O_2)$ / 10^8 M^{-1} s^{-1}
$L^{36}(PtCl)_2$	259 (104000), 281 (122000), 336 (27300), 384 (12400), 420 (11800)	515, 543	736	0.57 [0.04]	7600	7.3	76	56	0.96	10.9
$L^{38}(PtCl)_2$	270 (142000), 339sh (21900), 347 (21400), 390 (8700), 420sh (8670), 435 (9530)	522, 547sh	775	0.77 [0.02]	7500	7.6	102	31	1.11	11.0
$L^{39}(PtCl)_2$	267 (97000), 282sh (92200), 395 (14900), 425 (10400)	-	668	0.49 [0.04]	1800*	1.8	263	277	0.24	24.3
$L^{40}Pt_2L^1$	250 (168000), 273 (165000), 299sh (123000), 495 (13700), 440 (23700)	-	767	0.13 [0.06]	700*	-	22	141	-	5.5

4.4 Chapter 4 summary

Various novel dinuclear complexes have been synthesised and their photophysical properties studied. Class I sandwich complexes utilising a rigid xanthene scaffold, where the xanthene linker is connected *via* the central phenyl ring of the N^C^N-coordinating ligand, display mainly broad long-wavelength excimeric emission, with quantum yields ranging from 0.11 to 0.61 ($L^{32}(PtI)_2$ had a particularly low PLQY of 0.01). The emission is likely arising from intramolecular interactions, as their mononuclear analogues displayed purely monomer-like emission. $L^{32}(PtCl)_2$, where the pyridine ring is substituted with CF_3 groups at the 4-position, showed contribution from both a monomolecular and bimolecular species to the PL. Substituting the chloro ancillary ligand for isothiocyanate led to purely excimeric emission, blue-shifted in comparison to the parent chloro-complex (λ_{max} = 714 nm compared to 766 nm) as seen for thiocyanate complexes presented in Chapters 2 and 3. The opposite was seen when the ancillary chloro ligand was replaced by iodo, leading to purely monomeric emission for $L^{32}(PtI)_2$. The ancillary ligand clearly plays a role in governing excimer interactions.

Interlocked complexes featuring two xanthene units were synthesised to give three novel complexes $L^{31}Pt_2L^{35}$, $L^{32}Pt_2L^{35}$, and $L^{33}Pt_2L^{35}$, where the N^C^N ligand consists of unsubstituted pyridine rings, 4-CF_3 substituted pyridine, and pyrimidine rings respectively. Purely deep red/NIR excimeric emission was observed for all with λ_{max} red-shifted in the order $L^{31}Pt_2L^{35}$ < $L^{33}Pt_2L^{35}$ < $L^{32}Pt_2L^{35}$, following the same trends observed in previous chapters where pyridines substituted with CF_3 groups in the 4-position lead to significantly red-shifted excimeric emission. Even $L^{32}Pt_2L^{35}$ exhibited purely excimeric emission that was independent of concentration (unlike the Class I parent $L^{32}(PtCl)_2$), indicating that interlocking the molecule favours intramolecular interactions. PLQYs for these novel interlocked structures ranged from 0.09 to 0.29.

Dinuclear complexes fixed onto a rigid linker that holds the Pt(N^C^N) units approx. 7 Å apart were studied and compared to the xanthene analogues. These complexes

were designed in order to study *inter*molecular interactions, as interactions to form a zip-like structure could be anticipated, whereas the two Pt(N^C^N) units are held too far apart to expect *intra*molecular interactions. These complexes displayed simply monomeric emission (PLQYs of 0.57 and 0.77) with some appearance of an excimeric band at elevated concentration in DCM solution. This concentration-dependent emission led to the assignment of intermolecular excimers. It is postulated that these complexes are forming zip-like structures potentially involving more than two Pt(N^C^N) units, hence very red-shifted excimeric emission was observed, up to λ_{max} = 780 nm, compared to the analogous Class I xanthene compounds. It would be interesting to study the emission of these complexes in the solid-state to see if purely long-wavelength emission can be achieved.

Finally, 'foldamer' complexes utilising diphenylacetylene as a flexible linker were synthesised and their photophysical properties studied. This linker enables intramolecular interfacial interactions leading to concentration-independent broad long-wavelength emission, with a PLQY of 0.49 and a λ_{max} = 679 nm for the parent Class I compound $L^{39}(PtCl)_2$, where the Pt(N^C^N) units are connected to the linker *via* the central phenyl ring. This suggests the complexes exist in the 'closed form' in DCM solution, where the Pt(N^C^N) units are interacting. A Class II complex $L^{40}Pt_2L^1$, where the Pt units are connected to the diphenylacetylene unit *via* an acetylene co-ligand, exhibited the same concentration-independent emission with a λ_{max} = 766 nm, but with some monomeric contribution from an impurity of the monomolecular species PtL^1Cl due to degradation of this complex in solution. Future work should involve carrying out photophysical analysis of these compounds in various polar and non-polar solvents to see if the closed form and the open form can be isolated, as well as discovering a method to interchange between the two.

Overall, these dinuclear complexes have been synthesised to display intra- and/or intermolecular excimeric emission. The mechanism of emission suggests these excimers, even if intramolecular in nature, still require some energy/motion of the units relative to one another to form as, more often than not, the 77 K and solid-state emission spectra reveal purely monomeric emission. This is likely the reason

why trace amounts of monomer-like lower energy emission can be seen for some complexes. These novel compounds reported have helped to address questions regarding the mode of emission and interactions present in these molecules (i.e. inter- or intramolecular excimers, or ground state interactions), and complexes displaying purely deep red/NIR emission have been prepared.

Chapter 5

5. Dinuclear Pt(II) complexes featuring ditopic bis-bidentate linkers

5.1 Introduction

Numerous cyclometallated platinum(II) complexes featuring N^C aromatic chelate derivatives, such as 2-phenylpyridine (ppy) and 2-thienylpyridine (thpy), have been reported in the literature. These complexes can be categorised as follows: homoleptic complexes $Pt(N^C)_2$ where the two bidentate ligands are the same, heteroleptic complexes Pt(N^C)(N^C') where the bidentate ligands are different, and complexes with a single N^C unit and a non-cyclometallating ancillary ligand (LX) to complete the coordination sphere, Pt(N^C)(LX), as well as $Pt(N^C)(L^L)^+$ though we will focus here on only charge-neutral complexes.

5.1.1 Homoleptic $Pt(N^C)_2$ complexes

The homoleptic bis-cyclometallated complex featuring 2-phenylpyridine ligands, $Pt(N^C\text{-}ppy)_2$ (**Figure 5.1**), was first synthesised in 1984 by Von-Zelewsky and co-workers, closely followed by analogues with 2-thienyl-pyridine, $Pt(N^C\text{-}thpy)_2$, and derivatives.[142,143] It is the *cis* isomer that forms preferentially due to the trans effect of the cyclometallating carbon. $Pt(N^C\text{-}ppy)_2$ (**30**) is non-emissive due to efficient d-d deactivation, whereas the energy gap between the emissive state and the higher energy d-d state in $Pt(N^C\text{-}thpy)_2$ (**31**) is of the order of 3700 cm^{-1}, sufficient to rule out deactivation of the thiolate d-d state at room temperature.[144] Despite having an

impressive quantum yield of 0.35 in degassed solution,[145,146] Pt(N^C-thpy)$_2$ is not suitable for use in OLEDs due to its thermal instability, meaning it is not amenable to the thermal decomposition methods of OLED fabrication. However, by spin-casting the emitting layer from a solution containing TPD (*N,N'*-bis(3-tolyl)-1,1'-biphenyl-4,4'-diamine) as the host matrix and the Pt complex as the guest, devices have been fabricated successfully with an EL efficiency of 11.5%, as the TPD host is an excellent sensitiser of the Pt complex.[145,146]

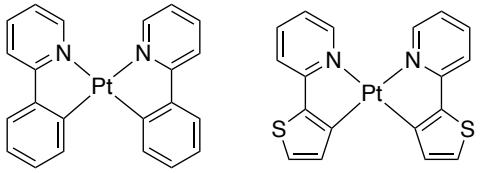

30 Pt(N^C-ppy)$_2$ **31** Pt(N^C-thpy)$_2$

Figure 5.1: *Structure of homoleptic bidentate complexes. Note the cis geometry due to the trans effect of the cyclometallated carbon.*

5.1.2 Heteroleptic complexes

The introduction of one cyclometallating N^C unit to form heteroleptic complexes can be readily achieved upon reaction of the corresponding HN^C proligand with K_2PtCl_4, proceeding through a chloro-bridged dimer (**Equation 5.1**). These dimers can be cleaved under mild conditions by N^N-coordinating diamine or diimines, such as 1,2-diaminoethane (en) or 2,2'-bipyridine (bpy) respectively, to give $[Pt(N^C)(N^N)]^+$ complexes,[147] although emission from such complexes usually originates from excited states with largely diimine character rather than involving the cyclometallated ligand. Heteroleptic (N^C)Pt(LX) complexes are formed by cleavage of the chloro-bridged dimer with bidentate anionic ligands LX such as β-diketonates (O^O) (**Equation 5.2**) - for example acetylacetonate (acac) - and can offer several advantages over bis N^C-derivatives.

$$K_2PtCl_4 + N^CH \rightarrow (N^C)Pt(\mu\text{-}Cl)_2Pt(N^C) \qquad (5.1)$$

$$(N^C)Pt(\mu\text{-}Cl)_2Pt(N^C) + 2(\beta\text{-diketone}) \xrightarrow{Na_2CO_3} (N^C)Pt(O^O) \qquad (5.2)$$

The complexes (N^C-ppy)Pt(O^O) and (N^C-thpy)Pt(O^O) have comparable emission wavelengths, efficiencies, and lifetimes to the analogous $(N^C)Pt(en)^+$ complexes, though with the added benefit of charge neutrality making them amenable to OLED processing procedures. Pt(thpy)(acac) (**32**) is an orange emitter (**Table 5.1**), whilst Pt(ppy)(acac) (**33**) emits in the green region of the spectrum (**Figure 5.2**). The more electron-rich nature of the thiophene ring compared to benzene red shifts the emission of thienylpyridine complexes compared to those of ppy. Incorporating a thiophene ring serves to raise the energy of the HOMO, consequently lowering the HOMO-LUMO gap and achieving a red-shift in the emission.

Table 5.1: *Photophysical properties of **32** and **33**. References: a) Thompson et al.[34], and b) Kozhevnikov et al.[2]*

Complex	Solvent	λ_{max} / nm	τ / μs	Φ
32: Pt(thpy)(acac)	2-methyltetrahydrofuran	575	4.5	0.11[a]
	DCM	554	21	0.36[b]
33: Pt(ppy)(acac)	2-methyltetrahydrofuran	486	2.6	0.15[a]

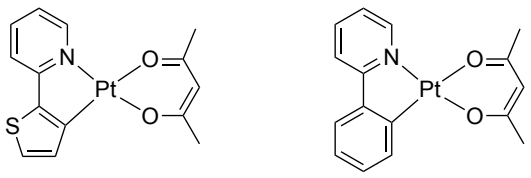

32 **33**

Figure 5.2: *Structure of Pt(thpy)(acac) (**32**) and Pt(ppy)(acac) (**33**).*

The nature of the ancillary ligand can affect the nature of the lowest emitting excited state by varying the electron-donating or -withdrawing character of the LX ligand to increase or decrease the electron density at the metal centre. This in turn will alter the proportion of MLCT character mixed into the lowest energy transition, thus changing both the colour of emission and radiative lifetime of the excited state. A study by Thompson *et al.* demonstrated this by systematically changing substituent

groups on the N^C ligand of (N^C)Pt(O^O) complexes, where O^O represents acac or the *t*-butyl substituted analogue dipivaloylmethane (dpm), chosen to improve the solubility of such complexes.[34]

All of the complexes studied in that work are intensely luminescent in glass at 77 K with PLQYs as high as 0.25, but only some are emissive in solution at RT. Emission was assigned to states of mixed MLCT/LC character ($d_{Pt}/\pi_{N^C} \rightarrow \pi^*_{N^C}$) based on electrochemical measurements and DFT studies, which showed that the HOMO in these complexes resides mainly on the Pt and ligand orbitals with the LUMO largely localised on the N^C ligand. This can be used to rationalise the observed trends in emission energies, following the general colour-tuning principles referred to throughout this thesis for cyclometallated Pt(II) complexes. Incorporating an electronegative fluorine substituent onto the 4' and 6' positions (**35**) of the phenyl ring of (ppy)Pt(dpm) (**36**) leads to a blue shift of the emission (**Figure 5.3**), by stabilisation of the HOMO. Adding an electron-donating dimethylamino group to the 4-position of the pyridyl ring (**34**) led to a further blue shift in the emission by raising the energy of the LUMO.

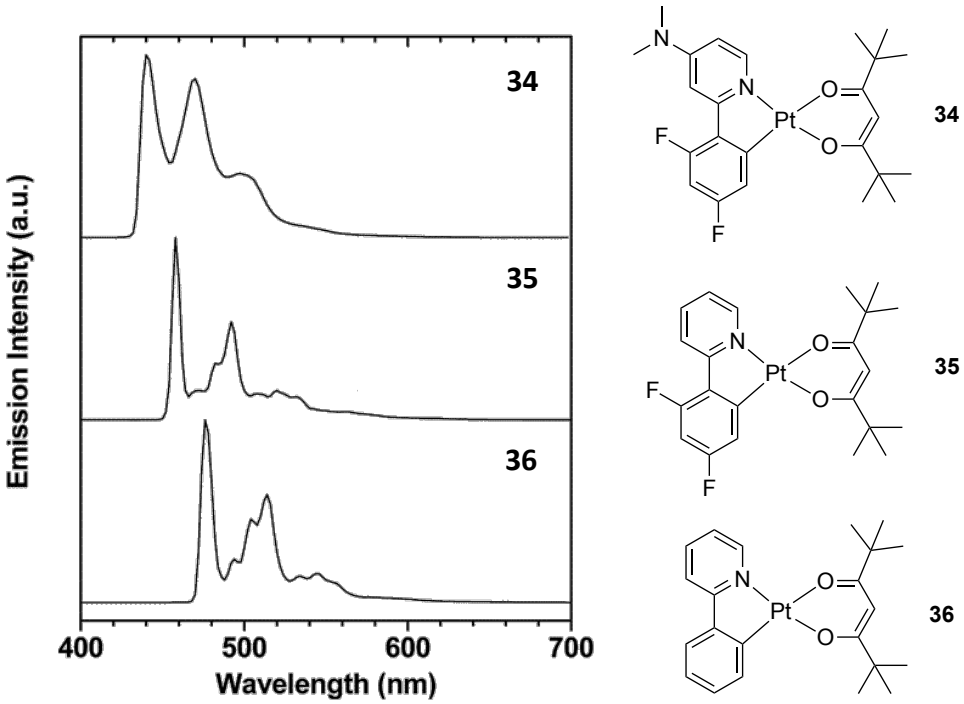

Figure 5.3: *Bidentate (N^C)Pt(O^O) complexes reported by Thompson et al. showing blue-shifted emission from bottom to top upon substitution of F groups into the phenyl ring and/or NMe_2 to the pyridyl ring.*[34]

A red shift in the emission was achieved through the incorporation of more electron-rich 5-membered thiophene and pyrrole rings into the systems, giving complexes **37** and **38** respectively (**Figure 5.4**). They display orange-red emission with λ_{max} up to 600 nm. Similarly, increasing the conjugation of the π system of N^C ligands lowered the energy of the ^{3}LC transition in the resulting complexes by simultaneously raising the HOMO and lowering the LUMO energy, in comparison to 2-phenylpyridine. Nonetheless, a study by Kozhevnikov *et al.* showed that increasing the conjugation in Pt(thpy)(acac), by conjugating extra thiophene rings onto the cyclometallated thiophene to form (oligothienyl)pyridines, is not an adequate design strategy to achieve NIR emission; increasing the conjugation decreases the contribution of the metal d orbitals to the HOMO, and therefore the influence of SOC from the metal in promoting both ISC and triplet radiative decay. In some cases, dual fluorescence was observed for their complexes with extended conjugation, with a decreasing intensity of phosphorescence due to the combined effects of a lower yield of triplet formation, a decreased $T_1 \rightarrow S_0$ radiative decay rate, and increased nonradiative decay, as predicted by the energy gap law.[2] This problem was side-stepped in follow-up studies by introducing a second Pt(II) ion,[148,149] a strategy that will be discussed in the section below.

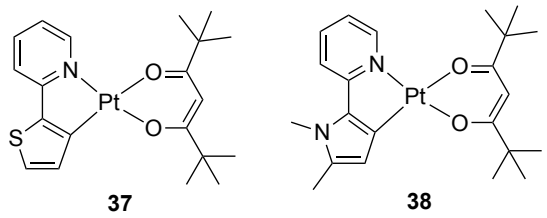

Figure 5.4: *Red/orange-emitting (N^C)Pt(O^O) complexes reported by Thompson et al.*

Yagi *et al.* carried out a photokinetic study on the excimer phosphorescence of Pt(N^C)(acac) complexes, based on 5'-benzoylated ppy (**Figure 5.5**).[150] The monomer emission for **39** in DCM solution is blue-green with λ = 479 and 513 nm, and slightly blue-shifted by 5 nm for the benzoyl substituted complex **40**. PMMA-doped films of the complexes were fabricated and studied. As the doping concentration increased for **39** from 3 to 10 wt%, a new emission band around 600 nm appeared which was not present for analogous complexes without the benzoyl substituent. This long-

wavelength band was assigned to excimer emission as the spectral shape of the absorption spectrum was the same regardless of doping concentration. Moreover, the excitation spectrum of both the monomer and excimer bands were identical, indicating that the species contributing to the broad long-wavelength emission is not present in the ground state, i.e., an excimer. The PLQY of the PMMA-doped films was relatively high for each complex regardless of doping level, ranging from 0.40 to 0.62, and despite the excimer formation which is usually associated with concentration quenching. It is well known that the ^{3}MC states of bidentate (N^C)Pt(O^O)-type complexes adopt highly distorted structures, and thus non-radiative decay is facilitated through the ^{3}MC state. On the other hand, non-radiative decay through structural relaxation should be suppressed in rigid media and is likely the reason why **39** and **40** are highly emissive in PMMA film. Complex **41** in particular formed radiative excimers with high efficiency, with a PLQY of 0.53 at a doping level of 3 wt%, where the relative intensity of the excimer emission was more than three times that of the monomer emission. For this reason, the group fabricated OLEDs doped with this complex to obtain white light, showing a maximum luminance of 11500 cd m^{-2} and a maximum current efficiency of 16.0 cd A^{-1}.

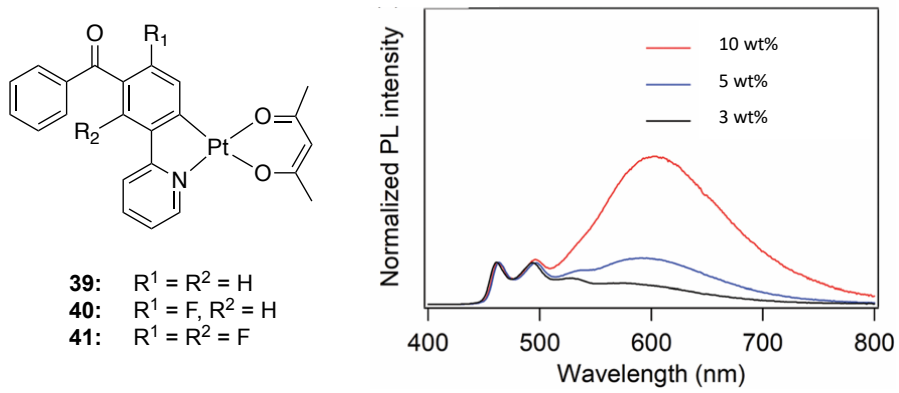

Figure 5.5: *Structure of benzoyl-substituted complexes reported by Yagi et al. and the emission spectrum of PMMA-doped films of complex **41** under an atmosphere of nitrogen, demonstrating excimer formation with increasing doping level.*

5.1.3 Multinuclear Pt(II) complexes featuring bidentate-coordinating ligands

It has already been discussed how the incorporation of a second Pt(II) atom into a complex can shift the emission towards the NIR region of the spectrum, whilst simultaneously diminishing the effect of the energy-gap law (see Section 4.1.1). Kozhevnikov *et al.* presented a dinuclear cyclometallated complex (**41**) with a ditopic, bis-bidentate 4,6-bis(2-thienyl)pyrimidine derivative as a bridging ligand (**Figure 5.6**), with acac completing the coordination sphere, that emits very brightly in the red region of the spectrum (λ_{max} = 610 nm, Φ = 0.85 and τ = 12 μs, in degassed DCM solution at RT), with the emission tailing into the NIR.[148] A striking result is the unusually high intensity of the lowest energy absorption band at 500 nm for **41**, with an extinction coefficient exceeding 50 000 M^{-1} cm^{-1}. This even exceeds in intensity all the bands in the UV region, which are usually significantly more intense than those in the visible region. The band is assigned to a mixed MLCT/LC state.

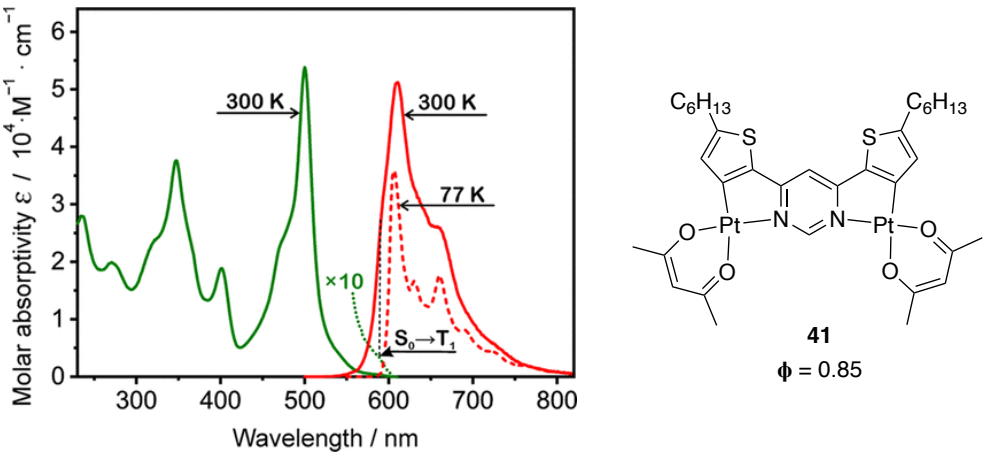

Figure 5.6: *Absorption spectrum of **41** in DCM at 300 K (solid green line), with an expansion of the low-energy region highlighting the spin-forbidden $S_0 \rightarrow T_1$ transition (dotted green line); emission spectra of the complex under the same conditions (solid red line) and at 77 K (dashed red line). Figure taken from reference 148.*

Additionally, for **41**, $k_r = 7.1 \times 10^4$ s^{-1}, a value that is over 4× that of the corresponding mononuclear complex Pt(thpy)(acac) (**32**), as well as $\Sigma k_{nr} = 1.3 \times 10^4$ s^{-1} being half of that of **32**, despite the emissive state of the former being significantly lower in energy

by around 1700 cm^{-1}; the dinuclear design clearly rigidifies the structure, suppressing non-radiative decay pathways. SOC clearly remains high for **41** since there is no ligand fluorescence and k_r of phosphorescence is very high. This suggests that the presence of the second metal centre allows the T_1 state to couple effectively with higher-lying states of the singlet manifold *via* SOC, which in turn have high oscillator strengths, promoting emission. This was supported by temperature-dependent studies down to 1.7 K which revealed an unusually large zero-field splitting of the triplet state for a Pt(II)-based complex, suggesting very efficient SOC pathways. The triplet state can mix with a ^{1}MLCT state involving different d orbitals, as shown by TD-DFT studies, which is a key prerequisite for effective SOC.

A follow-up study found that increasing the conjugation by adding an extra thiophene unit to the existing moiety (**Figure 5.7**), and also by switching the acac to dpm, shifted the emission into the NIR region with λ_{max} = 725 nm in toluene and essentially no "contamination" from visible light < 700 nm.[149] Though complex **42** has a lower PLQY than the shorter counterpart **41** at Φ = 0.17, this value is still remarkably high for solution phosphorescence that is squarely in the NIR. Complex **42** was used as an NIR emitter in solution-processed OLEDs where an EQE of 3.6% was reached using **42** doped into TBP:PBD at 5% w/w, with a turn-on voltage of 5.6 V (at 0.01 mW cm^{-2}). The maximum radiosity of 2.7 mW cm^{-2} was also particularly high compared to most reported NIR-emitting phosphorescent OLEDs. This result shows that dinuclear

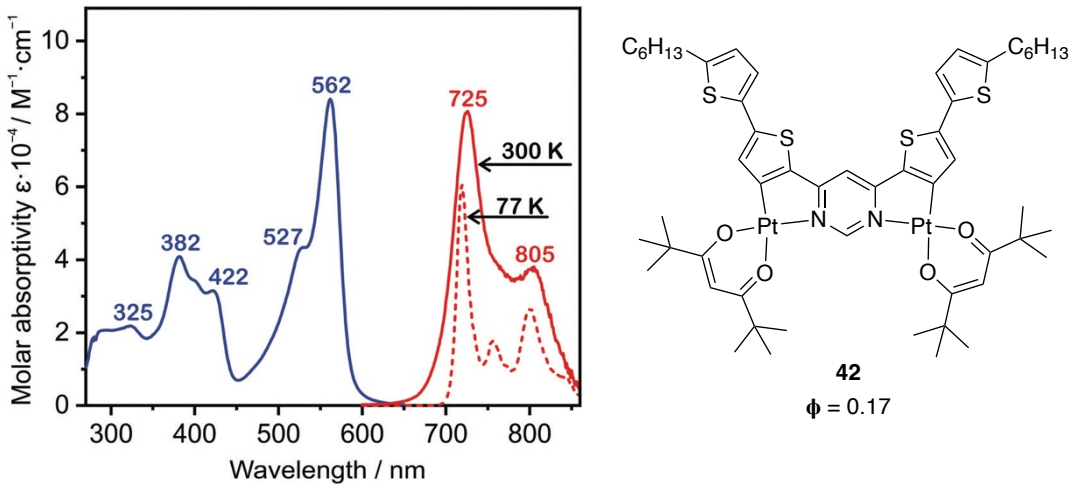

Figure 5.7: *Absorption and emission spectra (at RT and 77 K) of complex **42** pictured, showing NIR emission.*

complexes can offer a way of side-stepping the problem of decreased efficiency that usually accompanies the extension of the π-conjugation of the ligand in such complexes.

Other examples of red/NIR-emitting dinuclear Pt(II) complexes bearing bidentately bound Pt ions include a "zig-zag" type dinuclear complex reported by Zhu *et al.* from which a device was fabricated that showed NIR emission peaking at 724 nm with a shoulder at 783 nm, though with a lower EQE than complex **42** of 0.97% and a radiosity of 146 μW cm^{-2} at 2 wt% doping concentration.[124] Kozhevnikov *et al.* also reported a series of dinuclear Pt(II) complexes using 2,3- and 2,5-substituted isomers of a ditopic bis-bidentate diphenylpyrazine as a bridging ligand between the two Pt(II) ions, with dpm once again completing the coordination spheres.[151] Introduction of the second metal ion, for all complexes investigated, led to a red-shift in the emission due to a significant stabilization of the LUMO, which resides on the N-heterocycle. Increasing the conjugation within the heterocycle on going from pyrazine through quinoxaline to a phenazine unit also had a much more significant effect on the LUMO, leading to progressive shifts of the emission towards the red region of the spectrum. Of additional interest is the effect of the second metal ion on the radiative rate constant k_r, which increases upon introduction of the second metal ion despite the red shift. Typically, a decrease in k_r with decreasing energy of the excited state is usually observed for structurally related complexes since the oscillator strength of a transition is dependent on v^3 in the Einstein coefficient for spontaneous emission. The increased k_r may be observed due to the higher degree of SOC expected from the presence of the second heavy metal ion, as discussed in Section 4.1.1.

An OLED with the highest reported EQE for a dinuclear Pt(II) complex so far was designed by Sun *et al.* The complexes feature two Pt(II) ions that are bidentately bound to the same triphenylamine core (**Figure 5.8**).[152] The dinuclear complexes showed superior PLQYs compared to their mononuclear counterparts (from 0.03-0.07 for the mononuclear analogues to 0.11-0.22 for the dinuclear complexes). Complexes **43** and **44** also exhibit high PLQYs in doped CBP films, 0.79 and 0.42 respectively, and showed preferential horizontal orientation in doped films, which

prompted fabrication of OLEDs. Complex **43** is a yellow emitter (λ_{EL} = 553 nm) that was incorporated into an OLED with a maximum EQE of 22.4%, a new record at the time for OLEDs based on dinuclear Pt(II) complexes. Complex **44** is a red emitter (λ_{EL} = 606 nm) also with a remarkably high EQE of 21.1%. The complexes also both demonstrated turn-on voltages of 3.9-4.8 V, comparable if not lower than other solution-processed OLEDs based on dinuclear Pt(II) complexes. It is clear that dinuclear Pt(II) complexes, featuring bidentate-coordinating ligands, could be a design strategy towards efficient red/NIR emitters, with the presence of the two heavy metals seeming to somewhat circumvent the energy-gap law.

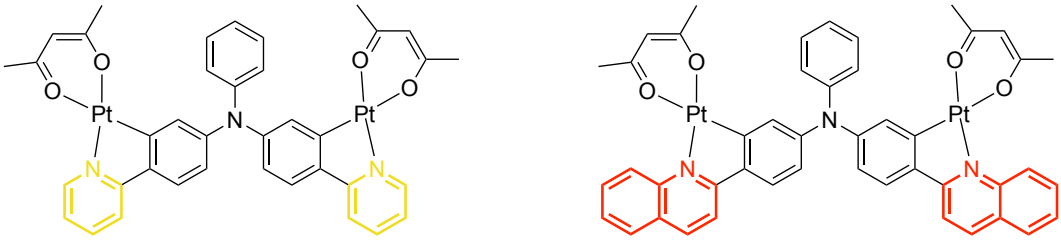

43
λ_{EL} = 553 nm
EQE = 22.4%

44
λ_{EL} = 606 nm
EQE = 21.1%

Figure 5.8: *Dinuclear Pt(II) complexes reported by Sun et al. with high efficiencies in OLED devices.*

5.1.4 Pt(II) complexes featuring bidentate triazole ligands

In this chapter, triazole pyridine ligands will be used as N^N$^-$-binding ligands, in place of the O^O$^-$ β-diketones, in some complexes. A brief review of such ligands is provided here. Azole ligands, such as triazoles, can be combined with a heterocycle such as pyridine to give ligands with synergistic strong σ-donating and π-accepting character. Many have been studied as ligands for luminescent Pt(II) complexes, amongst other applications,[153] including the aforementioned extremely high efficiency NIR-emitting pyrazolyl-pyrazinolate complexes reported by Chi *et al.* (see Section 1.6.2).[74] Triazoles are defined as 5-membered rings containing 3 nitrogen atoms. They are classed as 1,2,3- or 1,2,4-triazoles depending upon the positions of the N atoms in the ring. 1,2,4-Triazoles with anionic coordination (**Figure 5.9**) are of particular interest due to the functionality that can be incorporated into the ring

which can aid with solubility and influence the luminescence properties of the resulting complexes. Pt(II) complexes containing these triazole ligands can be synthesised in the same way outlined above for heteroleptic Pt(II) complexes, where the triazole ligand is used to break open the chloro-bridged dimer instead of, for example, a β-diketonate such as acac.

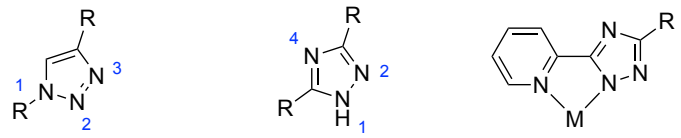

Figure 5.9: *Structure of 1,2,3- and 1,2,4-triazoles with the anionic binding mode of a 1,2,4-triazole-pyridine ligand.*

There are few examples of Pt(II) complexes containing bidentate 1,2,4-triazole ligands that are strongly luminescent in solution, and fewer still that have been incorporated into devices. Naziruddin *et al.* reported a blue-emitting Pt(II) complex **45** (λ = 474, 501 nm) featuring a pyridine-triazole ligand along with a bidentate N-heterocyclic carbene pyrazolate ligand (**Figure 5.10**), that demonstrated a high PLQY in the solid state (PLQY of 0.11 in neat film and 0.49 for 10 wt% in PMMA film).[154]

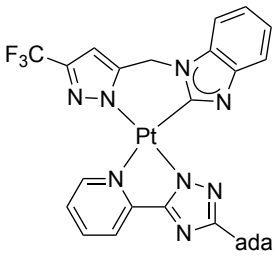

45

Figure 5.10*: Blue-emitting Pt(II) complex featuring a 1,2,4-triazole ligand. Ada = adamantane.*

Li *et al.* reported complex **46** featuring the ligand 3,5-bis(2-pyridyl)-1,2,4-triazole ('ptp'), which forms columnar stacks stabilised by strong intermolecular Pt···Pt interactions (3.298 Å) as seen from the crystal structure (**Figure 5.11**), meaning the complex is able to form excimers.[155] The symmetry of the coordination sphere due to the homoleptic Pt(N^N)$_2$ design allows for the formation of fully-overlapped excimers. Three types of phosphorescent emissions were observed in neat and

doped thin films (**Figure 5.11**): structured monomer emission in the blue-green region (λ_{max} = 480 nm), unstructured excimer emission in the yellow region (λ_{max} = 550 nm), and broad unstructured MMLCT extended excimer emission in the orange-red region of the spectrum (λ_{max} = 600 nm) due to the formation of oligomers. A slight red shift is observed for the excimer band at higher concentrations; it is well known, best established for pyrene,[65] that a greater overlap between the two planar monomer units results in a red shift for the excimer emission band, suggesting increased overlap of the complex at higher doping levels. OLEDs were fabricated by sequential thermal evaporation, and the same shift from monomer to excimer emission was also observed in the EL. The EQE reached a maximum of 6.6%, and near-white EL was achieved by optimising the doping concentration to vary the ratio of monomer to excimer.

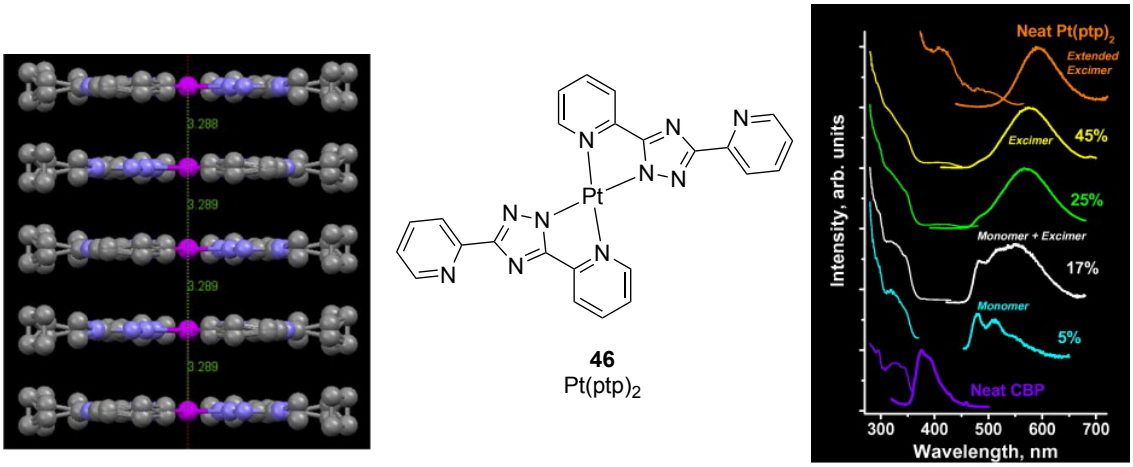

Figure 5.11: *Crystal structure of complex **46** (left) revealing infinite columnar stacking with Pt···Pt interactions (left). PL spectra of complex **46** in thin films showing a shift from monomer to excimer emission upon increasing the wt% doping concentration of the complex in CBP.*

Walden *et al.* reported similar homoleptic Pt(II) complexes featuring triazole ligands but with the added benefit of increased solubility due to the introduction of aryl rings with *t*-butyl substituents (**Figure 5.12**).[101] This allowed solution-processed OLEDs to be fabricated with an EQE of 12.5% for complex **47** and a maximum luminance of 28 700 cd m^{-2}. Despite the pendant aryl groups eliminating close Pt···Pt contacts (though retaining close interfacial distances of the aromatic ligands in adjacent molecules),

the complex showed green monomer emission in solution and intense red emission at elevated concentrations, both in solution and in films, due to bimolecular excited states.

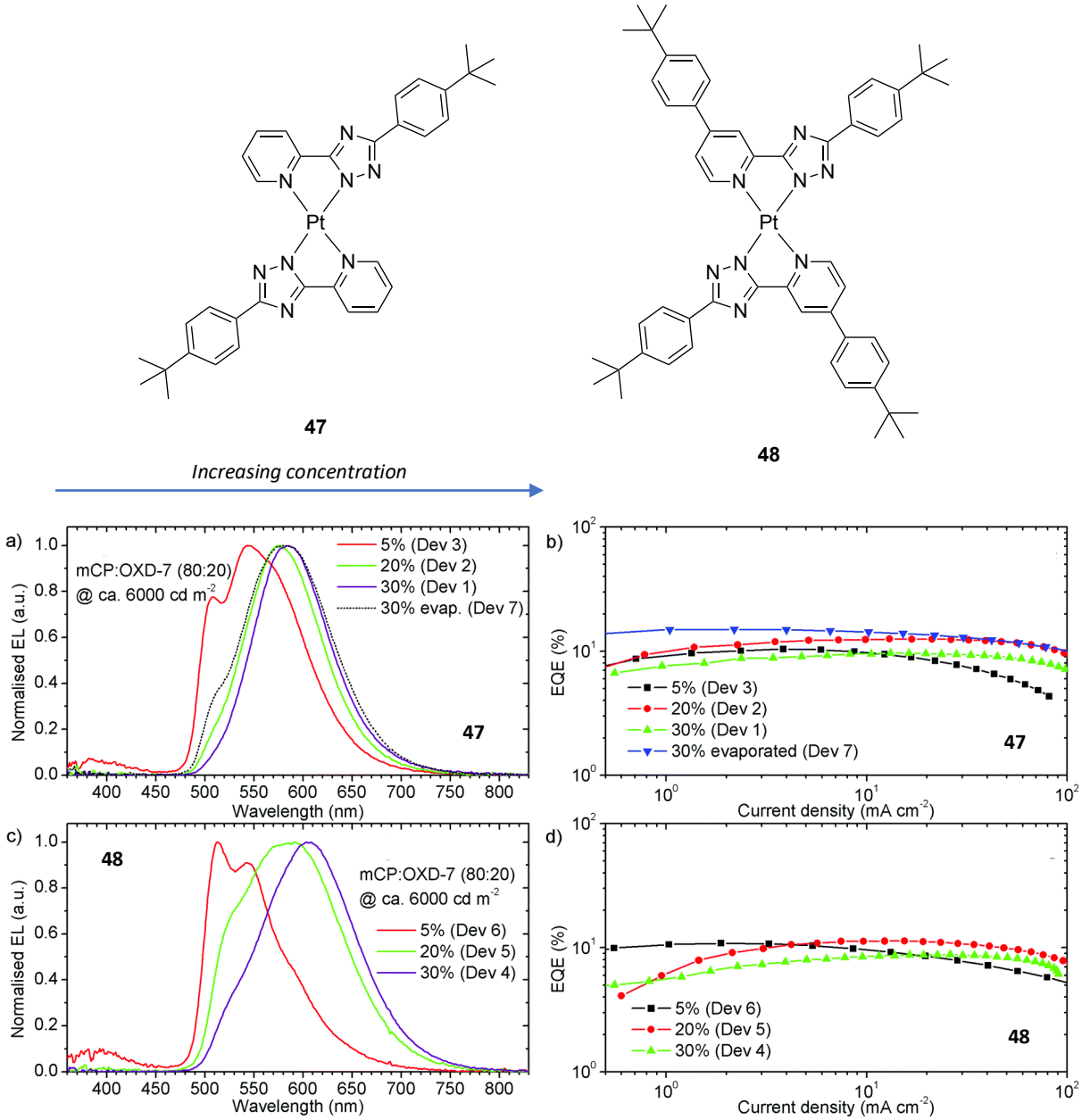

***Figure 5.12**: Characteristics of OLED devices of complexes **47** and **48** reported by Walden et al. EL spectra are normalised to λ_{max} (left) and EQE versus current density are shown on the right. The % for each devices indicates concentration of the emitter in wt%.*[101]

Time-resolved studies also revealed different environments of the bimolecular excited states, with those appearing to emit at the lowest energy interestingly having the longest lifetimes, in contrast with the energy-gap law. This observation was

rationalised by the PES of the excimer becoming repulsive upon emission, highlighting again the intriguing potential of the use of excimers in potentially overcoming the consequences of the energy-gap law to achieve efficient red/NIR emitters.

5.2 Aims and objectives

There is not a great deal of research into the excimeric interactions between Pt(II) complexes featuring bidentate ligands, though the literature review above has shown that varying the substituents on, for example, the ppy ligands of Pt(ppy)(acac) can increase the propensity for excimer formation whilst shifting the emission energy. Incorporating two Pt(II) ions by extending the conjugation of the ligands has been shown to red shift the emission whilst retaining high PLQYs, with the presence of the second heavy metal likely increasing SOC and aiding in circumventing the energy-gap law. With this in mind, the aim of the work described in this chapter is to synthesise Pt(II) complexes with bidentate ligands anchored onto a xanthene scaffold, similar to the tridentate complexes reported in Chapter 4, based on ppy, thpy and variants with extended conjugation such as isoquinolines. Although complexes with bidentate ligands can undergo distortion from D_{4h} to D_{2d} symmetry in the excited state, which has long been recognised as a potential sink for the excited state energy,[1] there are some examples of promising emitters reported in the literature. It would be beneficial to probe further the interactions between such complexes. Excimeric interactions will be investigated to see if the presence of the xanthene scaffold can promote intramolecular interactions, with the overall objective of achieving red/NIR emission. Acac and 1,2,4-triazole compounds will be investigated as co-ligands in these target complexes (**Figure 5.13**). Additionally, some flexible linkers will be proposed, and the results of some initial studies on the described towards the end of the chapter.

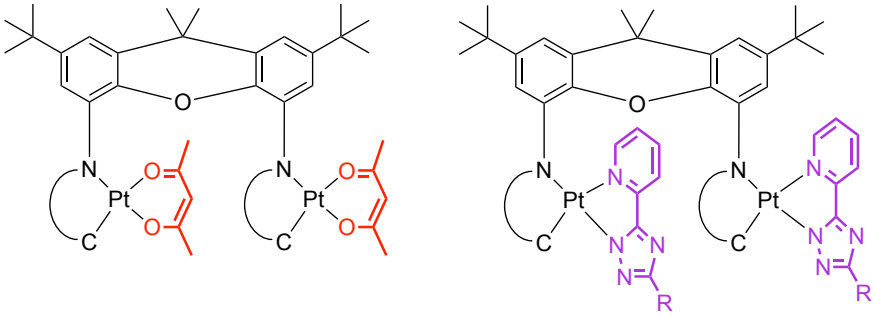

Figure 5.13: *Design strategy of Pt(II) complexes with bidentate ligands on a xanthene scaffold featuring acac (left) and 1,2,4-triazole ligands (right). Note: N^C will be ppy, thpy or related alternatives. Isomers can also be targeted in which the phenyl ring of the N^C ligand is linked to the xanthene, rather than the pyridine as shown here.*

5.3 Results and discussion

5.3.1 Synthesis

Proligand synthesis

Bis-bidentate ligands were prepared by successive Suzuki, Stille and Miyaura cross-coupling reactions. Both the 2,4- and 2,5-isomers of bromo-substituted ppy and thpy were initially synthesised (**Scheme 5.1** and **Scheme 5.2**) before coupling onto the xanthene to give the proligands H_2L^{41-44} in good yields. Note that the N^C group in these two proligands is attached to the xanthene through the pyridine ring.

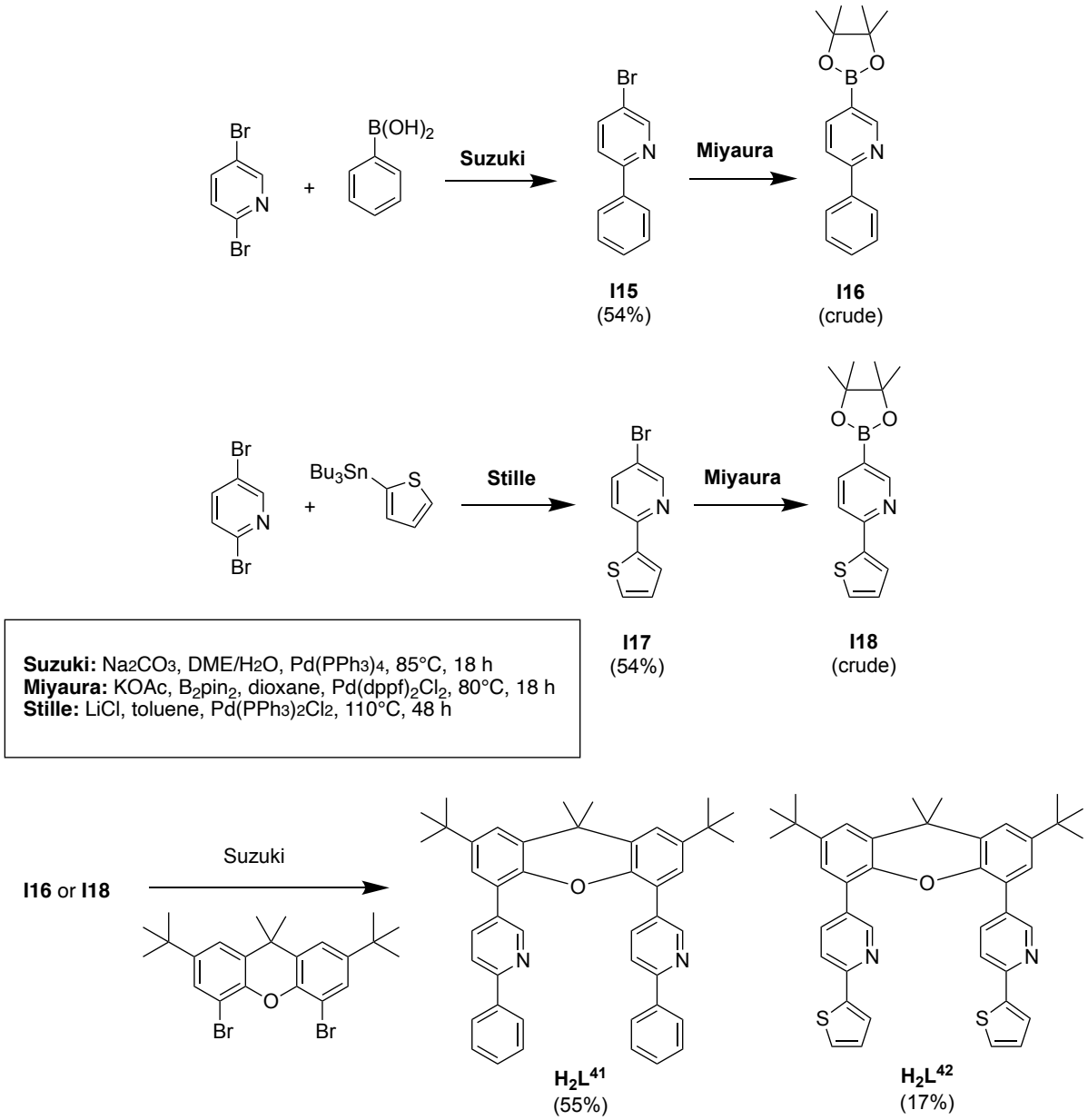

Scheme 5.1: *Synthesis of bidentate proligands H_2L^{41} and H_2L^{42} featuring the 2,5-isomers of ppy and thpy.*

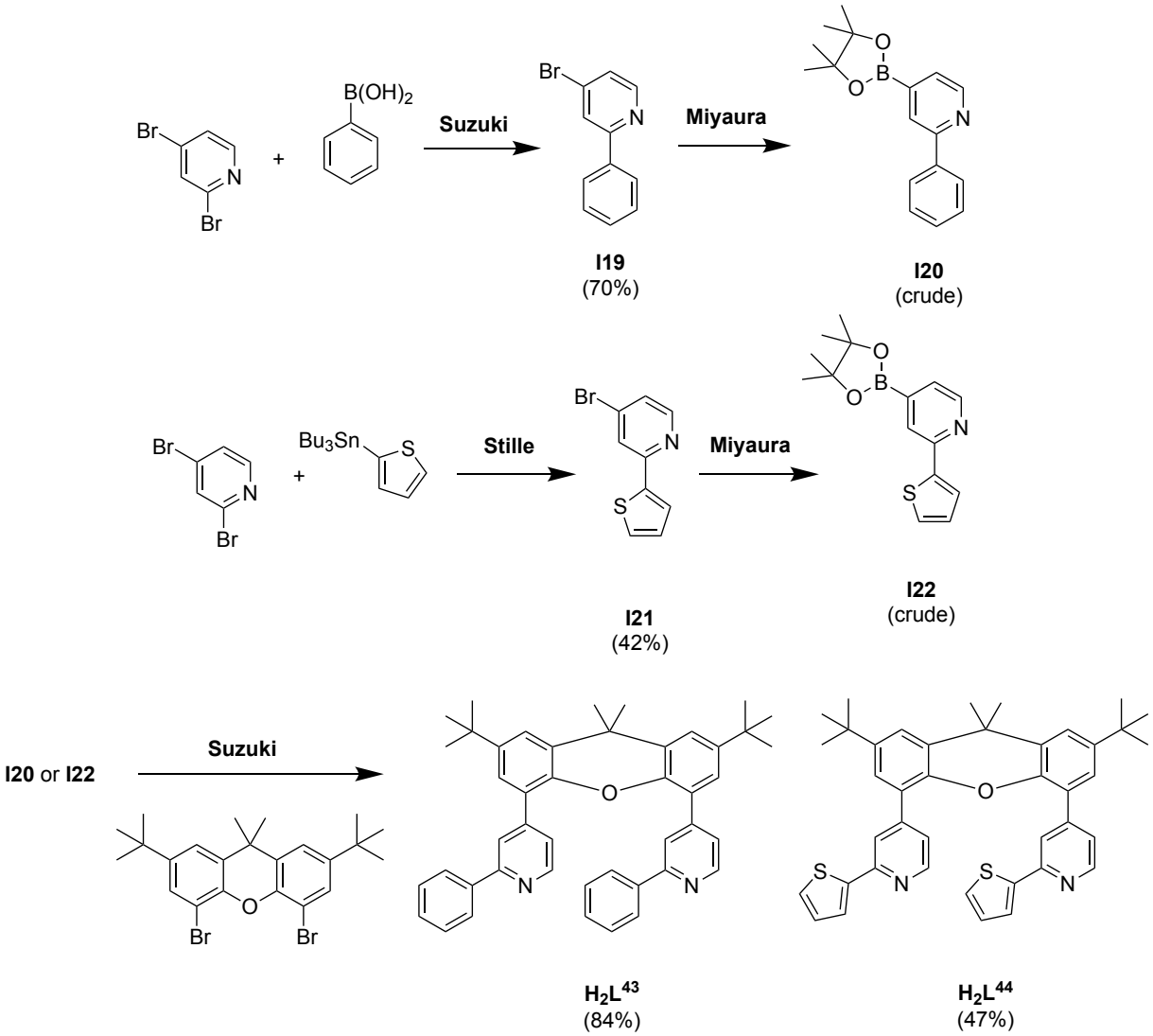

Scheme 5.2: *Synthesis of bidentate proligands H_2L^{43} and H_2L^{44} featuring the 2,4-isomers of ppy and thpy.*

Proligands were targeted with increased conjugation of the heterocycle, i.e. using isoquinolines instead of pyridine. The synthesis of the precursor **P8** featuring the 1-isoquinoline isomer with 3-bromobenzeneboronic acid was outlined in Chapter 3, and this gave H_2L^{45} in high yield upon reaction with xanthene-Br_2 (**Scheme 5.3**). **P14** was prepared in the same way using 4-bromobenzeneboronic acid to give the 'straight' proligand when reacted with xanthene-Br_2 (**Scheme 5.4**). For these proligands, the N^C group is attached to the xanthene anchor through the phenyl ring as opposed to the heterocycle, as dibromo-substituted isoquinolines are not a commercially or synthetically viable option. Interestingly the synthesis of H_2L^{45}

proceeded with no issues, as opposed to the tridentate version HL^{34} (Section 4.3.1.1) where the Suzuki coupling only proceeded at one bromine reactive site to give the mono proligand with only one N^C^N unit anchored to xanthene. There is clearly less steric hindrance involved with the bidentate version, which is likely the reason for the relative ease of synthesis of H_2L^{45}.

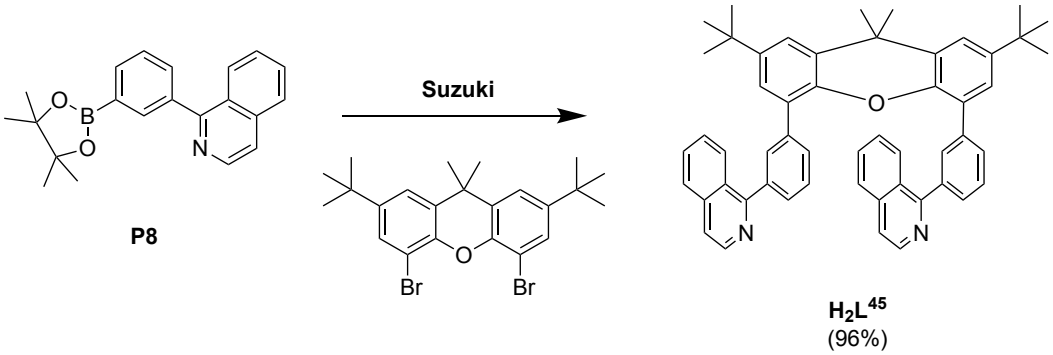

Scheme 5.3: *Synthesis of H_2L^{45} featuring 1-isoquinoline in the N^C unit.*

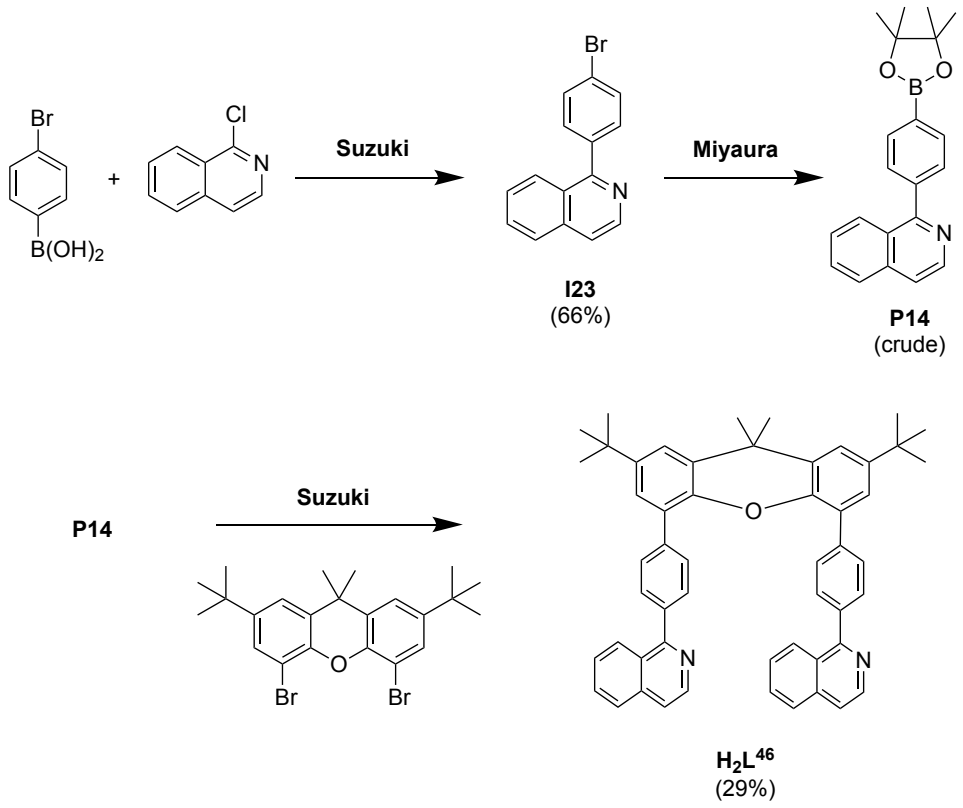

Scheme 5.4: *Synthesis of the proligand H_2L^{46}.*

A side product of the Suzuki-Miyaura coupling of **I23** (**Scheme 5.4**) where a second coupling occurs to give **I24** with two phenyl rings, prompted the synthesis of proligand H_2L^{47} (**Scheme 5.5**). It was also postulated that the added phenyl ring could provide a little extra flexibility to the system which may allow closer Pt···Pt intramolecular interactions in the resulting complex.

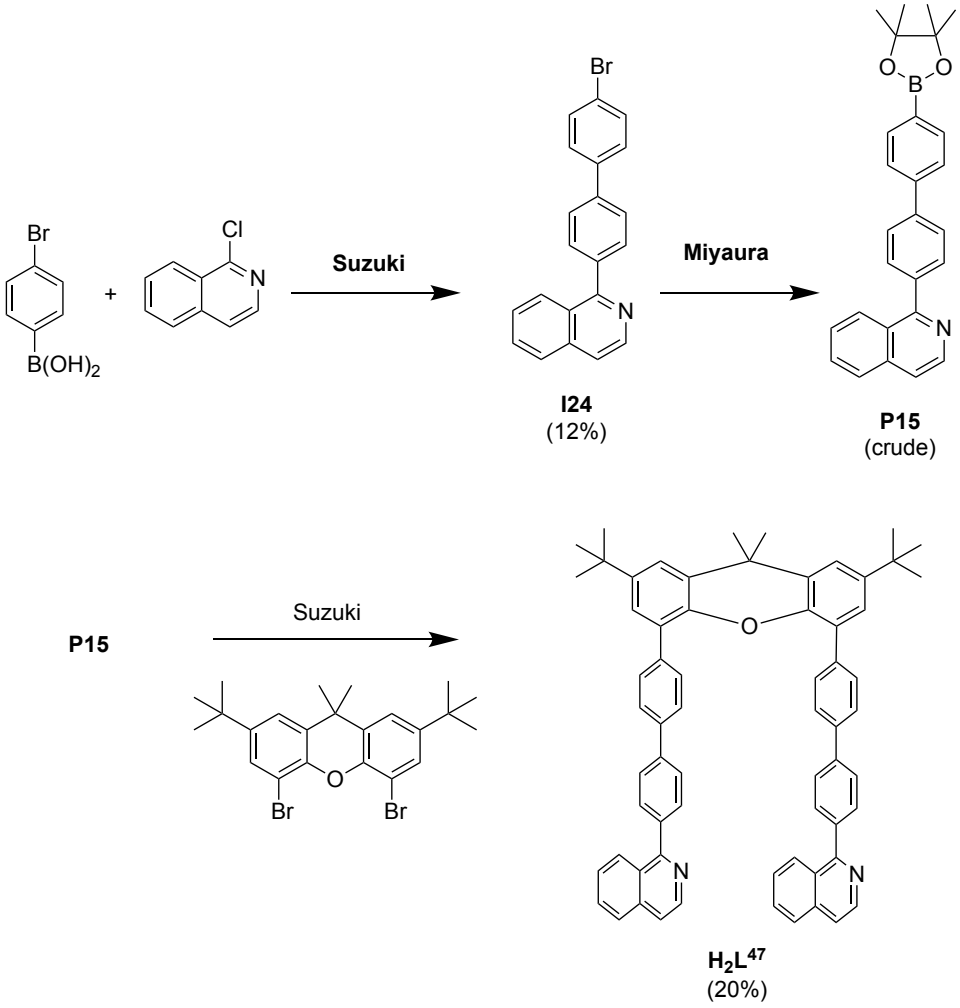

Scheme 5.5: *Synthesis of H_2L^{47} featuring an additional phenyl ring in between the xanthene linker and the N^C unit.*

Complexation

Complexation proceeded in two steps: firstly, the relevant proligand was reacted with K_2PtCl_4 in refluxing acetic acid under an inert atmosphere overnight, and secondly, the product of this reaction, likely a chloro-bridged dimer, was reacted with acetylacetone (or later a triazole compound) and sodium carbonate in 2-ethoxyethanol, again under an inert atmosphere (**Scheme 5.6**). Acetic acid was used

here for the first step as opposed to an ethanol/water (3:1 v/v mixture as reported in the literature,[101] as the harsher acetic acid conditions were required in order to introduce a Pt ion at both bidentate binding sites of the ligand. The reaction was initially tried in ethanol/water, which gave a mixture of mono- and bis-substituted final products, hence acetic acid was used as the solvent moving forward.

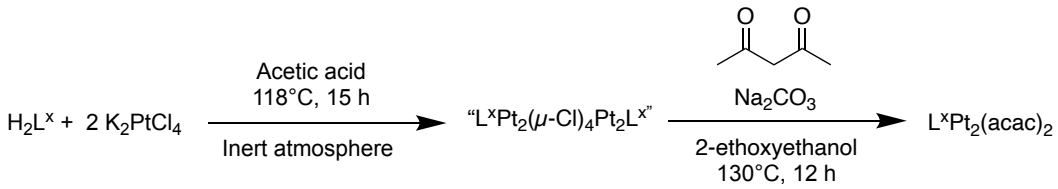

Scheme 5.6: *Two step synthesis of dinuclear Pt complexes featuring bidentate ligands.*

It was expected that the reaction of the bidentate proligands with K_2PtCl_4 in acetic acid would proceed *via* a μ-Cl dimer (as discussed above in Section 5.1.2). In fact, isolation and crystallisation of the product from the reaction between H_2L^{44} and K_2PtCl_4 in refluxing acetic acid using an inert atmosphere, revealed the structure shown in **Scheme 5.7**, where instead of the chloro-bridged dimer, each Pt ion is coordinated to one Cl and two of the N^C-xanthene units. This product was confirmed by MALDI mass spectrometry and X-ray crystallography, albeit from a small weakly diffracting crystal that showed whole molecule disorder and therefore the structure could not be solved completely as seen in **Scheme 5.7**. Photophysical properties of the pure complex were investigated, and the remainder was reacted with acac, though the isolated product $L^{44}Pt_2(acac)_2$ could not be purified to a suitable standard for analysis.

For the remaining proligands, no pure complex was isolated at this stage after step 1 of the synthesis, so each was simply reacted on in the next step to give the acac-substituted final complexes (**Figure 5.14**). Purification was achieved by preparative column chromatography, and in some cases analytically pure complexes could not be isolated so the photophysical properties of these complexes, namely $L^{43}Pt_2(acac)_2$ and $L^{44}Pt_2(acac)_2$, were not studied. The relatively low yields of the complexes, for $L^{45}Pt_2(acac)_2$ in particular, could be due to step 1 of the synthesis forming complexes such as that depicted in **Scheme 5.7**, as each complex here can only produce one of

the final desired products where two Pt ions are required, as opposed to a chloro-bridged dimer where the stoichiometry would be such that two equivalents of final product could be formed.

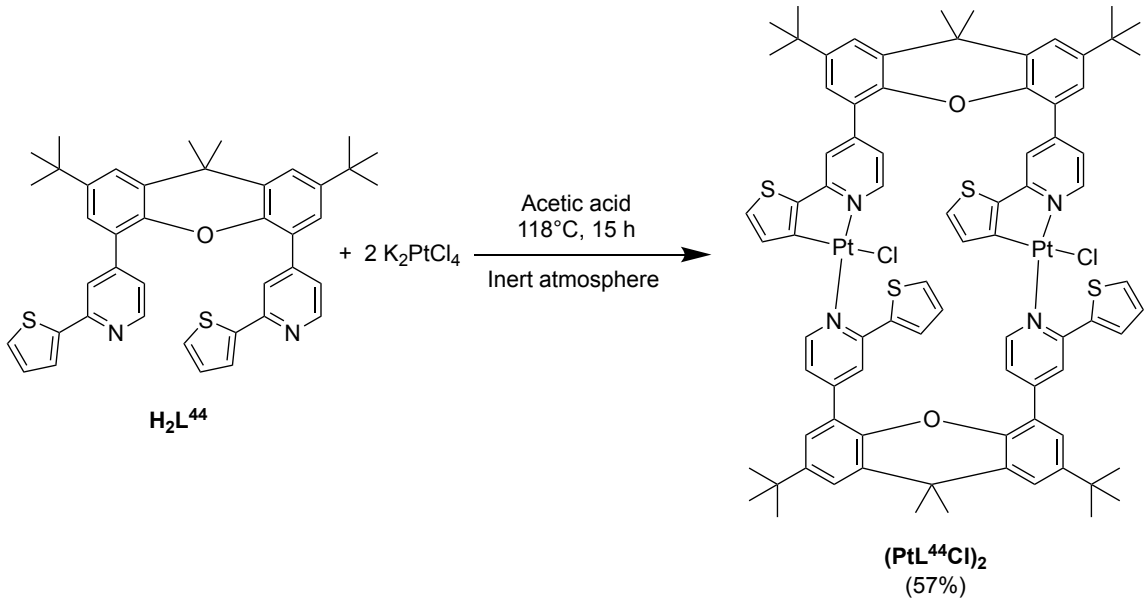

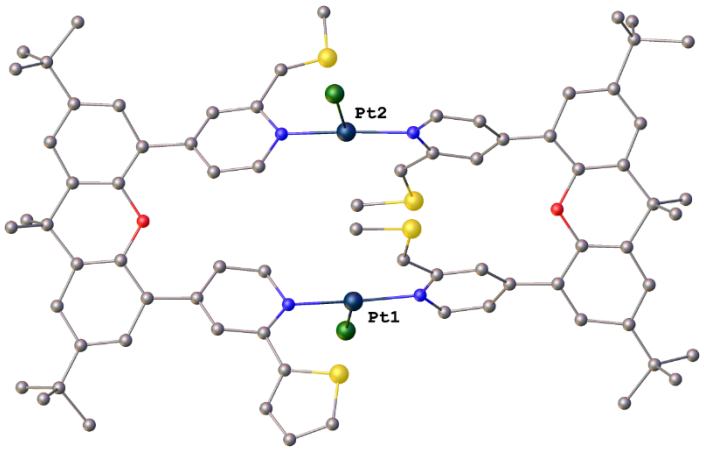

Scheme 5.7: *Synthesis of $(PtL^{44}Cl)_2$ and its molecular structure (disordered, with missing atoms as the structure could not be completely solved) determined by X-ray crystallography.*

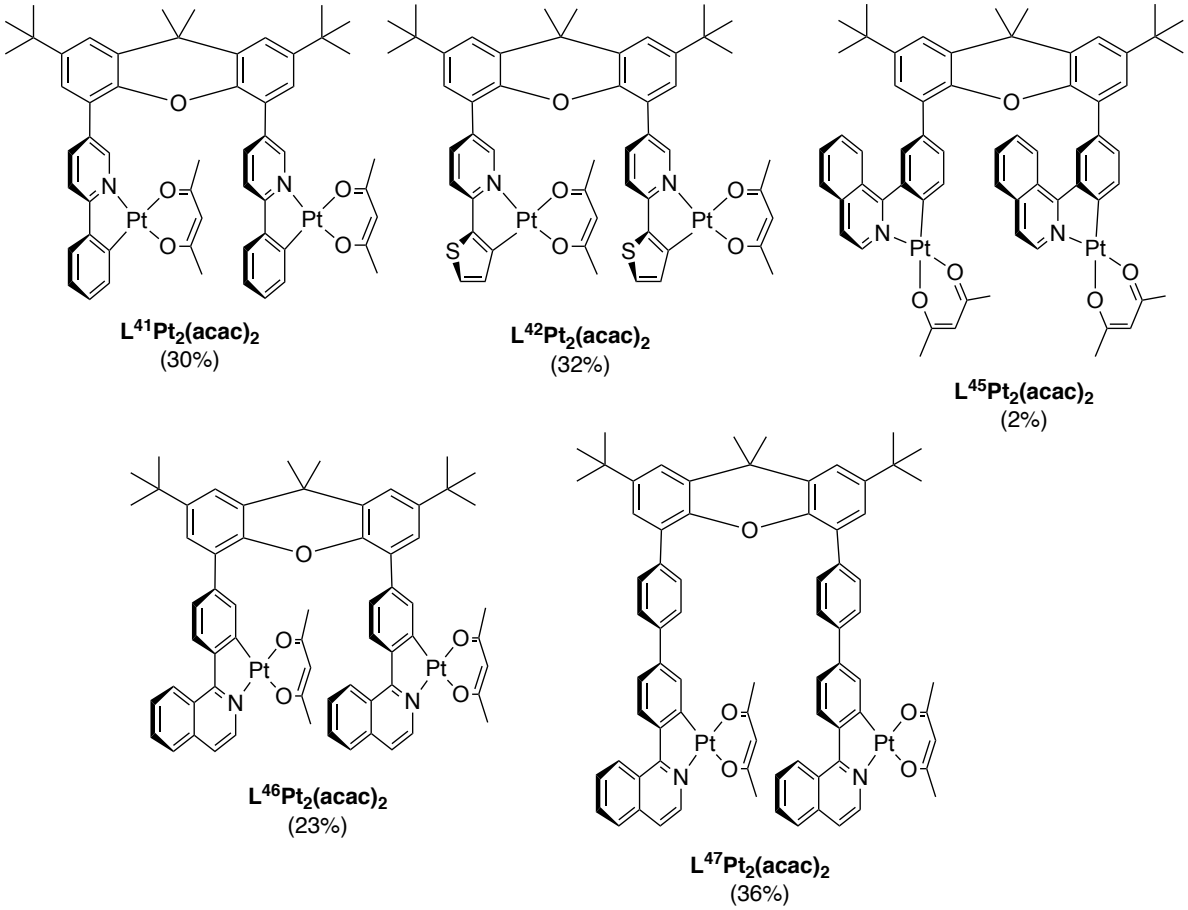

Figure 5.14: *Structure of dinuclear Pt(II) complexes featuring bidentate ligands with xanthene as a linker.*

Crystals of $L^{47}Pt_2(acac)_2$ suitable for X-ray diffraction were grown by slow evaporation from the complex in a DCM/MeOH mixture and the molecular structure is shown in **Figure 5.15**. The extra phenyl ring in the structure between the N^C-coordinating ligand and the xanthene anchor provides additional flexibility to the structure, twisting the two Pt units into a geometry favoured for metallophilic interactions with a Pt···Pt distance of 3.2233(5) Å, shorter than the sum of the van der Waals' radii of two Pt atoms. Intramolecularly the Pt units are disposed such that the N^C ligand of one unit is overlapping with the acac ligand of the other unit.

The use of a *t*-Bu-substituted 1,2,4-triazole (synthesised by Dr Melissa Walden[135]) in the second step in place of acetylacetone yielded the triazole-substituted complexes shown in **Scheme 5.8**. The low yields reflect the difficulty in purifying these complexes. The structures are drawn based on the *cis*-coordination usually displayed

for bis-cyclometallated Pt complexes, where the strong *trans* influence of the σ-donating C^- atom makes it unfavourable for them to be placed opposite one another. Since no crystals suitable for x-ray diffraction were obtained, the exact coordination of the triazole compounds cannot be confirmed. Walden *et al.* reported crystals of complexes **47** and **48** featuring the same triazole ligand that displayed triazole rings in a *trans* configuration where the N^- triazole atoms are opposite one another, suggesting that the N *trans* effect in these complexes is less important. Perhaps the different conformations of these complexes are all synthesised in various amounts, along with the added complication of having two Pt centres in the same complex, which could be a reason why it was so difficult to obtain a clean NMR spectrum.

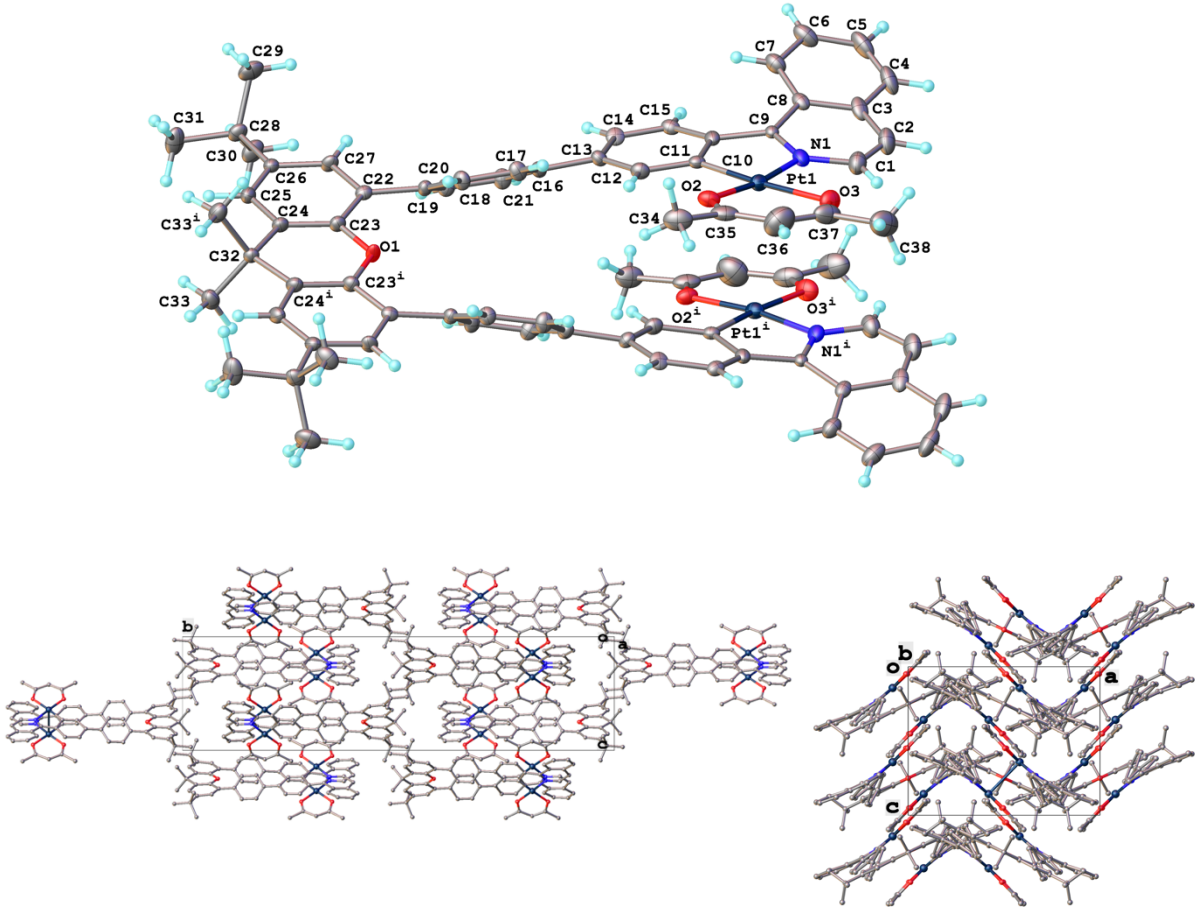

Figure 5.15: *Molecular structure and crystal packing of $L^{47}Pt_2(acac)_2$.*

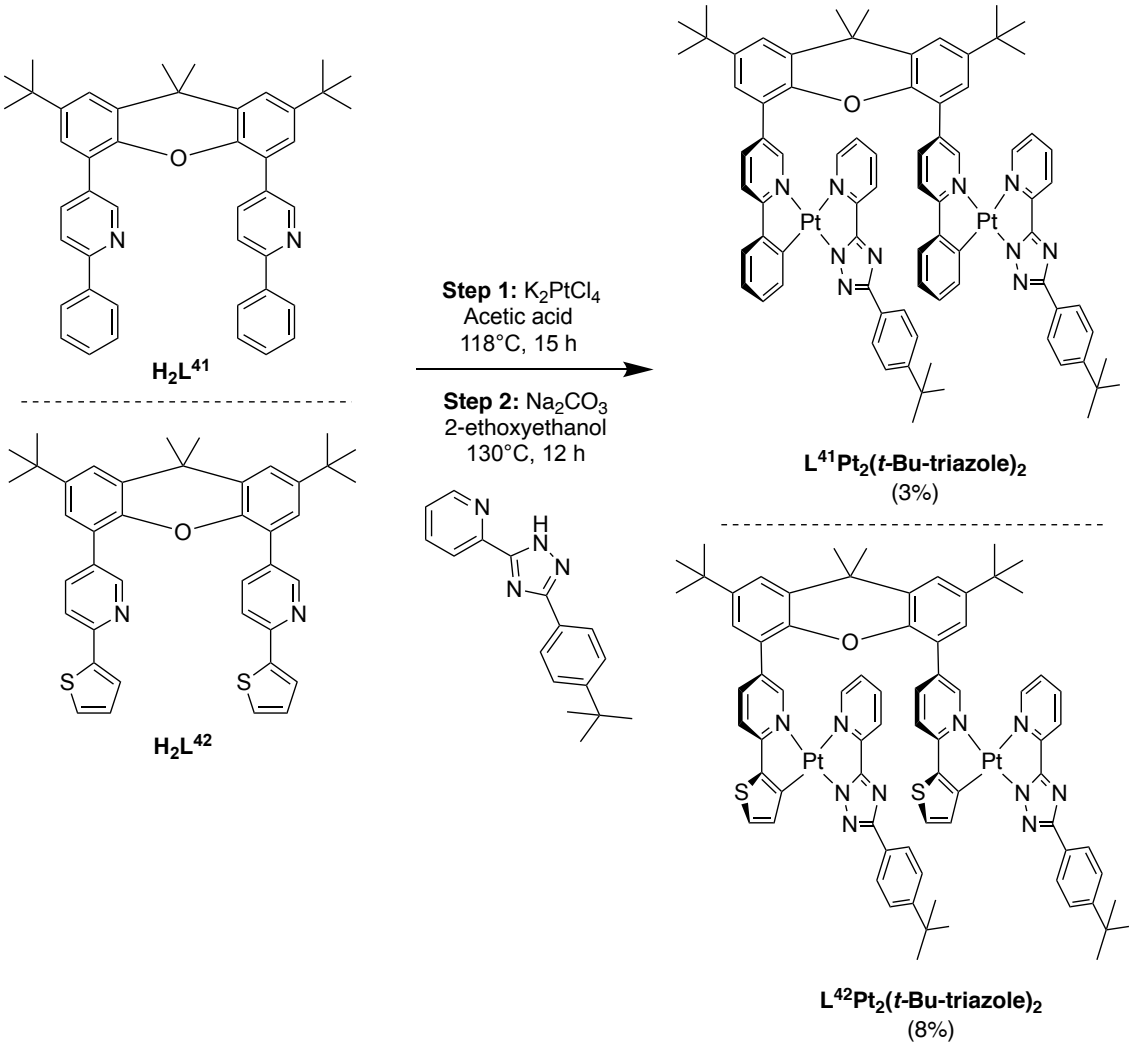

Scheme 5.8: *Synthesis of triazole-substituted dinuclear Pt complexes linked to a xanthene scaffold.*

Indeed, the reaction of H_2L^{42} with an OMe-substituted triazole compound (synthesised by Dr Melissa Walden) resulted in a complex that readily formed crystals suitable for x-ray diffraction. The molecular structure revealed the product to be a mononuclear complex featuring the triazole in the *trans* configuration, with the N^- of the triazole opposite to the C^- of the thiophene ring (**Figure 5.16**). This configuration is perhaps stabilised by some interaction between the pendant OMe-phenyl ring of the triazole and the xanthene ring. The distance measured between the plane of the aromatic ring of xanthene and the OMe-phenyl group of the triazole ligand is 4.0872(12) Å, implying that weak π-stacking interactions are present. The trans configuration of the triazole ligand can be rationalised by looking at the bond lengths (**Table 5.2**); remarkably the Pt1-N2 (triazole) distance is even slightly longer

than Pt1-N1, implying the trans effect is less important here. The molecule also packs in pairs in the crystal structure (**Figure 5.17**).

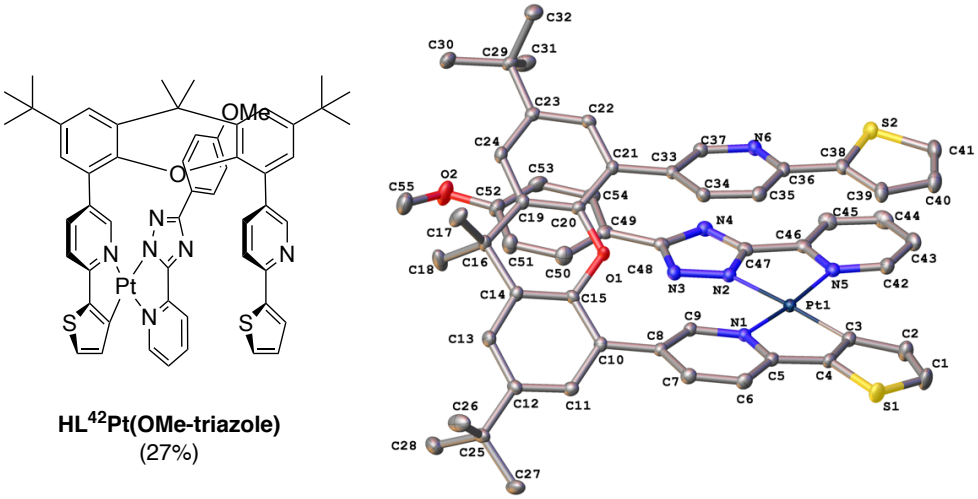

***Figure 5.16**: Molecular structure of HL[42]Pt(OMe-triazole) and yield indicated in brackets.*

***Table 5.2:** Selected bond lengths and angles for HL[42]Pt(OMe-triazole)*

Bond lengths / Å		Bond angles / °	
Pt1-N1	2.0287(17)	N1-Pt1-N5	175.17(7)
Pt1-N2	2.0569(16)	N2-Pt1-C3	177.17(8)
Pt1-N5	2.0435(17)	N5-Pt1-N2	78.34(7)
Pt1-C3	2.021(2)	N1-Pt1-C3	80.96(8)

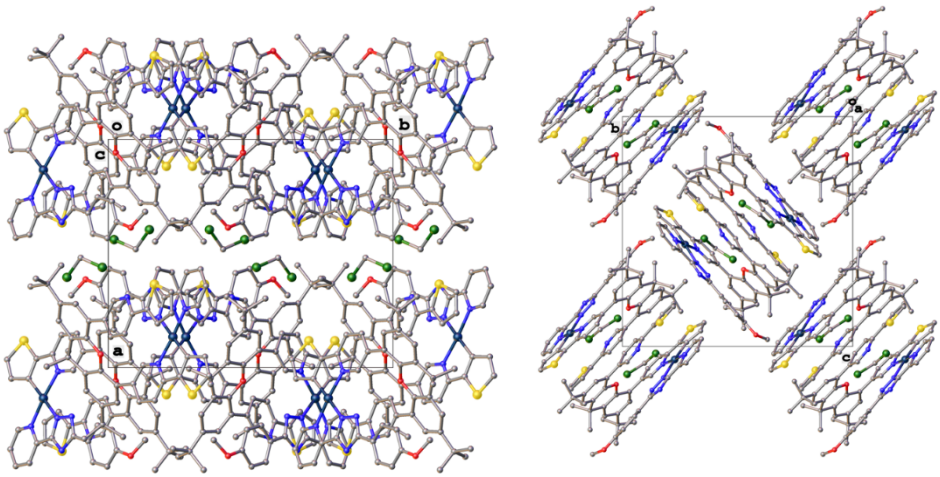

***Figure 5.17:** Crystal packing of HL[42]Pt(OMe-triazole).*

5.3.2 Photophysical properties

Absorption

A summary of all spectroscopic data for the complexes presented in this chapter can be found in **Table 5.3**. Absorption spectra of complexes of the type $L^xPt_2(acac)_2$ are shown in **Figure 5.18**. The tail of the lowest energy absorption band is red shifted in the order $L^{41}Pt_2(acac)_2$ < $L^{42}Pt_2(acac)_2$ < $L^{45}Pt_2(acac)_2$ < $L^{46}Pt_2(acac)_2$ < $L^{47}Pt_2(acac)_2$. Breaking this trend down into substituent effects, this is as expected; going from the ppy substituted $L^{41}Pt_2(acac)_2$ to $L^{42}Pt_2(acac)_2$ containing thpy ligands results in a red shift of the absorption due to the more electron-rich thiophene ring.[34] The remaining three complexes all feature ligands with extended conjugation (isoquinoline in place of pyridine) so their absorption spectra are red-shifted. $L^{47}Pt_2(acac)_2$ has the most red-shifted band likely due to the additional phenyl ring in the structure between the N^C-coordinating ligand and the xanthene ring allowing extra flexibility in the system

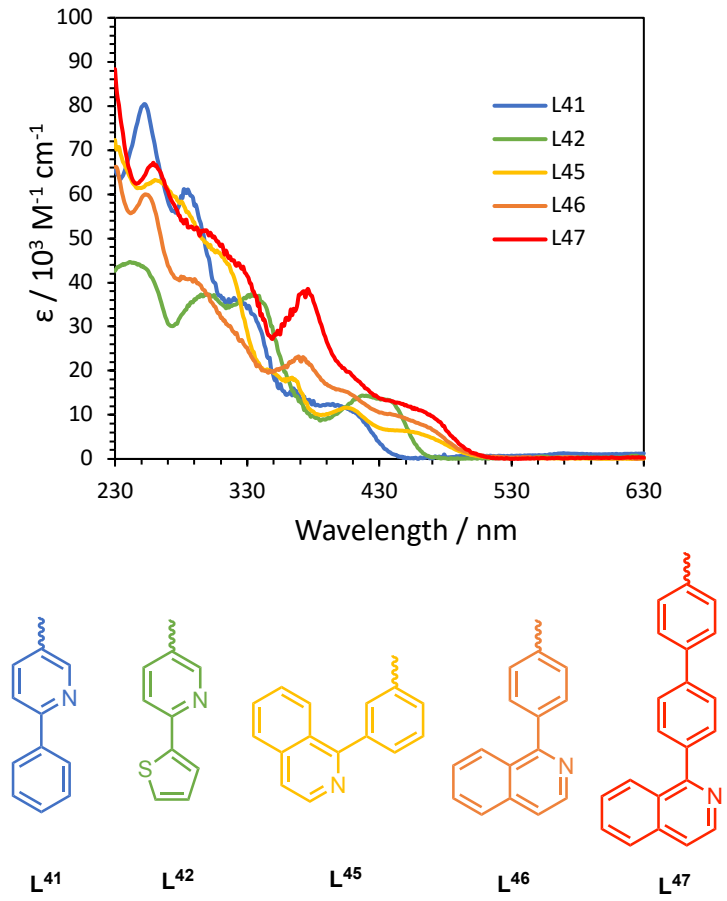

Figure 5.18: *Absorption spectra of complexes of the type $L^xPt_2(acac)_2$, showing the structure of the N^C-coordinating ligand in each case.*

so the Pt centres can interact more favourably, giving rise to this lower energy, tentatively assigned MMLCT state.

The absorption spectrum for $(PtL^{44}Cl)_2$ is compared to that of the acac-substituted complex that is most similar in structure, $L^{42}Pt_2(acac)_2$, in **Figure 5.19**. Both feature similar absorption profiles with LC states below 330 nm, and the lowest energy MC band is of similar energy for both centred around 430 nm, though less intense for $(PtL^{44}Cl)_2$. Absorption spectra for all triazole-substituted complexes are shown in **Figure 5.20**. $HL^{42}Pt$(OMe-triazole) is the most strongly absorbing complex of the three despite there being only one Pt centre. The tail of the lowest energy absorption band is red-shifted for $L^{42}Pt_2$(*t*-Bu-triazole)$_2$ with respect to $L^{41}Pt_2$(*t*-Bu-triazole)$_2$, again due to the more electron rich thiophene rings in the former as opposed to the phenyl rings of the ppy ligands of the latter. The absorption profile is very similar for $HL^{42}Pt$(OMe-triazole) and $L^{42}Pt_2$(*t*-Bu-triazole)$_2$, though with the former being more intense, suggesting the electronic effects of the OMe and *t*-Bu substituents on the triazole ring are very similar, both being slightly electron-donating.

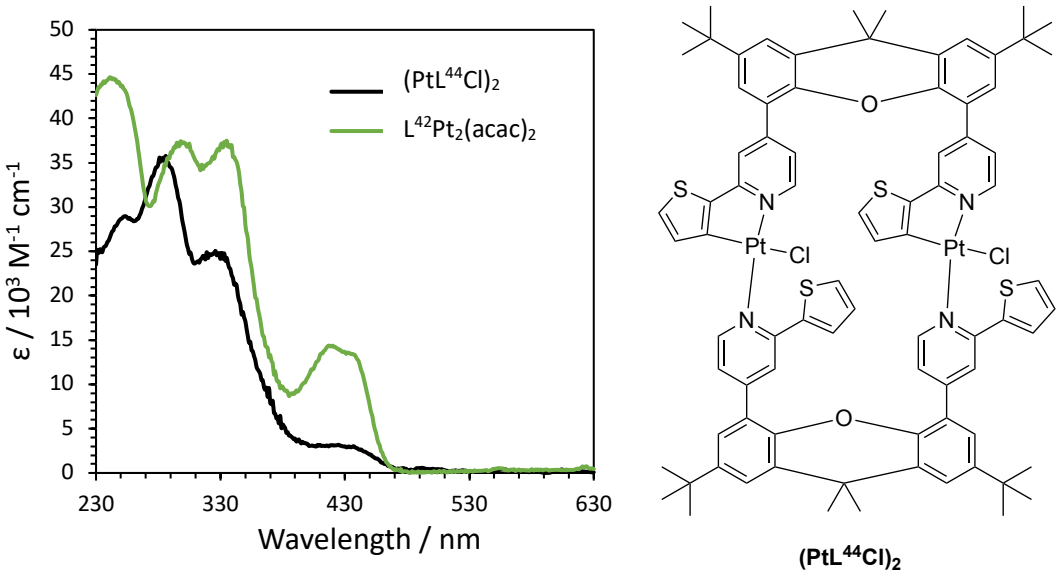

Figure 5.19: *Absorption spectrum of $(PtL^{44}Cl)_2$ compared with $L^{42}Pt_2(acac)_2$.*

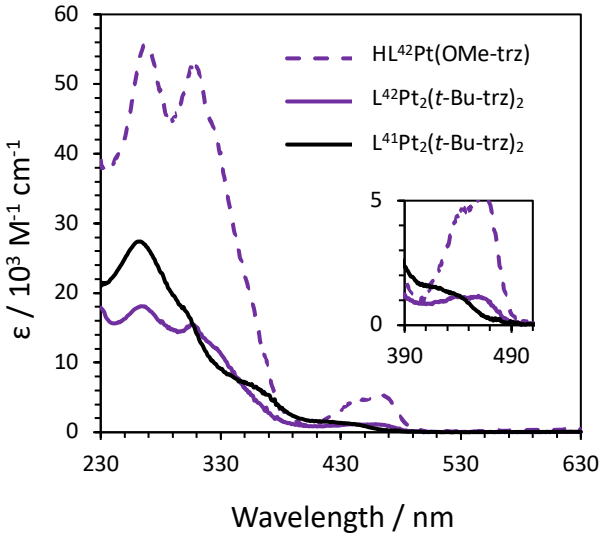

Figure 5.20: *Absorption spectra of triazole complexed $HL^{42}Pt$(OMe-triazole) and $L^{41,42}Pt_2$(t-Bu-triazole)$_2$.*

Emission

The emission spectra of complexes $L^xPt_2(acac)_2$ in dilute degassed DCM solution are shown in **Figure 5.21**, with quantum yields ranging from 0.02 to 0.21. The onset of emission is red shifted in the order $L^{41}Pt_2(acac)_2$ < $L^{42}Pt_2(acac)_2$ < $L^{45}Pt_2(acac)_2$ < $L^{46}Pt_2(acac)_2$ < $L^{47}Pt_2(acac)_2$, following the same trend as the absorption spectra which can be rationalised in the same way. All complexes except $L^{42}Pt_2(acac)_2$ feature a low-energy broader band along with the more structured monomer emission even in dilute solution, likely due to excimeric interactions which will be discussed in more detail below when considering the emission spectra at various concentrations.

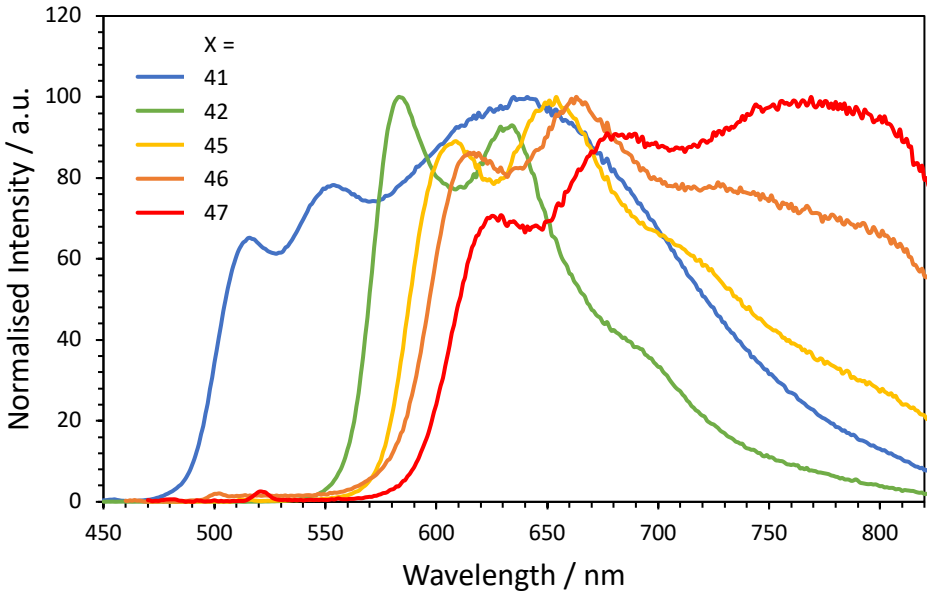

Figure 5.21: *Emission spectra of complexes $L^xPt_2(acac)_2$ in dilute degassed DCM solution at RT.*

The chloro-substituted dimer intermediate $(PtL^{44}Cl)_2$ is also intensely luminescent in DCM solution (**Figure 5.22**) with an impressive PLQY of 0.47 and a relatively long lifetime of 26 μs (**Table 5.3**) that does not significantly change with concentration; the second pyridine ring and monodentate chloro ancillary ligand are sufficient to displace the d-d states to high enough energy to favour luminescence. The emission of $(PtL^{44}Cl)_2$ is blue-shifted compared to the closest analogous acac complex $L^{42}Pt_2(acac)_2$ that differs only in the position of attachment of the thpy ligand to the xanthene linker. This demonstrates first-hand the greater σ-donating effect of the acac ligand compared to pyridine and Cl^- as this serves to simultaneously raise the deactivating MC states whilst lowering the MLCT state, leading to a red shift in the emission of 15 nm.

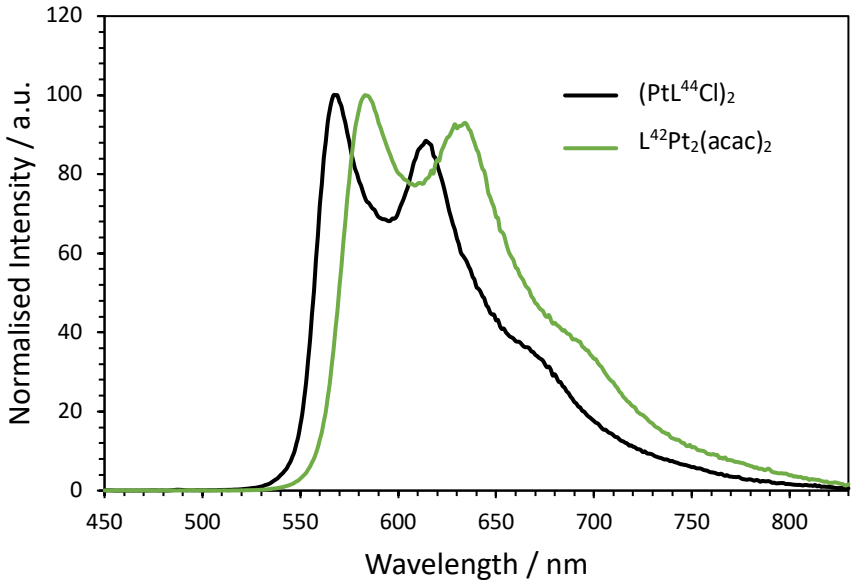

***Figure 5.22**: Emission spectra of $(PtL^{44}Cl)_2$ and $L^{42}Pt_2(acac)_2$ in degassed DCM solution at RT at concentrations of 5.1×10^{-6} M and 4.8×10^{-6} M respectively.*

Emission spectra of all complexes were recorded in dilute and saturated DCM solution, and at various concentrations in between; $L^{42}Pt_2(acac)_2$, where L^{42} features thpy, has the same emission spectrum irrespective of concentration, showing purely monomeric emission as seen in **Figure 5.22**. This suggests that complexes featuring thpy are less likely to form excimers. This complex also has an almost zero value for k_{SQ}. However, the PLQY for this complex is only 0.18 as k_{nr} is relatively large compared to k_r (40×10^3 and 8×10^3 s^{-1} respectively).

The equivalent complex $L^{41}Pt_2(acac)_2$ with ppy in place of thpy exhibits a broad, long-wavelength emission band peaking at 635 nm (**Figure 5.23**), though the emission spectrum is concentration-independent over the concentration range investigated. This implies that this band arises from an excimer that is intramolecular in nature and therefore unaffected by concentration. The lifetime of the species emitting at 650 nm is the same as that at 520 nm at all concentrations investigated, implying that the excimer decay follows that of the monomer.

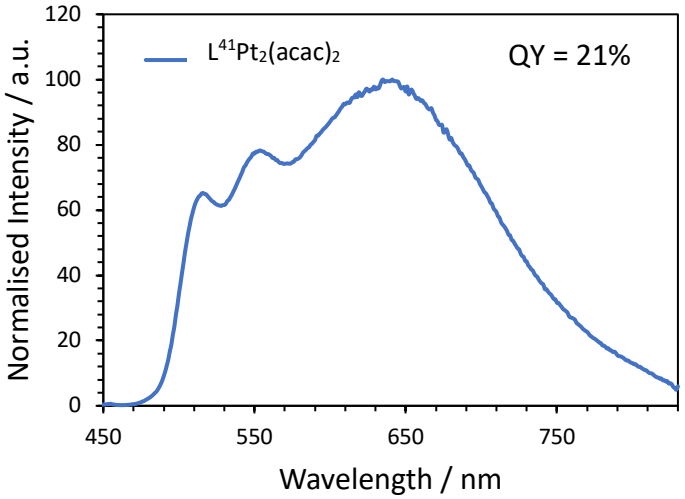

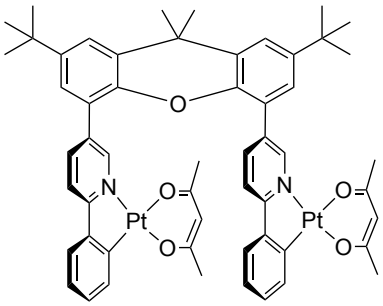

Conc / 10^{-5} M	τ at 520 nm / ns	τ at 650 nm / ns
28.9	1700	1700
6.07	1900	1900
0.32	2000	2000

Figure 5.23: *The emission spectrum of $L^{41}Pt_2(acac)_2$ in degassed DCM solution is identical at all concentrations investigated, shown in the table along with lifetimes of the monomer (at 520 nm) and excimer band (at 650 nm).*

$L^{45}Pt_2(acac)_2$ displays purely monomeric emission that does not change over the concentration range investigated (**Figure 5.24**). It would be interesting to study this complex in a neat film to see if excimeric interactions are present in the solid state. Despite not showing signs of strong Pt(N^C) intramolecular interactions, $L^{45}Pt_2(acac)_2$ has a very low PLQY of only 0.01.

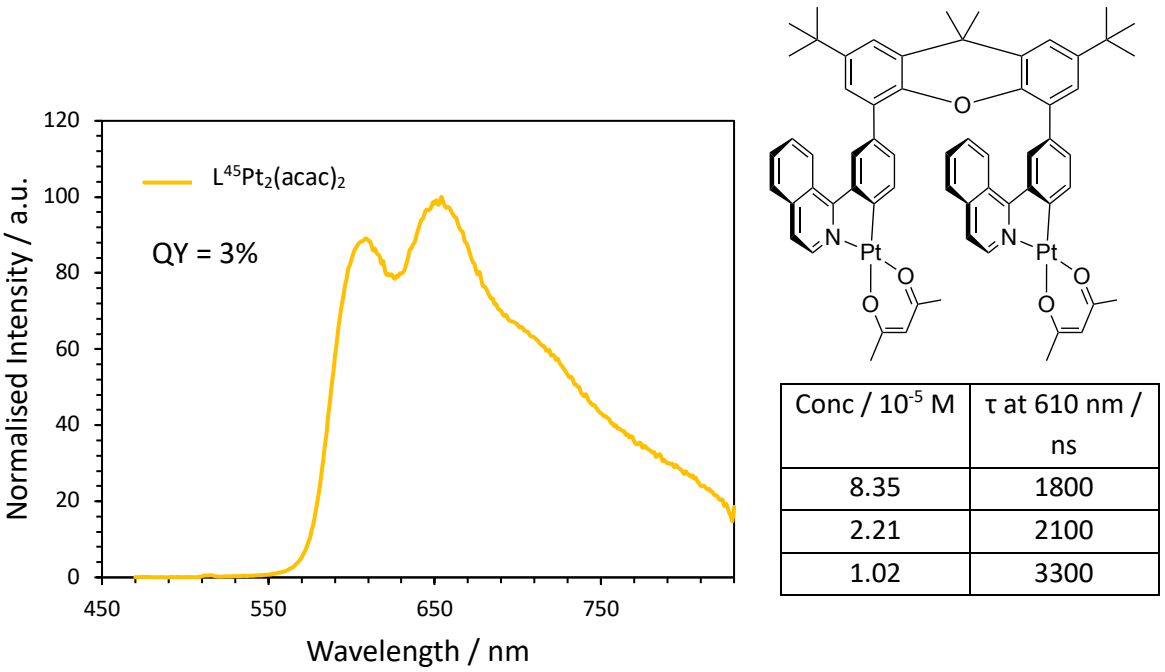

Conc / 10^{-5} M	τ at 610 nm / ns
8.35	1800
2.21	2100
1.02	3300

***Figure 5.24**: The emission spectrum of $L^{45}Pt_2(acac)_2$ in degassed DCM solution is identical at all concentrations investigated, shown in the table along with the corresponding lifetimes of the monomer (at 520 nm) and excimer band (at 650 nm).*

$L^{46}Pt_2(acac)_2$ differs from $L^{45}Pt_2(acac)_2$ only by the coordination position of the phenyl ring to the xanthene scaffold; both complexes have a similar emission profile, though the former shows an excimeric band centred around 800 nm that increases slightly with increasing concentration (**Figure 5.25**). This suggests that intermolecular interactions also come into play for $L^{46}Pt_2(acac)_2$, though intramolecular interactions are also likely to be present as this excimeric band can be observed even in dilute solution (7.3×10^{-6} M). $L^{46}Pt_2(acac)_2$ also has a low PLQY of 0.02.

The excimer emission band of $L^{47}Pt_2(acac)_2$ is more prominent than for $L^{46}Pt_2(acac)_2$ at all concentrations investigated, and the band exceeds in intensity the monomer emission. This is likely due to the close Pt···Pt interaction in $L^{47}Pt_2(acac)_2$ enabled by the additional phenyl ring between the N^C ligand and the xanthene ring giving more flexibility to the system. The emission of $L^{47}Pt_2(acac)_2$ also changes with concentration (**Figure 5.26**); the emission profile of the solutions at 3.4×10^{-6} M to 2.4×10^{-5} M stays relatively constant. In the most saturated solution at 1.28×10^{-4} M, the excimer band increases in intensity, suggesting that intermolecular interactions

start to play a role. Another possible explanation is that at elevated concentration, the Pt(N^C) units are forced even closer together within each molecule, thereby increasing the intramolecular interaction. The lifetime measured at 750 nm did not change over the concentration range investigated.

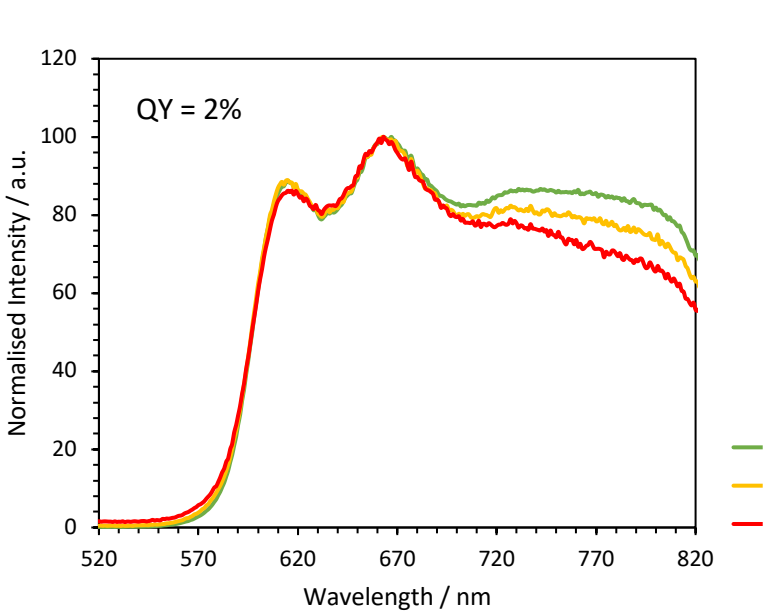

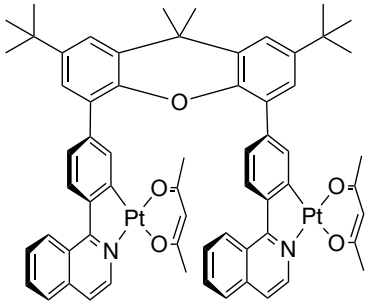

Conc / 10^{-5} M	τ at 625 nm / ns	τ at 750 nm / ns
2.39	2300	110
0.34	2500	110
12.8	1900	110

Figure 5.25: *Concentration-dependent emission spectra of $L^{46}Pt_2(acac)_2$ in degassed DCM solution at RT.*

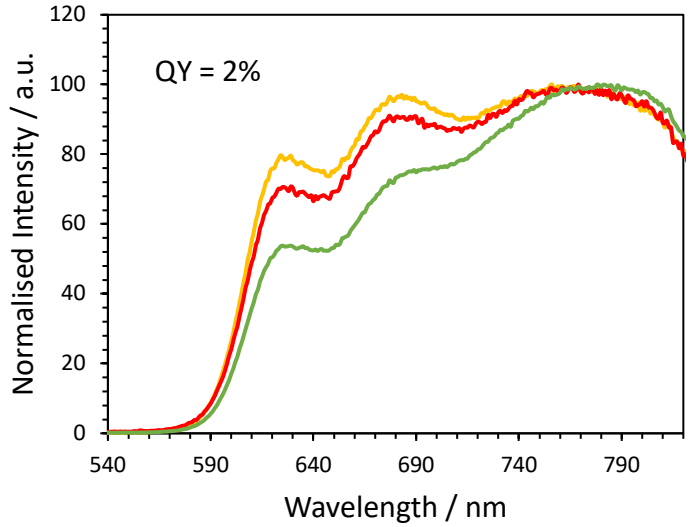

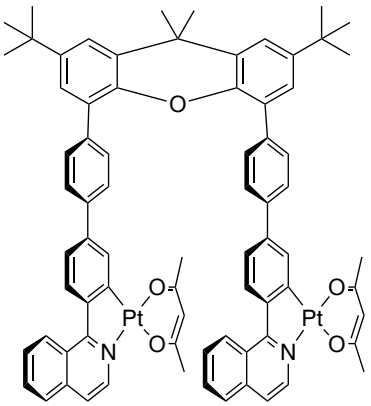

Conc / 10^{-5} M	τ at 615 nm / ns	τ at 800 nm / ns
11.0	2600	300
2.39	2600	300
0.73	2800	350

Figure 5.26: *Concentration-dependent emission spectra of $L^{47}Pt_2(acac)_2$ in degassed DCM solution at RT, normalised to λ_{max} which is the excimer band in this case.*

Complexes featuring triazole ligands

The emission of triazole-substituted complexes in dilute DCM solution is shown in **Figure 5.27**. As predicted from the absorption spectra, the emission spectra of $L^{42}Pt_2$(*t*-Bu-triazole)$_2$ and HL^{42}Pt(OMe-triazole) are identical, suggesting that there is no influence of the *t*-Bu or OMe substituents. Moreover, there is no effect of having the second Pt centre in the complex on the monomeric emission, other than reducing the PLQY from 0.35 for HL^{42}Pt(OMe-triazole) to 0.24 for $L^{42}Pt_2$(*t*-Bu-triazole)$_2$. The spectrum of $L^{41}Pt_2$(*t*-Bu-triazole)$_2$ is much broader than that of $L^{42}Pt_2$(*t*-Bu-triazole)$_2$, in moving from thpy to ppy, potentially due to some excimer formation, though if this is the case then the excimer is emitting at relatively high energy.

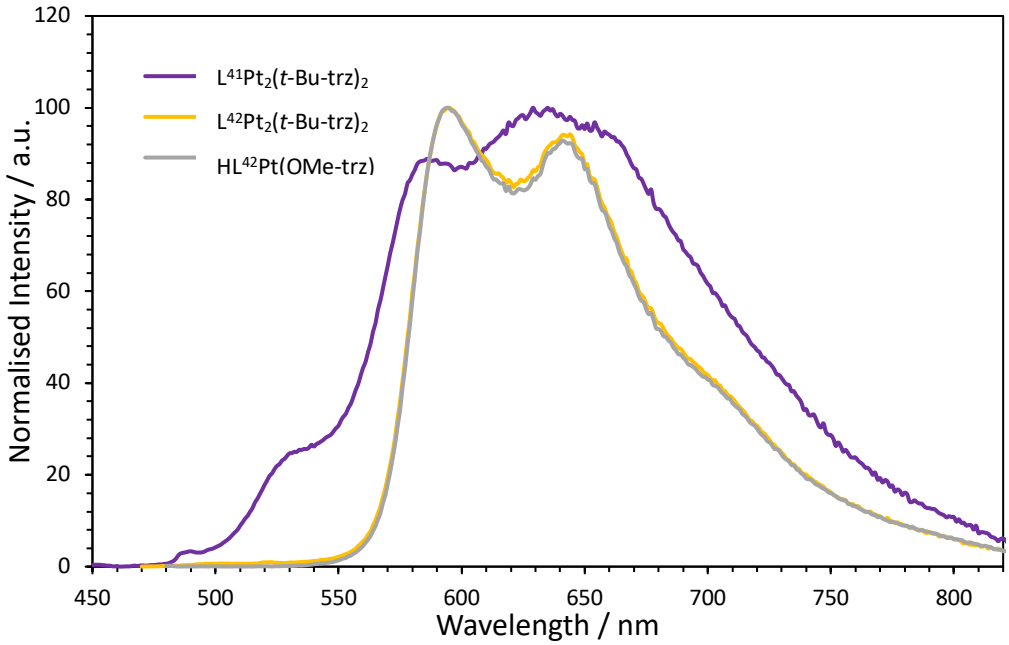

Figure 5.27: *Emission spectra of $L^{41}Pt_2$(t-Bu-triazole)$_2$, $L^{42}Pt_2$(t-Bu-triazole)$_2$ and HL^{42}Pt(OMe-triazole) in degassed DCM solution at concentrations of 1.29 × 10^{-5} M, 1.54 × 10^{-5} M, and 5.44 × 10^{-6} M respectively.*

The emission spectra of $L^{42}Pt_2$(*t*-Bu-triazole)$_2$ and HL^{42}Pt(OMe-triazole), where both complexes feature thpy, do not change with concentration, over the range investigated, which was up to 6.8 × 10^{-4} M and 2.3 × 10^{-4} M for each respectively. This follows the observed trend for the acac-substituted complexes above where $L^{42}Pt_2$(acac)$_2$ did not form excimers. On the contrary, the emission spectrum of $L^{41}Pt_2$(*t*-Bu-triazole)$_2$ does change with concentration; as the concentration

increases, the monomer-like bands at 531 and 587 nm disappear (**Figure 5.28**). The lifetime also becomes extremely short at 1.6 × 10^{-4} M. This is likely due to the emission at 1.6 × 10^{-4} M being solely from the excimer species, as opposed to the lower concentrations where the monomer is present, as at 660 nm there will be some overlap of the monomer emission with the excimer so this will be reflected in the lifetime. More information confirming the structure of these complexes, such as a crystal structure, would be helpful in interpreting the data.

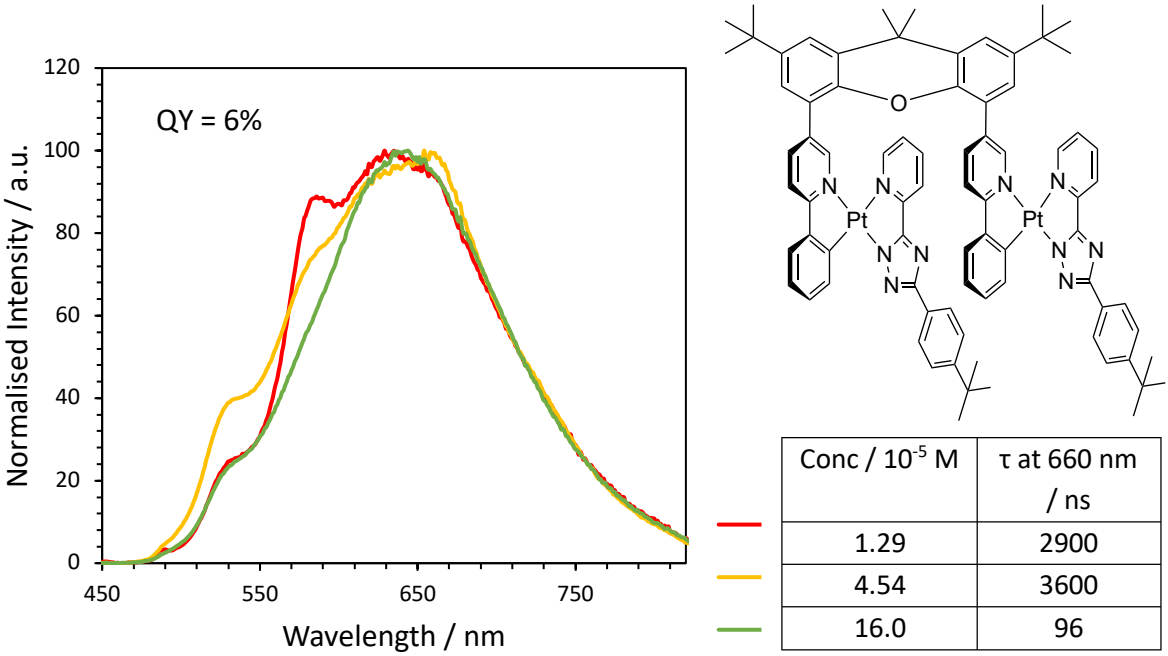

Conc / 10^{-5} M	τ at 660 nm / ns
1.29	2900
4.54	3600
16.0	96

Figure 5.28: *Concentration-dependent emission spectra of $L^{41}Pt_2$(t-Bu-triazole)$_2$ in degassed DCM solution, normalised to λ_{max} which is the broad excimer emission in each case.*

Complexes featuring triazole ligands reported by Walden *et al.*[101] showed red emission at elevated concentration due to bimolecular excited states, and green emission in dilute solution. Although the complexes presented here also feature ppy so are not a direct comparison, it does suggest that the xanthene unit is promoting excimeric interactions for $L^{41}Pt_2$(*t*-Bu-triazole)$_2$ as the emission is dominated by the broad band even in dilute solution.

Table 5.3: *A summary of the photophysical properties of dinuclear complexes featuring bidentate ligands in dilute degassed (aerated in parentheses) DCM solution at 298 K.*

Complex	λ_{abs} / nm (ε / M^{-1} cm^{-1})	λ_{em} / nm (monomer)	λ_{em} / nm (excimer)	Φ_{lum} [aer]	τ / ns [aer]	τ_0 / μs	k_r / 10^3 s^{-1}	$\sum k_{nr}$ / 10^3 s^{-1}	k_{SQ} / 10^9 M^{-1} s^{-1}	$k_Q(O_2)$ / 10^8 M^{-1} s^{-1}
$(PtL^{44}Cl)_2$	259 (27700), 294 (32600), 337 (23600), 425 (3110)	568, 618, 675	-	0.47 [0.02]	26000 [780]	26.5	18	20	0.01	5.7
$L^{41}Pt_2(acac)_2$	255 (70400), 291 (51400), 330 (30800), 371 (12200), 400 (10800)	521, 558	635	0.21 [0.02]	2000 [250]	2.0	105	392	0.31	16.3
$L^{42}Pt_2(acac)_2$	250 (43500), 307 (35700), 341 (34500), 425 (13600), 430 (13100), 443 (11200)	583, 636, 694	-	0.18 [0.01]	21000 [570]	20.8	8	40	0.04	7.7
$L^{45}Pt_2(acac)_2$	270 (63500), 318 (44300), 355 (18400), 369 (17000), 410 (11300), 465 (5260)	611, 654	-	0.03 [0]	3300 [320]	3.0	8	294	2.8	7.4
$L^{46}Pt_2(acac)_2$	255 (59300), 292 (38600), 372 (22900), 407 (14700), 435 (10100), 459sh (7520)	619, 664, 732	802	0.02 [0.01]	2800 [240]	-	6	351	-	17.6
$L^{47}Pt_2(acac)_2$	265 (63100), 311 (46800), 333 (39200), 380 (34200), 450 (11900)	628, 682	774	0.02 [0.01]	2800 [340]	1.03	6	397	2.5	11.6
$L^{41}Pt_2$(*t*-Bu-triazole)$_2$	266 (25600), 303sh (16000), 354 (6770), 425 (1370)	531, 586	639	0.06 [0.03]	2900 [120]	-	22	349	-	36.3
$L^{42}Pt_2$(*t*-Bu-triazole)$_2$	260 (22900), 307sh (17300), 439 (1170), 450 (1070)	595, 645, 702sh	-	0.24 [0.02]	16000 [760]	-	15	47	-	5.7
$HL^{42}Pt$(OMe-triazole)	275 (49400), 314 (47500), 333 (34600), 448 (4350), 405 (1570), 465 (4830)	594, 645, 701sh	-	0.35 [0.02]	15000 [620]	14.9	24	44	0.01	7.0
$L^{48}Pt_2(ppy)_2$	256 (95100), 281 (67800), 316 (37200), 330 (34200), 373 (21700), 395 (12800)	486, 518, 554	654	0.08 [0.03]	3680 [230]	0.7	23	249	2.46	18.4

5.3.3 An alternative flexible linker

Preliminary research was carried out at the end of this project into an alternative linker, featuring two acac units that is flexible so that intramolecular interactions between the Pt(N^C) units are possible but not forced. Only one pure complex was isolated and its photophysical properties studied, still it gives an insight into this concept of a flexible linker for bidentate Pt(II) complexes and has provided ideas for future work. The compound used as a linker, L^{48} (**Scheme 5.9**) was reported in the late 80s by Maverick *et al.*[156] where it was used to bind to Cu(II), and has since been reported in complexes with V(II)[157] and Fe(III)[158], and more recently again with Cu(II) in prism structures[159,160], though the linker has never been used to coordinate to Pt(II).

5.3.3.1 Synthesis

The linker L^{48} was synthesised in two steps: firstly, *m*-xylene was brominated using N-bromosuccinimde (NBS) with a catalytic amount of benzoyl peroxide and carbon tetrachloride as the solvent (**Scheme 5.9**). This intermediate **I23** was then added to a stirred mixture of acetylacetone and sodium carbonate in acetone at 0°C, which was then heated to reflux overnight to yield the proligand L^{48} in 20% yield.

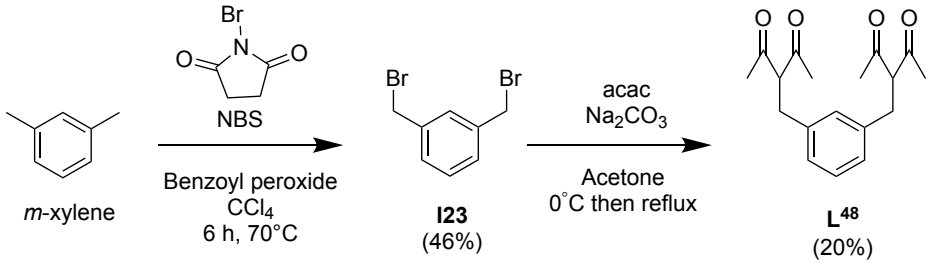

Scheme 5.9: *Synthesis of L^{48}.*

L^{48} can then replace acac in the same kind of synthesis described above in section 5.3.1; ppy was reacted with K_2PtCl_4 to obtain the μ-Cl dimer which was then reacted with L^{48} to give the final complex $L^{48}Pt_2(ppy)_2$ (**Scheme 5.10**). This reaction was low yielding as significant amounts of mononuclear product were present and isolation of the desired dinuclear complex required a preparative column with DCM as the

eluent and numerous recrystallisations from DCM/hexane. The reaction was also attempted with thpy in place of ppy, though the desired product could not be successfully purified.

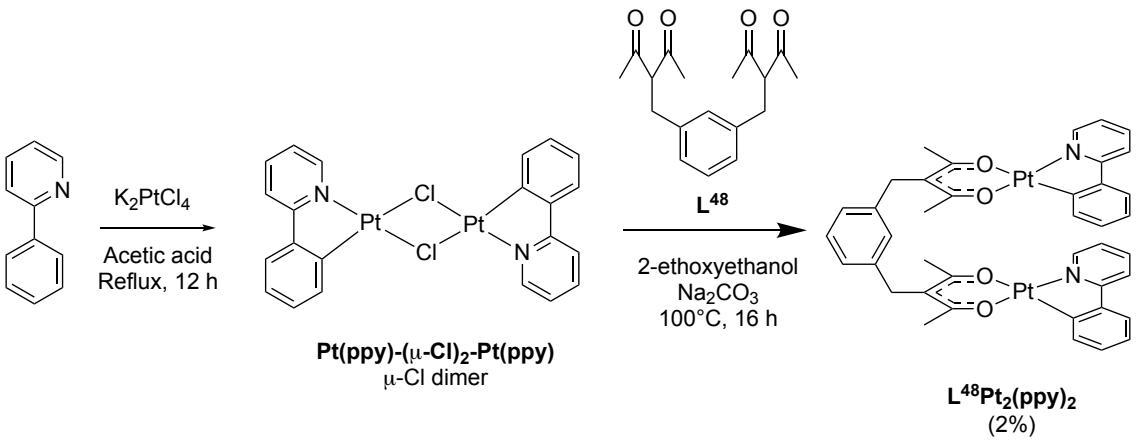

Scheme 5.10: *Synthesis of $L^{48}Pt_2(ppy)_2$.*

5.3.3.2 Photophysical properties

The absorption spectrum of $L^{48}Pt_2(ppy)_2$ exhibits high intensity LC transitions below 330 nm and a broader MC band between 330 and 430 nm (**Figure 5.29a**). The absorption spectrum does not change with concentration, with no appearance of an MMLCT band that would suggest the complex is aggregating; the Beer-Lambert law is obeyed.

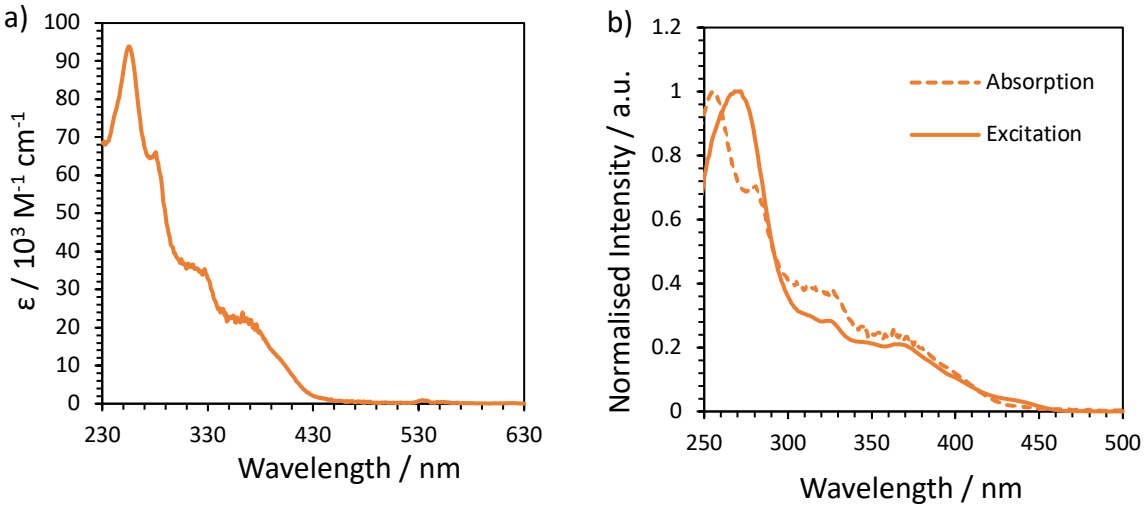

Figure 5.29*: a) Absorption spectrum of $L^{48}Pt_2(ppy)_2$, and b) comparison to the excitation spectrum at 520 nm in degassed DCM solution at concentration 2.89 × 10^{-6} M.*

The emission spectrum of $L^{48}Pt_2(ppy)_2$ in dilute DCM solution consists of purely structured monomer emission with the 0,1 component being the most intense transition peaking at 519 nm (**Figure 5.30**). As the concentration is increased, we observe the appearance of a broad long wavelength band peaking at 655 nm. This is likely due to an intermolecular excimer as the band is only observed at high concentration, suggesting that the species is not present in the closed form as there is no evidence of intramolecular excimer formation (**Figure 5.31**). The absorption spectrum matches the excitation spectrum (at λ_{em} = 510 nm) implying there is only one chromophore present (**Figure 5.29b**). Moreover, a rise time in the emission can be observed from the TCSPC decay (**Figure 5.32**) giving more evidence that the bimolecular species is intermolecular in nature as it requires time to form, i.e. for diffusion of one monomer in the ground state to find another in the excited state and form an excimer. The value of k_{SQ} is also relatively large at 2.46×10^9 M^{-1} s^{-1} (**Table 5.3**).

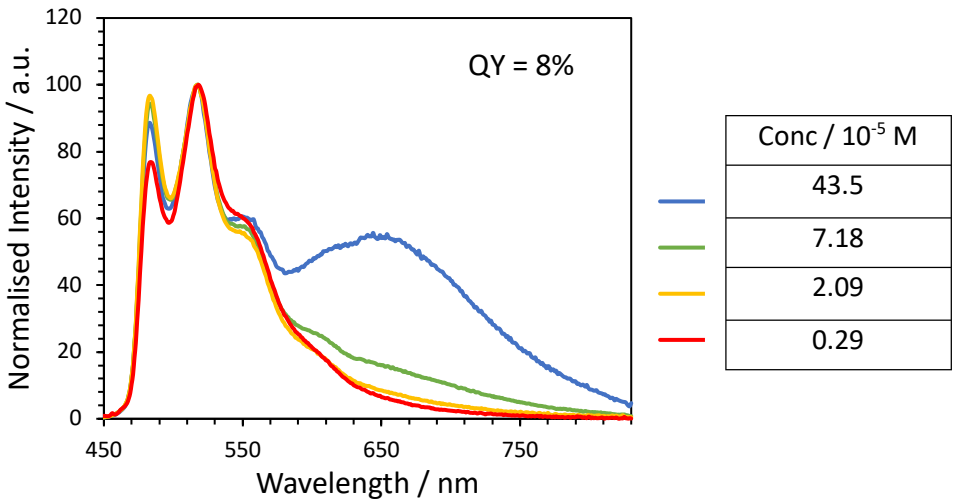

***Figure 5.30**: Concentration-dependent emission of $L^{48}Pt_2(ppy)_2$ in degassed DCM solution at RT, normalised to λ_{max} which is the 0,1 transition in this case at 519 nm.*

More photophysical studies in different solvents of various polarities would be interesting to see if this affects the ratio of the monomer to excimer emission, and if intramolecular interactions (i.e. the closed form) can be forced. There are many more complexes of this type that could be explored, including also attaching the ppy N^C

ligand onto a similar linker that would enclose the complex and force the intramolecular interactions. This will be discussed further in Chapter 6 (Future Work).

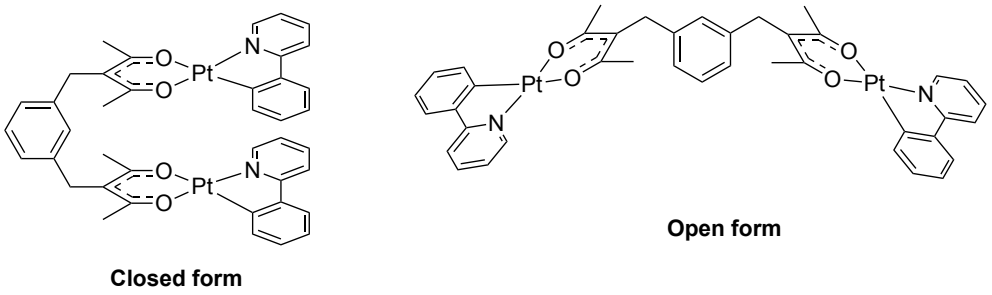

Figure 5.31: Possible conformations (closed and open form) of $L^{48}Pt_2(ppy)_2$.

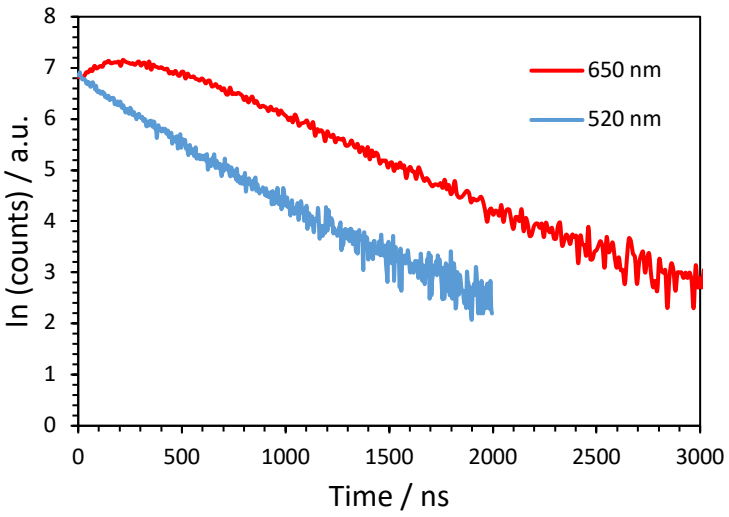

Figure 5.32: TCSPC decay curves for the monomer and excimer emission of $L^{48}Pt_2(ppy)_2$, probed at 520 and 650 nm respectively.

5.4 Chapter 5 summary

A series of dinuclear Pt(II) complexes featuring bidentate N^C ligands tethered onto a xanthene scaffold have been synthesised and their photophysical properties analysed. Overall, the PLQYs of the complexes of the type $L^xPt_2(acac)_2$ are lower than the complexes presented in Chapter 4 with tridentate ligands (0.12 to 0.16 for Class I and 0.09 to 0.29 for interlocked compounds); here they range from 0.02 to 0.21, the higher values only observed for complexes $L^{41}Pt_2(acac)_2$ and $L^{42}Pt_2(acac)_2$ with

the highest energy monomer emission. As the monomer emission is red shifted by incorporating isoquinoline rings with extended conjugation, the PLQY drops to 2%. The lower PLQY values compared to analogous complexes with tridentate ligands presented in Chapter 4 can be possibly rationalised by the denticity of the ligands; higher denticity favours more efficient emission due to the rigidity of the structure. Nevertheless, novel compounds have been presented with the ability to tune the colour of emission through structural modification of the N^C moiety, as well as enabling intramolecular excimeric interactions that emit in the NIR region of the spectrum, with a λ_{max} of 777 nm for the most red-shifted excimer emission seen for $L^{47}Pt_2(acac)_2$.

Further complexes were made with triazole ligands in place of acac. Only $L^{41}Pt_2$(*t*-Bu-triazole)$_2$ (where the N^C unit in L^{41} is ppy) showed evidence of an intramolecular excimer, whereas both $L^{42}Pt_2$(*t*-Bu-triazole)$_2$ and HL^{42}Pt(OMe-triazole) (where the N^C unit in L^{42} is thpy) only showed monomer emission in degassed DCM solution at all concentrations investigated. No complex featuring thpy as the N^C ligand showed excimer formation; the linker is not able to force excimeric interactions in these complexes despite holding them in a favourable geometry suggesting that complexes based on thpy are not prone to excimer formation. The emission spectral profile of $L^{42}Pt_2$(*t*-Bu-triazole)$_2$ and HL^{42}Pt(OMe-triazole) were identical implying that the different substituents on the triazole ring do not affect the wavelength of emission, as well as the presence of the second Pt centre. Further research is needed into these types of complexes, in particular a crystal structure to confirm the conformation of the triazole ligands in the complexes.

Finally, complex $L^{48}Pt_2(ppy)_2$ was presented featuring a flexible linker that could allow intramolecular interactions but does not force them. In dilute degassed DCM solution, only structured monomer emission was observed. A broad long wavelength excimer emission band peaking at 654 nm appeared as the concentration increased, likely due to intermolecular excimers as opposed to intramolecular.

Chapter 6

6. Concluding remarks and future work

The overarching aim of this project was to achieve red-shifted emission in the NIR region of the electromagnetic spectrum through structural modification of Pt(II) complexes featuring cyclometallating ligands. A range of mono- and dinuclear Pt(II) complexes has been prepared and their photophysical properties studied. The PL was tuned towards the deep-red/NIR region of the spectrum by exploiting excimeric interactions, both intermolecularly for mononuclear complexes, and intramolecularly for dinuclear complexes. NIR OLEDs were prepared using a selection of these complexes that showed some impressive results, with λ_{max} squarely in the NIR with no contamination from visible light.

Chapter 2 focused on the synthesis of Pt(II) complexes with symmetric N^C^N-coordinating ligands. Modification of the ancillary ligand produced interesting results. Exchanging the ancillary chloro ligand for SCN/NCS led to blue-shifted excimer emission in solution but a significant red shift of the PL in the solid state, assigned to the formation of extended aggregates. PtL^1SCN, in particular, showed an impressive λ_{max} of 944 nm in a NIR OLED with the onset of emission starting at $\lambda >$ 700 nm and an EQE of 0.3% (**Figure 6.1**). Exchanging the chloro ancillary ligand for iodo led to a fourfold increase in the EQE relative to PtL^1Cl (4.1% and 0.8% respectively), whilst retaining a similar value of λ_{max} as for the parent chloro complex (λ_{max} = 736 nm and 765 nm respectively). The most efficient NIR OLED achieved has EQE = 4.7 % and reaches a maximum radiosity of 5.09 mW cm^{-2} with λ_{EL} = 726 nm, using PtL^2I as the EML.

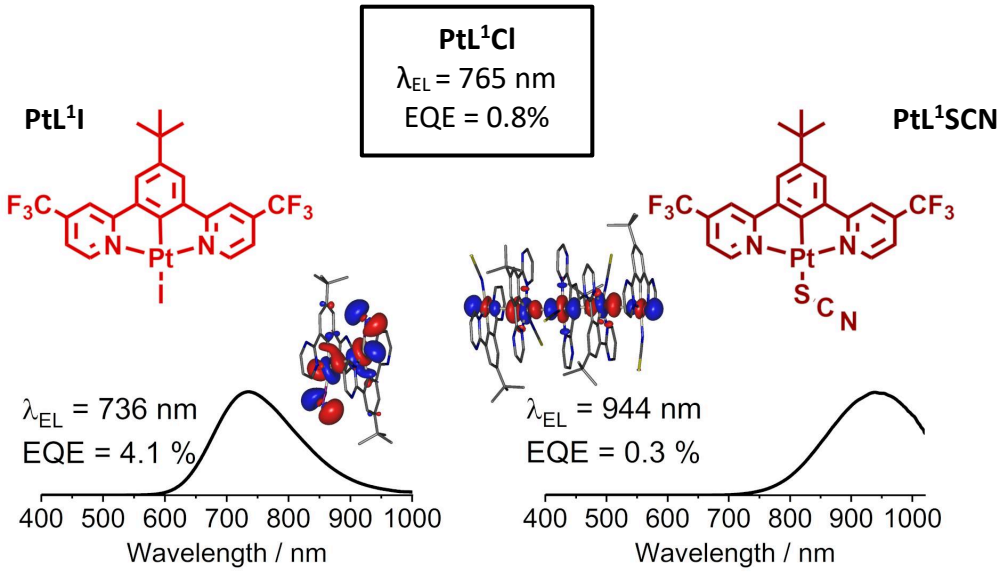

Figure 6.1: *PtL[1]I (left) showed a fourfold increase in the EQE compared to PtL[1]Cl. PtL[1]SCN (right) showed significantly red shifted EL compared to PtL[1]Cl. OLED devices were fabricated by Dr Piotr Pander (Durham University Physics Department).*

Future work in this area should be aimed at studying the emission of more thiocyanate complexes in the solid state, for example PtL[3]NCS featuring 1-isoquinoline (**Figure 6.2**). The monomer and excimer emission for this complex is already red shifted due to the extended conjugation of the isoquinoline rings compared to pyridine, so it would be interesting to study the emission of this complex in the solid state. The corresponding isomer with 3-substituted isoquinoline units could also be targeted and studied as we have shown that complexes featuring 3-substituted isoquinoline are more prone to excimer formation.

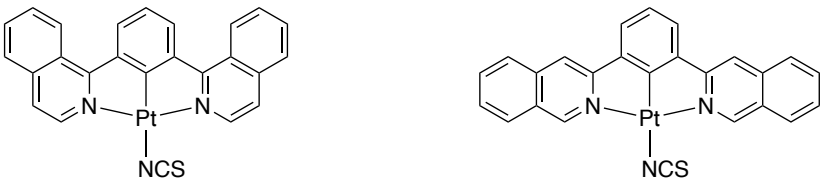

PtL[3]NCS

Synthesised in this work

Solution-state λ_{max} (excimer) = 760 nm

PtL[4]NCS

Potential target

Figure 6.2: *The solid-state emission of PtL[3]NCS should be studied, as well as synthesising PtL[4]NCS and studying the photophysical properties in both solution and solid-state.*

Moreover, both SCN and NCS binding modes were observed during this work, with the most red shifted EL seen for PtL^1SCN which exhibited binding to the Pt via S. It would be useful to establish a tool to confirm the binding mode of such complexes instead of relying upon crystal structures, for example using salicylic acid as a standard to compare the IR spectra. It has also been postulated that the thiocyanate complexes can isomerise in solution, if the energies of the S and N bound complexes are comparable. It would be interesting to synthesise a wider range of these complexes to see how varying the N^C^N ligand affects the binding mode of the thiocyanate ligand. The ligand exchange reaction could also be carried out at different temperatures and in various solvents to see if this affects which isomer is obtained.

A range of Pt(II) complexes featuring asymmetrically substituted N^C^N-coordinating ligands was synthesised utilising palladium cross-coupling reactions to target the ligands. The excimer emission of the complexes varied depending on the substituents, even if the monomer emission was dictated by the heterocycle of the lowest energy (**Figure 6.3**). Incorporating heterocycles with EWGs red shifted the excimer emission, whilst EDGs resulted in a blue shift. Complexes featuring pyrimidine rings sat somewhere in between, whilst 3-substituted isoquinoline slightly red-shifted the excimer. Incorporating 1-substituted isoquinoline reduced the propensity of the complexes to form excimers, though when they do form, they are significantly red shifted by around 70 nm compared to the analogous pyridine complex.

DFT studies could be carried out in future work to support these experimental results. It would be useful to see where the LUMO is located, especially for the 3-substituted isoquinoline complexes where we observed unimolecular emission with overlapping peaks, seeming to suggest contribution from both the 3-substituted isoquinoline unit and the pyridine ring to the emissive state. Supporting these experimental results with computational/theoretical analysis could help to provide a tool to tune the excimer emission energy of Pt(N^C^N)Cl-type complexes.

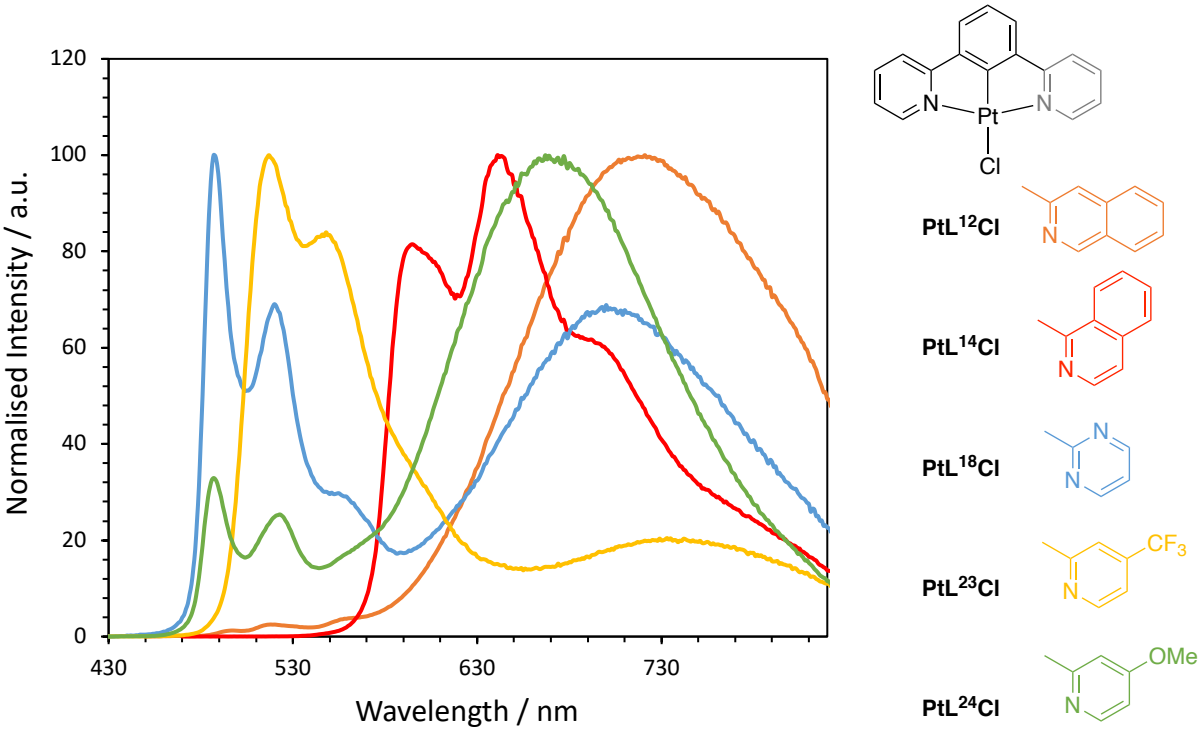

Figure 6.3: *Photoluminescence emission spectra of complexes bearing one unsubstituted pyridine ring in concentrated degassed DCM solution a 298 K showing excimer formation. Spectra are normalised to* λ_{max}.

Dinuclear sandwich complexes with tridentate (Chapter 4) or bidentate (Chapter 5) ligands also offer a route to deep-red/NIR emission as the substituted-xanthene linker employed holds the Pt(N^C^N) units in a favourable geometry to form intramolecular excimers. Purely broad long-wavelength excimer emission was observed for most sandwich complexes presented, even in dilute solution. For $L^{32}(PtCl)_2$, a combination of monomeric and excimeric emission was observed (**Figure 6.4**). Incorporating an additional xanthene linker into the molecular design to form the interlocked complex $L^{32}Pt_2L^{35}$ resulted in purely excimeric emission.

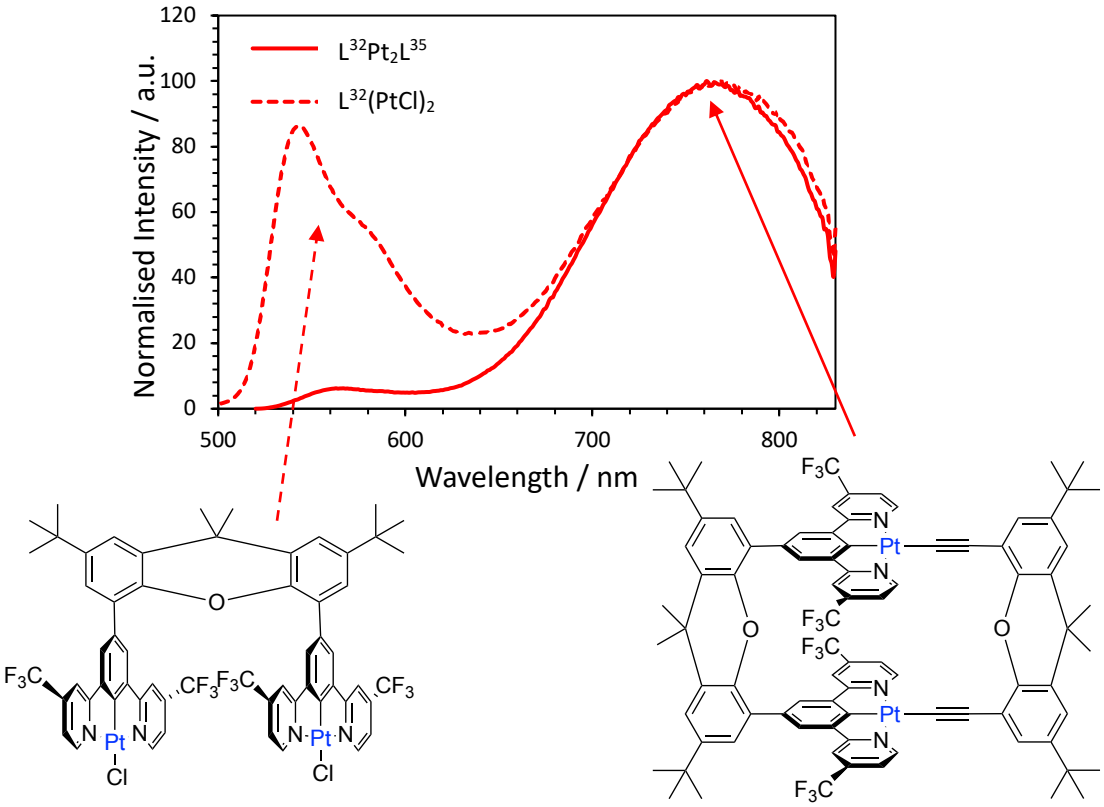

***Figure 6.4**: Interlocking the sandwich complex with an additional xanthene unit led to purely excimeric emission in dilute DCM solution.*

An additional linker was designed to hold the Pt(N^C^N) units roughly 7 Å apart, which led to complexes that showed concentration-dependent excimeric emission assigned to intermolecular interactions (**Figure 6.5**). This area was only investigated at the end of this project, so more research needs to be done in the area, though we have seen some promising results. The excimeric emission was significantly red shifted compared to the xanthene-linked analogues, potentially suggesting these complexes are forming zip-like structures involving multiple Pt(N^C^N) units in the excited state interaction, hence the red shift in the emission. It would be interesting to study these complexes in the solid-state to see if the PL is dominated by the aggregated/excimeric species. Additionally, a small aromatic planar molecule such as pyrene could be titrated into a solution of the dinuclear sandwich complex, and the emission studied to see if excimeric interactions are formed where in which the small molecule slots itself in between the Pt(N^C^N) units. This could be interesting to see if the excimeric emission could be shifted further towards the NIR region.

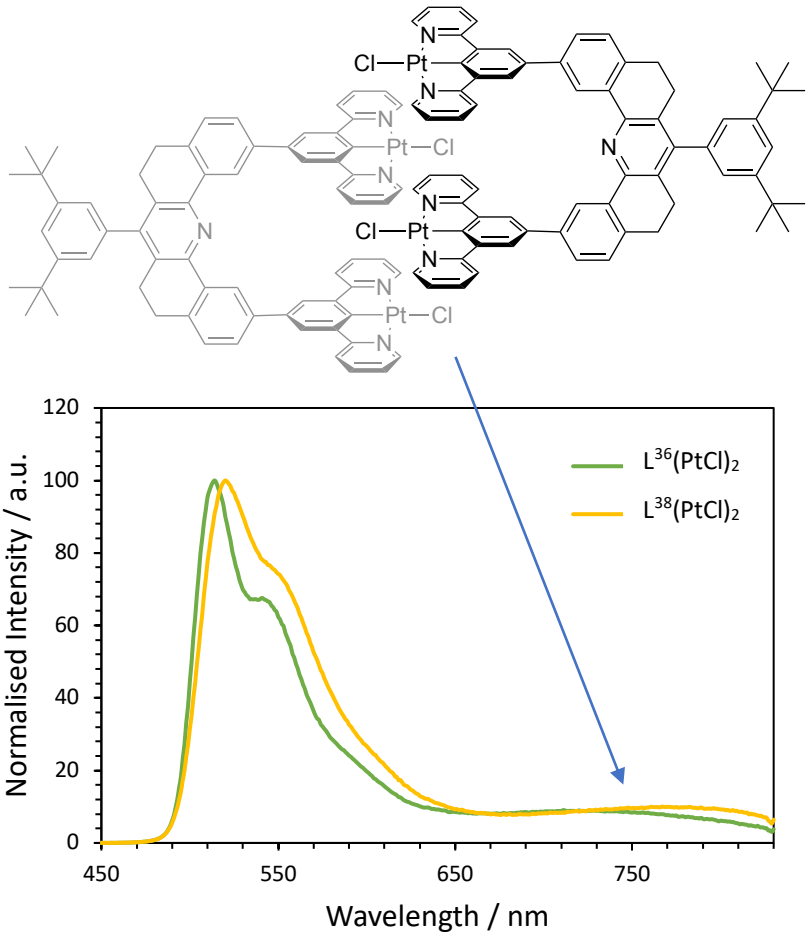

Figure 6.5: *Emission spectra of $L^{36}(PtCl)_2$ and $L^{38}(PtCl)_2$ (analogous complex with pyrimidine rings in place of pyridine) in concentrated degassed DCM solution reveals some concentration-dependent excimer formation potentially due to the formation of a zip-like structure as pictured.*

A flexible linker bearing acac units was employed to give the complex $L^{48}Pt_2(ppy)_2$. Despite there being possible open and closed forms of this complex (**Figure 6.6**), where the closed form should show intramolecular excimers, concentration-dependent excimer emission was observed suggesting the observed excimer is intermolecular in nature. Future studies could be directed towards measuring the emission spectra in various solvents of different polarities to see if certain solvents favour the intramolecular interactions. Another target complex is proposed (**Figure 6.7**) where the ppy units are also linked together. This complex is very similar to the interlocked complexes presented in Chapter 4, and should force intramolecular interactions for these complexes (i.e. the closed form), whilst the arms of the linker

should still allow some flexibility in order for the Pt units to arrange themselves in the most favourable geometry.

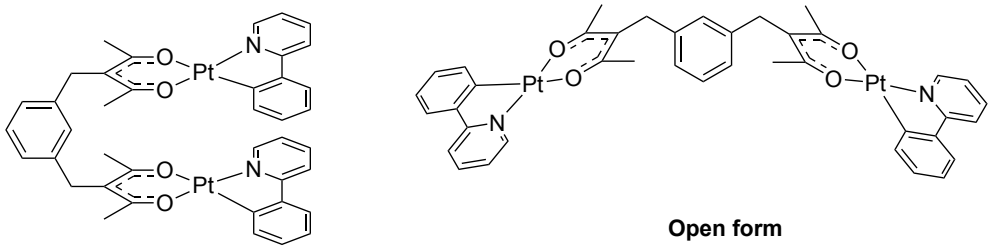

***Figure 6.6**: Possible closed and open conformations of $L^{48}Pt_2(ppy)_2$.*

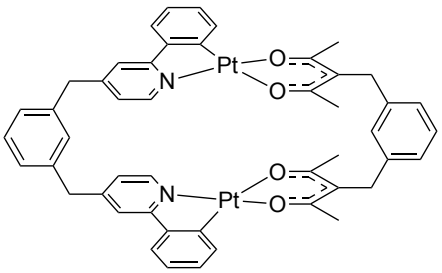

***Figure 6.7:** Target interlocked complex based on $L^{48}Pt_2(ppy)_2$ that should force intramolecular interactions between the Pt(N^C) units and hopefully lead to intramolecular excimer formation.*

Another potential area for research is mixed metal Pt(II)/Ir(III) complexes, as discussed in Section 4.1.1. There is another possible bidentate N^C-binding site for $PtL^{30}Cl$ presented in Chapter 2. This complex was reacted with another equivalent of K_2PtCl_4, which was anticipated to form a chloro-bridged dimer structure, which could then be cleaved by acac (**Scheme 6.1**). The reaction was unsuccessful and only $PtL^{30}Cl$ was recovered. Ir(III) could potentially be incorporated into the design to form a complex with one Ir(III) centre and three Pt(II) centres (**Figure 6.8**), similar to complex **19** reported by Turnbull *et al.* (section 4.1.1).[122] The synthetic route can be tried both ways by first incorporating Ir(III) and then Pt(II), or by using $PtL^{30}Cl$ as a starting material to react with $IrCl_3$. Nevertheless, it would be interesting to synthesise this molecule to see if the emission can be red-shifted with respect to $PtL^{30}Cl$.

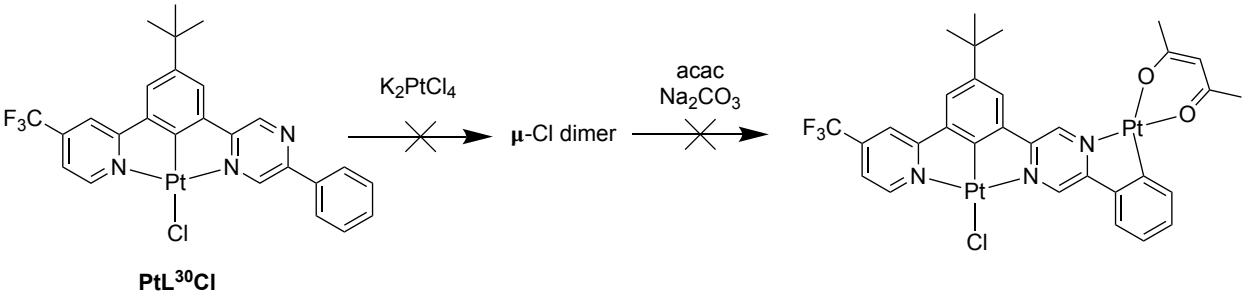

PtL^{30}Cl

Scheme 6.1: *Unsuccessful synthesis of a diplatinum complex based on PtL^{30}Cl.*

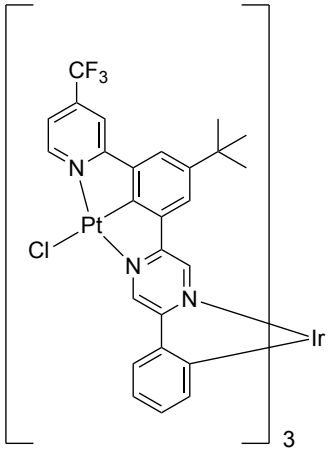

Figure 6.8: *Potential mixed-metal target complex for future work.*

Chapter 7

7. Experimental

7.1 Materials and methods

Commercial chemicals were used as supplied without further purification. Reactions requiring an inert atmosphere were carried out using Schlenk-line techniques under an atmosphere of argon or nitrogen. Thin layer chromatography analysis was performed on F254 silica plates and visualised by UV irradiation at 254 or 365 nm. NMR spectra were recorded on a Bruker Avance-400 spectrometer (400 MHz), a Varian VNMRS-600 (600 MHz) or a Varian VNMRS-700 (700 MHz). Two-dimensional NMR experiments, including homonuclear correlation spectroscopy (COSY), heteronuclear multiple bond correlation spectroscopy (HMBC) and heteronuclear single quantum coherence spectroscopy (HSQC), were used to aid assignments. Chemical shift values (δ) are reported in parts per million (ppm), coupling constants (J) are reported in Hertz (Hz), C^q denotes a quaternary carbon, and the spectra are referenced to residual protio solvent peaks: $CDCl_3$ = 7.26 (^1H), 77.2 (^{13}C); DMSO = 2.50 (^1H), 39.5 (^{13}C), CD_2Cl_2 = 5.32 (^1H), 53.8 (^{13}C).

Electrospray ionisation mass spectra (ESI) were recorded using a Waters Acquity TQD Tandem Quadrupole mass spectrometer or a Waters SQD mass spectrometer and an Aquity UPLC, with a column using water containing formic acid (0.1% /v) and either acetonitrile or methanol as the carrier solvent. Atmospheric pressure solids analysis probe (ASAP) ionisation mass spectra were obtained using a LCT Premier XE mass spectrometer and an Acquity UPLC from Waters Ltd at 350°C. High-resolution mass spectra were obtained using a Quantum time-of-flight (QTof) mass spectrometer.

Elemental analysis was performed by Dr. Emily Unsworth using an Exeter CE-440 Elemental Analyser device (Durham University elemental analysis service). Infrared analysis was carried out using a Perkin-Elmer Spectrum 100 Series FT-IR Frontier Spectrometer.

UV-Vis absorption spectra were recorded on a Biotech instruments UVIKON XS Spectrometer. Samples were contained in optically matched quartz cuvettes with a path length of 1 cm, and all spectra were run against a reference of pure solvent. Extinction coefficients (ε) were determined by a dilution technique of four stock solutions and graphical application of the Beer-Lambert law. Emission and excitation spectra in solution were acquired using an Instruments S.A. Fluoromax-2 spectrometer equipped with a Hamamatsu R928 photomultiplier tube. Samples that were to be measured in the absence of air were modified with appropriate glassware to allow connection to a high vacuum line. To remove air prior to the measurement, the sample was degassed within the cuvette by three freeze-pump-thaw cycles. Emission was detected at 90° to the excitation source with appropriate filters used where required to remove second-order peaks. All emission spectra were corrected for dark count and for the spectral response of the detector. Excitation spectra were automatically corrected upon measurement for lamp output through use of a beam splitter, which directs 8% of the excitation light to a reference photodiode.

Luminescence quantum yields were determined relative to a reference solution of ruthenium (II) tris-(2,2'-bipyridine) chloride (Φ_{std} = 0.04 ± 0.002 in air-equilibrated aqueous solution).[161] To measure the quantum yield, a sample of complex in DCM was prepared so that the absorbance at the chosen excitation wavelength was below 0.1 to minimise inner-filter effects. Quantum yields were calculated relative to the standard by applying **Equation 7.1** where Φ is the luminescence quantum yield, D is the integrated area under the corrected emission spectrum, $A(\lambda_x)$ is the absorbance at the excitation wavelength, and *n* is the refractive index of the solution. Subscripts, std, refer to the corresponding values for the standard. Quoted Φ values have an associated error of approx. ± 20%.

$$\Phi = \Phi_{\mathrm{std}} \left(\frac{\mathrm{D}}{\mathrm{D_{std}}}\right) \left(\frac{\mathrm{A_{std}}(\lambda_x)}{\mathrm{A}(\lambda_x)}\right) \left(\frac{n}{n_{\mathrm{std}}}\right)^2 \qquad (7.1)$$

Excited-state lifetime measurements were made using an Edinburgh Instruments OB 920 fluorimeter. Luminescence lifetimes of the complexes up to approximately 10 µs were measured by time-correlated single-photon counting, following excitation at 405 nm with an EPL-405 pulsed-diode laser. The emission was detected at 90° to the excitation source using a Peltier-cooled R928 after passage through a monochromator. The estimated uncertainty in quoted lifetimes, based on years of repeated measurements in the group using the equipment and comparison to well-known standards, is ±10% or better. Lifetimes in excess of 10 µs were measured by multi-channel scaling following excitation with a µs-pulsed xenon lamp. The lifetimes were obtained by least squares fitting to a monoexponential decay unless stated otherwise, and goodness-of-fit was confirmed by the residuals (assuring a X^2 value close to 1). Low temperature (77 K) experiments were performed using a glass vacuum cold finger apparatus built in house. A small amount of sample was placed in a 4 mm o.d. glass tube, which was inserted into the cold finger filled with liquid nitrogen.

Self-quenching constants were calculated from the slope of a plot of k_{obs} against concentration. The associated error on the k_{obs} value is the same as the error on the lifetime (±10%) as these values are inversely proportional to one another.[162] The concentration of each solution was determined from the absorbance and extinction coefficient using the Beer-Lambert law. Therefore, the error in the concentration value can be calculated using **Equation 7.2**, where Δc is the error in the concentration. The uncertainty in the extinction coefficient was calculated by linear regression of the slope fitted to obtain the values. It is difficult to determine exactly the associated error of an absorbance measurement, which will be larger at A < 0.05 due to a lower signal-to-noise ratio, and A > 1.5 due to inner filter effects. The uncertainty of the absorbance value is greater when reading from a slope, so a flat portion of the spectrum was chosen for each concentration to give a more accurate measurement. The errors have been overestimated in all cases.

$$(\frac{\Delta c}{c})^2 = (\frac{\Delta A}{A})^2 + (\frac{\Delta \varepsilon}{\varepsilon})^2 \quad (7.2)$$

OLED devices were fabricated by Dr Piotr Pander (Department of Physics, Durham University). OLEDs were fabricated by the vacuum thermal evaporation method. The

hole injection layer (HAT-CN) was deposited first followed by the hole-transport/electron-blocking layer (TSBPA). Subsequently, platinum(II) complexes were deposited as the emissive layer (EML). PO-T2T served as the electron transport/hole blocking layer, while LiF was the electron injection layer and Al the cathode. Devices of 4 × 2 mm pixel size were fabricated. Dipyrazino[2,3-f :2',3'-h]quinoxaline-2,3,6,7,10,11-hexacarbonitrile (HAT-CN, Lumtec, sublimed), 4,4'-(diphenylsilanediyl)bis(*N*,*N*-diphenylaniline) (TSBPA, Lumtec, sublimed), 2,4,6-tris[3-(diphenylphosphinyl)phenyl]-1,3,5-triazine (PO-T2T, LUMTEC), 1,3-bis(carbazol-9-yl)benzene (mCP, Lumtec, sublimed), 1,3,5-tri[(3-pyridyl)-phen-3-yl]benzene (TmPyPB, Lumtec), LiF (99.995%, Sigma Aldrich), and aluminium pellets (99.9995%, Lesker) were purchased from the companies indicated in parentheses. Pre-patterned indium-tin-oxide (ITO) coated glass substrates were used with a sheet resistance of 20 Ω cm^{-2} and ITO thickness of 100 nm. The substrates were pre-cleaned with oxygen plasma before use. All organic and inorganic layers were thermally evaporated using a Kurt J. Lesker Spectros II deposition system at 10^{-6} mbar base pressure. All organic materials and aluminium were deposited at a rate of 1 Å s^{-1} except for the EML which was deposited at a rate of 0.1-0.3 1 Å s^{-1}. The LiF layer was deposited at a rate of 0.1–0.2 Å s^{-1}. Characterisation of OLED devices was conducted in a 10 inch integrating sphere (Labsphere) connected to a Source Measure Unit Keithley 2400 and coupled with a spectrometer USB4000 (Ocean Optics).[163]

Single-crystal X-ray data were collected on a Bruker D8Venture diffractometer (I μS microfocus sources, focusing mirrors, CMOS Photon100detector) using λMoKα (λ = 0.71073 Å) radiation, equipped with Cryosteam (Oxford cryosystems) open-flow nitrogen cryostats. The temperature of the crystals was maintained at 120.0 K. All structures were solved by direct methods and refined by full-matrix least squares on F2 for all data using SHELXTL[164] and OLEX2[165] software by Dr. D. S. Yufit (Durham University).

7.2 General synthetic procedures

Suzuki cross-coupling reaction

The appropriate boronic acid or ester derivative (1 equiv.), halogenated pyridine/ isoquinoline (1 or 2 equiv.) and 1 M sodium carbonate (8 equiv.) were added with ethylene glycol dimethyl ether (DME) to a dry Schlenk and degassed using three freeze-pump-thaw cycles. Tetrakis(triphenylphosphine)-palladium(0) (5 mol %) was added under a flow of nitrogen and the reaction mixture heated at reflux overnight under an atmosphere of nitrogen (85°C, approx. 20 h). The crude mixture was washed with water and extracted into dichloromethane (DCM) before drying over anhydrous $MgSO_4$. The solution was filtered and the solvent removed under reduced pressure before purification by column chromatography.[48,166]

Stille cross-coupling reaction

The appropriate halogenated precursor (1 equiv.) and tin reagent (1.25 equiv.), e.g. 2-(tributylstannyl)pyridine, were added with dry toluene and lithium chloride (8 equiv.) to a dry Schlenk and degassed by three freeze-pump-thaw cycles. Bis(triphenylphosphine)-palladium(II) dichloride (8 mol %) was added under a flow of nitrogen and the reaction mixture heated at reflux (110°C) for 48 h. Saturated KF was added to the solution and stirred at room temperature for 30 min. Subsequently the crude product was filtered, washed with toluene and the solvent removed under reduced pressure. The organic product was extracted into DCM, washed with 5% $NaHCO_3$ and dried over anhydrous $MgSO_4$ before purification by column chromatography.[49]

Miyaura cross-coupling reaction

The relevant bromobenzene (1 equiv.), bis(pinacolato)diboron, B_2Pin_2, (1.2 equiv.) and potassium acetate (6 equiv.) were added with 1,4-dioxane (10 mL per mmol of substrate) to a dry Schlenk and degassed by three freeze-pump-thaw cycles. [1,1'-Bis(diphenylphosphino)ferrocene]dichloropalladium(II) (10 mol %) was added under a flow of nitrogen and the reaction mixture heated at 80°C overnight. The 1,4-

dioxane solvent was removed under reduced pressure and the crude solid was filtered and washed with DCM to extract the product. After removal of the solvent under reduced pressure the crude product was purified by column chromatography or used in further reactions without purification.[53]

Complexation with platinum: General Procedure 1

Potassium tetrachloroplatinate(II) was added to a solution of the appropriate ligand in acetic acid in a dry Schlenk and the solution was degassed using three freeze-pump-thaw cycles. The reaction mixture was then heated at reflux (118°C) for 60 h under nitrogen before cooling to room temperature. Water was added and the solid product separated on the centrifuge; the crude product was washed with water, methanol, and then finally diethyl ether. The solid product was extracted into DCM and the solvent removed under reduced pressure to give the desired complex.[42]

Complexation General Procedure 2

2,7-Di-*tert*-butyl-4,5-diethynyl-9,9-dimethylxanthene (1 equiv.) and NaOMe (0.5 M, 5 equiv.) were stirred in dry MeOH at RT (30 mins). Pt(N^C^N)Cl (2 equiv.) dissolved in dry DCM was added to the solution and stirred at 60°C for 48 h. On cooling to RT, the solvent was removed under reduced pressure and the resulting solid washed with water, MeOH and Et_2O before recrystallisation in DCM/hexane to yield the pure product.

Chloride Metathesis

The appropriate chloro-complex was suspended in acetone in a round-bottom flask. Silver trifluoromethanesulfonate (AgOTf) was added and the reaction stirred at RT for 1-1.5 h. The complex in solution was separated from the precipitated silver chloride (AgCl) *via* centrifugation. The potassium salt of the desired ancillary ligand (KI or KSCN) was added to the acetone solution and stirred at RT for 1-2 h. The complex precipitated from the reaction and was isolated *via* centrifugation and washed with water, ethanol and diethyl ether before extraction into DCM.

7.3 Chapter 2 Synthesis

7.3.1 Intermediates and precursors

P1: 1,3-Di(pinacolatoboron)-5-(t-butyl)benzene

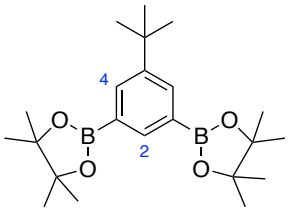

This compound was prepared *via* the Miyaura borylation reaction using 1,3-dibromo-5-*t*-butylbenzene (1.00 g, 3.43 mmol), B_2Pin_2 (1.92 g, 7.53 mmol), KOAc (2.02 g, 20.6 mmol), $PdCl_2$(dppf) (0.251 g, 0.34 mmol) and 1,4-dioxane (35 mL). Purification by column chromatography on silica (DCM, R_f = 0.4) gave the pure product as an off-white solid (1.32 g, 44%); δH (700 MHz; $CDCl_3$) 8.10 (1H, t, J 1.2, H^2), 7.91 (2H, d, J 1.2, H^4), 1.35 (9H, s, $H^{t\text{-}Bu}$), 1.33 (24H, s, H^{Bpin}); δ C (176 MHz, $CDCl_3$) 149.3 (C^5), 138.7 (C^2), 134.5 (C^4), 127.8 (C^1), 83.6 (O<u>C</u>$(CH_3)_2$), 34.7 (<u>C</u>$(CH_3)_3$), 31.4 (C(<u>C</u>$H_3)_3$), 24.86 (OC(<u>C</u>$H_3)_2$); MS (AP^+) *m/z* 387.2 [B^{11} M+H]$^+$, 385.2 [B^{10} M+H]$^+$; HRMS (AP^+) *m/z* 385.2921 [M+H]$^+$, calc. for 385.2951 [$C_{22}H_{37}O_4{}^{10}B_2$].

I1: N-Benzyl-2,2-diethoxyacetamide

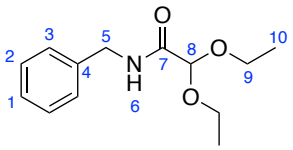

This compound was made following reported literature procedures[88] to give the product as a yellow oil (2.24 g, 94%); δ H (600 MHz; $CDCl_3$) 7.31-7.19 (5 H, m, H^1, H^2 and H^3), 6.95 (1 H, br s, H^6), 4.80 (1 H, s, H^8), 4.42 (2 H, d, J 6.1, H^5), 3.61 (4 H, ddq, J 44.7, 9.4, 7.0, H^9), 1.19 (6 H, t, J 7.0, H^{10}); δ C (600 MHz; $CDCl_3$) 167.8 (C^7), 137.9 (C^4), 128.6 (C^1, C^2 or C^3), 127.7 (C^1, C^2 or C^3), 127.5 (C^1, C^2 or C^3), 98.5 (C^8), 62.4 (C^9), 42.9 (C^5), 15.1 (C^{10}); MS ESI (ES^+) *m/z* 238 ([M+H]$^+$, 100%).

Isoquinolin-3-ol

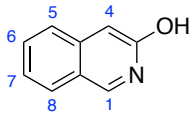

This compound was synthesised following reported literature procedures[89,167] to give the product as a bright yellow solid (755 mg, 59%); δ H (400 MHz; $CDCl_3$) 8.75 (1 H, s, H^1), 7.83 (1 H, d, J 8.4, H^5 or H^8), 7.66 (1 H, d, J 8.5, H^5 or H^8), 7.60-7.53 (1 H, m, H^6 or H^7), 7.31 (1 H, ddd, J 8.6, 6.9, 1.4, H^6 or H^7), 7.03 (1 H, s, H^4); MS ESI (ES^+) *m/z* 146.8 ($[M+H]^+$, 100%).

3-Isoquinolyl triflate

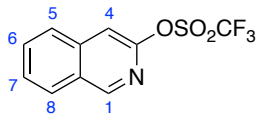

This compound was synthesised following reported literature procedures.[90] The product was purified by column chromatography on silica (hexane: ethyl acetate, gradient to 80:20, R_f = 0.6 in 70:30) to yield the pure compound as a white solid (428 mg, 69%); δ H (400 MHz, $CDCl_3$) 9.10 (1 H, s, H^1), 8.09 (1 H, dd, J 8.4, 1.0, H^5 or H^8), 7.94 (1 H, dd, J 8.4, 1.0, H^5 or H^8), 7.82 (1 H, ddd, J 8.2, 6.9,1.2, H^6 or H^7), 7.72 (1 H, ddd, J 8.2, 6.9, 1.2, H^6 or H^7), 7.61 (1 H, d, J 1.0, H^4); δ F (376 MHz, $CDCl_3$) −73.07; MS ESI (ES^+) *m/z* 278.5 ($[M+H]^+$, 100%).

I2: 1,5-Dibromo-2,4-dimethylbenzene

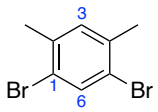

This compound was synthesised following reported literature procedures.[168] *m*-Xylene (4.30 g, 40 mmol) and iodine (0.206 g, 0.81 mmol) were added to a Schlenk wrapped in aluminium foil in an ice-bath. Bromine (14.9 g, 95 mmol) was added dropwise with stirring over 1 h, and the reaction mixture warmed to room temperature overnight. Aqueous KOH (100 mL, 20% mol) was added and the aqueous layer decanted from the solid. The solid was washed with water and extracted into DCM before drying over anhydrous $MgSO_4$. The solution was filtered and the solvent removed under reduced pressure before purification by

recrystallization from hot ethanol to yield the pure product as a white solid (5.86 g, 55%); δ H (400 MHz, $CDCl_3$) 7.70 (1 H, s, H^6), 7.12 (1 H, s, H^3), 2.33 (6 H, s, H^{Me}); δ C (101 MHz, $CDCl_3$) 136.9, 134.9, 132.6, 122.0, 58.5; MS ASAP (AP^+) *m/z* 264.9 ($[M+H]^+$, 100%).

P2

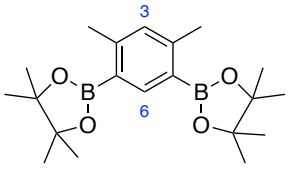

This compound was prepared *via* the Miyaura cross-coupling reaction using **I2** (1.00 g, 3.79 mmol), B_2Pin_2 (2.13 g, 8.34 mmol), KOAc (2.23 g, 22.8 mmol), $PdCl_2$(dppf) (0.227 g, 0.38 mmol) and 1,4-dioxane (30 mL). The crude mixture was purified by column chromatography (hexane: DCM gradient, R_f = 0.5 in 20:80) to yield the pure product as a white solid (544 mg, 40%); δ H (400 MHz, $CDCl_3$) 8.13 (1 H, s, H^6), 6.99 (1 H, d, J 1.3, H^3), 2.51 (6 H, d, J 0.7, H^{Me}), 1.35 (24 H, s, H^{Bpin}); MS ASAP (AP^+) *m/z* 359.25 ($[M+H]^+$, 100%). The experimental data obtained were in good agreement with the literature.[169]

7.3.2 Proligands

HL¹

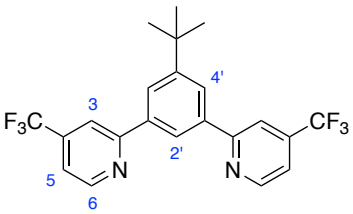

This proligand was prepared *via* the Suzuki cross-coupling reaction using **P1** (661 mg, 1.71 mmol), 2-bromo-4-(trifluoromethyl)pyridine (774 mg, 3.42 mmol), aqueous Na_2CO_3 (1450 mg, 13.7 mmol), $Pd(PPh_3)_4$ (99 mg, 0.09 mmol) and DME (10 mL). The crude mixture was purified by column chromatography (hexane: ethyl acetate slow gradient, R_f = 0.2 in 90:10) to yield the pure product as a cloudy oil (514 mg, 71%); δ

H (700 MHz, $CDCl_3$) 8.91 (2 H, dd, J 4.9, 0.9, H^6), 8.43 (1 H, t, J 1.7, $H^{2'}$), 8.17 (2 H, d, J 1.6, $H^{4'}$), 8.01 (2 H, dt, J 1.7, 0.8, H^3), 7.48 (2 H, ddd, J 5.0, 1.6, 0.8, H^5), 1.47 (9 H, s, $H^{t\text{-}Bu}$); δ C (176 MHz, $CDCl_3$) 158.8 (C^q), 152.9 ($C^{q\text{-}t\text{-}Bu}$), 150.6 (C^6), 139.2 (C^{CF_3}), 138.7 (C^q), 125.6 ($C^{4'}$), 123.7 (C^q), 123.2 ($C^{2'}$), 122.2 (C^q), 117.7 (C^5), 116.3 (C^3), 31.4 ($C^{t\text{-}Bu}$); δ F (376 MHz, $CDCl_3$) -64.65 (s); MS ESI (ES+) *m/z* 425.4 ($[M+H]^+$, 100%); HRMS (ES^+) *m/z* 425.1435 $[M+H]^+$, calc. for $[C_{22}H_{19}N_2F_6]$ 425.1452.

HL²

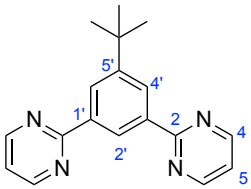

This proligand was prepared *via* the Suzuki cross-coupling reaction using **P1** (992 mg, 2.57 mmol), 2-bromo-4-(trifluoromethyl)pyridine (817 mg, 5.14 mmol), aqueous Na_2CO_3 (2180 mg, 20.5 mmol), $Pd(PPh_3)_4$ (148 mg, 0.128 mmol) and DME (20 mL). The crude mixture was purified by column chromatography (hexane: ethyl acetate gradient, R_f = 0.3 in 70:30) to yield the pure product as a white solid (535 mg, 72%); δ H (700 MHz, $CDCl_3$) 9.36 (1H, t, J 1.6, $H^{2'}$), 8.84 (4H, d, J 4.8, H^4), 8.64 (2H,d, J 1.6, $H^{4'}$), 7.19 (2H, t, J 4.8, H^5), 1.48 (9H, s,$H^{t\text{-}Bu}$); δ C (176 MHz, $CDCl_3$) 164.9 (s, C^2), 157.2 (s, C^4), 152.1 (s, $C^{5'}$), 137.8 (s, $C^{1'}$), 127.5 (s, $C^{4'}$), 125.7 (s, $C^{2'}$), 119.1 (s, C^5), 35.1 (s, $C^{t\text{-}Bu}$), 31.5 (s, $C^{t\text{-}Bu}$); MS ESI (ES+) *m/z* 291.3 $[M + H]^+$; HRMS (ES+) *m/z* 291.1612 $[M + H]^+$, calc. for $[C_{18}H_{19}N_4]$ 291.1610.

HL³: 1,3-Di(1-isoquinolyl)benzene

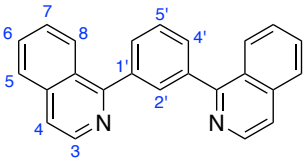

This ligand was prepared *via* the Suzuki cross-coupling method using benzene-1,3-diboronic acid (101 mg, 0.61 mmol), 1-chloroisoquinoline (200 mg, 1.22 mmol), aqueous Na_2CO_3 (518 mg, 4.89 mmol), $Pd(PPh_3)_4$ (35 mg, 0.03 mmol) and DME (7.5 mL) to yield the crude product as a brown oil. The product was purified by column

chromatography on silica (hexane: ethyl acetate, gradient to 70:30, R_f = 0.3 in 50:50) to yield the pure proligand as an off-white solid (149 mg, 73%); δ H (700 MHz; $CDCl_3$) 8.62 (2 H, d, J 5.7, H^3), 8.20 (2 H, d, J 8.5, H^8), 8.03 (1 H, t, J 1.7, $H^{2'}$), 7.88 (2 H, d, J 8.4, H^5), 7.86 (2 H, dd, J 7.6, 1.8, $H^{4'}$), 7.72 (1 H, t, J 7.6, $H^{5'}$), 7.70-7.64 (4 H, m, H^4 and H^6), 7.54 (2 H, t, J 7.7, H^7); δ C (400 MHz; $CDCl_3$) 160.4 (C^q), 142.3 (C^3), 139.8 (C^q), 131.5 ($C^{2'}$), 130.2 ($C^{4'}$), 130.1 ($C^{5'}$), 128.6 (C^4), 127.6 (C^8), 127.3 (C^7), 127.0 (C^5), 126.8 (C^q), 120.1 (C^6); MS ESI (ES^+) *m/z* 333.4 ($[M+H]^+$, 100%). The experimental data obtained were in good agreement with the literature.[89]

HL^4: 1,3-Di(3-isoquinolyl)benzene

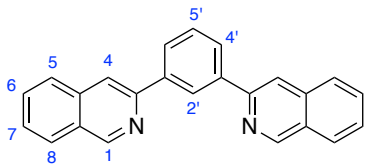

This compound was prepared *via* the Suzuki cross-coupling reaction using 1,3-phenylenediboronic acid (100 mg, 0.603 mmol), 3-bromoisoquoline (251 mg, 1.21 mmol), aqueous Na_2CO_3 (511 mg, 4.82 mmol), $Pd(PPh_3)_4$ (35 mg, 0.030 mmol) and DME (5 mL). The crude mixture was purified by column chromatography on silica (hexane: ethyl acetate, R_f = 0.4 in 70:30) to yield the product as a white solid (180 mg, 90%); δH (400 MHz, $CDCl_3$) 9.40 (2 H, d, J 1.0, H^1), 8.91 (1 H, td, J 1.9, 0.5, $H^{2'}$), 8.25 (2 H, s, H^4), 8.22 (2 H, dd, J 7.7, 1.8, $H^{4'}$), 8.03 (2 H, dq, J 8.2, 1.0, H^8), 7.93 (2 H, dq, J 8.6, 1.0, H^5), 7.72 (2 H, ddd, J 8.2, 6.8, 1.3, H^6), 7.67 (1 H, td, J 7.8, 0.5, $H^{5'}$), 7.61 (2 H, ddd, J 8.1, 6.9, 1.1, H^7); δC (100 MHz, $CDCl_3$) 152.4 (C^1), 151.2 (C^q), 140.1 (C^q), 136.7 (C^q), 130.6 (C^6), 129.3 ($C^{5'}$), 127.9 (C^q), 127.6 (C^8), 127.2 ($C^{4'}$ or C^7), 127.1 ($C^{4'}$ or C^7), 127.0 (C^5), 125.6 ($C^{2'}$), 116.8 (C^4); MS ESI (ES^+) *m/z* 333.3 ($[M+H]^+$, 100%). The experimental data obtained were in good agreement with the literature.[56]

HL[5]: 1,3-Di(2-quinolyl)benzene

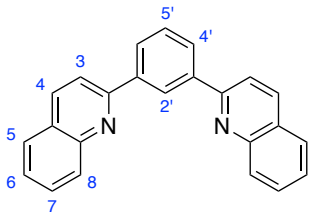

This proligand was synthesised *via* the Suzuki cross-coupling reaction of 2-chloroquinoline (208 mg, 1.27 mmol) and benzene-1,3-diboronic acid (105 mg, 0.64 mmol) with aqueous Na_2CO_3 (539 mg, 5.09 mmol), $Pd(PPh_3)_4$ (37 mg, 0.03 mmol) and DME (5 mL) to yield the crude product as an off-white oily solid. The product was purified by column chromatography on silica (hexane: ethyl acetate, gradient to 70:30, R_f = 0.3 in 70:30) to yield the pure proligand as a white solid (150 mg, 71%); δ H (700 MHz, $CDCl_3$) 8.97 (1 H, t, J 1.8, $H^{2'}$), 8.32-8.27 (4 H, m, $H^{4'}$ and H^3 or H^4), 8.25 (2 H, d, J 8.5, H^8), 8.05 (2 H, d, J 8.5, H^3 or H^4), 7.90 (2 H, d, J 8.0, H^5), 7.76 (2 H, ddd, J 8.5, 6.8, 1.4, H^7), 7.70 (1 H, td, J 7.7, 0.5, $H^{5'}$), 7.55 (2 H, ddd, J 8.0, 6.8, 1.4, H^6); δ C (100 MHz, $CDCl_3$) 157.1 (C^q), 148.2 (C^q), 140.2 (C^q), 137.0 ($C^{4'}$, and C^3 or C^4), 129.8 (C^q), 129.5 ($C^{5'}$), 128.6 ($C^{4'}$, and C^3 or C^4), 127.5 (C^5), 127.3 (C^7), 126.8 ($C^{2'}$), 126.4 (C^6), 119.2 (C^3 or C^4); MS ESI (ES^+) *m/z* 333.3 (M^+, 100%).[170]

HL[6]

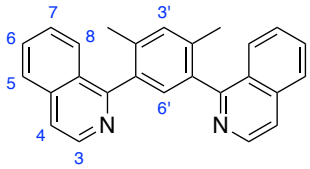

This proligand was prepared *via* the Suzuki cross-coupling reaction with **P2** (150 mg, 0.42 mmol), 1-chloroisoquinoline (137 mg, 0.84 mmol), aqueous Na_2CO_3 (355 mg, 3.35 mmol), $Pd(PPh_3)_4$ (24 mg, 0.02 mmol) and DME (4 mL). Purification by column chromatography (hexane: ethyl acetate gradient, R_f = 0.2 in 50:50) gave the pure product as a pale yellow solid (100 mg, 66%); δ H (700 MHz, $CDCl_3$) 8.58 (2 H, d, J 5.7, H^3), 7.87-7.79 (4 H, m, H^5 and H^8), 7.65 – 7.60 (4 H, m, H^4 and H^7), 7.46 (2 H, t, J 8.2, H^6), 7.34 (1 H, s, $H^{6'}$), 7.32 (1 H, s, $H^{3'}$), 2.15 (6 H, s, H^{Me}); δ C (176 MHz, $CDCl_3$) 161.0 (C^q), 142.0 (C^3), 136.7 (C^q), 136.4 (C^q), 136.3 (C^q), 132.3 ($C^{6'}$), 130.7 ($C^{3'}$), 130.1 (C^7), 127.9 (C^8), 127.6 (C^q), 127.3 (C^6), 126.7 (C^5), 119.9 (C^4), 19.6 (C^{Me}), 19.6 (C^{Me}); MS ESI

(ES$^+$) *m/z* 361.7 ([M+H]$^+$, 48%), 362.3 (100%); HRMS (ES$^+$) *m/z* 361.1693 [M+H]$^+$, calc. for [$C_{26}H_{21}N_2$] 361.1705.

HL^7

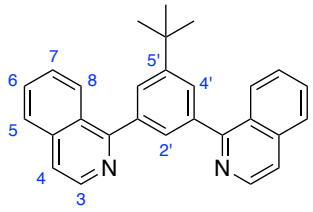

This proligand was prepared *via* the Suzuki cross-coupling reaction using crude **P1** (330 mg, 0.856 mmol), 1-chloroisoquinoline (280 mg, 1.71 mmol), aqueous Na_2CO_3 (726 mg, 6.85 mmol), $Pd(PPh_3)_4$ (50 mg, 0.043 mmol) and DME (7 mL). The crude mixture was purified by column chromatography on silica (hexane: ethyl acetate gradient, R_f = 0.2 in 70:30) to yield the pure product as a yellow oil (234 mg, 70%); δ H (400 MHz, $CDCl_3$) 8.66 (1 H, d, J 5.7), 8.20 (1 H, dq, J 8.6, 0.9), 7.93 – 7.88 (2 H, m), 7.83 (1 H, t, J 1.6), 7.73 – 7.67 (2 H, m), 7.56 (1 H, ddd, J 8.3, 6.9, 1.3), 1.49 (5 H, s); MS ESI (ES$^+$) *m/z* 389.2 ([M+H]$^+$, 100%). The experimental data obtained were in good agreement with the literature.[171]

HL^8

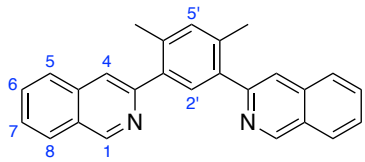

This compound was prepared *via* the Suzuki cross-coupling reaction using **P2** (57 mg, 0.16 mmol), 3-isoquinolyl triflate (100 mg, 0.36 mmol), aqueous Na_2CO_3 (136 mg, 1.28 mmol), $Pd(PPh_3)_4$ (9 mg, 0.01 mmol) and DME (1.5 mL) to give the crude product as a dark yellow oil. The product was purified by column chromatography (hexane: ethyl acetate, gradient to 60:40, R_f = 0.3 in 50:50) to yield the pure proligand as a white solid (37 mg, 64%); δ H (700 MHz, $CDCl_3$) 9.33 (2 H, s, H^1), 8.00 (2 H, dd, J 8.2, 1.2, H^8), 7.85-7.81 (2 H, m, H^5), 7.80 (2 H, s, H^4), 7.72-7.66 (3 H, m, H6 and $H^{2'}$ or $H^{5'}$), 7.59 (2 H, ddd, J 8.2, 6.8, 1.2, H^7), 7.28 (1 H, s, $H^{2'}$ or $H^{5'}$), 2.47 (6 H, s, H^{Me}); δC (176 MHz, $CDCl_3$) 153.5 (C^3), 151.7 (C^1), 138.1 ($C^{1'}$), 136.3 (C^q), 135.9 ($C^{4'}$), 133.3 ($C^{2'}$ or $C^{5'}$),

131.9 (C^6 or $C^{2'}$ or $C^{5'}$), 130.3 (C^6 or $C^{2'}$ or $C^{5'}$), 127.5 (C^8), 127.2 (C^q), 127.0 (C^7), 126.7 (C^5), 120.2 (C^4), 20.1 (C^{Me}); MS ESI (ES^+) *m/z* 361.2 ($[M+H]^+$, 100%); HRMS (ES^+) *m/z* 361.1708 $[M+H]^+$, calc. for $[C_{26}H_{21}N_2]^+$ 361.1705. The experimental data obtained were in good agreement with the literature.[59,172]

***HL*[9]**

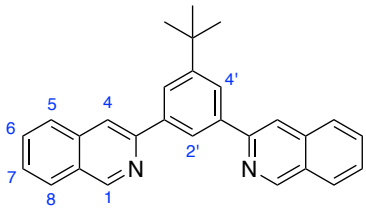

This compound was prepared *via* the Suzuki cross-coupling reaction using crude **P1** (330 mg, 0.856 mmol), 3-bromoisoquinoline (356 mg, 1.712 mmol), aqueous Na_2CO_3 (726 mg, 6.85 mmol), $Pd(PPh_3)_4$ (50 mg, 0.043 mmol) and DME (7 mL). The crude mixture was purified by column chromatography on silica (hexane: ethyl acetate gradient, R_f = 0.3 in 80:20) to yield the pure product as a white solid (214 mg, 64%); δ H (600 MHz, $CDCl_3$) 9.38 (2 H, t, J 0.9, H^1), 8.64 (1 H, t, J 1.6, $H^{2'}$), 8.25 (2 H, d, J 1.6, $H^{4'}$), 8.21 (2 H, d, J 1.0, H^4), 8.01 (2 H, dq, J 8.1, 0.9, H^8), 7.92 (2 H, dd, J 8.3, 1.1, H^5), 7.71 (2 H, ddd, J 8.1, 6.8, 1.2, H^6), 7.59 (2 H, ddd, J 8.0, 6.8, 1.1, H^7), 1.52 (9 H, s, $H^{t\text{-}Bu}$); δ C (151 MHz, $CDCl_3$) 152.3 (C^1), 151.8 (C^q), 139.9 (C^q), 136.7 (C^q), 130.5 (C^6), 127.8 (C^q), 127.6 (C^8), 126.9 (C^5), 126.9 (C^7), 126.0 (C^q), 124.5 ($C^{4'}$), 123.1 ($C^{2'}$), 116.8 (C^4), 35.2 ($C^{t\text{-}Bu}$), 31.6 ($C^{t\text{-}Bu}$); MS ESI (ES^+) *m/z* 389.4 ($[M+H]^+$, 50%) ; HRMS (ES^+) *m/z* 389.2001 $[M+H]^+$, calc. for $[C_{28}H_{25}N_2]$ 389.2018.

***HL*[10]**

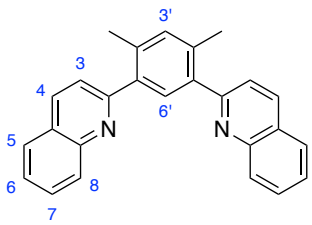

This proligand was prepared *via* the Suzuki cross-coupling reaction using **P2** (150 mg, 0.42 mmol), 2-chloroquinoline (137 mg, 0.84 mmol), aqueous Na_2CO_3 (355 mg, 3.35 mmol), $Pd(PPh_3)_4$ (24 mg, 0.02 mmol) and DME (4 mL). Purification by column

chromatography (hexane: ethyl acetate gradient to 70:30, R_f = 0.3 in 80:20) yielded the pure product as a white solid (91 mg, 60%); δ H (600 MHz, $CDCl_3$) 8.18 (2 H, d, J 8.4, H^3), 8.15 (2 H, d, J 8.5, H^8), 7.83 (2 H, dd, J 8.3, 1.4, H^5), 7.71 (2 H, ddd, J 8.4, 6.8, 1.4, H^7), 7.69 (1 H, s, $H^{6'}$), 7.58 (2 H, d, J 8.4, H^4), 7.53 (2 H, ddd, J 8.1, 6.7, 1.2, H^6), 7.29 (1 H, s, $H^{3'}$), 2.47 (6 H, s, H^{Me}); δ C (151 MHz, $CDCl_3$) 160.0 (C^q), 147.9 (C^q), 138.5 (C^q), 136.3 (C^q), 136.0 (C^3), 133.5 ($C^{3'}$), 131.2 ($C^{6'}$), 129.6 (C^8), 129.5 (C^7), 127.5 (C^5), 126.7 (C^q), 126.3 (C^6), 122.5 (C^4), 20.1 (C^{Me}); MS ESI (ES+) m/z 361.4 ([M+H]+, 100%); HRMS (ES^+) *m/z* 361.1709 $[M+H]^+$, calc. for $[C_{26}H_{21}N_2]$ 361.1705.

***HL*[11]**

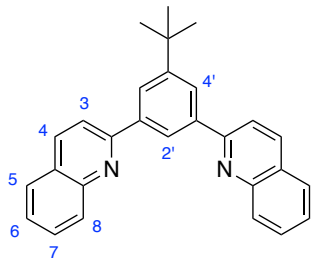

This proligand was prepared *via* the Suzuki cross-coupling reaction using **P1** (67 mg, 0.17 mmol), 2-chloroquinoline (57 mg, 0.35 mmol), aqueous Na_2CO_3 (148 mg, 1.39 mmol), $Pd(PPh_3)_4$ (10 mg, 0.01 mmol) and DME (2 mL). Purification by column chromatography (hexane: ethyl acetate slow gradient, R_f = 0.3 in 90:10) gave the pure product as a white solid (11 mg, 16%); δ H (700 MHz, $CDCl_3$) 8.70 (1 H, t, J 1.6, $H^{2'}$), 8.32 (2 H, d, J 1.6, $H^{4'}$), 8.26 (2 H, d, J 8.5, H^3), 8.23 (2 H, d, J 8.4, H^8), 8.02 (2 H, d, J 8.5, H^4), 7.87 – 7.83 (2 H, m, H^5), 7.74 (2 H, ddd, J 8.4, 6.8, 1.4, H^7), 7.54 (2 H, ddd, J 8.0, 6.8, 1.2, H^6), 1.52 (9 H, s, $H^{t\text{-}Bu}$); δ C (176 MHz, $CDCl_3$) 157.7 (C^q), 152.3 (C^q), 148.3 (C^q), 140.0 (C^q), 136.7 (C^3), 129.8 (C^8), 129.6 (C^7), 127.4 (C^5), 127.2 (C^q), 126.2 (C^6), 125.8 ($C^{4'}$), 124.3 ($C^{2'}$), 119.4 (C^4), 31.5 ($C^{t\text{-}Bu}$), 30.9 ($C^{q\text{-}t\text{-}Bu}$); MS ESI (ES^+) *m/z* 389.4 ($[M+H]^+$, 82%); HRMS (ES^+) *m/z* 389.2016 $[M+H]^+$, calc. for $[C_{28}H_{25}N_2]$ 389.2018.

7.3.3 PtL^{n}Cl Complexes

PtL^{1}Cl

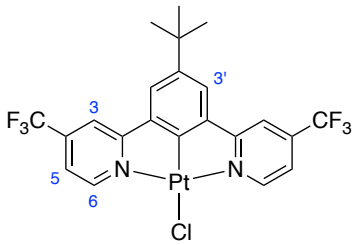

This complex was prepared by *Complexation General Procedure 1* of HL^1 (151 mg, 0.36 mmol) with K_2PtCl_4 (168 mg, 0.41 mmol) in acetic acid (15 mL) to give the product as a red or yellow solid depending upon the polymorph (see Section 2.3.2) (127 mg, 55%); δ H (700 MHz, $CDCl_3$) 9.49 (2 H, d, J 5.9, H^6), 7.89 – 7.84 (2 H, m, H^3), 7.62 (2 H, s, H$^{3'}$), 7.47 (2 H, dd, J 5.9, 1.8, H^5), 1.45 (9 H, s, H$^{t\text{-Bu}}$); δ C (176 MHz, $CDCl_3$) 168.9 (C^q), 160.4 (C^q), 153.3 (C^6), 147.3 (C^q), 140.9 (C^{CF_3}), 139.5 (C^q), 123.1 (C^q), 122.8 (C$^{3'}$), 121.5 (C^q), 119.1 (C^5), 115.2 (C^3), 31.5 (C$^{t\text{-Bu}}$); δ F (376 MHz, $CDCl_3$) -65.00 (s); MS ASAP (AP$^+$) *m/z* 659.1 ([M-Cl+MeCN]$^+$, 100%); HRMS (AP$^+$) *m/z* 658.1186 [M-Cl+MeCN]$^+$, calc. for [$C_{24}H_{20}N_3F_6{}^{194}Pt$] 658.1188; Found: C, 40.02; H, 2.59; N, 4.26, calc. for $C_{22}H_{17}ClF_6N_2Pt$: C, 40.41; H, 2.62; N, 4.28.

PtL^{2}Cl

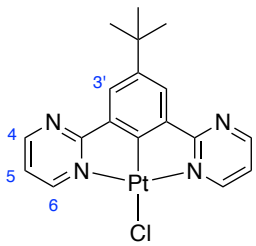

This complex was prepared by *Complexation General Procedure 1* of HL^2 (200 mg, 0.69 mmol) with K_2PtCl_4 (326 mg, 0.79 mmol) in acetic acid (20 mL) to give the product as a dark green or yellow solid depending upon the polymorph (264 mg, 74%); δ H (700 MHz, $(CD_3)_2SO$) 9.19 (2H, dd, J 5.7, 2.2, H^6), 9.10 (2H, dd, J 4.8, 2.2, H^4), 7.80 (2H, s, H$^{3'}$), 7.60 (2H, dd, J 5.7, 4.8, H^5), 1.37 (9H, s, CH_3); MS MS ASAP (AS$^+$)

m/z 525.1 ([M-Cl+MeCN]$^+$, 100%); HRMS (AS$^+$) *m/z* 524.1351 [M-Cl+MeCN]$^+$, calc. for 524.1345 [$C_{20}H_{20}N_5{}^{194}Pt$]; Found: C, 41.24; H, 3.32; N, 10.60, calc. for $C_{18}H_{17}ClN_4Pt$: C, 41.58; H, 3.30; N, 10.78.

PtL^{3}Cl

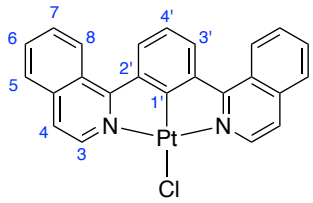

This complex was prepared by *Complexation General Procedure 1* of HL^3 (50 mg, 0.15 mmol) and K_2PtCl_4 (71 mg, 0.17 mmol) in acetic acid (6.5 mL) to yield the pure product as a bright orange solid (73 mg, 87%); δ H (400 MHz; $CDCl_3$) 9.54 (2 H, d, J 6.4, J ^{195}Pt-^{1}H 36, H^3), 9.01 (2 H, d, J 8.6, H^5 or H^8), 8.31 (2 H, d, J 8.1, H$^{3'}$), 7.97 (2 H, d, J 8.2, H^5 or H^8), 7.87 (2 H, t, J 7.7, H^6 or H^7), 7.83-7.76 (2 H, m, H^6 or H^7), 7.70 (2 H, d, J 6.4, H^4), 7.46 (1 H, t, J 8.0, H$^{4'}$); MS ESI (ES$^+$) *m/z* 567.2 ([M–Cl+MeCN]$^+$, 29%). This sample was too weak to obtain a ^{13}C NMR spectrum. The experimental data obtained were in good agreement with the literature.[56]

PtL^{4}Cl

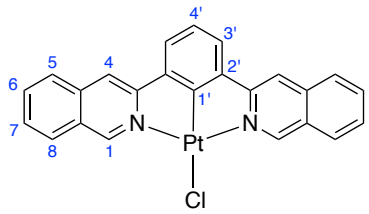

This complex was prepared using *Complexation General Procedure 1* with HL^4 (110 mg, 0.331 mmol) and K_2PtCl_4 (156 mg, 0.377 mmol) in acetic acid (10 mL) to yield the product as a yellow solid (110 mg, 59%); δ H (700 MHz, $CDCl_3$) 10.14 – 10.02 (2 H, m, H^1), 8.09 (2 H, d, J 8.1, H^8), 7.99 (2 H, s, H^4), 7.89 (2 H, d, J 8.2. H^5), 7.82 (2 H, t, J 7.5, H^6), 7.65 (2 H, t, J 7.5, H^7), 7.51 (2 H, d, J 7.6, H$^{3'}$), 7.29 (1 H, t, J 7.6, H$^{4'}$)); MS TOF (ES$^+$) *m/z* 526.1 ([M-Cl]$^+$, 100%).[56] This sample was too weak to obtain a ^{13}C spectrum. The experimental data obtained were in good agreement with the literature.[56]

PtL^{5}Cl

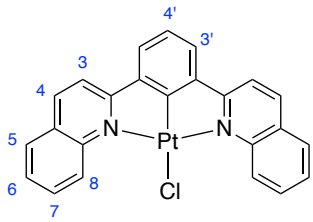

This complex was prepared by *Complexation General Procedure 1* of HL^5 (50 mg, 0.15 mmol) and K_2PtCl_4 (71 mg, 0.17 mmol) in acetic acid (7 mL) to yield the pure product as a blood orange solid (42 mg, 52%); δ H (600 MHz, CD_2Cl_2) 9.98 (2 H, d, J 8.8, H^8), 8.50 (2 H, d, J 8.6, H^4), 7.92 (6 H, dt, J 16.3, 8.4, H$^{5\text{-}7}$), 7.76 (2 H, d, J 7.6, H$^{3'}$), 7.66 (2 H, t, J 7.6, H^3), 7.42 (1 H, t, J 7.6, H$^{4'}$); HRMS (ES$^+$) *m/z* 566.1136 [M-Cl+MeCN]$^+$, calc. for [$C_{26}H_{18}N_3{}^{194}Pt$] 566.1128. This sample was too insoluble to obtain a ^{13}C NMR.

PtL^{6}Cl

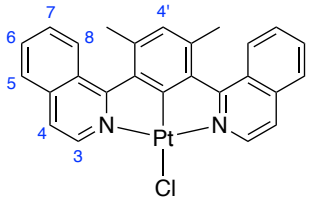

This complex was prepared using *Complexation General Procedure 1* with HL^6 (50 mg, 0.14 mmol) and K_2PtCl_4 (67 mg, 0.16 mmol) in acetic acid (6 mL) to yield the product as a dark orange/red solid (49 mg, 60%); δ H (700 MHz, $CDCl_3$) 9.31 (2 H, d, J 6.3, H^3), 8.13 (2 H, dq, J 8.7, 1.0, H^8), 7.87 (2 H, ddd, J 8.7, 1.2, 0.6, H^5), 7.77 (2 H, ddd, J 8.1, 6.8, 1.1, H^6), 7.63 (2 H, d, J 6.3, H^4), 7.60 (2 H, ddd, J 8.6, 6.8, 1.2, H^7), 6.98 (1 H, s, H$^{4'}$); δ C (176 MHz, $CDCl_3$) 170.6 (C^q), 169.0 (C^q), 143.1 (C^3), 139.6 (C^q), 139.3 (C^q), 137.4 (C^q), 131.8 (C^6), 130.5 (C$^{4'}$), 128.9 (C^8), 126.7 (C^5), 126.6 (C^7), 125.7 (C^q), 120.6 (C^4), 23.9 (C^{Me}); MS ASAP (AP$^+$) *m/z* 595.2 ([M-Cl+MeCN]$^+$, 100%); HRMS (AP$^+$) *m/z* 595.1470 [M-Cl+MeCN]$^+$, calc. for [$C_{28}H_{22}N_3{}^{195}Pt$] 595.1462.

PtL^{7}Cl

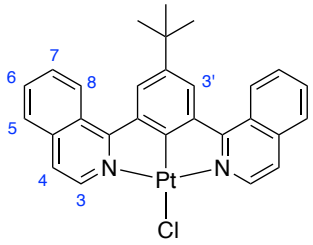

This complex was prepared using *Complexation General Procedure 1* with HL^{7} (80 mg, 0.206 mmol) and K_2PtCl_4 (98 mg, 0.235 mmol) in acetic acid (8 mL) to yield the product as a pale orange solid (34 mg, 27%); δ H (600 MHz, $CDCl_3$) 9.48 (2 H, d, J 6.3, H^{3}), 8.94 (2 H, d, J 8.6, H^{8}), 8.34 (2 H, s, H$^{3'}$), 8.00-7.91 (2 H, m, H^{5}), 7.84 (2 H, ddd, J 8.2, 6.8, 1.1, H^{6}), 7.79 (2 H, ddd, J 8.4, 6.8, 1.4, H^{7}), 7.65 (2 H, d, J 6.3, H^{4}) 1.54 (9 H, s, H$^{t\text{-Bu}}$) ; δ C (151 MHz, $CDCl_3$) 167.7 (C$^{1'}$), 164.5 (C$^{2'}$), 145.4 (C$^{4'}$), 143.9 (C^{3}), 137.8 (C^{q}), 131.7 (C^{6}), 128.7 (C^{6}), 128.0 (C^{5}), 126.4 (C$^{3'}$), 125.4 (C^{8}), 121.5 (C^{4}), 31.7 (C$^{t\text{-Bu}}$); HRMS (AP^{+}) *m/z* 622.1760 [M-Cl+MeCN]$^{+}$, calc. for [$C_{30}H_{26}N_3{}^{194}Pt$] 622.1754.

PtL^{8}Cl

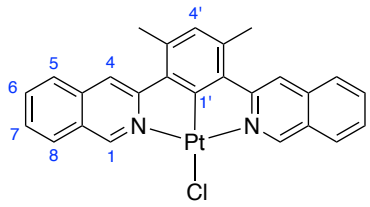

This complex was prepared by *Complexation General Procedure 1* of HL^{8} (35 mg, 0.10 mmol) and K_2PtCl_4 (46 mg, 0.11 mmol) in acetic acid (4 mL) to yield the pure product as a yellow solid (33 mg, 58%); δ H (400 MHz, $CDCl_3$) 10.26 (2 H, s, J ^{195}Pt-^{1}H 44, H^{1}), 8.15 (2 H, s, H^{4}), 8.10 (2 H, d, J 8.3, H^{5} or H^{8}), 7.89 (2 H, d, J 8.3, H^{5} or H^{8}), 7.81 (2 H, t, J 7.4, H^{6} or H^{7}), 7.65 (2 H, t, J 7.4, H^{6} or H^{7}), 6.90 (1 H, s, H$^{4'}$), 2.81 (6 H, s, H^{Me}); MS ASAP (AP^{+}) *m/z* 595.1 ([M-Cl+MeCN]$^{+}$, 100%); HRMS (AP^{+}) *m/z* 594.1423 [M(^{194}Pt)-Cl+MeCN]$^{+}$, calc. for [$C_{28}H_{22}N_3{}^{194}Pt$] 594.1441. This sample was too weak to obtain a ^{13}C NMR spectrum.

PtL^{9}Cl

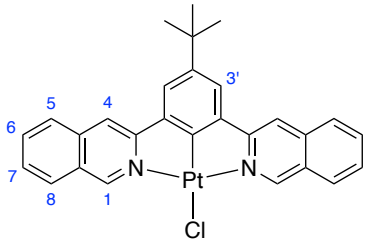

This complex was prepared using *Complexation General Procedure 1* with HL^{9} (75 mg, 0.193 mmol) and K_2PtCl_4 (91 mg, 0.220 mmol) in acetic acid (8 mL) to yield the product as a yellow solid (54 mg, 45%); δ H (600 MHz, CD_2Cl_2) 10.03 (2 H, s, H^{1}), 8.13 (2 H, d, J 8.2, H^{8}), 8.10 (2 H, s, H^{4}), 7.97-7.92 (2 H, m, H^{5}), 7.86 (2 H, ddd, J 8.1, 6.8, 1.2, H^{6}), 7.68 (2 H, ddd, J 8.1, 6.8, 1.2, H^{7}), 7.65 (2 H, s, H$^{3'}$), 1.52 (9 H, s, H$^{t\text{-Bu}}$); δ C (151 MHz, CD_2Cl_2) 156.0 (C^{1}), 133.0 (C^{6}), 128.8 (C^{8}), 128.1 (C^{7}), 126.7 (C^{5}), 120.4 (C$^{3'}$), 115.4 (C^{4}), 31.4 (C$^{t\text{-Bu}}$); MS ASAP (AP^{+}) *m/z* 623.2 ([M-Cl+MeCN]$^{+}$, 100%); HRMS (AP^{+}) *m/z* 622.1756 [M(^{194}Pt)-Cl+MeCN]$^{+}$, calc. for [$C_{30}H_{26}N_3{}^{194}Pt$] 622.1754.

7.3.4 PtL^{n}X Complexes where X = I or NCS/SCN

PtL^{1}I

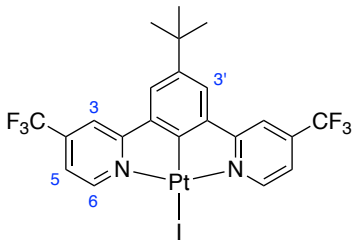

This complex was prepared by the *chloride metathesis reaction* with PtL^{1}Cl (50 mg, 0.076 mmol), AgOTf (24 mg, 0.092 mmol) and KI (excess) to give the product as a yellow solid (41 mg, 60%); δ H (400 MHz, CD_2Cl_2) 10.08 (2 H, d, J 6.1, H^{6}), 7.99 (2 H, s, H^{3}), 7.73 (2H , s, H$^{3'}$), 7.51 (2 H, d, J 6.1, H^{5}), 1.50 (9 H, s, H$^{t\text{-Bu}}$); δ F (376 MHz, $CDCl_3$) -65.50 (s); δ C (151 MHz, HSQC, CD_2Cl_2) 158.3 (C^{6}), 123.2 (C$^{3'}$), 119.9 (C^{5}), 115.3 (C^{3}), 30.9 (CH_3); the solubility was too poor to resolve the quaternary carbons; MS ASAP (AS^{+}) *m/z* 659.1 ([M-I+MeCN]$^{+}$, 100%); HRMS (AS^{+}) *m/z* 658.1196 [M+H]$^{+}$, calc. for [$C_{24}H_{20}N_3F_6{}^{194}Pt$] 658.1188; Anal. calc. for $C_{22}H_{17}F_6IN_2Pt$: C, 35.45; H, 2.30; N, 3.76 %; found C, 35.51; H, 2.29; N, 3.65 %.

PtL^{1}SCN

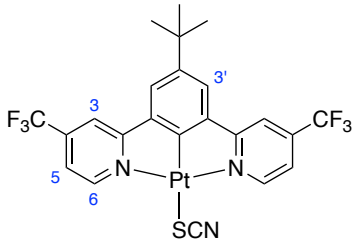

This complex was prepared by the *chloride metathesis reaction* with PtL^{1}Cl (50 mg, 0.076 mmol), AgOTf (24 mg, 0.092 mmol) and KSCN (15 mg, 0.150 mmol) to give the product as a green yellow solid (33 mg, 64%); δ H (400 MHz, CD_2Cl_2) 8.99 (2 H, d, J 5.7, H^6), 7.99 (2 H, s, H^3), 7.69 (2 H, s, H$^{3'}$), 7.59 (2 H, d, J 5.7, H^5), 1.48 (9 H, s, H$^{t\text{-Bu}}$); δ F (376 MHz, CD_2Cl_2) -65.46 (s); δ C (151 MHz, HSQC, CD_2Cl_2) 153.2 (C^6), 122.9 (C$^{3'}$), 119.7 (C^5), 115.7 (C^3), 30.9 (CH_3); the solubility was too poor to resolve the quaternary carbons; HRMS (AP$^+$) *m/z* 676.0767 [M+H]$^+$, calc. for [$C_{23}H_{18}N_3F_6S^{194}Pt$] 676.0752; ν_{max}/cm^{-1} 2073.9s (SCN); Anal. calc. for $C_{23}H_{17}F_6N_3PtS{\cdot}0.1CH_2Cl_2$: C, 40.50; H, 2.53; N, 6.13 %; found C, 40.35; H, 2.46; N, 6.08 %.

PtL^{2}I

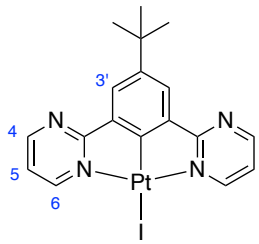

This complex was prepared by the *chloride metathesis reaction* with PtL^{2}Cl (25 mg, 0.048 mmol), AgOTf (15 mg, 0.060 mmol) and KI (38 mg, 0.229 mmol) to give the product as a dark green solid (8 mg, 27%); δ H (600 MHz, CD_2Cl_2) 9.90 (2 H, dd, J 5.8, H^6), 8.90 (2 H, dd, J 4.8, 2.3, H^4), 7.97 (2 H, s, H$^{3'}$), 7.26 (2 H, dd, J 5.8, 4.8, H^5), 1.45 (9 H, s, H$^{t\text{-Bu}}$); δ C (151 MHz, HSQC, CD_2Cl_2) 163.2 (C^6), 158.2 (C^4), 126.9 (C$^{3'}$), 119.3 (C^5), 31.0 (CH_3); the solubility was too poor to resolve the quaternary carbons; MS ASAP (AP$^+$) *m/z* 525.1 ([M-I+MeCN]$^+$, 100%), 612.0 ([M+H]$^+$, 2%); HRMS (AP$^+$) *m/z* 524.1349 [M-I+MeCN]$^+$, calc. for [$C_{20}H_{20}N_5{}^{194}Pt$] 524.1345; Anal. calc. for $C_{19}H_{17}N_5PtS{\cdot}0.2CH_2Cl_2$: C, 34.79; H, 2.79; N, 8.92 %; found C, 34.90; H, 2.64; N, 8.70 %.

PtL²NCS

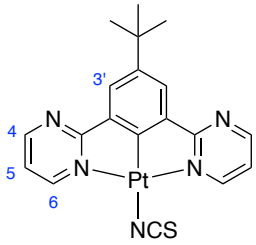

This complex was prepared by the *chloride metathesis reaction* with PtL^2Cl (25 mg, 0.048 mmol), AgOTf (15 mg, 0.060 mmol) and KSCN (47 mg, 0.480 mmol) to give the product as a burgundy red/purple solid (11 mg, 42%); δ H (600 MHz, CD_2Cl_2) 8.96 (2 H, dd, J 4.8, 2.3, H^4), 8.89 (2 H, dd, J 5.7, 2.3, H^6), 7.87 (2 H, s, $H^{3'}$), 7.34 (2 H, dd, J 5.6, 4.8, H^5), 1.43 (9H, s, $H^{t\text{-}Bu}$); δ C (151 MHz, HSQC, CD_2Cl_2) 159.4 (C^4), 158.0 (C^6), 126.8 ($C^{3'}$), 119.3 (C^5), 30. (CH_3); the solubility was too poor to resolve the quaternary carbons; MS ASAP (AP^+) *m/z* 525.1 $[M\text{-}NCS+MeCN]^+$; HRMS (AP^+) *m/z* 524.1336 $[M\text{-}NCS+MeCN]^+$, calc. for $[C_{20}H_{20}N_5{}^{194}Pt]$ 524.1345; ν_{max}/cm^{-1} 2107.9s (NCS); Anal. calc. for $C_{19}H_{17}N_5PtS{\cdot}0.1CH_2Cl_2$: C, 41.63; H, 3.15; N, 12.71 %; found C, 41.63; H, 3.10; N, 12.72 %.

PtL³NCS

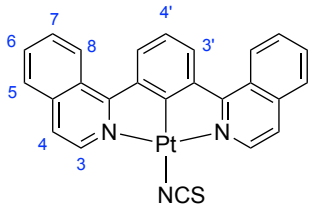

This complex was prepared by the *chloride metathesis reaction* with PtL^3Cl (10 mg, 0.018 mmol), AgOTf (6 mg, 0.021 mmol) and KSCN (17 mg, 0.180 mmol) to give the product as an orange solid (10 mg, 95%); δ H (600 MHz, CD_2Cl_2) 8.86 (2 H, d, J 8.6, H^8), 8.64 (2 H, d, J 6.2, H^3), 8.16 (2 H, d, J 8.0, $H^{3'}$), 7.89 (2 H, d, J 8.2, H^5), 7.83 (2 H, t, J 7.5, H^6), 7.76 (2 H, t, J 7.7, H^7), 7.59 (2 H, d, J 6.4, H^4), 7.38 (1 H, t, J 7.9, $H^{4'}$); MS ASAP (AP^+) *m/z* 567.1 $[M\text{-}NCS+MeCN]^+$; HRMS $(AP)^+$ *m/z* 566.1140 $[M\text{-}NCS+MeCN]^+$, calc. for $[C_{26}H_{18}N_3{}^{194}Pt]$ 566.1128. This sample was too insoluble to obtain a ^{13}C NMR spectrum.

PtL^{7}I

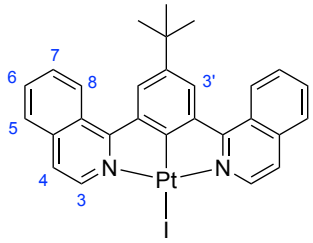

This complex was prepared by the *chloride metathesis reaction* with PtL^{7}Cl (50 mg, 0.081 mmol), AgOTf (25 mg, 0.097 mmol) and KI (27 mg, 0.163 mmol) to give the product as an orange solid (33 mg, 58%); δ H (600 MHz, CD_2Cl_2) 9.94 (2 H, d, J 6.5, H^3), 8.97 (2 H, d, J 8.6, H^8), 8.35 (2 H, s, $H^{3'}$), 7.95 (2 H, d, J 8.2, H^5), 7.88 (2 H, ddd, J 8.1, 6.8, 1.1, H^6), 7.83 (2 H, ddd, J 8.1, 6.8, 1.1, H^6), 7.60 (2 H, d, J 6.5, H^4), 1.57 (9 H, s, $H^{t\text{-}Bu}$); δ C (151 MHz, CD_2Cl_2) 148.7 (C^3), 132.0 (C^6), 128.9 (C^7), 127.8 (C^5), 126.8 ($C^{3'}$), 125.7 (C^8), 121.8 (C^4), 31.3 ($C^{t\text{-}Bu}$); MS ASAP (AP^+) *m/z* 623.2 $[M\text{-}I+MeCN]^+$; HRMS (AP^+) *m/z* 622.1767 $[M\text{-}I+MeCN]^+$, calc. for $[C_{30}H_{26}N_3{}^{194}Pt]$ 622.1754.

PtL^{7}NCS

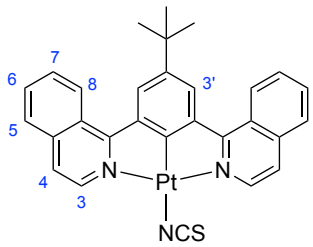

This complex was prepared by the *chloride metathesis reaction* with PtL^{7}Cl (50 mg, 0.081 mmol), AgOTf (25 mg, 0.097 mmol) and KSCN (9 mg, 0.093 mmol) to give the product as a burgundy red solid (20 mg, 39%); δ H (400 MHz, CD_2Cl_2) 8.47 (4 H, d, J 14.9, H^3), 7.90 (2 H, s), 7.87 – 7.78 (4 H, m), 7.69 (2 H, s), 7.34 (2 H, s), 1.42 (9 H, s); this sample was too insoluble to obtain a ^{13}C NMR spectrum; MS ASAP (AP^+) *m/z* 623.2 $[M\text{-}NCS+MeCN]^+$; HRMS (AP^+) *m/z* 622.1750 $[M\text{-}NCS+MeCN]^+$, calc. for $[C_{30}H_{26}N_3{}^{194}Pt]$ 622.1754.

7.4 Chapter 3 Synthesis

7.4.1 Intermediates and Precursors

P3: 2-(3-bromophenyl)pyridine

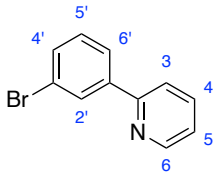

This compound was prepared *via* the Stille cross-coupling method with 1,3-dibromobenzene (250 mg, 1.06 mmol), 2-(tributylstannyl)pyridine (488 mg, 1.33 mmol), $Pd(PPh_3)_2Cl_2$ (60 mg, 0.09 mmol), LiCl (360 mg, 8.48 mmol) and dry toluene (15 mL) to give the crude product as a yellow/brown oily solid. The compound was purified by column chromatography on silica (hexane: ethyl acetate, gradient to 80:20, R_f = 0.3 in 90:10) to yield the pure product as a clear oil (111 mg, 45%); δ H (400 MHz, $CDCl_3$) 8.72 (1 H, ddd, J 4.8, 1.8, 1.0, H^6), 8.20 (1 H, t, J 1.9, $H^{2'}$), 7.93 (1 H, ddd, J 7.8, 1.8, 1.0, $H^{4'}$), 7.78 (1 H, ddd, J 8.0, 7.3, 1.1, H^4), 7.72 (1 H, dt, J 8.0, 1.1, H^3), 7.56 (1 H, ddd, J 7.9, 2.0, 1.0, $H^{6'}$), 7.36 (1 H, t, J 7.9, $H^{5'}$), 7.29-7.25 (1 H, m, H^5); δ C (100 MHz, $CDCl_3$) 155.9 (C^q), 149.8 (C^6), 141.4 (C^q), 136.9 (C^4), 131.9 ($C^{6'}$), 130.3 ($C^{5'}$), 130.1 ($C^{2'}$), 125.4 ($C^{4'}$), 123.1 (C^q), 122.7 (C^5), 120.6 (C^3); MS ESI (ES^+) *m/z* 233.3 (M^+, 100%). The experimental data obtained were in good agreement with the literature.[173]

This compound was also prepared *via* the Suzuki cross-coupling reaction with 2-bromopyridine (0.944 g, 5.98 mmol) and 3-bromophenylboronic acid (1.00 g, 4.98 mmol) with aqueous Na_2CO_3 (4.22 g, 39.8 mmol), $Pd(PPh_3)_4$ (0.288 g, 0.249 mmol) and DME (15 mL). The crude mixture was purified by column chromatography on silica (hexane: ethyl acetate gradient, R_f = 0.3 in 90:10) to yield the pure product as a clear oil (0.916 g, 79%).

P4

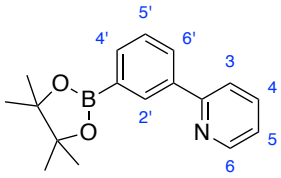

This ligand precursor was prepared *via* the Miyaura cross-coupling reaction using **P3** (111 mg, 0.47 mmol), B_2Pin_2 (145 mg, 0.57 mmol), KOAc (140 mg, 1.42 mmol), $PdCl_2$(dppf) (17 mg, 0.02 mmol) and 1,4-dioxane as the solvent (5 mL). The crude black/brown solid was purified by column chromatography (DCM: methanol, gradient to 70:30, product eluted at 25% MeOH) to yield the product as a brown oily solid (55 mg, 41%); δ H (700 MHz, $CDCl_3$) 8.65 (1 H, ddd, J 4.9, 1.8, 0.9, H^6), 8.33 (1 H, s, $H^{2'}$), 8.07 (1 H, ddd, J 7.8, 2.0, 1.3, $H^{6'}$), 7.83 (1 H, dt, J 7.3, 1.2, $H^{4'}$), 7.76 (1 H, dt, J 8.0, 1.2, H^3), 7.73 (1 H, td, J 7.7, 1.8, H^4), 7.48-7.45 (1 H, m, $H^{5'}$), 7.21 (1 H, ddd, J 7.3, 4.9, 1.3, H^5), 1.34 (12 H, s, H^{Bpin}); δ C (176 MHz, $CDCl_3$) 157.5 (C^2), 149.5 (C^6), 138.6 ($C^{1'}$ or $C^{3'}$), 136.8 (C^4), 135.3 ($C^{4'}$), 133.2 ($C^{2'}$), 131.1 ($C^{1'}$ or $C^{3'}$), 129.9 ($C^{6'}$), 128.2 ($C^{5'}$), 122.1 (C^5), 120.9 (C^3), 83.9 (C^{Bpin}), 24.6 ($C^{Me\text{-}Bpin}$); MS ESI (ES^+) *m/z* 282.2 ($[M+H]^+$, 100%); HRMS (ES^+) *m/z* 281.1705 $[M(^{10}B)+H]^+$, calc. for $[C_{17}H_{21}NO_2{}^{10}B]^+$ 281.1702. The experimental data obtained were in good agreement with the literature.[174]

P5

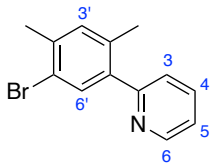

This ligand precursor was prepared *via* the Stille cross-coupling reaction with 1,5-dibromo-2,4-dimethylbenzene (500 mg, 1.89 mmol), 2-(tributylstannyl)pyridine (558 mg, 1.52 mmol), $Pd(PPh_3)_2Cl_2$ (85 mg, 0.12 mmol), LiCl (514 mg, 12.12 mmol) and dry toluene (20 mL). The crude mixture was purified by column chromatography (hexane: ethyl acetate gradient to 80:20, R_f = 0.3 in 90:10) to yield the pure product as a clear oil (100 mg, 25%); δ H (700 MHz, $CDCl_3$) 8.68 (1 H, ddd, J 4.9, 1.8, 0.9, H^6), 7.73 (1 H, td, J 7.7, 1.8, H^4), 7.57 (1 H, s, $H^{6'}$), 7.36 (1 H, dt, J 7.8, 1.1, H^3), 7.24 (1 H, ddd, J 7.6, 4.9, 1.2, H^5), 7.14 (1 H, s, $H^{3'}$), 2.40 (3 H, d, J 0.7, H^{Me}), 2.28 (3 H, s, H^{Me}); δ C (176 MHz, $CDCl_3$) 158.5 (C^q), 149.3 (C^6), 139.7 (C^q), 137.6 (C^q), 136.2 (C^4), 134.9 (C^q),

133.1 ($C^{6'}$), 133.1 ($C^{3'}$), 124.0 (C^{3}), 121.8 (C^{5}), 121.7 (C^{q}), 22.5 (C^{Me}), 19.7 (C^{Me}); MS ESI (ES^+) *m/z* 261.5 (M^+, 100%); HRMS (ES^+) *m/z* 262.0236 $[M+H]^+$, calc. for $[C_{13}H_{13}NBr]$ 262.0231.

P6

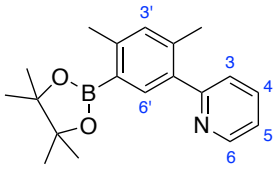

This compound was prepared *via* the Miyaura cross-coupling reaction using **P5** (100 mg, 0.38 mmol), B_2Pin_2 (117 mg, 0.46 mmol), KOAc (224 mg, 2.29 mmol), $PdCl_2$(dppf) (28 mg, 0.04 mmol) and 1,4-dioxane (4 mL). The crude product was used in further reactions without purification.

I3

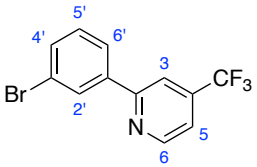

This compound was prepared *via* the Suzuki cross-coupling reaction using 3-bromophenylboronic acid (1.00 g, 4.98 mmol), 2-bromo-4-(trifluoromethyl)pyridine (1.35 g, 5.98 mmol), aqueous Na_2CO_3 (4.22 g, 39.83 mmol), $Pd(PPh_3)_4$ (288 mg, 0.25 mmol) and DME (15 mL). The crude mixture was purified by column chromatography (hexane: ethyl acetate slow gradient, R_f = 0.5 in 90:10) to yield the pure product as a white solid (707 mg, 47%); δ H (400 MHz, $CDCl_3$) 8.89 (1 H, dt, J 5.0, 0.8), 8.23 (1 H, t, J 1.8), 7.96 (1 H, ddd, J 7.8, 1.8, 1.0), 7.93 (1 H, s), 7.61 (1 H, ddd, J 7.9, 2.0, 1.0), 7.50 (1 H, ddd, J 5.1, 1.6, 0.8), 7.39 (1 H, t, J 7.9); δ F (376 MHz, $CDCl_3$) -64.79 (s); δ C (101 MHz, $CDCl_3$) 157.1, 150.8, 139.9, 139.5, 132.8, 130.5, 130.2, 125.5, 123.3, 121.5, 118.2, 116.1; MS ESI (ES+) m/z 302.2 (M+, 100%). The experimental data obtained were in good agreement with the literature.[175]

I4

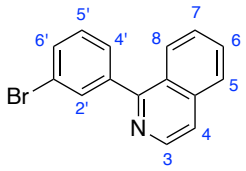

This compound was prepared *via* the Suzuki cross-coupling reaction using 3-bromophenylboronic acid (1.00 g, 4.98 mmol), 1-chloroisoquinoline (0.978 g, 5.98 mmol), aqueous Na_2CO_3 (4.22 g, 39.8 mmol), $Pd(PPh_3)_4$ (0.288 g, 0.249 mmol) and DME (40 mL). The crude mixture was purified by column chromatography on silica (hexane: ethyl acetate gradient, R_f = 0.3 in 90:10) to yield the pure product as a white solid (1.11 g, 78%); δ H (400 MHz, $CDCl_3$) 8.6 (1 H, d, J 5.7), 8.1 (1 H, dq, J 8.5, 1.0), 7.9 (1 H, dt, J 8.5, 1.1), 7.9 (1 H, t, J 1.8), 7.7 (1 H, ddd, J 8.2, 6.9, 1.2), 7.7 (1 H, dd, J 5.7, 0.9), 7.7 (2 H, ddt, J 7.9, 2.8, 1.1), 7.6 (1 H, ddd, J 8.3, 6.9, 1.3), 7.4 (1 H, t, J 7.8). The experimental data obtained were in good agreement with the literature.[176]

P7

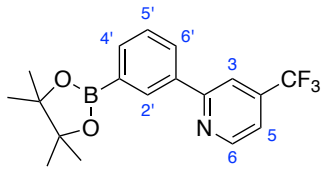

This compound was prepared *via* the Miyaura borylation reaction using **I3** (707 mg, 2.34 mmol), B_2Pin_2 (716 mg, 2.81 mmol), KOAc (1380 mg, 14.1 mmol), $PdCl_2$(dppf) (171 mg, 0.23 mmol) and 1,4-dioxane (20 mL). The crude product was used in further reactions without purification.

P8

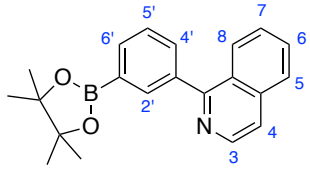

This compound was prepared *via* the Miyaura borylation reaction using **I4** (980 mg, 3.45 mmol), B_2pin_2 (1055 mg, 4.14 mmol), KOAc (2031 mg, 20.7 mmol) and $PdCl_2$(dppf) (252 mg, 0.0.345 mmol) in 1,4-dioxane (35 mL). The crude mixture was

purified by flash column chromatography (hexane: ethyl acetate, R_f = 0.5 in 70:30) to give the product as a white solid (686 mg, 60%); δ H (600 MHz, $CDCl_3$) 8.59 (1 H, d, J 5.7 , H^3), 8.13 (1 H, t, J 1.5, $H^{2'}$), 8.06 (1 H, dq, J 8.5, 0.9, H^5), 7.93 (1 H, dt, J 7.4, 1.3, H^7), 7.86 (1 H, dt, J 8.2, 1.0, $H^{4'}$), 7.76 (1 H, ddd, J 7.6, 1.9, 1.3, H^8), 7.67 (1 H, ddd, J 8.2, 6.8, 1.2, $H^{5'}$), 7.63 (1 H, dd, J 5.7, 0.9, H^4), 7.52 (2 H, tdd, J 6.8, 2.6, 0.9, $H^{6'}$ and H^6), 1.33 (12 H, s, H^{Bpin}); δ C (151 MHz, $CDCl_3$) 160.9 (C^q), 142.2 (C^3), 139.0 (C^q), 136.8 (C^q), 136.2 $C^{2'}$), 134.9 (C^7), 132.6 (C^8), 129.9 ($C^{5'}$), 127.6 (C^6), 127.1 ($C^{6'}$), 127.0 (C^5), 126.7 ($C^{4'}$), 126.8 (C^q), 119.8 (C^4), 83.9 ($C^{q\text{-}Bpin}$), 24.9 (C^{Bpin}); MS ESI (ES^+) *m/z* 332.4 ($[M+H]^+$, 100%); HRMS (ES^+) *m/z* 331.1870 $[M+H]^+$, calc. for $[C_{21}H_{23}NO_2{}^{10}B]$ 331.1858.

I5: 2-(3-Bromophenyl)pyrimidine

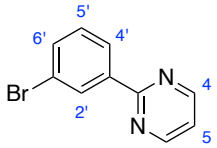

This compound was prepared *via* the Suzuki cross-coupling reaction using 3-bromophenylboronic acid (1.50 g, 7.47 mmol), 2-bromopyrimidine (1.43 g, 8.96 mmol), aqueous Na_2CO_3 (6.33 g, 59.8 mmol), $Pd(PPh_3)_4$ (0.432 g, 0.373 mmol) and DME (30 mL). The crude mixture was purified by column chromatography on silica (hexane: ethyl acetate gradient, R_f = 0.3 in 90:10) to yield the pure product as a white solid (1.30 g, 75%); δ H (400 MHz, $CDCl_3$) 8.84 (2 H, d, J 4.8), 8.65 (1 H, ddd, J 2.1, 1.6, 0.4), 8.41 (1 H, ddd, J 7.9, 1.6, 1.1), 7.64 (1 H, ddd, J 7.9, 2.1, 1.1), 7.39 (1 H, td, J 7.9, 0.4), 7.25 (1 H, t, J 4.8). The experimental data obtained were in good agreement with the literature.[177]

P10

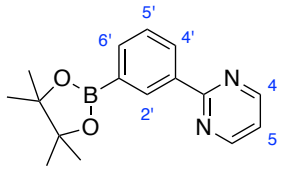

This compound was prepared *via* the Miyaura borylation reaction using **I5** (800 mg, 3.40 mmol), B_2pin_2 (1040 mg, 4.08 mmol), KOAc (2000 mg, 20.4 mmol) and

$PdCl_2$(dppf) (249 mg, 0.340 mmol) in 1,4-dioxane (30 mL). The crude product was used in further reactions without purification.

I6

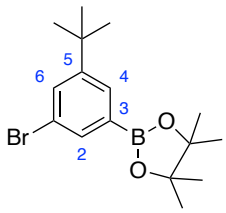

This compound was prepared *via* the Miyaura borylation reaction using 1,3-dibromo-5-*tert*-butylbenzene (1.00 g, 3.43 mmol), B_2pin_2 (0.873 g, 3.43 mmol), KOAc (2.02 g, 20.6 mmol) and $PdCl_2$(dppf) (0.251 g, 0.343 mmol) in 1,4-dioxane (35 mL). The crude product was used in further reactions without purification.

I7

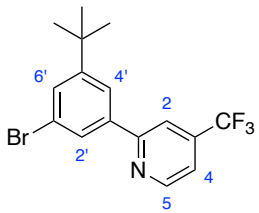

This compound was prepared *via* the Suzuki cross-coupling reaction using crude **I6** (1.16 g, 3.43 mmol), 2-bromo-4-(trifluoromethyl)pyridine (0.968 g, 4.28 mmol), aqueous Na_2CO_3 (2.90 g, 27.4 mmol), $Pd(PPh_3)_4$ (0.198 g, 0.171 mmol) and DME (20 mL). The crude mixture was purified by column chromatography on silica (hexane: ethyl acetate gradient, R_f = 0.5 in 90:10) to yield the pure product as a white solid (429 mg, 35%); δ H (400 MHz, $CDCl_3$) 8.93 – 8.87 (1 H, m, H^5), 8.00 (2 H, dt, J 9.2, 1.7, $H^{4'}$ and $H^{6'}$), 7.90 (1 H, dt, J 1.6, 0.8, H^2), 7.65 (1 H, t, J 1.7, $H^{2'}$), 7.53 – 7.47 (1 H, m. H^4); MS ESI (ES^+) *m/z* 358.1 ($[M+H]^+$, 93%); HRMS (ES^+) *m/z* 358.0434 $[M+H]^+$, calc. for 358.0418 [$C_{16}H_{16}NF_3Br$].

P11

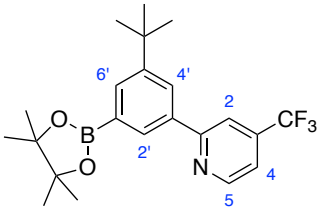

This compound was prepared *via* the Miyaura borylation reaction using **I7** (372 mg, 1.04 mmol), B_2pin_2 (318 mg, 1.25 mmol), KOAc (612 mg, 6.23 mmol) and $PdCl_2$(dppf) (76 mg, 0.104 mmol) in 1,4-dioxane (10 mL). The crude mixture was purified by column chromatography on silica (hexane: ethyl acetate gradient, R_f = 0.4 in 90:10) to give the product as a white solid (283 mg, 67%); δ H (600 MHz, $CDCl_3$) 8.86 (1 H, d, J 5.0, H^5), 8.22 (1 H, t, J 2.0, $H^{2'}$), 8.17-8.14 (1 H, m, $H^{4'}$ or $H^{6'}$), 7.96 (1 H, s, H^2), 7.93 (1 H, dd, J 2.1, 0.9, $H^{4'}$ or $H^{6'}$), 7.43 (1 H, dd, J 5.1, 1.5, H^4), 1.41 (9 H, s, $H^{t\text{-}Bu}$), 1.37 (12 H, s, H^{Bpin}); δ C (151 MHz, $CDCl_3$) 159.3 (C^q), 151.3 (C^q), 150.3 (C^5), 133.2 ($C^{4'}$ or $C^{6'}$), 130.5 ($C^{4'}$ or $C^{6'}$), 127.2 ($C^{2'}$), 117.3 (C^4), 116.4 (C^2), 83.9 (C^q), 34.9 ($C^{Bpin\text{-}q}$), 31.4 ($C^{t\text{-}Bu}$), 25.0 (C^{Bpin}); δ F (376 MHz, $CDCl_3$) -64.63 (CF_3); MS ESI (ES^+) *m/z* 406.4 $[M+H]^+$.

I7

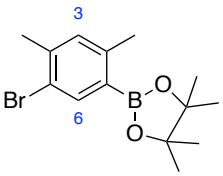

This compound was prepared *via* the Miyaura borylation reaction using 1,5-dibromo-2,4-dimethylbenzene (550 mg, 2.08 mmol), B_2pin_2 (443 mg, 3.43 mmol), KOAc (1020 mg, 10.4 mmol) and $PdCl_2$(dppf) (127 mg, 0.174 mmol) in 1,4-dioxane (20 mL). The crude product was used in further reactions without purification.

I8

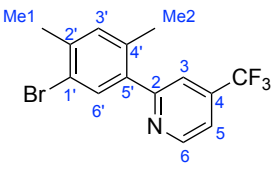

This compound was prepared *via* the Suzuki cross-coupling reaction using crude **I7** (648 mg, 2.08 mmol), 2-bromo-4-(trifluoromethyl)pyridine (589 mg, 2.60 mmol), aqueous Na_2CO_3 (1770 mg, 16.7 mmol), $Pd(PPh_3)_4$ (120 mg, 0.104 mmol) and DME (15 mL). The crude mixture was purified by column chromatography on silica (hexane: ethyl acetate gradient, R_f = 0.3 in 90:10) to yield the pure product as a clear oil (124 mg, 18%); δ H (700 MHz, $CDCl_3$) 8.87 (1 H, dt, J 5.1, 0.7, H^6), 7.59 (1 H, dt, J 1.6, 0.8, H^3), 7.59 (1 H, s, $H^{6'}$), 7.47 (1 H, ddd, J 5.1, 1.7, 0.7, H^5), 7.17 (1 H, t, J 0.9, $H^{3'}$), 2.41 (3 H, s, H^{Me1}), 2.30 (3 H, s, H^{Me2}); δ C (176 MHz, $CDCl_3$) 159.8 (C^2), 150.2 (C^6), 138.6 ($C^{5'}$), 138.2 ($C^{4'}$), 135.0 ($C^{2'}$), 133.4 ($C^{3'}$), 133.1 ($C^{6'}$), 123.6 (C^4), 122.0 ($C^{1'}$), 119.5 (C^3), 117.4 (C^5), 22.5 (C^{Me1}), 19.7 (C^{Me2}); δ F (376 MHz, $CDCl_3$) -64.7; MS ESI (ES^+) *m/z* 330.1 (M^+, 99%), 332.1 ($[M+H]^+$, 100%); HRMS (ES^+) *m/z* 330.0108 $[M+H]^+$, calc. for $[C_{14}H_{12}NF_3Br]$ 330.0105.

P12

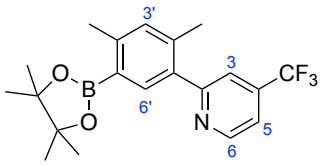

This compound was prepared *via* the Miyaura borylation reaction using **I8** (124 mg, 0.376 mmol), B_2pin_2 (115 mg, 0.451 mmol), KOAc (221 mg, 2.26 mmol) and $PdCl_2$(dppf) (28 mg, 0.038 mmol) in 1,4-dioxane (4 mL). The crude product was used in further reactions without purification.

P13

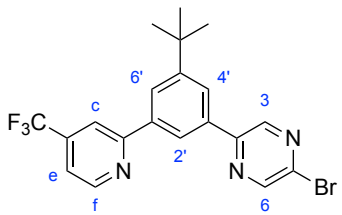

This compound was isolated as a side product from the Suzuki reaction between **P11** (286 mg, 0.706 mmol) and 2,5-dibromopyrazine (84 mg, 0.353 mmol) with aqueous Na_2CO_3 (299 mg, 2.83 mmol), $Pd(PPh_3)_4$ (21 mg, 0.018 mmol) and DME (3 mL). The crude mixture was purified by column chromatography on silica (hexane: ethyl

acetate gradient, R_f = 0.3 in 90:10) to yield the pure product as a yellow solid (73 mg, 47%); δ H (400 MHz, $CDCl_3$) 8.94 (1 H, dt, J 5.1. 0.8), 8.90 (1 H, d, J 1.4), 8.79 (1 H, d, J 1.5), 8.44 (1 H, t, J 1.7), 8.20 (1 H, t, J 1.8), 8.15 (1 H, t, J 1.8), 8.04 – 7.98 (1 H, m), 7.52 (1 H, ddd, J 5.1, 1.6, 0.7), 1.49 (9 H, s, $H^{t\text{-}Bu}$); MS ESI (ES^+) *m/z* 438.3 ($[M+H]^+$, 100%); HRMS (ES^+) *m/z* 436.0640 $[M+H]^+$, calc. for 436.0636 $[C_{20}H_{18}N_3F_3Br]$.

7.4.2 Proligands

HL^{12}: 1-(3-Isoquinolyl)-3-(2-pyridyl)benzene

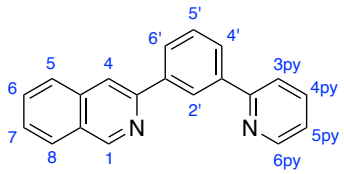

This proligand was prepared *via* the Suzuki cross-coupling reaction of 3-isoquinolyl triflate (284 mg, 1.02 mmol) and crude **P4** (240 mg, 0.85 mmol) with aqueous Na_2CO_3 (724 mg, 6.83 mmol), $Pd(PPh_3)_4$ (49 mg, 0.04 mmol) and DME (7 mL). The crude mixture was purified by column chromatography (hexane: ethyl acetate, gradient to 80:20, R_f = 0.3 in 80:20) to yield the pure product as a clear oil (96 mg, 44%); δ H (600 MHz, $CDCl_3$) 9.42 (1 H, s, H^1), 8.78 (1 H, ddd, J 4.9, 1.8, 1.0, H^{6py}), 8.74 (1 H, dt, J 1.9, 1.0, $H^{2'}$), 8.26 (1 H, s, H^4), 8.20 (1 H, ddd, J 7.8, 1.9, 1.1, $H^{4'}$ or $H^{6'}$), 8.08-8.01 (2 H, m, $H^{4'}$ or $H^{6'}$, and H^5), 7.92-7.96 (2 H, m, H^8 and H^{3py}), 7.87 (1 H, td, J 7.7, 1.8, H^{4py}), 7.76 (1 H, ddd, J 8.2, 6.8, 1.2, H^7), 7.62-7.66 (2 H, m, H^6 and $H^{5'}$), 7.33 (1 H, ddd, J 7.4, 4.9, 1.2, H^{5py}); δ C (151 MHz, $CDCl_3$) 210.8 (C^q), 156.8 (C^q), 151.8 (C^1), 149.9 (C^q), 148.9 (C^{6py}), 139.1 (C^q), 139.0 (C^q), 137.8 (C^{4py}), 137.0 (C^q), 131.4 (C^7), 129.6 (C^6 or $C^{5'}$), 128.1 ($C^{4'}$ or $C^{6'}$), 127.9 ($C^{4'}$, and $C^{6'}$ or C^5), 127.7 (C^6 or $C^{5'}$), 127.5 ($C^{4'}$ and $C^{6'}$ or C^5), 127.1 (C^8 or C^{3py}), 125.9 ($C^{2'}$), 122.6 (C^{5py}), 121.4 (C^8 or C^{3py}), 117.7 (C^4); MS ESI (ES^+) *m/z* 283.2 ($[M+H]^+$, 100%); HRMS (ES^+) *m/z* 283.1240 $[M+H]^+$, calc. for $[C_{20}H_{15}N_2]$ 283.1235.

***HL*[13]**

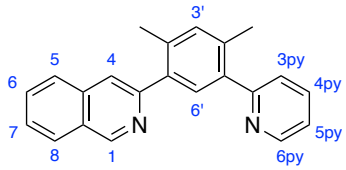

This proligand was prepared *via* the Suzuki cross-coupling reaction using crude **P6** (118 mg, 0.38 mmol), 3-isoquinolyl triflate (106 mg, 0.38 mmol), aqueous Na_2CO_3 (323 mg, 3.05 mmol), $Pd(PPh_3)_4$ (22 mg, 0.02 mmol) and DME (3 mL). The crude reaction mixture was purified by column chromatography (hexane: ethyl acetate gradient, R_f = 0.3 in 50:50) to yield the pure product as a white solid (35 mg, 30%); δ H (600 MHz, $CDCl_3$) 9.32 (1 H, t, J 0.9, H^1), 8.69 (1 H, ddd, J 4.9, 1.8, 0.9, H^{6py}), 7.99 (1 H, dt, J 8.3, 1.0, H^5), 7.82 (1 H, dd, J 8.2, 1.0, H^8), 7.78 (1 H, d, J 1.0, $H^{6'}$), 7.74 – 7.65 (2 H, m, H^{4py} and H^7), 7.59 (1 H, ddd, J 8.1, 6.9, 1.1, H^6), 7.57 (1 H, s, $H^{3'}$), 7.45 (1 H, dt, J 7.8, 1.1, H^{3py}), 7.24 (1 H, s, H^4), 7.21 (1 H, ddd, J 7.5, 4.9, 1.2, H^{5py}), 2.44 (3 H, s, H^{Me}), 2.42 (3 H, s, H^{Me}); δ C (151 MHz, $CDCl_3$) 159.8 (C^q), 153.4 (C^q), 151.7 (C^1), 149.1 (C^{6py}), 138.1 (C^q), 138.0 (C^q), 136.3 (C^q), 136.2 (C^q), 136.1 (C^{4py}), 135.5 (C^q), 133.3 (C^4), 131.5 ($C^{3'}$), 130.4 (C^7), 127.5 (C^5), 127.2 (C^q), 127.0 (C^6), 126.7 (C^8), 124.2 (C^{3py}), 121.5 (C^{5py}), 120.1 ($C^{6'}$), 20.1 (C^{Me}), 20.0 (C^{Me}); MS ESI (ES^+) *m/z* 311.4 ($[M+H]^+$, 100%); HRMS (AP^+) *m/z* 311.1563 $[M+H]^+$, calc. for $[C_{22}H_{19}N_2]$ 311.1548.

***HL*[14]**

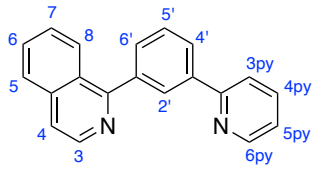

This proligand was prepared *via* the Suzuki cross-coupling reaction using crude **P4** (250 mg, 0.89 mmol), 1-chloroisoquinoline (175 mg, 1.07 mmol), aqueous Na_2CO_3 (754 mg, 7.11 mmol), $Pd(PPh_3)_4$ (51 mg, 0.04 mmol) and DME (7 mL). The crude mixture was purified by column chromatography (hexane: ethyl acetate, gradient to 70:30, R_f = 0.2 in 70:30) to yield the pure product as a yellow oil (106 mg, 42%); δ H (700 MHz, $CDCl_3$) 8.69 (1 H, ddd, J 4.8, 1.8, 0.9, H^{6py}), 8.63 (1 H, d, J 5.7, H^3), 8.32 – 8.28 (1 H, m, $H^{2'}$), 8.16 (2 H, ddq, J 16.4, 8.5, 1.1, H^8 and, $H^{4'}$ or $H^{6'}$), 7.90 (1 H, d, J 8.2, H^5), 7.81 (1 H, dt, J 8.0, 1.0, H^{3py}), 7.77 – 7.73 (2 H, m, H^{4py} and, $H^{4'}$ or $H^{6'}$), 7.70 (1 H,

ddd, J 8.2, 6.8, 1.1, H^6), 7.69 – 7.67 (1 H, m, H^{6py}), 7.66 – 7.62 (1 H, m, H^3), 7.55 (1 H, ddd, J 8.3, 6.8, 1.2, H^7), 7.24 (1 H, ddd, J 7.5, 4.8, 1.2, H^{5py}); δ C (176 MHz, $CDCl_3$) 171.1 (C^q), 160.4 (C^q), 157.1 (C^q), 149.7 (C^{6py}), 141.9 (C^3), 139.6 (C^q), 136.9 (C^q), 136.8 ($C^{4'}$, $C^{6'}$ or C^{4py}), 130.4 ($C^{4'}$, $C^{6'}$, or C^{4py}), 130.2 (C^6), 128.8 ($C^{5'}$), 128.5 ($C^{2'}$), 127.6 ($C^{4'}$, $C^{6'}$ or C^8), 127.4 ($C^{4'}$, $C^{6'}$ or C^8), 127.3 (C^7), 127.0 (C^5), 126.8 (C^q), 122.3 (C^{5py}), 120.7 (C^{3py}), 120.1 (C^4); MS ESI (ES^+) *m/z* 283.4 ($[M+H]^+$, 100%); HRMS (ES^+) *m/z* 283.1238 $[M+H]^+$, calc. for $[C_{20}H_{15}N_2]$ 283.1235.

HL[15]

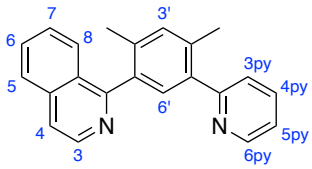

This proligand was prepared *via* the Suzuki cross-coupling reaction using crude **P6** (324 mg, 1.05 mmol), 1-chloroisoquinoline (290 mg, 1.05 mmol), aqueous Na_2CO_3 (889 mg, 8.38 mmol), $Pd(PPh_3)_4$ (61 mg, 0.08 mmol) and DME (8 mL). The crude mixture was purified by column chromatography (hexane: ethyl acetate gradient, R_f = 0.1 in 60:40) followed by recrystallisation from hexane/DCM to yield the pure product as a yellow oil (78 mg, 24%); δ H (700 MHz, $CDCl_3$) 8.66 (1 H, dd, J 4.9, 1.7, H^{6py}), 8.61 (1 H, d, J 5.8, H^3), 7.89 (1 H, d, J 8.2, H^6), 7.79 (1 H, d, J 8.5, H^8), 7.74 – 7.68 (3 H, m, H^{4py}, H^4 and H^5), 7.51 (1 H, t, J 7.6, H^7), 7.46 (1 H, d, J 7.9, H^{3py}), 7.39 (1 H, s, $H^{6'}$), 7.28 (1 H, s, $H^{3'}$), 7.21 (1 H, dd, J 7.6, 4.8, H^{5py}), 2.45 (3 H, s, H^{Me}), 2.10 (3 H, s, H^{Me}); δ C (176 MHz, $CDCl_3$) 163.9 (C^q), 161.1 (C^q), 159.7 (C^q), 148.9 (C^{6py}), 141.9 (C^3), 137.8 (C^q), 136.6 (C^{4py}, C^4, or C^5), 136.2 (C^q), 132.9 ($C^{3'}$), 132.7 (C^q), 131.0 ($C^{6'}$), 130.2 (C^q), 128.0 (C^8), 127.5 (C^7), 126.9 (C^6), 126.2 (C^q), 124.4 (C^{4py}, C^4, or C^5), 124.3 (C^{3py}), 121.6 (C^{5py}), 120.4 (C^{4py}, C^4, or C^5); MS ESI (ES^+) m/z 311.4 ([M+H]+, 100%); HRMS (ES^+) *m/z* 311.1525 $[M+H]^+$, calc. for $[C_{22}H_{19}N_2]$ 311.1548.

HL[16]

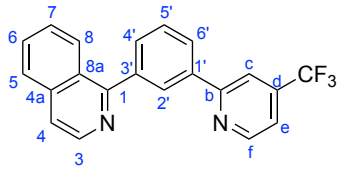

This proligand was prepared *via* the Suzuki cross-coupling method using crude **P8** (550 mg, 1.66 mmol), 2-bromo-4-(trifluoromethyl)pyridine (375 mg, 1.66 mmol), aqueous Na_2CO_3 (1410 mg, 13.3 mmol), $Pd(PPh_3)_4$ (96 mg, 0.083 mmol) and DME (13 mL). The crude mixture was purified by column chromatography on silica (hexane: ethyl acetate, R_f = 0.2 in 80:20) to yield the pure product as a yellow oil (328 mg, 56%); δ H (700 MHz, $CDCl_3$) 8.87 (1 H, d, J 5.0, H^f), 8.64 (1 H, d, J 5.6, H^3), 8.36 (1 H, s, $H^{2'}$), 8.21 (1 H, dt, J 8.0, 1.3, $H^{6'}$), 8.13 (1 H, d, J 8.5, H^8), 8.02 (1 H, s, H^c), 7.92 (1 H, d, J 8.2, H^5), 7.81 (1 H, d, J 7.5, $H^{4'}$), 7.72 (2 H, dd, J 8.6, 6.7, H^4 and H^6), 7.69 (1 H, t, J 7.7, $H^{5'}$), 7.59 – 7.56 (1 H, m, H^7), 7.47 – 7.45 (1 H, m, H^7); δ C (176 MHz, $CDCl_3$) 160.0 (C^1), 158.3 ($C^{1'}$), 150.7 (C^f), 139.2 (C^{CF_3}), 138.3 ($C^{3'}$), 137.0 (C^{4a} or C^{8a}), 131.3 ($C^{4'}$), 129.0 ($C^{5'}$), 128.6 ($C^{2'}$), 127.6 (C^7), 127.5 (C^8), 127.4 ($C^{6'}$), 127.1 (C^5), 126.7 (C^{4a} or C^{8a}), 123.7 (C^d), 122.1 (C^b), 120.4 (C^4), 117.7 (C^e), 116.2 (C^c); δ F (376 MHz, $CDCl_3$) -64.8; MS ESI $(ES)^+$ *m/z* 351.2 ($[M+H]^+$, 100%); HRMS (ES^+) *m/z* 351.1097 $[M+H]^+$, calc. for $[C_{21}H_{14}N_2F_3]$ 351.1109.

HL[17]

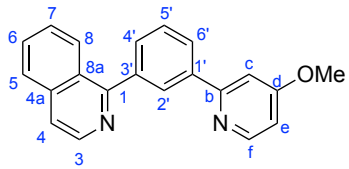

This compound was prepared *via* the Suzuki cross-coupling reaction using crude **P8** (833 mg, 2.52 mmol), 2-chloro-4-methoxypyridine (361 mg, 2.52 mmol), aqueous Na_2CO_3 (2132 mg, 20.1 mmol), $Pd(PPh_3)_4$ (145 mg, 0.126 mmol) and DME (20 mL). The crude mixture was purified by column chromatography on silica (hexane: ethyl acetate gradient, R_f = 0.3 in 30:70) to yield the pure product as a clear oil (725 mg, 92%); δ H (600 MHz, $CDCl_3$) 8.62 (1 H, d, J 5.6, H^3), 8.51 (1 H, d, J 5.7, H^f), 8.25 (1 H, t, J 1.8, $H^{2'}$), 8.13 (2 H, dddd, J 9.5, 8.5, 1.9, 1.0, $H^{6'}$ and H^7), 7.88 (1 H, dd, J 8.3, 1.0, H^5), 7.73 (1 H, dt, J 7.6, 1.5, $H^{4'}$), 7.68 (1 H, ddd, J 8.1, 6.8, 1.2, H^6), 7.66 (1 H, dd, J 5.7, 0.9,

H^4), 7.63 (1 H, t, J 7.7, $H^{5'}$), 7.53 (1 H, ddd, J 8.3, 6.9, 1.2, H^8), 7.29 (1 H, d, J 2.4, H^c), 6.77 (1 H, dd, J 5.7, 2.4, H^e), 3.88 (3 H, s, H^{OMe}); δ C (151 MHz, $CDCl_3$) 166.4 (C^b), 160.5 (C^1), 158.9 ($C^{1'}$), 150.9 (C^f), 142.2 (C^3), 139.9 (C^{8a}), 139.7 ($C^{3'}$), 136.8 (C^{4a}), 130.5 ($C^{4'}$), 130.0 (C^6), 128.7 ($C^{5'}$), 128.5 ($C^{2'}$), 127.5 ($C^{6'}$ or C^7), 127.3 ($C^{6'}$ or C^7), 127.3 (C^8), 126.9 (C^5), 126.8 (C^d), 120.0 (C^4), 108.4 (C^e), 106.9 (C^c), 55.2 (C^{OMe}); MS ESI (ES^+) *m/z* 313.3 ($[M+H]^+$, 60%); HRMS (ES^+) *m/z* 313.1334 $[M+H]^+$, calc. for $[C_{21}H_{17}N_2O]$ 313.1341.

HL[18]

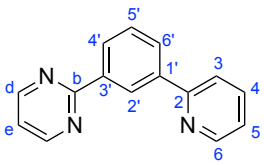

This proligand was prepared *via* the Suzuki cross-coupling reaction using crude **P4** (275 mg, 0.978 mmol), 2-bromopyrimidine (155 mg, 0.978 mmol), aqueous Na_2CO_3 (829 mg, 7.82 mmol), $Pd(PPh_3)_4$ (57 mg, 0.049 mmol) and DME (8 mL). The crude mixture was purified by column chromatography on silica (hexane: ethyl acetate gradient, R_f = 0.3 in 70:30) to yield the pure product as a yellow oil (102 mg, 45%); δ H (400 MHz, $CDCl_3$) 9.08 (1 H, s, $H^{2'}$), 8.87 (2 H, d, J 4.8, H^d), 8.76 (1 H, dd, J 4.9, 1.5, H^6), 8.53 (1 H, dd, J 7.8, 1.5, $H^{4'}$ or $H^{6'}$), 8.22 (1 H, dd, J 7.8, 1.7, $H^{4'}$ or $H^{6'}$), 7.95 – 7.89 (1 H, m, H^3), 7.82 (1 H, tt, J 7.8, 1.4, H^4), 7.65 (1 H, t, J 7.8, $H^{5'}$), 7.32 – 7.29 (1 H, m, H^5), 7.25 (1 H, t, J 4.8, H^e); δ C (101 MHz, $CDCl_3$) 164.5 (C^b), 157.3 (C^d), 157.0 (C^2), 149.6 (C^6), 139.7 ($C^{1'}$ or $C^{3'}$), 138.1 ($C^{1'}$ or $C^{3'}$), 137.0 (C^4), 129.4 ($C^{4'}$ or $C^{6'}$), 129.2 ($C^{5'}$), 128.7 ($C^{4'}$ or $C^{6'}$), 126.7 ($C^{2'}$), 122.3 (C^5), 120.8 (C^3), 119.3 (C^e). MS ES (ES^+) *m/z* 234.2 ($[M+H]^+$, 100%); HRMS (ES^+) *m/z* 234.1038 $[M+H]^+$, calc. for $[C_{15}H_{12}N_3]$ 234.1031.

HL[19]

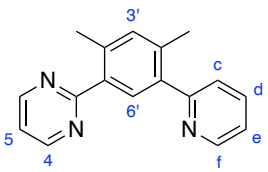

This proligand was prepared *via* the Suzuki cross-coupling reaction using crude **P6** (324 mg, 1.048 mmol), 2-bromopyrimidine (167 mg, 1.05 mmol), aqueous Na_2CO_3

(889 mg, 8.38 mmol), $Pd(PPh_3)_4$ (61 mg, 0.08 mmol) and DME (8 mL). The crude mixture was purified by column chromatography (hexane: ethyl acetate gradient, R_f = 0.2 in 40:60) to yield the pure product as a white solid (91 mg, 33%); δ H (700 MHz, $CDCl_3$) 8.81 (2 H, d, J 4.8, H^4), 8.67 (1 H, ddd, J 4.9, 1.9, 1.0, H^f), 7.95 (1 H, s, $H^{6'}$), 7.72 (1 H, td, J 7.7, 1.8, H^d), 7.46 (1 H, dt, J 7.8, 1.1. H^c), 7.22 – 7.20 (2 H, m, H^e and $H^{3'}$), 7.17 (1 H, t, J 4.8, H^5), 2.60 (3 H, s, H^{Me}), 2.41 (3 H, s, H^{Me}); δ C (176 MHz, $CDCl_3$) 167.4 (C^q), 159.6 (C^q), 156.7 (C^4), 149.1 (C^f), 138.1 (C^q), 137.4 (C^q), 137.2 (C^q), 136.0 (C^d), 135.6 (C^q), 134.0 ($C^{3'}$), 132.1 ($C^{6'}$), 124.2 (C^c), 121.5 (C^e), 118.3 (C^5), 20.9 (C^{Me}), 20.1 (C^{Me}); MS ESI (ES+) *m/z* 262.4 ([M+H]+, 100%); HRMS (ES^+) *m/z* 262.1345 $[M+H]^+$, calc. for $[C_{17}H_{16}N_3]$ 262.1344.

HL[20]

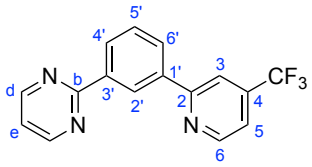

This proligand was prepared *via* the Suzuki cross-coupling reaction using crude **P10** (600 mg, 2.13 mmol), 2-bromo-4-(trifluoromethyl)pyridine (481 mg, 2.13 mmol), aqueous Na_2CO_3 (1800 mg, 17.0 mmol), $Pd(PPh_3)_4$ (123 mg, 0.106 mmol) and DME (15 mL). The crude mixture was purified by column chromatography on silica (hexane: ethyl acetate, R_f = 0.2 in 80:20) to yield the pure product as a pale yellow solid (495 mg, 77%); δ H (700 MHz, $CDCl_3$) 9.09 (1 H, t, J 1.9, $H^{2'}$), 8.90 (1 H, d, J 5.0, H^6), 8.86 (2 H, d, J 4.8, H^d), 8.56 (1 H, dt, J 7.8, 1.4, $H^{4'}$), 8.22 (1 H, ddd, J 7.7, 1.8, 1.1, $H^{6'}$), 8.07 (1 H, s, H^3), 7.65 (1 H, t, J 7.7, $H^{5'}$), 7.49 – 7.44 (1 H, m, H^5), 7.24 (1 H, t, J 4.8, H^e); δ C (176 MHz, $CDCl_3$) 164.2 (C^b), 158.4 (C^2), 157.3 (C^d), 150.6 (C^6), 138.3 ($C^{1'}$), 138.3 ($C^{3'}$), 129.5 ($C^{4'}$), 129.4 ($C^{5'}$), 129.4 ($C^{6'}$), 126.7 ($C^{2'}$), 123.7 (C^4), 122.2 (C^{CF_3}), 119.4 (C^e), 117.7 (C^5), 116.2 (C^3); δ F (376 MHz, $CDCl_3$) -64.7; MS ESI (ES^+) *m/z* 302.2 ($[M+H]^+$, 100%); HRMS (ES^+) *m/z* 302.0901 $[M+H]^+$, calc. for $[C_{16}H_{11}N_3F_3]$ 302.0905.

***HL*[21]**

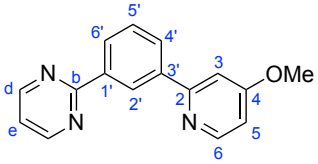

This compound was prepared *via* the Suzuki cross-coupling reaction using crude **P10** (480 mg, 1.70 mmol), 2-chloro-4-methoxypyridine (244 mg, 1.70 mmol), aqueous Na_2CO_3 (1440 mg, 13.6 mmol), $Pd(PPh_3)_4$ (98 mg, 0.085 mmol) and DME (15 mL). The crude mixture was purified by column chromatography on silica (hexane: ethyl acetate gradient, R_f = 0.3 in 50:50) to yield the pure product as an off-white solid (307 mg, 69%); δ H (700 MHz, $CDCl_3$) 9.00 (1 H, td, J 1.8, 0.6, $H^{2'}$), 8.79 (2 H, dd, J 4.8, 0.5, H^{d}), 8.51 (1 H, dd, J 5.7, 0.6, H^{6}), 8.47 (1 H, ddd, J 7.7, 1.8, 1.1, $H^{6'}$), 8.13 (1 H, ddd, J 7.7, 1.9, 1.1, $H^{4'}$), 7.57 (1 H, td, J 7.7, 0.6, $H^{5'}$), 7.34 (1 H, dd, J 2.4, 0.5, H^{3}), 7.16 (1 H, t, J 4.8, H^{e}), 6.76 (1 H, dd, J 5.7, 2.4, H^{5}), 3.89 (3 H, s, H^{OMe}); δ C (176 MHz, $CDCl^{3}$) 166.4 (C^{4}), 164.5 (C^{b}), 158.8 (C^{2}), 157.2 (C^{d}), 150.9 (C^{6}), 139.8 ($C^{3'}$), 138.0 ($C^{1'}$), 129.4 ($C^{4'}$), 129.0 ($C^{5'}$), 128.7 ($C^{6'}$), 126.7 ($C^{2'}$), 119.2 (C^{e}), 108.3 (C^{5}), 106.9 (C^{3}), 55.2 (C^{3}); MS ESI (ES^+) *m/z* 264.1 ($[M+H]^+$, 100%); HRMS (ES^+) *m/z* 264.1128 $[M+H]^+$, calc. for $[C_{16}H_{14}N_3O]$ 264.1137.

***HL*[22]**

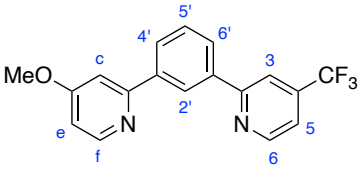

This proligand was prepared *via* the Suzuki cross-coupling reaction using 2-chloro-4-methoxypyridine (395 mg, 2.75 mmol), crude **P7** (800 mg, 2.29 mmol), aqueous Na_2CO_3 (1940 mg, 18.33 mmol), $Pd(PPh_3)_4$ (132 mg, 0.12 mmol) and DME (10 mL). The crude mixture was purified by column chromatography (hexane: ethyl acetate gradient, R_f = 0.1 in 80:20) to yield the pure product as a yellow oil (63 mg, 8%); δ H (600 MHz, $CDCl_3$) 8.88 (1 H, dt, J 5.1, 0.7, H^{6}), 8.63 (1 H, t, J 1.9, $H^{2'}$), 8.56 (1 H, d, J 5.7, H^{c}), 8.10 (1 H, ddd, J 7.7, 1.9, 1.0, $H^{4'}$ or $H^{6'}$), 8.06 (1 H, ddd, J 7.8, 1.8, 1.1, $H^{4'}$ or $H^{6'}$), 8.04 (1 H, dt, J 1.7, 0.9, H^{3}), 7.61 (1 H, td, J 7.8, 0.6, $H^{5'}$), 7.46 (1 H, ddd, J 5.0, 1.6, 0.8, H^{5}), 7.33 (1 H, d, J 2.4, H^{f}), 6.82 (1 H, dd, J 5.7, 2.4, H^{e}), 3.93 (3 H, s, H^{OMe}); δ C

(151 MHz, $CDCl_3$) 166.6 (C^q), 158.5 (C^q), 150.8 (C^c), 150.6 (C^6), 139.3 (C^q), 139.0 (C^q), 138.5 (C^q), 129.4 ($C^{5'}$), 128.4 ($C^{4'}$ or $C^{6'}$), 127.7 ($C^{4'}$ or $C^{6'}$), 125.7 ($C^{2'}$), 117.7 (C^5), 116.2 (C^3), 108.3 (C^e), 107.2 (C^f), 55.3 (C^{OMe}); MS ESI (ES+) m/z 331.3 ([M+H]+, 100%); HRMS (ES^+) *m/z* 331.1069 $[M+H]^+$, calc. for $[C_{18}H_{14}N_2OF_3]$ 331.1058.

HL[23]

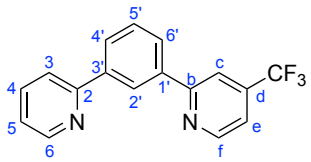

This compound was prepared *via* the Suzuki cross-coupling reaction using crude **P4** (295 mg, 1.05 mmol), 2-bromo-4-(trifluoromethyl)pyridine (237 mg, 1.05 mmol), aqueous Na_2CO_3 (889 mg, 8.39 mmol), $Pd(PPh_3)_4$ (60 mg, 0.052 mmol) and DME (8 mL). The crude mixture was purified by column chromatography on silica (hexane: ethyl acetate gradient, R_f = 0.3 in 70:30) to yield the pure product as a clear oil (19 mg, 6%); δ H (700 MHz, $CDCl_3$) 8.89 (1 H, d, J 5.0, H^f), 8.74 (1 H, ddd, J 4.8, 1.8, 1.0, H^6), 8.67 (1 H, t, J 1.9, $H^{2'}$), 8.12 – 8.08 (2 H, m, $H^{4'}$ and $H^{6'}$), 8.04 (1 H, s, H^c), 7.85 (1 H, dt, J 8.0, 1.1, H^3), 7.80 (1 H, td, J 7.6, 1.8, H^4), 7.64 – 7.59 (1 H, m, $H^{5'}$), 7.47 (1 H, ddd, J 5.1, 1.6, 0.8, H^e), 7.28 (1 H, ddd, J 7.4, 4.8, 1.2, H^5); δ C (176 MHz, $CDCl_3$) 158.5 (C^a), 156.8 (C^2), 150.6 (C^f), 149.6 (C^6), 140.0 ($C^{3'}$), 139.2 (C^d), 138.6 ($C^{1'}$), 137.0 (C^4), 129.4 ($C^{5'}$), 128.3 ($C^{4'}$ or $C^{6'}$), 127.6 ($C^{4'}$ or $C^{6'}$), 125.6 ($C^{2'}$), 123.7 (C^{CF_3}), 122.5 (C^5), 120.8 (C^3), 117.7 (C^e), 116.2 (C^c); δ F (376 MHz, $CDCl_3$) -64.7; MS ESI (ES^+) *m/z* 302.1 ($[M+H]^+$, 100%); HRMS (ES^+) *m/z* 301.0952 $[M+H]^+$, calc. for $[C_{17}H_{12}N_2F_3]$ 301.0953.

HL[24]

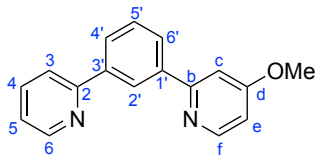

This compound was prepared *via* the Suzuki cross-coupling reaction using crude **P4** (295 mg, 1.05 mmol), 2-chloro-4-methoxypyridine (151 mg, 1.05 mmol), aqueous Na_2CO_3 (889 mg, 8.39 mmol), $Pd(PPh_3)_4$ (60 mg, 0.052 mmol) and DME (8 mL). The

crude mixture was purified by column chromatography on silica (hexane: ethyl acetate gradient, R_f = 0.2 in 60:40) to yield the pure product as a clear oil (110 mg, 48%); δ H (599 MHz, $CDCl_3$) 8.70 (1 H, ddd, J 4.7, 1.9, 1.0, H^6), 8.58 (1 H, t, J 1.8, $H^{2'}$), 8.52 (1 H, d, J 5.8, H^f), 8.03 (2 H, ddt, J 18.1, 8.0, 1.4, $H^{4'}$ and $H^{6'}$), 7.81 (1 H, dt, J 8.0, 1.1, H^3), 7.73 (1 H, td, J 7.7, 1.9, H^4), 7.56 (1 H, t, J 7.7, $H^{5'}$), 7.32 (1 H, d, J 2.4, H^c), 7.22 (1 H, ddd, J 7.4, 4.8, 1.2, H^5), 6.77 (1 H, dd, J 5.7, 2.4, H^e), 3.88 (3 H, d, J 1.9, H^{OMe}); δ C (151 MHz, $CDCl_3$) 166.4 (C^d), 158.9 (C^b), 157.2 (C^2), 150.8 (C^f), 149.6 (C^6), 139.9 ($C^{1'}$ and $C^{3'}$), 136.7 (C^4), 129.1 ($C^{5'}$), 127.5 ($C^{4'}$ and $C^{6'}$), 125.5 ($C^{2'}$), 122.2 (C^5), 120.7 (C^3), 108.3 (C^3), 107.0 (C^c), 55.2 (C^{OMe}); MS ESI (ES^+) *m/z* 264.1 ($[M+H]^+$, 100%); HRMS (ES^+) *m/z* 263.1173 $[M+H]^+$, calc. for $[C_{17}H_{15}N_2O]$ 263.1184.

***HL*[25]**

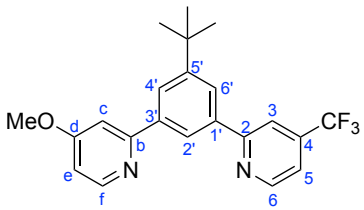

This proligand was prepared *via* the Suzuki cross-coupling reaction using crude **P11** (486 mg, 1.20 mmol), 2-chloro-4-methoxypyridine (172 mg, 1.20 mmol), aqueous Na_2CO_3 (1020 mg, 9.59 mmol), $Pd(PPh_3)_4$ (69 mg, 0.060 mmol) and DME (10 mL). The crude mixture was purified by column chromatography on silica (hexane: ethyl acetate gradient, R_f = 0.2 in 80:20) to yield the pure product as a yellow oil (151 mg, 33%); δ H (700 MHz, $CDCl_3$) 8.89 (1 H, d, J 5.0, H^6), 8.61 (1 H, d, J 5.9, H^f), 8.37 (1 H, t, J 1.6, $H^{2'}$), 8.17 (1 H, s, $H^{6'}$), 8.13 (1 H, s, $H^{4'}$), 8.05 (1 H, s, H^3), 7.48 – 7.43 (1 H, m, H^5), 7.34 (1 H, d, J 2.4, H^c), 6.88 (1 H, s, H^e), 3.98 (3 H, s, H^{OMe}), 1.47 (9 H, s, H^{tBu}); δ C (176 MHz, $CDCl_3$) 150.5 (C^6), 139.3, 138.5, 127.8, 125.9 ($C^{4'}$), 125.8, 123.7, 123.3 ($C^{2'}$), 117.6 (C^5), 116.5 (C^3), 108.4 (C^e), 107.9 (C^c), 55.6 (C^{OMe}), 31.4 ($C^{t\text{-}Bu}$); MS ESI (ES^+) *m/z* 387.3 ($[M+H]^+$, 100%); HRMS (ES^+) *m/z* 387.1676 $[M+H]^+$, calc. for $[C_{22}H_{22}N_2OF_3]$ 387.1684.

***HL*[26]**

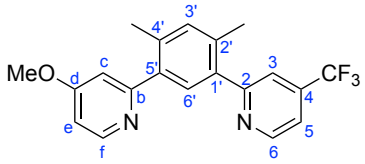

This compound was prepared *via* the Suzuki cross-coupling reaction using crude **P12** (142 mg, 0.376 mmol), 2-chloro-4-methoxypyridine (54 mg, 0.376 mmol), aqueous Na_2CO_3 (319 mg, 3.01 mmol), $Pd(PPh_3)_4$ (22 mg, 0.019 mmol) and DME (3 mL). The crude mixture was purified by column chromatography on silica (hexane: ethyl acetate gradient, R_f = 0.6 in 30:70) to yield the pure product as a clear oil (12 mg, 9%); δ H (600 MHz, $CDCl_3$) 8.84 (1 H, d, J 5.2, H^6), 8.18 (1 H, dd, J 5.9, 1.3, H^f), 7.63 (1 H, s, H^3), 7.43 (1 H, d, J 5.3, H^5), 7.23 – 7.18 (1 H, m, $H^{3'}$ and $H^{6'}$), 6.83 (1 H, t, J 1.8, H^c), 6.74 (1 H, dt, J 5.8, 1.8, H^e), 3.84 (3 H, d, J 1.3, H^{OMe}), 2.40 (3 H, d, J 1.2, H^{Me}), 2.12 (3 H, d, J 1.3, H^{Me}); δ C (151 MHz, $CDCl_3$) 150.2 (C^f), 149.9 (C^6),132.6 ($C^{6'}$), 130.7 ($C^{3'}$), 119.6 (C^3), 116.9 (C^5), 109.7 (C^e) 109.4 (C^c); MS ESI (ES^+) *m/z* 359.2 ($[M+H]^+$, 100%).

***HL*[27]**

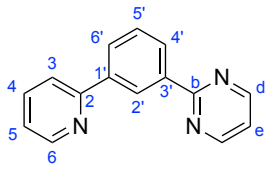

This proligand was prepared *via* the Suzuki cross-coupling reaction using crude **P4** (275 mg, 0.978 mmol), chloropyrazine (112 mg, 0.978 mmol), aqueous Na_2CO_3 (829 mg, 7.82 mmol), $Pd(PPh_3)_4$ (57 mg, 0.049 mmol) and DME (8 mL). The crude mixture was purified by column chromatography on silica (hexane: ethyl acetate gradient, R_f = 0.2 in 70:30) to yield the pure product as an off-white solid (120 mg, 53%); δ H (400 MHz, $CDCl_3$) 9.17 (1 H, s, H^c), 8.77 (1 H, dd, J 4.9, 1.4, H^6), 8.70 (2 H, dt, J 2.7, 1.4, H^f and $H^{2'}$), 8.57 (1 H, d, J 2.4, H^e), 8.18 – 8.07 (2 H, m, $H^{4'}$ and $H^{6'}$), 7.85 (2 H, ddd, J 13.5, 8.2, 6.7, H^3 and H^4), 7.66 (1 H, t, J 7.8, $H^{5'}$), 7.31 (1 H, ddd, J 6.9, 5.1, 1.3, H^5); δ C (101 MHz, $CDCl_3$) 156.8 (C^q), 152.6 (C^q), 149.8 (C^6), 144.2 (C^f or $C^{2'}$), 143.1 (C^e), 142.4 (C^c), 140.2 (C^q), 137.0 (C^3 or C^4), 136.9 (C^q), 129.6 ($C^{5'}$), 128.4 ($C^{4'}$ or $C^{6'}$), 127.4 ($C^{4'}$ or $C^{6'}$), 125.6 (C^f or $C^{2'}$), 122.5 (C^5), 120.8 (C^3 or C^4); MS ES (ES^+) *m/z* 234.1 ($[M+H]^+$, 100%); HRMS (ES^+) *m/z* 234.1036 $[M+H]^+$, calc. for $[C_{15}H_{12}N_3]$ 234.1031.

***HL*[29]**

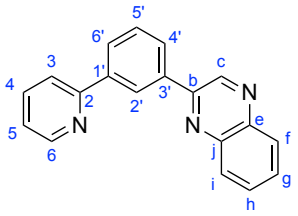

This proligand was prepared *via* the Suzuki cross-coupling reaction using crude **P4** (275 mg, 0.978 mmol), 2-chloroquinoxaline (161 mg, 0.978 mmol), aqueous Na_2CO_3 (829 mg, 7.82 mmol), $Pd(PPh_3)_4$ (57 mg, 0.049 mmol) and DME (8 mL). The crude mixture was purified by column chromatography on silica (hexane: ethyl acetate gradient, R_f = 0.3 in 70:30) to yield the pure product as a white solid (179 mg, 65%); δ H (700 MHz, $CDCl_3$) 9.42 (1 H, s, H^c), 8.84 (1 H, t, J 1.8, $H^{2'}$), 8.75 (1 H, ddt, J 4.9, 1.8, 0.8, H^6), 8.25 (1 H, ddt, J 7.7, 1.9, 0.9, $H^{4'}$), 8.20 – 8.16 (1 H, m, H^i), 8.16 – 8.11 (2 H, m, $H^{6'}$ and H^f), 7.87 (1 H, dq, J 8.0, 0.9, H^3), 7.82 – 7.77 (2 H, m, H^4 and H^h), 7.75 (1 H, ddd, J 6.9, 1.5, 0.7, H^g), 7.68 (1 H, t, J 7.7, $H^{5'}$), 7.28 (1 H, ddt, J 7.4, 4.8, 0.9, H^5); δ C (176 MHz, $CDCl_3$) 156.8 (C^2), 151.6 ($C^{3'}$), 149.8 (C^6), 143.4 (C^c), 142.3 (C^e), 141.7 (C^b), 140.4 ($C^{1'}$), 137.3 (C^j), 136.9 (C^4), 130.3 (C^h), 129.7 (C^i), 129.7 ($C^{5'}$), 129.6 (C^g) 129.1 (C^f), 128.6 ($C^{6'}$), 128.0 ($C^{4'}$), 126.1 ($C^{2'}$), 122.5 (C^5), 120.8 (C^3); MS ES (ES^+) *m/z* 284.1 ($[M+H]^+$, 100%); HRMS (ES^+) *m/z* 284.1180 $[M+H]^+$, calc. for $[C_{19}H_{14}N_3]$ 284.1188.

***HL*[30]**

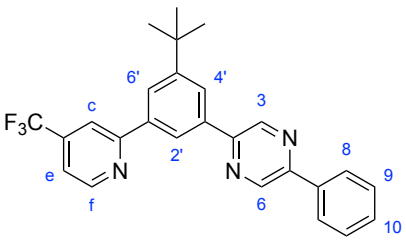

This proligand was prepared *via* the Suzuki cross-coupling reaction using **P13** (80 mg, 0.183 mmol), phenylboronic acid (22 mg, 0.183 mmol), aqueous Na_2CO_3 (155 mg, 1.46 mmol), $Pd(PPh_3)_4$ (11 mg, 0.009 mmol) and DME (2 mL). The crude mixture was purified by column chromatography on silica (hexane: ethyl acetate gradient, R_f = 0.3 in 90:10) to yield the product as a clear oil (50 mg, 63%); δ H (600 MHz, $CDCl_3$) 9.17 (1 H, d, J 1.5, H^3), 9.12 (1 H, d, J 1.5, H^6), 8.95-8.83 (1 H, m, H^f), 8.49 (1 H, t, J 1.7, $H^{2'}$), 8.21 (1 H, t, J 1.7, $H^{4'}$), 8.19 (1 H, , t, J 1.7, $H^{6'}$), 8.11-8.06 (2 H, m, H^8), 8.01 (1 H, dt, J

1.6, 0.8, H^c), 7.59-7.51 (2 H, m, H^9), 7.51-7.44 (2 H, m, H^e and H^{10}), 1.48 (9 H, s, $H^{t\text{-}Bu}$); δ C (151 MHz, $CDCl_3$) 153.0 (C^q), 150.7 (C^f), 141.5 (C^3), 141.1 (C^6), 129.9 (C^{10}), 128.8 (C^9), 126.8 (C^q), 125.7 ($C^{6'}$), 125.3 ($C^{4'}$), 122.8 ($C^{2'}$), 117.8 (C^e), 116.5 (C^c), 31.5 ($C^{t\text{-}Bu}$); MS ESI (ES^+) *m/z* 434.4 ($[M+H]^+$, 100%); HRMS (ES^+) *m/z* 434.1848 $[M+H]^+$, calc. for $[C_{26}H_{23}N_3F_3]$ 434.1844.

7.4.3 PtL^{n}Cl Complexes

PtL^{12}Cl

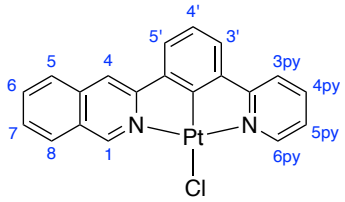

This complex was prepared by *Complexation General Procedure 1* using HL^{12} (50 mg, 0.18 mmol) and K_2PtCl_4 (84 mg, 0.20 mmol) in acetic acid (5 mL) to yield the product as a yellow solid (52 mg, 57%); δ H (700 MHz, $CDCl_3$) 10.06 (1 H, s, H^1), 9.39 (1 H, d, J 5.5, H^{6py}), 8.09 (1 H, d, J 7.6, H^5), 7.99 (1 H, s, H^4), 7.96 – 7.91 (1 H, m, H^{4py}), 7.89 (1 H, d, J 8.2, H^8), 7.85 – 7.80 (1 H, m, H^7), 7.69 (1 H, d, J 7.6, H^{3py}), 7.65 (1 H, t, J 7.6, H^6), 7.54 (1 H, d, J 7.6, $H^{3'}$ or $H^{5'}$), 7.43 (1 H, d, J 7.6, $H^{3'}$ or $H^{5'}$), 7.30-7.28 (1 H, m, H^{5py}), 7.26 (1 H, d, J 7.6, $H^{4'}$); MS ASAP (AP^+) *m/z* 517.1 ($[M\text{-}Cl+MeCN]^+$, 100%); HRMS (AP^+) *m/z* 516.0972 $[M\text{-}Cl+MeCN]^+$, calc. for $[C_{22}H_{16}N_3{}^{194}Pt]$ 516.0971. This sample was too weak to obtain a ^{13}C NMR spectrum.

PtL^{13}Cl

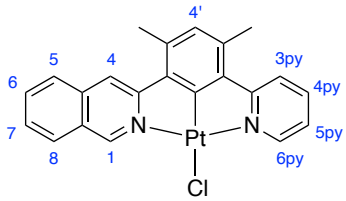

This complex was prepared by *Complexation General Procedure 1* with HL^{13} (22 mg, 0.07 mmol) with K_2PtCl_4 (34 mg, 0.08 mmol) in acetic acid (3 mL) to yield the product as a pale yellow solid (19 mg, 50%); δ H (700 MHz, $CDCl_3$) 10.14 (1 H, s, H^1), 9.55 –

9.48 (1 H, m, H^{6py}), 8.09 (1 H, s, H^{4}), 8.01 (1 H, d, J 8.1, H^{5}), 7.88 (1 H, ddd, J 8.2, 7.4, 1.7, H^{4py}), 7.82 (2 H, dd, J 14.3, 8.1, H^{8} and H^{3py}), 7.76 (1 H, ddd, J 8.1, 6.8, 1.2, H^{7}), 7.59 (1 H, ddd, J 7.9, 6.8, 1.1, H^{6}), 7.21 (1 H, ddd, J 7.2, 5.6, 1.4, H^{5py}), 6.80 (1 H, s, $H^{4'}$), 2.76 (3 H, s, H^{Me}), 2.64 (3 H, s, H^{Me}); δ C (176 MHz, $CDCl_3$) 168.1 (C^{q}), 160.6 (C^{q}), 155.6 (C^{1}), 152.3 (C^{6py}), 141.8 (C^{q}), 138.6 (C^{4py}), 137.2 (C^{q}), 136.3 (C^{q}), 136.0 (C^{q}), 135.8 (C^{q}), 133.6 (C^{q}), 133.0 (C^{q}), 132.7 (C^{7}), 131.0 ($C^{4'}$), 128.6 (C^{5}), 128.0 (C^{6}), 127.1 (C^{8}), 122.1 (C^{3py}), 122.0 (C^{5py}), 119.0 (C^{4}), 22.2 (C^{Me}), 21.9 (C^{Me}); MS ASAP (AP^{+}) *m/z* 545.1 ([M-Cl+MeCN]$^{+}$, 100%); HRMS (AP^{+}) *m/z* 544.1284 [M-Cl+MeCN]$^{+}$, calc. for $[C_{24}H_{20}N_3{}^{194}Pt]$ 544.1284.

PtL^{14}Cl

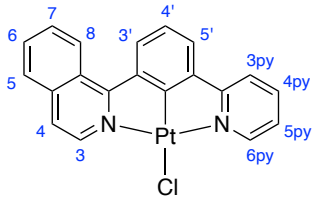

This complex was prepared by *Complexation General Procedure 1* with HL^{14} (54 mg, 0.19 mmol) and K_2PtCl_4 (90 mg, 0.22 mmol) in acetic acid (5 mL) to yield the product as an orange solid (39 mg, 40%); δ H (700 MHz, $CDCl_3$) 9.42 (2 H, dd, J 9.4, 6.1, H^{3} and H^{6py}), 8.93 (1 H, d, J 8.7, H^{5}), 8.19 (1 H, d, J 7.9, $H^{3'}$ or $H^{5'}$), 7.96 (1 H, td, J 7.8, 1.6, H^{4py}), 7.91 (1 H, d, J 8.2, H^{8}), 7.85 – 7.78 (1 H, m, H^{7}), 7.77 – 7.70 (2 H, m, H^{6} and H^{3py}), 7.62 (1 H, d, J 6.4, H^{4}), 7.52 (1 H, d, J 7.6, $H^{3'}$ or $H^{5'}$), 7.32 (2 H, td, J 7.5, 3.7, H^{5py} and $H^{5'}$); δ C (176 MHz, $CDCl_3$) 151.8 (C^{6py}), 144.1 (C^{3}), 139.0 (C^{4py}), 131.7 (C^{7}), 129.0 ($C^{3'}$ or $C^{5'}$), 128.7 (C^{6}), 127.9 (C^{8}), 125.4 (C^{5}), 124.1 ($C^{3'}$ or $C^{5'}$), 123.2 (C^{5py}), 122.8 ($C^{4'}$), 121.7 (C^{4}), 119.1 (C^{3py}), the quaternary carbon peaks were not observed; MS ASAP (AP^{+}) *m/z* 517.1 ([M-Cl+MeCN]$^{+}$, 100%); HRMS (AP^{+}) 516.0969 [M-Cl+MeCN]$^{+}$, calc. for $[C_{22}H_{16}N_3{}^{194}Pt]$ 516.0971.

PtL^{15}Cl

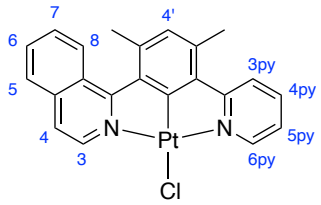

This complex was prepared by *Complexation General Procedure 1* with HL^{15} (67 mg, 0.22 mmol) with K_2PtCl_4 (102 mg, 0.25 mmol) in acetic acid (7 mL) to give the product as an orange solid (87 mg, 75%); δ H (600 MHz, $CDCl_3$) 9.54 – 9.42 (1 H, m, H^{6py}), 9.30 (1 H, d, J 6.3, H^3), 8.10 (1 H, d, J 8.6, H^5), 7.94 – 7.87 (1 H, m, H^{4py}), 7.85 (2 H, t, J 9.2, H^8 and H^{3py}), 7.76 (1 H, ddd, J 8.1, 6.8, 1.1, H^7), 7.62 (1 H, d, J 6.3, H^4), 7.58 (1 H, ddd, J 8.3, 6.8, 1.3, H^6), 7.23 (1 H, td, J 5.7, 2.8, H^{5py}), 6.94 (1 H, s, $H^{4'}$), 2.68 (3 H, s, H^{Me}), 2.43 (3 H, s, H^{Me}); δ C (151 MHz, $CDCl_3$) 170.0 (C^q), 168.1 (C^q), 164.8 (C^q), 152.2 (C^{6py}), 143.2 (C^3), 139.5 (C^q), 138.7 (C^{4py}), 138.5 (C^q), 137.6 (C^q), 137.1 (C^q), 136.7 (C^q), 131.8 (C^7), 130.5 ($C^{4'}$), 128.9 (C^5), 126.6 (C^6), 126.6 (C^8), 125.4 (C^q), 122.1 (C^{3py}), 122.1 (C^{5py}), 120.7 (C^4), 23.5 (C^{Me}), 21.8 (C^{Me}); MS ASAP (AP^+) *m/z* 545.1 ([M-Cl+MeCN]$^+$, 100%); HRMS (AP^+) *m/z* 544.1297 [M-Cl+MeCN]$^+$, calc. for [$C_{24}H_{20}N_3{}^{194}Pt$] 544.1284.

PtL^{16}Cl

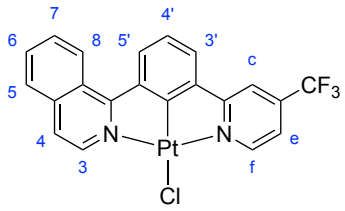

This complex was prepared using *Complexation General Procedure 1* with HL^{16} (168 mg, 0.480 mmol) and K_2PtCl_4 (227 mg, 0.547 mmol) in acetic acid (15 mL) to yield the product as a yellow solid (119 mg, 41%); δ H (600 MHz, $CDCl_3$) 9.65 (1 H, d, J 5.9, H^f), 9.37 (1 H, d, J 6.4, H^3), 8.94 (1 H, d, J 8.6, H^8), 8.26 (1 H, d, J 7.9, $H^{5'}$), 7.96 – 7.91 (1 H, m, H^5), 7.88 (1 H, s, H^c), 7.84 (1 H, ddd, J 8.1, 6.8, 1.0, H^6), 7.77 (1 H, ddd, J 8.4, 6.8, 1.4, H^7), 7.65 (1 H, d, J 6.4, H^4), 7.60 (1 H, d, J 7.7, $H^{3'}$), 7.56 – 7.48 (1 H, m, H^e), 7.38 (1 H, t, J 7.8, $H^{4'}$); δ C (151 MHz, $CDCl_3$) 152.8 (C^f), 147.9 (C^q), 143.9 (C^3), 132.1 (C^6), 130.1 ($C^{5'}$), 129.0 (C^7), 128.0 (C^5), 125.4 (C^8), 124.5 ($C^{3'}$), 123.1 ($C^{4'}$), 122.0 (C^4), 119.0

(C^e), 115.2 (C^c); MS ASAP (AP^+) *m/z* 544.1 ([M-Cl]$^+$, 100%); HRMS (AP^+) *m/z* 543.0569 [M-Cl]$^+$, calc. for [$C_{21}H_{12}N_2F_3{}^{194}Pt$] 543.0579.

PtL^{17}Cl

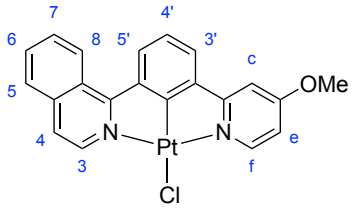

This complex was prepared using *Complexation General Procedure 1* with HL^{17} (77 mg, 0.247 mmol) and K_2PtCl_4 (117 mg, 0.281 mmol) in acetic acid (7 mL) to yield the product as a yellow solid (65 mg, 49%); δ H (600 MHz, $CDCl_3$) 9.45 (1 H, d, J 6.4, H^3), 9.21 (1 H, d, J 6.5, H^f), 8.95 (1 H, d, J 8.7, H^8), 8.20 (1 H, d, J 7.8, $H^{5'}$), 7.93 (1 H, d, J 8.2, H^5), 7.83 (1 H, dd, J 7.8, 6.7, H^6), 7.75 (1 H, t, J 7.5, H^7), 7.63 (1 H, d, J 6.3, H^4), 7.50 (1 H, d, J 7.6, $H^{3'}$), 7.33 (1 H, t, J 7.8, $H^{4'}$), 7.22 (1 H, d, J 2.8, H^c), 6.83 (1 H, dd, J 6.6, 2.8, H^e), 4.01 (3 H, s, H^{OMe}); δ C (151 MHz, $CDCl_3$) 131.2 (C^6), 129.3 ($C^{5'}$), 128.7 (C^7), 125.2 (C^8), 123.9 ($C^{3'}$), 122.4 ($C^{4'}$), 121.7 (C^4), 108.1 (C^e), 103.9 (C^c); MS ASAP (AP^+) *m/z* 547.1 ([M-Cl+MeCN]$^+$, 100%); HRMS (AP^+) *m/z* 546.1077 [M-Cl+MeCN]$^+$, calc. for [$C_{23}H_{18}N_3O^{194}Pt$] 546.1077.

PtL^{18}Cl

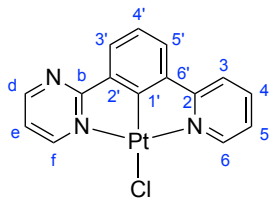

This complex was prepared using the *Complexation General Procedure 1* with HL^{18} (62 mg, 0.266 mmol) and K_2PtCl_4 (126 mg, 0.303 mmol) in acetic acid (6 mL) to yield the product as an orange solid (95 mg, 77%); δ H (700 MHz, $CDCl_3$) 9.48 (1 H, dd, J 5.7, 2.2, H^f), 9.29 (1 H, dt, J 5.7, 0.9, H^6), 8.91 (1 H, dd, J 4.8, 2.3, H^d), 7.96 (1 H, td, J 7.8, 1.6, H^4), 7.75 (1 H, dd, J 7.6, 0.9, $H^{3'}$), 7.72 (1 H, dd, J 7.9, 1.3, H^3), 7.54 (1 H, dd, J 7.7, 0.9, $H^{5'}$), 7.30 (1 H, ddd, J 7.3, 5.6, 1.4, H^5), 7.28 (1 H, t, J 7.6, $H^{4'}$), 7.26 (1 H, dd, J 4.3, 1.4, H^e); δ C (176 MHz, $CDCl_3$) 175.3 (C^q), 166.6 (C^q), 161.2 (C^q), 158.3 (C^f), 158.2

(C^{d}), 152.3 (C^{6}), 141.1 (C^{q}), 139.4 (C^{4}), 137.8 (C^{q}), 127.6 ($C^{3'}$), 126.0 ($C^{5'}$), 123.4 ($C^{4'}$), 123.3 (C^{5}), 119.3 (C^{3}), 118.6 (C^{e}); MS ASAP (AP^{+}) *m/z* 468.1 ([M-Cl+MeCN]$^{+}$, 100%); HRMS (AP^{+}) *m/z* 466.0807 [M-Cl+MeCN]$^{+}$, calc. for [$C_{17}H_{14}N_4{}^{192}Pt$] 466.0829.

PtL^{19}Cl

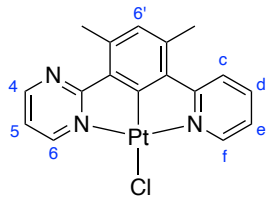

This complex was prepared using *Complexation General Procedure 1* with HL^{19} (53 mg, 0.20 mmol) and K_2PtCl_4 (96 mg, 0.23 mmol) in acetic acid (6 mL) to give the product as a yellow orange solid (85 mg, 85%); δ H (600 MHz, $CDCl_3$) 9.49 (1 H, dd, J 5.7, 2.4, H^{6}), 9.34 (1 H, dd, J 5.7, 1.7, H^{f}), 8.86 (1 H, dd, J 4.8, 2.4, H^{4}), 7.93 – 7.85 (1 H, m, H^{d}), 7.82 (1 H, d, J 8.1, H^{c}), 7.19 (1 H, ddd, J 7.3, 5.6, 1.4, H^{e}), 7.16 – 7.11 (1 H, m, H^{5}), 6.77 (1 H, s, $H^{4'}$), 2.70 (3 H, s, H^{Me}), 2.64 (3 H, s, H^{Me}); δ C (151 MHz, $CDCl_3$) 176.2 (C^{q}), 167.4 (C^{q}), 163.2 (C^{q}), 157.8 (C^{6}), 157.3 (C^{4}), 152.2 (C^{f}), 141.5 (C^{q}), 138.9 (C^{d}), 138.5 (C^{q}), 137.2 (C^{q}), 133.3 (C^{q}), 130.5 ($C^{4'}$), 122.2 (C^{c}), 122.1 (C^{e}), 117.3 (C^{5}), 22.0 (C^{Me}), 20.0 (C^{Me}); MS ASAP (AP^{+}) m/z 496.1 ([M-Cl+MeCN]$^{+}$, 100%); HRMS (AP^{+}) *m/z* 495.1098 [M-Cl+MeCN]$^{+}$, calc. for [$C_{19}H_{17}N_4{}^{194}Pt$] 495.1080.

PtL^{20}Cl

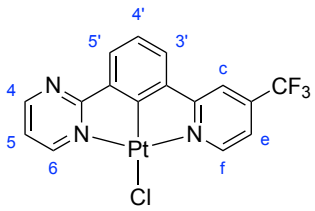

This complex was prepared using *Complexation General Procedure 1* with HL^{20} (68 mg, 0.226 mmol) and K_2PtCl_4 (107 mg, 0.257 mmol) in acetic acid (8 mL) to yield the product as a yellow solid (94 mg, 78%); δ H (600 MHz, CD_2Cl_2) 9.48 (1 H, d, J 5.9, H^{f}), 9.41 (1 H, dd, J 5.7, 2.3, H^{6}), 8.95 (1 H, dd, J 4.8, 2.3, H^{4}), 7.94 (1 H, d, J 1.9, H^{c}), 7.83 (1 H, dd, J 7.7, 0.9, $H^{5'}$), 7.67 (1 H, dd, J 7.7, 0.9, $H^{3'}$), 7.60-7.51 (1 H, m, H^{e}), 7.36 (1 H, t, J 7.7, $H^{4'}$), 7.33 (1 H, dd, J 5.7, 4.8, H^{5}); δ C (151 MHz, CD_2Cl_2) 158.8 (C^{4}), 153.1 (C^{f}),

128.6 ($C^{5'}$), 126.4 ($C^{3'}$), 123.7 ($C^{4'}$), 119.7 (C^{e}), 119.0 (C^{5}), 115.4 (C^{e}); MS ASAP (AP^+) *m/z* 495.0 ([M-Cl]$^+$, 100%); HRMS (AP^+) *m/z* 535.0640 [M-Cl+MeCN]$^+$, calc. for [$C_{18}H_{12}N_4F_3{}^{194}Pt$] 535.0641; Anal calc. for $C_{16}H_9ClF_3N_3Pt$: C, 36.21; H, 1.71; N, 7.92; Found: C, 36.15; H, 1.66; N, 7.84.

PtL^{21}Cl

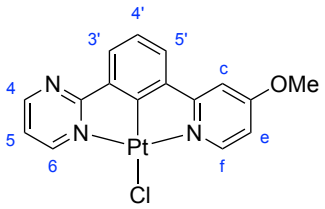

This complex was prepared using *Complexation General Procedure 1* with HL^{21} (100 mg, 0.380 mmol) and K_2PtCl_4 (180 mg, 0.433 mmol) in acetic acid (10 mL) to yield the product as a yellow solid (132 mg, 70%); δ H (700 MHz, $CDCl_3$) 9.50 – 9.37 (1 H, m, H^6), 8.98 (1 H, d, J 6.6, H^f), 8.88 – 8.81 (1 H, m, H^4), 7.69 (1 H, d, J 7.6, $H^{3'}$), 7.44 (1 H, d, J 7.6, $H^{5'}$), 7.23 – 7.16 (2 H, m, H^5 and $H^{4'}$), 7.12 (1 H, d, J 2.9, H^c), 6.75 – 6.71 (1 H, m, H^e), 3.94 (3 H, s, H^{OMe}); δ C (176 MHz, $CDCl_3$) 175.3 (C^q), 168.0 (C^q), 160.7 (C^q), 158.3 (C^6), 158.2 (C^4), 153.3 (C^f), 141.3 (C^q), 127.7 ($C^{3'}$), 125.9 ($C^{5'}$), 123.3 ($C^{4'}$), 118.6 (C^5), 108.2 (C^e), 106.1 (C^c), 56.1 (C^{OMe}); HRMS (AP^+) *m/z* 497.0886 [M-Cl+MeCN]$^+$, calc. for [$C_{17}H_{19}O_5{}^{194}Pt$] 497.0873; Anal calc. for $C_{16}H_{12}ClN_3OPt{\cdot}0.3CH_2Cl_2$: C, 37.77; H, 2.45; N, 8.11; Found: C, 37.96; H, 2.34; N, 8.25.

PtL^{22}Cl

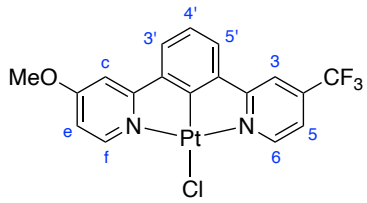

This complex was prepared by *Complexation General Procedure 1* with HL^{22} (54 mg, 0.16 mmol) and K_2PtCl_4 (77 mg, 0.19 mmol) in acetic acid (5 mL) to yield the product as a yellow solid (69 mg, 76%); δ H (400 MHz, $CDCl_3$) 9.62 (1 H, d, J 6.0, H^6), 9.11 (1 H, d, J 6.7, H^f), 7.87 (1 H, d, J 5.0, H^3), 7.59 – 7.52 (1 H, m, $H^{3'}$ or $H^{5'}$), 7.52 – 7.46 (2 H, m, $H^{3'}$ or $H^{5'}$), 7.33 – 7.27 (1 H, m, $H^{4'}$), 7.21 (1 H, d, J 2.9, H^c), 6.83 (1 H, dd, J 6.7, 2.8,

H^e); MS ASAP (AP^+) *m/z* 565.1 ([M-Cl+MeCN]$^+$, 100%); HRMS (AP^+) *m/z* 564.0810 [M-Cl+MeCN]$^+$, calc. for [$C_{20}H_{15}N_3OF_3{}^{194}Pt$] 546.0794. This sample was too weak to obtain a ^{13}C NMR spectrum.

PtL^{23}Cl

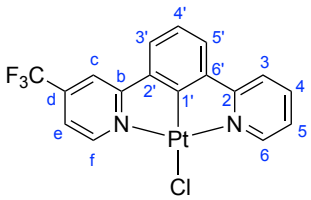

This complex was prepared using *Complexation General Procedure 1* with HL^{23} (19 mg, 0.063 mmol) and K_2PtCl_4 (30 mg, 0.072 mmol) in acetic acid (4 mL) to yield the product as a yellow solid (19 mg, 57%); δ H (700 MHz, $CDCl_3$) 9.56 (1 H, d, J 5.9, H^f), 9.36 – 9.25 (1 H, m, H^6), 7.96 (1 H, td, J 7.7, 1.6, H^4), 7.83 (1 H, s, H^c), 7.71 (1 H, d, J 7.9, H^3), 7.54 – 7.48 (2 H, m, $H^{3'}$ and $H^{5'}$), 7.48 – 7.45 (1 H, m, H^e), 7.31 (1 H, ddd, J 7.3, 5.6, 1.5, H^5), 7.27 (1 H, d, J 7.7, $H^{4'}$); δ C (176 MHz, $CDCl_3$) 168.8 (C^q), 167.1 (C^q), 162.7 (C^q), 153.1 (C^f), 152.4 (C^6), 141.2 (C^q), 139.5 (C^q), 139.4 (C^4), 125.0 ($C^{3'/5'}$), 124.6 ($C^{3'/5'}$), 123.4 (C^5), 123.2 ($C^{4'}$), 119.4 (C^3), 119.1 (C^e), 115.1 (C^c); HRMS (AP^+) *m/z* 534.0677 [M-Cl+MeCN]$^+$, calc. for [$C_{19}H_{13}N_3F_3{}^{194}Pt$] 534.0688.

PtL^{24}Cl

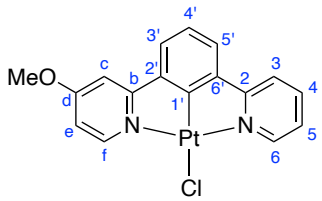

This complex was prepared using *Complexation General Procedure 1* with HL^{24} (110 mg, 0.419 mmol) and K_2PtCl_4 (198 mg, 0.478 mmol) in acetic acid (11 mL) to yield the product as a yellow solid (68 mg, 34%); δ H (700 MHz, $CDCl_3$) 9.39 – 9.29 (1 H, m, H^6), 9.07 (1 H, d, J 6.6, H^f), 7.92 (1 H, td, J 7.7, 1.6, H^4), 7.68 – 7.63 (1 H, m, H^3), 7.42 (1 H, dd, J 7.6, 0.8, $H^{5'}$), 7.38 (1 H, dd, J 7.7, 0.8, $H^{3'}$), 7.28 – 7.23 (2 H, m, H^5), 7.19 (1 H, t, J 7.6, $H^{4'}$), 7.13 (1 H, d, J 2.8, H^c), 6.75 (1 H, dd, J 6.6, 2.8, H^e), 3.97 (3 H, s, H^{OMe}); δ C (176 MHz, $CDCl_3$) 168.6 (C^b), 167.9 (C^d), 167.2 (C^2), 161.4 ($C^{6'}$), 153.1 (C^f), 152.1 (C^6),

140.9 ($C^{2'}$), 138.8 (C^{4}), 124.1 ($C^{5'}$), 124.0 ($C^{3'}$), 123.1 (C^{5}), 122.7 ($C^{4'}$), 119.1 (C^{3}), 108.1 (C^{e}), 105.9 (C^{c}), 56.0 (C^{OMe}); MS ASAP (AP^{+}) *m/z* 456.1 ([M-Cl]$^{+}$, 100%); HRMS (AP^{+}) *m/z* 455.0669 [M-Cl]$^{+}$, calc. for [$C_{17}H_{13}N_2O^{194}Pt$] 455.0655.

PtL^{25}Cl

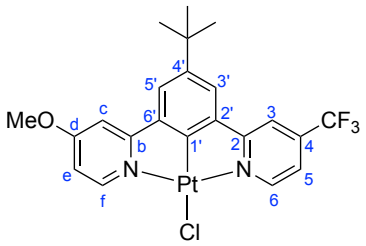

This complex was prepared using *Complexation General Procedure 1* with HL^{25} (66 mg, 0.171 mmol) and K_2PtCl_4 (81 mg, 0.195 mmol) in acetic acid (6 mL) to yield the product as a yellow solid (62 mg, 59%); δ H (700 MHz, $CDCl_3$) 9.55 (1 H, d, J 5.9, H^{6}), 9.04 (1 H, d, J 6.6, H^{f}), 7.83 (1 H, d, J 1.9, H^{3}), 7.55 (1 H, d, J 1.4, $H^{3'}$), 7.51 (1 H, d, J 1.4, $H^{5'}$), 7.43 (1 H, dd, J 6.1, 1.9, H^{5}), 7.19 (1 H, d, J 2.8, H^{c}), 6.77 (1 H, dd, J 6.6, 2.8, H^{e}), 4.00 (3 H, s, H^{OMe}), 1.43 (9 H, s, H^{tBu}); δ C (176 MHz, $CDCl_3$) 169.0 (C^{q}), 168.7 (C^{q}), 168.1 (C^{q}), 159.1 (C^{q}), 153.3 (C^{f}), 153.0 (C^{6}), 146.6 (C^{q}), 140.9 (C^{q}), 139.0 (C^{q}), 122.2 ($C^{5'}$), 121.9 ($C^{3'}$), 118.9 (C^{5}), 114.9 (C^{3}), 108.0 (C^{e}), 106.1 (C^{c}), 56.1 (C^{OMe}), 35.3 (C^{tBu}), 31.5 (C^{tBu}); HRMS (AP^{+}) *m/z* 620.1404 [M-Cl+MeCN]$^{+}$, calc. for [$C_{24}H_{23}N_3OF_3{}^{194}Pt$] 620.1420.

PtL^{30}Cl

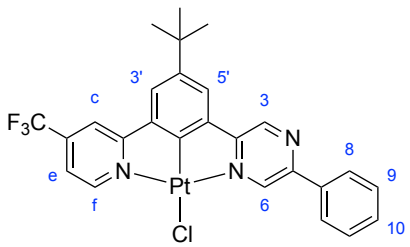

This complex was prepared using *Complexation General Procedure 1* with HL^{30} (50 mg, 0.115 mmol) and K_2PtCl_4 (95 mg, 0.229 mmol) in acetic acid (5 mL) to yield the product as a yellow orange solid (16 mg, 21%); δ H (600 MHz, $CDCl_3$) 9.65 (1 H, s, H^{6}), 9.50 (1 H, d, J 6.0, H^{f}), 9.07 (1 H, s, H^{3}), 8.07 (2 H, d, J 6.8, H^{8}), 7.85 (1 H, s, H^{c}), 7.71 (1 H, s, H^{10}), 7.59 (1 H, s, $H^{5'}$), 7.56 – 7.46 (4 H, m, $H^{3'}$, H^{9} and H^{e}), 2.09 (6 H, s, $H^{t\text{-}Bu}$); MS

ASAP (AP$^+$) *m/z* 668.2 ([M-Cl+MeCN]$^+$, 100%); HRMS (AP$^+$) *m/z* 667.1570 [M-Cl+MeCN]$^+$, calc. for [$C_{28}H_{24}N_4F_3{}^{194}Pt$] 667.1580. This sample was too insoluble to obtain a ^{13}C NMR spectrum.

7.4.4 PtL^{n}NCS Complexes

PtL^{16}NCS

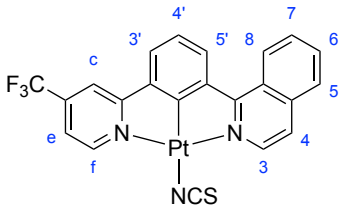

This complex was prepared by the *chloride metathesis reaction* with PtL^{16}Cl (15 mg, 0.026 mmol), AgOTf (8 mg, 0.031 mmol) and KSCN (excess) to give the product as a red solid (5 mg, 37%); δ H (700 MHz, CD_2Cl_2) 9.04 (1 H, d, J 5.9), 8.94 (1 H, d, J 8.8), 8.77 (1 H, d, J 6.2), 8.26 (1 H, d, J 8.), 8.03 (1 H, d, J 8.1), 7.96 (1 H, s), 7.93 (1 H, t, J 7.4), 7.86 (1 H, t, J 7.8), 7.76 (1 H, d, J 6.3), 7.63 (1 H, d, J 7.7), 7.59 (1 H, d, J 5.8), 7.42 (1 H, t, J 7.8); δ F (376 MHz, CD_2Cl_2) −65.42; HRMS (AP$^+$) *m/z* 584.0837 [M-NCS+MeCN]$^+$, calc. for [$C_{23}H_{15}N_3F_3{}^{194}Pt$] 584.0845. This sample was too insoluble to obtain a ^{13}C NMR spectrum.

PtL^{19}NCS

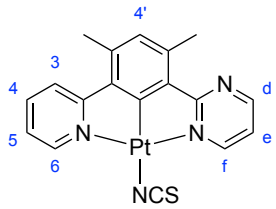

This complex was prepared by the *chloride metathesis reaction* with PtL^{19}Cl (15 mg, 0.031 mmol), AgOTf (10 mg, 0.037 mmol) and KSCN (excess) to give the product as an orange solid (3 mg, 19%); δ H (700 MHz, CD_2Cl_2) 8.84 (1 H, dd, J 4.8, 2.3, H^f), 8.82 (1 H, dd, J 5.6, 2.4, H^d), 8.64 (1 H, d, J 5.5, H^6), 7.91 (1 H, td, J 7.9, 1.7, H^4), 7.77 (1 H, d, J 8.2, H^3), 7.20 (1 H, dd, J 7.2, 5.4, H^5), 7.16 (1 H, dd, J 5.6, 4.7, H^e), 6.73 (1 H, s, H$^{4'}$), 2.60 (3 H, s, H^{Me}), 2.54 (3 H, s, H^{Me}); δ C (176 MHz, CD_2Cl_2) 157.8 (C^d), 157.7 (C^f), 151.8

(C^6), 139.6 (C^4), 131.1 ($C^{4'}$), 122.8 (C^5), 122.7 (C^3), 118.0 (C^e), 21.3 (C^{Me}), 19.8 (C^{Me}); HRMS (AP^+) *m/z* 495.1076 $[M\text{-}NCS+MeCN]^+$, calc. for $[C_{19}H_{17}N_4{}^{194}Pt]$ 495.1080.

7.5 Chapter 4 Synthesis

7.5.1 Class I Sandwich Compounds

Intermediates and precursors

I9: 1,3-Di(pinacolatoboron)-5-bromobenzene

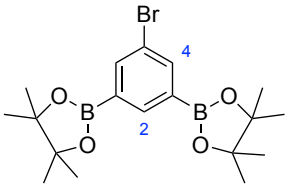

This compound was synthesised *via* the Miyaura borylation reaction using 1,3,5-tribromobenzene (2.00 g, 6.35 mmol), B_2Pin_2 (3.56 g, 14.0 mmol), KOAc (3.74 g, 38.1 mmol), $PdCl_2$(dppf) (0.465 g, 0.64 mmol) and 1,4-dioxane (40 mL). The crude product was used in further reactions without purification.

Dpyb-Br

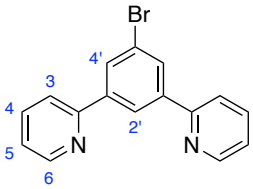

This ligand precursor was prepared *via* the Stille cross-coupling reaction using 1,3,5-tribromobenzene (1.00 g, 3.18 mmol), 2-(tributylstannyl)pyridine (2.34 g, 6.35 mmol), $Pd(PPh_3)_2Cl_2$ (0.72 g, 0.25 mmol), LiCl (1.08 g, 25.4 mmol) and dry toluene (20 mL). The crude mixture was purified by column chromatography (hexane: ethyl acetate gradient to 80:20, R_f = 0.2 in 80:20) to yield the pure product as an off-white solid (223 mg, 23%); δ H (400 MHz, $CDCl_3$) 8.67 (2 H, ddd, J 4.8, 1.8, 1.0), 8.51 (1 H, t, J 1.6), 8.18 (2 H, d, J 1.6), 7.77 – 7.66 (4 H, m), 7.21 (2 H, ddd, J 7.1, 4.8, 1.5); MS ESI (ES^+) *m/z* 311.6 (M^+, 100%). The experimental data obtained were in good agreement with the literature.[61]

This compound was also prepared *via* the Suzuki cross-coupling reaction using crude 1,3-di(pinacolatoboron)-5-bromobenzene (1.30 g, 3.18 mmol), 2-bromopyridine (1.01 g, 6.36 mmol), aqueous Na_2CO_3 (2.70 g, 25.4 mmol), $Pd(PPh_3)_4$ (0.184 g, 0.159 mmol) and DME (25 mL). The crude mixture was purified by column chromatography on silica (hexane: ethyl acetate gradient, R_f = 0.3 in 70:30) to yield the pure product as an off-white solid (0.350 g, 35%).

Dpyb-Bpin

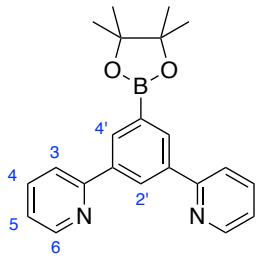

This compound was prepared *via* the Miyaura borylation reaction using Dpyb-Br (853 mg, 2.74 mmol), B_2pin_2 (839 mg, 3.29 mmol), KOAc (1610 mg, 16.4 mmol) and $PdCl_2$(dppf) (200 mg, 0.274 mmol) in 1,4-dioxane (25 mL). Purification by flash column chromatography (hexane: ethyl acetate on silica, R_f = 0.2 in 70:30) yielded the product as a white solid (920 mg, 94%); δ H (400 MHz, $CDCl_3$) 8.75 (1 H, t, J 1.9), 8.71 (2 H, ddd, J 4.8, 1.8, 0.9), 8.46 (2 H, d, J 1.9), 7.88 (2 H, dt, J 8.0, 1.0), 7.74 (2 H, ddd, J 8.0, 7.5, 1.8), 7.22 (2 H, ddd, J 7.5, 4.8, 1.1), 1.36 (12 H, s); MS ESI (ES^+) *m/z* 311.6 ($[M+H]^+$, 100%).

CF_3dpyb-Br

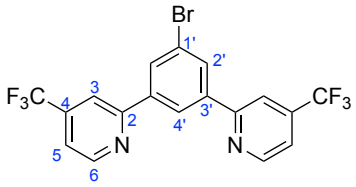

This compound was prepared *via* the Suzuki cross-coupling reaction using crude 1,3-di(pinacolatoboron)-5-bromobenzene (2.59 g, 6.35 mmol), 2-bromo-4-(trifluoromethyl)pyridine (2.87 g, 0.013 mmol), aqueous Na_2CO_3 (5.39 g, 50.8 mmol),

$Pd(PPh_3)_4$ (0.367 g, 0.318 mmol) and DME (25 mL). The crude mixture was purified by column chromatography on silica (hexane: ethyl acetate gradient, R_f = 0.4 in 90:10) to yield the pure product as a white solid (0.740 g, 26%); δ H (400 MHz, $CDCl_3$) 8.95 (2 H, d, J 5.0, H^6), 8.68 (1 H, t, J 1.6, $H^{4'}$), 8.33 (2 H, d, J 1.6, $H^{2'}$), 8.06 (2 H, dt, J 1.7, 0.8, H^3), 7.57 (2 H, dt, J 4.9, 1.3, H^5); δ F (376 MHz, $CDCl_3$) -64.7; MS ESI (ES^+) *m/z* 447.0 ($[M+H]^+$, 100%); HRMS (ES^+) *m/z* 446.9937 $[M+H]^+$, calc. for $[C_{18}H_{10}N_2BrF_6N_2]$ 446.9932.

CF_3dypb-Bpin

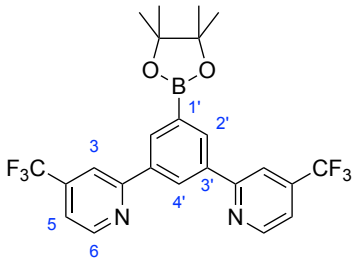

This compound was prepared *via* the Miyaura borylation reaction using CF_3dypb-Br (340 mg, 0.762 mmol), B_2pin_2 (233 mg, 0.915 mmol), KOAc (449 mg, 4.57 mmol) and $PdCl_2$(dppf) (56 mg, 0.076 mmol) in 1,4-dioxane (10 mL). Purification by flash column chromatography (hexane: ethyl acetate on silica, R_f = 0.3 in 80:20) yielded the product as a white solid (305 mg, 81%); δ H (400 MHz, $CDCl_3$) 9.00 – 8.86 (3 H, m, H^6 and $H^{4'}$), 8.53 (2 H, d, J 1.9, $H^{2'}$), 8.11 (2 H, dt, J 1.5, 0.8, H^3), 7.51 (2 H, ddd, J 5.0, 1.6, 0.8, H^5), 1.43 (12 H, s, H^{Bpin}); MS ESI $(ES)^+$ *m/z* 495.4 ($[M+H]^+$, 100%); HRMS (ES^+) *m/z* 494.1709 $[M+H]^+$, calc. for $[C_{24}H_{22}N_2O_2{}^{10}BF_6]$ 494.1715.

dpmb-Br

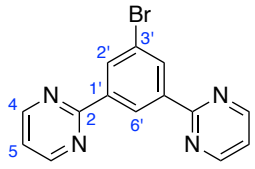

This compound was prepared *via* the Suzuki cross-coupling reaction using crude 1,3-di(pinacolatoboron)-5-bromobenzene (2.59 g, 6.35 mmol), 2-bromopyrimidine (2.02 g, 12.7 mmol), aqueous Na_2CO_3 (5.39 g, 50.8 mmol), $Pd(PPh_3)_4$ (0.367 g, 0.318 mmol) and DME (40 mL). The crude mixture was purified by column chromatography on

silica (hexane: ethyl acetate gradient, R_f = 0.3 in 70:30) to yield the pure product as a white solid (0.717 g, 36%); δ H (600 MHz, $CDCl_3$) 9.48 (1 H, q, J 1.7, $H^{6'}$), 8.87 – 8.80 (4 H, m, H^4), 8.75 – 8.71 (2 H, m, $H^{2'}$), 7.24 (2 H, d, J 7.3, H^5); δ C (151 MHz, $CDCl_3$) 163.1 (C^2), 157.3 (C^4), 139.8 ($C^{1'}$), 133.2 ($C^{2'}$), 126.6 ($C^{6'}$), 123.3 ($C^{3'}$), 119.7 (C^5); HRMS (ES^+) *m/z* 313.0103 $[M+H]^+$, calc. for $[C_{14}H_{10}N_4Br]$ 313.0089.

dpmb-Bpin

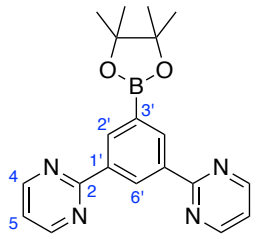

This compound was prepared *via* the Miyaura borylation reaction with dpmb-Br (375 mg, 0.194 mmol), B_2pin_2 (365 mg, 1.43 mmol), KOAc (703 mg, 7.16 mmol) and $Pd(dppf)Cl_2$ (87 mg, 0.119 mmol) in 1,4-dioxane (10 mL). The crude product was purified by column chromatography on silica (hexane: ethyl acetate gradient, 60:40) to yield the pure product as a pale yellow solid (350 mg, 81%); δ H (600 MHz, $CDCl_3$) 9.64 (1 H, t, J 1.8), 9.02 (2 H, d, J 1.9), 8.88 (4 H, d, J 4.8), 7.25 (2 H, d, J 7.7), 1.38 (12 H, s); HRMS (ES^+) *m/z* 361.395 $[M+H]^+$, calc. for $[C_{20}H_{22}N_4BrO_2]$ 361.184.

diqb-Br

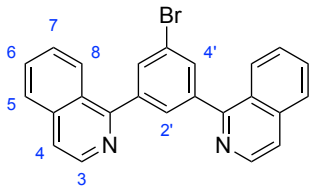

This compound was synthesised *via* the Suzuki cross-coupling reaction of 1,3-di(pinacolatoboron)-5-bromobenzene (579 mg, 1.42 mmol) and 1-chloroisquinoline (464 mg, 2.84 mmol) with aqueous Na_2CO_3 (1200 mg, 11.4 mmol), $Pd(PPh_3)_4$ (82 mg, 0.071 mmol) and DME (10 mL). The crude mixture was purified by column chromatography on silica (hexane: ethyl acetate gradient, R_f = 0.3 in 70:30) to yield the pure product as a pale yellow solid (173 mg, 30%); δ H (700 MHz, $CDCl_3$) 8.61 (2 H, d, J 5.7, H^3), 8.14 (2 H, d, J 8.6, H^8), 8.00 (2 H, d, J 1.5, $H^{4'}$), 7.95 (1 H, t, J 1.5, $H^{2'}$),

7.87 (2 H, dd, J 8.2, 1.1, H^5), 7.71 – 7.65 (4 H, overlapping m, H^4 and H^6), 7.55 (2 H, ddd, J 8.3, 6.9, 1.2, H^7); δ C (176 MHz, $CDCl_3$) 171.1, 158.7, 142.1, 141.4, 136.8, 132.9, 130.3, 130.2, 127.7, 127.1, 126.5, 122.6, 120.6; MS ASAP (AP^+) *m/z* 411.1 ($[M+H]^+$, 100%); HRMS (ES^+) *m/z* 411.0505 $[M+H]^+$, calc. for $[C_{24}H_{16}N_2Br]$ 411.0497.

diqb-Bpin

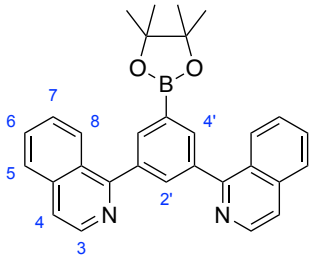

This compound was prepared *via* the Miyaura borylation reaction using diqb-Br (173 mg, 0.421 mmol), B_2pin_2 (129 mg, 0.505 mmol), KOAc (248 mg, 2.53 mmol) and $PdCl_2$(dppf) (31 mg, 0.042 mmol) in dioxane (5 mL). The crude product was used in further reactions without purification.

Proligands

H_2L^{31}

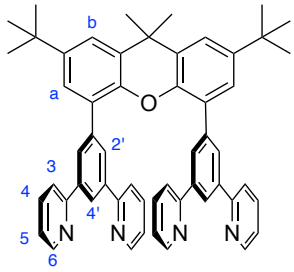

This ligand precursor was prepared *via* the Suzuki cross-coupling reaction using dpyb-Bpin (200 mg, 0.56 mmol), 4,5-dibromo-2,7-di-*t*-butyl-9,9-dimethylxanthene (122 mg, 0.254 mmol), aqueous Na_2CO_3 (215 mg, 2.03 mmol), $Pd(PPh_3)_4$ (15 mg, 0.01 mmol) and DME (2 mL). The crude mixture was purified by column chromatography (hexane: ethyl acetate gradient, R_f = 0.3 in ethyl acetate) to yield the pure product as a white solid (80 mg, 40%); δ H (400 MHz, $CDCl_3$) 8.54 (4 H, ddd, J 4.8, 1.8, 1.0, H^6), 8.14 (2 H, t, J 1.7, $H^{4'}$), 8.00 (4 H, d, J 1.7, $H^{2'}$), 7.51 (2 H, d, J 2.4, H^a or H^b), 7.44 – 7.34 (8 H, m, H^3 and H^4), 7.30 (2 H, d, J 2.4, H^a or H^b), 6.91 (4 H, ddd, J 6.6, 4.8, 1.6, H^5),

1.84 (6 H, s, H^{Me}), 1.39 (18 H, s, $H^{t\text{-}Bu}$); MS ESI (ES+) m/z 783.1 (M+, 87%). The experimental data obtained were in good agreement with the literature.[129]

H_2L^{32}

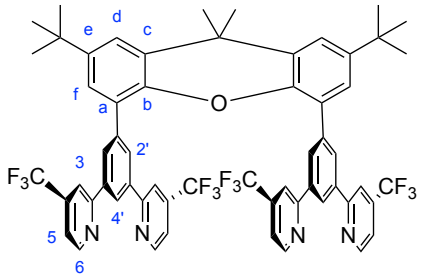

This compound was prepared *via* the Suzuki cross-coupling reaction using crude CF_3dpyb-Bpin (754 mg, 1.53 mmol), 4,5-dibromo-2,7-di-*tert*-butyl-9,9-dimethylxanthene (333 mg, 0.693 mmol), aqueous Na_2CO_3 (588 mg, 5.54 mmol), $Pd(PPh_3)_4$ (40 mg, 0.035 mmol) and DME (6 mL). The crude mixture was purified by column chromatography on silica (hexane: ethyl acetate gradient, R_f = 0.2 in 90:10) to yield the pure product as a white solid (603 mg, 82%); δ H (400 MHz, $CDCl_3$) 8.70 (4 H, d, J 5.0, H^6), 8.24 (2 H, t, J 1.7, $H^{4'}$), 7.99 (4 H, d, J 1.7, $H^{2'}$), 7.68 (4 H, d, J 1.5, H^3), 7.55 (2 H, d, J 2.3, H^f), 7.26 – 7.23 (2 H, m, H^d), 7.14 (4 H, dd, J 5.0, 1.5, H^5), 1.87 (6 H, s, H^{Me}), 1.40 (18 H, s, H^{tBu}); MS ESI (ES^+) *m/z* 1053.9 (M^+, 82%).

H_2L^{33}

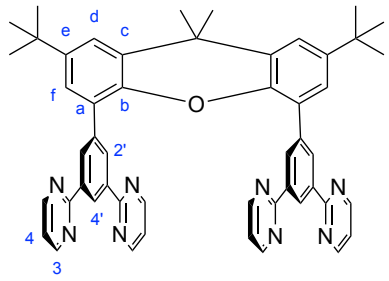

This compound was prepared *via* the Suzuki cross-coupling reaction using crude dpmb-Bpin (598 mg, 1.66 mmol), 4,5-dibromo-2,7-di-*tert*-butyl-9,9-dimethylxanthene (362 mg, 0.755 mmol), aqueous Na_2CO_3 (640 mg, 6.04 mmol), $Pd(PPh_3)_4$ (44 mg, 0.038 mmol) and DME (6 mL). The crude mixture was purified by column chromatography on silica (hexane: ethyl acetate gradient, R_f = 0.1 in 20:80)

to yield the pure product as an off-white solid (356 mg, 60%); δ H (600 MHz, $CDCl_3$) 8.92 (2 H, d, J 1.8, $H^{6'}$), 8.54 (8 H, d, J 4.4, H^3), 8.46 (4 H, d, J 1.4, $H^{2'}$), 7.45 (2 H, d, J 2.3, H^d), 7.26 (2 H, d, J 2.3, H^f), 6.72 (4 H, t, J 4.5, H^4), 1.81 (6 H, s, H^{Me}), 1.36 (18 H, s, H^{tBu}); δ C (151 MHz, $CDCl_3$) 163.9 (C^1), 156.6 (C^3), 144.9 (C^e), 144.8 (C^b), 138.7 (C^c), 136.6 ($C^{3'}$), 131.7 ($C^{2'}$), 128.9 ($C^{1'}$), 128.8 (C^a), 126.0 ($C^{4'}$), 125.7 (C^f), 122.4 (C^d), 118.1 (C^4), 34.7 (C^g), 34.5 (C^h), 33.5 (C^{Me}), 31.6 (C^{tBu}); MS ESI (ES^+) *m/z* 787.4 ($[M+H]^+$, 100%); HRMS (ES^+) *m/z* 787.3875 $[M+H]^+$, calc. for $[C_{51}H_{47}N_8O]$ 787.3873.

HL[34]

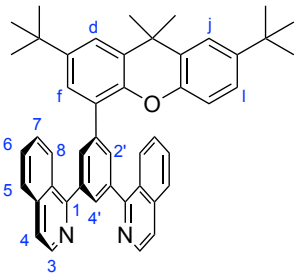

This proligand was prepared *via* the Suzuki cross-coupling reaction using 1,3-di(1-isoquinolyl)-5-(pinacolatoboron)benzene (193 mg, 0.421 mmol), 4,5-dibromo-2,7-di-*tert*-butyl-9,9-dimethylxanthene (92 mg, 0.191 mmol), aqueous Na_2CO_3 (162 mg, 1.53 mmol), $Pd(PPh_3)_4$ (11 mg, 0.010 mmol) and DME (2 mL). The crude mixture was purified by column chromatography on silica (hexane: ethyl acetate gradient, R_f = 0.2 in 80:20) to yield the product as a white solid (40 mg, 20%); δ H (400 MHz, $CDCl_3$) 8.68 (2 H, d, J 5.6), 8.46 (2 H, dd, J 8.5, 1.1), 8.11 (3 H, q, J 1.1), 7.93 (2 H, d, J 8.2), 7.77 – 7.68 (4 H, m), 7.62 (2 H, ddd, J 8.3, 6.8, 1.3), 7.48 (1 H, d, J 2.4), 7.43 (2 H, dd, J 6.5, 2.3), 7.18 (1 H, dd, J 8.5, 2.3), 7.00 – 6.91 (1 H, m), 1.72 (6 H, s), 1.38 (9 H, s), 1.34 (9 H, s); MS ESI (ES^+) *m/z* 653.4 ($[M+H]^+$, 100%); HRMS (ES^+) *m/z* 653.3551 $[M+H]^+$, calc. for $[C_{47}H_{45}N_2O]$ 653.3532.

Complexes

L[31](PtCl)$_2$

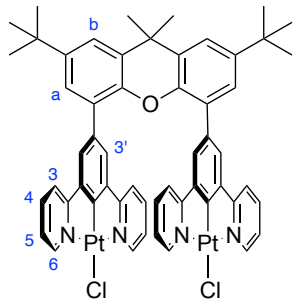

This complex was synthesised by *Complexation General Procedure 1* with H_2L^{31} (45 mg, 0.06 mmol) and K_2PtCl_4 (54 mg, 0.13 mmol) in acetic acid (5 mL) to give the product as a yellow solid (56 mg, 79%). The experimental data obtained were in good agreement with the literature.[129]

L[32](PtCl)$_2$ and HL[32]PtCl

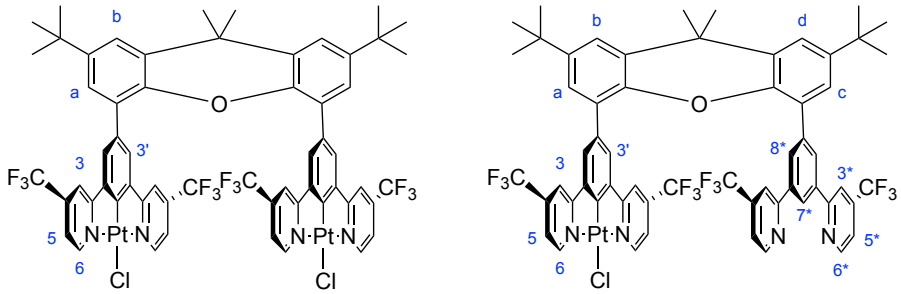

These complexes were prepared using *Complexation General Procedure 1* with HL^{32} (50 mg, 0.047 mmol) and K_2PtCl_4 (98 mg, 0.237 mmol) in acetic acid (10 mL). The crude solid was purified by preparative column chromatography on silica (DCM: MeOH gradient) to yield a mixture of the dinuclear product $L^{32}(PtCl)_2$ as a yellow-orange solid (6.5 mg, 9%) and the mononuclear product $HL^{32}PtCl$ as a yellow solid (23 mg, 38%).

$L^{32}(PtCl)_2$: δ H (700 MHz, $CDCl_3$) 9.53 (4 H, d, J 5.8, {^{195}Pt 31.8}, H^6), 7.54 (2 H, d, J 2.4, H^d or H^f), 7.48 (4 H, s, $H^{2'}$), 7.41 (4 H, s, H^3), 7.38 (4 H, dd, J 5.8, 1.9, H^5), 7.22 (2 H, d, J 2.3, H^d or H^f), 1.83 (6 H, s, H^{Me}), 1.41 (18 H, s, $H^{t\text{-}Bu}$); δ C (176 MHz, $CDCl_3$) 167.9 (C^2), 161.8 ($C^{4'}$), 154.0 (C^6), 146.2 (C^e), 144.1 (C^b), 139.3 ($C^{1'}$), 129.3 (C^c), 128.1 (C^a), 126.7 ($C^{2'}$), 125.8 (C^d or C^f), 123.3 (C^d or C^f), 119.6 (C^5), 115.1 (C^3), 34.7 (C^g), 34.1

($C^{t\text{-}Bu}$), 33.7 (C^{Me}); MS ESI (ES^+) *m/z* 1555.7 $[M+MeCN]^+$; HRMS ASAP (AP^+) *m/z* 1477.8969 $[M\text{-}Cl]^+$, calc. for $[C_{59}H_{44}ClF_{12}N_4OPt_2]$ 1478.2312.

$HL^{32}PtCl$: δ H (600 MHz, $CDCl_3$) 9.43 (2 H, d, J 5.9, H^6), 8.78 (2 H, d, J 4.9, H^{6*}), 8.56 (1 H, t, J 1.7, H^{7*}), 8.14 (2 H, d, J 1.7, H^{8*}), 7.67 (2 H, dt, J 1.5, 0.7, H^{3*}), 7.56 (2 H, t, J 2.3, H^b and H^d), 7.39 (2 H, s, $H^{3'}$), 7.36 (2 H, d, J 2.0, H^3), 7.33 – 7.28 (3 H, m, H^c and H^5), 7.23 (1 H, d, J 2.3, H^a), 7.10 (2 H, ddd, J 5.0, 1.5, 0.7, H^{5*}), 1.85 (6 H, s, H^{Me}), 1.42 (9 H, s, $H^{t\text{-}Bu}$), 1.40 (9 H, s, $H^{t\text{-}Bu}$); δ C (151 MHz, $CDCl_3$) 168.1 (C^q), 156.2 (C^q), 152.9 (C^6), 150.7 (C^{6*}), 128.9 (C^{8*}), 126.9 ($C^{3'}$), 126.1 (C^c), 125.3 (C^a), 123.1 (C^b), 123.2 (C^d), 122.6 (C^{7*}), 118.8 (C^5), 117.1 (C^{5*}), 115.0 (C^3), 114.6 (C^{3*}), 34.9 ($C^{q\text{-}tBu}$), 34.7 ($C^{q\text{-}Me}$), 33.4 (C^{Me}), 31.6 ($C^{t\text{-}Bu}$); δ F (376 MHz, $CDCl_3$) −64.60, −65.47; MS ESI (ES^+) *m/z* 1248.9 $[M\text{-}Cl]^+$; HRMS ASAP (AP^+) *m/z* 1285.2949 $[M]^+$, calc. for $[C_{59}H_{45}ClF_{12}N_4OPt]$ 1285.2825.

$L^{33}(PtCl)_2$ and $HL^{33}PtCl$

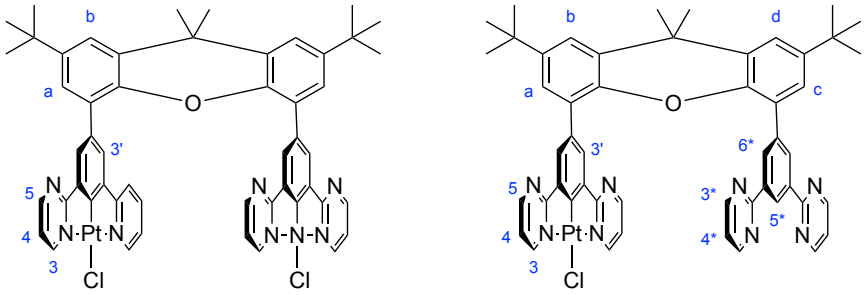

These complexes were prepared using *Complexation General Procedure 1* with HL^{33} (61 mg, 0.078 mmol) and K_2PtCl_4 (161 mg, 0.388 mmol) in acetic acid (6 mL). The crude solid was purified by preparative column chromatography on silica (DCM: MeOH gradient, R_f $L^{33}(PtCl)_2$ = 0.4 in 5%, R_f $HL^{33}PtCl$ = 0.1 in 2%) to yield a mixture of the dinuclear product $L^{33}(PtCl)_2$ as an orange solid (10 mg, 10%) and the mononuclear product $HL^{33}PtCl$ as a yellow solid (22 mg, 28%).

$L^{33}(PtCl)_2$: δ H (600 MHz, $CDCl_3$) 9.45 (4 H, dd, J 5.7, 2.3, H^3), 8.47 (4 H, dd, J 4.7, 2.3, H^5), 7.78 (4 H, s, $H^{3'}$), 7.48 (2 H, d, J 2.4, H^b), 7.24 (2 H, d, J 2.3, H^a), 7.10 – 7.04 (4 H, m, H^4), 1.79 (6 H, s, H^{Me}), 1.38 (18 H, s, $H^{t\text{-}Bu}$); MS ASAP (AP^+) *m/z* 1209.3 $[M\text{-}Cl]^+$; HRMS (AP^+) *m/z* 1208.3348 $[M\text{-}Cl]^+$, calc. for $[C_{51}H_{44}ClN_8O^{194}Pt^{195}Pt]$ 1208.2660. This sample was too insoluble to obtain a ^{13}C NMR spectrum.

HL[33]PtCl: δ H (600 MHz, $CDCl_3$) 9.29 (2 H, dd, J 5.7 2.3, H^3), 8.88 (1 H, t, J 1.7, H^{5*}), 8.62 (4 H, d, J 4.7, H^{3*}), 8.53 (2 H, d, J 4.7, H^{6*}), 8.44 (2 H, dd, J 4.7, 2.2, H^5), 7.75 (2 H, s, $H^{3'}$), 7.48 (1 H, d, J 2.3, H^b), 7.46 (1 H, d, J 2.4, H^d), 7.27 (2 H, d, J 2.3, H^a and H^c), 6.95 (2 H, dd, J 5.7, 4.7, H^4), 6.81 (2 H, t, J 4.7, H^{4*}), 1.80 (6 H, s, H^{Me}), 1.39 (9 H, s, $H^{t\text{-}Bu}$), 1.37 (9 H, s, $H^{t\text{-}Bu}$); δ C (151 MHz, $CDCl_3$) 157.9 (C^3), 157.8 (C^5), 156.9 (C^{3*}), 131.9 (C^{6*}), 131.3 ($C^{3'}$), 126.0 (C^a), 125.6 (C^{5*}), 125.3 (C^c), 118.3 (C^{4*}), 117.8 (C^4), 33.5 (C^{Me}), 31.6 ($C^{t\text{-}Bu}$); MS ASAP (AP^+) *m/z* 1017.3 $[M+H]^+$; HRMS (AP^+) *m/z* 1017.3191 $[M+H^+]$, calc. for $[C_{51}H_{45}ClN_8OPt]$ 1017.3137.

L[34]PtCl

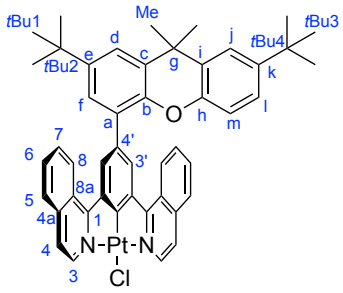

This complex was prepared using *Complexation General Procedure 1* with HL^{34} (40 mg, 0.041 mmol) and K_2PtCl_4 (38 mg, 0.092 mmol) in acetic acid (5 mL) to yield the product as a dark orange solid (13 mg, 22%); δ H (700 MHz, $CDCl_3$) 9.53 (2 H, d, J 6.3, H^3), 9.05 (2 H, d, J 8.7, H^8), 8.50 (2 H, s, $H^{3'}$), 7.93 (2 H, d, J 8.4, H^5), 7.81 (2 H, ddd, J 8.0, 6.7, 1.0, H^6), 7.68 (2 H, d, J 6.0, H^4), 7.67 – 7.65 (2 H, m, H^7), 7.56 (1 H, d, J 2.3, H^d), 7.49 (1 H, d, J 2.3, H^j), 7.41 (1 H, d, J 2.4, H^f), 7.17 (1 H, dd, J 8.5, 2.3, H^l), 6.94 (1 H, d, J 8.5, H^m), 1.77 (6 H, s, H^{Me}), 1.42 (9 H, s, H^{tBu}), 1.35 (9 H, s, H^{tBu}); δ C (176 MHz, $CDCl_3$) 167.2 (C^1), 148.5 (C^q), 146.0 (C^q), 145.7 (C^q), 145.5 (C^q), 143.9 (C^3), 142.5 (C^q), 137.6 (C^{4a}), 133.0 ($C^{4'}$ or C^a), 131.7 (C^6), 130.9 ($C^{3'}$), 130.7 (C^q), 129.6 (C^q), 129.4 (C^q), 128.8 (C^7), 127.9 (C^5), 126.7 (C^{8a}), 125.8 (C^f), 125.7 (C^8), 124.3 (C^l), 122.5 (C^j), 122.3 (C^d), 121.6 (C^4), 115.6 (C^m), 34.9 (C^g), 34.6 (C^{tBu2}), 34.5 (C^{tBu4}), 32.2 (C^{Me}), 31.6 (C^{tBu1} or C^{tBu3}), 31.6 (C^{tBu1} or C^{tBu3}); MS ASAP (AP^+) *m/z* 846.3 ($[M\text{-}Cl]^+$, 10%); HRMS (AP^+) *m/z* 845.2999 $[M\text{-}Cl]^+$, calc. for $[C_{47}H_{43}N_2O^{194}Pt]$ 845.3002.

L[32](PtNCS)$_2$

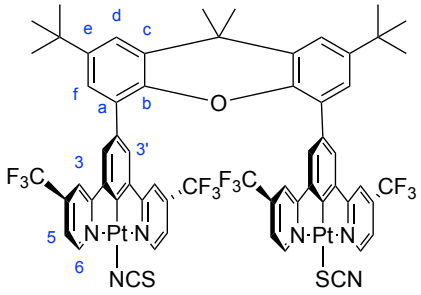

This complex was prepared by the *chloride metathesis reaction* of $L^{32}(PtCl)_2$ (11 mg, 0.007 mmol) with AgOTf (4 mg, 0.016 mmol) and KSCN (10 mg, 0.103 mmol) in acetone (5 mL) to give the product as a red solid (8.6 mg, 79%); δ H (600 MHz, CD_2Cl_2) 8.97 (4 H, d, J 5.8, H^6), 7.57 (2 H, d, J 2.3, H^d), 7.53-7.45 (4 H, m, $H^{3'}$), 7.41 (8 H, m, H^3 and H^5), 7.25 (2 H, d, J 2.3, H^f), 1.83 (6 H, s, H^{Me}), 1.40 (18 H, s, $H^{t\text{-}Bu}$); δ C (151 MHz, CD_2Cl_2) 127.1 (C^3 or C^5), 125.1 (C^f), 123.4 (C^d), 119.7 (C^3 or C^5), 115.6 ($C^{3'}$), 33.2 (C^{Me}), 31.2 ($C^{t\text{-}Bu}$); δ F (376 MHz, CD_2Cl_2) -65.6; HRMS (AP^+) *m/z* 1500.2421 $[M\text{-}NCS]^+$, calc. for $[C_{60}H_{44}F_{12}N_5OPt_2S]$ 1500.2430. Only some peaks were observed for the ^{13}C NMR spectrum, aided by HSQC, due to insolubility.

L[32](PtI)$_2$

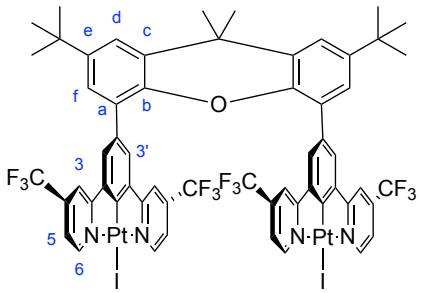

This complex was prepared by the *chloride metathesis reaction* of $L^{32}(PtCl)_2$ (11.5 mg, 0.008 mmol) with AgOTf (2 mg, 0.009 mmol) and KI (1.5 mg, 0.015 mmol) in acetone (5 mL) to give the product as an orange solid (13 mg, 98%); δ H (400 MHz, $CDCl_3$)10.14 (4 H, d, J 5.9, H^6), 7.59 (2 H, d, J 2.3, H^f), 7.54 (4 H, d, J 5.2, H^5), 7.43 (4 H, s, $H^{3'}$), 7.38 (4 H, s, H^3), 7.22 (2 H, s, H^d), 1.86 (6 H, s, H^{Me}), 1.45 (18 H, s, $H^{t\text{-}Bu}$); HRMS (AP^+) *m/z* 1569.1752 $[M\text{-}I]^+$, calc. for $[C_{59}H_{44}F_{12}IN_4OPt_2]$ 1569.1661. This sample was too insoluble to obtain a ^{13}C NMR spectrum.

$L^{33}(PtNCS)_2$

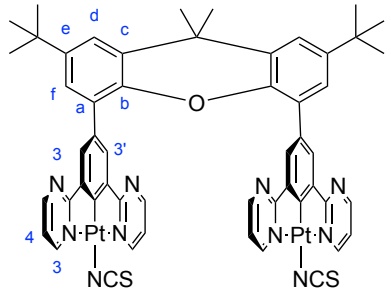

This complex was prepared by the *chloride metathesis reaction* of $L^{33}(PtCl)_2$ (11 mg, 0.009 mmol) with AgOTf (3 mg, 0.011 mmol) and KSCN (10 mg, 0.103 mmol) in acetone (5 mL) to give the product as a red solid (11 mg, 96%). This sample was too insoluble for characterisation.

7.5.2 Class II Sandwich Compounds

Intermediates and Precursors

I10: 2,7-di-tert-butyl-4,5-diiodo-9,9-dimethylxanthene

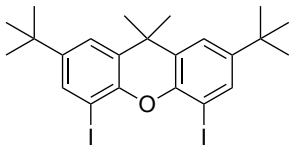

n-BuLi (2.5 M in hexanes, 1.66 mL, 4.14 mmol) was added dropwise to a stirred solution of 4,5-dibromo-2,7-di-*t*-butyl-9,9-dimethylxanthene (0.9 g, 1.87 mmol) in 20 ml of dry THF maintained at −20 °C. The resulting beige suspension was stirred for 2 h. Next a solution of I_2 (0.6 g, 4.7 mmol) in 10 mL of dry THF was added and the reaction mixture was slowly warmed to RT overnight. The reaction mixture was poured onto saturated sodium thiosulfate solution and extracted with DCM. The organic layer was washed with brine and dried over $MgSO_4$. The solvents were removed *in vacuo* and the residue was recrystallised from DCM. A white powder was obtained (679 mg, 64 %). The experimental data obtained were in good agreement with the literature.[178]

I11: 2,7-di-tert-butyl-4,5-bis((trimethylsilyl)ethynyl)-9,9-dimethylxanthene

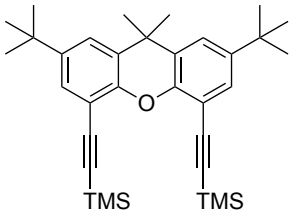

$Pd(dppf)_2Cl_2$ (74 mg, 0.10 mmol) and copper(I) iodide (32 mg, 0.17 mmol) were added successively to a solution of 2,7-di-tert-butyl-4,5-diiodo-9,9-dimethylxanthene (300 mg, 0.52 mmol) and trimethysilylacetylene (0.24 mL, 1.58 mmol) in dry NEt_3 (3 mL) under argon at RT. The reaction mixture was stirred at 60 °C for 24 h and the NEt_3 was then removed under reduced pressure. The residue was diluted with H_2O (5 mL) and DCM (5 mL). The product was extracted into DCM (3 x 10 mL), and the combined organic phases were dried over $MgSO_4$ and evaporated. The crude produced was purified by flash column chromatography on silica gel (30:1, hexane/ethyl acetate) and a white solid was obtained (277 mg, 86 %). The experimental data obtained were in good agreement with the literature.[130]

H_2L^{35}: 2,7-di-tert-butyl-4,5-diethynyl-9,9-dimethylxanthene

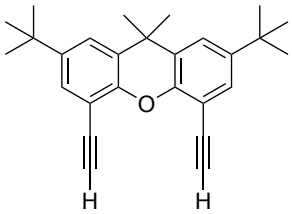

A solution of K_2CO_3 (150 mg, 1.09 mmol) in MeOH (3 mL) was added to a solution of 2,7-di-tert-butyl-4,5-bis((trimethylsilyl)ethynyl)-9,9-dimethylxanthene (100 mg, 0.174 mmol) in DCM (3 mL). After stirring at RT for 12 h, the solvent was removed *in vacuo*. The residue was diluted with H_2O (20 mL) and DCM (20 mL). The product was extracted into DCM (3 x 10 mL), and the combined organic phases were dried over $MgSO_4$ and evaporated. The crude produced was purified by flash column chromatography on silica gel (30:1, hexane/ethyl acetate) and a white solid was obtained (70 mg, 95 %). The experimental data obtained were in good agreement with the literature.[130]

(L³Pt)₂L³⁵

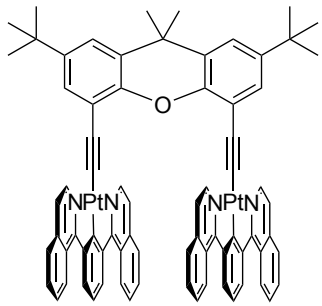

Di-tert-butyl-4,5-bis((trimethylsilyl)ethynyl)-9,9-dimethylxanthene (7.5 mg, 0.02 mmol) was suspended in dry MeOH (1 mL). A solution of 0.5 M NaOMe in MeOH (27 mg, 0.5 mmol) was added and the mixture stirred for 30 mins at RT. Following this, PtL^3Cl (22 mg, 0.04 mmol) dissolved in DCM was added to the mixture and this was set to stir at 60 °C for 48 h. On cooling to RT, the solvent was removed under reduced pressure and the resulting solid was then washed with H_2O, MeOH and Et_2O. Recrystallisation in DCM/Hexane gave trace amounts of the pure product with not enough for a full characterisation; δ H (700 MHz, $CDCl_3$) 9.67 (4 H, d, J 6.2), 8.34 (4 H, d, J 8.5), 7.68 (4 H, d, J 7.8), 7.54 (2 H, d, J 2.3), 7.40 (4 H, d, J 7.9), 7.35 (4 H, ddd, J 7.9, 6.6, 1.0), 7.30 (2 H, d, J 2.4), 7.28 (4 H, ddd, J 8.1, 6.6, 1.4), 7.14 (4 H, d, J 6.2), 7.00 (2 H, t, J 7.7), 1.77 (6 H, s), 1.37 (18 H, s).

7.5.3 Interlocked complexes

Complexes

L³¹Pt₂L³⁵

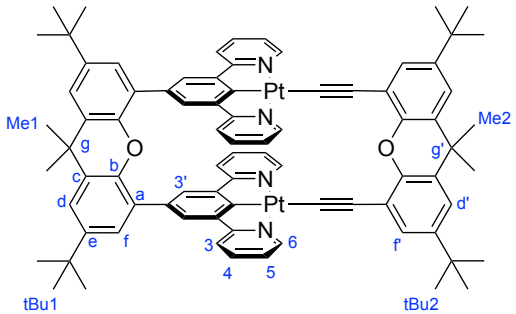

2,7-Di-*tert*-butyl-4,5-diethynyl-9,9-dimethylxanthene (9 mg, 0.024 mmol) and NaOMe (4 mg, 0.73 mmol) were stirred in MeOH (20 mL) at RT (30 mins). $L^{31}(PtCl)_2$

(30 mg, 0.024 mmol) was added in DCM (20 mL) and the resulting mixture reacted according to *Complexation General Procedure 2* to give the product as a yellow solid (31 mg, 83%); δ H (700 MHz, $CDCl_3$) 9.72 – 9.63 (4 H, m, H^6), 7.56 (2 H, d, J 2.4, H^d or H^f), 7.48 (2 H, d, J 2.3, H^d or H^f), 7.37 (4 H, s, $H^{3'}$), 7.28 – 7.22 (8 H, m, H^4, H^d and H^f), 7.17 (4 H, d, J 7.8, H^3), 6.96 – 6.90 (4 H, m, H^5), 1.82 (6 H, s, H^{Me}), 1.70 (6 H, s, H^{Me}), 1.39 (18 H, s, H^{tBu}), 1.35 (18 H, s, H^{tBu}); δ C (176 MHz, $CDCl_3$) 179.1, 168.9, 156.6 (C^6), 148.7, 145.5 ($C^{e/e'}$), 144.4, 143.9 ($C^{e'/e'}$), 142.5, 141.7, 136.7 ($C^{4/d'/f'}$), 132.4, 129.9, 129.1 ($C^{c/c'}$), 129.1 ($C^{d/f}$), 128.8 ($C^{c/c'}$), 125.7 ($C^{4/d'/f'}$), 124.9 ($C^{3'}$), 123.0 (C^5), 122.2 ($C^{d/f}$), 120.0 ($C^{4/d'/f'}$), 118.3 (C^3), 116.0, 53.4, 50.9, 34.8, 34.6 ($C^{g/g'}$), 34.4 ($C^{g/g'}$), 33.6 (C^{Me}), 33.1 (C^{Me}), 31.6 (C^{tBu}), 31.6 (C^{tBu}), 31.4; MS ASAP (AP^+) *m/z* 1540.2 $[M+H]^+$; HRMS (AP^+) *m/z* 1540.5468 $[M+H]^+$, calc. for $[C_{82}H_{76}N_4O_2Pt_2]$ 1540.5363; Anal. calc. for $C_{82}H_{76}N_4O_2Pt_2 \cdot 3CH_2Cl_2$: C, 56.89; H, 4.61; N, 3.12 %; found C, 56.63; H, 4.96; N, 2.98 %.

$L^{32}Pt_2L^{35}$

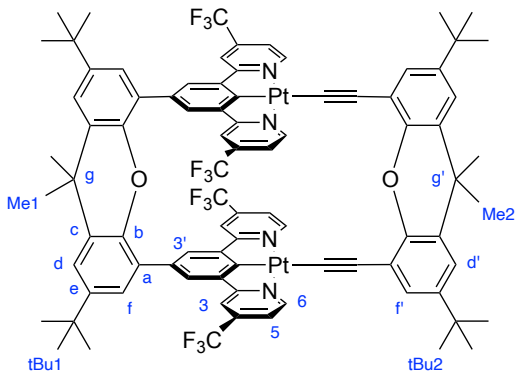

2,7-Di-*tert*-butyl-4,5-diethynyl-9,9-dimethylxanthene (5.6 mg, 0.015 mmol) and NaOMe (4 mg, 0.076 mmol) were stirred in MeOH (15 mL) at RT (30 mins). $L^{32}(PtCl)_2$ (23 mg, 0.015 mmol) was added in DCM (15 mL) and the resulting mixture reacted according to *Complexation General Procedure 2* to give the product as a red solid (8.8 mg, 32%); δ H (600 MHz, $CDCl_3$) 9.90 (4 H, d, J 5.6, H^6), 7.55 (2 H, t, J 2.3, H^d or H^f), 7.52 (4 H, dd, J 4.0, 2.1, $H^{d'}$ and $H^{f'}$), 7.38 (4 H, dt, J 4.5, 2.4, H^3), 7.31 (2 H, t, J 2.3, H^d or H^f), 7.27 (4 H, d, J 6.0, $H^{3'}$), 7.26-7.23 (4 H, m, H^5), 1.71 (6 H, d, J 2.2, H^{Me}), 1.60 (6 H, d, J 2.1, H^{Me}), 1.36 (18 H, d, J 2.2, $H^{t\text{-}Bu}$), 1.31 (18 H, d, J 2.4, $H^{t\text{-}Bu}$); δ C (151 MHz, $CDCl_3$) 157.7 (C^6), 129.2 (C^d or C^f), 128.8 (C^3), 126.4 ($C^{d'}$ or $C^{f'}$), 125.7 (C^5), 123.5, 122.9

($C^{d'}$ or $C^{f'}$), 120.7 (C^{d} or C^{f}), 119.7 ($C^{3'}$), 114.8, 32.9 (C^{Me}), 32.0 (C^{Me}), 31.6 ($C^{t\text{-}Bu}$), 31.3 ($C^{t\text{-}Bu}$); HRMS (AP^{+}) *m/z* 1812.5026 $[M+H]^{+}$, calc. for $[C_{86}H_{72}F_{12}N_4O_2Pt_2]$ 1812.4858.

$L^{33}Pt_2L^{35}$

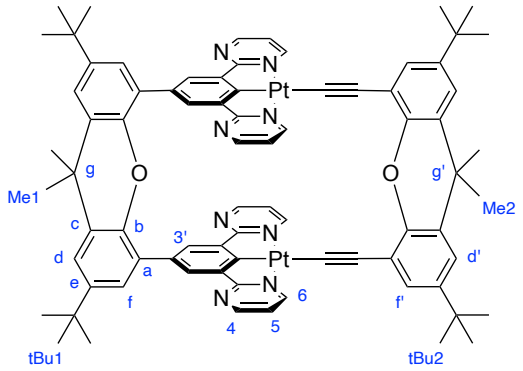

2,7-Di-*tert*-butyl-4,5-diethynyl-9,9-dimethylxanthene (6 mg, 0.015 mmol) and NaOMe (4 mg, 0.080 mmol) were stirred in MeOH (15 mL) at RT (30 mins). $L^{33}(PtCl)_2$ (20 mg, 0.016 mmol) was added in DCM (15 mL) and the resulting mixture reacted according to *Complexation General Procedure 2* to give the product as a yellow solid (6.3 mg, 25%); δ H (600 MHz, CD_2Cl_2) 9.70 (4 H, d, J 6.5, H^6), 8.44 (4 H, s, H^4), 7.75 (4 H, d, J 0.9, $H^{3'}$), 7.51 (2 H, s, H^{d}), 7.46 (2 H, s, $H^{d'}$), 7.31 (2 H, s, $H^{f'}$) 7.27 (2 H, s, H^{f}), 7.02 (4 H, t, J 5.2, H^5), 1.80 (6 H, s, H^{Me}), 1.70 (6 H, s, H^{Me}), 1.39 (18 H, d, J 0.8, $H^{t\text{-}Bu}$), 1.37 (18 H, s, $H^{t\text{-}Bu}$); δ C (151 MHz, $CDCl_3$) 162.7 (C^6), 156.4 (C^4), 131.0 ($C^{3'}$), 128.9 (C^{d}), 125.5 (C^{f}), 122.2 ($C^{d'}$), 120.5 ($C^{f'}$), 118.6 (C^5), 33.2 (C^{Me}), 32.9 (C^{Me}), 31.6 ($C^{t\text{-}Bu}$), 31.5 ($C^{t\text{-}Bu}$); HRMS (AP^{+}) *m/z* 1542.5154 $[M^{+}]$, calc. for $[C_{78}H_{72}N_8O_2Pt_2]$ 1542.5135.

7.5.4 Alternative Linkers

Proligands

H_2L^{37}

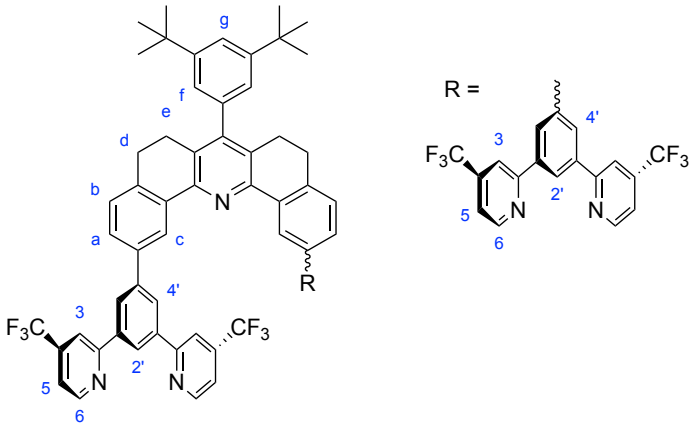

This proligand was prepared using a Suzuki reaction with **I13** (100 mg, 0.159 mmol), CF_3dpyb-Bpin (165 mg, 0.334 mmol), aqueous Na_2CO_3 (135 mg, 1.27 mmol), $Pd(PPh_3)_4$ (9 mg, 0.008 mmol) and DME (2 mL). The crude mixture was purified by column chromatography on silica (hexane: ethyl acetate gradient, R_f = 0.3 in 70:30) to yield the product as a white solid (59 mg, 31%); δ H (700 MHz, $CDCl_3$) 8.86 (2 H, s, H^{Ar}), 8.62 (4 H, d, J 4.9, H^6), 8.41 (2 H, s, H^{Ar}), 8.32 (4 H, s, H^{Ar}), 7.85 (4 H, s, H^{Ar}), 7.56 (2 H, s, H^{Ar}), 7.42 (1 H, d, J 2.0, H^g), 7.31-7.24 (6 H, m, H^5 and H^{Ar}), 7.03 (2 H, d, J 1.8, H^d), 2.83 (4 H, t, J 7.6, H^a or H^b), 2.70 (4 H, t, J 7.2, H^a or H^b), 1.33 (18 H, s, $H^{t\text{-}Bu}$); δ C (176 MHz, $CDCl_3$) 150.5 (C^6), 127.9, 127.2, 124.3, 123.1 (C^d), 121.2 (C^g), 117.7 (C^5), 116.0, 31.6 ($C^{t\text{-}Bu}$), 28.1 (C^a or C^b), 26.2 (C^a or C^b); δ F (376 MHz, $CDCl_3$) -64.78; MS ASAP (AP^+) *m/z* 1204.4 ($[M+H]^+$, 50%); HRMS (AP^+) *m/z* 1204.4160 $[M+H]^+$, calc. for $[C_{71}H_{54}F_{12}N_5]$ 1204.4187.

H_2L^{38}

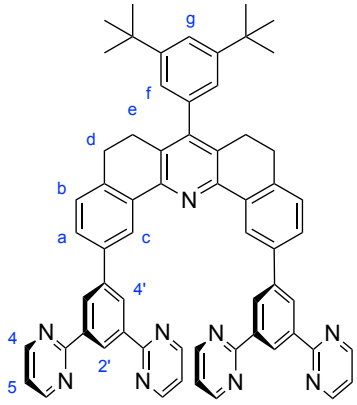

This proligand was prepared using a Suzuki reaction with **I13** (104 mg, 0.165 mmol), dpmb-Bpin (125 mg, 0.347 mmol), aqueous Na_2CO_3 (140 mg, 1.32 mmol), $Pd(PPh_3)_4$ (9.5 mg, 0.008 mmol) and DME (2 mL). The crude mixture was purified by column chromatography on silica (hexane: ethyl acetate gradient, R_f = 0.3 in ethyl acetate) to yield the product as a white solid (66 mg, 44%); δ H (600 MHz, $CDCl_3$) 9.37 (2 H, t, J 1.6, $H^{2'}$), 9.24 (2 H, d, J 2.0, H^c), 9.07 (4 H, d, J 1.6, $H^{4'}$), 8.65 (8 H, d, J 4.8, H^4), 7.87 (2 H, dd, J 7.7, 2.0, H^a), 7.50 (1 H, t, J 1.8, H^g), 7.37 (2 H, d, J 7.8, H^b), 7.15-7.07 (6 H, m, H^5 and H^f), 2.96 (4 H, t, J 7.2, H^d), 2.80 (4 H, t, J 7.2, H^e), 1.41 (18 H, s, $H^{t\text{-}Bu}$); δ C (151 MHz, $CDCl_3$) 157.1 (C^4), 128.5 ($C^{4'}$), 128.1 (C^b),127.1 (C^a), 126.5 ($C^{2'}$), 123.8 (C^c), 123.1 (C^5), 121.3 (C^g), 119.3 (C^f), 31.3 ($C^{t\text{-}Bu}$), 27.9 (C^d), 26.0 (C^e); MS ESI (ES^+) *m/z* 933.5 (M^+, 11%).

H_2L^{39}

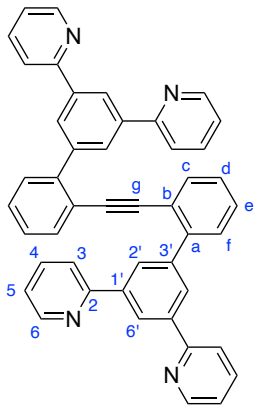

This compound was prepared *via* the Suzuki cross-coupling reaction using crude Dpyb-Bpin (403 mg, 1.13 mmol), **I14** synthesised by Dr Amit Sil (172 mg, 0.511 mmol), aqueous Na_2CO_3 (433 mg, 4.09 mmol), $Pd(PPh_3)_4$ (30 mg, 0.026 mmol) and DME (4

mL). The crude mixture was purified by column chromatography on silica (hexane: ethyl acetate gradient, R_f = 0.5 in 100% ethyl acetate) to yield the pure product as an off-white solid (137 mg, 42%); δ H (600 MHz, $CDCl_3$) 8.69 – 8.64 (4 H, m, H^6), 8.62 (2 H, t, J 1.7, $H^{6'}$), 8.28 (4 H, d, J 1.6, $H^{2'}$), 7.83 – 7.78 (4 H, m, H^3), 7.70 (4 H, td, J 7.7, 1.7, H^4), 7.51 (2 H, dt, J 7.2, 1.1, H^f), 7.30 (4 H, t, J 7.5, H^d and H^e), 7.22 (4 H, ddd, J 7.5, 4.7, 1.1, H^5), 7.06 (2 H, td, J 7.6, 1.3, H^c); δ C (151 MHz, $CDCl_3$) 156.9 (C^2), 149.4 (C^6), 142.9 (C^a), 141.1 (C^g), 139.3 ($C^{1'}$), 136.8 (C^4), 133.2 (C^d or C^e), 129.3 (C^f), 128.5 ($C^{2'}$), 128.4 (C^d or C^e), 127.1 (C^c), 124.6 ($C^{6'}$), 122.2 (C^5), 121.6 (C^b), 120.9 (C^3), 92.5 (C^g); MS ESI $(ES)^+$ *m/z* 639.5 ($[M+H]^+$, 38%); HRMS (ES^+) *m/z* 639.2574 $[M+H]^+$, calc. for $[C_{46}H_{31}N_4]$ 639.2549.

Complexes

L^{36}(PtCl)$_2$

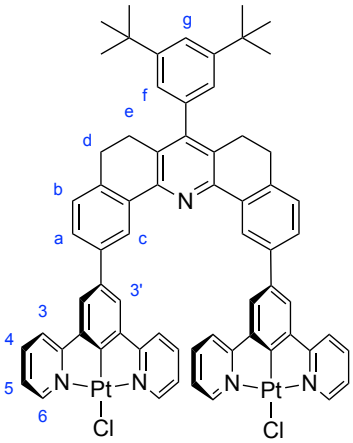

This complex was prepared using *Complexation General Procedure 1*, stirring at reflux for 1 week, with H_2L^{36} (38 mg, 0.0408 mmol) and K_2PtCl_4 (85 mg, 0.204 mmol) in acetic acid (10 mL) to yield the product as a dark yellow solid (25 mg, 44%); δ H (600 MHz, $CDCl_3$) 8.95 (4 H, s, H^6), 7.58 (4 H, s, $H^{3'}$), 7.50 (1 H, s, H^g), 7.26 (12 H, m, H^{Ar}), 7.04 (8 H, m, H^{Ar}), 2.65 (8 H, m, H^d and H^e), 1.44 (18 H, s, $H^{t\text{-}Bu}$); HRMS (AP^+) *m/z* 1392.3335 $[M^+]$, calc. for $[C_{67}H_{55}Cl_2N_5Pt_2]$ 1392.3209. This sample was too insoluble to obtain a ^{13}C NMR spectrum.

L[38](PtCl)$_2$

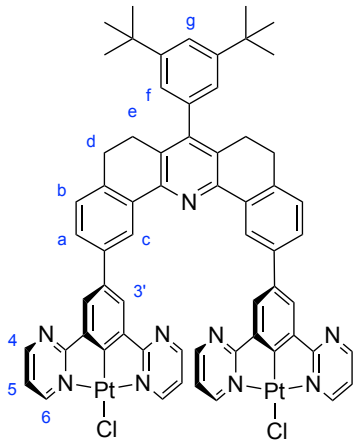

This complex was prepared using *Complexation General Procedure 1*, stirring at reflux for 1 week, with H_2L^{38} (30 mg, 0.032 mmol) and K_2PtCl_4 (67 mg, 0.160 mmol) in acetic acid (7 mL) to yield the product as a dark orange or green solid depending on the polymorph (15 mg, 34%); δ H (600 MHz, $CDCl_3$) 8.86 (2 H, s, H^c), 8.73 (4 H, s, H^6), 8.54 (4 H, s, $H^{3'}$), 7.50 (1 H, s, H^g), 7.29 (2 H, s, H^{Ar}), 7.23-7.09 (6 H, m, H^f and H^{Ar}), 6.96 (4 H, s, H^{Ar}), 2.85 (8 H, d, J 35.4, H^d and H^e), 1.41 (18 H, s, $H^{t\text{-}Bu}$); δ C (151 MHz, $CDCl_3$) 157.3 ($C^{3'}$), 127.1, 123.1, 121.2 (C^g), 118.7, 31.6 ($C^{t\text{-}Bu}$), 28.0 (C^d or C^e), 26.1 (C^d or C^e); MS ASAP (AP^+) *m/z* 1393.3 (M^+, 11%); HRMS (AP^+) *m/z* 1393.3359 [M^+], calc. for [$C_{63}H_{51}Cl_2N_9Pt_2$] 1393.2928.

L[39](PtCl)$_2$

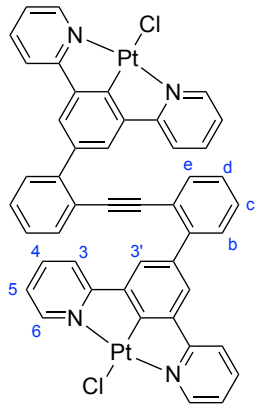

This complex was prepared using *Complexation General Procedure 1* with H_2L^{39} (43 mg, 0.067 mmol) and K_2PtCl_4 (84 mg, 0.202 mmol) in acetic acid (8 mL). The crude solid was purified using preparative column chromatography on silica (DCM: MeOH, gradient, R_f = 0.1 in 2% MeOH) to yield the product as an orange solid (15 mg, 20%);

δ H (600 MHz, CD_2Cl_2) 9.05-8.92 (4 H, m, H^6), 7.87-7.69 (8 H, m, H^4 and H^{Ar}), 7.42 (4 H, s, $H^{3'}$), 7.41-7.35 (4 H, m, H^{Ar}), 7.23-7.19 (4 H, m, H^3), 7.16 (4 H, ddd, J 7.2, 5.6, 1.5, H^5); δ C (151 MHz, CD_2Cl_2) 137.9, 128.9, 124.7, 123.0 (C^5), 118.9 (C^3); MS ASAP (AP^+) *m/z* 1097.2 ($[M+H]^+$, 2%).

7.6 Chapter 5 Synthesis

7.6.1 Intermediates and precursors

I15: 2-phenyl-5-bromopyridine

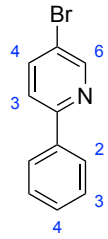

This compound was prepared by the Suzuki cross-coupling reaction using 2,5-dibromopyridine (1.00 g, 4.22 mmol), phenylboronic acid (0.643 g, 5.28 mmol), aqueous Na_2CO_3 (3.58 g, 33.8 mmol), $Pd(PPh_3)_4$ (0.244 g, 0.211 mmol) and DME (30 mL). The crude mixture was purified by column chromatography on silica (hexane: ethyl acetate gradient, R_f = 0.6 in 90:10) to yield the product as a white solid (536 mg, 54%); δ H (400 MHz, $CDCl_3$) 8.77 (1 H, dd, J 2.4, 0.8), 8.03 – 7.95 (2 H, m), 7.91 (1 H, dd, J 8.5, 2.4), 7.66 (1 H, dd, J 8.5, 0.8), 7.56 – 7.42 (3 H, m); MS ESI $(ES)^+$ *m/z* 234.0 $[M^+]$. The experimental data obtained were in good agreement with the literature.[179]

I16: 2-phenyl-5-bispinacolatoboron-pyridine

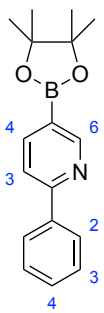

This compound was prepared *via* the Miyaura cross-coupling reaction using **I15** (400 mg, 1.71 mmol), B_2Pin_2 (523 mg, 2.05 mmol), KOAc (1000 mg, 10.3 mmol), $PdCl_2$(dppf) (125 mg, 0.171 mmol) and 1,4-dioxane (20 mL). The crude product was used in further reactions without purification.

I17: 2-(2-thiophene)-5-bromopyridine

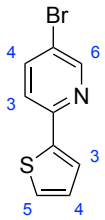

This compound was prepared *via* the Stille cross-coupling method with 2,5-dibromopyridine (1.00 g, 4.22 mmol), 2-(tributylstannyl)thiophene (1.97 g, 5.28 mmol), $Pd(PPh_3)_2Cl_2$ (0.237 g, 0.338 mmol), LiCl (1.43 g, 33.8 mmol) and dry toluene (40 mL). The crude mixture was purified by column chromatography on silica (hexane: ethyl acetate gradient, R_f = 0.5 in 90:10) to yield the pure product as a clear oil (464 mg, 46%); δ H (400 MHz, $CDCl_3$) 8.63 (1 H, dd, J 2.3, 0.8), 7.81 (1 H, dd, J 8.5, 2.4), 7.65 – 7.51 (2 H, m), 7.44 (1 H, dd, J 5.0, 1.1), 7.13 (1 H, dd, J 5.0, 3.7); MS ESI (ES^+) *m/z* 240.0 [M^+].

I18: 2-thiophene-5-bispinacolatoboron-pyridine

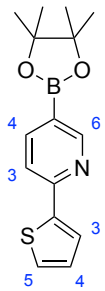

This compound was prepared *via* the Miyaura cross-coupling reaction using **I17** (360 mg, 1.50 mmol), B_2Pin_2 (459 mg, 1.80 mmol), KOAc (883 mg, 8.99 mmol), $PdCl_2$(dppf) (110 mg, 0.150 mmol) and 1,4-dioxane (15 mL). The crude product was used in further reactions without purification.

I19: 2-phenyl-4-bromopyridine

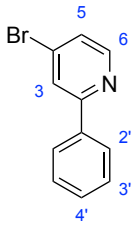

This compound was prepared by the Suzuki cross-coupling reaction using 2,4-dibromopyridine (715 mg, 3.02 mmol), phenylboronic acid (460 mg, 3.77 mmol), aqueous Na_2CO_3 (2560 mg, 21.1 mmol), $Pd(PPh_3)_4$ (174 mg, 0.151 mmol) and DME (20 mL). The crude mixture was purified by column chromatography on silica (hexane: ethyl acetate gradient, R_f = 0.6 in 80:20) to yield the product as a colourless oil (494 mg, 70%); δ H (400 MHz, $CDCl_3$) 8.53 (1 H, d, J 5.2), 8.03 – 7.95 (2 H, m), 7.93 (1 H, d, J 1.8), 7.55 – 7.45 (3 H, m), 7.42 (1 H, dd, J 5.2, 1.8); MS ESI (ES^+) *m/z* 234.1 [M^+]. The experimental data obtained were in good agreement with the literature.[180]

I20: 2-phenyl-4-bispinacolatoboron-pyridine

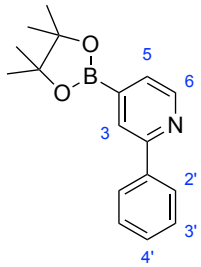

This compound was prepared *via* the Miyaura cross-coupling reaction using **I19** (347 mg, 1.48 mmol), B_2Pin_2 (453 mg, 1.78 mmol), KOAc (873 mg, 8.89 mmol), $PdCl_2$(dppf) (108 mg, 0.148 mmol) and 1,4-dioxane (15 mL). The crude product was used in further reactions without purification.

I21: 2-(2-thiophene)-4-bromopyridine

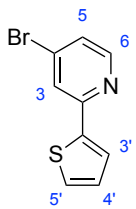

This compound was prepared *via* the Stille cross-coupling method with 2,4-dibromopyridine (500 mg, 2.11 mmol), 2-(tributylstannyl)thiophene (985 mg, 2.64 mmol), $Pd(PPh_3)_2Cl_2$ (118 mg, 0.168 mmol), LiCl (716 mg, 16.9 mmol) and dry toluene (20 mL). The crude mixture was purified by column chromatography on silica (hexane: ethyl acetate gradient, R_f = 0.4 in 90:10) to yield the pure product as a white solid (212 mg, 42%); δ H (400 MHz, $CDCl_3$) 8.39 (1 H, dd, J 5.3, 0.7), 7.83 (1 H, dd, J 1.8, 0.6), 7.59 (1 H, dd, J 3.7, 1.1), 7.45 (1 H, dd, J 5.1, 1.1), 7.32 (1 H, dd, J 5.3, 1.8), 7.13 (1 H, dd, J 5.1, 3.7); MS ESI (ES^+) *m/z* 240.0 [M^+].

I22: 2-thiophene-4-bispinacolatoboron-pyridine

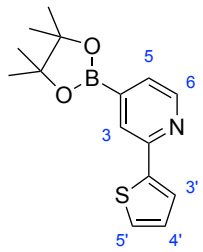

This compound was prepared *via* the Miyaura cross-coupling reaction using **I21** (212 mg, 0.883 mmol), B_2Pin_2 (270 mg, 1.06 mmol), KOAc (520 mg, 5.30 mmol), $PdCl_2$(dppf) (65 mg, 0.088 mmol) and 1,4-dioxane (9 mL). The crude product was used in further reactions without purification.

I23: 1,3-bis(bromomethyl)benzene

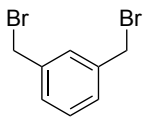

m-Xylene (500 mg, 4.71 mmol) was added to a Schlenk tube with NBS (2000 mg, 11.8 mmol) and benzoyl peroxide (57 mg, 0.236 mmol) in CCl_4 (5 mL) and heated to reflux for 24 hours. The solid was removed by filtration after cooling to RT, and the required filtrate washed with water, brine, and then extracted with DCM. The combined organics were dried over $MgSO_4$ and purified by column chromatography on silica (hexane: ethyl acetate, R_f = 0.5 in 90:10) to give the desired product as a white solid (566 mg, 46%); δ H (400 MHz, $CDCl_3$) 7.45 (1 H, s), 7.36 (3 H, d, J 1.4), 4.51 (4 H, s). The experimental data obtained were in good agreement with the literature.[181,182]

7.6.2 Proligands

H_2L^{41}

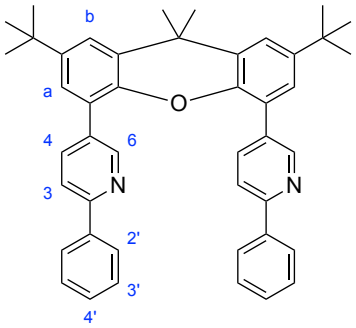

This compound was prepared by the Suzuki cross-coupling reaction using **I16** (481 mg, 1.71 mmol), 4,5-dibromo-2,7-di-*t*-butyl-9,9-dimethylxanthene (373 mg, 0.778 mmol), aqueous Na_2CO_3 (660 mg, 6.22 mmol), $Pd(PPh_3)_4$ (45 mg, 0.039 mmol) and DME (6 mL). The crude mixture was purified by column chromatography on silica (hexane: ethyl acetate gradient, R_f = 0.3 in 90:10) to yield the product as a white solid (268 mg, 55%); δ H (600 MHz, $CDCl_3$) 8.71 (2 H, dd, J 2.3, 0.8, H^6), 7.80 – 7.75 (4 H, m, $H^{2'}$), 7.61 (2 H, dd, J 8.2, 2.3, H^4), 7.51 (2 H, d, J 2.3, H^b), 7.39 – 7.30 (4 H, m, H^3 and $H^{4'}$), 7.29 – 7.26 (4 H, m, $H^{3'}$), 7.24 (2 H, d, J 2.3, H^a), 1.76 (6 H, s, H^{Me}), 1.37 (18 H, s, $H^{t\text{-}Bu}$); δ C (151 MHz, $CDCl_3$) 146.0 (C^6), 138.0 (C^4), 132.5 (C^q), 130.6 (C^q), 128.8 ($C^{4'}$), 128.7 ($C^{3'}$), 126.7 ($C^{2'}$), 125.7 (C^a), 122.5 (C^b), 119.4 (C^3), 31.8 (C^{Me}), 31.6 ($C^{t\text{-}Bu}$); HRMS (AP^+) *m/z* 629.3552 [M^+], calc. for [$C_{45}H_{45}N_2O$] 629.3532.

H_2L^{42}

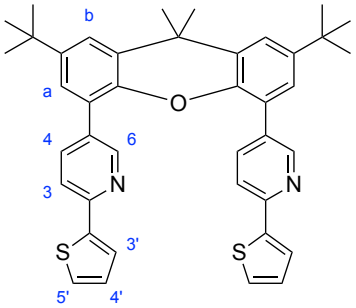

This compound was prepared by the Suzuki cross-coupling reaction using **I18** (430 mg, 1.50 mmol), 4,5-dibromo-2,7-di-*t*-butyl-9,9-dimethylxanthene (327 mg, 0.681 mmol), aqueous Na_2CO_3 (577 mg, 5.45 mmol), $Pd(PPh_3)_4$ (39 mg, 0.034 mmol) and

DME (5 mL). The crude mixture was purified by column chromatography on silica (hexane: ethyl acetate gradient, R_f = 0.2 in 90:10) to yield the product as a white solid (73 mg, 17%); δ H (600 MHz, $CDCl_3$) 8.56 (2 H, dd, J 2.3, 0.8, H^6), 7.51 - 7.49 (4 H, m, H^b and H^3), 7.33 (2 H, dd, J 5.1, 1.1, $H^{3'}$), 7.23 (2 H, d, J 8.2, H^4), 7.20 (2 H, d, J 2.3, H^a), 7.14 (2 H, s (br), $H^{6'}$), 6.95 (2 H, dd, J 5.1, 3.6, $H^{4'}$), 1.75 (6 H, s, H^{Me}), 1.35 (18 H, s, $H^{t\text{-}Bu}$); δ C (151 MHz, $CDCl_3$) 149.4 (C^6), 146.0 (C^q), 137.9 (C^3), 132.2 (C^q), 130.6 (C^q), 128.1 ($C^{4'}$), 127.3 ($C^{3'}$), 125.4 (C^a), 122.5 (C^b), 117.7 (C^4), 31.5 (C^{Me}), 31.4 ($C^{t\text{-}Bu}$); MS ESI (ES^+) *m/z* 641.5 $[M+H]^+$.

H_2L^{43}

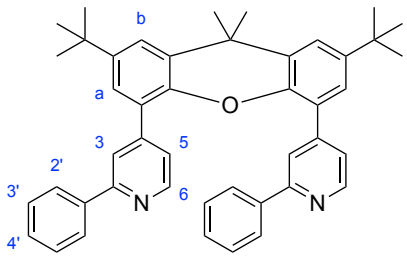

This compound was prepared by the Suzuki cross-coupling reaction using **I20** (417 mg, 1.48 mmol), 4,5-dibromo-2,7-di-*t*-butyl-9,9-dimethylxanthene (324 mg, 0.674 mmol), aqueous Na_2CO_3 (571 mg, 5.39 mmol), $Pd(PPh_3)_4$ (39 mg, 0.034 mmol) and DME (7 mL). The crude mixture was purified by column chromatography on silica (hexane: ethyl acetate gradient, R_f = 0.3 in 70:30) to yield the product as a white solid (355 mg, 84%); δ H (600 MHz, $CDCl_3$) 8.22 (2 H, d, J 5.0, H^6), 7.75 – 7.69 (4 H, m, $H^{2'}$), 7.63 (2 H, d, J 1.4, H^3), 7.53 (2 H, d, J 2.3, H^b), 7.37 – 7.28 (6 H, m, $H^{3'}$ and $H^{4'}$), 7.22 (2 H, d, J 2.3, H^a), 7.09 – 7.04 (2 H, m, H^5), 1.77 (6 H, s, H^{Me}), 1.37 (18 H, s, $H^{t\text{-}Bu}$); δ C (151 MHz, $CDCl_3$) 148.8 (C^6), 146.1 (C^q), 145.2 (C^q), 130.3 (C^q), 128.7 ($C^{3'}$), 128.5 ($C^{4'}$), 126.9 ($C^{2'}$), 125.6 (C^a), 123.3 (C^b), 122.4 (C^5), 121.4 (C^3), 32.4 (C^{Me}), 31.4 ($C^{t\text{-}Bu}$); MS ESI (ES^+) *m/z* 629.6 $[M+H]^+$; HRMS (ES^+) *m/z* 629.3534 $[M+H]^+$, calc. for $[C_{45}H_{45}N_2O]$ 629.3532.

H_2L^{44}

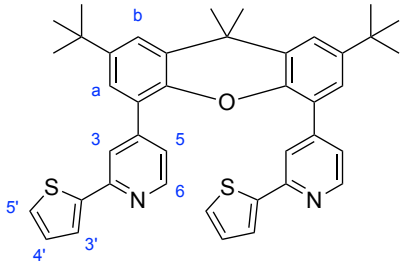

This compound was prepared by the Suzuki cross-coupling reaction using **I22** (254 mg, 0.884 mmol), 4,5-dibromo-2,7-di-*t*-butyl-9,9-dimethylxanthene (193 mg, 0.402 mmol), aqueous Na_2CO_3 (341 mg, 3.22 mmol), $Pd(PPh_3)_4$ (23 mg, 0.020 mmol) and DME (4 mL). The crude mixture was purified by column chromatography on silica (hexane: ethyl acetate gradient, R_f = 0.2 in 80:20) to yield the product as a white solid (122 mg, 47%); δ H (600 MHz, $CDCl_3$) 8.18 (2 H, d, J 5.0), 7.62 – 7.52 (4 H, m), 7.33 (2 H, d, J 4.9), 7.28 – 7.22 (4 H, m), 7.09 – 7.01 (2 H, m), 7.00 – 6.91 (2 H, m), 1.81 (6 H, s, H^{Me}), 1.40 (18 H, s, $H^{t\text{-}Bu}$); HRMS (ES^+) *m/z* 641.2665 $[M+H]^+$, calc. for $[C_{41}H_{41}N_2OS_2]$ 641.2660.

L^{48}

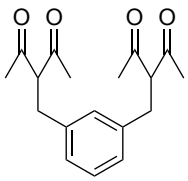

Acetylacetone (720 mg, 7.20 mmol) was stirred in acetone (5 mL) at 0°C before addition of sodium carbonate in portions and resultant stirring for 15 mins. 1,3-bis(bromomethyl)benzene (**I23**) in acetone (5 mL) was added dropwise over 15 mins and then the reaction mixture stirred at reflux for 24 h. The mixture was cooled to RT, filtered, and the solvent removed under reduced pressure to give the product without the need for purification (227 mg, 20%). The experimental data obtained were in good agreement with the literature.[156]

7.6.3 Complexes

Complexation General Procedure 3

Step 1:

The relevant proligand (1 equiv.) was added to a Schlenk flask with K_2PtCl_4 (2 equiv.) in acetic acid and degassed by three freeze-pump-thaw cycles before being heated to reflux for 15 h. The resulting suspension was cooled and the solvent removed *via* centrifugation before washing with acetic acid and ethanol to give the resulting chloro-Pt dimer.

Step 2:

The relevant chloro-Pt dimer (1 equiv.) was added to a Schlenk flask with acetylacetone (5 equiv.), sodium carbonate (10 equiv.) and 2-ethoxyethanol and degassed by three freeze-pump-thaw cycles. The reaction mixture was heated to 100 °C for 16 h, before cooling. The solvent was removed under reduced pressure and the crude solid purified by preparative column chromatography on silica with DCM as the eluent.

Complexation General Procedure 4

Step 1:

The relevant proligand (1 equiv.) was added to a Schlenk flask with K_2PtCl_4 (2 equiv.) in acetic acid and degassed by three freeze-pump-thaw cycles before being heated to reflux for 15 h. The resulting suspension was cooled, and the solvent removed *via* centrifuge before washing with acetic acid and ethanol to achieve the resulting chloro-Pt dimer.

Step 2:

The relevant chloro-Pt dimer (1 equiv.) was added to a Schlenk flask with the relevant triazole ligand (2 equiv.) in dry DCM/MeOH and degassed by three freeze-pump-thaw cycles. The reaction mixture was heated to 50 °C for 24 h, before cooling. The solvent was removed under reduced pressure and the crude mixture purified by column chromatography.

(L^{44}PtCl)$_2$

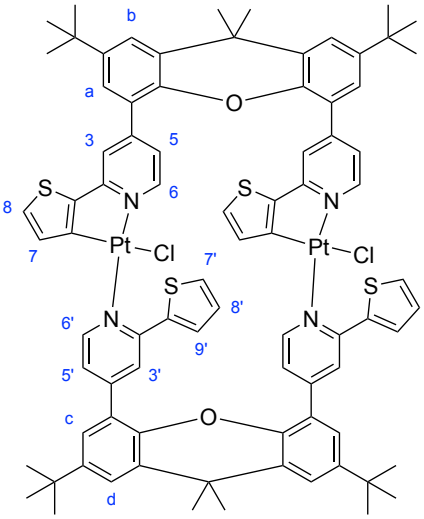

This complex was synthesised using *Complexation General Procedure 3* (step 1 only) with H_2L^{44} (230 mg, 0.359 mmol) and K_2PtCl_4 (298 mg, 0.718 mmol) in acetic acid (10 mL) to give the product as an orange solid (354 mg, 57%); δ H (600 MHz, $CDCl_3$) 9.35 – 9.28 (2 H, m, H^6), 8.89 (2 H, d, J 6.1, $H^{6'}$), 8.00 (2 H, dd, J 3.8, 1.3, $H^{7'}$), 7.81 (2 H, d, J 2.0, $H^{3'}$), 7.61 (2 H, d, J 2.4, H^d), 7.53 (2 H, d, J 2.4, H^b), 7.37 (2 H, d, J 4.7, H^7), 7.32 – 7.29 (6 H, m, H^3, $H^{5'}$ and $H^{9'}$), 7.28 (2 H, d, J 2.4, H^c), 7.26 (2 H, d, J 2.4, H^a), 7.00 (2 H, dd, J 6.1, 2.0, H^5), 6.90 (2 H, dd, J 6.1, 2.0, $H^{8'}$), 6.32 (2 H, d, J 4.7, H^8), 1.80 (6 H, s, H^{Me}), 1.78 (6 H, s, H^{Me}), 1.38 (18 H, s, $H^{t\text{-}Bu}$), 1.37 (18 H, s, $H^{t\text{-}Bu}$); δ C (151 MHz, $CDCl_3$) 153.7 ($C^{6'}$), 151.3 (C^6), 129.8 ($C^{7'}$), 129.2 ($C^{9'}$), 129.1 (C^8), 128.9 (C^7), 126.6 ($C^{8'}$), 126.6 (C^c), 126.0 (C^a), 125.7 ($C^{3'}$), 124.9 (C^d), 124.7 (C^b), 124.5 (C^3), 118.6 (C^5), 117.9 ($C^{5'}$); MS MALDI (M^+) *m/z* 1740.0 (M^+). This sample was too insoluble to observe the quaternary carbon peaks in the ^{13}C NMR spectrum.

L^{41}Pt$_2$(acac)$_2$

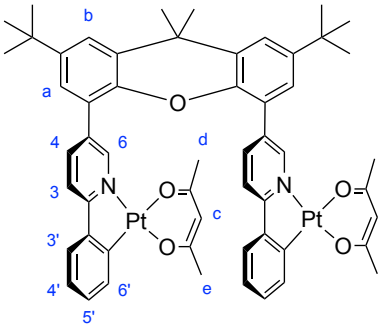

This complex was prepared by *Complexation General Procedure 3* with H_2L^{41} (90 mg, 0.143 mmol) and K_2PtCl_4 (119 mg, 0.286 mmol) in acetic acid (20 mL) for step 1, and the resulting product with acetylacetone (72 mg, 0.715 mmol), Na_2CO_3 (152 mg, 1.43 mmol) in 2-ethoxyethanol (10 mL) for step 2 to give the product as a yellow-orange solid (52 mg, 30%); δ H (600 MHz, $CDCl_3$) 9.01 (2 H, d, J 2.0, H^6), 7.68 (2 H, dd, J 8.3, 2.0, H^4), 7.52 – 7.48 (4 H, m, H^b and $H^{5'}$), 7.40 (2 H, d, J 8.3, H^3), 7.26 (2 H, d, J 2.3, H^a), 7.19 – 7.10 (2 H, m, $H^{4'}$), 6.85 (4 H, ddd, J 13.7, 8.0, 6.6, $H^{3'}$ and $H^{6'}$), 5.42 (2 H, s, H^c), 1.96 (6 H, s, H^e), 1.85 (6 H, s, H^d), 1.75 (6 H, s, H^{Me}), 1.37 (18 H, s, $H^{t\text{-}Bu}$); δ C (151 MHz, $CDCl_3$) 147.1 (C^6), 138.8 (C^4), 130.2 (C^b), 128.8 ($C^{4'}$), 125.4 (C^a), 123.7 ($C^{3'}$), 123.6 ($C^{6'}$), 122.6 ($C^{5'}$), 117.7 (C^3), 102.5 (C^c), 31.5 ($C^{t\text{-}Bu}$), 31.3 (C^{Me}), 28.2 (C^d), 27.1 (C^e);HRMS (AP^+) *m/z* 1214.3513 [M^+], calc. for [$C_{55}H_{56}N_2O_5Pt_2$] 1214.3483.

$L^{42}Pt_2(acac)_2$

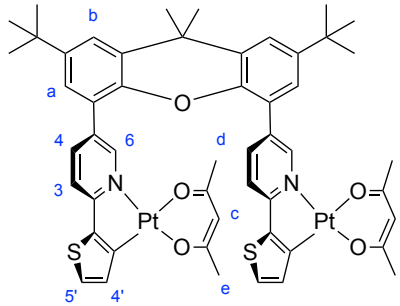

This complex was prepared by *Complexation General Procedure 3* with H_2L^{42} (50 mg, 0.078 mmol) and K_2PtCl_4 (65 mg, 0.156 mmol) in acetic acid (5 mL) for step 1, followed by reaction of the product with acetylacetone (39 mg, 0.390 mmol), Na_2CO_3 (83 mg, 0.780 mmol) in 2-ethoxyethanol (5 mL) to give the product as a yellow solid (31 mg, 32%); δ H (600 MHz, $CDCl_3$) 8.79 (2 H, d, J 1.9, H^6), 7.60 (2 H, dd, J 8.3, 2.0, H^4), 7.47 (2 H, d, J 2.3, H^b), 7.36 (2 H, d, J 4.7, $H^{4'}$), 7.23 (2 H, d, J 2.3, H^a), 7.08 (2 H, d, J 8.2, H^3), 6.99 (2 H, d, J 4.7, $H^{5'}$), 5.40 (2 H, s, H^c), 1.88 (6 H, s, H^e), 1.78 (6 H, s, H^d), 1.74 (6 H, s, H^{Me}), 1.36 (18 H, s, $H^{t\text{-}Bu}$); δ C (151 MHz, $CDCl_3$) 147.1 (C^6), 146.1 (C^q), 145.6 (C^q), 139.0 (C^4), 130.4 (C^q), 129.9 ($C^{5'}$), 127.4 ($C^{4'}$), 125.5 (C^a), 122.4 (C^b), 116.3 (C^3), 102.8 (C^c), 32.0 (C^{Me}), 31.4 ($C^{t\text{-}Bu}$), 28.1 (C^d), 26.6 (C^e); HRMS ASAP (AP^+) *m/z* 1227.2712 [M^+], calc. for [$C_{51}H_{52}N_2O_5Pt_2S_2$] 1227.2687.

L^{45}Pt$_2$(acac)$_2$

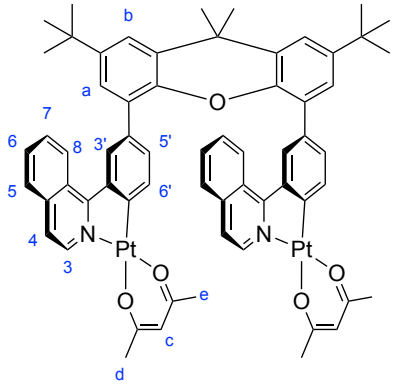

This complex was prepared by *Complexation General Procedure 3* with H_2L^{45} (156 mg, 0.214 mmol) and K_2PtCl_4 (178 mg, 0.427 mmol) in acetic acid (15 mL) for step 1, followed by reaction of the product with acetylacetone (107 mg, 1.08 mmol), Na_2CO_3 (227 mg, 2.14 mmol) in 2-ethoxyethanol (15 mL) according to step 2 to give the product as an orange solid (5 mg, 2%); δ H (600 MHz, $CDCl_3$) 8.80 (2 H, d, J 6.4, H^3), 8.18 (2 H, d, J 8.7, H^8), 7.96 (2 H, s, $H^{3'}$), 7.50 (2 H, d, J 8.2, H^5), 7.46 (2 H, d, J 2.4, H^b), 7.43 – 7.37 (2 H, m, H^6), 7.23 – 7.17 (6 H, m, H^7, H^4 and H^a), 6.89 – 6.78 (4 H, m, $H^{5'}$ and $H^{6'}$), 5.46 (2 H, s, H^c), 2.06 (6 H, s, H^e), 1.94 (6 H, s, H^d), 1.82 (6 H, s, H^{Me}), 1.36 (18 H, s, $H^{t\text{-}Bu}$); δ H (151 MHz, $CDCl_3$) 139.2 (C^3), 130.0 (C^6), 129.8 ($C^{5'}$ and $C^{6'}$), 129.6 ($C^{3'}$), 127.4 (C^7), 126.7 (C^8), 126.6 (C^5), 126.2 (C^4), 121.1 (C^b), 120.1 (C^a), 32.7 (C^{Me}), 31.3 ($C^{t\text{-}Bu}$), 28.4 (C^e), 27.3 (C^d); HRMS (AP$^+$) *m/z* 1215.3417 [M-acac]$^+$, calc. for [$C_{58}H_{52}N_2O_3Pt_2$] 1215.3350.

L^{46}Pt$_2$(acac)$_2$

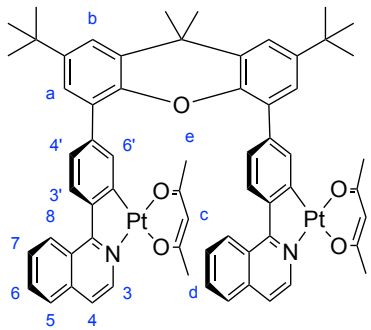

This complex was prepared by *Complexation General Procedure 3* with H_2L^{46} (50 mg, 0.069 mmol) and K_2PtCl_4 (57 mg, 0.137 mmol) in acetic acid (5 mL) for step 1, followed by reaction of the product with acetylacetone (34 mg, 0.343 mmol), Na_2CO_3

(73 mg, 0.686 mmol) in 2-ethoxyethanol (7 mL) according to step 2 to give the product as a dark orange solid (21 mg, 23%); δ H (600 MHz, $CDCl_3$) 8.62 (2 H, d, J 6.4, H^3), 8.31 (2 H, d, J 8.7, $H^{3'}$), 7.78 (2 H, d, J 1.8, H^6), 7.57 (2 H, d, J 8.3, H^8), 7.48 – 7.40 (4 H, m, H^5 and H^b), 7.35 (2 H, d, J 8.0, H^a), 7.32 – 7.26 (2 H, m, $H^{6'}$), 7.11 – 7.05 (4 H, m, $H^{4'}$ and H^7), 6.95 (2 H, d, J 6.4, H^4), 5.47 (2 H, s, H^c), 2.00 (6 H, s, H^d), 1.94 (6 H, s, H^e), 1.77 (6 H, s, H^{Me}), 1.38 (18 H, s, $H^{t\text{-}Bu}$); δ C (151 MHz, HSQC, $CDCl_3$) 130.2 (C^6), 130.1 ($C^{6'}$), 127.8 (C^8), 127.7 ($C^{4'}$), 126.4 (C^a), 126.0 (C^5), 125.8 (C^7), 125.7 ($C^{3'}$), 120.8 (C^b), 118.7 (C^4), 102.7 (C^c), 31.6 ($C^{t\text{-}Bu}$), 31.6 (C^{Me}), 28.4 (C^d), 27.1 (C^e); HRMS (AP^+) *m/z* 1215.3389 $[M\text{-acac}]^+$, calc. for $[C_{58}H_{52}N_2O_3Pt_2]$ 1215.3350.

$L^{47}Pt_2(acac)_2$

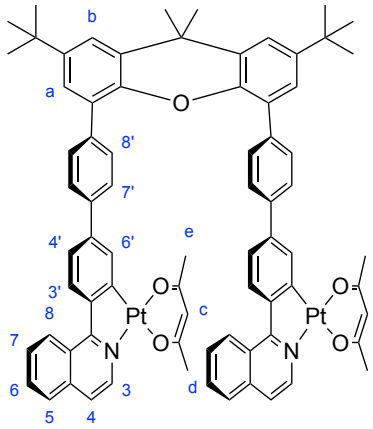

This complex was prepared by *Complexation General Procedure 3* with H_2L^{47} (44 mg, 0.050 mmol) and K_2PtCl_4 (41 mg, 0.010 mmol) in acetic acid (5 mL) for step 1, followed by reaction of the product with acetylacetone (25 mg, 0.249 mmol), Na_2CO_3 (53 mg, 0.249 mmol) in 2-ethoxyethanol (5 mL) according to step 2 to give the product as a red solid (26 mg, 36%); δ H (600 MHz, $CDCl_3$) 8.64 (2 H, d, J 6.4, H^3), 8.44 (2 H, d, J 8.7, H^8), 7.97 (2 H, d, J 2.0, $H^{6'}$), 7.70 (2 H, d, J 8.3, $H^{3'}$), 7.59 – 7.53 (4 H, m, $H^{7'}$), 7.47 – 7.43 (4 H, m, H^5 and H^a), 7.44 – 7.41 (4 H, m, $H^{8'}$), 7.37 (2 H, ddd, J 8.0, 6.7, 1.0, H^6), 7.29 (2 H, d, J 2.3, H^b), 7.17 (2 H, ddd, J 8.3, 6.7, 1.4, H^7), 7.07 (2 H, dd, J 8.2, 2.0, $H^{4'}$), 7.03 (2 H, d, J 6.4, H^4), 5.41 (2 H, s, H^c), 2.00 (6 H, s, H^d), 1.91 (6 H, s, H^e), 1.75 (6 H, s, H^{Me}), 1.37 (18 H, s, $H^{t\text{-}Bu}$); δ C (151 MHz, $CDCl_3$) 138.9 (C^3), 130.4 (C^6), 129.9 ($C^{8'}$), 128.8 ($C^{3'}$), 127.8 ($C^{6'}$), 127.7 (C^7), 126.6 (C^5), 126.4 ($C^{7'}$), 125.9 (C^8), 125.8 (C^b),

122.2 ($C^{4'}$), 120.8 (C^{a}), 118.6 (C^{4}), 31.4 ($C^{t\text{-}Bu}$), 30.7 (C^{Me}), 28.1 (C^{e}), 27.3 (C^{d}); HRMS (AP^+) *m/z* 1367.4126 $[M\text{-acac}]^+$, calc. for $[C_{70}H_{60}N_2O_3Pt_2]$ 1367.3977.

$L^{41}Pt_2$(t-Bu-triazole)$_2$

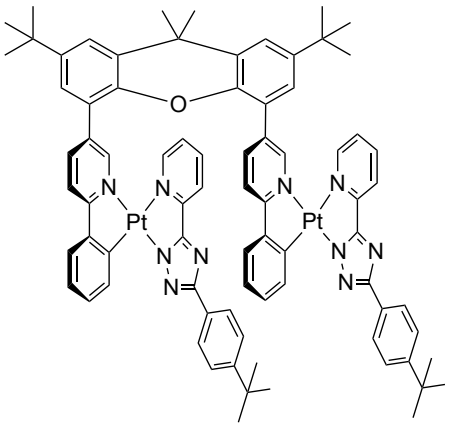

This complex was prepared by *Complexation General Procedure 4* with H_2L^{41} (75 mg, 0.119 mmol) and K_2PtCl_4 (99 mg, 0.239 mmol) in acetic acid (15 mL) for step 1, and the resulting product with *t*-Bu-triazole (66 mg, 0.238 mmol) in DCM (2 mL) and MeOH (2 mL) for step 2 to give the product as a red solid in trace amounts (3 mg, 3%); δ H (400 MHz, $CDCl_3$) 10.57 (2 H, s), 8.60 (2 H, s), 8.16 (2 H, s), 7.96 (4 H, s), 7.72 (4 H, d, J 2.4), 7.19 (8 H, d, J 8.2), 7.12 (4 H, s), 7.02 (2 H, s), 6.96 (2 H, d, J 2.3), 6.82 (4 H, dd, J 18.0, 7.3), 2.14 (6 H, s), 1.32 (18 H, s), 1.27 (18 H, s); HRMS (AP^+) *m/z* 1571.5747 $[M+H]^+$, calc. for $[C_{79}H_{76}N_{10}OPt_2]$ 1571.5577.

$L^{42}Pt_2$(t-Bu-triazole)$_2$

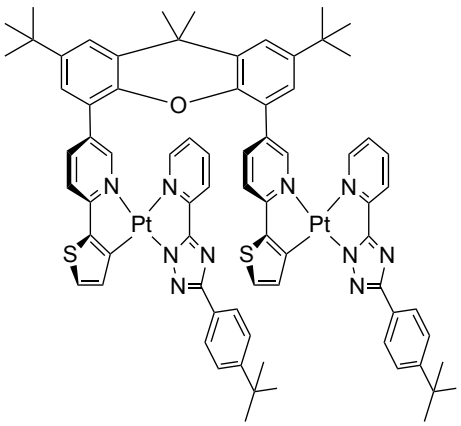

This complex was prepared by *Complexation General Procedure 4* with H_2L^{42} (50 mg, 0.078 mmol) and K_2PtCl_4 (65 mg, 0.156 mmol) in acetic acid (10 mL) for step 1, and with the resulting product from step 1 and OMe-triazole (22 mg, 0.078 mmol) in DCM (2 mL) and MeOH (2 mL) for step 2 to give the product as a red solid (5 mg, 8%); δ H (400 MHz, $CDCl_3$) 10.59 (2 H, s), 9.03 (2 H, d, J 5.9), 8.24 (2 H, d, J 7.8), 8.21 – 8.15 (2 H, m), 8.04 (2 H, t, J 7.6), 7.80 (2 H, dd, J 8.2, 1.9), 7.63 (2 H, d, J 8.4), 7.60 – 7.50 (4 H, m), 7.43 (2 H, d, J Hz), 7.27 – 7.20 (2 H, m), 7.18 – 7.03 (4 H, m), 6.90 (2 H, dd, J 3.7, 1.1), 6.84 (2 H, dd, J 5.0, 3.6), 2.20 (6 H, s), 1.91 (18 H, s), 1.41 (18 H, s); HRMS (AP^+) *m/z* 1584.4786 $[M+H]^+$, calc. for $[C_{75}H_{72}N_{10}OPt_2S_2]$ 1584.4719.

HL^{42}Pt(OMe-triazole)

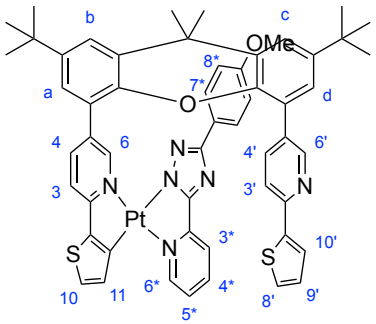

This complex was prepared by *Complexation General Procedure 4* with H_2L^{42} (82 mg, 0.128 mmol) and K_2PtCl_4 (106 mg, 0.256 mmol) in acetic acid (6 mL) for step 1, and with the resulting product from step 1 and OMe-triazole (65 mg, 0.256 mmol) in DCM (3 mL) and MeOH (3 mL) for step 2 to give the product as a red solid (19 mg, 27%); δ H (600 MHz, $CDCl_3$) 10.50 (1 H, d, J 1.9, H^6), 8.97 (1 H, d, J 5.8, H^{6*}), 8.16 (1 H, d, J 7.8, H^{3*}), 8.12 (1 H, d, J 2.2, $H^{5'}$), 8.05 – 7.96 (1 H, m, H^{4*}), 7.77 (1 H, dd, J 8.1, 1.9, H^4), 7.68 – 7.63 (2 H, m, H^{7*}), 7.56 (1 H, d, J 2.3, H^b), 7.50 – 7.44 (3 H, m, H^c, $H^{4'}$, and H^{10}), 7.39 (1 H, d, J 8.0, H^3), 7.22 (1 H, d, J 2.3, H^a), 7.19 – 7.13 (2 H, m, H^{5*} and $H^{3'}$), 7.08 – 7.02 (2 H, m, $H^{8'}$ and H^{11}), 6.97 (1 H, d, J 2.3, H^d), 6.86 – 6.82 (1 H, m, $H^{10'}$), 6.78 (1 H, dd, J 4.9, 3.6, $H^{9'}$), 6.62 – 6.57 (2 H, m, H^{8*}), 3.76 (3 H, s, H^{OMe}), 1.87 (6 H, s, H^{Me}), 1.56 (18 H, s, $H^{t\text{-}Bu}$); δ C HSQC (151 MHz, $CDCl_3$) 152.4 (C^6), 151.2 (C^{6*}), 149.5 ($C^{5'}$), 140.0 (C^4), 138.9 (C^{4*}), 136.8 (C^{10}), 131.2 ($C^{8'}$), 127.4 ($C^{9'}$), 127.0 (C^{7*}), 126.7 ($C^{4'}$), 126.6 (C^{11}), 126.2 (C^a), 126.2 (C^d), 124.1 ($C^{10'}$), 123.7 (C^b), 122.9 (C^{5*}), 122.8 (C^c), 120.5 (C^{3*}), 117.6

($C^{3'}$), 116.3 (C^{3}), 113.4 (C^{8*}), 55.1 (C^{OMe}), 33.6 ($C^{t\text{-}Bu}$), 31.6 (C^{Me}), 31.4 (C^{Me}); HRMS (AP^{+}) *m/z* 1085.3127 [M^{+}], calc. for [$C_{55}H_{50}N_6O_2PtS_2$] 1085.3142.

$L^{48}Pt_2(ppy)_2$

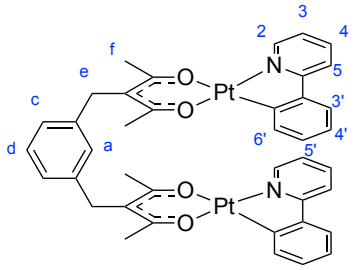

Phenylpyridine (100 mg, 0.644 mmol) was added with K_2PtCl_4 (267 mg, 0.644 mmol) to a Schlenk tube with acetic acid (20 mL) and degassed by three freeze-pump-thaw cycles. The mixture was heated to reflux for 15 h, and the resulting solid separated from the solution by centrifugation. The solid was washed with acetic acid and ethanol before drying under vacuum to give the μ-Cl dimer. This was then added to a Schlenk tube with L^{48} (117 mg, 0.386 mmol) and Na_2CO_3 (170 mg, 1.61 mmol) in 2-ethoxyethanol (10 mL) and degassed by three freeze-pump-thaw cycles. The reaction mixture was heated at reflux for 16 h, and the solvent removed under reduced pressure. Purification by column chromatography on silica (DCM, R_f = 0.5 in DCM) to give the product in trace amounts; δ H (600 MHz, CD_2Cl_2) 8.98 (2 H, ddd, J 5.8, 1.6, 0.8, H^2), 7.89 – 7.79 (2 H, m, H^4), 7.66 (2 H, dd, J 8.1, 1.3, H^5), 7.56 (2 H, dd, J 7.6, 1.3, $H^{c'}$), 7.49 (2 H, dd, J 7.8, 1.4, $H^{3'}$), 7.21 (1 H, t, J 7.5, H^d), 7.19 – 7.13 (4 H, m, H^3 and $H^{5'}$), 7.10 (2 H, td, J 7.5, 1.3, $H^{4'}$), 7.07 – 6.99 (3 H, m, H^a and H^c), 3.81 (4 H, s, H^e), 2.10 (12 H, s, H^f); δ C (151 MHz, CD_2Cl_2) 147.0 (C^2), 138.2 (C^4), 130.6 ($C^{6'}$), 128.9 ($C^{5'}$), 128.6 (C^d), 127.3 (C^a), 125.4 (C^e), 123.4 ($C^{4'}$), 123.0 ($C^{3'}$), 121.4 (C^4), 118.5 (C^5), 35.9 (C^e), 29.7 (C^f); MS ESI (ES^{+}) *m/z* 998.8 [M^{+}]; HRMS (AP^{+}) *m/z* 1039.2690 [M+MeCN]$^{+}$, calc. for [$C_{40}H_{36}N_2O_4Pt_2CH_3CN$] 1039.2231.

8. References

1 J. A. G. Williams, *Chem. Soc. Rev.*, 2009, **38**, 1783–1801.

2 D. N. Kozhevnikov, V. N. Kozhevnikov, M. Z. Shafikov, A. M. Prokhorov, D. W. Bruce and J. A. G. Williams, *Inorg. Chem.*, 2011, **50**, 3804–3815.

3 B. Zhang, L. Zhang, C. Liu, Y. Zhu, M. Tang, C. Du and M. Song, *Dalton. Trans.*, 2014, **43**, 7704–7707.

4 L. Zhang, L. Tian, M. Li, R. He and W. Shen, *Dalton. Trans.*, 2014, **43**, 6500–6512.

5 A. K. Chan, M. Ng, Y. Wong, M. Chan, W. Wong and V. W. Yam, *J. Am. Chem. Soc.*, 2017, **139**, 10750–10761.

6 T. Fleetham, G. Li and J. Li, *Adv. Mater.*, 2016, 1–16.

7 Z.-L. Gong and Y. Zhong, *Inorg. Chem.*, 2016, **55**, 10143–10151.

8 R. C. Evans, P. Douglas, J. A. G. Williams and D. L. Rochester, *J. Fluoresc.*, 2006, **16**, 201–206.

9 K. M. Wong, W. Tang, X. Lu, N. Zhu and V. W. Yam, *Inorg. Chem.*, 2005, **44**, 1005–1011.

10 J. Ni, Y. Wang, J. Wang, Y. Zhao, Y. Pan, H. Wang, X. Zhang, J. Zhang and Z. Chen, *Dalton. Trans.*, 2013, **42**, 13092–13100.

11 A. Casado-Sanchez, R. Gomez-Ballesteros, F. Tato, F. J. Soriano, G. Pascual-Coca, S. Cabrera and J. Aleman, *Chem. Commun.*, 2016, **52**, 9137–9140.

12 Q. Xu, W. Fu, G. Zhang, Z. Bian, J. Zhang, X. Han and W. Xu, *Catal. Commun.*, 2008, **10**, 49–52.

13 S. W. Botchway, M. Charnley, J. W. Haycock, A. W. Parker, D. L. Rochester, J. A. Weinstein and J. A. G. Williams, *Proc. Natl. Acad. Sci.*, 2008, **105**, 16071–16076.

14 Y. Dai, H. Xiao, J. Liu, Q. Yuan, D. Yang, C. Li, Z. Cheng, Z. Hou, P. Yang and J. Lin, *J. Am. Chem. Soc.*, 2013, **135**, 18920–18929.

15 W. A. Tarran, G. R. Freeman, L. Murphy, A. M. Benham, R. Kataky and J. A. G. Williams, *Inorg. Chem.*, 2014, **53**, 5738–5749.

16 M. Mauro, A. Aliprandi, D. Septiadi, S. Kehr and L. De Cola, *Chem. Soc. Rev.*,

2014, **43**, 4144–4166.

17 S. Huo, J. Carroll and D. A. K. Vezzu, *Asian J. Org. Chem.*, 2015, **4**, 1210–1245.

18 A. Hofmann, L. Dahlenburg and R. Van Eldik, *Inorg. Chem.*, 2003, **42**, 6528–6538.

19 J. A. G. Williams, S. Develay, D. L. Rochester and L. Murphy, *Coord. Chem. Rev.*, 2008, **252**, 2596–2611.

20 G. Li, T. Fleetham and J. Li, *Adv. Mater.*, 2014, **26**, 2931–2936.

21 L. Murphy, P. Brulatti, V. Fattori, M. Cocchi and J. A. G. Williams, *Chem. Commun.*, 2012, **48**, 5817–5819.

22 E. Rossi, L. Murphy, P. L. Brothwood, A. Colombo, C. Dragonetti, D. Roberto, R. Ugo, M. Cocchi and J. A. G. Williams, *J. Mater. Chem.*, 2011, **21**, 15501–15510.

23 E. Rossi, A. Colombo, C. Dragonetti, D. Roberto, F. Demartin, M. Cocchi, P. Brulatti, V. Fattori and J. A. G. Williams, *Chem. Commun.*, 2012, **48**, 3182–3184.

24 F. Nisic, A. Colombo, C. Dragonetti, D. Roberto, A. Valore, J. M. Malicka, M. Cocchi, G. R. Freeman and J. A. G. Williams, *J. Mater. Chem. C*, 2014, **2**, 1791–1800.

25 G. Cheng, Q. Wan, W. Ang, C. Kwong, W. To, P. Chow, C. Kwok and C. Che, *Adv. Opt. Mater.*, 2019, **1801452**, 1–7.

26 M. I. Daneshvar, J. M. Peralta, G. A. Casay, N. Narayanan, L. Evans, G. Patonay and L. Strekowski, *J. Immunol. Methods*, 1999, **226**, 119–128.

27 D. Septiadi, A. Aliprandi, M. Mauro and L. De Cola, *RSC Adv.*, 2014, **4**, 25709–25718.

28 S. Luo, E. Zhang, Y. Su, T. Cheng and C. Shi, *Biomaterials*, 2011, **32**, 7127–7138.

29 Z. Guo, S. Park, J. Yoon and I. Shin, *Chem. Soc. Rev.*, , DOI:10.1039/c3cs60271k.

30 J. G. Bünzli and S. V Eliseeva, *J. Rare Earths*, 2010, **28**, 824–842.

31 L. F. Gildea and J. A. G. Williams, in *Organic light-emitting diodes (OLEDs): Materials, Devices and Applications*, Woodhead Publishing Limited, Cambridge, 1st edn., 2013, pp. 77–113.

32 J. A. G. Williams, in *Photochemistry and Photophysics of Coordination Compounds II*, eds. V. Balzani and S. Campagna, Springer, Berlin, Heidelberg, 2007, pp. 205–268.

33 A. Zampetti, A. Minotto and F. Cacialli, *Adv. Funct. Mater.*, 2019, **29**, 1807623.

34 J. Brooks, Y. Babayan, S. Lamansky, P. I. Djurovich, I. Tsyba, R. Bau and M. E. Thompson, *Inorg. Chem.*, 2002, **41**, 4510–4511.

35 V. A. Krylova and M. E. Thompson, in *OLED Fundamentals: Materials, Devices and Processing of Organic Light-Emitting Diodes*, eds. D. J. Gaspar and E. Polikarpov, CRC Press, Florida, 1st edn., 2015, pp. 255–279.

36 J. A. G. Williams, A. Beeby, E. S. Davies, J. A. Weinstein and C. Wilson, *Inorg. Chem.*, 2003, **42**, 8609–8611.

37 D. N. Kozhevnikov, V. N. Kozhevnikov, M. M. Ustinova, A. Santoro, D. W. Bruce, B. Koenig, R. Czerwieniec, T. Fischer, M. Zabel and H. Yersin, *Inorg. Chem.*, 2009, **48**, 4179–4189.

38 G. W. Robinson, R. P. Frosch and I. R. Transitions, *J. Chem. Phys.*, 1963, **38**, 1187–1203.

39 C. Chan, T. Lai, C. Che and S. Peng, *J. Am. Chem. Soc.*, 1993, 11245–11253.

40 W. Lu, B. Mi, M. C. W. Chan, Z. Hui, C. Che, N. Zhu and S. Lee, *J. Am. Chem. Soc.*, 2004, **126**, 4958–4971.

41 W. Lu, N. Zhu and C. Che, *Chem. Commun.*, 2002, **3**, 900–901.

42 D. J. Cárdenas, A. M. Echavarren and M. C. Ramírez de Arellano, *Organometallics*, 1999, **18**, 3337–3341.

43 A. F. Rausch, L. Murphy, J. A. G. Williams and H. Yersin, *Inorg. Chem.*, 2009, **48**, 11407–11414.

44 A. F. Rausch, L. Murphy, J. A. G. Williams and H. Yersin, *Inorg. Chem.*, 2012, **51**, 312–319.

45 G. S. Tong and C. Che, *Chem. Eur. J.*, 2009, **15**, 7225–7237.

46 S. Garbe, M. Krause, A. Klimpel, I. Neundorf, P. Lippmann, I. Ott, D. Brünink, C. A. Strassert, N. L. Doltsinis and A. Klein, *Organometallics*, 2020, **39**, 746–756.

47 M. Beley, J. Collin, R. Louis, B. Metz and J. Sauvage, *J. Am. Chem. Soc.*, 1991, **113**, 8521–8522.

48 A. Suzuki and N. Miyaura, *Chem. Rev.*, 1995, **95**, 2457–2483.

49 B. J. K. Stille, *Angew. Chemie Int. Ed.*, 1986, **25**, 508–524.

50 E. Negishi, A. O. King and N. Okukado, *J. Org. Chem.*, 1977, **42**, 1821–1823.

51 S. J. Farley, D. L. Rochester, A. L. Thompson, J. A. K. Howard and J. A. G. Williams, *Inorg. Chem.*, 2005, **44**, 9690–9703.

52 D. L. Rochester, S. Develay, S. Záliš and J. A. G. Williams, *Dalton. Trans.*, 2009, 1728–1741.

53 T. Ishiyama, M. Murata and N. Miyaura, *J. Org. Chem.*, 1995, **60**, 7508–7510.

54 N. J. Turro, V. Ramamurthy and J. C. Scaiano, *Modern Molecular Photochemistry of Organic Molecules*, The Benjamin/Cummings Publishing Co., California, 1978.

55 H. Mustroph and S. Ernst, *Chem. Unserer Zeit*, 2011, **45**, 256–269.

56 Z. Wang, E. Turner, V. Mahoney, S. Madakuni, T. Groy and J. Li, *Inorg. Chem.*, 2010, **49**, 11276–11286.

57 B. M. Cocchi, D. Virgili, V. Fattori, D. L. Rochester and J. A. G. Williams, *Adv. Funct. Mater.*, 2007, **17**, 285–289.

58 R. C. Kwong, S. Sibley, T. Dubovoy, M. Baldo, S. R. Forrest and M. E. Thompson, *Chem. Mater.*, 1999, **11**, 3709–3713.

59 L. F. Parkes, Durham University, 2012.

60 X. Li, J. Hu, Y. Wu, R. Li, D. Xiao, W. Zeng, D. Zhang, Y. Xiang and W. Jin, *Dye. Pigment.*, 2017, **141**, 188–194.

61 C. Lin, Y. Liu, S. Peng, T. Shinmyozu and J. Yang, *Inorg. Chem.*, 2017, **56**, 4978–4989.

62 J. R. Sommer, A. H. Shelton, A. Parthasarathy, I. Ghiviriga, J. R. Reynolds and K. S. Schanze, *Chem. Mater.*, 2011, **23**, 5296–5304.

63 Y.-J. Cho, S.-Y. Kim, H.-J. Son, D. W. Cho and S. O. Kang, *Phys. Chem. Chem. Phys.*, 2017, **19**, 5486–5494.

64 J. Romanova, M. R. R. Prabhath and P. D. Jarowski, *J. Phys. Chem.*, 2016, **120**, 2002–2012.

65 T. Forster, *Angew. Chemie Int. Ed.*, 1969, **8**, 333–343.

66 H. Kunkely and A. Vogler, *J. Am. Chem. Soc.*, 1990, **112**, 5625–5627.

67 M. Z. Shafikov, A. F. Suleymanova, D. N. Kozhevnikov and B. Konig, *Inorg. Chem.*, 2017, **56**, 4885–4897.

68 J. Kang, X. Zhang, H. Zhou, X. Gai, T. Jia, L. Xu, J. Zhang, Y. Li and J. Ni, *Inorg. Chem.*, 2016, **55**, 10208–10217.

69 M. Cocchi, J. Kalinowski, V. Fattori, J. A. G. Williams and L. Murphy, *Appl. Phys. Lett.*, 2009, **073309**, 4–7.

70 J. Kalinowski, M. Cocchi, L. Murphy, J. A. G. Williams and V. Fattori, *Chem. Phys.*, 2010, **378**, 47–57.

71 H. Xiang, J. Cheng, X. Ma, X. Zhou and J. J. Chruma, *Chem. Soc. Rev.*, 2013, **42**, 6128–6185.

72 R. Englman, *Mol. Phys.*, 1970, **18**, 145–164.

73 W. Chen, P. Chou and Y. Cheng, *J. Phys. Chem. C*, 2019, **123**, 10225–10236.

74 K. T. Ly, H. Lin, Y. Shiau, S. Liu, P. Chou, C. Tsao, Y. Huang and Y. Chi, *Nat. Photonics*, 2017, **11**, 63–68.

75 H. Chen, J. Lee, B. Lin, S. Chen and S. Wu, *Nature*, 2018, **7**, 17113–17168.

76 B. K. T. Kamtekar, A. P. Monkman and M. R. Bryce, *Adv. Mater.*, 2010, **22**, 572–582.

77 T. Fleetham, Y. Ji, L. Huang, T. S. Fleetham and J. Li, *Chem. Sci.*, 2017, **8**, 7983–7990.

78 M. A. Baldo, D. F. O'Brien, Y. You, A. Shoustikov, S. Sibley, M. E. Thompson and S. R. Forrest, *Nature*, 1998, **395**, 151–154.

79 Y. Sun, C. Borek, K. Hanson, P. I. Djurovich, M. E. Thompson, J. Brooks, J. J. Brown and S. R. Forrest, *Appl. Phys. Lett.*, 2007, **90**, 213503.

80 S. Drouet, C. O. Paul-roth, V. Fattori, M. Cocchi and J. A. G. Williams, *New J. Chem.*, 2011, **35**, 438–444.

81 J. R. Sommer, R. T. Farley, K. R. Graham, Y. Yang, J. R. Reynolds, J. Xue and K. S. Schanze, *Appl. Mater. Interfaces*, 2009, **1**, 274–278.

82 M. T. Whited, P. I. Djurovich, S. T. Roberts, A. C. Durrell, C. W. Schlenker, S. E. Bradforth and M. E. Thompson, *J. Am. Chem. Soc.*, 2011, 88–96.

83 L. Huang, C. D. Park, T. Fleetham and J. Li, *Appl. Phys. Lett.*, 2016, **109**, 233302.

84 K. R. Graham, Y. Yang, J. R. Sommer, A. H. Shelton, K. S. Schanze, J. Xue and J. R. Reynolds, *Chem. Mater.*, 2011, **23**, 5305–5312.

85 J. M. Chem, E. Rossi, L. Murphy, P. L. Brothwood, A. Colombo, C. Dragonetti, D. Roberto, R. Ugo and J. A. G. Williams, *J. Mater. Chem. C*, 2011, **21**, 15501–15510.

86 US 9,836,165 B2, 2017.

87 L. Murphy, Durham University, 2010.

88 P. Ramesh and N. W. Fadnavis, *Chem. Lett.*, 2015, **44**, 138–140.

89 L. F. Gildea, A. S. Batsanov and J. A. G. Williams, *Dalton. Trans.*, 2013, **42**, 10388–10393.

90 B. Ventura, F. Barigelletti, F. Durola, L. Flamigni, J. Sauvage and O. S. Wenger, *Dalton. Trans.*, 2008, 491–498.

91 B. M. Still, P. G. A. Kumar, J. R. Aldrich-Wright and W. S. Price, *Chem. Soc. Rev.*, 2007, **36**, 665–686.

92 X. Zhang, J. Y. Wang, J. Ni, L. Y. Zhang and Z. N. Chen, *Inorg. Chem.*, 2012, **51**, 5569–5579.

93 C. Y. Lien, Y. F. Hsu, Y. H. Liu, S. M. Peng, T. Shinmyozu and J. S. Yang, *Inorg. Chem.*, 2020, **59**, 11584–11594.

94 S. J. Anderson, P. L. Goggin and R. J. Goodfellow, *Dalton. Trans.*, 1960, 1959–1964.

95 G. P. Mcquillan and I. A. Oxton, *Dalton. Trans.*, 1978, 1460–1464.

96 P. S. Pregosin, H. Streit and L. M. Venanzi, *Inorganica Chim. Acta*, 1980, **38**, 237–242.

97 M. J. Coyer, R. H. Herber, J. Chen, M. Croft and S. P. Szu, *Inorg. Chem.*, 1994, **33**, 716–721.

98 A. Weller, *Pure Appl. Chem.*, 1968, **16**, 115–124.

99 P. Pander, A. Sil, R. J. Salthouse, C. W. Harris, M. T. Walden, D. S. Yufit, J. A. G. Williams and F. B. Dias, *J. Mater. Chem. C*, 2022, **10**, 15084–15095.

100 Y.-C. Wei, S. F. Wang, Y. Hu, L.-S. Liao, D.-G. Chen, K.-H. Chang, C.-W. Wang, S.-H. Liu, W.-H. Chan, J.-L. Liao, W.-Y. Hung, T.-H. Wang, P.-T. Chen, H.-F. Hsu, Y. Chi and P.-T. Chou, *Nat. Photonics*, 2020, **14**, 570–577.

101 M. T. Walden, P. Pander, D. S. Yufit, F. B. Dias and J. A. G. Williams, *J. Mater. Chem. C*, 2019, **7**, 6592–6606.

102 P. Pander, A. V. Zaytsev, A. Sil, J. A. G. Williams, P.-H. Lanoe, V. N. Kozhevnikov and F. B. Dias, *J. Mater. Chem. C*, 2021, **9**, 10276–10287.

103 M. Cocchi, J. Kalinowski, D. Virgili and J. A. G. Williams, *Appl. Phys. Lett.*, 2008, **92**, 113302.

104 W. Chen, C. Sukpattanacharoen, W. Chan, C. Huang, H. Hsu, D. Shen, W. Hung, N. Kungwan, D. Escudero, C. Lee and Y. Chi, *Adv. Funct. Mater.*, 2020, **30**, 2002494.

105 X. Yang, H. Guo, X. Xu, Y. Sun, G. Zhou, W. Ma and Z. Wu, *Adv. Sci.*, 2019, **6**, 1801930.

106 S. F. Wang, Y. Yuan, Y. C. Wei, W. H. Chan, L. W. Fu, B. K. Su, I. Y. Chen, K. J. Chou, P. T. Chen, H. F. Hsu, C. L. Ko, W. Y. Hung, C. S. Lee, P. T. Chou and Y. Chi, *Adv. Funct. Mater.*, 2020, **30**, 1–9.

107 M. Chapran, P. Pander, M. Vasylieva, G. Wiosna-Salyga, J. Ulanski, F. B. Dias and P. Data, *ACS Appl. Mater. Interfaces*, 2019, **11**, 13460–13471.

108 J. R. Sommer, R. T. Farley, K. R. Graham, Y. Yang, J. R. Reynolds, J. Xue and K. S. Schanze, *ACS Appl. Mater. Interfaces*, 2009, **1**, 274–278.

109 M. Z. Shafikov, P. Pander, A. V. Zaytsev, R. Daniels, R. Martinscroft, F. B. Dias, J. A. G. Williams and V. N. Kozhevnikov, *J. Mater. Chem. C*, 2021, **9**, 127–135.

110 K. Zhang, Y. Liu, Z. Hao, G. Lei, S. Cui, W. Zhu and Y. Liu, *Org. Electron.*, 2020, **87**, 105902.

111 K. Tuong Ly, R. W. Chen-Cheng, H. W. Lin, Y. J. Shiau, S. H. Liu, P. T. Chou, C. S. Tsao, Y. C. Huang and Y. Chi, *Nat. Photonics*, 2017, **11**, 63–68.

112 W. Xiong, F. Meng, H. Tan, Y. Wang, P. Wang, Y. Zhang, Q. Tao, S. Su and W. Zhu, *J. Mater. Chem. C*, 2016, **4**, 6007–6015.

113 X. Wu, D.-G. Chen, D. Liu, S.-H. Liu, S.-W. Shen, C.-I. Wu, G. Xie, J. Zhou, Z.-X. Huang, C.-Y. Huang, S.-J. Su, W. Zhu and P.-T. Chou, *J. Am. Chem. Soc.*, 2020, **142**, 7469–7479.

114 S. Develay, O. Blackburn, A. L. Thompson and J. A. G. Williams, *Inorg. Chem.*, 2008, **47**, 11129–11142.

115 T. T. Dang, J. Soulé, H. Doucet, A. Benmensour, A. Boucekkine, A. Colombo, C. Dragonetti, S. Righetto, D. Jacquemin, J. Boixel and V. Guerchais, *Eur. J. Inorg. Chem.*, 2016, 4774–4782.

116 B. Schulze, C. Friebe, E. Birckner, A. Winter and U. S. Schubert, *Organometallics*, 2018, **37**, 145–155.

117 T. Kayano, S. Takayasu, K. Sato and K. Shinozaki, *Chem. A Eur. J.*, 2014, **20**, 16583–16589.

118 S. Chang, J. Kavitha, S. Li, C. Hsu, Y. Chi, Y. Yeh, P. Chou, G. Lee, A. J. Carty, Y. Tao and C. Chien, *Inorg. Chem.*, 2006, **45**, 137–146.

119 S. Culham, P. H. Lanoë, V. L. Whittle, M. C. Durrant, J. A. G. Williams and V. N.

Kozhevnikov, *Inorg. Chem.*, , DOI:10.1021/ic401131x.

120 S. Ernst and W. Kaim, *J. Am. Chem. Soc.*, 1986, **108**, 3578–3586.

121 V. N. Kozhevnikov, M. C. Durrant and J. A. G. Williams, *Inorg. Chem.*, 2011, **50**, 6304–6313.

122 G. Turnbull, J. A. G. Williams and V. N. Kozhevnikov, *Chem. Commun.*, 2017, **53**, 2729–2732.

123 E. V Puttock, M. T. Walden and J. A. G. Williams, *Coord. Chem. Rev.*, 2018, **367**, 127–162.

124 S. Yang, F. Meng, X. Wu, Z. Yin, X. Liu, C. You, Y. Wang, S. Su and W. Zhu, *J. Mater. Chem. C*, 2018, **6**, 5769–5777.

125 S. Lamansky, P. Djurovich, D. Murphy, F. Abdel-razzaq, H. Lee, C. Adachi, P. E. Burrows, S. R. Forrest and M. E. Thompson, *J. Am. Chem. Soc.*, 2001, **123**, 4304–4312.

126 D. N. Kozhevnikov, V. N. Kozhevnikov, M. Z. Sha, A. M. Prokhorov, D. W. Bruce and J. A. G. Williams, *Inorg. Chem.*, 2011, **50**, 3804–3815.

127 M. Z. Shafikov, S. Tang, C. Larsen, M. Bodensteiner, V. N. Kozhevnikov and L. Edman, *J. Mater. Chem. C*, 2019, **7**, 10672–10682.

128 R. Okamura, T. Wada, K. Aikawa, T. Nagata and K. Tanaka, *Inorg. Chem.*, 2004, **43**, 1479–1482.

129 S. Develay and J. A. G. Williams, *Dalton. Trans.*, 2008, 4562–4564.

130 R. Munoz-Rodriguez, E. Bunuel, J. A. G. Williams and D. J. Cárdenas, *Chem. Commun.*, 2012, **48**, 5980–5982.

131 Z. Guo, S. Yiu and M. C. W. Chan, *Chem. Eur. J.*, 2013, 8937–8947.

132 E. Garoni, J. Boixel, V. Dorcet, T. Roisnel, D. Roberto, D. Jacquemin and V. Guerchais, *Dalton. Trans.*, 2018, **47**, 224–232.

133 Y. Ai, M. H. Chan, A. K. Chan, M. Ng, Y. Li and V. W. Yam, *Proc. Natl. Acad. Sci.*, 2019, **116**, 13856–13861.

134 J. Lin, C. Zou, X. Zhang, Q. Gao, S. Suo, Q. Zhuo, X. Chang, M. Xie and W. Lu, *Dalton. Trans.*, 2019, **48**, 10417–10421.

135 M. T. Walden, Durham University, 2018.

136 J. Kabesova, M.;Gazo, *Chem. Rev.*, 1980, **34**, 800–841.

137 T. Korenaga, Y. Kawauchi, T. Kosaki, T. Ema and T. Sakai, *Bull. Chem. Soc. Jpn.*,

2005, **78**, 2175–2179.

138 D. Kim, H. P. Jong, M. J. Jun, Y. L. Jin, O. K. Sang and J. Ko, *Inorg. Chem.*, 2005, **44**, 7886–7894.

139 D. Kim, I. Jung, K. H. Song, S. O. Kang and J. Ko, *J. Organomet. Chem.*, 2006, **691**, 5946–5954.

140 X. Yang, H. Lu, X. Zhu, L. Zhou, G. Deng, Y. Yang and Y. Liang, *Org. Lett.*, 2019, **21**, 7284–7288.

141 Y. Ai, M. H. Chan, A. K. Chan, M. Ng, Y. Li and V. W. Yam, *Proc. Natl. Acad. Sci.*, 2019, **116**, 13856–13861.

142 L. Chassot, E. Müller and A. von Zelewsky, *Inorg. Chem.*, 1984, **23**, 4249–4253.

143 L. Chassot and A. Von Zelewsky, *Inorg. Chem.*, 1987, **26**, 2814–2818.

144 F. Barigelletti, D. Sandrini, M. Maestri, V. Balzani, A. Von Zelewsky, L. Chassot, P. Jolliet and U. Maeder, *Inorg. Chem.*, 1988, **27**, 3644–3647.

145 M. Cocchi, D. Virgili, C. Sabatini, V. Fattori, P. Di Marco, M. Maestri and J. Kalinowski, *Synth. Met.*, 2004, **147**, 253–256.

146 M. Cocchi, V. Fattori, D. Virgili, C. Sabatini, P. Di Marco, M. Maestri and J. Kalinowski, *Appl. Phys. Lett.*, 2004, **7**, 1052–1054.

147 P.-I. Kvam, M. V. Puzyk, K. P. Balashev and J. Songstad, *Acta Chem. Scand.*, 1995, 49, 335–343.

148 M. Z. Shafikov, R. Daniels, P. Pander, F. B. Dias, J. A. G. Williams and V. N. Kozhevnikov, *ACS Appl. Mater. Interfaces*, , DOI:10.1021/acsami.8b18928.

149 M. Z. Shafikov, P. Pander, A. V. Zaytsev, R. Daniels, R. Martinscroft, F. B. Dias, J. A. G. Williams and V. N. Kozhevnikov, *J. Mater. Chem. C*, 2021, **9**, 127–135.

150 N. Okamura, T. Maeda, H. Fujiwara, A. Soman, K. N. N. Unni, A. Ajayaghosh and S. Yagi, *Phys. Chem. Chem. Phys.*, 2018, **20**, 542–552.

151 S. Culham, P. Lanoe, V. L. Whittle, M. C. Durrant, J. A. G. Williams and V. N. Kozhevnikov, *Inorg. Chem.*, 2013, **52**, 10992–11003.

152 Y. Sun, B. Liu, Y. Guo, X. Chen, Y. T. Lee, Z. Feng, C. Adachi, G. Zhou, Z. Chen and X. Yang, *ACS Appl. Mater. Interfaces*, 2021, **13**, 36020–36032.

153 B. J. Pages, J. Sakoff, J. Gilbert, Y. Zhang, F. Li, D. Preston, J. D. Crowley and J. R. Aldrich-Wright, *J. Inorg. Biochem.*, 2016, **165**, 92–99.

154 A. R. Naziruddin, A. Galstyan, A. Iordache, C. G. Daniliuc, C. A. Strassert and L.

De Cola, *Dalton. Trans.*, 2015, **44**, 8467–8477.

155 M. Li, W. H. Chen, M. Te Lin, M. A. Omary and N. D. Shepherd, *Org. Electron.*, 2009, **10**, 863–870.

156 A. W. Maverick and D. P. Martone, *Polyhedron*.

157 P. J. Bonitatebus, S. K. Mandal and W. H. Armstrong, *Chem. Commun.*, 1998, **941**, 939–940.

158 S. Dutta, P. Biswas, S. K. Dutta and K. Nag, *New J. Chem.*, 2009, **33**, 847–852.

159 G. F. Gao, M. Li, S. Z. Zhan, Z. Lv, G. H. Chen and D. Li, *Chem. - A Eur. J.*, 2011, **17**, 4113–4117.

160 S. Z. Zhan, J. H. Li, G. H. Zhang, X. W. Liu, M. Li, J. Zheng, S. W. Ng and D. Li, *Chem. Commun.*, 2019, **55**, 11992–11995.

161 K. Suzuki, A. Kobayashi, S. Kaneko, K. Takehira, T. Yoshihara, H. Ishida, Y. Shiina, S. Oishi and S. Tobita, *Phys. Chem. Chem. Phys.*, 2009, **11**, 9850–9860.

162 I. Hughes and T. Hase, *Measurements and their uncertainties a practical guide to modern error analysis*, Oxford University Press, 2010.

163 D. de Sa Pereira, A. P. Monkman and P. Data, *J. Vis. Exp.*, 2018, **2018**, 1–6.

164 G. M. Sheldrick, *Acta Crystallogr. Sect. A*, 2008, **64**, 112–122.

165 O. V Dolomanov, L. J. Bourhis, R. J. Gildea, J. A. K. Howard and H. Puschmann, *J. Appl. Crystallogr.*, 2009, **42**, 339–341.

166 H. Doucet, *European J. Org. Chem.*, 2008, 2013–2030.

167 B. S. Pilgrim, A. E. Gatland, C. H. A. Esteves, C. T. McTernan, G. R. Jones, M. R. Tatton, P. A. Procopiou and T. J. Donohoe, *Org. Biomol. Chem.*, 2016, **14**, 1065–1090.

168 M. C. Bonifacio, C. R. Robertson, J. Jung, B. T. King and S. Cheme, *J. Org. Chem.*, 2005, **70**, 8522–8526.

169 Y. Yang and H. Gong, *Chem. Commun.*, 2019, **55**, 3701–3704.

170 C. S. Cho, *J. Organomet. Chem.*, 2005, **690**, 4094–4097.

171 B. Tong, H. Ku, I. Chen, Y. Chi, H. Kao, C.-C. Yeh, C.-H. Chang, S.-H. Liu, G.-H. Lee and P.-T. Chou, *J. Mater. Chem. C*, 2015, **2**, 3460–3471.

172 R. Salthouse, University of Durham, 2018.

173 A. M. Clark, C. E. F. Rickard, W. R. Roper and L. J. Wright, *Organometallics*, 1999, **18**, 2813–2820.

174 P. G. Bomben, B. D. Koivisto and C. P. Berlinguette, *Inorg. Chem.*, 2010, **2**, 4960–4971.

175 J. Kan, S. Huang, J. Lin, M. Zhang and W. Su, *Angew. Chemie Int. Ed.*, 2015, **54**, 2199–2203.

176 Q. Yu, L. Hu, Y. Wang, S. Zheng and J. Huang, *Angew. Chemie Int. Ed.*, 2015, **54**, 15284–15288.

177 S. Warratz, D. J. Burns, C. Zhu, K. Korvorapun, T. Rogge, J. Scholz, C. Jooss, D. Gelman and L. Ackermann, *Angew. Chemie Int. Ed.*, 2017, **56**, 1557–1560.

178 L. A. Van Der Veen, P. K. Keeven, P. C. J. Kamer and P. W. N. M. Van Leeuwen, *J. Chem. Soc. Dalton. Trans.*, 2000, 2105–2112.

179 H. A. Duong, W. Wu and Y. Y. Teo, *Organometallics*, 2017, **36**, 4363–4366.

180 X. Zhang, X. Feng, C. Zhou, X. Yu, Y. Yamamoto and M. Bao, *Org. Lett.*, 2018, **20**, 7095–7099.

181 A. J. Beneto, J. Sivamani, V. Ashokkumar, R. Balasaravanan, K. Duraimurugan and A. Siva, *New J. Chem.*, 2015, **39**, 3098–3104.

182 B. Sket and M. Zupan, *J. Org. Chem.*, 1986, **51**, 929–931.

Chapter 9

9. Appendix

9.1 Publications arising from this work

1. "Excimer or Aggregate? Near Infrared Electro- and Photoluminescence from Multimolecular Excited States of N^C^N-Coordinated Platinum(II) Complexes"

Piotr H. Pander, Amit Sil, Rebecca J. Salthouse, Christopher W. Harris, Melissa T. Walden, Dimitrii S. Yufit, J. A. Gareth Williams and Fernando B. Dias.

Journal of Materials Chemistry C, 2022, **10**, 15084-15095.

2. "Near-infrared electroluminescence beyond 940 nm in Pt(N^C^N)X complexes: influencing aggregation with the ancillary ligand X"

Rebecca J. Salthouse, Piotr H. Pander, Dimitrii S. Yufit, Fernando B. Dias and J. A. Gareth Williams.

Chemical Science, DOI https://doi.org/10.1039/D2SC05023D.

9.2 Crystal structure information

Crystal data and structure refinement for PtL^1Cl

Identification code	19srv176
Empirical formula	$C_{22}H_{17}ClF_6N_2Pt$ x $CHCl_3$
Formula weight	773.28
Temperature/K	120.0
Crystal system	triclinic
Space group	P-1
a/Å	9.6801(7)
b/Å	10.9554(8)
c/Å	12.8666(10)
α/°	68.534(3)
β/°	84.144(3)
γ/°	78.223(3)
Volume/Å^3	1242.56(16)
Z	2
ρ_{calc}g/cm^3	2.067
μ/mm^{-1}	6.138
F(000)	740.0
Crystal size/mm^3	0.06 × 0.04 × 0.005
Radiation	MoKα (λ = 0.71073)
2Θ range for data collection/°	4.062 to 59.998
Index ranges	-13 ≤ h ≤ 13, -15 ≤ k ≤ 15, -18 ≤ l ≤ 18
Reflections collected	27731
Independent reflections	7266 [R_{int} = 0.0524, R_{sigma} = 0.0599]
Data/restraints/parameters	7266/0/328
Goodness-of-fit on F^2	1.007
Final R indexes [I>=2σ (I)]	R_1 = 0.0298, wR_2 = 0.0463
Final R indexes [all data]	R_1 = 0.0472, wR_2 = 0.0492
Largest diff. peak/hole / e Å^{-3}	1.04/-0.95

Crystal data and structure refinement for PtL^1Cl (MeOH solvate)

Identification code	21srv417
Empirical formula	$C_{22.88}H_{20.88}ClF_6N_2O_{0.88}Pt$
Formula weight	682.33
Temperature/K	120.0
Crystal system	monoclinic
Space group	$P2_1/c$
a/Å	14.9746(5)
b/Å	23.6254(8)
c/Å	14.2787(5)
α/°	90
β/°	113.5820(10)
γ/°	90
Volume/Å^3	4629.7(3)
Z	8
ρ_{calc}g/cm^3	1.958
μ/mm^{-1}	6.243
F(000)	2625.0
Crystal size/mm^3	0.24 × 0.02 × 0.02
Radiation	Mo Kα (λ = 0.71073)
2Θ range for data collection/°	4.55 to 60
Index ranges	-21 ≤ h ≤ 21, -33 ≤ k ≤ 33, -20 ≤ l ≤ 19
Reflections collected	111237
Independent reflections	13487 [R_{int} = 0.0693, R_{sigma} = 0.0398]
Data/restraints/parameters	13487/122/680
Goodness-of-fit on F^2	1.152
Final R indexes [I>=2σ (I)]	R_1 = 0.0398, wR_2 = 0.0884
Final R indexes [all data]	R_1 = 0.0484, wR_2 = 0.0917
Largest diff. peak/hole / e Å^{-3}	2.92/-1.87

Crystal data and structure refinement for PtL^2Cl

Identification code	19srv279
Empirical formula	$C_{18}H_{17}ClN_4Pt$
Formula weight	519.90
Temperature/K	120.0
Crystal system	monoclinic
Space group	$P2_1/c$
a/Å	6.8240(9)
b/Å	21.121(3)
c/Å	11.2367(14)
α/°	90
β/°	90.107(4)
γ/°	90
Volume/Å^3	1619.5(4)
Z	4
ρ_{calc}g/cm^3	2.132
μ/mm^{-1}	8.836
F(000)	992.0
Crystal size/mm^3	0.29 × 0.01 × 0.01
Radiation	MoKα (λ = 0.71073)
2Θ range for data collection/°	4.106 to 53.996
Index ranges	-8 ≤ h ≤ 8, -26 ≤ k ≤ 26, -14 ≤ l ≤ 14
Reflections collected	20830
Independent reflections	3545 [R_{int} = 0.1113, R_{sigma} = 0.0905]
Data/restraints/parameters	3545/7/222
Goodness-of-fit on F^2	1.070
Final R indexes [I>=2σ (I)]	R_1 = 0.0494, wR_2 = 0.0924
Final R indexes [all data]	R_1 = 0.0784, wR_2 = 0.1016
Largest diff. peak/hole / e Å^{-3}	2.08/-2.91

Crystal data and structure refinement for PtL^3Cl

Identification code	19srv246
Empirical formula	$C_{24}H_{16}ClN_2Pt$
Formula weight	562.93
Temperature/K	230
Crystal system	monoclinic
Space group	C2/c
a/Å	15.453(2)
b/Å	15.333(2)
c/Å	7.9555(13)
α/°	90
β/°	105.168(5)
γ/°	90
Volume/$Å^3$	1819.3(5)
Z	4
$\rho_{calc}g/cm^3$	2.055
μ/mm^{-1}	7.872
F(000)	1076.0
Crystal size/mm^3	0.239 × 0.13 × 0.053
Radiation	MoKα (λ = 0.71073)
2Θ range for data collection/°	5.314 to 60.066
Index ranges	-21 ≤ h ≤ 21, -21 ≤ k ≤ 21, -11 ≤ l ≤ 10
Reflections collected	15605
Independent reflections	2669 [R_{int} = 0.0349, R_{sigma} = 0.0275]
Data/restraints/parameters	2669/0/129
Goodness-of-fit on F^2	1.038
Final R indexes [I>=2σ (I)]	R_1 = 0.0229, wR_2 = 0.0462
Final R indexes [all data]	R_1 = 0.0332, wR_2 = 0.0489
Largest diff. peak/hole / e $Å^{-3}$	0.62/-0.69

Crystal data and structure refinement for PtL^6Cl

Identification code	21srv201
Empirical formula	$C_{26}H_{19}ClN_2Pt$
Formula weight	589.97
Temperature/K	120.0
Crystal system	orthorhombic
Space group	$P2_12_12_1$
a/Å	7.7299(7)
b/Å	15.5317(15)
c/Å	16.4222(15)
α/°	90
β/°	90
γ/°	90
Volume/Å^3	1971.6(3)
Z	4
ρ_{calc}g/cm^3	1.988
μ/mm^{-1}	7.269
F(000)	1136.0
Crystal size/mm^3	0.09 × 0.02 × 0.005
Radiation	MoKα (λ = 0.71073)
2Θ range for data collection/°	4.96 to 54.992
Index ranges	-10 ≤ h ≤ 9, -20 ≤ k ≤ 20, -21 ≤ l ≤ 21
Reflections collected	21735
Independent reflections	4513 [R_{int} = 0.0918, R_{sigma} = 0.0837]
Data/restraints/parameters	4513/39/274
Goodness-of-fit on F^2	1.053
Final R indexes [I>=2σ (I)]	R_1 = 0.0498, wR_2 = 0.0970
Final R indexes [all data]	R_1 = 0.0669, wR_2 = 0.1033
Largest diff. peak/hole / e Å^{-3}	1.03/-1.40
Flack parameter	0.000(8)

Crystal data and structure refinement for PtL^7Cl

Identification code	21srv113
Empirical formula	$C_{28}H_{23}ClN_2Pt$
Formula weight	618.02
Temperature/K	120.0
Crystal system	triclinic
Space group	P-1
a/Å	8.5278(4)
b/Å	11.9242(5)
c/Å	12.2789(5)
α/°	102.760(2)
β/°	104.635(2)
γ/°	110.132(2)
Volume/$Å^3$	1067.18(8)
Z	2
$\rho_{calc}g/cm^3$	1.923
μ/mm^{-1}	6.719
F(000)	600.0
Crystal size/mm^3	0.07 × 0.04 × 0.02
Radiation	MoKα (λ = 0.71073)
2Θ range for data collection/°	4.322 to 59.996
Index ranges	-11 ≤ h ≤ 11, -16 ≤ k ≤ 16, -17 ≤ l ≤ 17
Reflections collected	25925
Independent reflections	6215 [R_{int} = 0.0372, R_{sigma} = 0.0346]
Data/restraints/parameters	6215/0/292
Goodness-of-fit on F^2	1.033
Final R indexes [I>=2σ (I)]	R_1 = 0.0221, wR_2 = 0.0406
Final R indexes [all data]	R_1 = 0.0255, wR_2 = 0.0415
Largest diff. peak/hole / e $Å^{-3}$	0.98/-1.08

Crystal data and structure refinement for PtL^8Cl

Identification code	21srv126
Empirical formula	$C_{27}H_{23}ClN_2OPt$
Formula weight	622.01
Temperature/K	120.0
Crystal system	monoclinic
Space group	$P2_1/c$
a/Å	11.0717(5)
b/Å	9.4934(5)
c/Å	20.5787(10)
α/°	90
β/°	98.465(2)
γ/°	90
Volume/Å^3	2139.42(18)
Z	4
ρ_{calc}g/cm^3	1.931
μ/mm^{-1}	6.707
F(000)	1208.0
Crystal size/mm^3	0.32 × 0.08 × 0.06
Radiation	MoKα (λ = 0.71073)
2Θ range for data collection/°	5.048 to 60
Index ranges	-15 ≤ h ≤ 15, -13 ≤ k ≤ 13, -28 ≤ l ≤ 28
Reflections collected	50001
Independent reflections	6221 [R_{int} = 0.0353, R_{sigma} = 0.0201]
Data/restraints/parameters	6221/6/293
Goodness-of-fit on F^2	1.108
Final R indexes [I>=2σ (I)]	R_1 = 0.0219, wR_2 = 0.0479
Final R indexes [all data]	R_1 = 0.0243, wR_2 = 0.0488
Largest diff. peak/hole / e Å^{-3}	2.94/-0.78

Crystal data and structure refinement for PtL^2I

Identification code	21srv399
Empirical formula	$C_{18}H_{17}IN_4Pt$
Formula weight	611.34
Temperature/K	120.0
Crystal system	monoclinic
Space group	$P2_1/m$
a/Å	10.8783(3)
b/Å	6.7723(2)
c/Å	12.3368(3)
α/°	90
β/°	108.5190(10)
γ/°	90
Volume/Å^3	861.80(4)
Z	2
ρ_{calc}g/cm^3	2.356
μ/mm^{-1}	9.939
F(000)	568.0
Crystal size/mm^3	0.09 × 0.06 × 0.005
Radiation	Mo Kα (λ = 0.71073)
2Θ range for data collection/°	3.948 to 59.998
Index ranges	-15 ≤ h ≤ 15, -9 ≤ k ≤ 9, -17 ≤ l ≤ 17
Reflections collected	20699
Independent reflections	2710 [R_{int} = 0.0413, R_{sigma} = 0.0252]
Data/restraints/parameters	2710/0/143
Goodness-of-fit on F^2	1.203
Final R indexes [I>=2σ (I)]	R_1 = 0.0311, wR_2 = 0.0691
Final R indexes [all data]	R_1 = 0.0336, wR_2 = 0.0699
Largest diff. peak/hole / e Å^{-3}	2.08/-1.83

Crystal data and structure refinement for PtL[1]SCN

Identification code	21srv377
Empirical formula	$C_{22.4}H_{17}Cl_{0.6}F_6N_{2.4}PtS_{0.4}$
Formula weight	662.97
Temperature/K	120.0
Crystal system	tetragonal
Space group	$P4_2/n$
a/Å	21.2092(6)
b/Å	21.2092(6)
c/Å	9.3816(3)
α/°	90
β/°	90
γ/°	90
Volume/Å^3	4220.1(3)
Z	8
ρ_{calc}g/cm^3	2.087
μ/mm^{-1}	6.833
F(000)	2534.0
Crystal size/mm^3	0.23 × 0.02 × 0.01
Radiation	Mo Kα (λ = 0.71073)
2Θ range for data collection/°	3.84 to 54.998
Index ranges	-27 ≤ h ≤ 27, -27 ≤ k ≤ 27, -12 ≤ l ≤ 12
Reflections collected	65076
Independent reflections	4846 [R_{int} = 0.0933, R_{sigma} = 0.0578]
Data/restraints/parameters	4846/75/344
Goodness-of-fit on F^2	1.175
Final R indexes [I>=2σ (I)]	R_1 = 0.0622, wR_2 = 0.1183
Final R indexes [all data]	R_1 = 0.1036, wR_2 = 0.1311
Largest diff. peak/hole / e Å^{-3}	1.59/-1.59

Crystal data and structure refinement for PtL^3NCS

Identification code	21srv075
Empirical formula	$C_{27}H_{17}Cl_6N_3PtS$
Formula weight	823.28
Temperature/K	120.0
Crystal system	monoclinic
Space group	$P2_1/c$
a/Å	13.4022(3)
b/Å	24.7477(6)
c/Å	16.5832(4)
α/°	90
β/°	91.9820(10)
γ/°	90
Volume/$Å^3$	5496.9(2)
Z	8
$\rho_{calc}g/cm^3$	1.990
μ/mm^{-1}	5.789
F(000)	3168.0
Crystal size/mm^3	0.15 × 0.02 × 0.005
Radiation	MoKα (λ = 0.71073)
2Θ range for data collection/°	4.108 to 58
Index ranges	-18 ≤ h ≤ 18, -33 ≤ k ≤ 33, -22 ≤ l ≤ 22
Reflections collected	93934
Independent reflections	14625 [R_{int} = 0.0961, R_{sigma} = 0.0676]
Data/restraints/parameters	14625/15/712
Goodness-of-fit on F^2	1.051
Final R indexes [I>=2σ (I)]	R_1 = 0.0536, wR_2 = 0.0848
Final R indexes [all data]	R_1 = 0.0856, wR_2 = 0.0938
Largest diff. peak/hole / e $Å^{-3}$	1.03/-1.82

Crystal data and structure refinement for $PtL^{12}Cl$

Identification code	21srv073
Empirical formula	$C_{20}H_{13}ClN_2Pt$
Formula weight	511.86
Temperature/K	120.0
Crystal system	monoclinic
Space group	$P2_1/c$
a/Å	8.8991(5)
b/Å	9.8598(5)
c/Å	18.7913(10)
α/°	90
β/°	91.629(2)
γ/°	90
Volume/Å^3	1648.15(15)
Z	4
ρ_{calc}g/cm^3	2.063
μ/mm^{-1}	8.678
F(000)	968.0
Crystal size/mm^3	0.12 × 0.05 × 0.04
Radiation	MoKα (λ = 0.71073)
2Θ range for data collection/°	4.336 to 59.996
Index ranges	-12 ≤ h ≤ 12, -13 ≤ k ≤ 13, -26 ≤ l ≤ 26
Reflections collected	38105
Independent reflections	4776 [R_{int} = 0.0344, R_{sigma} = 0.0197]
Data/restraints/parameters	4776/0/217
Goodness-of-fit on F^2	1.058
Final R indexes [I>=2σ (I)]	R_1 = 0.0153, wR_2 = 0.0345
Final R indexes [all data]	R_1 = 0.0179, wR_2 = 0.0354
Largest diff. peak/hole / e Å^{-3}	0.79/-0.76

Crystal data and structure refinement for $PtL^{14}Cl$

Identification code	20srv221
Empirical formula	$C_{21}H_{17}ClN_2OPt$
Formula weight	543.91
Temperature/K	120.0
Crystal system	monoclinic
Space group	$P2_1/n$
a/Å	7.2548(4)
b/Å	9.1840(5)
c/Å	25.6786(14)
α/°	90
β/°	94.616(2)
γ/°	90
Volume/Å^3	1705.37(16)
Z	4
ρ_{calc}g/cm^3	2.118
μ/mm^{-1}	8.397
F(000)	1040.0
Crystal size/mm^3	0.13 × 0.12 × 0.01
Radiation	Mo Kα (λ = 0.71073)
2Θ range for data collection/°	4.712 to 59.998
Index ranges	-10 ≤ h ≤ 10, -12 ≤ k ≤ 12, -36 ≤ l ≤ 36
Reflections collected	30303
Independent reflections	4974 [R_{int} = 0.0770, R_{sigma} = 0.0533]
Data/restraints/parameters	4974/0/237
Goodness-of-fit on F^2	1.156
Final R indexes [I>=2σ (I)]	R_1 = 0.0426, wR_2 = 0.0738
Final R indexes [all data]	R_1 = 0.0570, wR_2 = 0.0782
Largest diff. peak/hole / e Å^{-3}	1.17/-2.48

Crystal data and structure refinement for $PtL^{18}Cl$

Identification code	20srv237
Empirical formula	$C_{15}H_{10}ClN_3Pt$
Formula weight	462.80
Temperature/K	120.0
Crystal system	orthorhombic
Space group	$P2_12_12_1$
a/Å	6.6652(4)
b/Å	10.7512(6)
c/Å	18.0704(11)
α/°	90
β/°	90
γ/°	90
Volume/Å^3	1294.90(13)
Z	4
ρ_{calc}g/cm^3	2.374
μ/mm^{-1}	11.033
F(000)	864.0
Crystal size/mm^3	0.08 × 0.03 × 0.01
Radiation	Mo Kα (λ = 0.71073)
2Θ range for data collection/°	4.408 to 57.996
Index ranges	-9 ≤ h ≤ 9, -14 ≤ k ≤ 14, -24 ≤ l ≤ 24
Reflections collected	19030
Independent reflections	3434 [R_{int} = 0.0708, R_{sigma} = 0.0524]
Data/restraints/parameters	3434/18/191
Goodness-of-fit on F^2	1.072
Final R indexes [I>=2σ (I)]	R_1 = 0.0420, wR_2 = 0.0941
Final R indexes [all data]	R_1 = 0.0475, wR_2 = 0.0964
Largest diff. peak/hole / e Å^{-3}	1.80/-3.43
Flack parameter	0.49(3)

Crystal data and structure refinement for $PtL^{19}Cl$

Identification code	19srv234
Empirical formula	$3(C_{17}H_{14}ClN_3Pt) \times 2(CHCl_3)$
Formula weight	1711.29
Temperature/K	120.0
Crystal system	monoclinic
Space group	$P2_1/c$
a/Å	11.2527(6)
b/Å	29.0710(14)
c/Å	16.1411(8)
α/°	90
β/°	94.342(2)
γ/°	90
Volume/$Å^3$	5265.0(5)
Z	4
$\rho_{calc}g/cm^3$	2.159
μ/mm^{-1}	8.457
F(000)	3248.0
Crystal size/mm^3	0.29 × 0.06 × 0.04
Radiation	MoKα (λ = 0.71073)
2Θ range for data collection/°	4.49 to 57.998
Index ranges	-15 ≤ h ≤ 15, -39 ≤ k ≤ 39, -22 ≤ l ≤ 22
Reflections collected	81546
Independent reflections	14001 [R_{int} = 0.0748, R_{sigma} = 0.0688]
Data/restraints/parameters	14001/6/663
Goodness-of-fit on F^2	1.041
Final R indexes [I>=2σ (I)]	R_1 = 0.0413, wR_2 = 0.0618
Final R indexes [all data]	R_1 = 0.0730, wR_2 = 0.0681
Largest diff. peak/hole / e $Å^{-3}$	1.22/-1.55

Crystal data and structure refinement for $PtL^{20}Cl$

Identification code	21srv074
Empirical formula	$C_{16}H_9ClF_3N_3Pt$
Formula weight	530.80
Temperature/K	120.0
Crystal system	triclinic
Space group	P-1
a/Å	8.0970(5)
b/Å	9.0699(6)
c/Å	9.9832(6)
α/°	88.760(2)
β/°	76.743(2)
γ/°	89.912(2)
Volume/Å^3	713.45(8)
Z	2
ρ_{calc}g/cm^3	2.471
μ/mm^{-1}	10.058
F(000)	496.0
Crystal size/mm^3	0.15 × 0.04 × 0.01
Radiation	MoKα (λ = 0.71073)
2Θ range for data collection/°	5.168 to 59.988
Index ranges	-11 ≤ h ≤ 11, -12 ≤ k ≤ 12, -14 ≤ l ≤ 14
Reflections collected	17039
Independent reflections	4148 [R_{int} = 0.0285, R_{sigma} = 0.0252]
Data/restraints/parameters	4148/0/217
Goodness-of-fit on F^2	1.046
Final R indexes [I>=2σ (I)]	R_1 = 0.0157, wR_2 = 0.0337
Final R indexes [all data]	R_1 = 0.0171, wR_2 = 0.0341
Largest diff. peak/hole / e Å^{-3}	0.97/-0.93

Crystal data and structure refinement for $PtL^{22}Cl$

Identification code	19srv240
Empirical formula	$C_{18}H_{12}ClF_3N_2OPt$
Formula weight	559.84
Temperature/K	120
Crystal system	triclinic
Space group	P-1
a/Å	9.1299(6)
b/Å	9.2461(6)
c/Å	9.6998(7)
α/°	95.250(2)
β/°	96.120(2)
γ/°	92.824(2)
Volume/Å^3	809.29(9)
Z	2
ρ_{calc}g/cm^3	2.297
μ/mm^{-1}	8.877
F(000)	528.0
Crystal size/mm^3	0.255 × 0.118 × 0.068
Radiation	MoKα (λ = 0.71073)
2Θ range for data collection/°	4.432 to 66.424
Index ranges	-14 ≤ h ≤ 14, -14 ≤ k ≤ 13, -14 ≤ l ≤ 14
Reflections collected	18547
Independent reflections	6175 [R_{int} = 0.0328, R_{sigma} = 0.0406]
Data/restraints/parameters	6175/0/236
Goodness-of-fit on F^2	1.039
Final R indexes [I>=2σ (I)]	R_1 = 0.0260, wR_2 = 0.0577
Final R indexes [all data]	R_1 = 0.0360, wR_2 = 0.0601
Largest diff. peak/hole / e Å^{-3}	2.86/-1.24

Crystal data and structure refinement for $PtL^{23}Cl$

Identification code	21srv104
Empirical formula	$C_{17}H_{10}ClF_3N_2Pt$
Formula weight	529.81
Temperature/K	120.0
Crystal system	monoclinic
Space group	$P2_1/c$
a/Å	12.4233(5)
b/Å	11.6995(4)
c/Å	11.3735(4)
α/°	90
β/°	112.9130(10)
γ/°	90
Volume/Å^3	1522.66(10)
Z	4
ρ_{calc}g/cm^3	2.311
μ/mm^{-1}	9.424
F(000)	992.0
Crystal size/mm^3	0.16 × 0.15 × 0.04
Radiation	MoKα (λ = 0.71073)
2Θ range for data collection/°	7.122 to 59.996
Index ranges	-17 ≤ h ≤ 17, -16 ≤ k ≤ 16, -16 ≤ l ≤ 16
Reflections collected	26494
Independent reflections	4410 [R_{int} = 0.0300, R_{sigma} = 0.0205]
Data/restraints/parameters	4410/0/225
Goodness-of-fit on F^2	1.108
Final R indexes [I>=2σ (I)]	R_1 = 0.0225, wR_2 = 0.0491
Final R indexes [all data]	R_1 = 0.0269, wR_2 = 0.0510
Largest diff. peak/hole / e Å^{-3}	1.41/-1.32

Crystal data and structure refinement for $PtL^{25}Cl$

Identification code	21srv112
Empirical formula	$C_{22}H_{20}ClF_3N_2OPt$
Formula weight	615.94
Temperature/K	120.0
Crystal system	monoclinic
Space group	$P2_1/m$
a/Å	12.1952(5)
b/Å	6.8897(3)
c/Å	12.9731(5)
α/°	90
β/°	113.4220(10)
γ/°	90
Volume/Å^3	1000.20(7)
Z	2
ρ_{calc}g/cm^3	2.045
μ/mm^{-1}	7.192
F(000)	592.0
Crystal size/mm^3	0.18 × 0.11 × 0.01
Radiation	MoKα (λ = 0.71073)
2Θ range for data collection/°	5.906 to 59.994
Index ranges	-17 ≤ h ≤ 17, -9 ≤ k ≤ 9, -18 ≤ l ≤ 18
Reflections collected	17936
Independent reflections	3125 [R_{int} = 0.0335, R_{sigma} = 0.0231]
Data/restraints/parameters	3125/7/202
Goodness-of-fit on F^2	1.073
Final R indexes [I>=2σ (I)]	R_1 = 0.0155, wR_2 = 0.0363
Final R indexes [all data]	R_1 = 0.0166, wR_2 = 0.0368
Largest diff. peak/hole / e Å^{-3}	0.71/-0.88

Crystal data and structure refinement for $PtL^{30}Cl$

Identification code	21srv383
Empirical formula	$C_{26.5}H_{22}Cl_2F_3N_3Pt$
Formula weight	705.46
Temperature/K	120.0
Crystal system	monoclinic
Space group	$P2_1/c$
a/Å	24.1378(8)
b/Å	6.7587(2)
c/Å	31.0271(11)
α/°	90
β/°	106.3418(14)
γ/°	90
Volume/Å^3	4857.3(3)
Z	8
ρ_{calc}g/cm^3	1.929
μ/mm^{-1}	6.043
F(000)	2728.0
Crystal size/mm^3	0.5 × 0.11 × 0.005
Radiation	Mo Kα (λ = 0.71073)
2Θ range for data collection/°	3.984 to 56.994
Index ranges	-32 ≤ h ≤ 32, -9 ≤ k ≤ 9, -41 ≤ l ≤ 41
Reflections collected	106162
Independent reflections	12294 [R_{int} = 0.0964, R_{sigma} = 0.0661]
Data/restraints/parameters	12294/90/647
Goodness-of-fit on F^2	1.157
Final R indexes [I>=2σ (I)]	R_1 = 0.0642, wR_2 = 0.1135
Final R indexes [all data]	R_1 = 0.1038, wR_2 = 0.1243
Largest diff. peak/hole / e Å^{-3}	1.94/-3.29

Crystal data and structure refinement for $L^{31}(PtCl)_2$

Identification code	20srv065
Empirical formula	$C_{56}H_{52}Cl_2N_4O_2Pt_2$
Formula weight	1274.09
Temperature/K	120.0
Crystal system	monoclinic
Space group	$P2_1/c$
a/Å	15.1276(13)
b/Å	27.580(2)
c/Å	11.1881(9)
α/°	90
β/°	93.815(5)
γ/°	90
Volume/Å^3	4657.6(7)
Z	4
ρ_{calc}g/cm^3	1.817
μ/mm^{-1}	12.508
F(000)	2488.0
Crystal size/mm^3	0.08 × 0.04 × 0.005
Radiation	CuKα (λ = 1.54178)
2Θ range for data collection/°	5.856 to 135.978
Index ranges	-17 ≤ h ≤ 18, -32 ≤ k ≤ 33, -13 ≤ l ≤ 13
Reflections collected	53291
Independent reflections	8467 [R_{int} = 0.2391, R_{sigma} = 0.1613]
Data/restraints/parameters	8467/0/597
Goodness-of-fit on F^2	0.961
Final R indexes [I>=2σ (I)]	R_1 = 0.0721, wR_2 = 0.1445
Final R indexes [all data]	R_1 = 0.1573, wR_2 = 0.1808
Largest diff. peak/hole / e Å^{-3}	1.73/-1.47

Crystal data and structure refinement for $L^{32}(PtSCN)_2$

Identification code	21srv388
Empirical formula	$C_{68.5}H_{61.5}F_{12}N_{8.5}O_{3.5}Pt_2S_2$
Formula weight	1742.06
Temperature/K	120.0
Crystal system	monoclinic
Space group	Pc
a/Å	14.9657(3)
b/Å	16.2514(4)
c/Å	27.9021(6)
α/°	90
β/°	103.4175(8)
γ/°	90
Volume/Å^3	6600.9(3)
Z	4
ρ_{calc}g/cm^3	1.753
μ/mm^{-1}	4.387
F(000)	3424.0
Crystal size/mm^3	0.07 × 0.03 × 0.006
Radiation	Mo Kα (λ = 0.71073)
2Θ range for data collection/°	3.796 to 54.998
Index ranges	-19 ≤ h ≤ 19, -21 ≤ k ≤ 21, -36 ≤ l ≤ 36
Reflections collected	136379
Independent reflections	30186 [R_{int} = 0.0661, R_{sigma} = 0.0623]
Data/restraints/parameters	30186/324/1718
Goodness-of-fit on F^2	1.031
Final R indexes [I>=2σ (I)]	R_1 = 0.0646, wR_2 = 0.1541
Final R indexes [all data]	R_1 = 0.0832, wR_2 = 0.1665
Largest diff. peak/hole / e Å^{-3}	3.99/-2.57
Flack parameter	-0.003(4)

Crystal data and structure refinement for $L^{31}Pt_2L^{35}$

Identification code	19srv323
Empirical formula	$C_{88}H_{82}Cl_{18}N_4O_2Pt_2$
Formula weight	2255.85
Temperature/K	120.0
Crystal system	monoclinic
Space group	$P2_1/n$
a/Å	20.6214(14)
b/Å	10.0682(7)
c/Å	23.5110(16)
α/°	90
β/°	94.520(2)
γ/°	90
Volume/Å^3	4866.2(6)
Z	2
ρ_{calc}g/cm^3	1.540
μ/mm^{-1}	3.412
F(000)	2232.0
Crystal size/mm^3	0.31 × 0.03 × 0.02
Radiation	Mo Kα (λ = 0.71073)
2Θ range for data collection/°	4.404 to 53.996
Index ranges	-26 ≤ h ≤ 26, -12 ≤ k ≤ 12, -30 ≤ l ≤ 30
Reflections collected	81882
Independent reflections	10614 [R_{int} = 0.1033, R_{sigma} = 0.0734]
Data/restraints/parameters	10614/165/444
Goodness-of-fit on F^2	1.032
Final R indexes [I>=2σ (I)]	R_1 = 0.1029, wR_2 = 0.2790
Final R indexes [all data]	R_1 = 0.1361, wR_2 = 0.3025
Largest diff. peak/hole / e Å^{-3}	5.14/-3.83

Crystal data and structure refinement for I11

Identification code	21srv345
Empirical formula	$C_{35}H_{35}Br_2N$
Formula weight	629.46
Temperature/K	120.0
Crystal system	monoclinic
Space group	C2/c
a/Å	20.8758(6)
b/Å	14.7694(4)
c/Å	11.5680(3)
α/°	90
β/°	123.3610(10)
γ/°	90
Volume/Å^3	2978.97(14)
Z	4
ρ_{calc}g/cm^3	1.403
μ/mm^{-1}	2.745
F(000)	1288.0
Crystal size/mm^3	0.21 × 0.19 × 0.05
Radiation	Mo Kα (λ = 0.71073)
2Θ range for data collection/°	4.472 to 59.996
Index ranges	-29 ≤ h ≤ 29, -20 ≤ k ≤ 20, -16 ≤ l ≤ 16
Reflections collected	26519
Independent reflections	4329 [R_{int} = 0.0379, R_{sigma} = 0.0275]
Data/restraints/parameters	4329/0/177
Goodness-of-fit on F^2	1.029
Final R indexes [I>=2σ (I)]	R_1 = 0.0335, wR_2 = 0.0769
Final R indexes [all data]	R_1 = 0.0456, wR_2 = 0.0824
Largest diff. peak/hole / e Å^{-3}	1.08/-1.19

Crystal data and structure refinement for $L^{47}Pt_2(acac)_2$

Identification code	21srv384
Empirical formula	$C_{75}H_{68}N_2O_5Pt_2$
Formula weight	1467.49
Temperature/K	120.0
Crystal system	orthorhombic
Space group	Pbcn
a/Å	13.8921(7)
b/Å	40.863(2)
c/Å	10.7577(6)
α/°	90
β/°	90
γ/°	90
Volume/Å^3	6106.9(6)
Z	4
ρ_{calc}g/cm^3	1.596
μ/mm^{-1}	4.631
F(000)	2912.0
Crystal size/mm^3	0.31 × 0.04 × 0.005
Radiation	Mo Kα (λ = 0.71073)
2Θ range for data collection/°	3.986 to 56.998
Index ranges	-18 ≤ h ≤ 18, -54 ≤ k ≤ 54, -14 ≤ l ≤ 14
Reflections collected	108128
Independent reflections	7757 [R_{int} = 0.0799, R_{sigma} = 0.0386]
Data/restraints/parameters	7757/24/384
Goodness-of-fit on F^2	1.254
Final R indexes [I>=2σ (I)]	R_1 = 0.0623, wR_2 = 0.1077
Final R indexes [all data]	R_1 = 0.0789, wR_2 = 0.1119
Largest diff. peak/hole / e Å^{-3}	1.15/-1.21

Crystal data and structure refinement for $HL^{42}Pt$(OMe-triaazole)

Identification code	21srv177
Empirical formula	$C_{56}H_{52}Cl_2N_6O_2PtS_2$
Formula weight	1171.14
Temperature/K	120.0
Crystal system	monoclinic
Space group	$P2_1/c$
a/Å	14.7021(5)
b/Å	18.2442(6)
c/Å	18.2446(6)
α/°	90
β/°	94.4730(10)
γ/°	90
Volume/Å^3	4878.8(3)
Z	4
ρ_{calc}g/cm^3	1.594
μ/mm^{-1}	3.122
F(000)	2360.0
Crystal size/mm^3	0.14 × 0.12 × 0.11
Radiation	MoKα (λ = 0.71073)
2Θ range for data collection/°	4.092 to 59.998
Index ranges	-20 ≤ h ≤ 20, -25 ≤ k ≤ 25, -25 ≤ l ≤ 25
Reflections collected	83920
Independent reflections	14219 [R_{int} = 0.0357, R_{sigma} = 0.0267]
Data/restraints/parameters	14219/0/631
Goodness-of-fit on F^2	1.036
Final R indexes [I>=2σ (I)]	R_1 = 0.0227, wR_2 = 0.0459
Final R indexes [all data]	R_1 = 0.0304, wR_2 = 0.0481
Largest diff. peak/hole / e Å^{-3}	0.75/-0.75